General Disclaimer

One or more of the Following Statements may affect this Document

- This document has been reproduced from the best copy furnished by the organizational source. It is being released in the interest of making available as much information as possible.

- This document may contain data, which exceeds the sheet parameters. It was furnished in this condition by the organizational source and is the best copy available.

- This document may contain tone-on-tone or color graphs, charts and/or pictures, which have been reproduced in black and white.

- This document is paginated as submitted by the original source.

- Portions of this document are not fully legible due to the historical nature of some of the material. However, it is the best reproduction available from the original submission.

Produced by the NASA Center for Aerospace Information (CASI)

(NASA-CR-132654) HYPERSONIC RESEARCH ENGINE PROJECT. PHASE 2: AEROTHERMODYNAMIC INTEGRATION MODEL DEVELOPMENT, DATA ITEM NO. 55-4-21 Final Technical Data Report, 10 Mar. 1968 - 22 Apr. (AiResearch Mfg. Co., G3/07 31373

N75-28071

Unclas

NASA-CR-132654

AIRESEARCH MANUFACTURING COMPANY OF CALIFORNIA

A DIVISION OF THE GARRETT CORPORATION

2525 WEST 190TH STREET • TORRANCE, CALIFORNIA 90509

HYPERSONIC RESEARCH ENGINE PROJECT - PHASE II
AEROTHERMODYNAMIC INTEGRATION MODEL DEVELOPMENT
FINAL TECHNICAL DATA REPORT
DATA ITEM NO. 55-4.21

10 MARCH 1968 THROUGH 22 APRIL 1974

NASA CONTRACT NO. NAS1-6666

Document No. AP-75-11133

RECEIVED
NASA STI FACILITY
INPUT BRANCH
AUG 1975

Number of pages 374

Original date 19 May 1975

Prepared by Engineering Staff

Edited by L.F. Jilly

Approved by

Edward N. Harris
HRE Program Manager

Revision	Date	Pages Affected (Revised, Added, Eliminated)

FOREWORD

This final technical data report is submitted to the NASA Langley Research Center by the AiResearch Manufacturing Company of Los Angeles, California. The document was prepared in accordance with the guidelines established in paragraph 5.7.3.2.2 of NASA Statement of Work L-4947-B (Revised).

Twenty interim technical data reports were previously submitted under the Aerothermodynamic Integration Model (AIM) task. This final report presents the development and test effort expended from beginning to completion of the AIM program and covers the period of 10 March 1968 through 22 April 1974.

ACKNOWLEDGEMENTS

Technical and Program Coordination	Louis Y. Kado
Aerodynamics	Dr. Yung H. Sun Lowell W. Pearson Walter C. Sainio
Heat Transfer	Anthony A. Vuigner
Structural	Elemer A. Katinszky
Test	Wilbur L. Andersen
Computer Program and Analyses	Albert E. Gaede

CONTENTS

Section		Page
1.	INTRODUCTION	1-1
	1.1 Program Summary	1-1
	1.2 Summary Description of the AIM	1-1
	1.2.1 Aerodynamics	1-2
	1.2.2 Mechanical Design	1-2
	1.2.3 Heat Transfer	1-2
	1.3 Summary of Tests	1-3
2.	ANALYTICAL DESIGN	2-1
	2.1 Aerodynamic	2-1
	2.1.1 Inlet Design	2-1
	2.1.2 Combustor Section	2-3A
	2.1.3 Combustor, Fuel Injectors	2-5
	2.1.4 Nozzle	2-17
	2.1.5 Gas Properties and Aerodynamic Loads	2-17
	2.1.6 Shock Interaction	2-21
	2.2 Heat Transfer Analysis and Design	2-22
	2.2.1 Aerodynamic Heating	2-22
	2.2.2 Coolant System Design	2-29
	2.2.3 Thermal Design Performance	2-32
	2.2.4 Fuel System Performance	2-50
	2.3 Structural	2-53
	2.3.1 Aerodynamic Loads	2-53
	2.3.2 Material Selection	2-53
	2.3.3 Component Analysis	2-54
3.	SPECIAL TEST SUPPORT EQUIPMENT	3-1
	3.1 Air-Metering Duct	3-1
	3.2 Instrumentation Rig	3-1

CONTENTS (Continued)

Section		Page
4.	DEVELOPMENT PROGRAMS	4-1
	4.1 Metal Joining	4-1
	4.1.1 Electron-Beam Welding	4-1
	4.1.2 Joining Copper to Nickel	4-4
	4.2 Machining Nickel	4-7
	4.3 Cowl Leading Edge Coolant Distribution	4-7
	4.4 Ignitor System	4-11
5.	TEST PROGRAM AND DATA ACQUISITION	5-1
	5.1 Test Program Summary	5-1
	5.2 Data Acquisition	5-7
6.	DATA REDUCTION AND METHOD OF CALCULATION	6-1
	6.1 Summary Description of Performance Program	6-1
	6.2 Calculation of Cooling Load Distribution	6-2
	6.3 Correlation of Cavity Forces	6-3
	6.4 Determination of External Drag	6-7
	6.5 Strut Force Calculation	6-10
	6.6 Performance Correction for Regeneratively Cooled System	6-13
	6.7 Performance Correction for Inlet Total Temperature	6-15
	6.8 Determination of Tunnel Mach Numbers	6-16
	6.9 Determination of Tunnel Gas Composition	6-16
7.	TEST DATA AND ANALYSIS	7-1
	7.1 Inlet Section	7-1
	7.1.1 Instrumentation	7-13
	7.1.2 Data Reduction	7-13
	7.1.3 Inlet Static Pressure Distributions	7-20
	7.1.4 Calculated Inlet Performance	7-42
	7.1.5 Inlet Unstart	7-47

CONTENTS (Continued)

Section		Page
7. (Cont)		
	7.1.6 Conclusions	7-59
	7.1.7 Recommendations	7-61
	7.2 Combustor Design	7-62
	7.2.1 Autoignition and Effects of Ignitors	7-64
	7.2.2 Effects of Altitude	7-69
	7.2.3 Supersonic and Subsonic Combustion	7-72
	7.2.4 Effects of Spike Translation	7-74
	7.2.5 Optimization of Fuel Schedule	7-74
	7.2.6 Effects of Angle of Attack	7-96
	7.2.7 Flow Field Between Struts	7-99
	7.2.8 Effects of Inlet Gas Composition	7-99
	7.2.9 Effects of Inlet Total Temperature	7-107
	7.2.10 Combustor Performance	7-110
	7.3 Nozzle Performance	7-124
	7.3.1 Supersonic and Subsonic Combustion	7-124
	7.3.2 Correlation of Nozzle Performance	7-137
	7.4 Engine Component Interactions	7-142
	7.4.1 Inlet-Combustor Interaction	7-142
	7.4.2 Combustor Stage Interaction	7-146
	7.4.3 Combustor-Nozzle Interaction	7-151
	7.5 Instrumentation Rig	7-154
	7.6 Cooling Load and Surface Temperature Distribution	7-161
	7.7 Overall Engine Performance	7-173
	7.7.1 Mach 6 Performance	7-178
	7.7.2 Mach 7 Performance	7-182
	7.7.3 Mach 5 Performance	7-187
	7.7.4 Overall Internal Performance Corrected for Regeneratively Cooled System	7-192
	7.8 Conclusions	7-194

CONTENTS (Continued)

Section		Page
REFERENCES		R-1
APPENDIXES		
A.	Description of Performance Output	A-1
B.	Cooling Loss Calculation	B-1
ATTACHMENTS		
	AiResearch Drawings	
	950501 Sheet 2	
	950502 Sheet 2	
	950506	
	950512 Sheets 1 and 2	
	950553	
	950592 Sheets 1 and 2	
	950593	
	950594	
	950610	
	950627	
	950671 Sheets 1 and 2	

ILLUSTRATIONS

Figure		Page
2.1-1	Selected Aerodynamic Contour	2-2
2.1-2	Phase II Boilerplate Engine Inlet Contraction Characteristics	2-3
2.1-3	Selected Combustor Configuration	2-4
2.1-4	Fuel Injector Locations	2-7
2.1-5	Concept of Mixing Parameter	2-6
2.1-6	Variation of Peak Chemical Efficiency With Z	2-9
2.1-7	Chemical Efficiency versus Z	2-10
2.1-8	Effect of Number of Injectors on Penetration Parameter	2-11
2.1-9	Mach 8 Injector Design	2-12
2.1-10	AIM Injector Sizing, Mach 7	2-13
2.1-11	AIM Injector Sizing	2-14
2.1-12	AIM Injector Sizing, Mach 6	2-15
2.1-13	AIM Injector Sizing	2-16
2.1-14	Estimated Force for Phase IIA Boilerplate Engine Test at Maximum Dynamic Pressure	2-20
2.2-1	Comparison in Heat Flux Between Plum Brook and OAL Gas Conditions	2-24
2.2-2	Heat Flux Distribution on Centerbody	2-25
2.2-3	Heat Flux Distribution on Outerbody	2-26
2.2-4	Heat Flux Along Strut Side Surface	2-27
2.2-5	Flow Turbulence Intensity Upstream of AIM (Plum Brook Facility)	2-30
2.2-6	AIM Cooling Circuits	2-33
2.2-7	Strut Leading Edge Cooling	2-34

ILLUSTRATIONS (Continued)

Figure		Page
2.2-8	Strut Side Surface Cooling	2-35
2.2-9	Cooling System of Outer Cowl and Support Leg Side Surface	2-36
2.2-10	Support Leg Leading Edge Cooling	2-37
2.2-11	Wall and Coolant Temperatures for $M_\infty = 6.65$	2-39
2.2-12	Wall and Coolant Temperatures for $M_\infty = 5.79$	2-40
2.2-13	Heat Transfer Effects at Spike Cone-Innerbody Interface	2-42
2.2-14	Cooling of Outerbody Leading Edge Tip - Zirconium-Copper Tip	2-44
2.2-15	Shock Impingement Effect	2-45
2.2-16	Fuel Injection Effects	2-47
2.2-17	Heating Effects Resulting From Struts	2-48
2.2-18	Heat Flux and Wall Temperatures of the Outer Cowl and Support Legs	2-49
2.2-19	AIM Hydrogen Injector Lines Pressure Drop Summary	2-51
2.2-20	AIM Fuel System Schematic	2-52
2.3-1	Stress Variation with Temperature for Annealed Nickel-200	2-55
2.3-2	Distribution of Hoop Stress with Axial Distance for Spike Outer Shell	2-57
2.3-3	Sandwich-Segment Fin-Size Spacing	2-58
2.3-4	Innerbody Assembly Surfaces	2-59
2.3-5	Distribution of Hoop Stress with Axial Distance for Nozzle Plug Outer Nickel Shell	2-61
2.3-6	Details of Leading Edge	2-62

ILLUSTRATIONS (Continued)

Figure		Page
2.3-7	AIM Aerodynamic Contours and Dimensional Changes	2-63
2.3-8	Maximum Fixed-End Loads at the Struts	2-65
2.3-9	Engine Main Mount Support Leg	2-67
3.1-1	AIM Airflow Meter Geometry	3-2
3.1-2	Air-Metering Duct Schematic	3-4
3.2-1	Instrumentation Probes	3-6
3.2-2	Instrumentation Assembly Surface Temperatures	3-7
3.2-3	Instrumentation Mount	3-8
4.1-1	Effect of Open-Annealing Conditions on Grain Size of Nickel-200	4-2
4.1-2	Typical Characteristics of a Missed E-B Weld Joint	4-3
4.1-3	Utilization of Mu-Metal Shielding	4-5
4.1-4	Weld Energy Levels for Various Metals	4-6
4.1-5	Low Cycle Fatigue Test Samples (Round and Rectangular)	4-8
4.1-6	Microphoto of Explosively Welded Copper to Nickel	4-9
4.2-1	Cowl Leading Edge	4-10
4.2-2	10X-Scale Cowl Leading Edge Plastic Model Schematic	4-12
4.2-3	10X-Scale Flow-Divider Configurations	4-13
4.2-4	Torch Ignitor Assembly Details	4-14
6.3-1	AIM Cavity	6-4
6.3-2	Correlation of Cavity Forces	6-6

ILLUSTRATIONS (Continued)

Figure		Page
6.4-1	Typical External Surface Pressure Distribution Between X_{CL} +4.116 to X_{CL} +6.366	6-9
6.4-2	AIM External Drag	6-11
6.4-3	Correlation of External Drag at Mach 6	6-12
6.5-1	Strut Base Pressure Estimate	6-14
6.8-1	Mach Number Calibration	6-17
6.9-1	Variation of Inlet Gas Composition in Reading 92	6-20
7.0-1	Mach 5 Pressure Distribution	7-7
7.0-2	Mach 6 Pressure Distribution	7-8
7.0-3	Mach 7 Pressure Distribution	7-9
7.1-1	General Configuration of the AIM	7-10
7.1-2	Flow Field Postulated for Inlet Starting	7-12
7.1-3	AIM Spike Tip and Cowl Leading Edge	7-14
7.1-4	AIM Spike Tip Positions	7-15
7.1-5	Mach 6 Typical Spike Static Pressure Distribution vs Theory	7-21
7.1-6	Mach 6 Typical Cowl Static Pressure Distribution vs Theory	7-22
7.1-7	Mach 6 Spike Pressure Distribution; Reduced Reynolds Number	7-23
7.1-8	Mach 6 Cowl Pressure Distribution; Reduced Reynolds Number	7-24
7.1-9	Mach 6 Spike Pressure Distribution vs Theory; Spike Position Change	7-25
7.1-10	Mach 6 Cowl Pressure Distribution vs Theory; Spike Position Change	7-26

ILLUSTRATIONS (Continued)

Figure		Page
7.1-11	Mach 6 Spike Pressure Distribution; 3 Degree Angle of Attack	7-27
7.1-12	Mach 6 Cowl Pressure Distribution; 3 Degree Angle of Attack	7-28
7.1-13	Mach 7 Typical Spike Static Pressure Distribution vs Theory	7-30
7.1-14	Mach 7 Typical Cowl Static Pressure Distribution vs Theory	7-31
7.1-15	Mach 7 Spike Pressure Distribution; 3 Degree Angle of Attack	7-32
7.1-16	Mach 7 Cowl Pressure Distribution; 3 Degree Angle of Attack	7-33
7.1-17	Mach 7 Spike Pressure Distribution; Increased Reynolds Number	7-34
7.1-18	Mach 7 Cowl Pressure Distribution; Increased Reynolds Number	7-35
7.1-19	Mach 5 Typical Spike Static Pressure Distribution vs Theory	7-36
7.1-20	Mach 5 Typical Cowl Static Pressure Distribution vs Theory	7-37
7.1-21	Mach 5 Spike Pressure Distribution; Reduced Reynolds Number	7-38
7.1-22	Mach 5 Cowl Pressure Distribution, Reduced Reynolds Number	7-39
7.1-23	Mach 5 Spike Pressure Distribution; 3 Degree Angle of Attack	7-40
7.1-24	Mach 5 Cowl Pressure Distribution; 3 Degree Angle of Attack	7-41
7.1-25	Typical Inlet Control Volume Force Distribution	7-44
7.1-26	Inlet Throat (Supersonic) Pressure Recovery	7-46

ILLUSTRATIONS (Continued)

Figure		Date
7.1-27	AIM Supersonic Pressure Recovery Test vs Theory	7-49
7.1-28	Estimated Effective Inlet Throat Mach Number and Pressure Recovery	7-50
7.1-29	Inlet Throat Pressure Recovery vs Hypersonic Similarity Parameter	7-51
7.1-30	Inlet Throat Mach Number vs Hypersonic Similarity Parameter	7-52
7.1-31	Inlet Throat Kinetic Energy Efficiency vs Hypersonic Similarity Parameter	7-53
7.1-32	Correlation of Inlet Total Pressure Recovery (Subsonic Combustion Mode)	7-54
7.1-33	Subsonic Pressure Recovery AIM vs 2/3-Scale Development Model	7-55
7.1-34	Fuel Equivalence Ratio vs Time	7-56
7.1-35	Pressure Variations Under Unstarting Conditions	7-57
7.1-36	Pressure Variations Under Unstarting Conditions	7-58
7.1-37	Pressure Variations Under Unstarting Conditions	7-60
7.2-1	Combustor Area Ratio	7-63
7.2-2	Interdigitization of Fuel Injectors	7-65
7.2-3	Pressure Distribution With and Without Ignitors - Mach 6	7-66
7.2-4	Time Plots of Equivalence Ratio and Measured Thrust	7-68
7.2-5	Effects of Altitude - Inner Cowl Pressure	7-70
7.2-6	Effects of Altitude - Centerbody	7-71
7.2-7	Effect of Initial Static Pressure and Temperature on Ignition Delay	7-73
7.2-8	Mach 6 Static Pressure Distribution, Centerbody	7-74

ILLUSTRATIONS (Continued)

Figure		Page
7.2-9	Mach 6 Static Pressure Distribution, Inner Cowl	7-75
7.2-10	Combustor Flow Parameters - Mach 6	7-77
7.2-11	Mach 7 Static Pressure Distribution, Inner Cowl	7-79
7.2-12	Mach 7 Combustor Flow Parameters	7-80
7.2-13	Mach 6 Static Pressure Distribution, Inner Cowl	7-81
7.2-14	Mach 5 Combustor Flow Parameters	7-82
7.2-15	Static Pressure Distribution, Inner Cowl	7-85
7.2-16	Mach 6 Correlation of Combustor Flow Momentum	7-87
7.2-17	Mach 6 Combustor Efficiency	7-89
7.2-18	Mach 6 Correlation of Combustor Flow Momentum	7-90
7.2-19	Mach 6 Comparison of Static Pressure Distribution for Different Fuel Injectors	7-91
7.2-20	Mach 6 Comparison of Static Pressure Distribution for Different Fuel Injectors	7-92
7.2-21	Mach 6 Combustor Flow Parameters	7-94
7.2-22	Mach 6 Combustor Flow Parameters	7-95
7.2-23	Mach 6 Inner Cowl Pressure Distribution ($\alpha = 0^0, 3^0$)	7-97
7.2-24	Mach 6 Centerbody Pressure Distribution ($\alpha = 0^0, 3^0$)	7-98
7.2-25	Mach 7 Inner Cowl Pressure Distribution ($\alpha = 0^0, 3^0$)	7-100
7.2-26	Mach 5 Inner Cowl Pressure Distribution ($\alpha = 3^0$)	7-101
7.2-27	Flow Field Between Struts	7-102
7.2-28	Flow Field Between Struts	7-103

ILLUSTRATIONS (Continued)

Figure		Page
7.2-29	Photograph of Strut Shock	7-104
7.2-30	Mach 7 Effects of Inlet Gas Composition	7-106
7.2-31	Mach 7 Effect of Inlet Total Temperature (Pressure Distribution)	7-108
7.2-32	Mach 7 Effect of Inlet Total Temperature (Flow Parameters)	7-109
7.2-33	Corrected and Uncorrected Mach 7.25 Internal Performance	7-111
7.2-34	Mach 5.1 Performance at Elevated Temperature	7-112
7.2-35	Mach 5 Effect of Inlet Total Temperature (Pressure Distribution)	7-113
7.2-36	Mach 5 Effect of Inlet Total Temperature (Flow Parameters)	7-114
7.2-37	Mach 6 Supersonic Combustor Efficiency	7-116
7.2-38	Mach 6 Super/Subsonic Combustor Efficiency	7-117
7.2-39	Mach 6 Total Pressure Recovery	7-118
7.2-40	Mach 6 Combustor Pressure Area Integral Factor	7-120
7.2-41	Mach 6 Combustor Effectiveness	7-122
7.2-42	Mach 7 Combustor Efficiency	7-123
7.2-43	Mach 5 Combustor Efficiency	7-125
7.2-44	Mach 5 Combustor Efficiency at Elevated Temperature	7-126
7.2-45	Mach 5 Combustor Pressure Area Integral Factor	7-127
7.3-1	Mach 6 AIM Nozzle Pressure Distribution	7-129
7.3-2	One-Third-Scale Nozzle Performance	7-131
7.3-3	Mach 6 Nozzle Performance From Momentum Calculations	7-132

ILLUSTRATIONS (Continued)

Figure		Page
7.3-4	Mach 6 Nozzle Performance From Thrust Measurements	7-133
7.3-5	Mach 6 Probable Nozzle Performance	7-135
7.3-6	Mach 6 Nozzle Performance Comparison	7-136
7.3-7	Mach 5 Nozzle Performance	7-138
7.3-8	Effect of Temperature on Mach 5 Nozzle Performance	7-139
7.3-9	Effect of Angle of Attack on Mach 5 Nozzle Performance	7-140
7.4-1	Mach 6 Inlet-Combustor Interaction (P vs X)	7-143
7.4-2	Mach 6 Inlet-Combustor Interaction (P vs ϕ)	7-144
7.4-3	Mach 6 Inlet Combustor Interaction (P vs X two stages)	7-145
7.4-4	Mach 7 Inlet Combustor Interaction (P vs X)	7-147
7.4-5	Mach 7 Inlet Unstart Point	7-148
7.4-6	Mach 6 Combustor Interaction (Pressure Distribution)	7-149
7.4-7	Mach 6 Combustor Interaction (Flow Parameters)	7-150
7.4-8	Heated Pattern on Strut	7-152
7.4-9	Bow Shock Pattern on Instrumentation	7-153
7.4-10	Photograph of Shock Pattern	7-155
7.5-1	Probe Location, View From Rear	7-156
7.5-2	Instrumentation Rig Probes	7-157
7.5-3	Mach 6 Flow Parameters at Combustor Exit	7-158
7.5-4	Mach 6 Flow Field (Yaw) at Combustor Exit	7-159
7.5-5	Mach 6 Flow Field (Pitch) at Combustor Exit	7-160

ILLUSTRATIONS (Continued)

Figure		Page
7.5-6	Mach 7 Flow Parameters at Combustor Exit	7-162
7.5-7	Mach 7 Flow Field (Yaw) at Combustor Exit	7-163
7.5-8	Mach 5 Flow Parameters at Combustor Exit	7-164
7.5-9	Mach 5 Flow Field (Yaw) at Combustor Exit	7-165
7.6-1	Mach 6 Overall Cooling Load	7-166
7.6-2	Temperature Distribution	7-168
7.6-3	Mach 6 Accumulative Cooling Load Distribution	7-169
7.6-4	Mach 7 Total Cooling Load	7-170
7.6-5	Mach 7 Accumulative Cooling Load Distribution	7-171
7.6-6	Mach 7 Surface and Gas Temperature	7-172
7.6-7	Mach 5 Total Cooling Load	7-174
7.6-8	Mach 5 Accumulative Cooling Load	7-175
7.6-9	Mach 5 Surface and Gas Temperatures	7-176
7.7-1	Comparison of Thrust Calculations	7-179
7.7-2	AIM Force Distribution	7-180
7.7-3	AIM Internal Performance	7-181
7.7-4	Mach 6 Performance at Different Freestream Total Pressures	7-183
7.7-5	Mach 6 Performance at Angle of Attack	7-184
7.7-6	Mach 6 Performance at Different Cowl Leading Edge Locations	7-185
7.7-7	Comparison of Mach 6 and 7 Combustor Pressures	7-186
7.7-8	Uncorrected Mach 7.25 Internal Performance	7-188
7.7-9	Corrected Mach 7.25 Internal Performance	7-189
7.7-10	Mach 5.1 Internal Performance	7-190

ILLUSTRATIONS (Continued)

Figure		Page
7.7-11	Mach 5.1 Performance at Angle of Attack	7-191
7.7-12	AIM Internal Performance	7-193

TABLES

Table		Page
2.1-1	AIM Injector Parameters	2-17
2.1-2	Range of Test Conditions for Phase IIA Boilerplate Engine	2-18
2.1-3	Summary of Forces	2-19
2.2-1	Summary of Aerodynamic Heating Design Points for OAL and Plum Brook Test Facilities, ϕ = 1.00	2-22
2.2-2	Comparison of Results Between Use of Flat-Plate and Duct-Flow Heat Transfer Equations	2-28
2.2-3	Summary of AIM Localized Heating Areas	2-31
2.2-4	Cooling Circuit	2-38
2.2-5	Combustor Transient Response Time	2-50
2.3-1	Zirconium Copper Properties	2-56
3.1-1	Flowmeter Coordinates	3-3
5-1	Summary of AIM Wind Tunnel Tests	5-2
5-2	Test Run Summary	5-3
6.6-1	Heat Added to Fuel vs Internal Cooling Losses	6-13
6.8-1	Facility Nozzle Inlet Sample Analysis	6-18
7.0-1	Summary of Test Points Used for Analyses	7-2
7.1-1	HRE-AIM Inlet Coordinates (Mach 6.0 Cowl Design Position)	7-11
7.1-2	Static Pressure Tap Distribution for Inlet Analysis	7-16
7.1-3	Test Points Selected for Inlet Analysis (No Fuel Injection)	7-19
7.1-4	Comparison of Estimated Wind Tunnel Characteristics Derived From Specific Measurements but Using Different Methods	7-43

1. INTRODUCTION

This report summarizes the design and the development effort performed under Contract NAS1-6666 on the Aerothermodynamic Integration Model (AIM) of the Hypersonic Research Engine (HRE) project.

The objective of this program was to (1) verify by test the feasibility of integrating the various analytical and experimental data available for the design of the hypersonic ramjet engine; and (2) determine by test the operational characteristic and the overall performance of the design selected.

The HRE-AIM was designed for operation at speeds of Mach 3 through Mach 8. Information available through the year 1970 was incorporated into this unit. Use of special materials and fabrication methods were necessary in many areas because of the extreme heating anticipated. Conventional materials and fabrication and metal joining methods were utilized wherever possible.

1.1 PROGRAM SUMMARY

The initial project plan for the HRE project consisted of three principal phases:

Phase I: Create the concept, perform design analysis, and define the development program for the various component sections of the HRE and ultimately define a ramjet engine operable over flight Mach numbers 3 through 8.

Phase II: Implement the research and development program defined at the conclusion of Phase I study program, and perform qualification tests on the HRE in anticipation of mounting it on a manned vehicle.

Phase III: Perform evaluation tests on the HRE when mounted on the aft lower ventral of the X-15A-2 research vehicle.

Approval to implement Phase II was received in February 1967. Approximately one year later, the X-15 research vehicle project phaseout began, and test plans for the Structural Assembly Model (SAM) and the Aerothermodynamic Integration Model (AIM) had to be modified to achieve all the objectives initially targetted. Still later in the program, the facility initially selected to test the AIM was to be closed, thereby requiring additional changes in program plans.

The basic project objectives were achieved, with the necessary adjustments incorporated into the SAM and AIM programs.

1.2 SUMMARY DESCRIPTION OF THE AIM

1.2.1 Aerodynamics

The objective of the AIM was to provide an engine capable of meeting performance requirements over the speed range from Mach 3 to Mach 8 as specified in the Statement of Work, and to provide a research tool to determine operational flexibility. Supersonic combustion was determined to be more efficient for flight conditions greater than Mach 7, and for flight conditions less than Mach 6, subsonic combustion was more efficient. Performance studies had indicated that high inlet-contraction ratio is required for operation at Mach 8 and low inlet-contraction ratio is necessary to pass the required airflow at lower flight speeds. Also, studies had indicated that a constant-area duct was required to achieve good supersonic combustion at higher Mach numbers, whereas a divergent combustor duct was necessary to prevent thermal choking at lower Mach numbers.

To satisfy these diverse requirements, a variable geometry inlet and a diverging combustor with a thermal throat were selected to obtain supersonic combustion above Mach 5 and subsonic combustion for Mach 3 through Mach 6. The thermal throat was designed for performance compromise between subsonic and supersonic combustion modes and to maximize stable combustor operation.

The nozzle section consisted of a shroud and a plug, the contour of which was obtained from tests performed by AiResearch.

1.2.2 Mechanical Design

The structural and mechanical design of the AIM was directed toward obtaining aerodynamic and operational information without major concern for its structural life as directed by the Statement of Work. The basic construction of the AIM was one of double-wall construction, wherein the aerodynamic surface (hot shell), fabricated from Nickel-200 material, was cooled by water and supported by a structural member (cold shell). Nickel-200 and zirconium copper was used on the aerodynamic surfaces because of its superior heat transfer capabilities and for its good mechanical properties at environments anticipated. Conventional fabrication methods were utilized wherever possible; however, special fabrication methods were required in many areas to satisfy special requirements specified by aerodynamics and by heat transfer.

1.2.3 Heat Transfer

The heat transfer analysis was initiated on basis of utilizing the wind tunnel located at the Ordnance Aerophysics Laboratories (OAL), Daingerfield, Texas. A major portion of the heat transfer analysis had been completed at the time the wind tunnel located at NASA-Lewis Research Center (NASA-LeRC) Plum Brook Station was selected, upon closing of OAL. Analysis indicated that the maximum heat fluxes imposed on the AIM were about equal, although the maximum heat flux occurred under different test conditions for the two facilities. The hot hypersonic airstream was generated utilizing a vitiated heater at OAL, and at NASA-LeRC the hot hypersonic airstream was obtained by

passing gaseous nitrogen through a hot carbon pebble-bed heater. Since the analysis had indicated that the peak heat fluxes were about equal, a decision was made to re-analyze only affected areas and to utilize the analysis completed; hence, in presentation of both the heat transfer and aerodynamic analyses in this report, a major portion will refer to the vitiated condition, although the tests were performed in a clean-air environment.

1.3 SUMMARY OF TESTS

The AIM was tested at the NASA Hypersonic Tunnel Facility at the Plum Brook Station of the Lewis Research Center with synthetic air at Mach 5, 6, and 7. The Mach 5 and 6 tests were conducted at true air temperature while Mach 7 tests were conducted at Mach 6 temperature ($3000^{\circ}R$) because of heater deficiency. The hydrogen fuel was heated up to $1500^{\circ}R$ prior to injection to simulate a regeneratively-cooled system.

A total of 6-1/2 months of engine testing was completed with 110 minutes of actual running time accumulated. The important achievements realized from this test program which advanced the state-of-the-art in hypersonic propulsion were:

1. Realistic engine performance levels for hypersonic flight were obtained from Mach 5 to 7.

Test Mach No.	Equivalence Ratio	Internal Thrust Coefficient	Internal Specific Impulse
5.1	1.0	0.910	2740
6.0	1.0	0.735	2360
7.25	1.0	0.570	2170

2. Engine inlet performance agreed well with theoretical prediction. Combustor efficiency of 95 percent was achieved. Nozzle vacuum thrust coefficient was lower than predicted.

3. The interaction effects in staged fuel injection were very important in achieving auto-ignition, high combustor efficiency, and overall performance. High supersonic combustor efficiency in a diverging duct was difficult to achieve. The strong stage interaction effects discovered during these tests may be used to great advantage in future designs.

4. The "transonic combustion" or "mixed combustion mode" was the most efficient heat addition process in the range of Mach numbers and temperatures tested in this program.

5. The effects of ignitors, altitudes, spike translation, fuel schedules, angle of attack, step and struts, inlet gas composition, inlet total temperature, and component interactions were investigated and correlated.

6. Stable subsonic and supersonic combustion and convertibility over a range of equivalence ratios at Mach 5 and 6 was demonstrated.

7. The overall cooling load and its distribution as compared with theoretical prediction was determined.

8. Acquisition of free jet test experience in a ground test facility with large model blockage and combustion.

11-15-67 Kenneth Kuo

PRECEDING PAGE BLANK NOT FILMED

FOLDOUT FRAME

ORIGINAL PAGE IS
OF POOR QUALITY

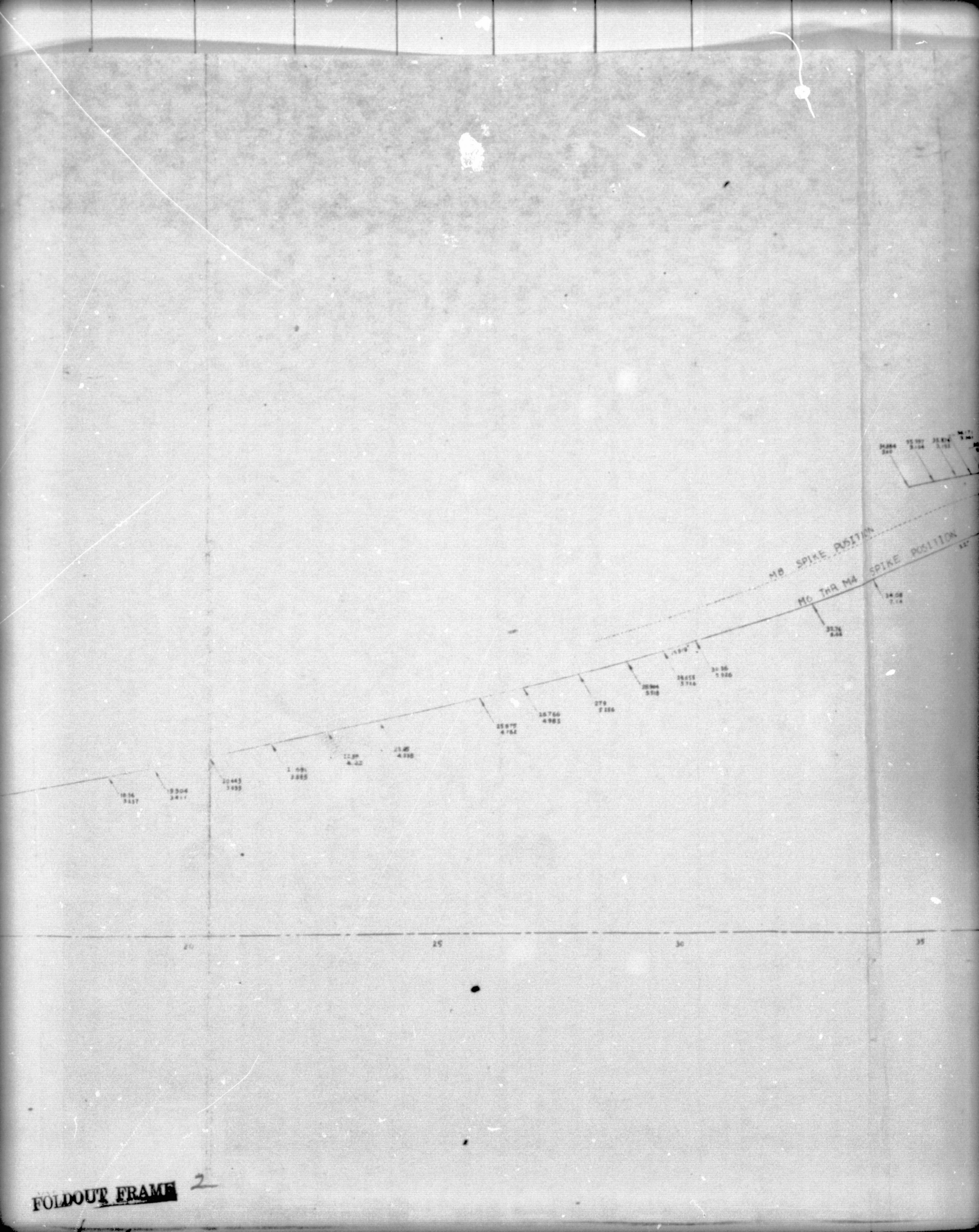

FOLDOUT FRAME 2

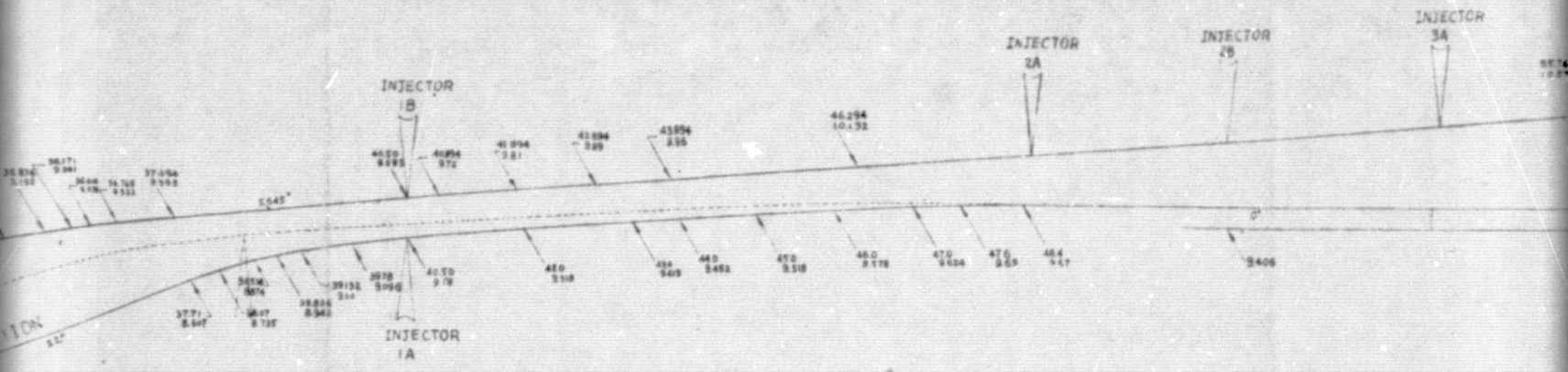

SPIKE POSITION SCHEDULE

	MACH NUMBER		
	4	6	8
SPIKE POSITION INCHES	34.884	34.884	36.990
MASS FLOW RATIO	0.78	1.0	1.0

FUEL INJECTION SCHEDULE

FLIGHT COND / INJECTOR	M4 Sub Comb	M6 Sub Comb	M6 Sup Comb	M8 Sup Comb
1A, 1B			$\phi = 0.59$	$\phi = 1.0$
2A, 2B			$\phi = 0.62$	
3A, 3B	$\phi = 1.0$	$\phi = 1.0$		

40 45 50 55

FOLDOUT FRAME 3

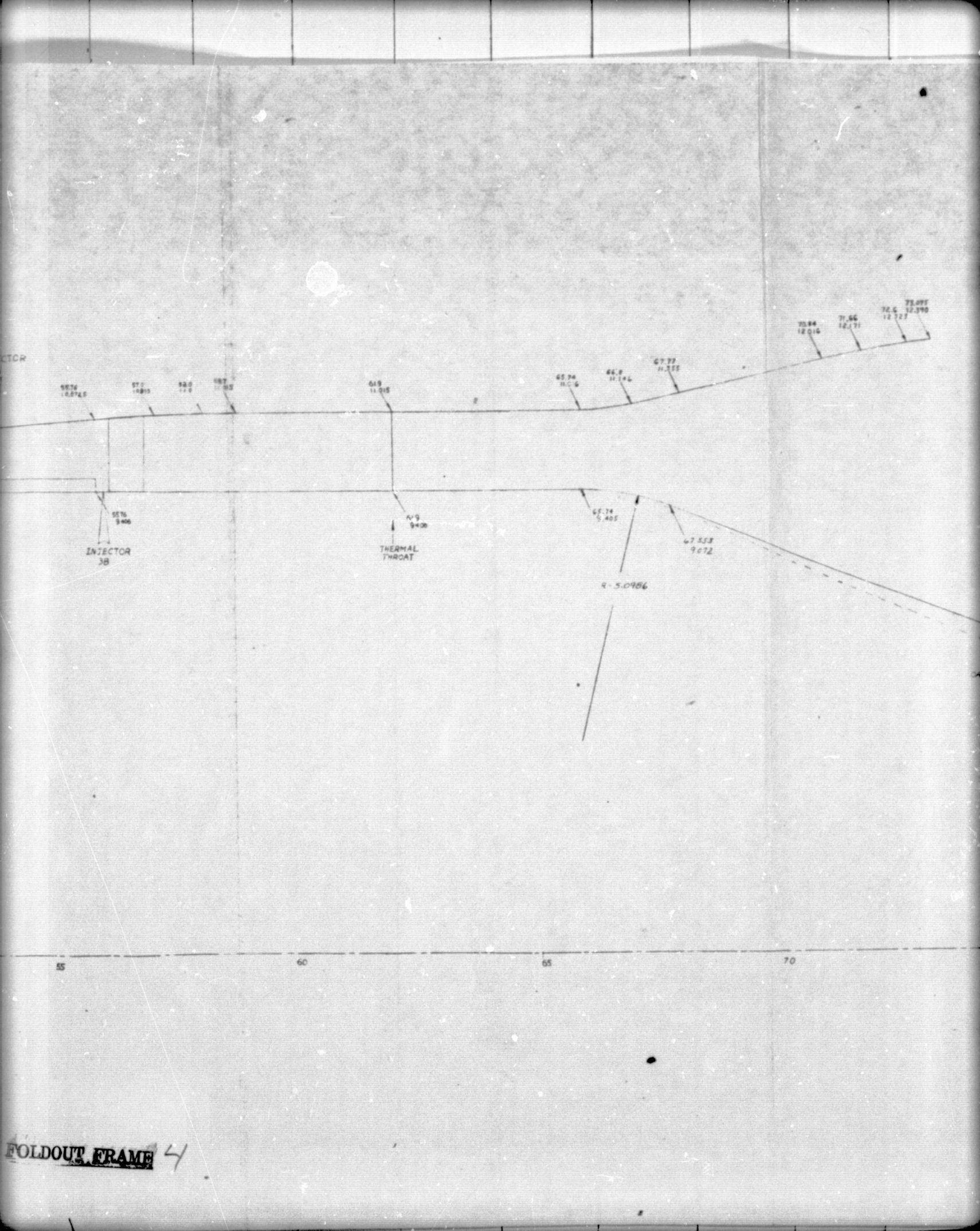

FOLDOUT FRAME 4

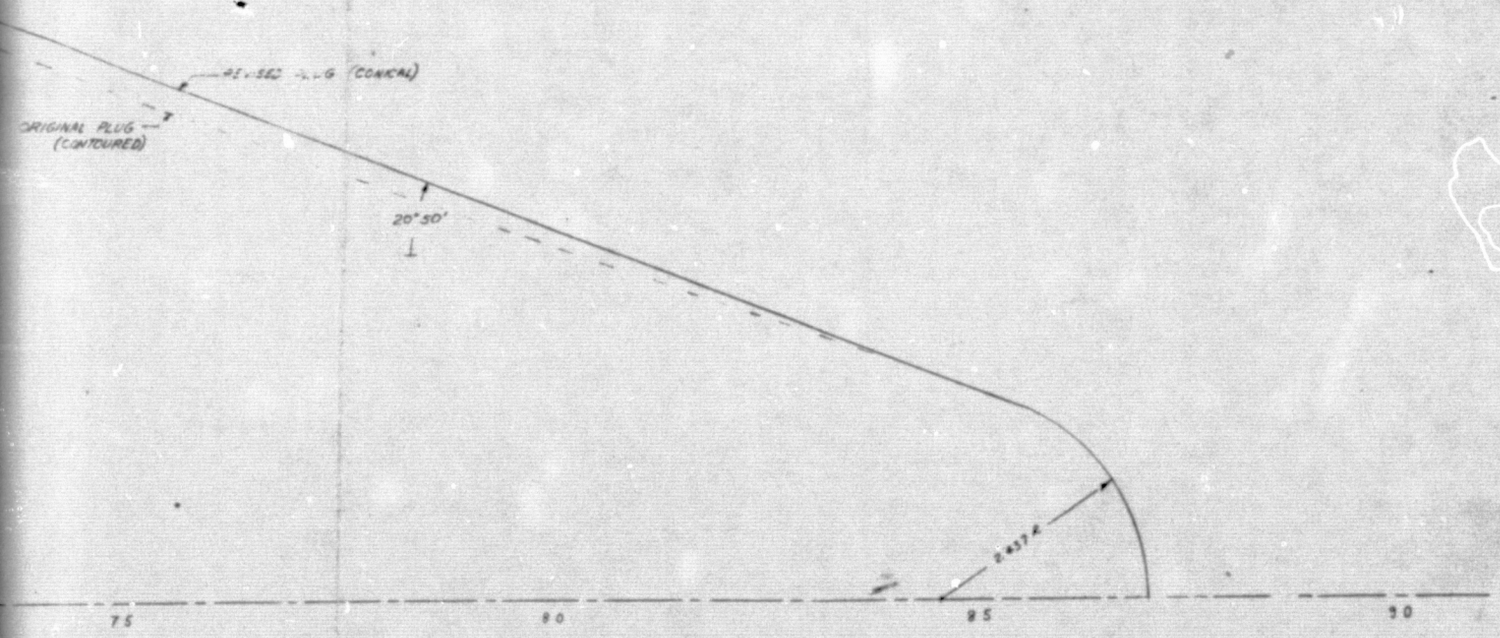

Figure 2.1-1. Selected Aerodynamic Contou

FOLDOUT FRAME 5

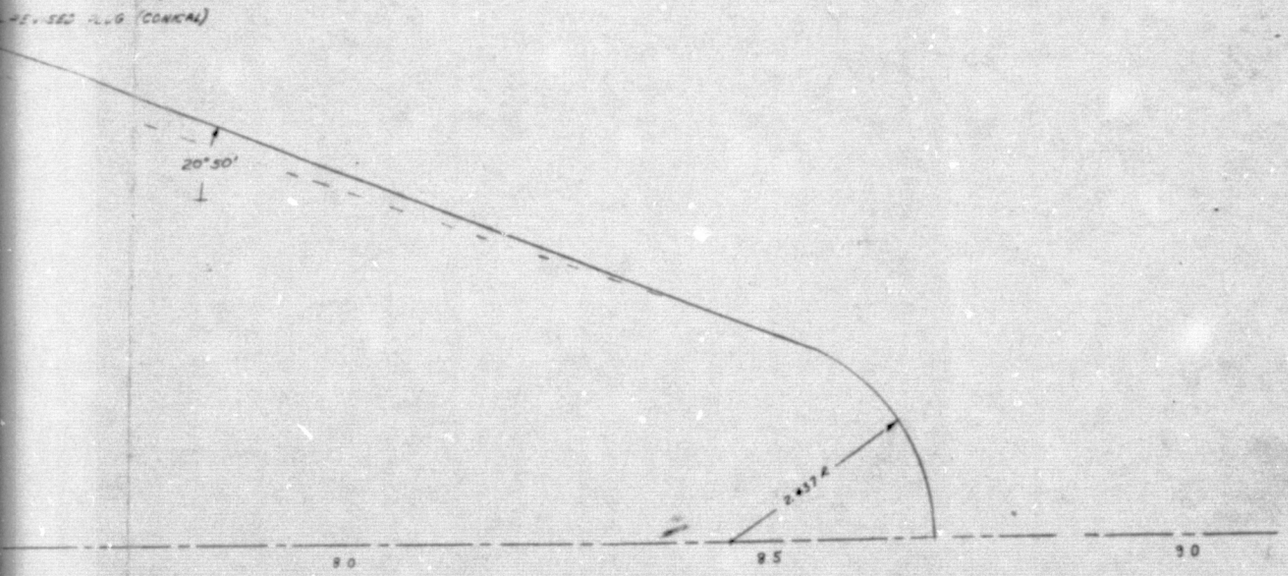

Figure 2.1-1. Selected Aerodynamic Contour

FOLDOUT FRAME

FRAME 5

2. ANALYTICAL DESIGN

2.1 AERODYNAMIC

The aerodynamic contour of the AIM was obtained from research and development tests performed by AiResearch and from data obtained from other Government-sponsored study programs. The details of events and considerations leading to the final aerodynamic contour were presented in series of technical reports submitted to the HRE Project Office, NASA-Langley Research Center, Hampton, Virginia. (Specifically Data Items 55-1, 55-2, and 55-3 covering the development of the HRE inlet, combustor, and nozzle, respectively.)

2.1.1 Inlet Design

The AIM incorporated an 18-in. dia axisymmetric inlet, in compliance with the original Statement of Work, and a translating inlet spike assembly to provide a variable inlet contraction ratio. The selected aerodynamic contour and the inlet contraction ratio is shown in Figures 2.1-1 and 2.1-2. Items considered in the extensive tradeoff study and considerations incorporated were:

(a) Obtain contraction ratio of 14.2 and 8 at operating Mach numbers of 8 and 6 respectively to achieve performance level targetted.

(b) Limit peak aerodynamic contraction ratio (CR m/m_o) at Mach 4 to insure obtaining an inlet start.

(c) Minimize the coalesced flow field to prevent bending the spike bow shock outward such that the shock-on-lip will occur at a smaller X/R ratio affecting the m/m_o schedule.

(d) Minimize the inlet throat upslope angle to facilitate integrating the inlet section with the combustor section.

(e) Minimize the length of the diffuser section to minimize difficulties in starting the inlet due to boundary layer growth.

The contour of the inlet spike was comprised of a 10-deg (half-angle) cone with a 1/8-in. tip radius followed by isentropic compression surfaces with a total external turning of 22 deg. The inlet section of the centerbody was designed with an upsloping throat of 5.65 deg with respect to the engine centerline. The inlet cowl assembly incorporated a leading edge tip radius of 0.03 in., and was designed to close off the inlet airflow when

PRECEDING PAGE BLANK NOT FILMED

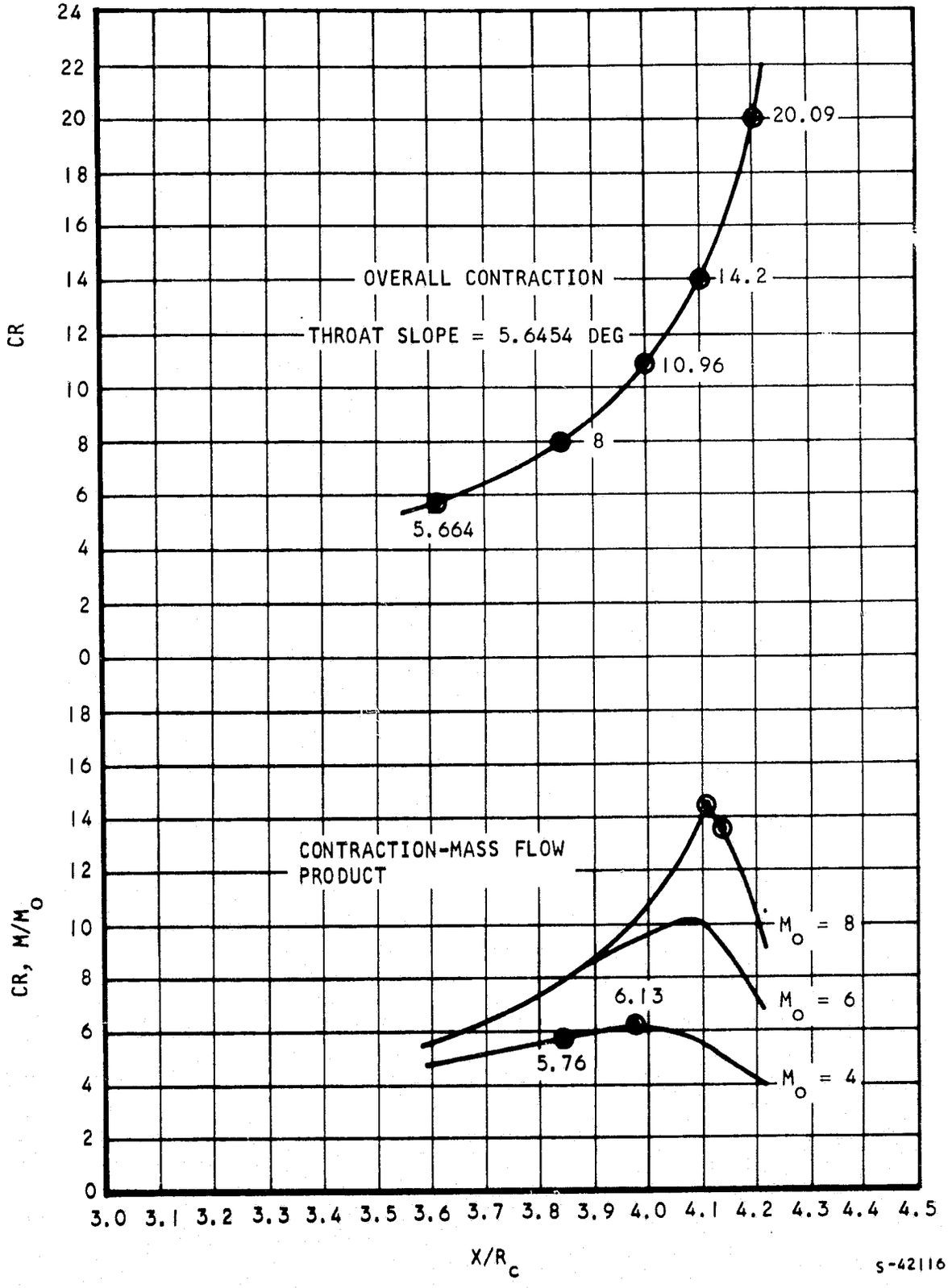

Figure 5-1. Phase II Boilerplate Engine Inlet Contraction Characteristics

PRECEDING PAGE BLANK NOT FILMED

the inlet spike assembly was in its fully extended position to reduce the heat transfer and the engine drag when the engine was not operating. Approximate overall contraction ratios of 14 and 8 were selected for operation at Mach 8 and 6 respectively.

2.1.2 Combustor Section

In the design of the combustor section consideration of many physical constraints and diverse geometric requirements to achieve efficient supersonic and subsonic combustion over test range of Mach 3 through Mach 8 resulted in extensive tradeoffs to optimize overall combustor performance. Items considered were:

(a) Inlet-combustor matching-- Incorporating a translating sp 'e assembly to satisfy the variable inlet requirements for operation over a wide range of speed resulted in an average upsloping air flow angle of 5.6 deg at the inlet throat. This condition required turning the air flow to an axial direction with a minimum loss.

(b) Combustor zone compatibility-- Since both supersonic and subsonic combustion modes must be obtained, area ratio along the duct must be compatible. In the supersonic combustion mode, the amount of fuel that may be injected from the first stage is primarily limited by the inlet unstart and thermal choking constraints, indicating that air flow in the combustor should not be less than Mach 1.3, and during subsonic combustion mode this combustor section must conform to requirements of a subsonic diffuser.

(c) Hard-throat concept-- The six struts which attach the innerbody to the outerbody formed the thermal throat for subsonic combustion. This blockage, however, creates a large drag in the supersonic combustion mode. Hence, a configuration which minimizes drag and offers minimum blockage (5 percent) was selected.

(d) Wetted area-- The wetted area must be kept to a minimum, in order to reduce the heat load and the friction force. The possibility of shortening the subsonic combustor length by sharing the area with the second-stage supersonic combustor section was considered; however, the hard-throat constraint and the interference with the sliding centerbody prevented utilization of this area for both modes of combustion.

(e) Fuel penetration and mixing-- The penetration and mixing studies were controlled by the maximum available fuel manifold pressure of 350 psia. Also, incorporation of a translating inlet spike assembly resulted in overlapping of the spike assembly with the innerbody for approximately 5 in. The overlap area could not be used to inject fuel.

The selected combustor configuration is shown in Figure 2.1-3. The combustor is basically divided into three sections between the inlet throat and the thermal throat. The first two sections are used for supersonic combustion and for subsonic diffusion. The third section is used for subsonic combustion. The first section (approximately 7-in. long) has a diffusion rate approximately equivalent to a half-angle cone angle of 1.5 deg. This slow divergence is primarily for good supersonic combustion performance at high flight Mach numbers. It also serves as the initial section of a subsonic diffuser for operation at low flight numbers in the subsonic combustion mode. The diffusion rate of the second section is equivalent to a half-cone angle of 11.2 deg. The higher divergence angle is required to accommodate the heat release without thermal choking at the lower Mach number flights. The third section starts just forward of the thermal throat and is used for subsonic combustion. The step at the start of this zone serves as the subsonic combustion flame holder.

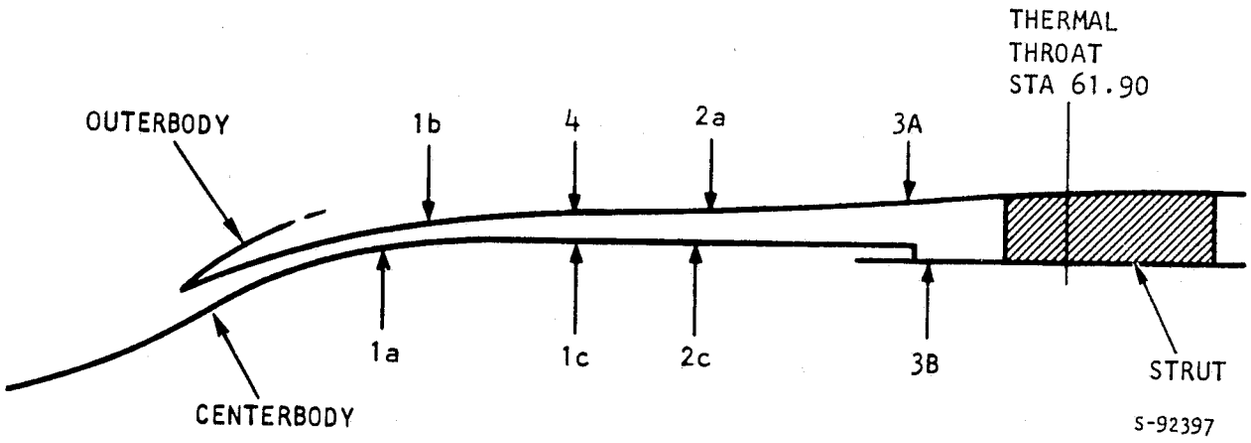

Figure 2.1-3. Selected Combustor Configuration

Four sets of fuel injectors were installed on the outerbody and on the centerbody. The forward fuel injection station (1a, 1b) was designated first-stage supersonic combustion fuel injectors and was placed almost at the inlet throat when the spike assembly is positioned for operation at Mach 6. It was anticipated that the fuel injection, at Mach 6 test condition, from this station will be limited to fuel equivalence ratio (ϕ) of approximately 0.20 and the remaining fuel will be injected from the second stage injectors. However, at Mach 8 flight conditions the inlet spike assembly will be positioned approximately 3 in. forward and ϕ of 1.0 or more could be injected from this fuel injector. The fuel injectors located at the third axial station (2a, 2c) were designated as second stage supersonic combustion fuel injectors when operating at flight conditions less than Mach 8 flight speed. An intermediate fuel injection station (4, 1c) was installed at the second axial station and was to be used as an alternative injector either at first stage supersonic combustion or second stage supersonic combustion. The fuel injectors located at the aft axial station (3A, 3B) were to be used primarily for subsonic combustion mode. This fuel injector station could also be used to provide fuel rich operation in the supersonic combustion mode. The injectors on the outerbody (3A) are

located approximately 2 in. forward of the end of the spike skirt when the spike is positioned for Mach 6 flight condition and the injectors on the innerbody (3B) were placed just downstream from the end of the spike assembly. It was anticipated that at Mach 4 flight condition the terminal shock will be located just downstream of the inlet throat and under Mach 6 flight condition shock will stabilize between fuel injectors 3A and 3B.

Ignitors were located at three stations to provide positive ignition. The ignitor utilizes gaseous hydrogen and oxygen and a capacitive discharge spark system to obtain initial ignition. Hydrogen gas was introduced through an Inconel tube located in the center of the ignitor chamber. This tube was also used as an electrode to initiate ignition. Oxygen gas was introduced through an annular passage with swirl vanes. The resultant swirling action of the oxygen cools the wall and the throat of the ignitor assembly The mixing effectiveness was intentionally limited to give stable burning and cooling of the ignitor body.

The first set of ignitors was mounted on the spike assembly to provide ignition for the first-stage supersonic combustor. The hot gas from the ignitor was ejected normal to the inlet airstream. The second set was located forward of the 2c fuel injector and the hot gas was directed 30 deg upstream and 30 deg circumferentially to provide penetration and agitation which may be necessary to ignite the second-stage combustion. The third set was installed just upstream of fuel injector 3A and the hot gas was directed 30 deg downstream and 30 deg circumferentially. The angular projection of the hot gas was selected to prevent possible impingement of the hot gas with the opposite wall.

2.1.3 Combustor, Fuel Injectors

The design of the combustor section and the location of the fuel injectors were derived from extensive research. The research included survey and analysis of combustor tests performed under Government-sponsored programs and from tests and analysis performed by AiResearch.

Programs examined were:

Conical combustor tested by General Electric Company.

Dual mode scramjet combustor with a constant section followed by two divergent sections. Designed and tested by Marquardt Corporation.

Tests performed by Applied Physics Laboratories, John Hopkins University on an 8-deg cone nozzle followed by a 1-1/2-deg divergent combustor.

Tests performed by AiResearch on a two-dimensional combustor having a 12-in.-long constant section followed by a variable divergent section.

Tests performed by Lockheed Aircraft Company under cognizance of AiResearch on a 2/3-scale inlet model of HRE with helium injection at the throat.

Tests performed by United Aircraft Research Laboratory. Analysis of these tests and parametric studies of chemical kinetics investigating effects of temperature, pressure, duct divergence, amount of vitration, and initial concentration of radicals lead to the combustor configuration shown in Figure 2.1-4.

2.1.3.1 Fuel Injector Design

Fuel injector design was based on the three-dimensional mixing concept evaluating the jet penetration parameter (z) and the jet spreading (/d) as shown in Figure 2.1-5. The jet penetration parameter (z) is the relative effectiveness of the penetration defined as the outer boundary of the jet divided by the minimum height required for complete combustion. Penetration is functionally related to the momentum flux ratio between the fuel jet and the airstream, and downstream diffusion.

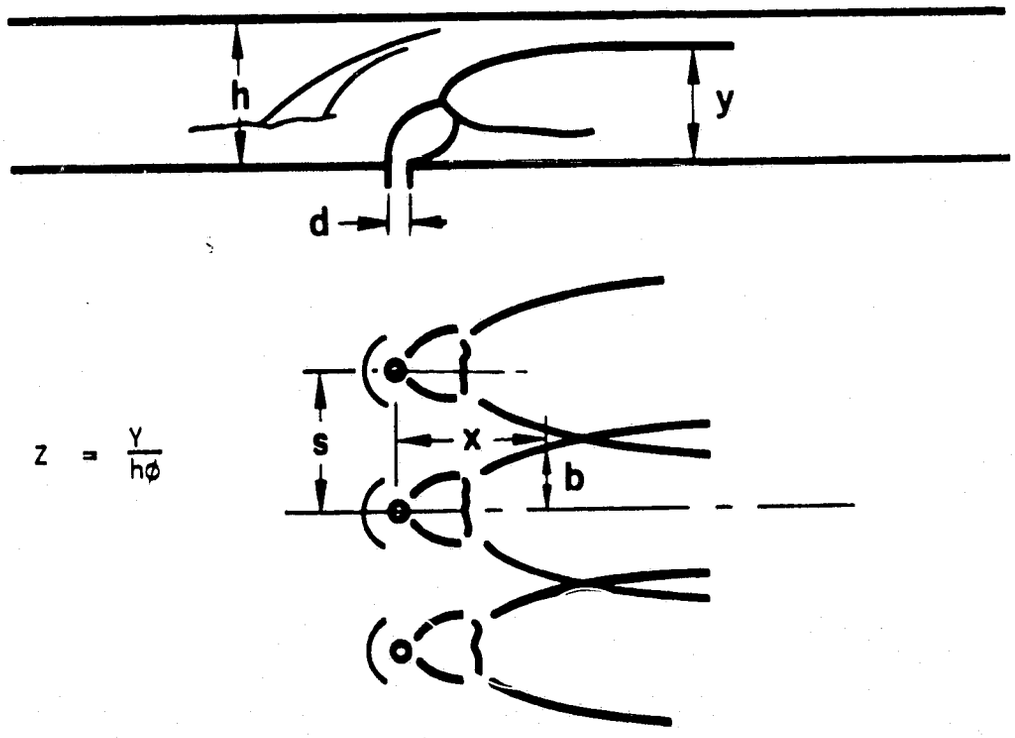

Figure 2.1-5. Concept of Mixing Parameter

The spreading parameter (b/s) defined as the ratio of jet-spreading to hole-spacing, was used to represent the spreading characteristic. It was postulated that the spreading parameter (b/s) is a function of the pressure ratio of the jet, the diameter of the injector hole (d), and the downstream

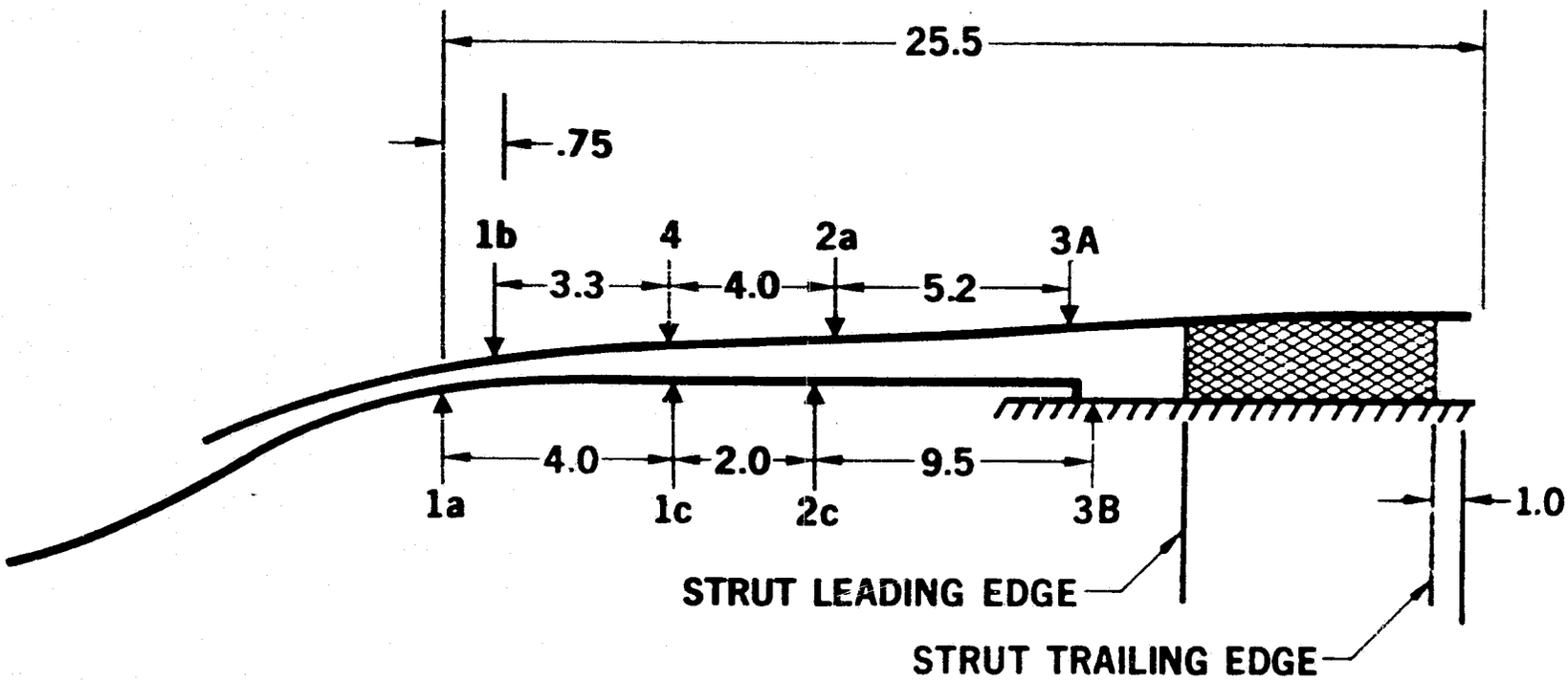

Figure 2.1-4. Fuel Injector Locations

distance (x). It was further assumed that width (b) is a linear function of the distance (x) as in a turbulent jet. The correlations of (z) and (b/s) from combustor component data versus efficiency are shown in Figures 2.1-6 and 2.1-7. In Figure 2.1-6, it showed that the peak efficiency is a strong function of the penetration parameter and levels off at a value of penetration parameter of about 1.7.

The relationship between penetration parameter and total number of injector holes for the first-stage injector combinations of 1a, 1b or 1a, 4 or 1c, and 4 were plotted in Figure 2.1-8. It indicated that penetration was most critical at Mach 8. Using z = 1.7 and injector set 1a and 4, a total of 74 injector holes was selected. The injector hole size was related to injector pressure and hole spacing as shown in Figure 2.1-9a. With an allowable injection pressure of 300 psia, the hole diameter was 0.119 in. and s/d = 14.2 for a single row or s/d = 7 for an interdigitized double row. Past experience indicated that s/d = 6 or 7 was in an acceptable range for good mixing, and this was also supported by Figure 2.1-9b which showed reasonable combustor length and efficiency as determined from combustor component tests. The use of injector set 1a and 4 instead of 1a and 1b for this design analysis was to provide added margin for possible inlet unstart problem at Mach 8.

The configuration selected for row (1c) was to be compatible with row (4) with 37 injector holes 0.119 in. in diameter and positioned at 103 deg with respect to airflow, to increase penetration. This configuration also provided the capability of using 1c and 4 as an alternative first-stage fuel injector set for supersonic combustion.

Design of the second-stage fuel injectors 2a and 2c involved utilizing parameters referenced above; however, their effects were modified and are shown in Figures 2.1-10 and 2.1-11. Z = 1.7 was again selected for these fuel injectors. The configuration selected for this stage was 60 injectors, 0.095 in. in diameter, positioned 117 deg with respect to the airstream, and interdigitized.

Information for design of the subsonic combustion was not as complete as that for supersonic combustion, since the two-dimensional combustor tests had been terminated prior to completing this stage. Calculation indicated that if fuel is injected in two locations; namely, one location upstream of the step created by the end of the spike assembly, and the other downstream from this step, a normal shock will stabilize between these injectors. Further, analysis indicated that there was no need to interdigitize the fuel injector ports. Parameters considered and their effects for subsonic combustion are shown in Figures 2.1-12 and 2.1-13. The configuration selected for row 3A was 105 injectors, 0.09 in. in diameter, positioned 120 deg with respect to the airstream, and for row 3B, 105 injectors, 0.09 in. in diameter, positioned 90 deg (perpendicular) to the airstream. Physical restrictions in installing 105 injectors equally spaced on the centerbody (row 3B) resulted in modifying the selected configuration to one shown in Table 2.1-1.

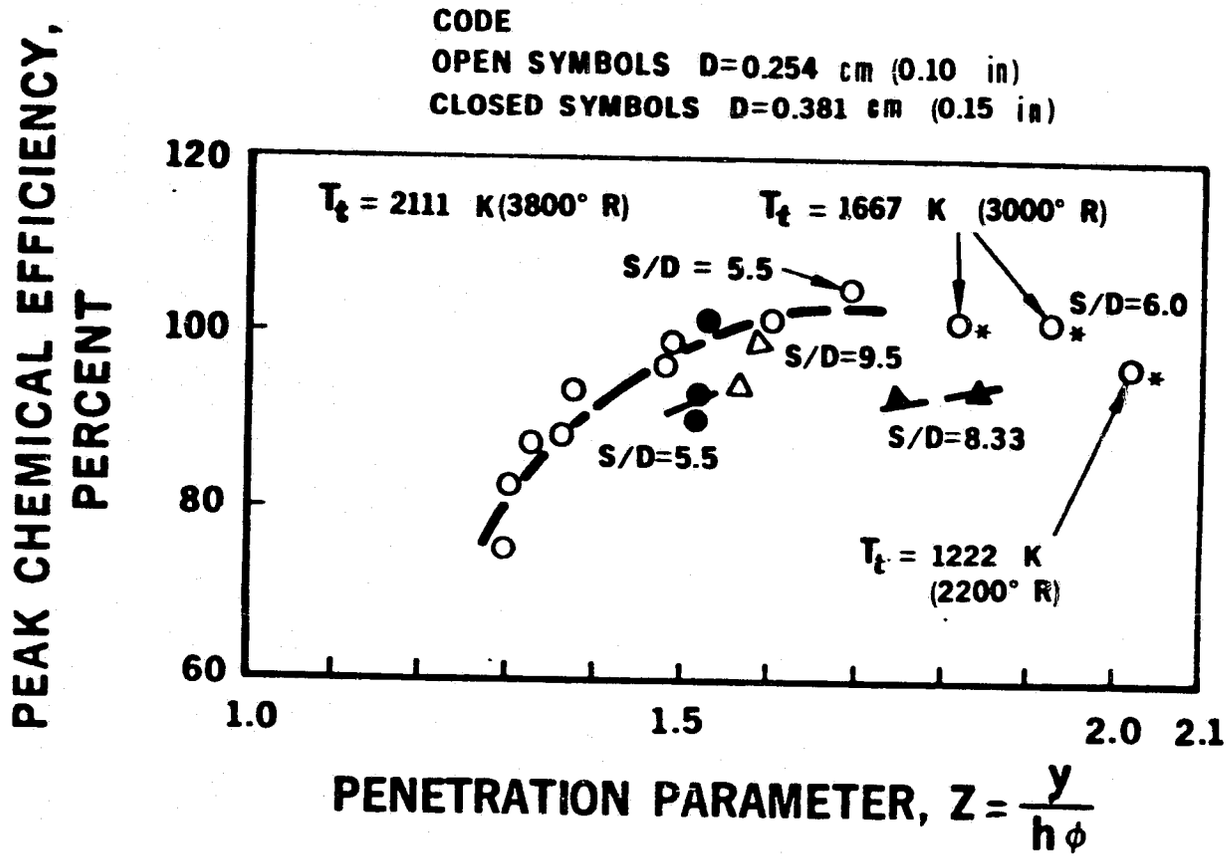

Figure 2.1-6. Variation of Peak Chemical Efficiency With Z

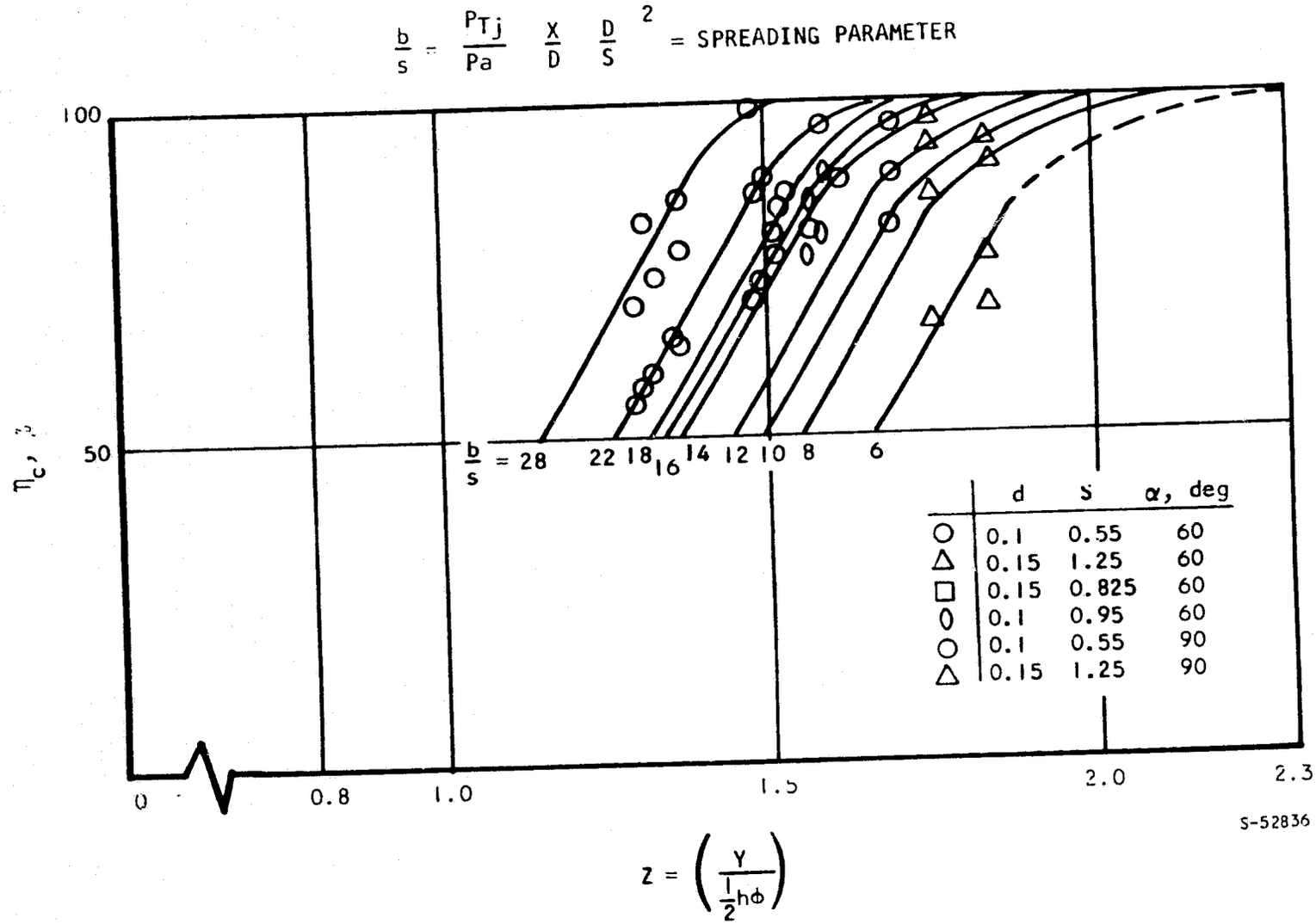

Figure 2.1-7. Chemical Efficiency versus Z

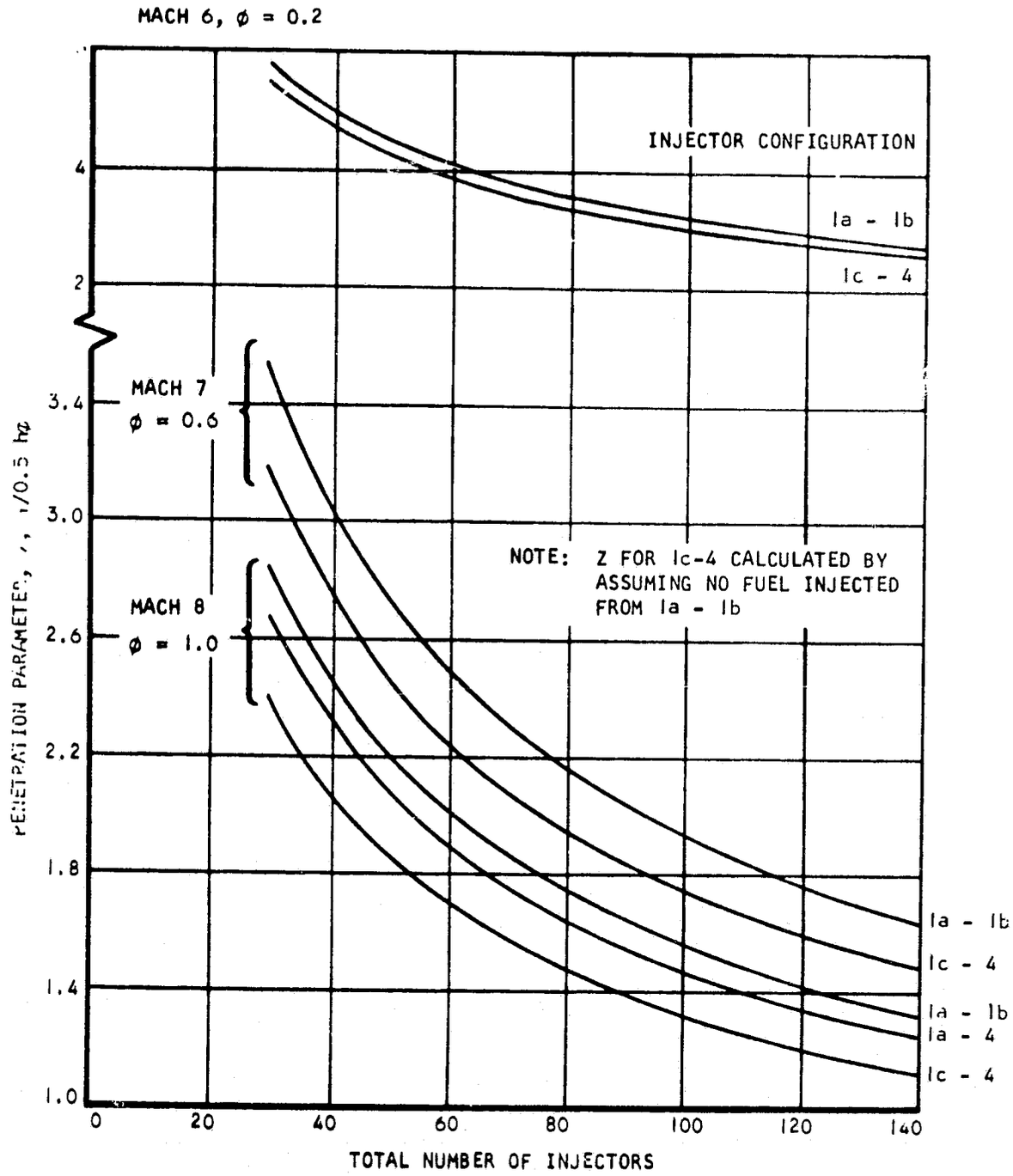

Figure 2.1-8. Effect of Number of Injectors on Penetration Parameter

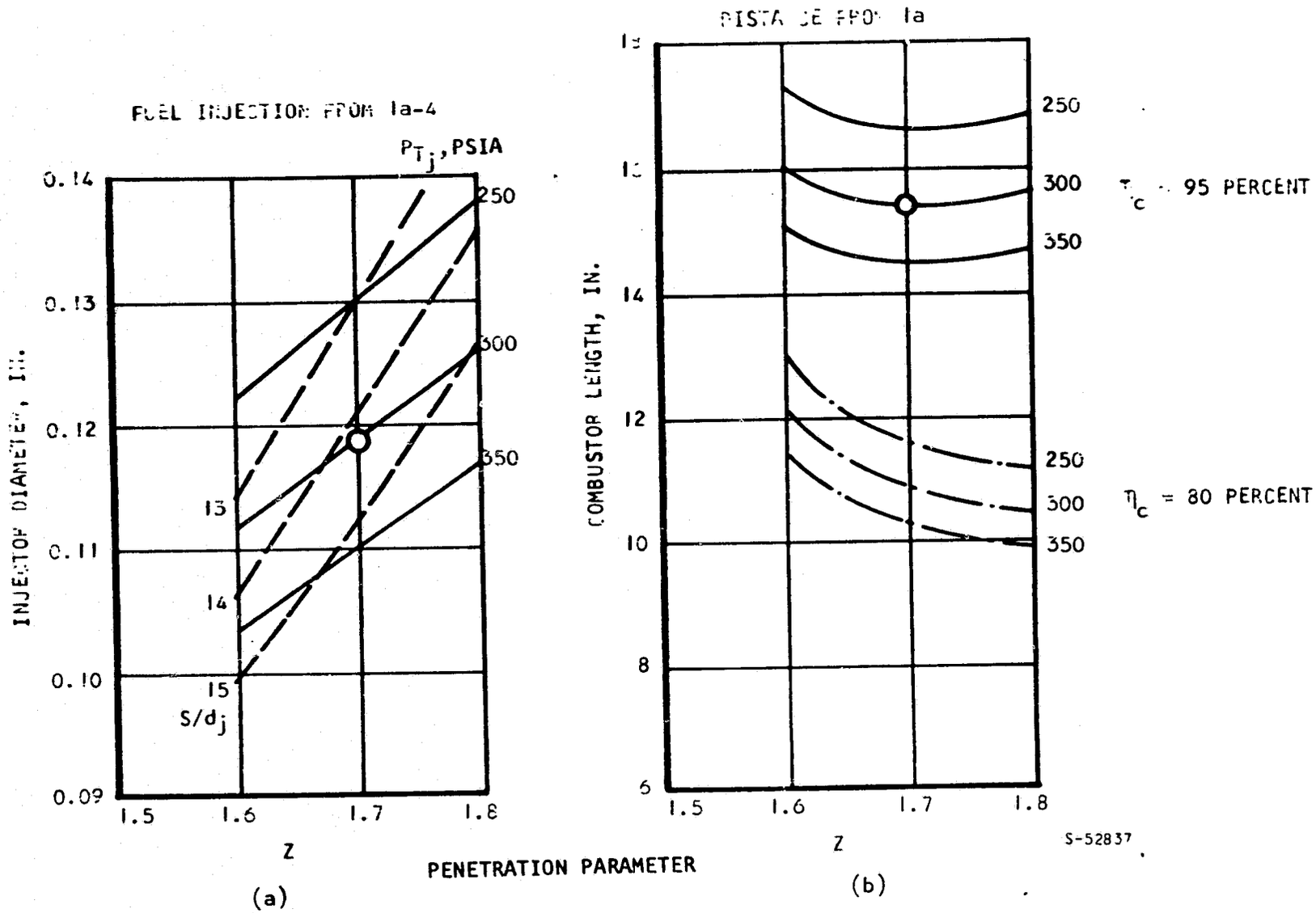

Figure 2.1-9. Mach 8 Injector Design

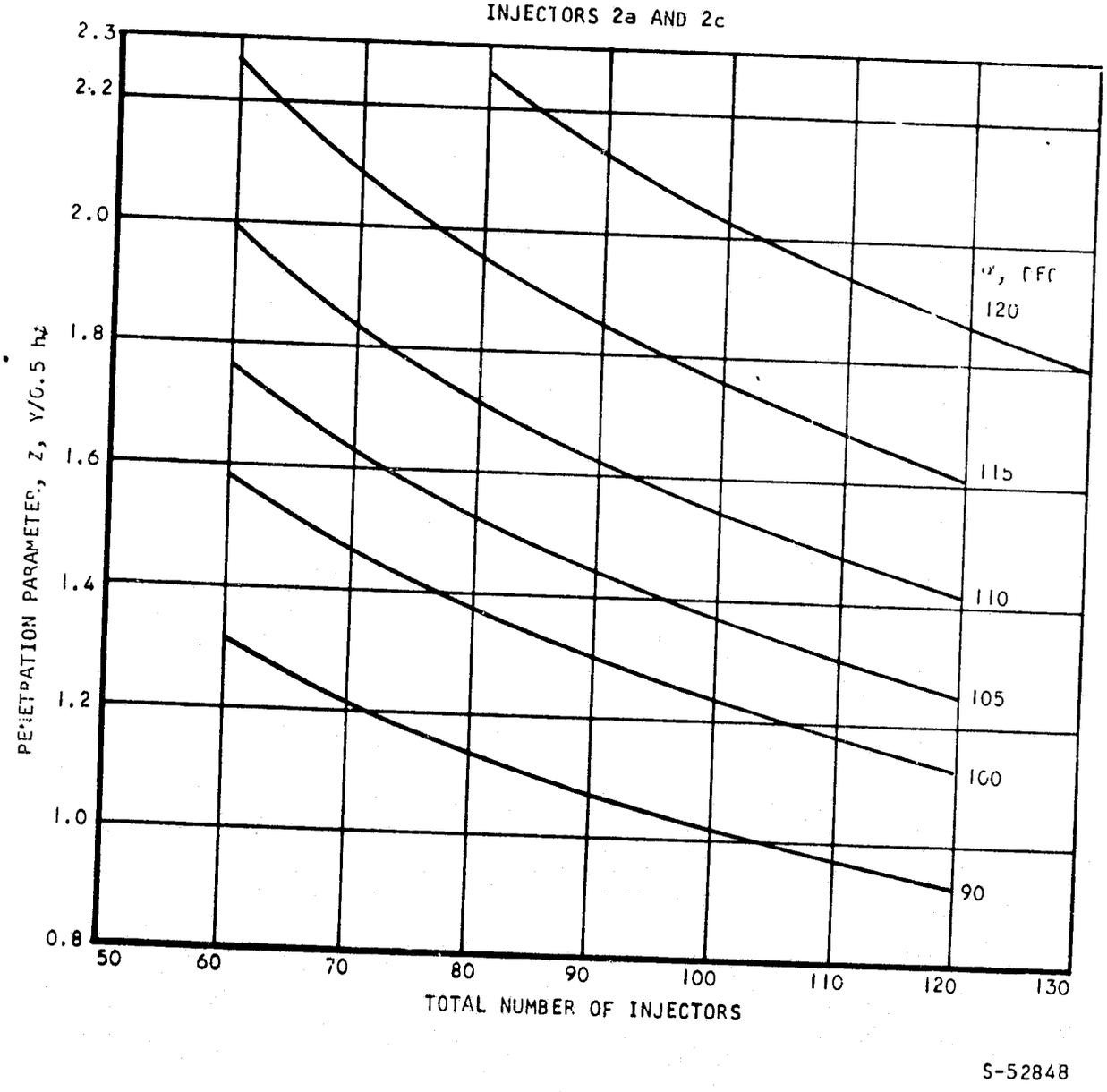

Figure 2.1-10. AIM Injector Sizing, Mach 7

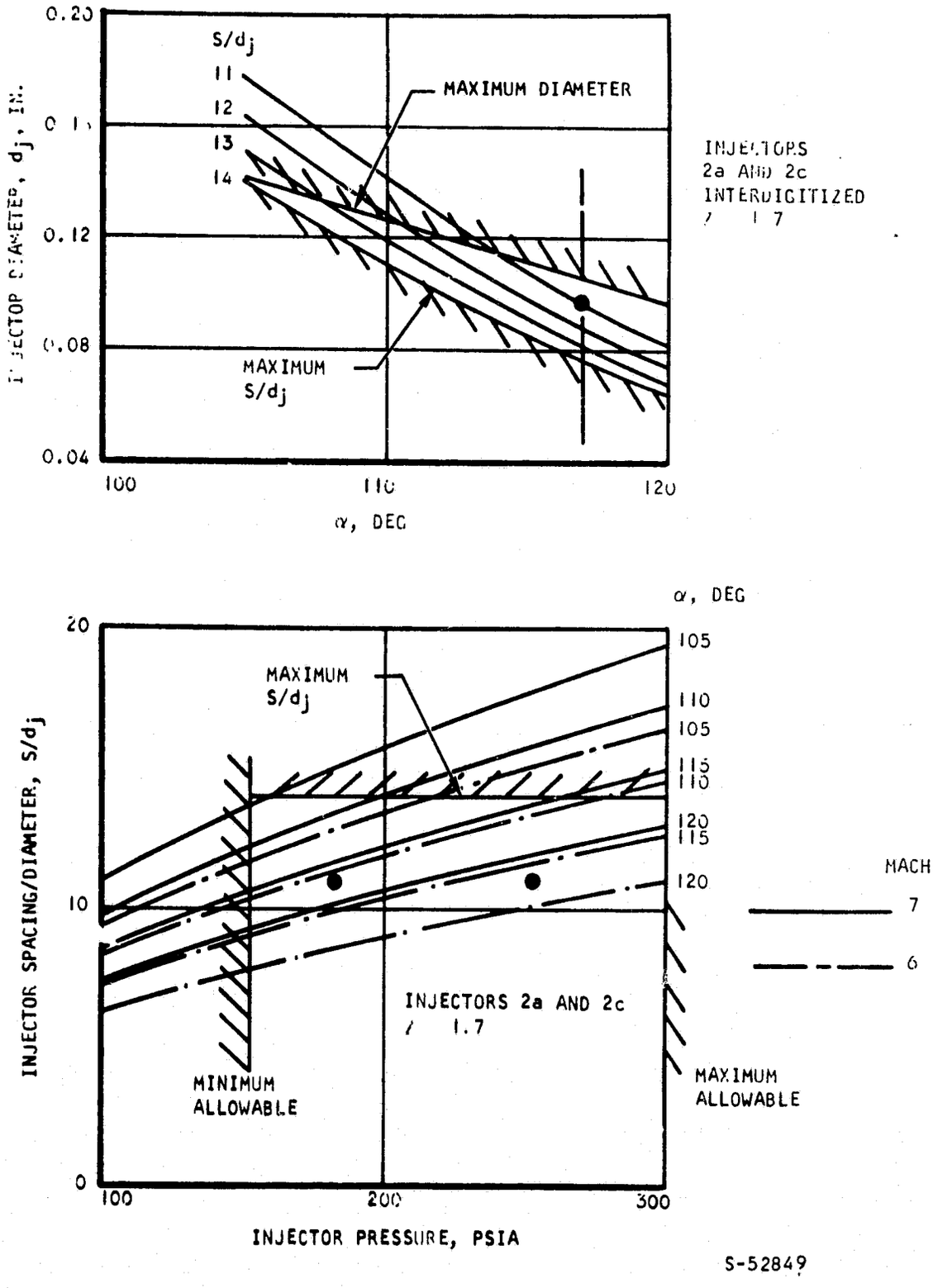

Figure 2.1-11. AIM Injector Sizing

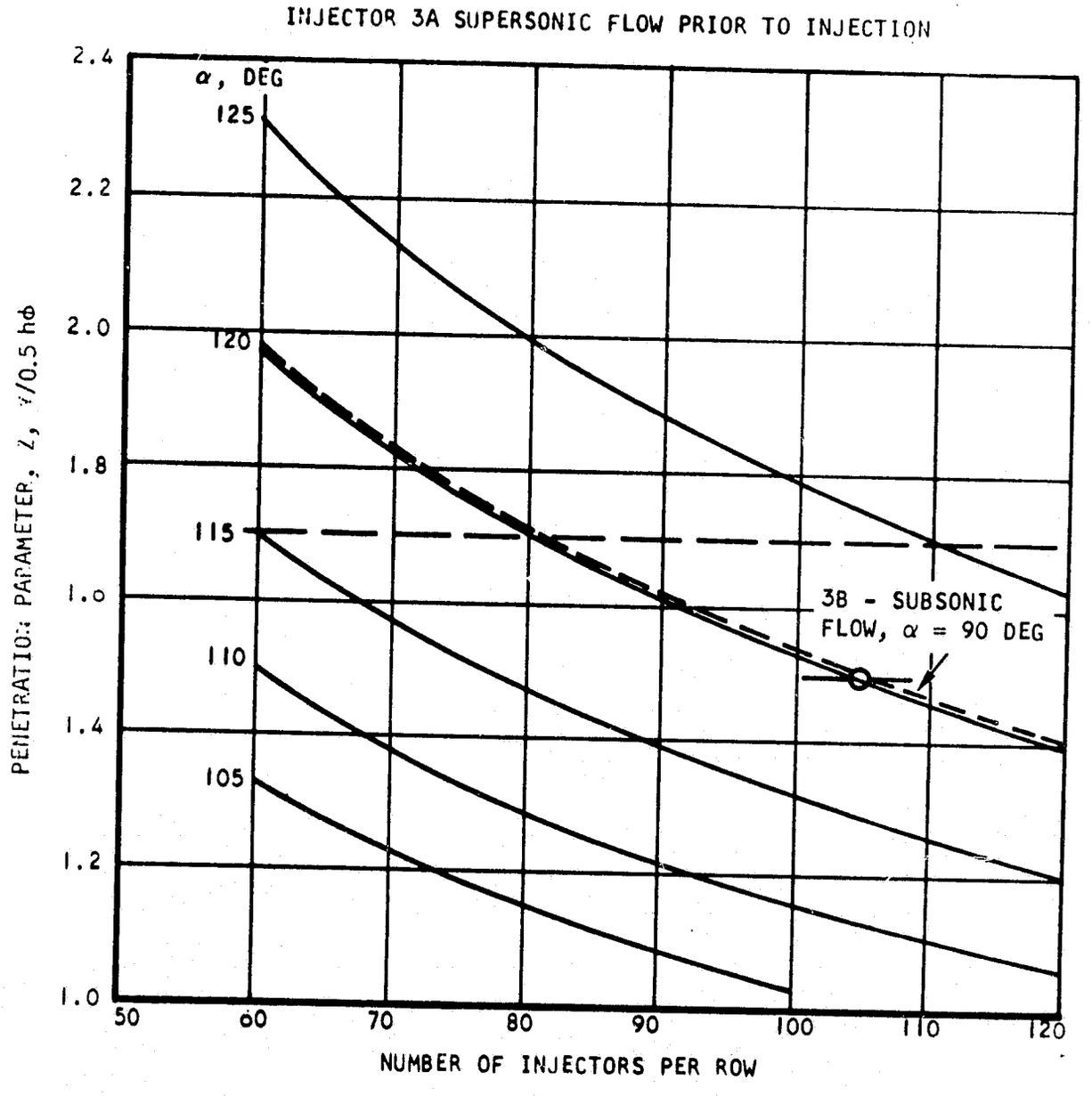

Figure 2.1-12. AIM Injector Sizing, Mach 6

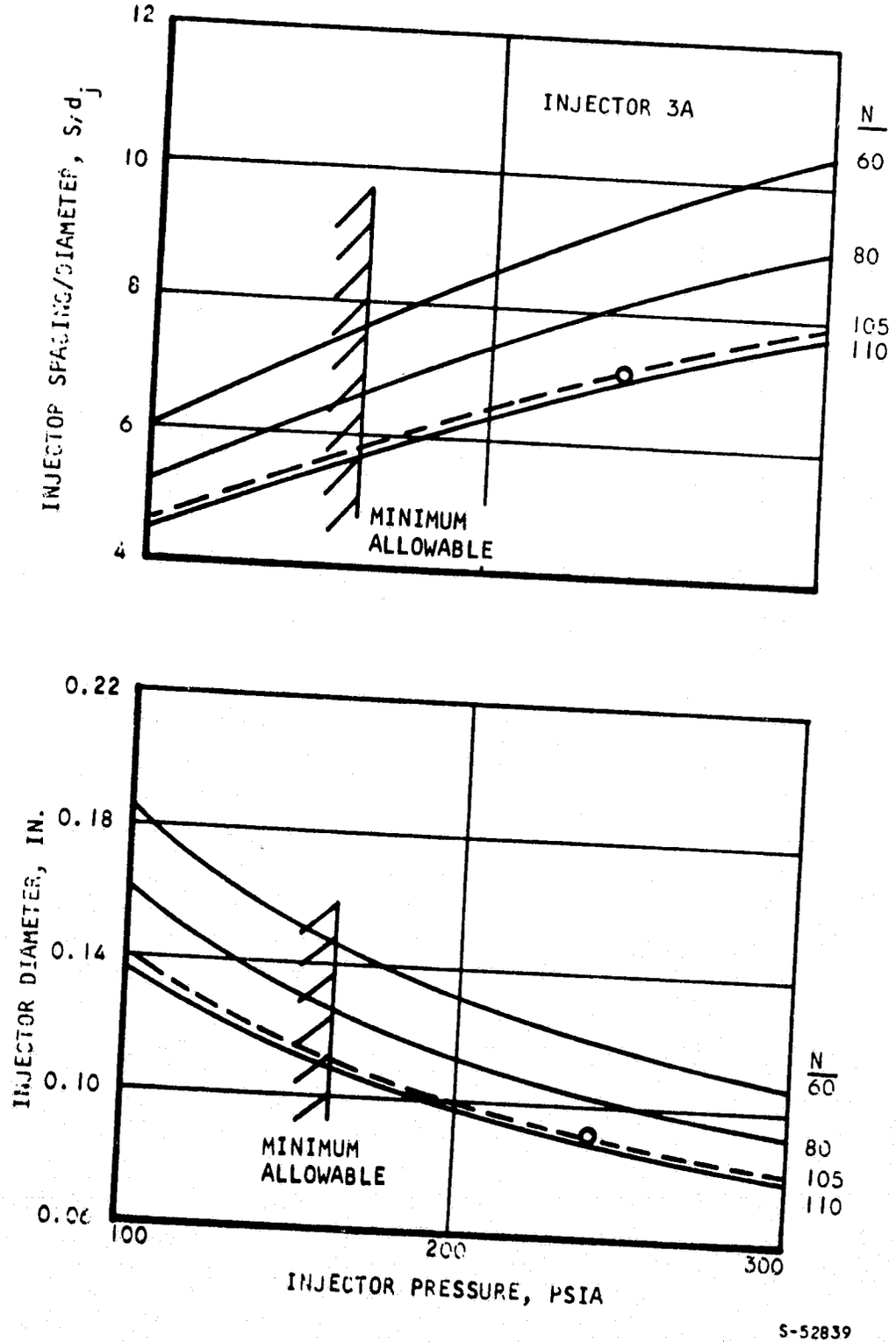

Figure 2.1-13. AIM Injector Sizing

TABLE 2.1-1

AIM INJECTOR PARAMETERS

Injector Row	Number of Injectors	Diameter, in.	Injection Angle, deg	S/d	Location	Mach 6 Position
1a	37	0.119	90	13.1	40.5	I.B.
1b	37	0.119	90	13.9	41.25	O.B.
1c	37	0.119	103	13.5	44.5	I.B.
4	37	0.119	90	14.2	44.5	O.B.
2a	60	0.095	117	11.4	48.5	O.B.
2c	60	0.095	117	10.6	46.5	I.B.
3A	105	0.09	120	7.0	53.75	O.B.
3B	105	0.09	90	6.3	55.9	I.B.

2.1.4 Nozzle

The nozzle section is a shrouded-plug design. Approximately 30 percent of the projected area is derived from the shroud, and the remaining 70 percent from the plug. The section leading to the nozzle entrance incorporated a nearly constant area and the plug was truncated at an optimum point determined from experimental data.

2.1.5 Gas Properties and Aerodynamic Loads

The gas properties used for the initial aerodynamic and heat transfer analysis were based on utilizing the vitiated air and test conditions specified for Ordinance Aerophysics Laboratories, Dangerfield, Texas.

The greatest aerodynamic load is imposed on the AIM under the test condition of freestream Mach number (M_∞) = 5.79, and the most severe heating of the AIM occurs at M_∞ = 6.65.

A summary of test conditions considered for the initial analysis is shown in Table 2.1-2, and summary of forces and thrust/drag coefficients is tabulated in Table 2.1-3. Figure 2.1-14 presents the estimated thrust/drag characteristic of the AIM over test conditions of Mach 3 through 7. This analysis does not include the external drag of the outer cowl body, since this component was mounted to a separate mount such that its reactive loads were not connected to the force balance system measuring the AIM thrust/drag characteristics.

TABLE 2.1-2

RANGE OF TEST CONDITIONS FOR PHASE IIA BOILERPLATE ENGINE

Mach No.	Clean or Vit Air	Inlet P_T, psia	Inlet T_T, °R	Inlet P_S, psia	Inlet T_S, °R	$\frac{A_o}{A_c}$	W_a, lb/sec	MW lb/lb-MOL	γ	f/a $\phi = 1$	Sub* or Sup Comb
3	Clean	30.5	1080	0.826	390	0.25	7.3	28.97	1.402	0.0293	Sub
3	Clean	62	1080	1.69	390	0.25	15.0	28.97	1.402	0.0293	Sub
4	Clean	83.8	1602	0.539	394	0.7	17.7	28.97	1.402	0.0293	Sub
4	Clean	170	1585	1.1	390	0.7	36.3	28.97	1.402	0.0293	Sub
5	Clean	150	2204	0.256	391	0.9	13.5	28.97	1.402	0.0293	Sub
5	Clean	150	2204	0.256	391	0.9	13.5	28.97	1.402	0.0293	Sup
5	Vit	150	2204	0.24	408	0.9	12.1	27.33	1.388	0.0308	Sub
5	Vit	450	2370	0.664	439	0.9	35.9	27.33	1.388	0.0308	Sub
5	Vit	150	2204	0.24	408	0.9	12.1	27.33	1.388	0.0308	Sup
6	Vit	466	2930	0.204	418	1	13.4	26.55	1.382	0.0317	Sub
6	Vit	930	3020	0.413	431	1	26.5	26.55	1.382	0.0317	Sub
6	Vit	466	2930	0.204	408	1	13.4	26.55	1.382	0.0317	Sup
6	Vit	930	3020	0.413	431	1	26.5	26.55	1.382	0.0317	Sup
7	Vit	500	3770	0.118	452	1	4.1	24.78	1.369	0.034	Sup
7	Vit	1000	3770	0.118	452	1	8.3	24.78	1.369	0.034	Sup

*Subsonic or Supersonic Combustion

TABLE 2.1-3

SUMMARY OF FORCES

Mach Number	3	4	5	6	7
$C_{D_{additive}}$	0.12	0.02	0.1	0	0
$C_{D_{pressure}}$	0.62 ±10%	0.49 ±10%	0.31 to 0.43	0.28 to 0.40	0.26 to 0.38
$C_{D_{friction}}$	0.009	0.008	0.007	0.006	0.005
Total $C_{D_{external}}$	0.749	0.520	0.327 to 0.447	0.286 to 0.406	0.265 to 0.385
$C_{D_{internal}}$	0.080	0.090	0.10	0.110	0.115
$C_{F_{NJ}}$	0.51	1.358	1.10	0.882	0.695
q_{min}, psia	5.21	6.04	4.17	5.06	1.98
q_{max}, psia	10.65	12.3	11.55	10.25	3.96
$Force_{(HOT)_{min}}$, lb	-320	+1290	+690 to +820	+610 to +765	+150 to +210
$Force_{(HOT)_{max}}$, lb	-650	+2620	+1920 to +2280	+1240 to +1550	+415 to +300
$Force_{(COLD)_{min}}$, lb	-1100	-940	-455 to -580	-505 to -660	-195 to -255
$Force_{(COLD)_{max}}$, lb	-2240	-1910	-1250 to -1600	-1030 to -1340	-390 to -510

NOTE: Drag and thrust coefficients referenced to A_c = 1.767 ft²

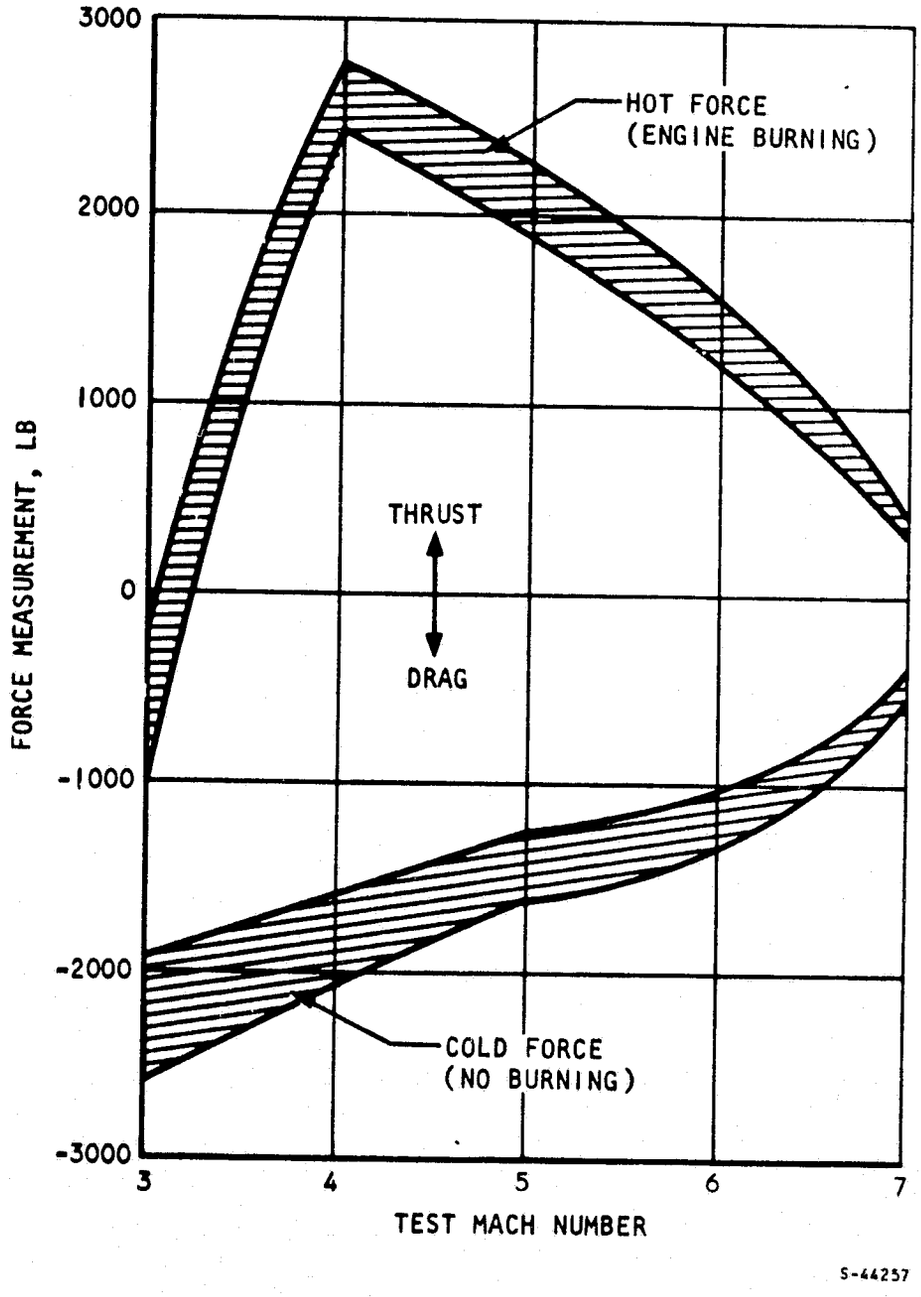

Figure 2.1-14. Estimated Force for Phase IIA Boilerplate Engine Test at Maximum Dynamic Pressure

Below Mach 4 the additive drag cannot be calculated accurately because of flow separation and subcritical spillage at the inlet, therefore, below Mach 4 the range presented in Figure 2.1-14 reflects a ±50-percent change in additive drag.

2.1.6 Shock Interaction

Probable location and configuration of the shock profile was calculated so that increase in heat transfer coefficients may be predicted for areas of high localized heating crated by the shock interaction. Areas considered were (1) intersection of the spike assembly bow shock with the tip of the cowl leading edge assembly, (2) intersection of the spike assembly bow shock with the standing shock of the engine support structure, and (3) the shock structure within the combustor at the outerbody/innerbody strut leading edge.

2.2 HEAT TRANSFER ANALYSIS AND DESIGN

This section summarizes the aerodynamic heating analyses, coolant system design, component thermal performance, and fuel system performance of the AIM. The heat transfer objectives were (1) to assess the overall, as well as local, aerodynamic heating--first for the OAL facility test conditions and ultimately for the LeRC Plum Brook facility test conditions; and (2) to provide a cooling design that would maintain engine structural integrity within facility coolant capabilities and allow for adequate aerothermodynamic test measurement.

Some of the heat transfer analyses and designs required several iterations before final selections were made. For brevity only the final iterations are summarized in the following sections.

2.2.1 Aerodynamic Heating

The aerodynamic heating analyses were performed using the aerodynamic data presented in Section 2.1. A complete assessment of the aerodynamic heating was required to define inputs to the cooling design and thermal performance. Presented below are descriptions of the test facility design points, comparative heating levels between the OAL and Plum Brook facilities, overall heating levels, comparative heating between analytical techniques, leading edge heating and a summary of localized aerodynamic heating effects.

2.2.1.1 Heat Transfer Design Point Description

Initially, the AIM was to be tested at the OAL facility in Dangerfield, Texas. Subsequently, the test site was changed to the Plum Brook facility of LeRC. The aerodynamic heating analyses of all engine surfaces (except the outer cowl body and support assembly) for the OAL conditions were completed when this change occurred. Since the design point heating analyses for both facilities were similar (as shown in Section 2.2.1.2 below), the OAL heating analysis was retained for most of the cooling design. The outer cowl body and support assembly heating, however, was updated for the Plum Brook facility. A summary of the heat transfer design points for both facilities is presented in Table 2.2-1.

TABLE 2.2-1

SUMMARY OF AERODYNAMIC HEATING DESIGN POINTS FOR OAL AND PLUM BROOK TEST FACILITIES, ϕ = 1.00

Test Facility	Freestream Mach Number	Freestream Total Pressure, psia	Freestream Total Temperature, ^{o}R	Inlet Air Flow Rate, lb/sec	AIM Combustion Mode
OAL	5.79	930	2940	30.40 (1)	Supersonic
OAL	6.65	1200	3770	34.64 (1)	Supersonic
PB	6.00	930	2930	34.58 (2)	Supersonic
PB	7.00	1200	3800	39.18 (2)	Supersonic

(1) Vitiated air
(2) Clean air

2.2.1.2 Comparison of Heating Between OAL and Plum Brook Facilities

Analyses were performed to determine the comparative aerodynamic heating between the OAL and Plum Brook test conditions. Results are shown in Figure 2.2-1 for the centerbody side of the engine combustor where heat fluxes were expected to be among the highest throughout the engine. The results show that the heat flux and heat loads are about equal for the two facility test conditions. Though the Plum Brook clean air mass flow rate is higher, the gas enthalpy is lower. The net effect is a slight reduction in Plum Brook facility heat load. This close comparison demonstrated that a complete aerodynamic heating reassessment for Plum Brook conditions was not required for coolant flow routing and component design. Thus, OAL heating conditions shown below were retained for design.

2.2.1.3 Overall Heating Levels

Aerodynamic heat fluxes were calculated for the OAL design point conditions of $M_\infty = 5.79$ and $M_\infty = 6.65$ (Table 2.2-1). These fluxes were calculated using AiResearch Computer Program H1760 (Aerodynamic Heat Transfer Evaluation Computer Program). This program uses the Eckert flat-plate reference enthalpy method with conical (spike and cowl) modifications factors of $\sqrt{3}$ and $\sqrt[5]{2}$, respectively, for laminar and turbulent flow conditions. Results of the analysis performed on the centerbody, outerbody, and strut side surfaces are presented in Figures 2.2-2, 2.2-3 and 2.2-4, respectively.

The heat flux curves in these figures do not include localized heating from shock impingement and surface protuberances. These local areas were each treated separately and are discussed in Section 2.2.1.6 below.

2.2.1.4 Comparison of Flat-Plate and Duct-Flow Heating for the Combustor Zone

In the combustor zone, between Stations 41 and 66, there was an uncertainty whether the hot gas boundary layer was thin enough to be considered independent of the adjacent wall (flat-plate flow) or thick enough to be affected by the adjacent wall (duct flow). Comparative analyses were performed to determine which flow pattern gave the larger heat fluxes. Results shown in Table 2.2-2 indicate that the duct-flow method gives slightly higher heat fluxes in specific areas over heat fluxes by the flat-plate method (Figures 2.2-2 and 2.2-3 using Computer Program H1760). These slightly higher fluxes did not require a change in cooling design, however.

2.2.1.5 Leading Edge Heating

The basic laminar stagnation point heat fluxes on the spike, cowl leading edge, struts, and outer cowl support legs were calculated by the method of Fay-Riddell (Reference 2-4). Lee's distribution (Reference 2-5) was then used to obtain the heat flux distribution around the stagnation point.

The effect of upstream turbulence was considered on the leading edges. To account for this, a factor of 1.8 on heat flux was initially used. This was based on Reference 2-6 which indicated that for a turbulence intensity of from

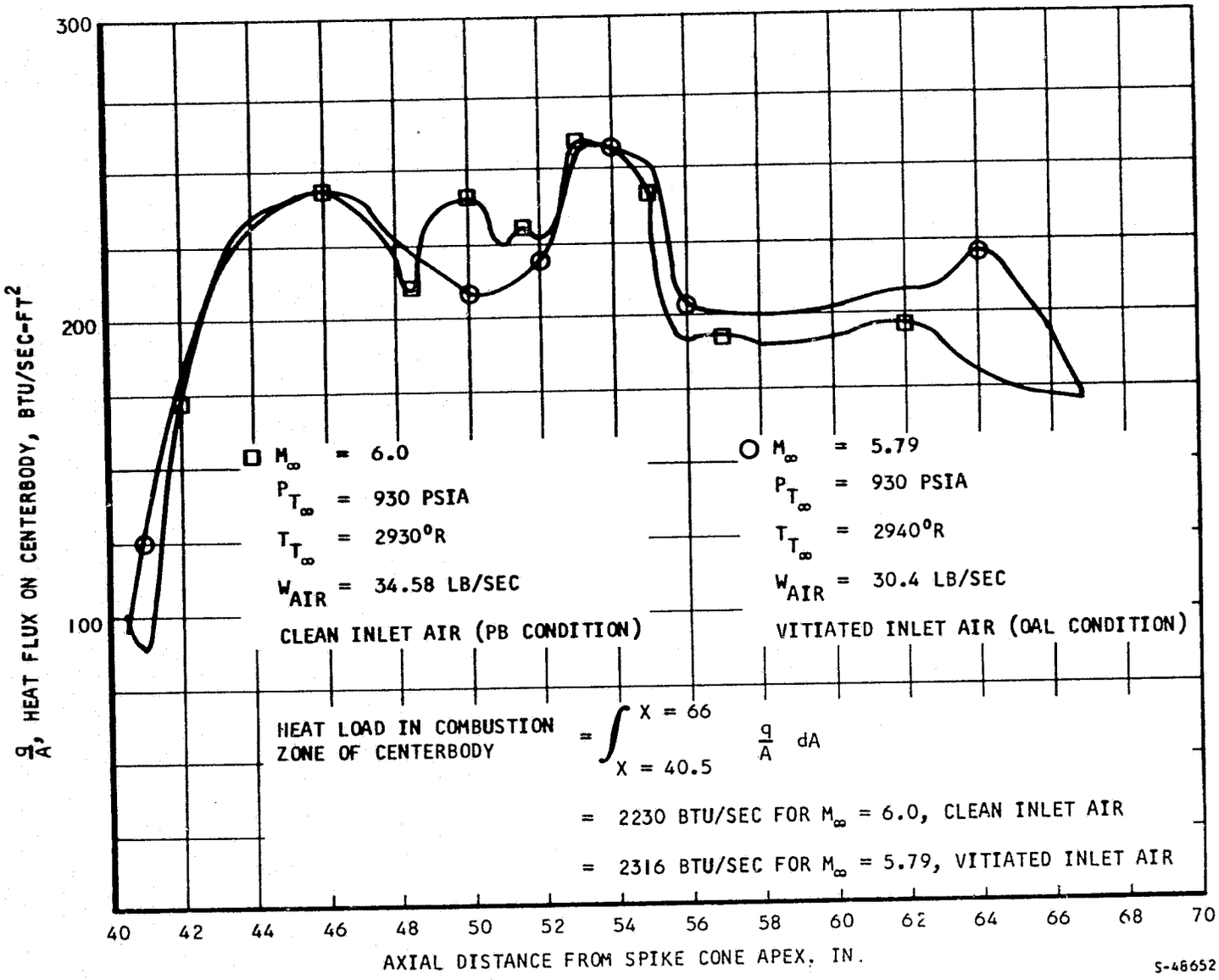

Figure 2.2-1. Comparison in Heat Flux Between Plum Brook and OAL Gas Conditions

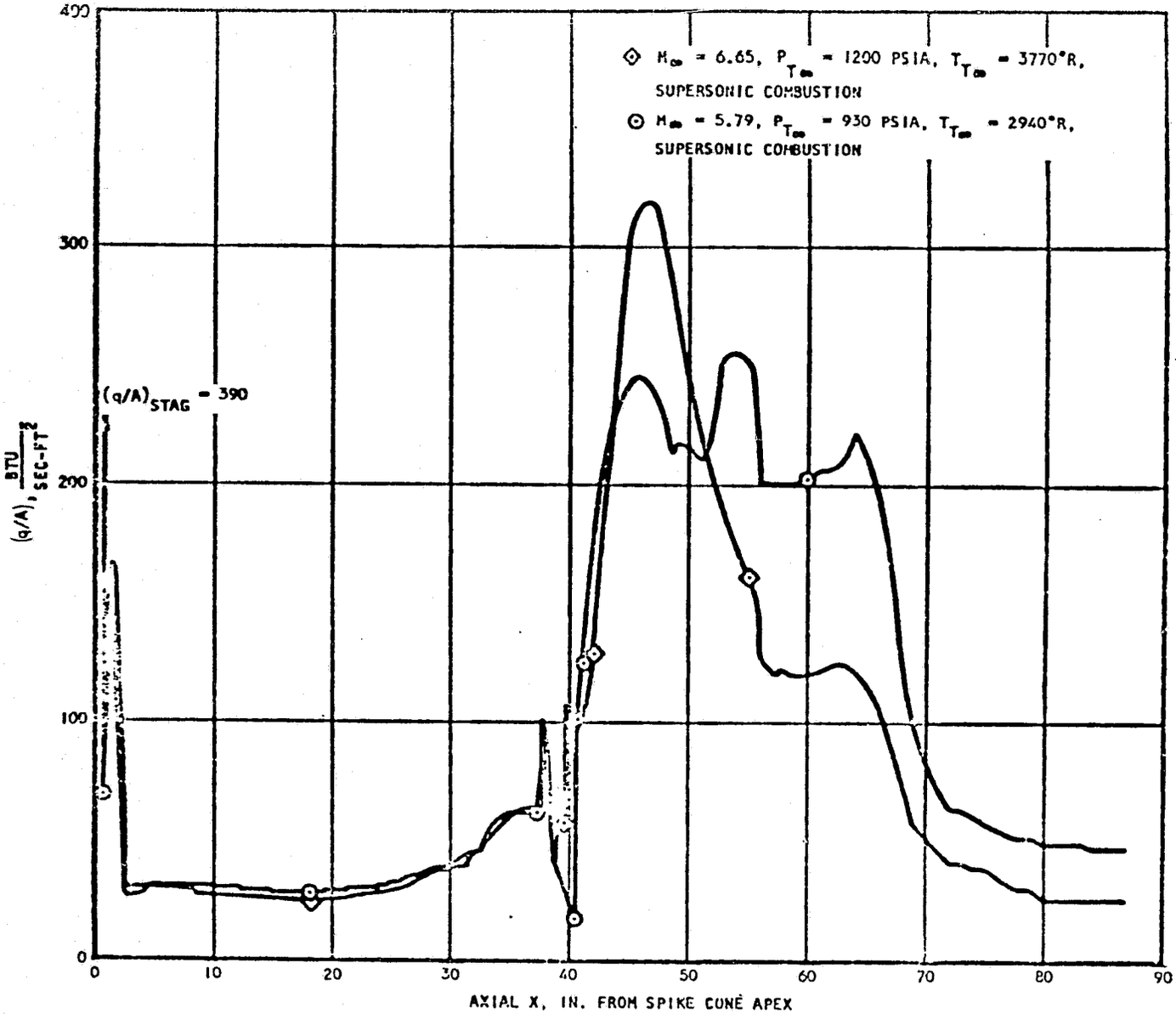

Figure 2.2-2. Heat Flux Distribution on Centerbody

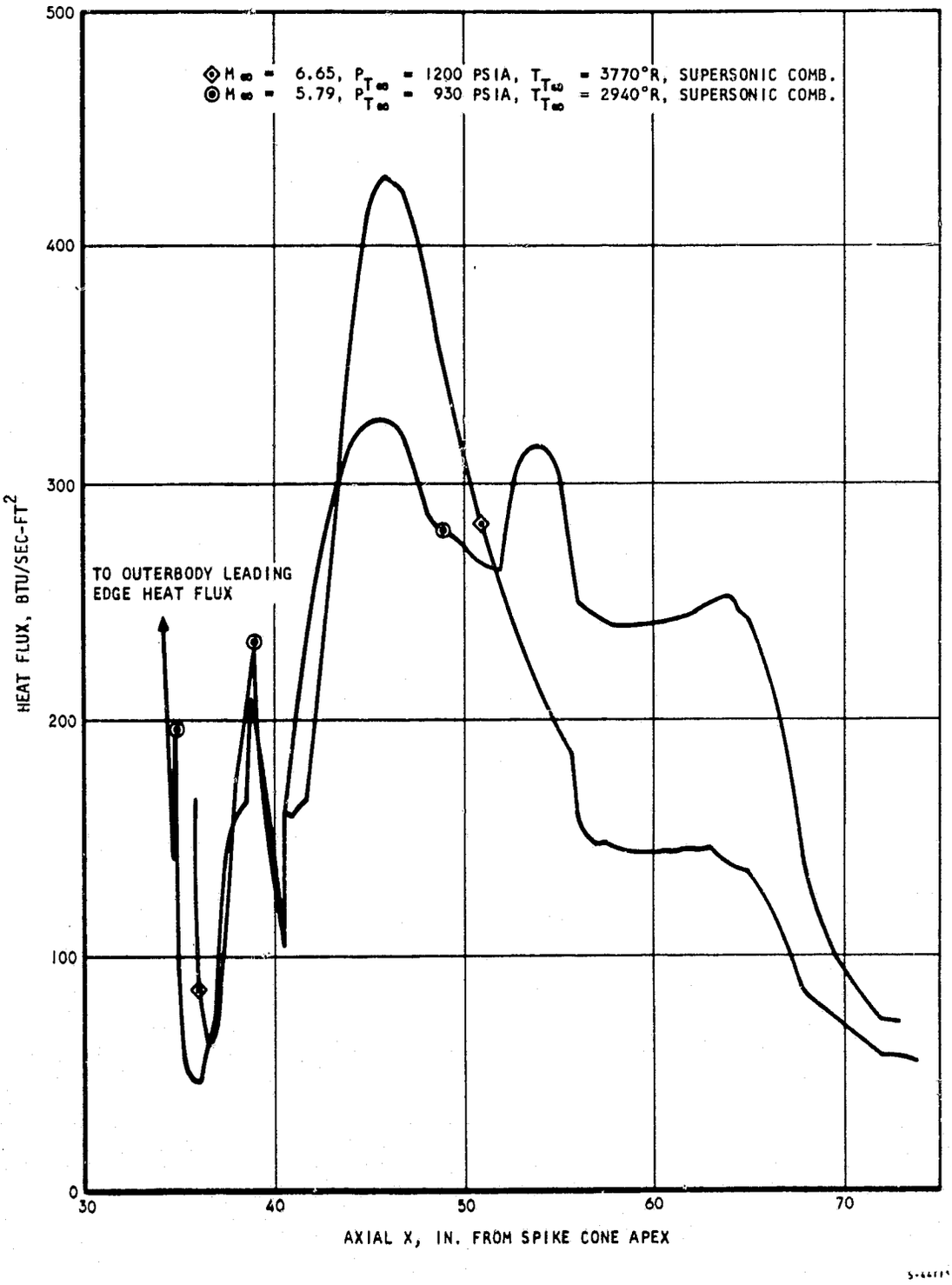

Figure 2.2-3. Heat Flux Distribution on Outerbody

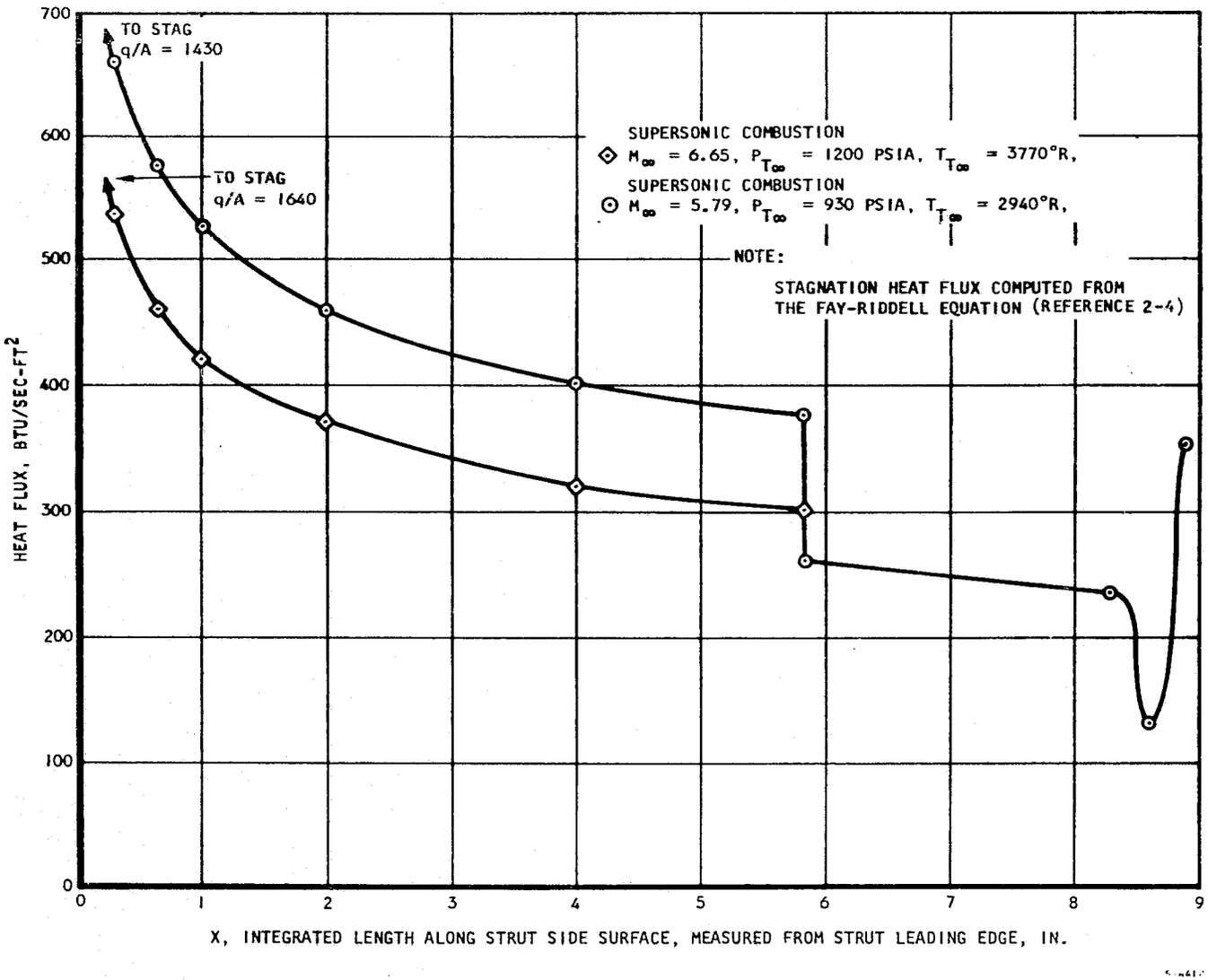

Figure 2.2-4. Heat Flux Along Strut Side Surface

TABLE 2.2-2

COMPARISON OF RESULTS BETWEEN USE OF FLAT-PLATE AND DUCT-FLOW HEAT TRANSFER EQUATIONS

Station	Flat Plate Heat Flux (HI760) Btu/sec ft^2				Duct Flow Heat Flux Btu/sec ft^2		$\frac{(q/A)_{Duct}}{(\frac{q}{A})_{F.P.\ Centerbody}}$		$\frac{(q/A)_{Duct}}{(\frac{q}{A})_{F.P.\ Outerbody}}$	
	Centerbody		Outerbody							
	M_∞ = 5.79	M_∞ = 6.65	M_∞ = 5.79	M_∞ = 6.65	M_∞ = 5.79	M_∞ = 6.65	M_∞ = 5.79	M_∞ = 6.65	M_∞ = 5.79	M_∞ = 6.65
43	209	196	294	285	213	204	1.020	1.04	0.73	0.72
45	242	298	327	413	248	322	1.026	1.08	0.76	0.78
46.5	244	319	322	429	-	348	-	1.09	-	0.81
50	215	244	274	313	208	245	0.970	1.005	0.85	0.78
55	250	160	305	197	235	149	0.940	0.934	0.76	0.76
60	202	120	241	144	179	105	0.885	0.872	0.74	0.73
65	210	118	242	135	187	104	0.890	0.881	0.77	0.77

Notes:
1. M_∞ = 5.79 corresponds to the inlet gas conditions of M_∞ = 5.79, P_{T_∞} = 930 psia, T_{T_∞} = 2940°R, vitiated air
2. M_∞ = 6.65 corresponds to the inlet gas conditions of M_∞ = 6.65, P_{T_∞} = 1200 psia, T_{T_∞} = 3770°R, vitiated air
3. Heat flux was computed with T_{wall} = 1000°R

2 to 10 percent, the laminar stagnation heat flux could increase by as much as 80 percent. The turbulence intensity is defined as

$$\frac{\sqrt{(\overline{u'})^2}}{u} = \sqrt{\frac{1}{3}\left[(u')^2 + (v')^2 + (w')^2\right]} / u$$

where u is the mean flow velocity, and u', v', and w' are the fluctuating components of the flow velocity in the three Cartesian coordinates.

Data submitted by NASA-LeRC subsequent to the leading edges cooling design indicated that the upstream flow turbulence intensity was less than 0.3 percent over the test range of Mach 4 through Mach 7 anticipated in the Plum Brook facility. Figure 2.2-5 presents the data submitted by LeRC. These low turbulence levels indicate that the 1.8 factor is conservative and that under actual test conditions, the extreme heating will not be experienced at the inlet spike tip, leading edge of the outerbody, and at the leading edge area of the outer cowl body support assembly. Turbulent airflow conditions are predicted, however, in front of the struts, since fuel injection and combustion will cause turbulence. Here the 1.8 factor was retained with the Fay-Riddell flux, but based on Plum Brook Mach 6 conditions ($1.8 \times 1230 \simeq$ Btu/sec ft^2). This is equivalent to a turbulence factor of 1.35 based on OAL Mach 6.65 conditions ($1.35 \times 1640 = 2210$ Btu/sec ft^2) shown in Figure 2.2-4.

In addition to upstream air turbulence, the cowl and support leg leading edges were subjected to localized heating from shock impingement. This impingement is described in Section 2.2.1.6 below. Numerical values of all leading edge heat fluxes are presented in Section 2.2.3 along with thermal performance results.

2.2.1.6 Localized Heating Areas

In addition to the overall and leading edge aerodynamic heating summarized above, several areas of the engine were expected to have high localized heating. This heating was created by local pressure rises resulting from shock impingement and flow recirculation. In turn, impingement and recirculation were caused generally by surface protuberances in the supersonic hot gas flow path. Though creating high local heat fluxes, these localized heating areas did not substantially increase overall engine heat load.

Each of these areas were analyzed individually and in conjunction with the local component thermal performance. Because of this, a general discussion of the magnitude of these local heating areas is deferred until Section 2.2.3, however, the location and type of these local heating areas are listed in Table 2.2-3 below.

2.2.2 Coolant System Design

This section summarizes the engine coolant system design. The object of the design was to maintain engine structural integrity within facility coolant

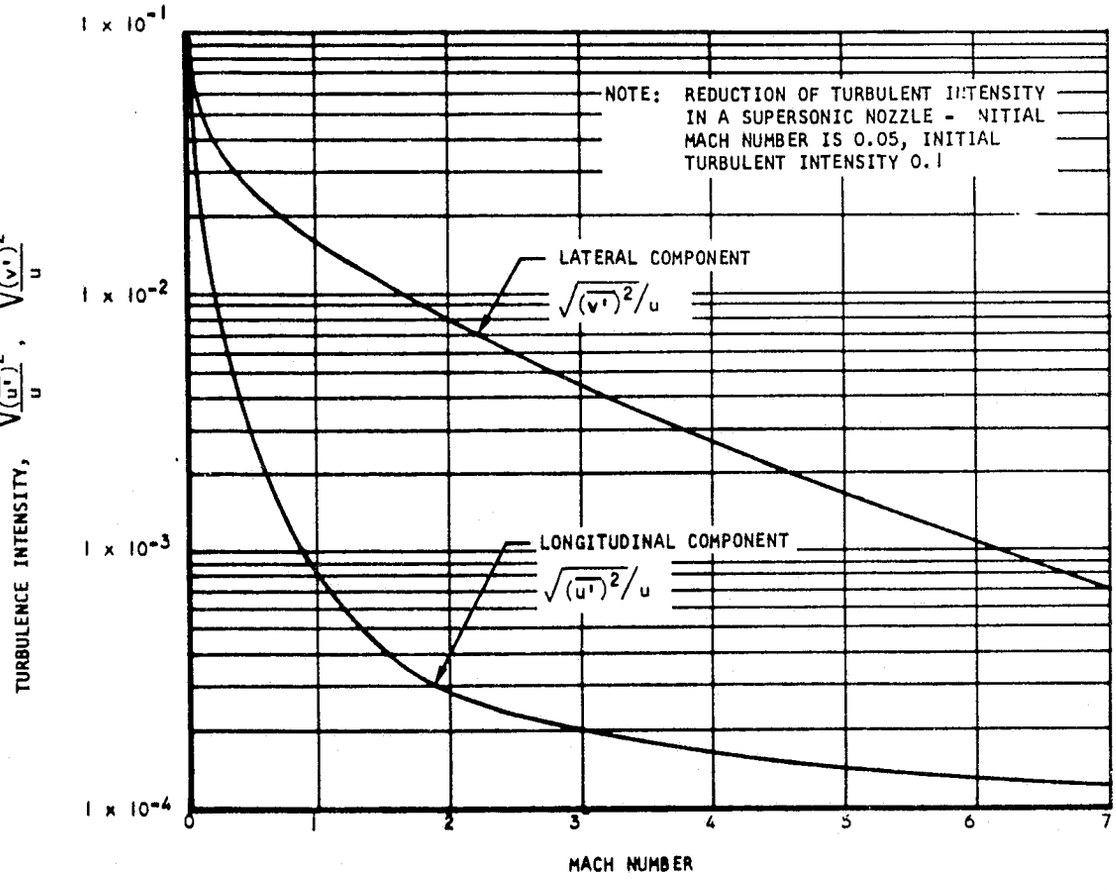

Figure 2.2-5. Flow Turbulence Intensity Upstream of AIM (Plum Brook Facility

TABLE 2.2-3

SUMMARY OF AIM LOCALIZED HEATING AREAS

Location of Localized Heating	Cause of Localized Heating
(1) Centerbody and outerbody from Sta. 39 to 46 in.	(a) Cowl leading edge shock impingement and reflections
	(b) Spike compression wave impingement and reflections
	(c) Pressure rise due to fuel injection
(2) Centerbody and outerbody from Sta. 40.4 to 55.9 in.	Fuel injection flow acting as a surface protuberance.
(3) Centerbody at Sta. 56 in.	Recirculation at end of spike (rearward facing step)
(4) Centerbody, outerbody and struts at strut leading edges	Strut leading edges acting as surface protuberance
(5) Cowl leading edge	Spike bow shock wave impingement
(6) Outer cowl at support leg leading edges	Support leg leading edges acting as surface protuberance
(7) Support leg leading edges	Interaction of cowl leading edge bow shock and support leg leading edge shock
(8) Support leg sides	Local flow separation

capabilities (water flow rate and pressure drop) and allow for adequate aerothermodynamic test measurement. A maximum allowable (Nickel-200) hot shell temperature of 1525°F was selected to maintain structural integrity for the minimum cycle life requirement of 100 cycles.

Presented below are a description of the coolant system flow routes and the coolant flow rate and pressure drop requirements.

2.2.2.1 Coolant Flow Route Descriptions

The five basic flow routes of the engine are presented in Figure 2.2-6. Details of two of these, the strut leading edge and strut sides flow routes, are shown in Figures 2.2-7 and 2.2-8, respectively.

The outer cowl and support legs are divided into four flow routes--upper cowl and outer cowl leg sides, lower cowl and inner support leg sides, and a support leg leading edge flow route for each of the two support legs. These flow routes are shown in Figures 2.2-9 and 2.2-10.

2.2.2.2 Coolant System Requirements

The coolant flow rate and pressure drop requirements for the above flow routes, and estimates of the flow route water heatups are presented in Table 2.2-4. These requirements are for the design point heating conditions described in Section 2.2.1.

2.2.3 Thermal Design Performance

The thermal performance of the AIM was performed using the aerodynamic heating data described in Section 2.2.1 and the coolant system described in Section 2.2.2. A complete evaluation of thermal performance was required to provide inputs to the engine structural evaluation described in Section 2.3. This evaluation, in turn, verified engine structural integrity for the minimum cycle life.

Presented below are thermal performance results of, first, the overall engine (excluding leading edges and localized heating) and then results of individual engine components (centerbody, outerbody, combustor, outer cowl, and support assembly) where leading edge and localized heating areas are considered.

2.2.3.1 Overall Thermal Performance

The overall temperature levels of the engine were calculated using the heat flux distributions in Figures 2.2-2 and 2.2-3, the water flow rate schedule in Table 2.2-4, and the coolant passage geometry shown in the attached AiResearch Drawing 350501, sheet 2. Results are presented in Figures 2.2-11 and 2.2-12, respectively, for OAL freestream Mach numbers of 6.65 and 5.79.

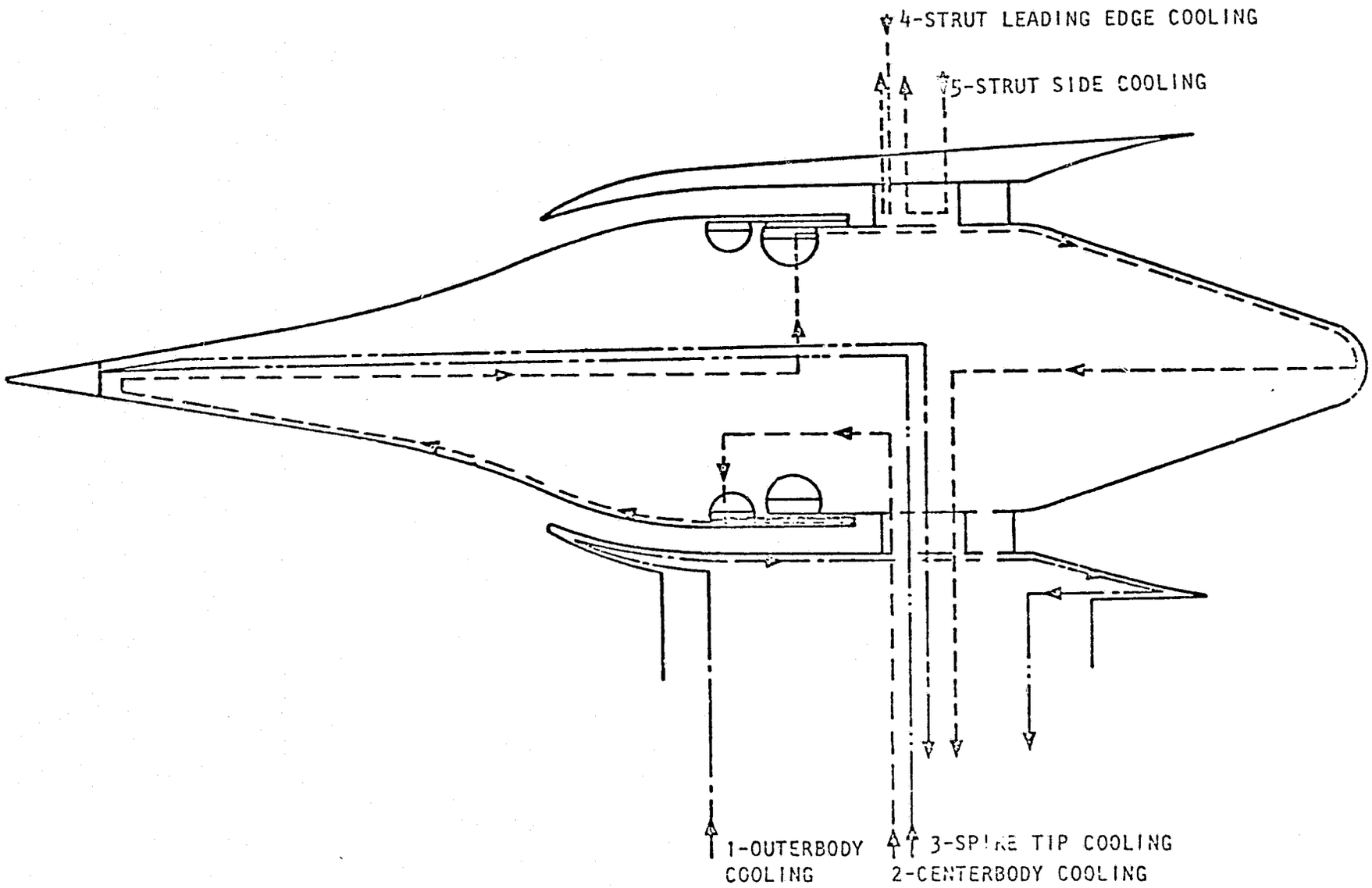

Figure 2.2-6. AIM Cooling Circuits

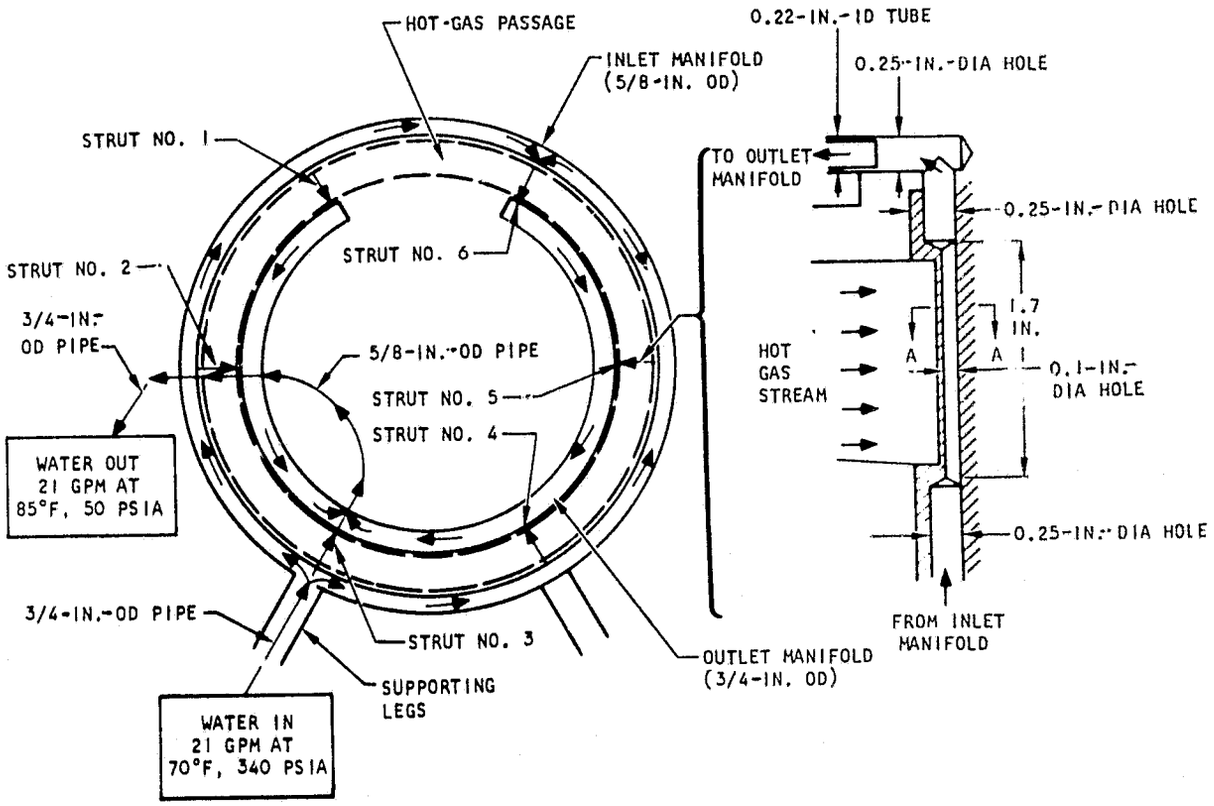

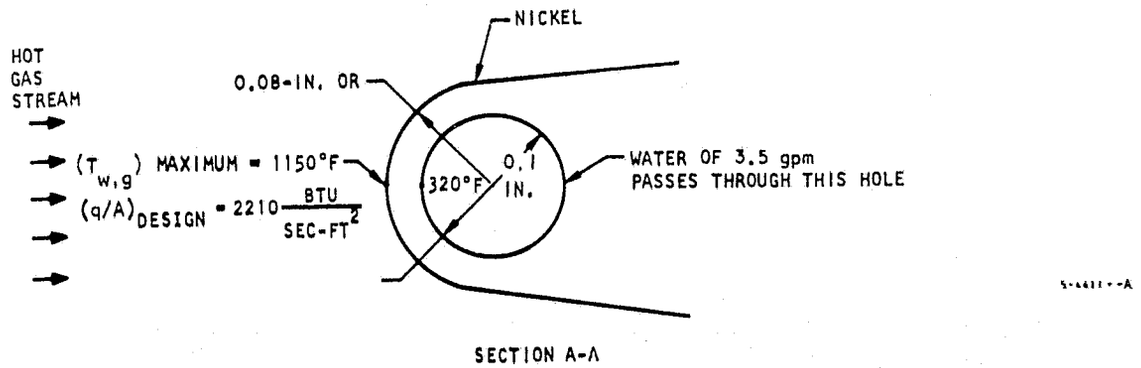

SECTION A-A

NOTE:
THE DESIGN HEAT FLUX FOR THE LEADING EDGE WAS TAKEN 1.35 TIMES THE FAY-RIDDELL STAGNATION HEAT FLUX (SEE FIGURE 2.2-4)

Figure 2.2-7. Strut Leading Edge Cooling

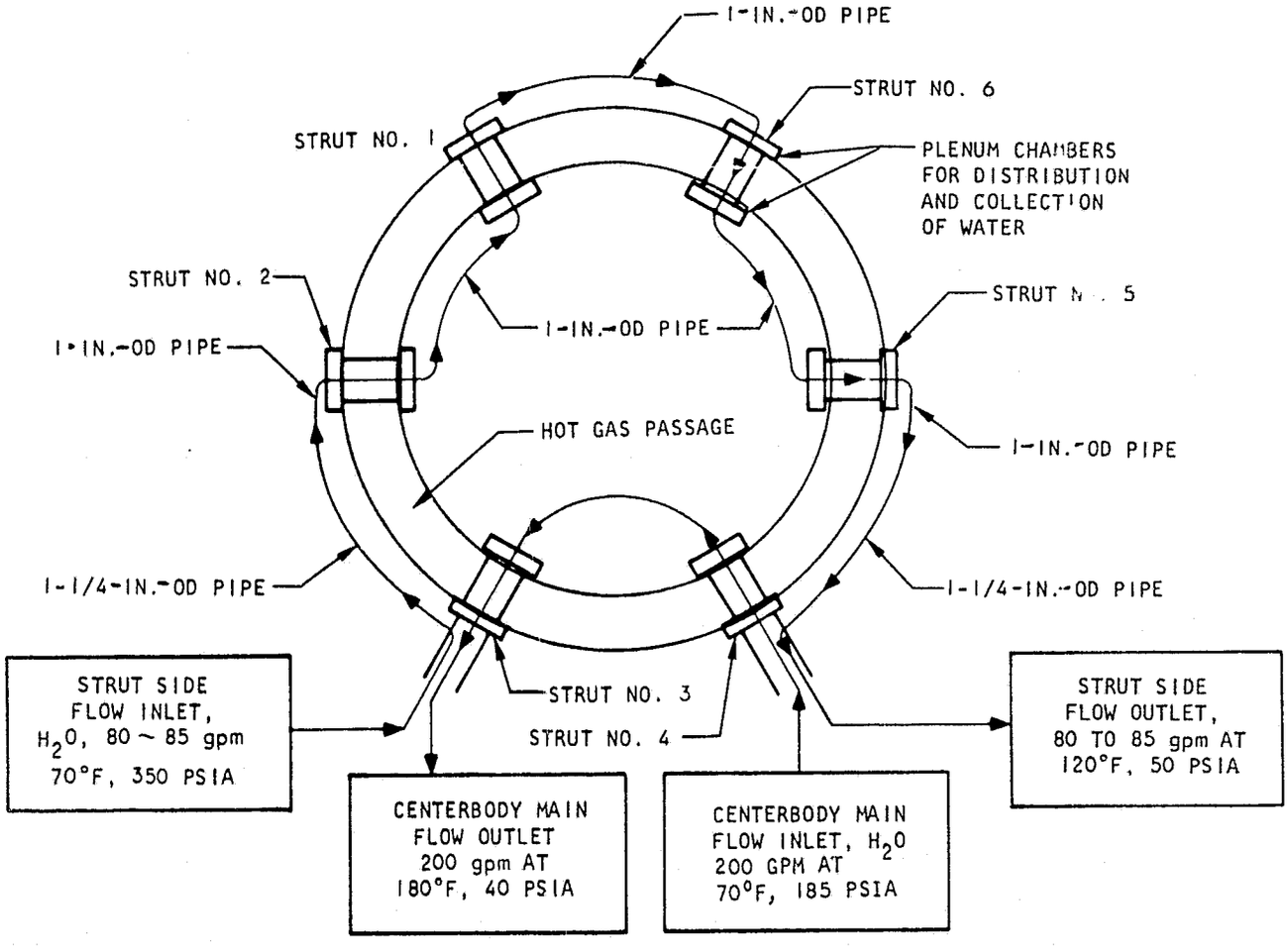

NOTES:

(a) STRUT SIDE SURFACES ARE COOLED BY WATER FLOWING THROUGH A NUMBER OF HOLES AND ANNULAR PASSAGES ALONG THE CIRCUMFERENCE OF THE STRUTS.

(b) HEAT FLUX DISTRIBUTION ON THE STRUT SIDE SURFACE IS SHOWN IN FIGURE 2.2-4
(c) MAXIMUM COOLANT SIDE METAL TEMPERATURE IS 300°F.
(d) MAXIMUM HOT GAS SIDE METAL TEMPERATURE IS 1100°F.
(e) FREE FLOW AREA AT STRUTS = 0.63 $IN.^2$ FOR STRUTS NO. 1, 2, 5, 6
= 1.7 $IN.^2$ FOR STRUTS NO. 3, 4.
(f) STRUTS NO. 3 AND 4 ARE COOLED BY MAIN CENTERBODY COOLANT FLOW.

Figure 2.2-8. Strut Side Surface Cooling

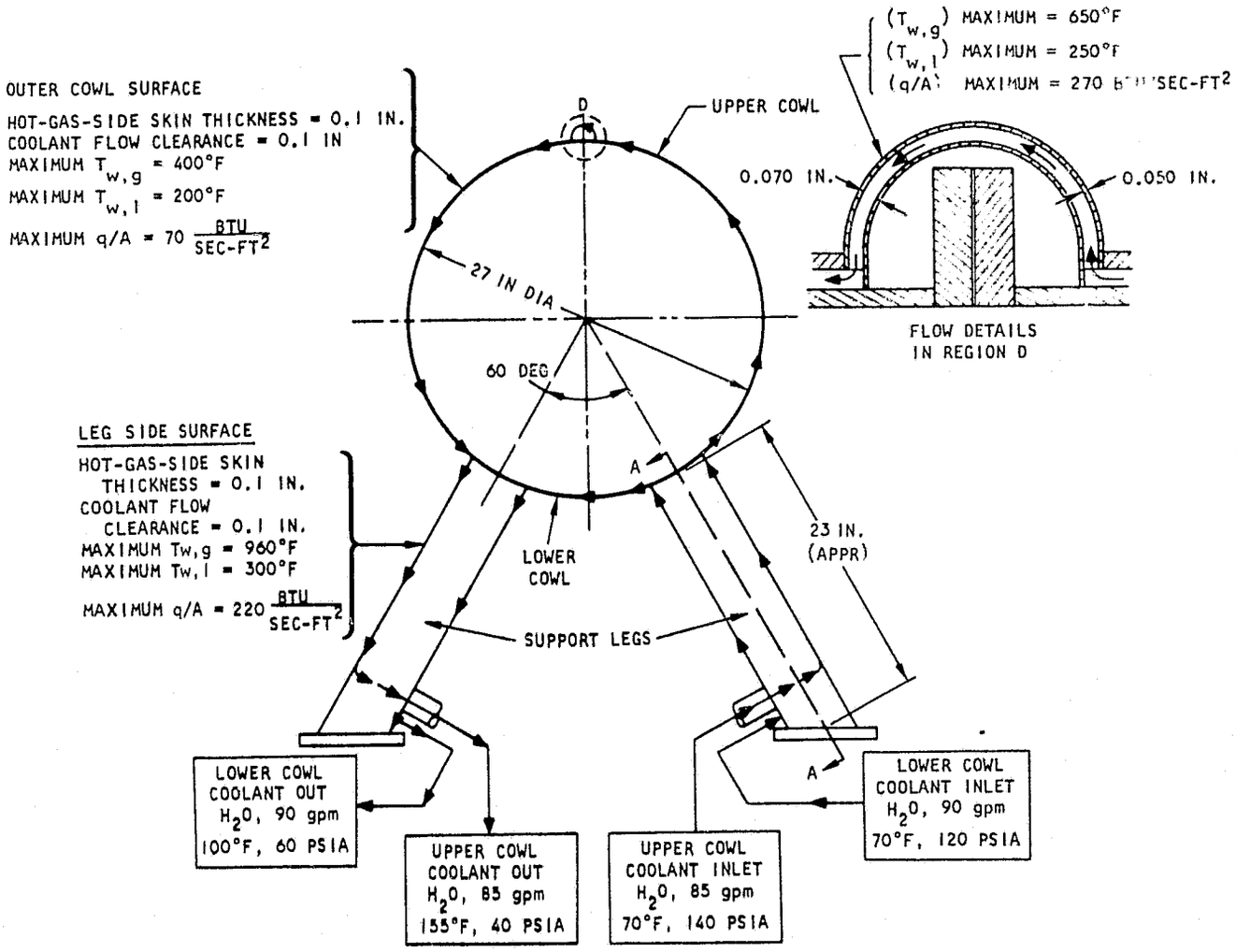

NOTES:

1) HOT GAS CONDITIONS FOR PLUM BROOK CONDITIONS (MACH 7, 1200 PSIA, 3800°R)
2) THE SKIN IN CONTACT WITH HOT GAS IS MADE OF STAINLESS STEEL

Figure 2.2-9. Cooling System of Outer Cowl and Support Leg Side Surface

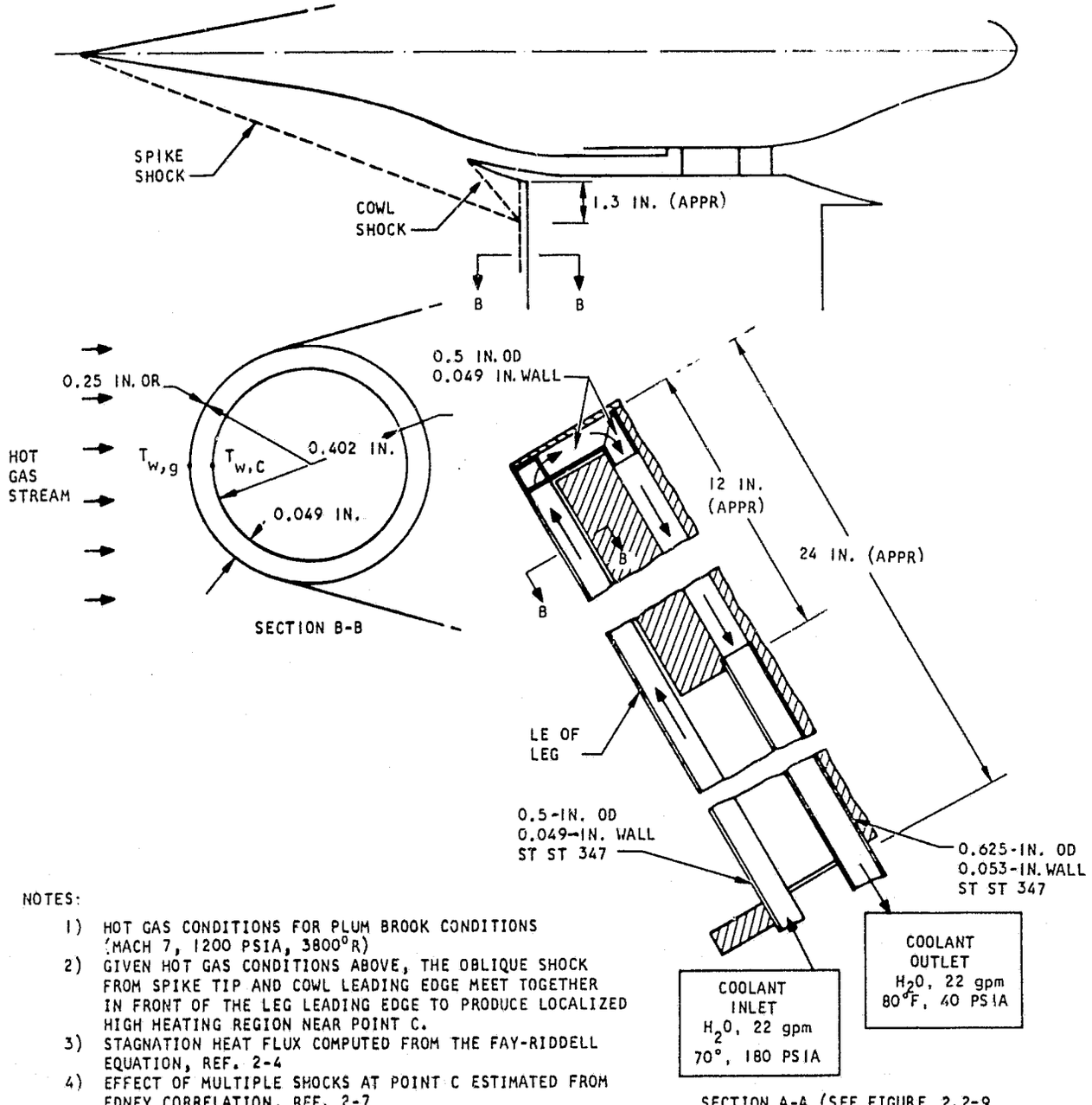

NOTES:

1) HOT GAS CONDITIONS FOR PLUM BROOK CONDITIONS (MACH 7, 1200 PSIA, 3800°R)
2) GIVEN HOT GAS CONDITIONS ABOVE, THE OBLIQUE SHOCK FROM SPIKE TIP AND COWL LEADING EDGE MEET TOGETHER IN FRONT OF THE LEG LEADING EDGE TO PRODUCE LOCALIZED HIGH HEATING REGION NEAR POINT C.
3) STAGNATION HEAT FLUX COMPUTED FROM THE FAY-RIDDELL EQUATION, REF. 2-4
4) EFFECT OF MULTIPLE SHOCKS AT POINT C ESTIMATED FROM EDNEY CORRELATION, REF. 2-7
5) THERMAL RESULTS SHOWN IN FIGURE 2.2-17.

Figure 2.2-10. Support Leg Leading Edge Cooling

TABLE 2.2-4

COOLING CIRCUIT

Circuit	Requirements					
	Gage			Actual		
	Flow, gpm	Inlet, psia	Outlet, psia	Flow, gpm	Inlet, psia	Outlet, psia
1. Outer Body	660	235	40	645	205	40
2. Centerbody	200	210	40	197	200	42
3. Spike Tip	7	225	70	9.2	248	78
4. Strut L.E.	21	360	50	20.3	415	41
5. Strut Side	85	350	50	78	350	46
6. OCB L.E.	22	260	40	22	192	52
7. OCB Fwd	15	135	40	15	140	38
8. OCB Aft	100	130	40	86	145	38
9. OCB Center	110	110	40	110	130	43

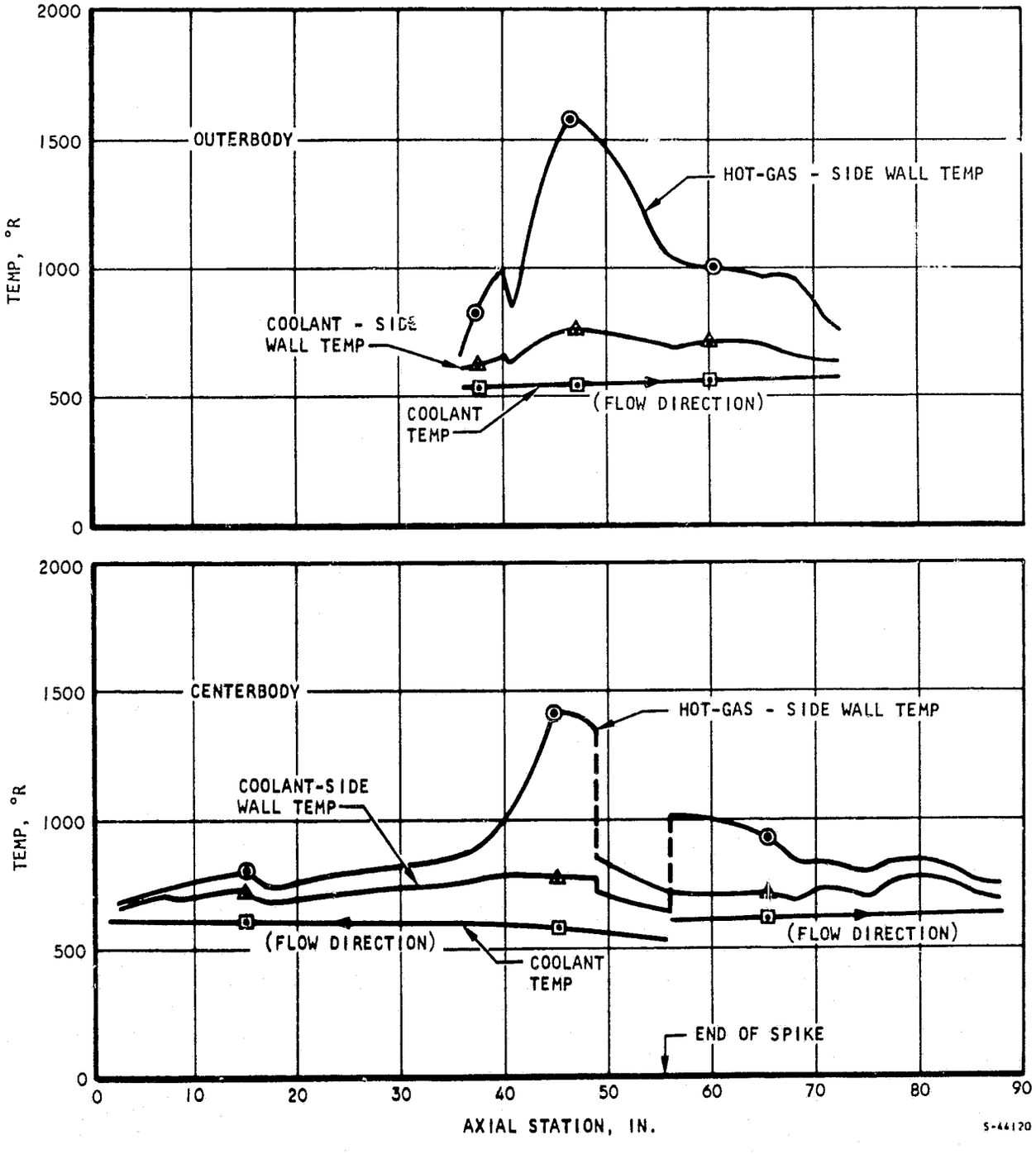

Figure 2.2-11. Wall and Coolant Temperatures for $M_\infty = 6.65$

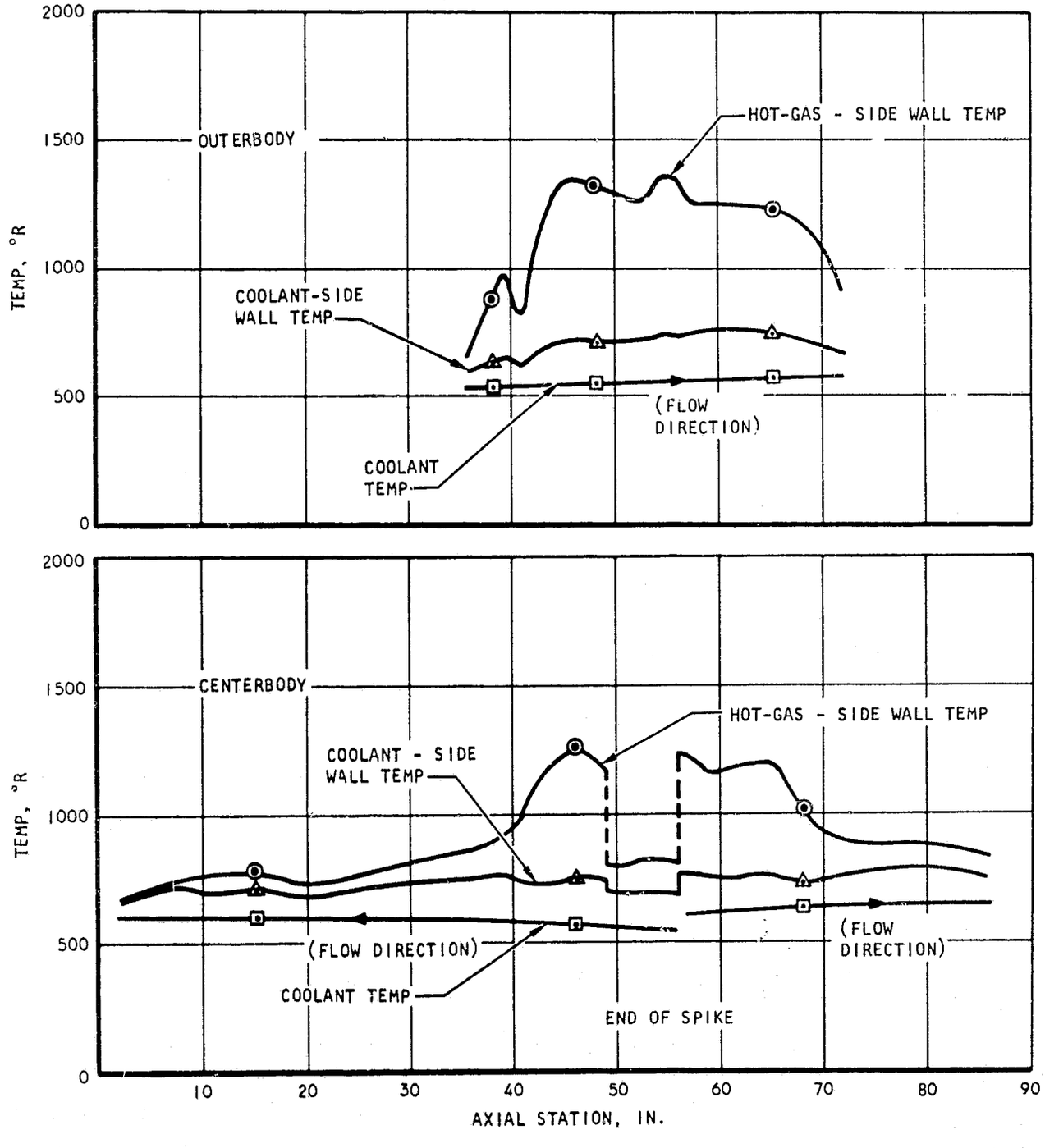

Figure 2.2-12. Wall and Coolant Temperatures for $M_\infty = 5.79$

2.2.3.2 Centerbody Thermal Performance

This section presents thermal results that are unique to the centerbody but not covered in Section 2.2.3.1, above.

2.2.3.2.1 Spike Tip

The zirconium copper spike tip section is cooled by a separate coolant circuit as shown in Figure 2.2-6 and attached AiResearch Drawing 350501, sheet 2. The stagnation point heat flux and hot wall temperature at the OAL freestream Mach number of 6.65 are 380 Btu/sec ft^2 and 995°F, respectively. With a 1.8 turbulence factor (see Section 2.2.1.6) the corresponding values are 632 Btu/sec ft^2 and 1148°F. For these latter values, the average water-wetted backside wall temperature is 285°F.

2.2.3.2.2 Spike Rearward-Facing Step

The end of the spike assembly located at Station 55.76 forms a rearward facing step for the oncoming supersonic air flow. This step produces a separation, followed by a free-mixing region, and then a reattachment to the surface further downstream on the innerbody. At the reattachment point, the flow is compressed, producing a recompression shock which results in an increased heat flux. The magnitude of the rise in heat transfer coefficient was calculated utilizing three methods (References 2-8, 2-9 and 2-10). A summary of results is presented in Figure 2.2-13 where it is noted that the maximum increase in the heat transfer coefficient ratio (h_b/h_a) is 1.3. An increase in heat flux to this level is well within the design heat transfer capability of the engine.

2.2.3.3 Outerbody Thermal Performance

This section presents thermal results that are unique to the outerbody but not covered in Section 2.2.3.1, above.

2.2.3.3.1 Cowl Leading Edge

In addition to stagnation point heating, the cowl leading edge was subject to upstream turbulence and shock-impingement effects. As discussed in Section 2.2.1.5, a multiplier of 1.8 was applied to the laminar stagnation heat flux to account for upstream turbulence. Though retained for design, this multiplier was later thought to be conservative due to low turbulence in the Plum Brook facility.

For optimum engine operation at Mach 5 and above, the translating spike was positioned so that the spike tip bow shock impinged directly on the cowl leading edge. Because of this, an impingement heating rate of ten-times the laminar stagnation value was estimated (References 2-4 and 2-11) to exist over a 0.003 in.-wide band of the 0.030 in. leading edge radius. The impingement effect was thought to laminarize the boundary layer at the impingement so the 1.8 turbulence factor was not applied here.

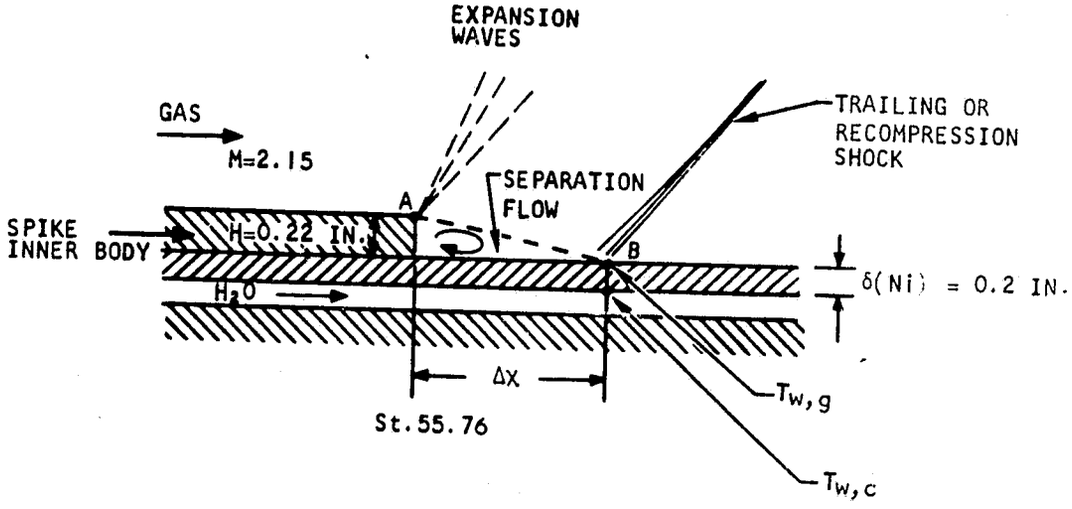

FREESTREAM CONDITIONS:

M_∞ = 6.65

P_{T_∞} = 1200 PSIA

T_{T_∞} = 3770°R

VITIATED INLET AIR

Reference	$\frac{\Delta X}{H}$	$\frac{h_B}{h_A}$	$(q/A)_B$ $\frac{Btu}{Sec\ Ft^2}$	$T_{w,g}$, °F	$T_{w,c}$, °F	T_{H_2O}, °F
Wuerer, et al (Reference 2-8)	5.5	1.3	190	610	262	160
Charwat, et al (Reference 2-9)	5.5	1.1	---	---	---	---
Smith, (Reference 2-10)	---	0.2	---	---	---	---
———	—	*2.0	277	800	300	160

*h_B/h_A = 2 is the upper limit below which no local boiling of coolant water is expected.

One-dimensional heat transfer analysis was used.

Figure 2.2-13. Heat Transfer Effects at Spike Cone-Innerbody Interface

Initially, OFHC copper was selected for the cowl leading edge tip section. However, after considering the effects of upstream turbulence and shock impingement, surface temperatures were beyond the capabilities of OFHC copper. Zirconium copper was then selected for its relatively high structural capabilities at temperatures anticipated with only a slight reduction in thermal conductivity.

The leading edge tip coolant passage is U-shaped. The coolant heat transfer coefficient was first calculated using the duct-flow heat transfer equation multiplied by a curvature factor of 1.55 as estimated from Mori's curved pipe flow correlation (Reference 2-12). Heat transfer analysis based on impingement cooling is also applicable here and is believed to be more appropriate than the use of duct flow analysis. Chupp's impingement cooling correlation (Reference 2-13) leads to a curvature multiplication factor of about 3. The net difference is utilizing these factors is approximately 100°F difference in the metal temperature on the coolant side only. Temperature at the tip of the cowl leading edge assembly is determined mainly by the hot gas conditions and very little effect was noted whether impingement cooling or duct flow cooling factors were used.

Based on the above heating and cooling considerations, the leading edge tip temperatures were calculated and results presented in Figure 2.2-14. For these results the more conservative factor of 1.55 was applied to the coolant heat transfer coefficient (duct flow).

2.2.3.3.2 Nozzle Shroud Assembly

The material selected for the trailing edge of the nozzle shroud assembly was initially OFHC copper but later changed to Nickel-200. This resulted from difficulties in joining OFHC copper to Nickel-200. The tip configuration was modified to accommodate the lower thermal conductivity of Nickel-200. A maximum gas side temperature of 1000°F and maximum coolant side temperature of 300°F was calculated. This was based on a heat flux of 44 Btu/sec ft^2 over the entire trailing edge surface and 100 Btu/sec ft^2 for the very tip of the trailing edge to account for the mild interaction when the internal and the external air flow converges.

2.2.3.4 Inlet and Combustor Thermal Performance

This section presents thermal results that are unique to the engine inlet and combustor. Though the inlet and combustor are formed by the hot shells of the innerbody and outerbody, the thermal results summarized below are common to both sides of the inlet and combustor.

2.2.3.4.1 Shock Impingement and Pressure Rises

In the inlet section of the engine, local gas pressure rises were predicted due to (1) impingement of the cowl leading edge bow shock on the centerbody, (2) impingement of the spike compression waves on the outerbody, and (3) fuel injection. Pressure rises due to fuel injection occurred downstream of the injectors. Thermal performance results in these areas are presented in Figure 2.2-15.

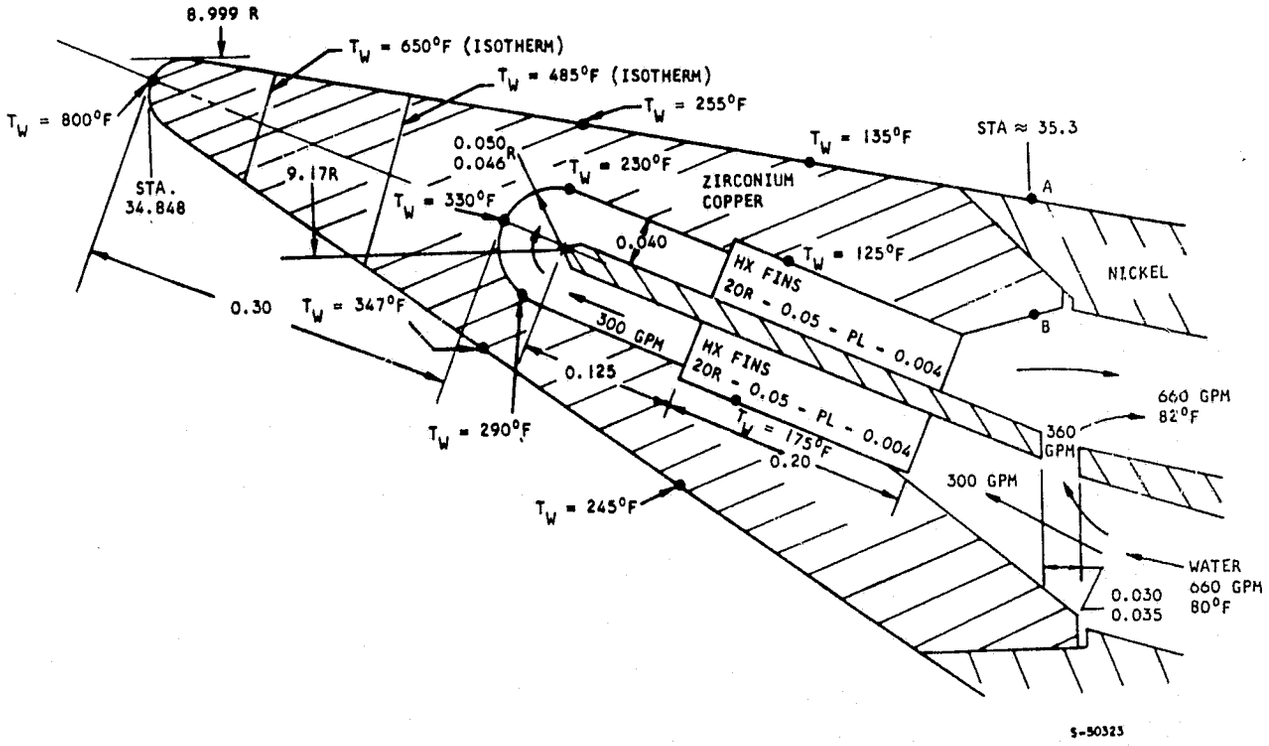

NOTES

1. DIMENSIONS IN INCHES
2. GAS CONDITIONS: M_∞ = 6.65, p_{T_∞} = 1200 PSIA, T_{T_∞} = 3770°R
3. SPIKE SHOCK IMPINGEMENT EFFECTS:
   $\frac{h(Peak)}{h(F-R)}$ = 10, h(Peak) = 0.171 x 10 = 1.71 Btu/sec/ft^2-°F
   ΔX(Peak Heating Width) = $\frac{2r_o}{20}$ = 0.003 in.
   h(F-R) = Fay-Riddell Stagnation Heat Transfer Coefficient with Spike Shock Inside Cowl Lip
4. MULTIPLICATION FACTOR DUE TO UPSTREAM AIR TURBULENCE EFFECT ON STAGNATION COEFFICIENT EXCEPT PEAK HEATING ZONE = 1.8 REFERENCE 2-6
   h_{STAG} = 0.171 x 1.8 = 0.308 Btu/sec ft^2-°F WITH SPIKE SHOCK INSIDE COWL LIP
   = 0.278 x 1.8 = 0.50 Btu/sec ft^2-°F WITH SPIKE SHOCK OUTSIDE COWL LIP
5. MULTIPLICATION FACTOR DUE TO CURVATURE ON COOLANT COEFFICIENT = 1.55 REFERENCE 2-12
   COOLANT HEAT TRANSFER COEFFICIENT AT IMPINGING POINT = 6.2 Btu/sec ft^2-°F
6. WHEN COMPRESSION WAVES FROM SPIKE COMPRESSION CORNER IMPINGES ON STATION = 35.3, T_A = 620°F, T_B = 360°F (ONE-DIMENSIONAL ANALYSIS)
7. $(\Delta p)_{WATER} \cong$ 50 PSI IN REGION SHOWN
8. THERMAL CONDUCTIVITY OF ZIRCONIUM-COPPER = 198 Btu/hr-ft^2-°F

Figure 2.2-14. Cooling of Outerbody Leading Edge Tip - Zirconium-Copper Tip

ORIGINAL PAGE IS
OF POOR QUALITY

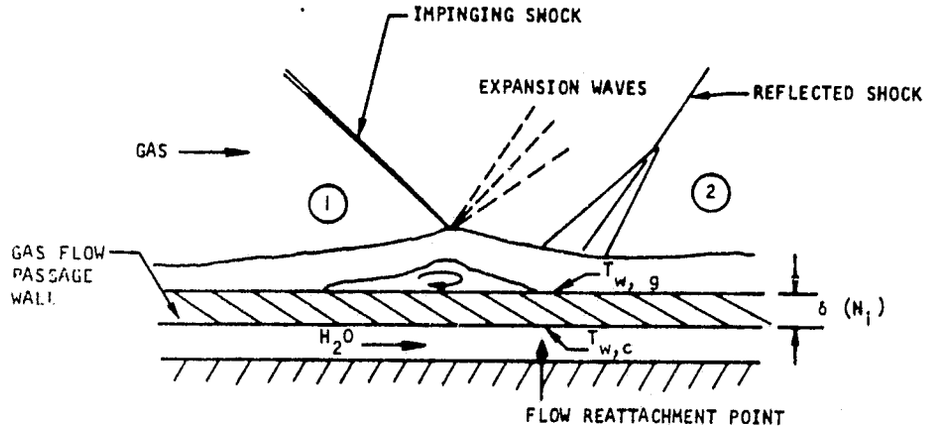

$$\frac{h_{peak}}{h_{(1)}} = \frac{P_2}{P_1}^{0.9}$$

(FROM REFERENCE 2-8)

FREESTREAM CONDITIONS:

M_∞ = 6.65

P_{T_∞} = 1200 PSIA

T_{T_∞} = 3770°R

VITIATED INLET AIR

Location	Station Numbers for P_{rise}	$\frac{P_2}{P_1}$	$\frac{h_{peak}}{h_{(1)}}$	$\frac{q}{A}$ peak, $\frac{Btu}{sec\ ft^2}$	$T_{w,g}$, °F	$T_{w,c}$, °F	T_{H_2O}, °F	$\delta(Ni)$, in.	Remarks
Centerbody	38 ~ 39	2.4	2.2	137	600	356	140	0.2	Cowl shock impingement slight water boiling predicted
Outerbody	36 ~ 39	9.95	7.9	500	1320	300	85	0.23	Impingement of compressor waves from spike compressor corner, no water boiling predicted.
Centerbody	40 ~ 46	5.0	4.25	500	1240	335	125	0.215	Pressure rise due to fuel injection from Injectors 1A and 1B
Outerbody	40 ~ 46	5.0	4.25	625	1525	330	90	0.21	Pressure rise due to fuel injection from Injectors 1A and 1B
Centerbody	---	3.0	2.7	---	---	---	---	---	This is due to fuel injection from Injectors 2A, 2B, and 4, and less heat flux is expected than that due to Injectors 1A and 1B

Note: One-dimensional heat transfer analysis was used.

Figure 2.2-15. Shock Impingement Effect

2.2.3.4.2 Fuel Injectors

In addition to creating pressure rises downstream of injection, injecting fuel into the supersonic air stream effectively produces a local surface protuberance near the wall. This causes flow separation upstream of the fuel injectors and an increased heat flux similar to that for shock impingement. Evidence of this reaction was observed during combustor testing at OAL and during the two-dimensional combustor rig testing.

The magnitude of the peak heat fluxes was determined from the available protuberance correlations (References 2-12 and 2-14). The shape of the interacting shocks and flow separation was constructed from Reference 2-15. Results of the thermal analyses are presented in Figure 2.2-16.

2.2.3.4.3 Struts

The struts are installed to position the centerbody with respect to the outerbody. The general thermal performance of the struts leading edge and sides, respectively, is summarized in Figures 2.2-7 and 2.2-8 of Section 2.2.2.1.

In addition, the strut leading edges are surface protuberances which create separation of hot gas flow and an associated pressure rise and higher heat flux. Analysis of this region was performed utilizing the heat flux associated with the outerbody, because analyses had indicated a higher heat flux on the outerbody side than on the innerbody side at the same axial station. The mechanical construction of the engine required a slotted joint in this area. Figure 2.2-17 presents the configuration of the joint and the results of the analyses which were based on References 2-14 and 2-17. Although results indicate that some local boiling will occur and surface temperatures will be higher than unaffected adjacent areas, the structural design limits of the engine will not be exceeded.

2.2.3.4.4 Combustor Transient Response

A transient analysis of the innerbody and outerbody hot shells was performed to determine the thermal response to steady state at the onset of combustion. The combustor shells were initially at 80°F and then a step change to combustion at a fuel equivalence ratio of 1.0 was imposed. Results summarized in Table 2.2-5 indicate that the time to steady state is in the order of 4 to 9 seconds depending on location.

2.2.3.5 Outer Cowl and Support Assembly

The heat transfer analyses of the outer cowl and support assembly were performed for the Plum Brook facility conditions of Mach 7, 1200 psia, and 3800°R. In addition to the overall heating, special consideration was given to shock interaction, surface protuberances, upstream turbulence, and airflow field created by the particular configuration of this structure.

Selected results on the outer cowl surface and leg-side surfaces are presented in Figure 2.2-9 (Section 2.2.2.1). Results of analyses for the above areas under special consideration are presented in Figure 2.2-18. The shock impingement on the leading edge of the support structure produces a

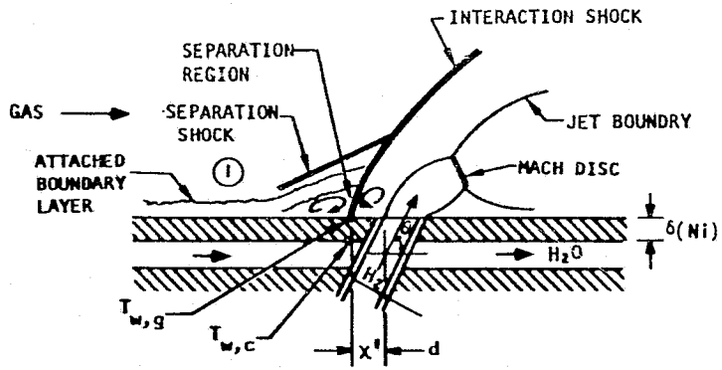

FREESTREAM CONDITIONS:

M_∞ = 6.65

P_{T_∞} = 1200 PSIA

T_{T_∞} = 3770°R

VITIATED INLET AIR

Location	Injector	Injector Station	θ, Deg	M_1	$\frac{x'}{d}$	$\frac{h_{peak}}{h_{①}}$	$(q/A)_{peak}$, $\frac{Btu}{Sec\ Ft^2}$	$T_{w,g}$, °F	$T_{w,c}$, °F	T_{H_2O}, °F	δ(Ni), in.	d, in.
Centerbody	1A	40.5	60	3.47	3.8	1	120	720	240	140	0.19	0.1
Outerbody	1B	41.37	60	3.47	0.97	2.6	400	990	255	85	0.2	0.1
Outerbody	2A	48.5	90	1.69	0.89	1.54	448	1080	274	90	0.2	0.16
Outerbody	2B	51.0	90	1.924	0.707	1.92	427	1040	265	90	0.2	0.232
Outerbody	4	44.5	90	1.51	1.56	1.0	380	940	250	90	0.2	0.16

Notes: (1) $h_{①}$ = Heat transfer coefficient in upstream undisturbed flow

(2) N_ρ local boiling of the coolant water is predicted

(3) One-dimensional heat transfer analysis was used

Figure 2.2-16. Fuel Injection Effects

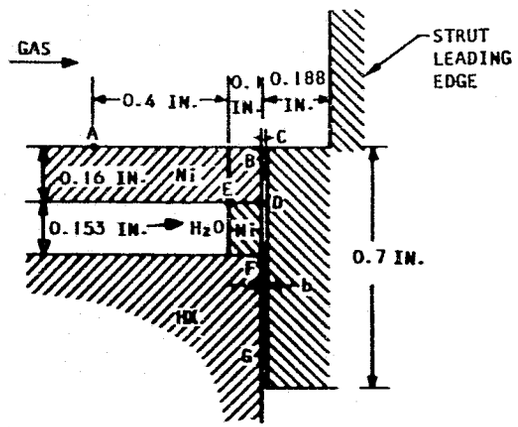

FREESTREAM CONDITIONS:

(I) M_∞ = 6.65, P_{T_∞} = 1200 PSIA, T_{T_∞} = 3770°R, VITIATED INLET AIR

(II) M_∞ = 5.79, P_{T_∞} = 930 PSIA, T_{T_∞} = 2940°R, VITIATED INLET AIR

Freestream Conditions	Local M	h_B/h_A	*With T_{wall} = 1000°R $(q/A)_A$ Btu/sec ft²	*With T_{wall} = 1000°R $(q/A)_B$ Btu/sec ft²	b, in.	Actual q/A, Btu/Sec Ft² A	Actual q/A, Btu/Sec Ft² B	Actual q/A, Btu/Sec Ft² C	T_A, °F	**T_B or T_C, °F	T_D, °F	***T_E, °F	T_F, °F	T_G, °F
I (M_∞ = 6.65)	2.30	1.61	149	240	—	—	—	—	—	—	—	—	—	—
II (M_∞ = 5.79)	1.67	1.24	274	340	0.002	264	220	755	680	1850	1095	408	741	885
					0.003	264	228	725	678	1756	1139	412	814	975

Notes:

* This is for comparison only. Subsequent analysis was performed for gas conditions (II), because $(q/A)_B$ is larger with gas conditions (II)

** Points B and C are the identical point except that Point B refers to the flat plate side and Point C to the slot side.

*** Local boiling of coolant water is expected near Point E. The values shown here are those without boiling.

Figure 2.2-17. Heating Effects Resulting from Struts

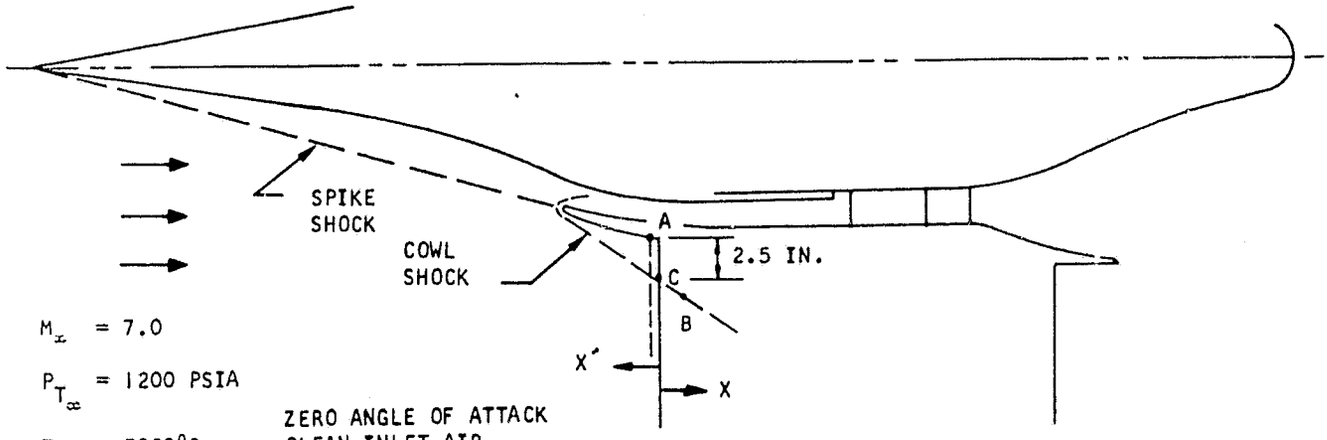

		q/A, Btu/sec Ft^2	$\frac{h_{gas}}{h_{F-R}}$	$T_{w,g}$, °F	$T_{w,c}$, °F	δ, in.	Remarks
Leg Leading Edge X = 0	At Point C	1900	19.7	1720	330	0.050	2-D Analysis
	Above C	430	3.2	1020	240	0.050	1-D Analysis
	Below C	267	1.8	680	195	0.050	1-D Analysis
Point B: Leg Side Cowl Shock Sweeping X = 1 in.		223	$\frac{h_{gas}}{h_l}$ = 4	1040	250	0.109	1-D Analysis, Local flow separation was assumed
Point A: Outer Cowl, Peak Heating X' = 0.025 in.		512	$\frac{h_{gas}}{h_o}$ = 12.7	1330	190	0.109	2-D Analysis, Peak heating is due to local protuberance

Notes:
- q/A = Local heat flux
- h_{gas} = Local gas side heat transfer coefficient
- B_{F-R} = Fay-Riddell stagnation heat transfer coefficient in cowl-shock free region (below Point C)
- h_l = Heat transfer coefficient on leg side surface at X = 1 in. Outside cowl-shock sweeping line (below Point B)
- h_o = Flat plate heat transfer coefficient on cowl surface upstream of Point A where air flow is not disturbed by presence of legs
- $T_{w,g}$ = Gas side wall temperature
- $T_{w,c}$ = Coolant side wall temperature
- δ = Wall thickness of stainless steel in contact with gas flow

Figure 2.2-18. Heat Flux and Wall Temperatures of the Outer Cowl and Support Legs

TABLE 2.2-5

COMBUSTOR TRANSIENT RESPONSE TIME

RESPONSE TIME FOR WALLS TO REACH STEADY-STATE THERMAL CONDITIONS FOR GAS CONDITIONS OF $M_\infty = 6.65, P_{T\infty} = 1200$ PSIA, $T_{T\infty} = 3770^\circ R$, AND ϕ (COMBUSTION) = 1						
	Centerbody			Outerbody		
Station, in.	62	67	72	62	67	72
Local total gas temp, $^\circ R$	4800	4800	4800	4800	4800	4800
Nickel wall thickness, in.	0.20	0.20	0.20	0.22	0.28	0.20
Water flow rate, gpm	200	200	200	660	660	500
Steady-state response time, sec	4.4	5.3	8.4	4.1	5.3	7.5

localized peak heat flux near the shock impingement point. Estimates made, indicated that the peak heat transfer coefficient could be 19.7-times larger than that calculated utilizing laminar stagnation heat transfer coefficient.

2.2.4 Fuel System Performance

The calculated pressure drop of each of the fuel systems is shown in Figure 2.2-19. The analysis was performed using fuel injector discharge coefficients of 0.60 and 1.00, scheduled maximum flow rates, and utilizing the various manifold systems necessary to obtain the fuel injector combination desired for test. See Figure 2.2-20 for manifold configuration. Various factors influence the exact discharge coefficient including the effects of cross-flow of the supersonic and near-sonic airflow. The ranges calculated were to be used as guidelines during test.

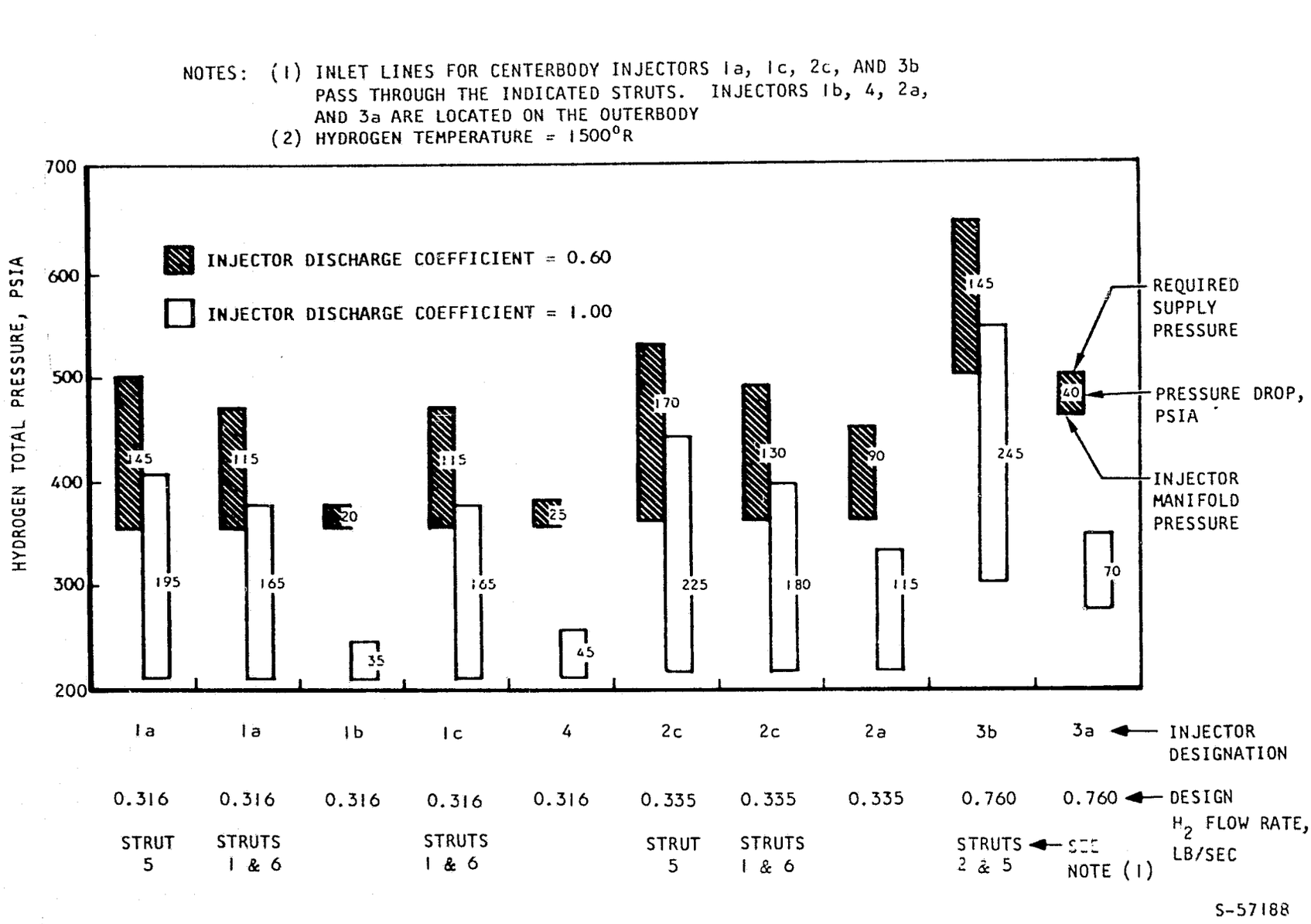

Figure 2.2-19. AIM Hydrogen Injector Lines Pressure Drop Summary

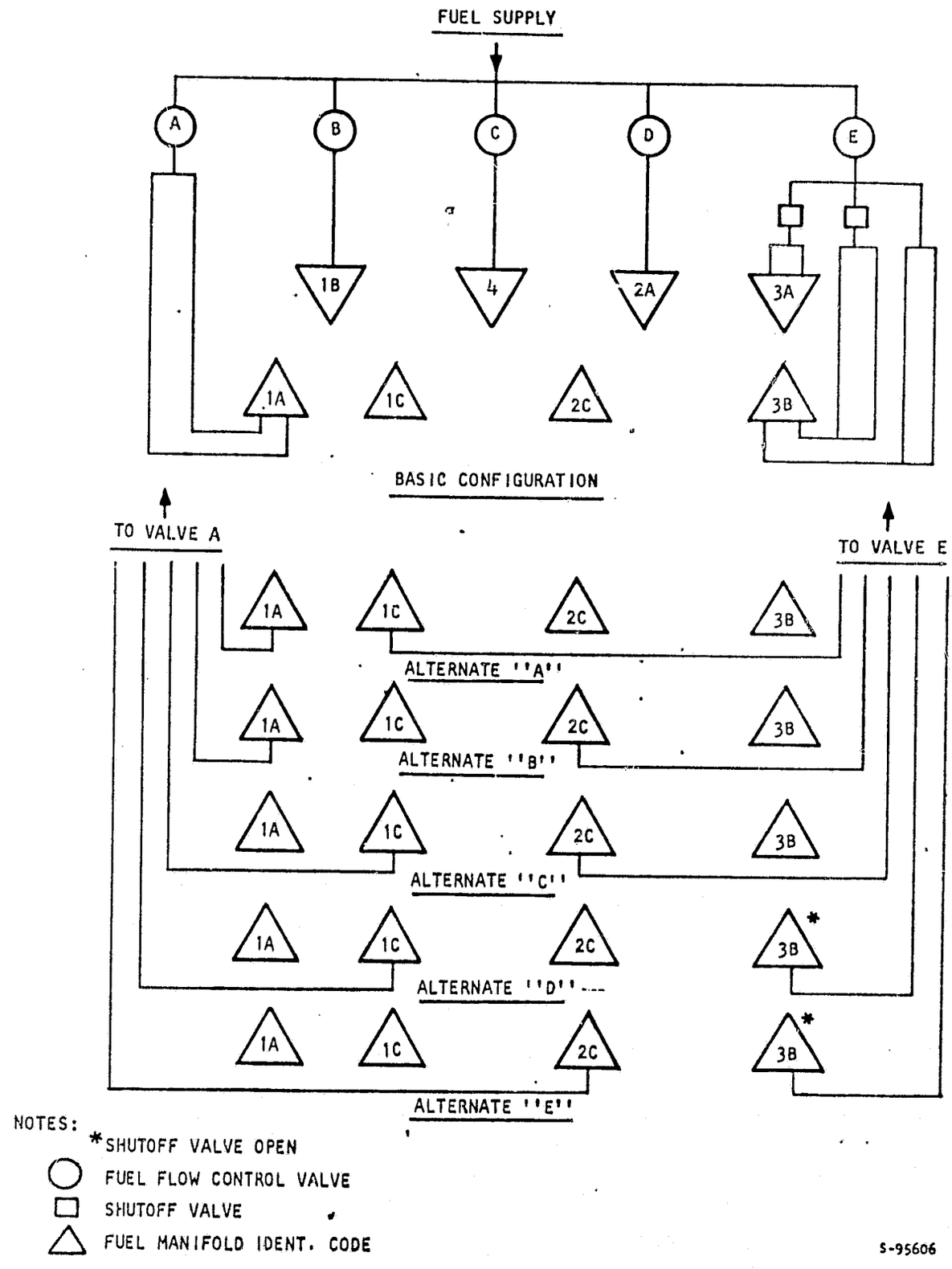

Figure 2.2-20. AIM Fuel System Schematic

2.3 STRUCTURAL

The AIM program was directed towards aerothermodynamic evaluation of the research ramjet engine and its operational cycle. The goal of the structural design effort was to assure adequate structural integrity and life to carry out the wind tunnel tests defined by the Statement of Work.

The following design criteria was established to insure compliance with the minimum structural requirements:

(a) Allowable stresses were defined as either 67 percent of the ultimate strength ($0.67F_{tu}$) or 85 percent of the yield strength ($0.85F_{ty}$), whichever was lower, if the load creating the stress was generated by an engine operating condition.

(b) For conditions involving buckling, a stability factor of 3 was used to account for the possible non-uniformities in the structures.

(c) For plate-fin structures, a stress concentration factor of 3 was used to account for the non-uniform loading of the fins.

(d) Structures were designed to withstand a proof pressure of 1.5-times operating coolant pressure at room temperature.

(e) It was assumed that the engine would be operated for 250 cycles. Due to uncertainties inherent in low cycle fatigue design calculations, the number of expected cycles was multiplied by a factor of eight, thus establishing a 2000 design-cycle requirement.

(f) Structures were designed to withstand inertia loads of 3.0 g's in the operating mode and 5.0 g's inertia load in all three axes for transportation purposes.

2.3.1 Aerodynamic Loads

The aerodynamic loads considered for structural analysis were (1) operational drag forces across the engine, (2) exterior unsymmetric load which may be incurred when engine is subject to tunnel unstart on one side only, and (3) internally-reached engine unsymmetric unstart.

Differential pressure of 20 psi across the axis of the engine was used for analysis involving pure drag and unsymmetric unstart loads.

2.3.2 Material Selection

Candidate materials for each component section of the engine were reviewed to select the most suitable material for each part. Three categories were established.

I Surfaces exposed to high heat fluxes

II Structures supporting high loads

III Plumbing and instrumentation hardware.

The material selected to satisfy the majority of components in Category I was Nickel-200. Nickel-200 was selected for its relatively high structural strength and substantial ductility, required to provide the design fatigue life. Zirconium copper was used where extreme heat fluxes were encountered, because of its ability to be cold worked in order to attain the tensile properties required for pressure containment with very little decrease in its thermal conductivity. Physical properties of these materials are shown in Figure 2.3-1 and Table 2.3-1.

Items considered in Category II were the main support legs of the engine, the actuator housing, and the outerbody support rings. AISI 4130 carbon steel was selected for the support legs and the actuator housing and Hastelloy X was selected for the outerbody support ring. Hastelloy X was selected for its high mechanical properties along with its compatibility with Nickel-200 material.

Category III items, including the coolant plumbing and miscellaneous hardware inside the engine were manufactured from 300-series stainless steel to resist corrosion and for ease in fabrication. Hastelloy X tubing was selected for specific areas requiring high strength.

2.3.3 Component Analysis

2.3.3.1 Inlet Spike Assembly

The inlet spike assembly consists of a double-walled forward section and a plate-fin aft section (see AiResearch drawing 950512). It was necessary to use plate-fin construction in the aft section because of high aerodynamic heat loads and limited physical space. The thickness of the double-walled forward section was a tradeoff between (1) the capability of the shells to withstand the hoop stresses imposed by the coolant pressure, and (2) limitations imposed by heat transfer requirements where the maximum allowable coolant side temperature of the hot shell was 300°F.

The hoop stress distribution of the spike forward section is presented in Figure 2.3-2. The maximum mean temperature of 700°F occurs during operation at axial station 45.0 in. The radius of the hot shell at this location is 9.52 in. The hoop stress is calculated to be 10,472 psi due to 220 psi coolant pressure.

Two layer plate-fin structure was used between Stations 49.6 and 55.6. The fin size and spacing is shown in Figure 2.3-3. Gold, palladium, and nickel brazing material (50 Au 25 Pd 25 Ni) was used to obtain best heat transfer characteristics. A stress level of 19,990 psi was calculated using a stress concentration factor of 3 for the fins. Fatigue cycle life of this section was calculated to be 33,000 cycles.

The cold shell was fabricated from 0.125-in.-thick stainless steel, from the tip to Station 36.5. Three stiffener rings were added between Stations 16.5 and 36.5 to prevent buckling. Maximum compressive stress of 20,000 psi was computed at Station 36.0. The spike assembly from Station 36.5 to the

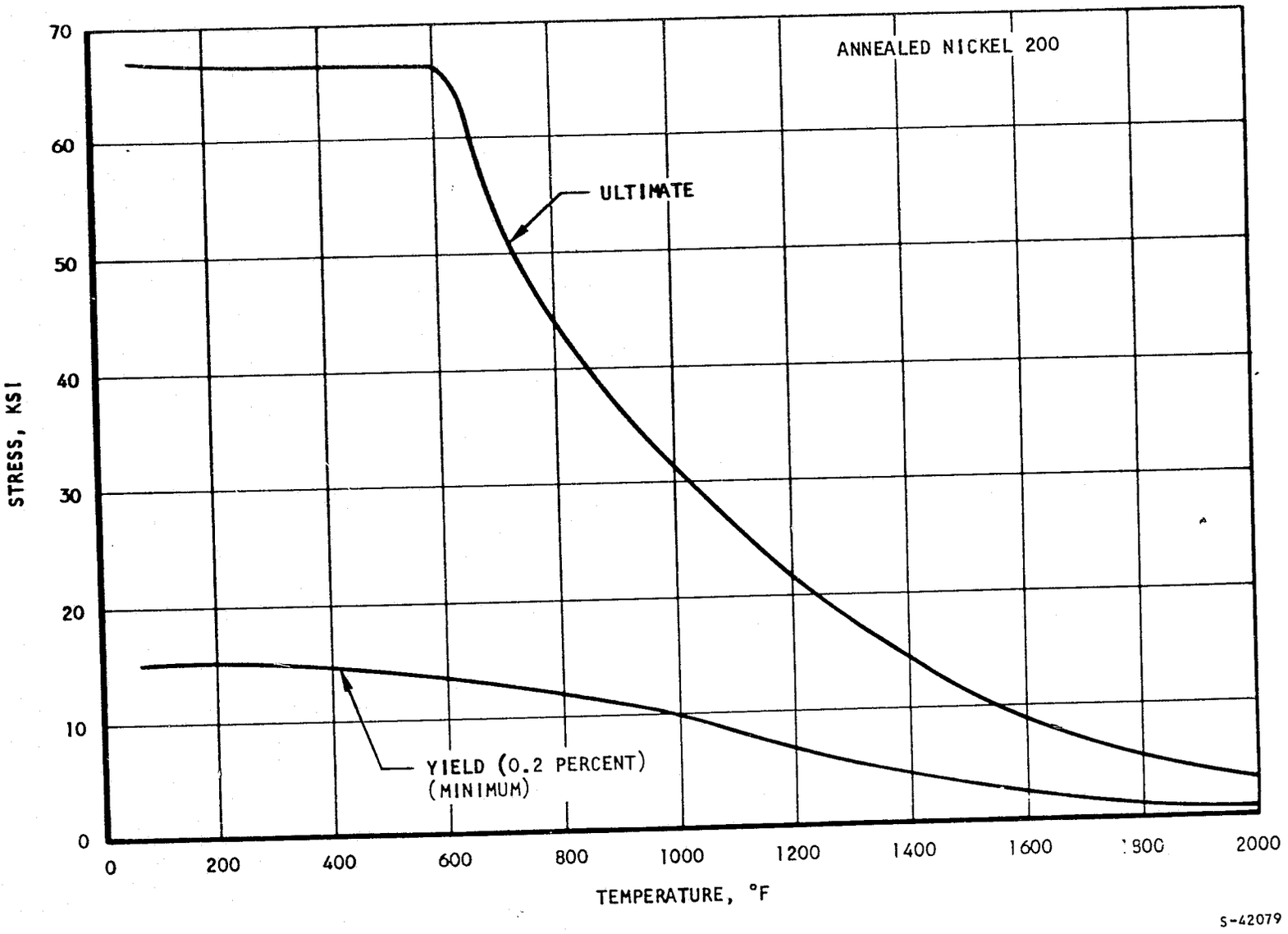

Figure 2.3-1. Stress Variation with Temperature for Annealed Nickel-200

TABLE 2.3-1

ZIRCONIUM COPPER PROPERTIES

Composition

Zirconium	0.13 - 0.20%	Selenium	2 ppm
Iron	22 ppm	Tellurium	1 ppm
Sulphur	12 ppm	Lead	5 ppm
Silver	12 ppm	Tin	1 ppm
Nickel	5 ppm	Bismuth	1 ppm
Antimony	5 ppm	Manganese	1/2 ppm
Arsenic	3 ppm	Oxygen-Free Copper	Remainder

Mechanical Properties

Heat Treatment: Solution-annealed at 900°C (1650°F) 30 minutes, quenched, cold-worked 35%, and aged at 425°C (795°F) 1 hour.

Properties	Room Temp.	250°C (480°F)	350°C (650°F)	400°C (750°F)	450°C (810°F)	500°C (930°F)	550°C (1020°F)	600°C (1110°F)
Ult. Strength, psi	54,700	54,500	55,000	54,800	54,700	54,100	51,200	46,300
Yield - 0.2% Offset, psi	47,400	47,200	47,100	46,800	46,800	47,600	43,700	40,300
Rockwell "B"	63.8	65.6	67.0	66.5	66.4	66.1	61.2	55.6
Vickers VPN	123	123	124	124	124	123	116	105
Conductivity, % IACS	87.0	86.7	87.5	86.4	87.3	90.0	92.2	94.5

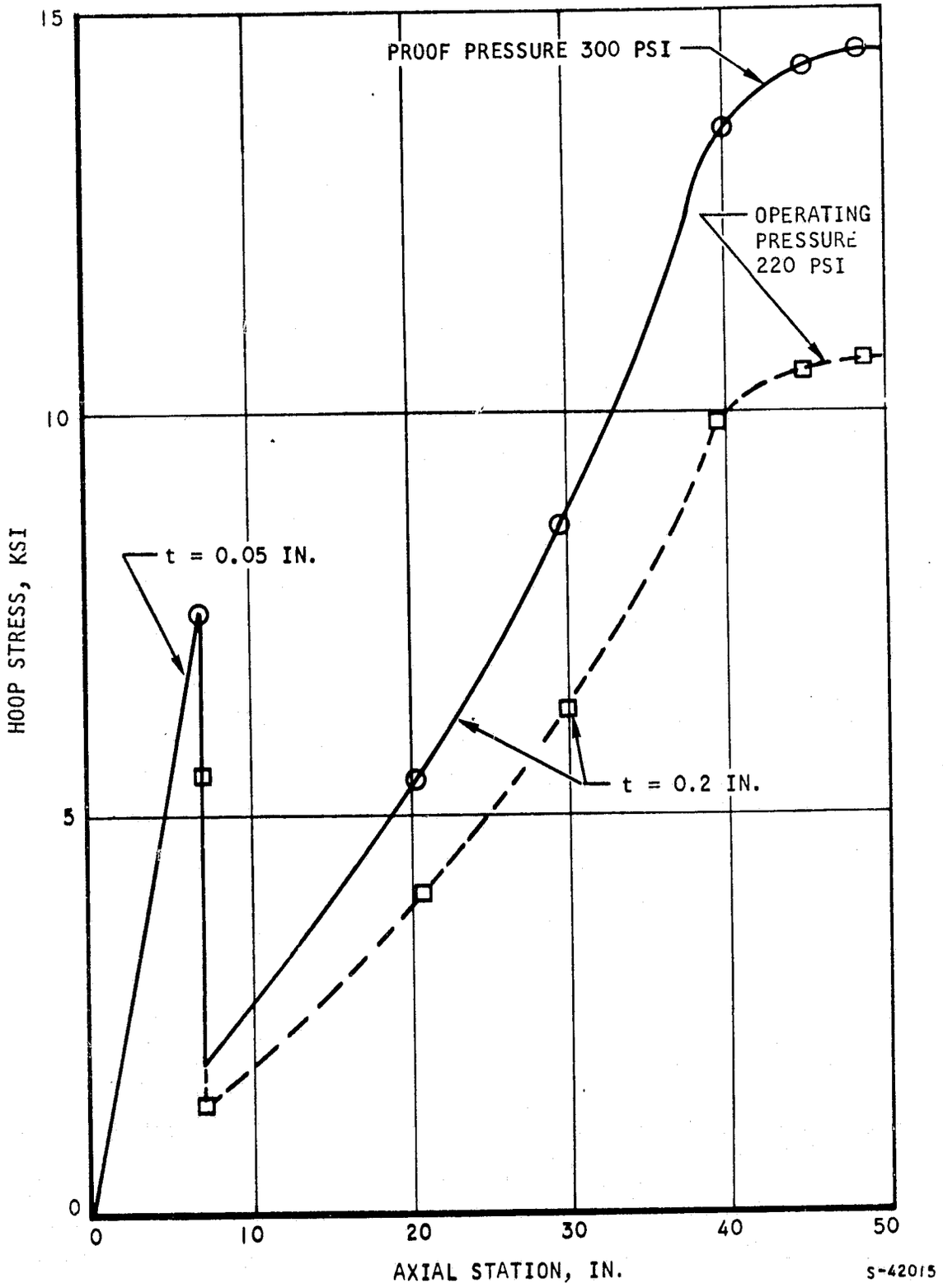

Figure 2.3-2. Distribution of Hoop Stress with Axial Distance for Spike Outer Shell

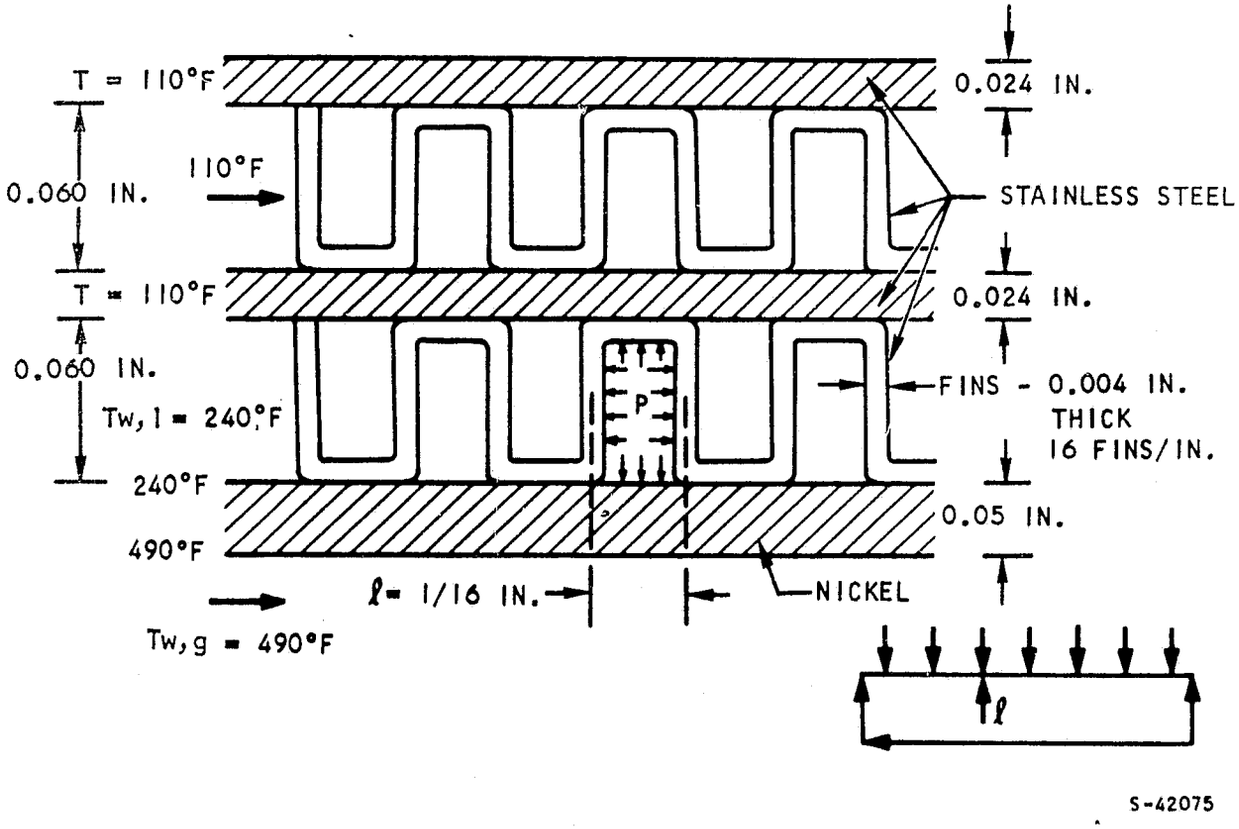

Figure 2.3-3. Sandwich-Segment Fin-Size Spacing

beginning of the plate-fin construction is basically a cylindrical section constructed of 0.1875-in.-thick stainless steel sections.

The inner mount cone was also fabricated from stainless steel material. Several openings were cut into the conical section to permit transfer of coolant lines and instrumentations. Reinforcements were installed in these areas to maintain desired stiffness of the structure.

2.3.3.2 Innerbody Assembly

The surfaces of the innerbody assembly consist of a nickel hot shell, nickel splitters and stainless steel cold shell. (See Figure 2.3-4 and AiResearch drawing 950553 for details.) Splitters were necessary to prevent distortion of the aerodynamic surface during operational mode. The closed coupling of the hot shell to the cold shell by the splitters created substantial end moments and plastic strains, but the fatigue cycle life of these areas was calculated to be well in excess of required minimum 250 cycles.

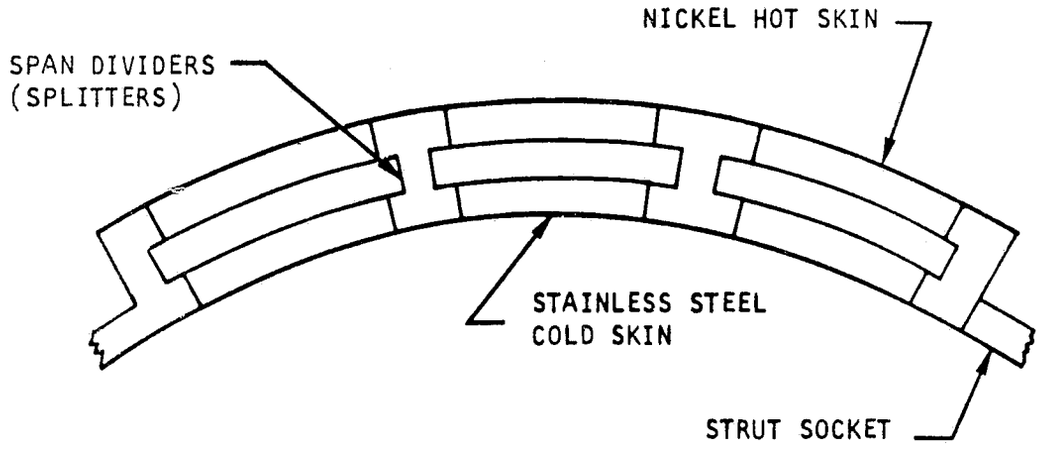

Figure 2.3-4. Innerbody Assembly Surfaces

The inlet spike actuator housing and the actuator housing mount flanges were designed to limit the deflection of the spike assembly when subjected to the unsymmetric unstart loads. The outside diameter of the actuator housing is rather small in comparison to the outside diameter of the innerbody, therefore the wall thickness of the actuator housing had to be thick in order to satisfy the spike tip deflection limitations. Consequently, the stresses in this heavy-walled housing were low due to every design load condition.

The strut socket and its associates support area was designed to limit deflection of the innerbody, in relation to the outerbody, during transportation and operation. Bow shock from the strut leading edge is expected to heat a small segment of the inner body and small surface cracks were expected to form in this area after a number of operational cycles. The structural integrity will not be affected by this condition.

The physical requirement that the manifolds be placed away from the injector locations and be connected by transfer tubes created differential thermal growth during operation. The analysis of the tube-header/injector assembly was modeled on the M.I.T. STRUDL computer program. The header was assumed to be displaced an amount equal to the unrestrained thermal growth. The resulting shear and bending stresses were found to be within acceptable limits of the structure.

2.3.3.3 Nozzle Plug Assembly

The construction of the nozzle plug assembly is similar to the forward section of the inlet spike assembly. The assembly consists of a nickel hot shell and a stainless steel cold shell with stiffeners to prevent buckling. The greatest compressive stress for the cold shell occurred at Station 68. The corresponding stress due to 300 psi proof pressure test was calculated to be 20,000 psi. Hoop stress profile for the nickel hot shell is shown in Figure 2.3-5.

2.3.3.4 Cowl Leading Edge Assembly

A complex composite structure (see Figure 2.3-6) consisting of five different sections and two different materials was necessary to carry the following applied loads:

(a) Internal coolant pressure load.

(b) External aerodynamic loads, including internal unsymmetric unstart.

(c) Loads due to temperature differences in mating parts during operation.

The copper tip area was designed to withstand:

(a) Extremely high heat loads due to the inlet spike bow shock impinging on the spike tip.

(b) High coolant pressure and large coolant volume required to prevent boiling of the coolant.

(c) Uniform and non-uniform aerodynamic loads experienced during engine operations.

Two forged nickel rings were used to restrain and transfer the various loads of the cowl leading edge assembly to the load carrying member of the outerbody. The differential temperatures of the external aerodynamic surface and the internal aerodynamic surface increase the shear and bending stress created by the pressurized coolant system. The profile of the calculated resultant deformation is shown in Figure 2.3-7.

2.3.3.5 Outerbody Assembly

The design of the outerbody assembly consists of a Nickel-200 hot shell attached to a Hastelloy X cold shell by Hastelloy X fins brazed with

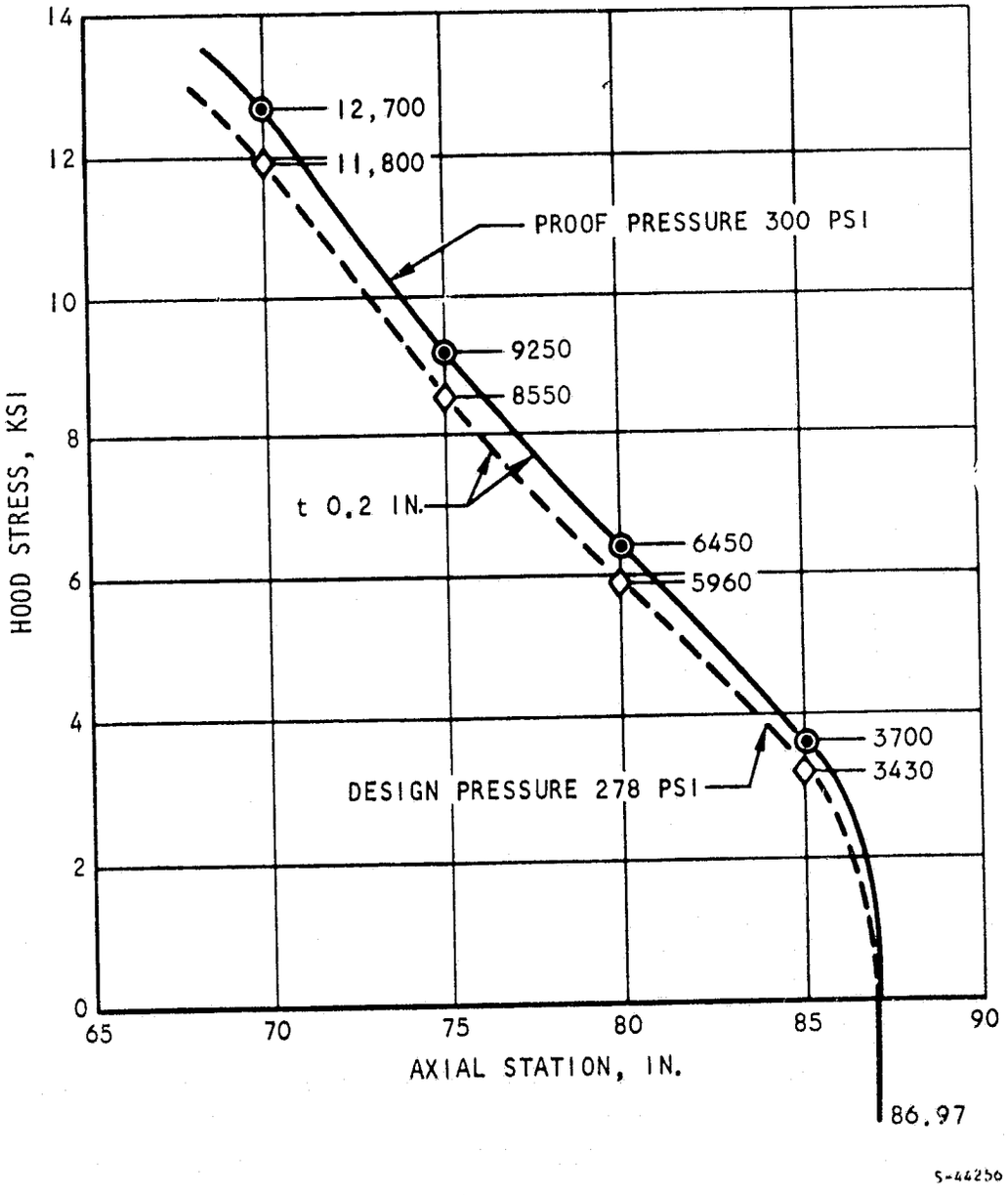

Figure 2.3-5. Distribution of Hoop Stress with Axial Distance for Nozzle Plug Outer Nickel Shell

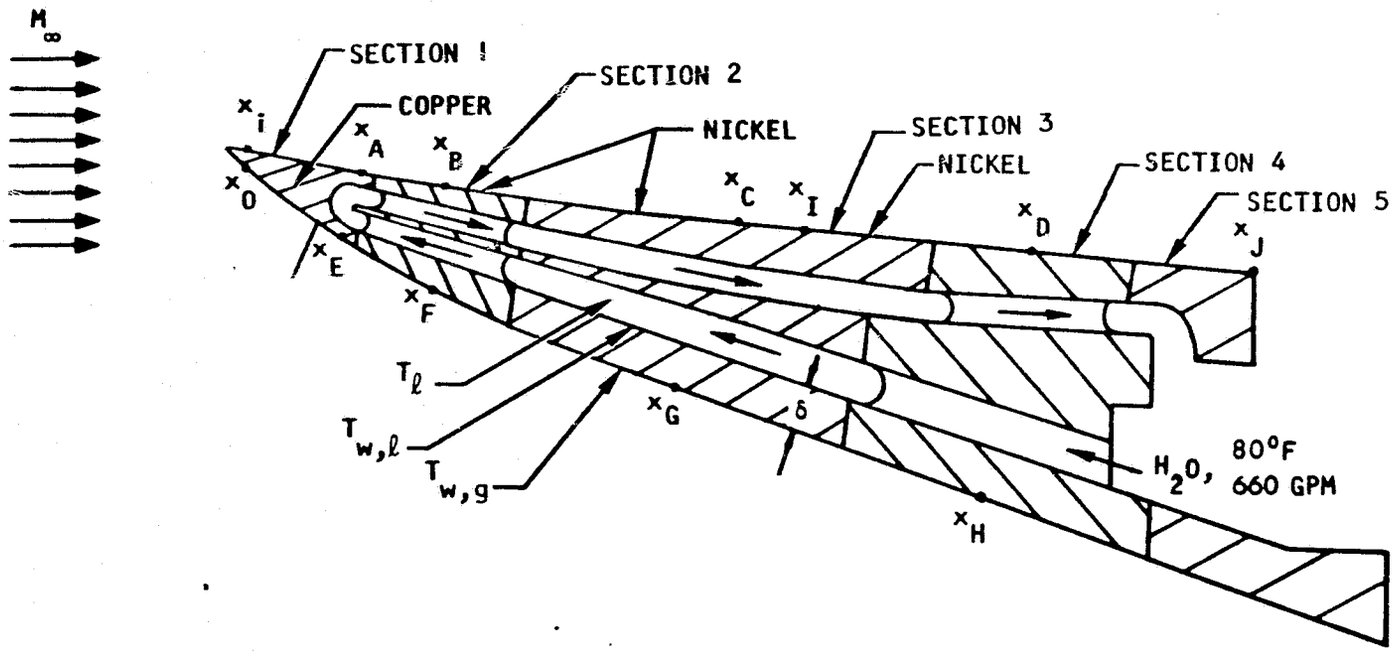

Figure 2.3-6. Details of Leading Edge

ORIGINAL PAGE IS
OF POOR QUALITY

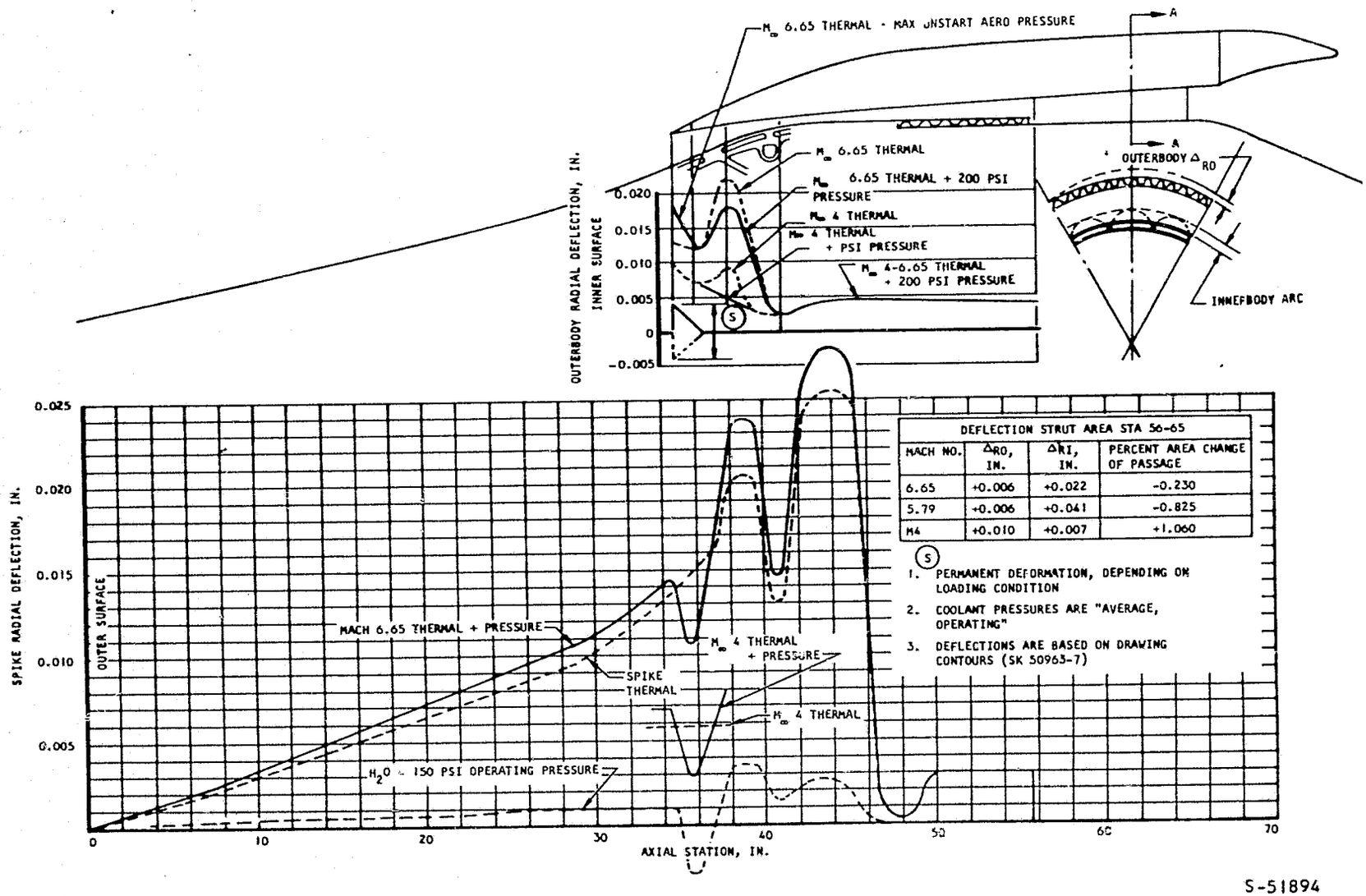

DEFLECTION STRUT AREA STA 56-65			
MACH NO.	ΔRO, IN.	ΔRI, IN.	PERCENT AREA CHANGE OF PASSAGE
6.65	+0.006	+0.022	-0.230
5.79	+0.006	+0.041	-0.825
M4	+0.010	+0.007	+1.060

(S)

1. PERMANENT DEFORMATION, DEPENDING ON LOADING CONDITION
2. COOLANT PRESSURES ARE "AVERAGE, OPERATING"
3. DEFLECTIONS ARE BASED ON DRAWING CONTOURS (SK 50963-7)

S-51894

Figure 2.3-7. AIM Aerodynamic Contours and Dimensional Changes

gold-palladium-nickel braze alloy. A third cylindrical shell, fabricated from Hastelloy C material was used at the forward section to provide means of distributing the coolant over the entire cylindrical area (see AiResearch drawing 950610).

The Hastelloy X cold shell and the fins were designed to restrain the nickel hot shell to satisfy aerodynamic requirements, thus the nickel hot shell is subject to plastic strain during each thermal cycle. A modified Euler column analysis with the tangent modulus being substituted for the elastic modules (to account for the nickel's plasticity) was used to determine the allowable unsupported length between the finned sections. To calculate the thermal cyclic life of the nickel hot shell, the equivalent triaxial resultant strain was calculated using the "Von Mises Distortion Energy Theorem."

2.3.3.6 Nozzle Shroud Assembly

The construction of the nozzle shroud assembly also utilized a nickel hot shell, stainless steel outer shell and stainless steel structural reinforcing members. (See AiResearch drawing 950506.) The maximum stress of 14,300 psi compression occurred at Station 71.74. The safety factor of 1.05 based on room temperature yield stress was deemed adequate. The compressive stress noted was caused by the proof pressure condition of 350 psi.

2.3.3.7 Strut Sockets

The innerbody strut sockets were designed to transmit the engine unsymmetric unstart loads and to provide adequate support during operation and transport of the AIM. A space frame program simulating the actuator and the support structure was used to determine shear loads transmitted to the strut sockets. The outerbody strut socket design problems were identical to those noted for the inner shell.

The effect of the support leg reactions on the outerbody and the load distribution through the shell and the struts were analyzed using the M.I.T. SABOR III shell program. Concentrated loads on the shells due to the leg reactions were simulated by appropriate Fourier series representation.

The cyclic life of the hydrogen fuel manifolds and fuel injectors was calculated on the basis of the Coffin formula.

2.3.3.8 Strut Assembly

The structural function of the struts was to maintain the position of the centerbody in relation to the outerbody and to transfer the load from the centerbody to the outerbody. The struts were constructed in such a manner as to provide access of plumbing and instrumentation into the centerbody section.

The struts were mounted in sockets provided in the centerbody and the outerbody so that the major shear loads may be reacted in bearing, permitting strut mounting bolts to be subject mainly to tensile loads resisting the moment. The geometry of the strut was defined to obtain maximum rigidity, hence the stress level of the strut itself is low. The fixed-end loads on the strut are shown in Figure 2.3-8.

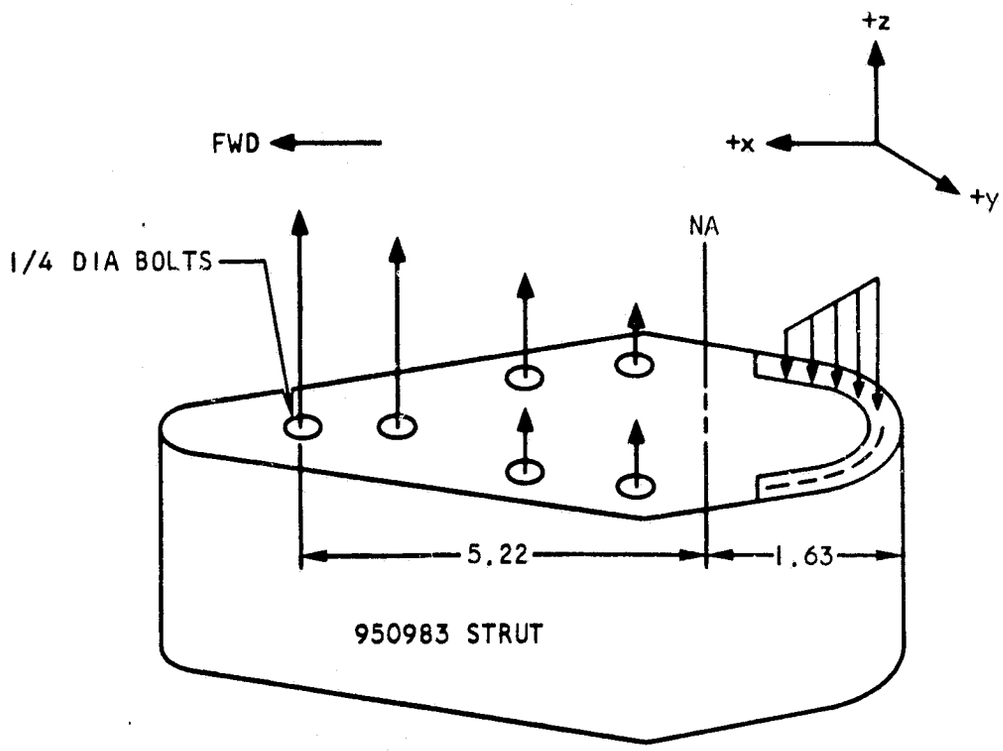

MAXIMUM DESIGN LOADS

Fx	=	9500 LB
Fy	=	250 LB
Fz	=	5000 LB
Mx	=	900 IN.-LB
My	=	12,600 IN.-LB
Mz	=	3700 IN.-LB

S-44259

Figure 2.3-8. Maximum Fixed-End Loads at the Struts

2.3.3.9 Engine Main Mount

The design criteria of the engine mount was based on supporting (1) aerodynamic load plus 3 g's and (2) transportation load of 5 g's impact as a minimum. The section modulus of the support legs was selected to minimize the deflection of the engine under test conditions.

The configuration of the assembly is shown in Figure 2.3-9. Channel-shaped support legs having a section modulus of 35.1 $in.^3$ in the axial direction and fabricated from AISI 4130 steel, heat treated to 125,000 psi yield strength were selected.

Nineteen 5/8 in. dia bolts tied the engine assembly to the facility mount plate interface. The bolt pattern was designed to maximize rigidity, hence the stress per bolt was low.

The mechanical joint at the mount support and the outerbody assembly incorporated use of six 3/8 in. dia ROSAN studs. Yield load capacity of each stud is 16,200 lb in tension, and 13,250 lb in shear. The loads calculated at this interface were 8,730 lb shear in the axial direction, 7,500 lb in the lateral direction, and 7,000 lb in the vertical direction. The load-carrying capacity of these studs was adequate.

The angular deflection of the support was calculated to be 0.001725 radians when the engine is subjected to engine unstart plus 3 g vibration.

2.3.3.10 Outer Cowl Body

The outer cowl body (OCB) was designed to provide aerodynamic cover for the external surface of the AIM. The aerodynamic drag of this part was isolated from measured thrust/drag forces produced by the AIM. AiResearch drawings 950671 and 950501 sheet 2 show the details of this part.

The calculated heat flux around the OCB was comparatively low, enabling the use of 300-series stainless steel material for the entire assembly. The assembly is basically a cylindrical barrel-like structure supported by two hollow-mount assemblies to permit access to instrumentation and plumbing lines necessary for operation of the engine.

Four separate cooling circuits were required to cool the outer cowl body. The outer skin was tied to the inner skin to prevent buckling and to carry the relatively high coolant pressures.

During operation, the OCB structure expands both axially and radially. The diameter of the OCB was fabricated correspondingly smaller in diameter to insure that the external airflow will always be subject to rearward facing step.

The flutter analysis of the OCB assembly was conducted with the assistance of a consultant experienced in the field of hypersonic flutter. Techniques outlined in report "A Survey on Panel Flutter" and "Cylindrical Shell Flutter--Theory and Experiment" by D.J. Johns were also utilized. The results of the analysis indicated that no flutter would be encountered.

ORIGINAL PAGE IS
OF POOR QUALITY

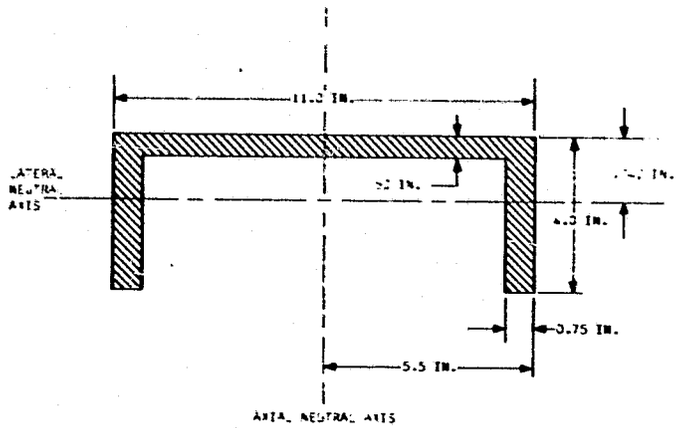

Axial Properties

$I_{AXIAL} = 93.0\ IN.^4$

$Z_{AXIAL} = \frac{493.0\ IN.^4}{5.5\ IN.} = 35.1\ IN.^3$

Lateral Properties

$I_{LATERAL} = 25.52\ IN.^4$

$Z_{LATERAL} = \frac{25.52\ IN.^4}{3.38\ IN.} = 7.65\ IN.^3$

Channel Support Dimensions and Section Properties

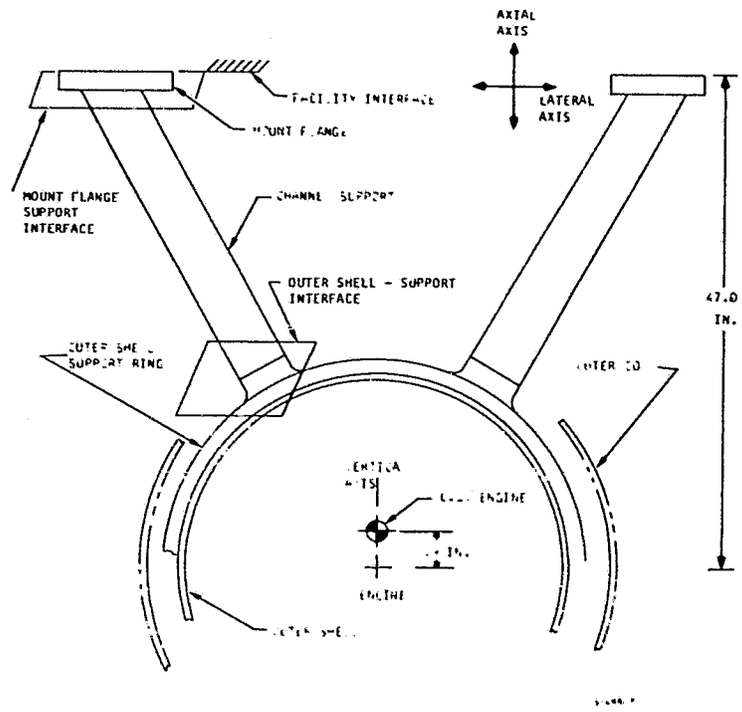

Structural Nomenclature

Figure 2.3-9. Engine Main Mount Support Leg

The only area on the OCB assembly which could experience plastic deformation is the forward part of the barrel-shaped section just forward of the leading edge of the support assembly.

The shock structure at this station causes high heating. The fatigue cycle life of this area was determined to be well above the minimum 250 cycles established.

3. SPECIAL TEST SUPPORT EQUIPMENT

3.1 AIR METERING DUCT

An air-metering device was deemed necessary to accurately measure the airflow through the AIM for a particular inlet spike position at a specific test condition. An annular-type airflow meter similar to those used for most wind tunnel tests was selected.

A one-fifth-scale model was built and tested at NASA-Langley to investigate flow coefficients. Review of the data indicated values of C_D of 0.945 to 0.965, using measured pitot pressures, and C_D = 0.84 to 1.0 was calculated using throat static pressures. Analysis of the data also indicated improvements could be obtained with minor modifications. The length of the duct was increased and profile of the convergent-divergent throat region was changed. The configuration selected and the locations of the instrumentation are shown in Figure 3.1-1, and the detail coordinates are presented in Table 3.1-1.

The accuracy of the airflow meter is determined by the combined accuracies of static-pressure total-temperature, and the throat area. An error analysis reveals that the uncertainty in weight flow can be expressed as

$$\frac{\Delta W}{W} = \left[\left(\frac{\Delta A^*}{A^*}\right)^2 + \frac{1}{4}\left(\frac{\Delta T_T}{T_T}\right)^2\right]^{1/2} + \left(\frac{\Delta P}{P}\right)^2$$

This indicates that the errors will be in the order of 1/2 percent in area, 1 percent in pressure, and 1 percent in total-temperature, giving a combined airflow error through the engine of 1-1/2 percent.

The construction of the air-metering duct was a double wall. The relatively low heat flux to which the air-metering duct will be subjected to, permitted use of SAE 1010 steel material.

Coolant requirements were such that coolant flow rates provided for the nozzle plug and the nozzle shroud were sufficient. Hence, the air-metering duct was designed to replace the nozzle shroud and plug. The coolant system and the temperature profile is shown in Figure 3.1-2 when subjected to the following test conditions.

$$M_\infty = 6,\ P_{T_\infty} = 930 \text{ psia},\ M_{LOCAL} = 0.3,\ P_T = 60 \text{ psia},\ T_T = 2940^\circ F,$$

$$W = 34.5 \text{ lb/sec}$$

3.2 INSTRUMENTATION RIG

The instrumentation rig consisted of five total/static pressure sensing probes and five total temperature/gas sampling probes arranged in such a manner as to obtain circumferential profile of the combustion products at the AIM combustor exit plane (see AiResearch drawing 950592). Difficulties were encountered in designing a total temperature/gas sampling probe in which the upstream gas can be fully captured without introducing errors caused by the

C-2

PRECEDING PAGE BLANK NOT FILMED

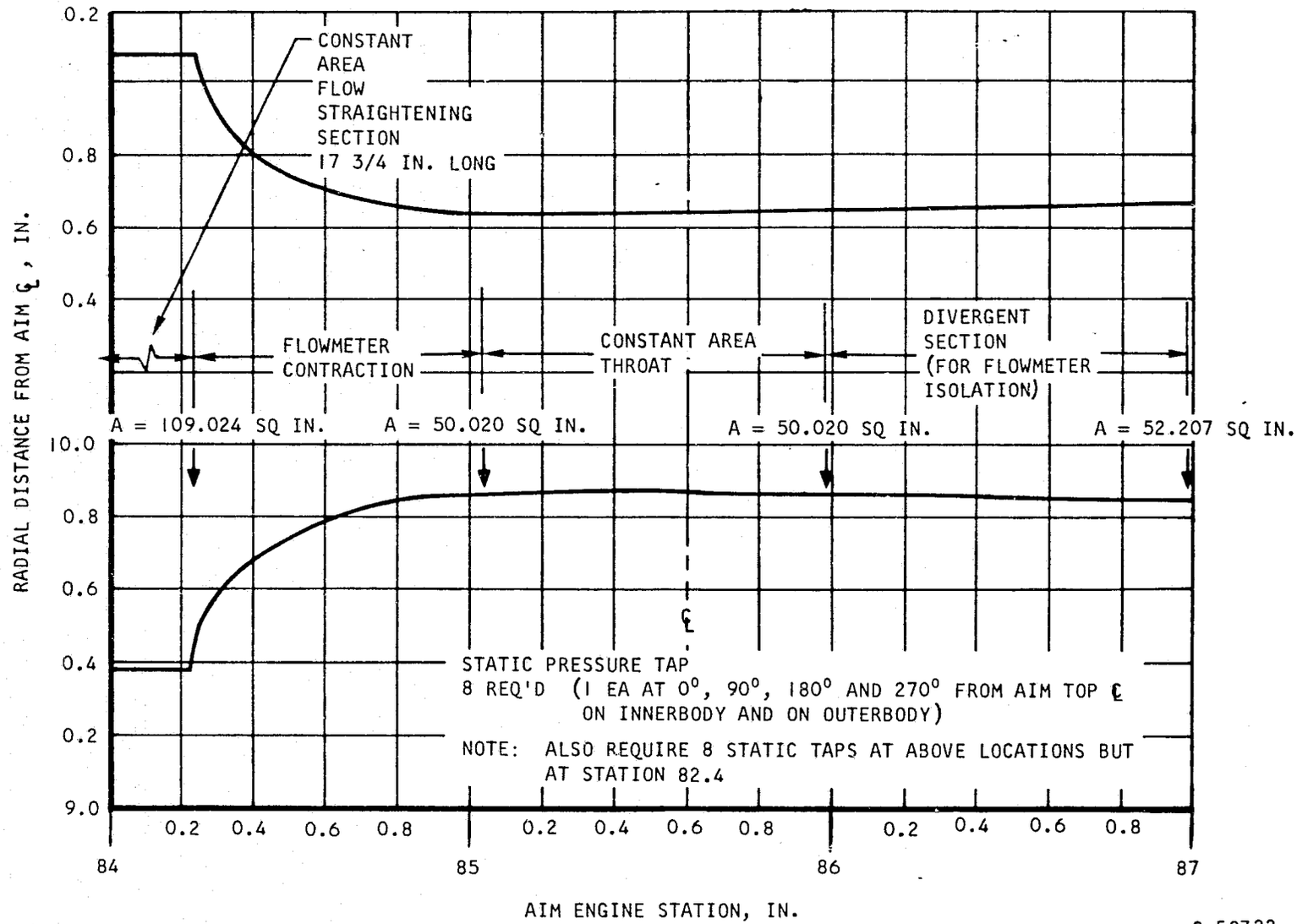

Figure 3.1-1. AIM Airflow Meter Geometry

TABLE 3.1-1

FLOWMETER COORDINATES

X, in.	Outer Wall R, in.	Inner Wall R, in.	Remarks	Area sq in.
66.233	-	9.383	inner wall L.E.	
66.459	11.079	9.383	outer wall L.E.	109.024
84.228	11.079	9.383	meter L.E.	
84.231	11.041	9.426	↑	
84.240	11.004	9.468		
84.255	10.967	9.509	contraction	
84.276	10.931	9.550	section	
84.335	10.863	9.627	↓	
84.415	10.801	9.697		
84.514	10.748	9.757		
84.628	10.705	9.806		
84.754	10.673	9.841		
84.821	10.661	9.856		
84.889	10.653	9.863		
84.958	10.648	9.869		
85.028	10.647	9.871	meter throat	50.020
85.978	10.647	9.871	meter throat	50.020
86.178	10.650	9.867	↑	
86.378	10.653	9.864	expansion	
86.578	10.656	9.860	section	
86.778	10.660	9.857	↓	
86.978	10.663	9.853	meter throat	52.207

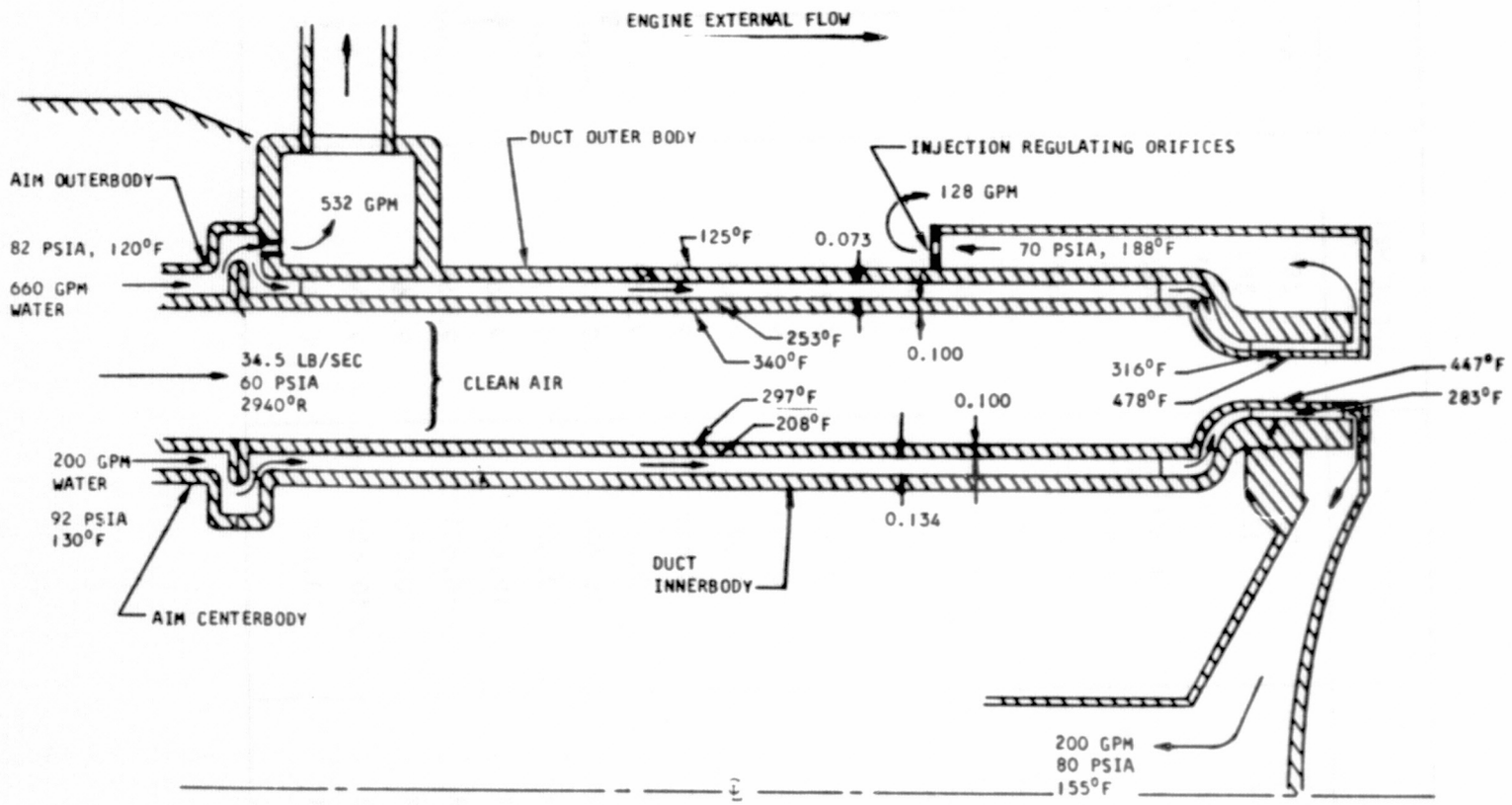

Figure 3.1-2. Air-Metering Duct Schematic

Chapman-Jouget detonation shock. Experience of NASA-LaRC and NASA-LeRC was utilized. The pressure probe was designed utilizing report NAS TND-3076 authored by J.D. Norris of LaRC and the total temperature/gas sampling probe designed from information obtained from L. Krause and G. Gawle of LeRC. Details of these probes are shown in Figure 3.2-1 and AiResearch drawings 950593 and 950594.

These probes were mounted on a cylindrical water cooled ring as shown in drawing 950592. The temperature profile of the mount ring for test condition at $M_\infty = 7.0$ and $M_{LOCAL} = 2.7$ is shown in Figure 3.2-2. The analysis included effects of shock as shown in Figure 3.2-3, and the effects of evaporation of the dumped coolant.

Analysis was also made to insure that the evaporation of the dumped coolant into the supersonic air stream would not create a reduction in the effective flow area and cause choking. Test condition considered was $M_\infty = 6.0$, $P_{T_\infty} = 9.30$ psia, $T_{T_\infty} = 2940^\circ R$, with local condition at the combustor exit of $M_L = 1.637$, $P = 19.33$ psia, $\alpha = 1.173$, $\frac{W}{A}$ gas $= 50$ lb/sec ft^2 and $H_T = 2260$ Btu/lb.

When the heat flows from the hot gas to the droplet, evaporation of the water droplet takes place. For an instantaneous droplet size of R, conservation of energy at the spherical interface leads to an equation

$$(\overline{q/A}) = \rho_\ell \cdot L \cdot \frac{dR}{dT}$$

where q/A = average heat flux to the droplet

ρ_ℓ = liquid water density

L = latent heat of water at saturation condition

t = time in seconds

Calculations indicate that the time required to reduce the volume of the droplet ($R_o = 0.01$ in.) 10 percent is 0.000358 sec. The velocity of the main gas stream at the combustor exit was estimated to be 4700 ft/sec. If it is assumed that the average speed of the droplet reaches one-half of the main air speed during this period, 10 percent evaporation will take place 10.1 in. downstream. Exit area of the AIM increases rapidly in this region and as the calculation had indicated, detrimental effects were not experienced during the test.

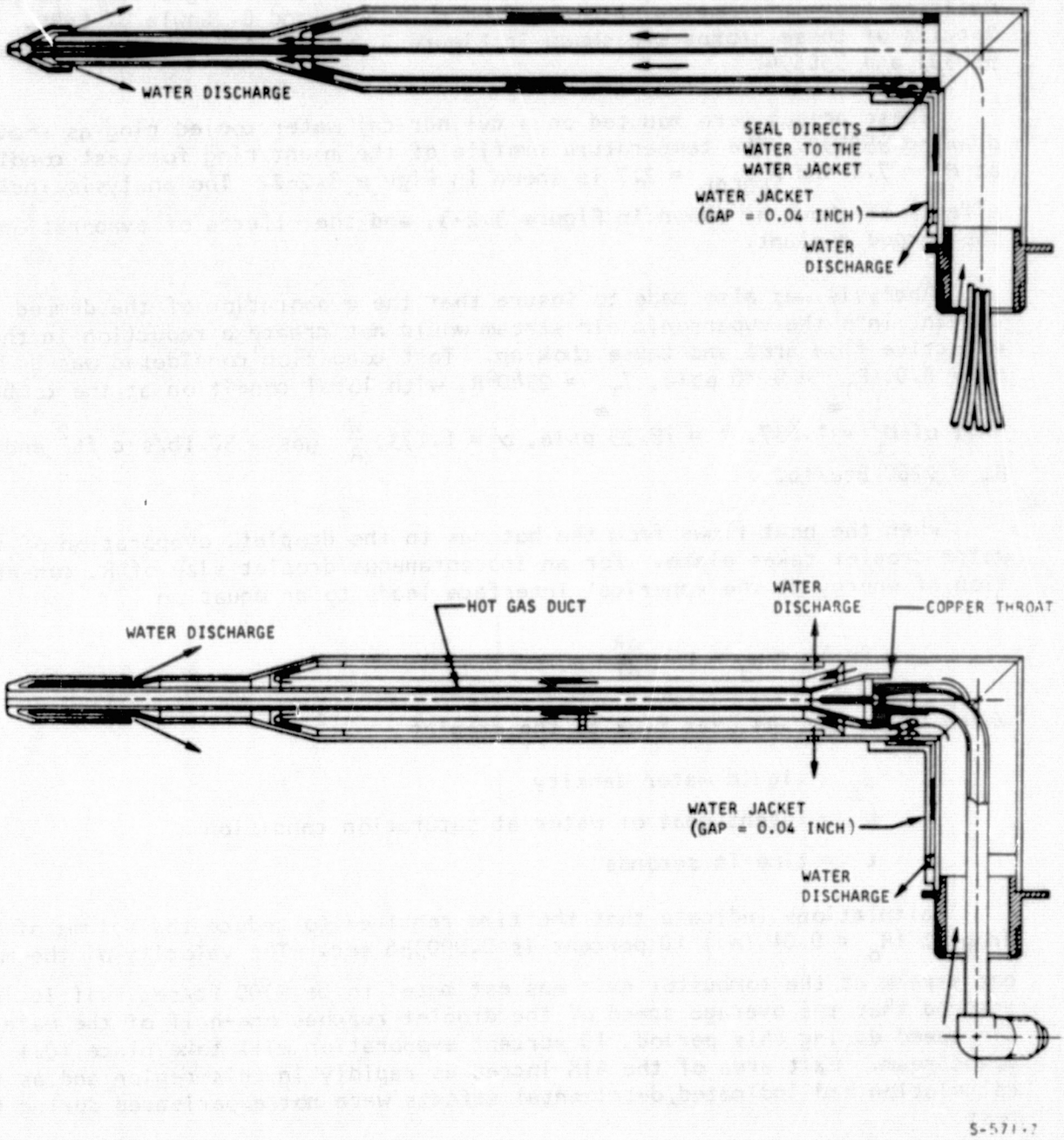

Figure 3.2-1. Instrumentation Probes

NOTES: 1. ALL TEMPERATURES IN °R
2. NUMBERS IN PARENTHESES CORRESPOND TO POSITION "A"
3. NUMBER IN RECTANGLE CORRESPONDS TO POSITION "B"
4. ALL OTHERS CORRESPOND TO POSITION "C"

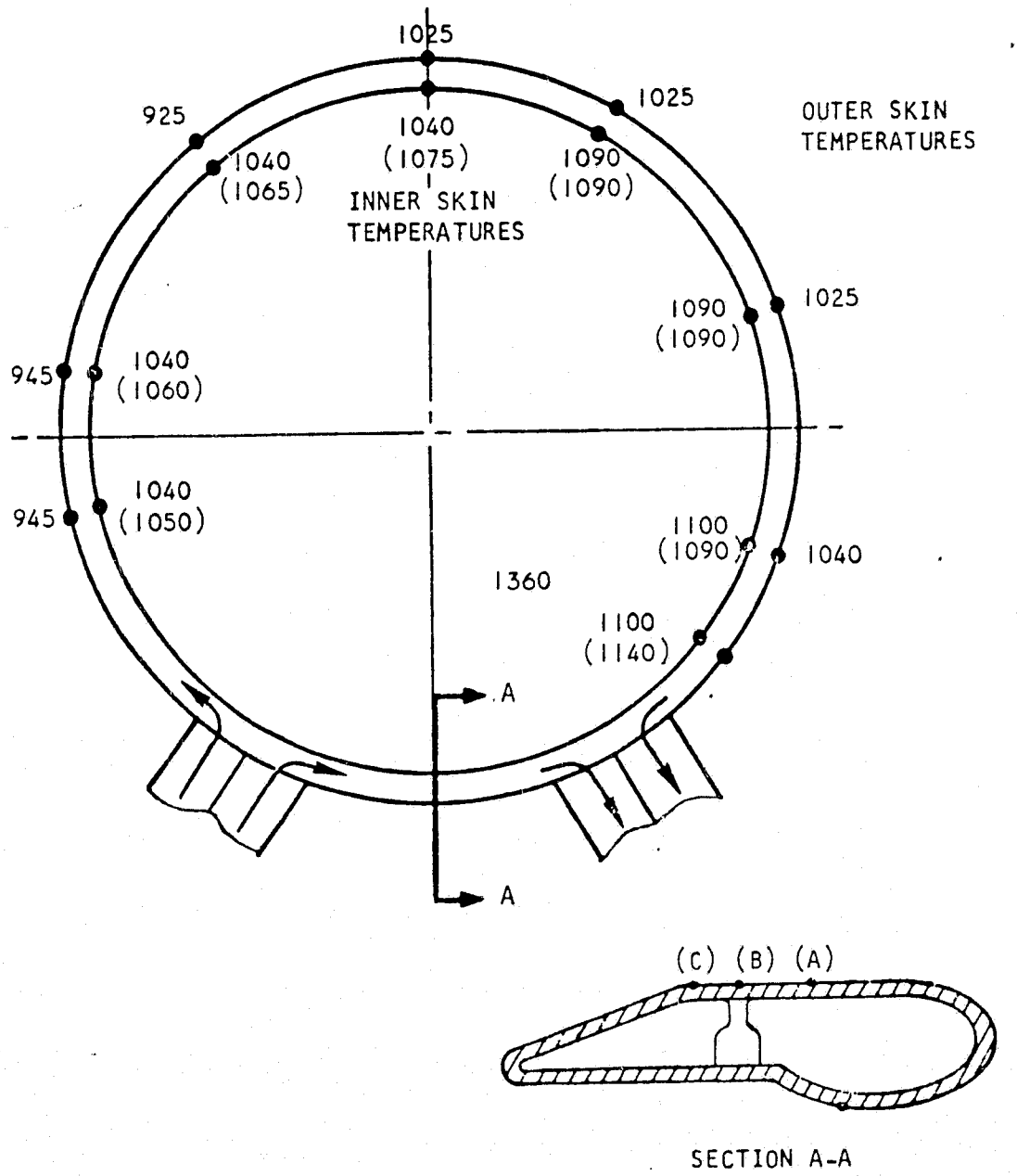

Figure 3.2-2. Instrumentation Assembly Surface Temperatures

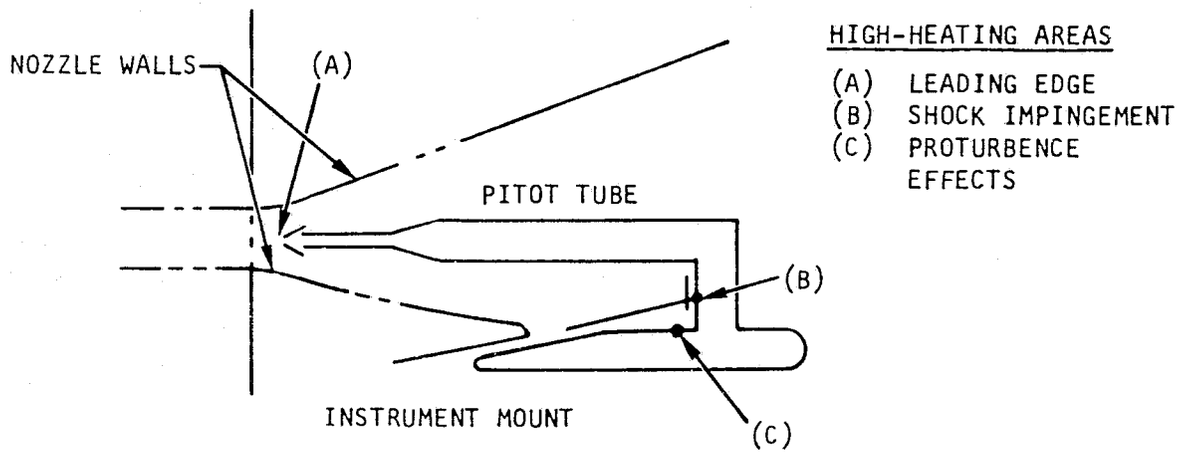

a. PITOT TUBE LOCATION RELATIVE TO THE ENGINE NOZZLE

Figure 3.2-3. Instrumentation Mount

4. DEVELOPMENT PROGRAMS

4.1 METAL JOINING

The construction of the AIM required joining Nickel-200 material to (1) Nickel-200, (2) stainless steel, (3) Hastelloy X, and (4) zirconium copper. Joining Nickel-200 to itself or to any other metal was a difficult task because of its high heat transfer characteristics and its susceptibility to excessive grain growth when subjected to high temperatures for any length of time. Figure 4.1-1 presents the relative grain growth for a given time at temperature conditions. Large grains have very detrimental effects on the mechanical properties of nickel, hence every effort was made to prevent excessive grain growth to satisfy structural requirements.

Electron-beam welding was used almost exclusively in the fabrication of the AIM, since tungsten inert gas (TIG) welding nickel 0.10 to 0.50 in. thick resulted in excessive heat-affected zone and distortion. Explosive welding and furnace brazing was used where structural design or difficulties prevented use of electron-beam welding.

4.1.1 Electron Beam Welding

Difficulties encountered in the welding heavy sections of nickel or joining dissimilar metals necessitated initiating a development program to understand all factors which influenced obtaining an acceptable weld, since survey of industry and other sources indicated that electron-beam welding of nickel 0.10 to 0.50 in. thick had not been attempted.

Difficulties encountered in utilizing the electron-beam (E.B.) welding were:

(a) Influence of extraneous magnetic field, deflecting the electron beam from its targeted position.

(b) Displacement of the weld joint from its positioned location due to thermal expansion or from residual stresses imparted during the machining process.

(c) Porosity in the welded joints resulting from outgassing of impurities in the metal or impurities on the surface of the metal.

4.1.1.1 Influence of Extraneous Magnetic Field

Whenever one or both parts being welded was fabricated from Nickel-200, random deflection of the electron beam from its targeted position was experienced. (See Figure 4.1-2.) It was determined that the residual magnetic field in the hardware was the principal contributor to this problem. Degausing the part prior to the welding process significantly reduced the amount of deflection.

PRECEDING PAGE BLANK NOT FILMED

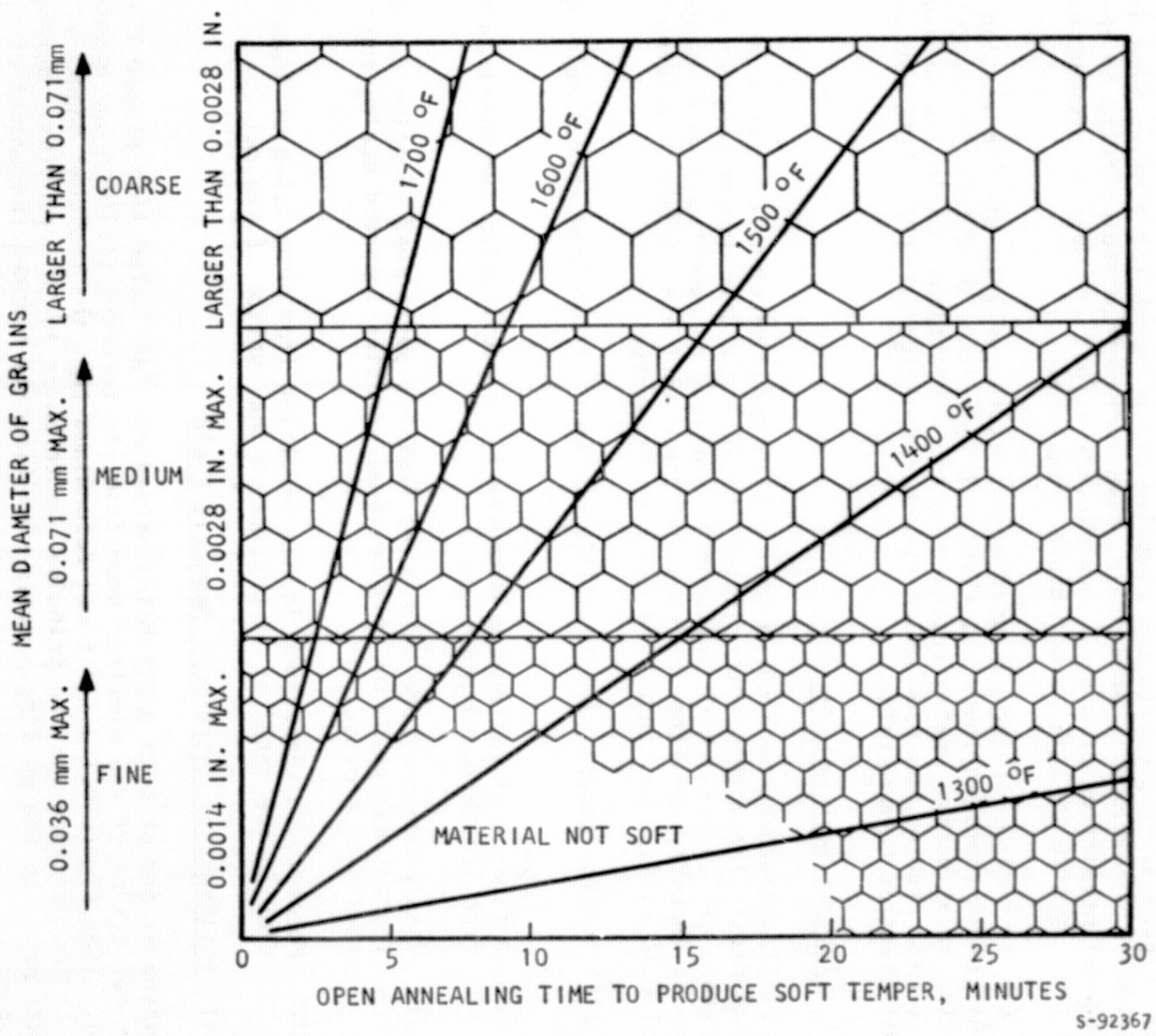

Figure 4.1-1. Effect of Open-Annealing Conditions on Grain Size of Nickel-200

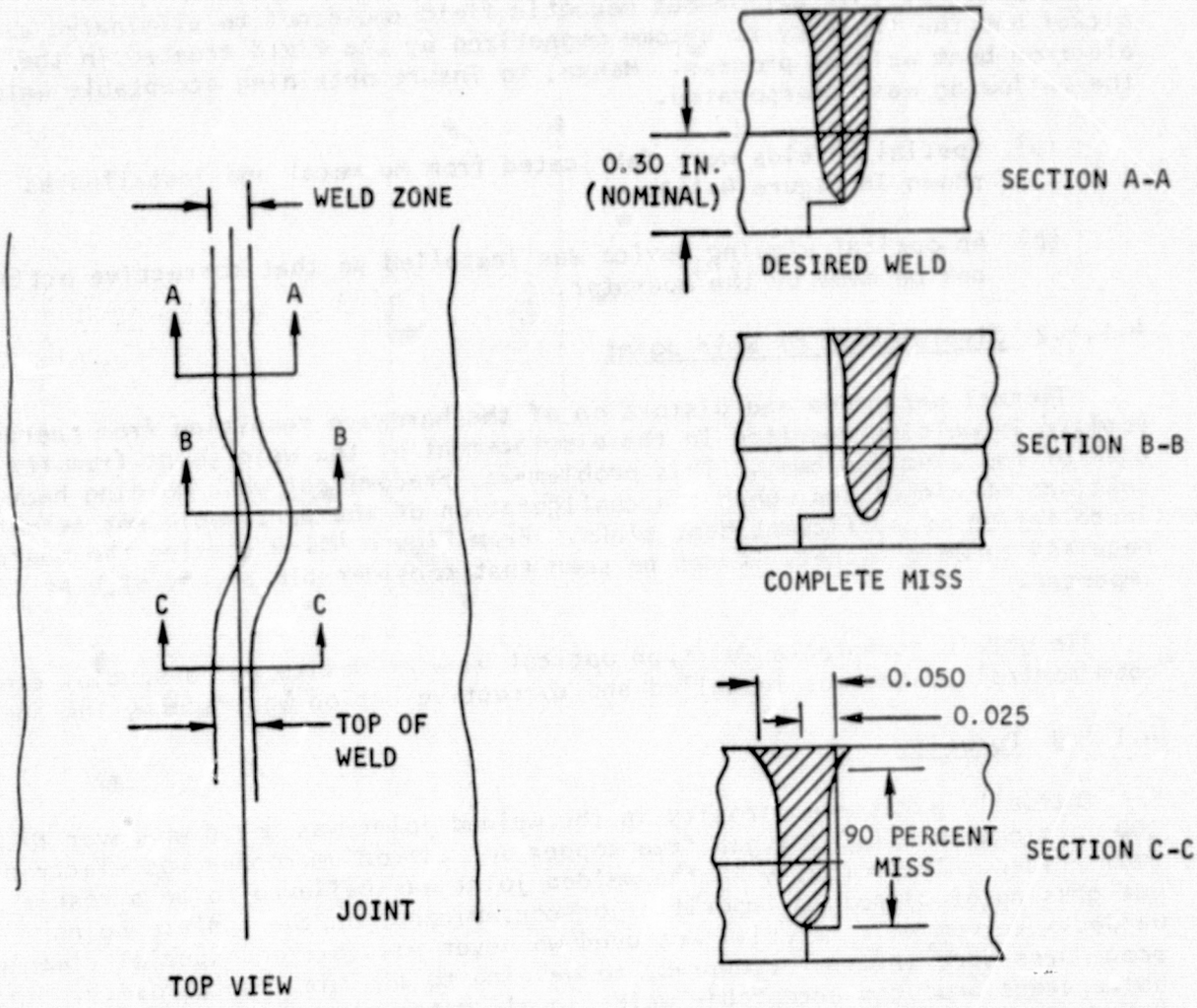

IN VIEW C-C IT IS SHOWN THAT FOR A TYPICAL 0.05-IN. WIDTH WELD, A 0.025-IN. MOVEMENT OF THE BEAM WILL RESULT IN A 90-PERCENT "MISSED" JOINT.

S-58321

Figure 4.1-2. Typical Characteristics of a Missed E-B Weld Joint

Effects of this extraneous magnetic field could not be eliminated since nickel has the tendency to become magnetized by the field created in the electron beam welding process. Hence, to insure obtaining acceptable welds, the following was incorporated.

(a) Special shields were fabricated from Mu metal and installed as shown in Figure 4.1-3.

(b) An optical viewing device was installed so that corrective action can be made by the operator.

4.1.1.2 Displacement of Weld Joint

Thermal expansion and distortion of the hardware resulting from energy applied in welding resulted in the displacement of the weld joint from the path of the electron beam. This problem was predominant when welding heavy sections of nickel and where the configuration of the part would not permit installation of sufficient heat sinks. From Figure 4.1-4 showing the energy required to weld nickel, it can be seen that considerable amount of heat is imparted.

To obtain acceptable welds, an optical viewing device and a special electron beam control system was installed and corrective action was made by the operator.

4.1.1.3 Porosity

Initially excessive porosity in the welded joint was noted whenever Nickel-200 forging, Inco 600, oxygen free copper or zirconium copper was electron-beam welded. The porosity in the welded joint was believed to be a result of out-gassing of dissolved impurities or contaminants on the surface being welded. Vacuum melt material was used whenever possible and special cleaning procedures were incorporated prior to welding to minimize the porosity. The above steps produced acceptable welds in all materials except copper. Reference 4-1 indicated that a number of factors affect the porosity in electron-beam welding of copper. This problem, along with the problem of deflected electron beam described in the following section, lead to decisions of utilizing explosive bonding for the nickel-copper joint.

4.1.2 Joining Copper to Nickel

The heat transfer and structural requirements of HRE-AIM required joining zirconium copper to nickel. Electron-beam welding first appeared to be the most expedicious method. However, problems associated with porosity and electron beam deflection indicated that structurally sound joints could not be obtained by using electron beam welding procedures. A number of alternate methods were considered and two methods considered best were:

(a) Plating nickel on zirconium copper and then making a nickel-to-nickel weld.

(b) Explosive bonding copper to nickel.

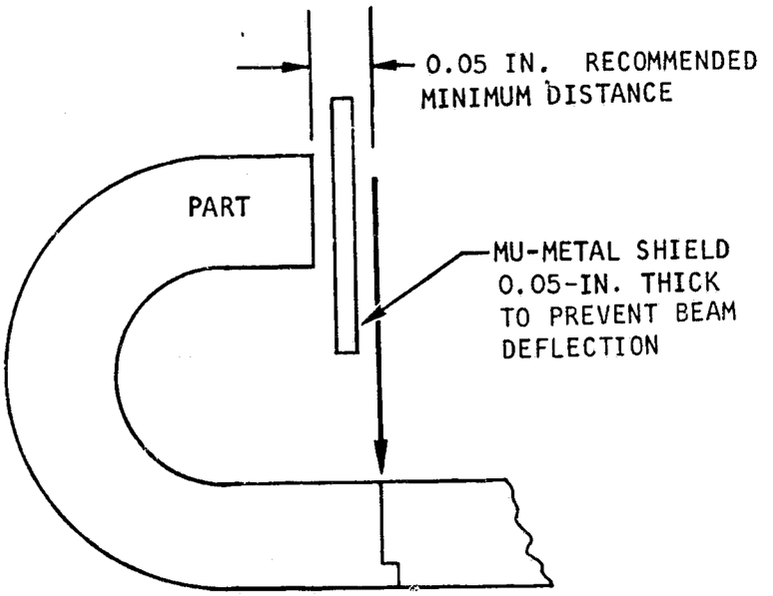

Mu Metal Shields

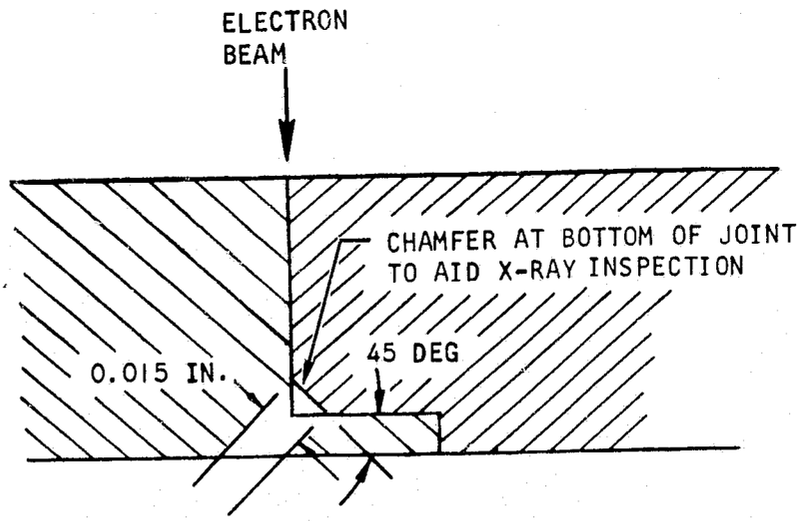

S-58322

Figure 4.1-3. Utilization of Mu-Metal Shielding

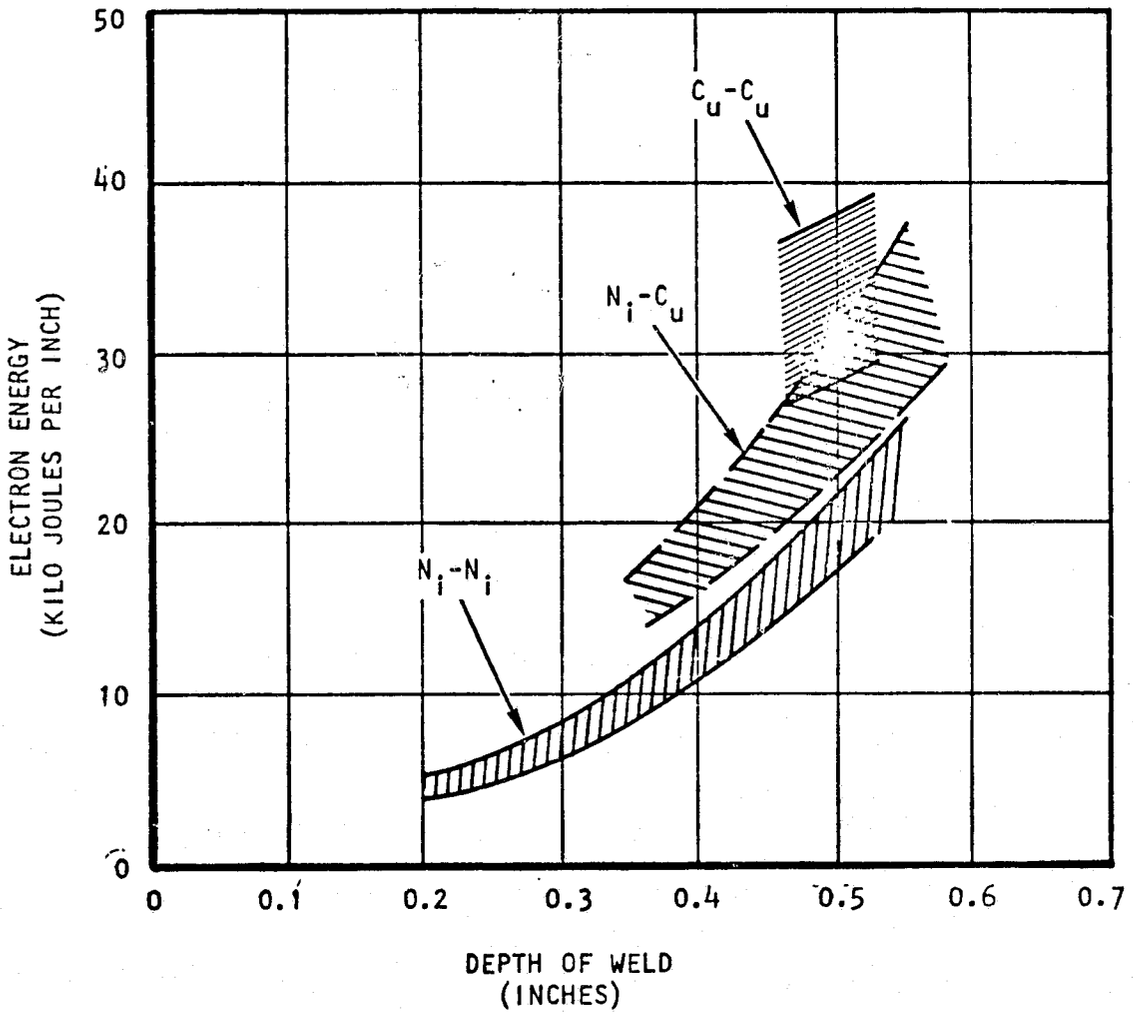

Figure 4.1-4. Weld Energy Levels for Various Metals

The survey revealed that Battalle Institute, Columbus, Ohio and E.I. Dupont, Explosive Division in Gibbstown, New Jersey had considerable experience in explosive bonding. Dupont was selected since they had been producing explosively bonded material for commercial use. Sample parts were ordered and tensile and fatigue tests were performed. Data revealed that the bonded joint was structurally sound and that all failures occurred in the parent copper side. (See Figure 4.1-5.) Figure 4.1-6 shows a microphoto of a typical joint.

4.2 MACHINING NICKEL

In the fabrication of the AIM component parts, aerodynamic requirements specified that the contoured surface be machined within ±0.003 in. of nominal specified, and that the surface finish be held within 16 to 32 rms.

Nickel-200 and zirconium copper material are soft, tough, and can easily be work-hardened. This condition was further complicated by the fact that a small stainless steel instrumentation tubing had been embedded in the aerodynamic surface. International Nickel Company and other sources were consulted for tool geometry and cutting speeds. Although some improvements were noted, finish and tolerances desired were not obtained.

Electrochemical grinding (ECG) process was developed. As the title indicates, this process is basically a deplating process where approximately 95 percent of the metal was removed by the electrochemical process and the remaining 5 percent of metal was removed by the grinding process in a single combined operation.

The ECG process virtually leaves the surface stress-free and surface finishes of approximately 8 rms were achieved.

The development program required establishing the following:

(a) Electrolyte compatible with nickel and zirconium copper

(b) Material and contour of the grinding wheel to optimize cutting speed and finish

(c) Electrical requirements to maximize material removal rate, yet obtain surface finish desired

(d) Method of maintaining correct surface cutting speed over wide range of diameter

4.3 COWL LEADING EDGE COOLANT DISTRIBUTION

The heat transfer requirements of the cowl leading edge assembly tip section required accurate coolant flow distribution. Spatial limitations did not permit use of manifolds or fixed orifices. It can be seen from the configuration of the coolant circuit shown in drawing 950502, Sheet 2 and Figure 4.2-1, that various factors such as flow separation and interaction will affect the coolant flow coefficient. Initial test indicated that the flow was

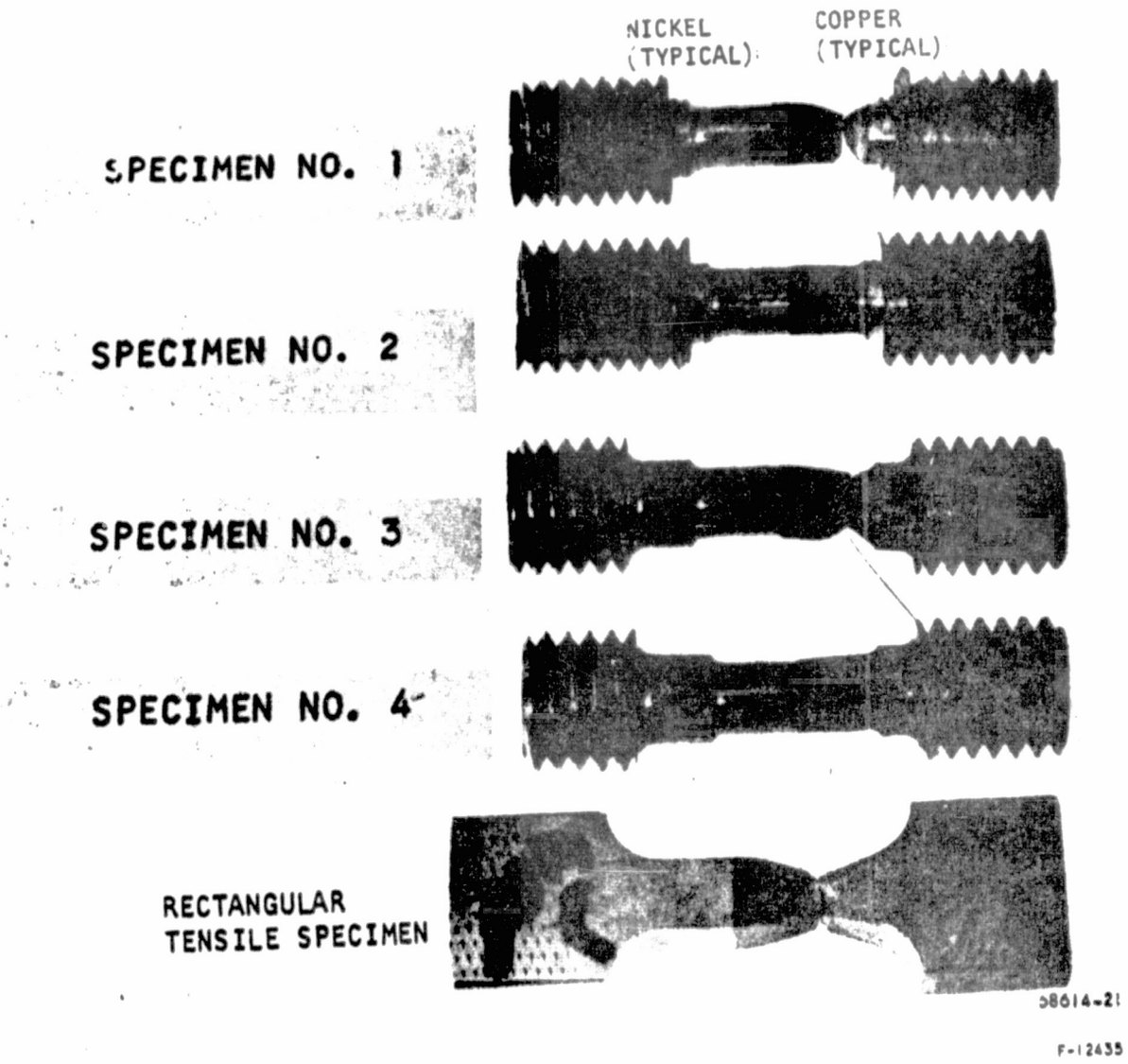

Figure 4.1-5. Low Cycle Fatigue Test Samples
(Round and Rectangular)

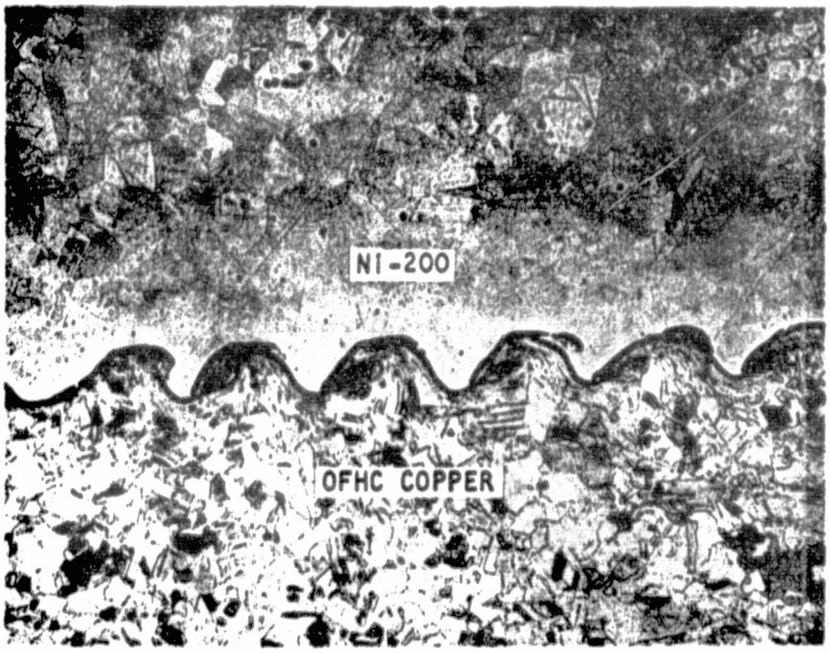

Mag. 25X

Interface parallel to shock wave direction.
Bond area was excellent. No microcracks noted in
Ni-200 or OFHC copper at magnifications up to
1500X. Etched with Anaconda Etch.

F-12249

Figure 4.1-6. Microphoto of Explosively Welded Copper to Nickel

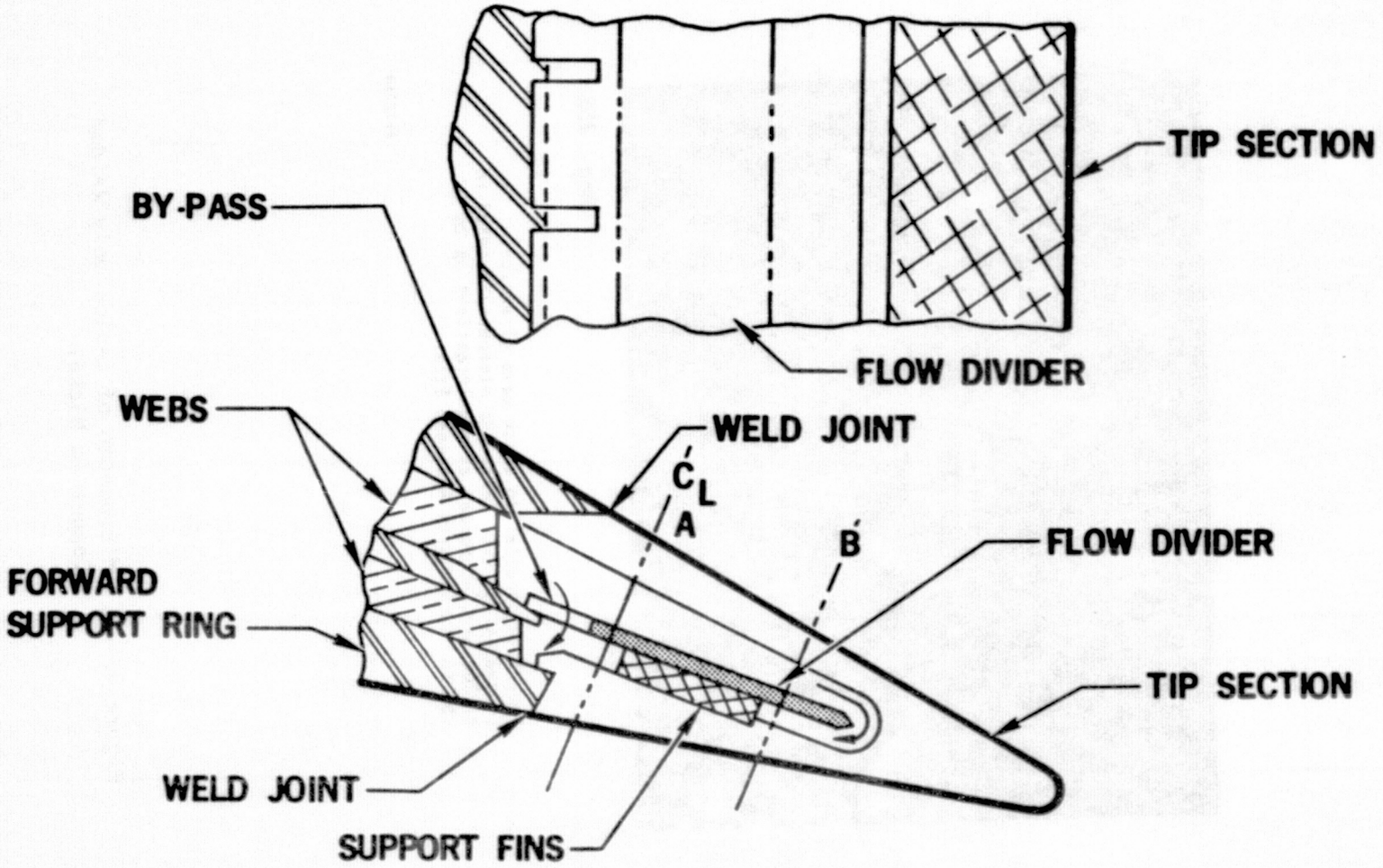

Figure 4.2-1. Cowl Leading Edge

not distributed as desired and that overall pressure drop was excessive. A 10-times scale model of the tip section was constructed from clear plastic (See Figure 4.2-2) so that the flow paths could be observed. Configuration of flow dividers evaluated are shown in Figure 4.2-3. The flow divider developed, which distributed the coolant flow best,with minimum sensitivity to flow-divider location,was that shown in Figure 4.2-3 (View 4). This configuration was incorporated into the cowl leading edge assembly.

4.4 IGNITOR SYSTEM

In compliance with the Statement of Work, the positive ignition system was provided on the AIM. Several systems were considered and investigated during the initial combustor test program performed at the Ordinance Aerophysics Laboratories. The most successful ignition system was a hydrogen-oxygen torch ignitor designed and developed by OAL. The space allocation within the AIM would not permit useage of the ignitor developed by OAL, hence, modifications were necessary.

The patent holder of the torch ignitor was consulted to insure modifications would not adversely affect the operation of the ignitor; then a development program was initiated to establish the following.

(a) Physical modification (shortening the assembly) had not affected the operational characteristics of the ignitors.

(b) Electrical energy requirements to insure ignition of the torch will be obtained at test conditions of NASA-LeRC.

(c) Cooling requirements of the combustion chamber to prevent damage to the adjacent components of the AIM were met.

(d) Energy level of the exhaust gas to insure ignition of the AIM combustor at test conditions.

The details of the torch ignitor assembly are shown in Figure 4.2-4 and Drawing 950627. The hot gas used to ignite the mixture in the combustor was obtained as follows:

(a) Oxygen supplied at port A of the ignitor enters cavity B and then passes through swirl vane C. The velocity of the swirl is such that the O_2 gas boundary layer continues to wash the walls of the ignitor assembly and the outlet port.

(b) The hydrogen supplied to port D enters cavity E and then proceeds through the center tube and into the ignitor combustion chamber. Here the hydrogen diffuses and mixes with the oxygen.

(c) Ignition of the mixture is obtained by a spark generated by the exector assembly utilizing the center tube and the swirl vanes as electrodes.

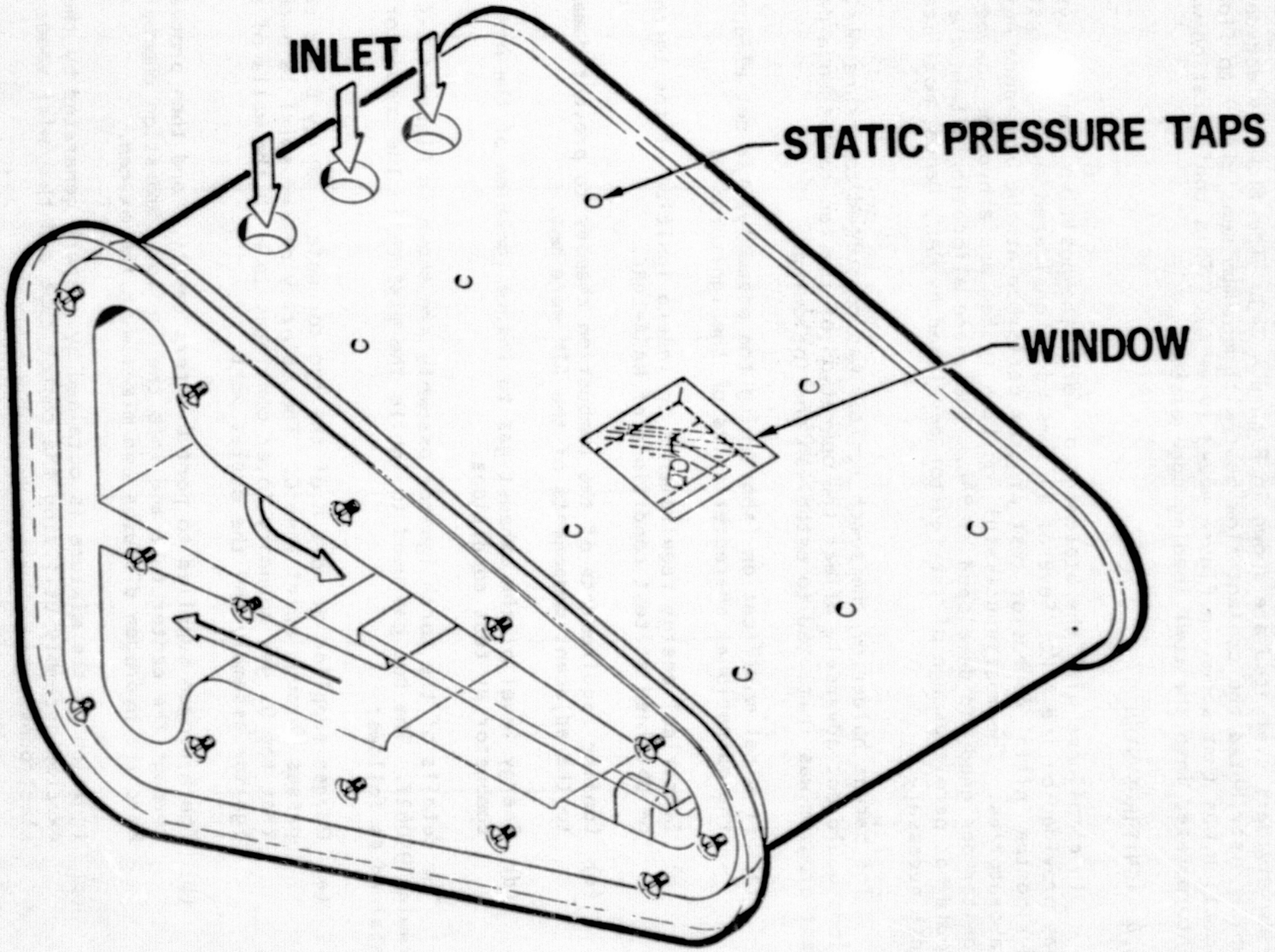

Figure 4.2-2. 10X-Scale Cowl Leading Edge Plastic Model Schematic

ALL DIMENSIONS IN INCHES

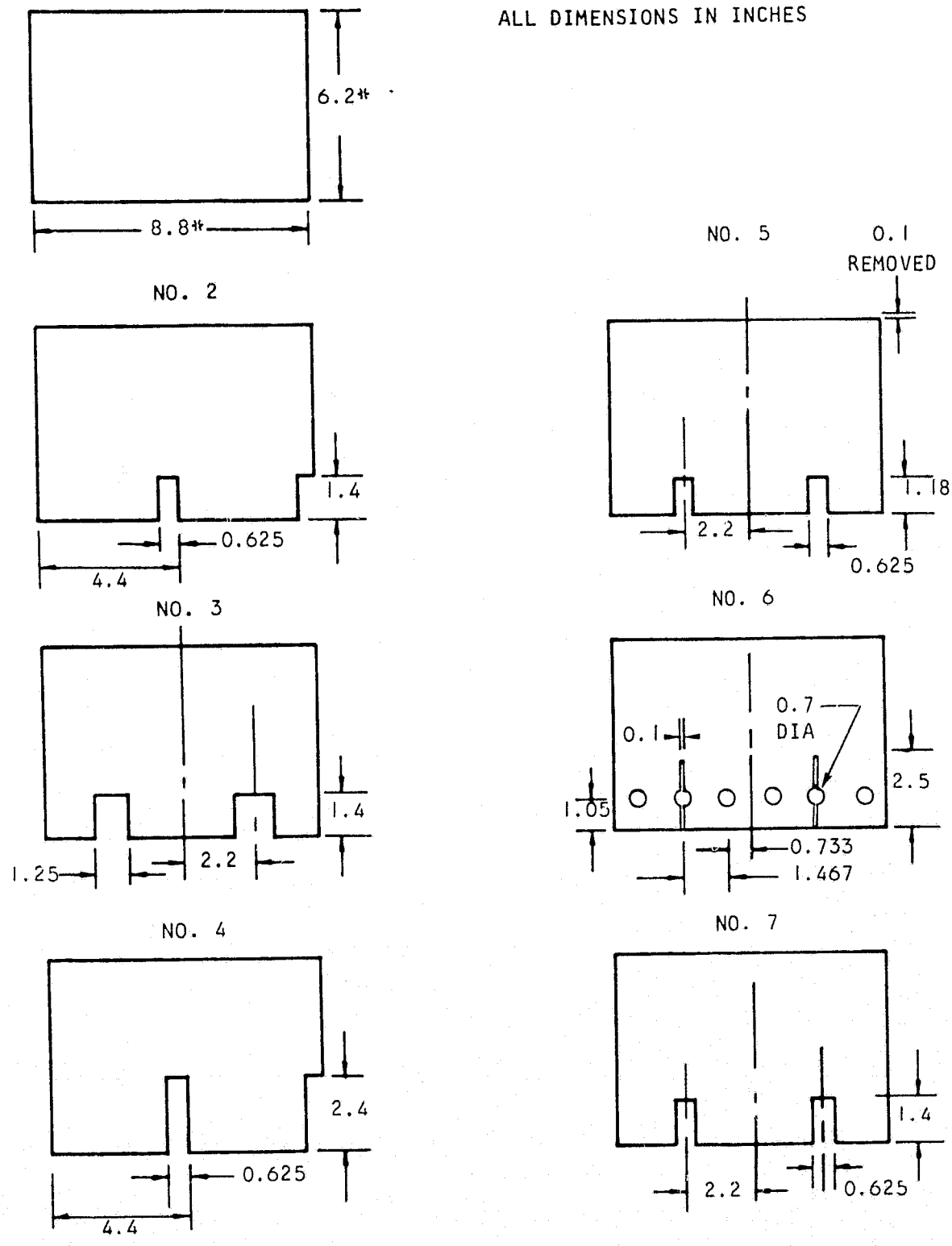

*Dimensions typical except for No. 5

Figure 4.2-3. 10X-Scale Flow-Divider Configurations

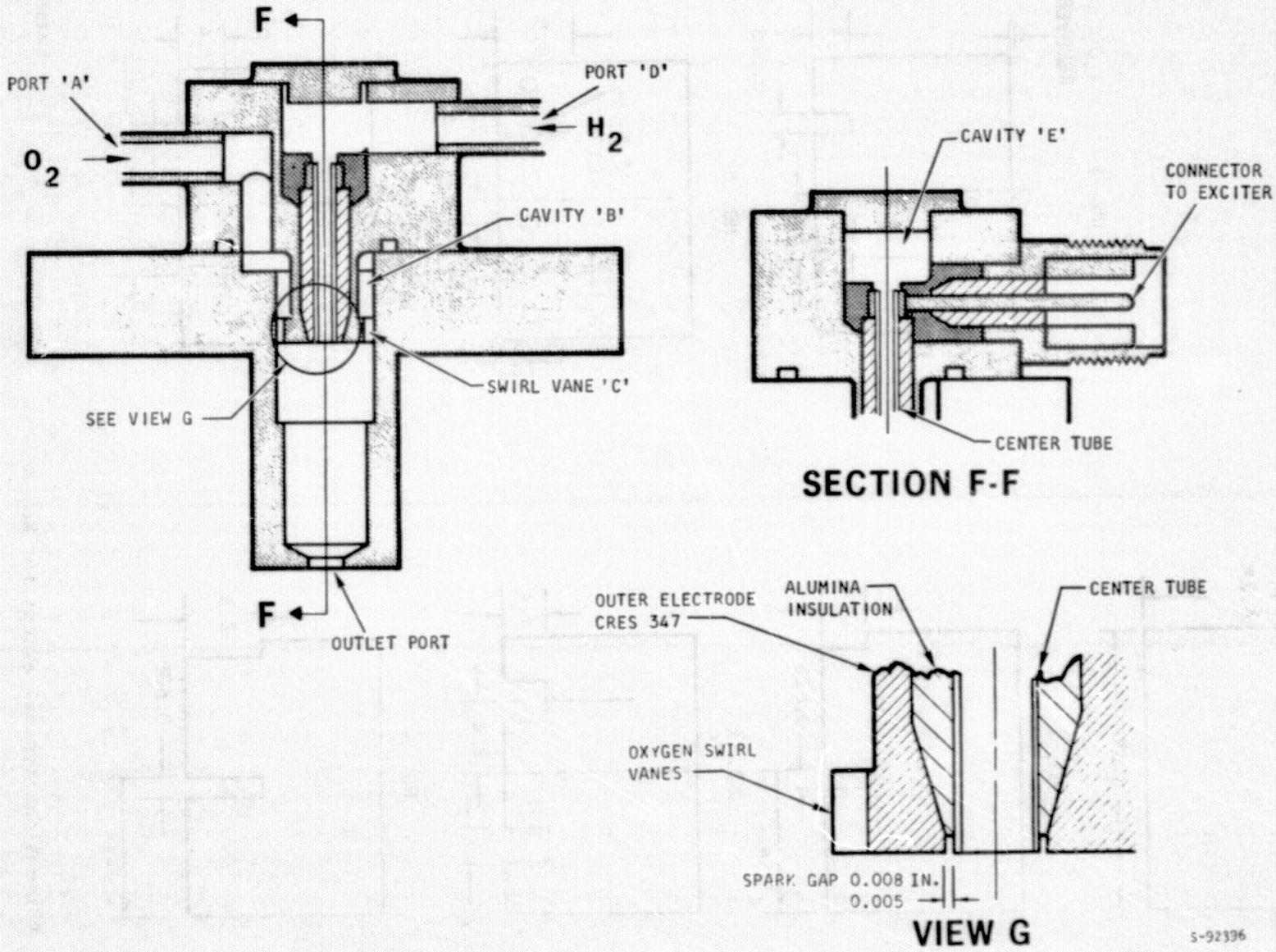

Figure 4.2-4. Torch Ignitor Assembly Details

Tests were performed at various oxygen-fuel ratios to determine its effect on combustion efficiency, ignitor chamber wall temperature, ignition limits, and to establish that once ignition was obtained , combustion would be sustained without addition of energy. Oxygen-fuel ratios of four through eight were evaluated and the ratio of eight was finally selected.

5. TEST PROGRAM AND DATA ACQUISITION

5.1 TEST PROGRAM SUMMARY

The AIM Test Plan was initially programmed for 46 tests. The plan was oriented toward obtaining the maximum information at Mach 6 before subjecting the AIM to higher structural risks of Mach 7. Information of special interest was (1) ignition delay and ignition limits, (2) autoignition, (3) Inlet-combustor interaction under subsonic and supersonic combustion mode, and (4) ability to make a transition from subsonic to supersonic combustion.

Table 5-1 presents the sequence of the original plan, along with the intended purpose. A 1500°R inlet total temperature was selected to minimize damage to the AIM in case the tunnel ambient may enter the cavity bounded by the AIM and the outer cowl body, or should other operational problems arise. During the inlet-combustor injector optimization tests, fuel equivalence ratio was to be varied; also, the instrumentation rig was to be installed to determine the quality and conditions of the combustion products.

The purge force calibration and the airflow calibration tests were designed to obtain information necessary to properly assess engine performance.

The tests were performed, in general, as planned, and a summary of these tests is shown in Table 5-2. The order and number of tests were modified to accommodate facility schedule requirements. Airflow calibration tests were deleted because of schedule limitations and due to the fact that subscale testing of the inlet section had indicated that the air flow through the inlet could be calculated with reasonable accuracy.

The fuel injector optimization tests were performed at a tunnel total pressure of 750 psia to minimize possible damage to the AIM when tunnel unstart, initiated by the intentional AIM inlet unstart, is experienced.

Each test was controlled by a preprogrammed-type computer program system to optimize obtaining useful data. The complexity of the facility controls and the short duration of each test did not lend itself to a manual control system. Several alternate test plans were incorporated into the tape and the selection of the plan pursued during the test was made at the discretion of the test director.

5.2 DATA ACQUISITION

The test data was recorded on tape in digital form. This data was reduced to engineering units by a computer program, and the reduced data was printed out, as well as fed into the central computer at NASA-LeRC, Cleveland, for storage. An option to access any of the stored data through a teletype terminal

PRECEDING PAGE BLANK NOT FILMED

TABLE 5-I

SUMMARY OF AIM WIND TUNNEL TESTS

RUN	M	PTO, PSIA	TTO, °R	α	FUEL SYSTEMS	FUEL SCHED.	INLET AX, IN.	COMBUSTION MODE	RUN TYPE AND PURPOSE
1	6	466	1500	0	-	-	4.23	-	Purge force, nominal case
2	6	466	1500	0	-	-	1.90	-	Purge force, effect of spike position
3	6	466	1500	3	-	-	4.23	-	Purge force, effect of angle of attack
4	6	466	2000	0	-	-	4.23	-	Operation checkout, effect of higher TTO
5	6	466	3000	0	-	-	0, 1.71, 2.52 4.23, aft stop	-	Airflow calibration, effect of altitude
6	6	930	2946	0	-	-	0, 1.71, 2.52 4.23, aft stop	-	Airflow calibration, nominal case
7	6	930	2946	3	-	-	0, 1.71, 2.52 4.23, aft stop	-	Airflow calibration, effect of angle of attack
8	6	930	2946	0	1a, 1b	1	4.23	Supersonic	Inlet-combustor performance, ignition and inlet unstart limits
9	6	930	2946	0	1a, 1b, 2a, 2c	2	4.23	Supersonic	Inlet-combustor performance, injector optimization
10	6	930	2946	0	1c, 4, 2a, 2c	2	4.23	Supersonic	Inlet-combustor performance, injector optimization
11	6	930	2946	0	1a, 1b, 1c, 4	3	4.23	Supersonic	Inlet-combustor performance, injector optimization
12	6	930	2946	0	TBD	TBD	4.23	Supersonic	Inlet-combustor performance, injector optimization
13	6	466	3000	0	1a, 1b, 2a, 2c	2	4.23	Supersonic	Inlet-combustor performance, effect of altitude
14	6	700	3000	0	1a, 1b, 2a, 2c	2	4.23	Supersonic	Inlet-combustor performance, effect of altitude
15	6	930	2946	0	1a, 1b, 2a, 2c	2	Aft stop	Supersonic	Inlet-combustor performance, effect of spike position
16	6	930	2946	0	1a, 1b, 2a, 2c	2	2.52	Supersonic	Inlet-combustor performance, effect of spike position
17	6	930	2946	0	1a, 1b, 2a, 2c	2	1.71	Supersonic	Inlet-combustor performance, effect of spike position
18	6	930	2946	0	3a, 3b	4	4.23	Subsonic	Inlet-combustor performance, subsonic combustion
19	6	930	2946	0	3a, 3b	5	4.23	Subsonic & transition	Engine performance, subsonic combustion and transition
20	6	930	2946	0	1a, 1b, 2a, 2c	2	4.23	Supersonic	Engine performance, nominal case
21	6	466	2946	0	1a, 1b, 2a, 2c	2	4.23	Supersonic	Engine performance, effect of altitude
22	6	930	2946	3	1a, 1b, 2a, 2c	2	4.23	Supersonic	Engine performance, effect of angle of attack
23	7	520	1500	0	-	-	2.88	-	Purge force
24	7	520	3965	0	-	-	2.34, 2.88 3.24	-	Airflow calibration, effect of altitude
25	7	1000	3840	0	-	-	1.98, 2.88 3.24	-	Airflow calibration, nominal case
26	7	1000	3840	3	-	-	2.34, 2.88 3.24	-	Airflow calibration, effect of angle of attack
27	7	520 & 1000	3965 3840	0	1a, 1b	6	2.88	Supersonic	Inlet-combustor performance, ignition and inlet unstart limits
28	7	1000	3840	0	1a, 1b, 2a, 2c	7	2.88	Supersonic	Inlet-combustor performance, injector optimization
29	7	1000	3840	0	1c, 4, 2a, 2c	7	2.88	Supersonic	Inlet-combustor performance, injector optimization
30	7	1000	3840	0	1a, 1b, 1c, 4	8	2.88	Supersonic	Inlet-combustor performance, injector optimization
31	7	1000	3840	0	TBD	TBD	2.88	Supersonic	Inlet-combustor performance, injector optimization
32	7	522	3965	0	1a, 1b, 2a, 2c	7	2.88	Supersonic	Inlet-combustor performance, effect of altitude
33	7	700	3965	0	1a, 1b, 2a, 2c	7	2.88	Supersonic	Inlet-combustor performance, effect of altitude
34	7	1000	3840	0	1a, 1b, 2a, 2c	7	3.24	Supersonic	Inlet-combustor performance, effect of spike position
35	7	1000	3840	0	1a, 1b, 2a, 2c	7	2.34	Supersonic	Inlet-combustor performance, effect of spike position
36	7	1000	3840	0	1a, 1b, 2a, 2c	7	1.98	Supersonic	Inlet-combustor performance, effect of spike position
37	7	1000	3840	0	1a, 1b, 2a, 2c	7	2.88	Supersonic	Engine performance, nominal case
38	7	522	3965	0	1a, 1b, 2a, 2c	7	2.88	Supersonic	Engine performance, effect of altitude
39	7	1000	3840	3	1a, 1b, 2a, 2c	7	2.88	Supersonic	Engine performance, effect of angle of attack
40	5	445	1500	0	1a, 1b, 2a, 2c	-	4.23	-	Purge force
41	5	206	2210	0	1a, 1b, 2a, 2c	-	4.23	-	Airflow calibration
42	5	415	2210	0	1a, 1b, 2a, 2c	9	4.23	Supersonic	Inlet-combustor performance, nominal case effect of altitude
43	5	415	2210	0	1a, 1b, 2a, 2c	TBD	4.23	Supersonic	Inlet-combustor performance, and ignitor flow rate
44	5	415	2210	0	1a, 1b, 2a, 2c	9	4.23	Supersonic	Engine performance, supersonic combustion
45	5	415	2210	0	3a, 3b	10	4.23	Subsonic	Engine performance, subsonic combustion
46	5	415	2210	3	1a, 1b, 2a, 2c	11	4.23	Subsonic & Supersonic	Engine performance, effect of angle of attack

ORIGINAL PAGE IS OF POOR QUALITY

ORIGINAL PAGE IS OF POOR QUALITY

TABLE 5-2

TEST RUN SUMMARY

Run No.	Reading No.	Date	Inlet Condition			Inlet Spike Position, in.	Fuel Injectors Used	Tunnel Config.	Time				Objective of Test	Comments
			Mach No.	P_{T0} Psia	T_{T0} °R				Run		Useful			
									Min	Sec	Min	Sec		
1	1 through 5	9/14/72	-	-	-	-	-	A	-	-	-	-	Pre-run reference No-airflow engine Purge system calibration	Data not valid due to mechanical interference between AIM and outer cowl body.
2	6	10/31/72	6	466	1500/2100	4.266	-	A	-	40	-	-	Facility and engine checkout	Test terminated due to cooling system overpressure abort system failure.
3	7	11/1	6	466	1500	4.266	-	A	2	26	-	-	Same as run 2	Tunnel nozzle started. Inlet started. Strong shocks in test section. Cell pressure = 2.0 psia.
4	8	11/2	6	466	1500	4.266	-	A	-	5	-	1	Establish facility operational procedure	Test aborted due to facility problem (TAFP).
5	9	11/16	6	466	1500	4.266	-	B1	-	-	-	-	Same as run 4	Facility shroud extended and washer added to assist tunnel start (TAFP).
	10	11/16	6	466	1500	4.266	-		-	-	-	-	Same as run 4	TAFP
	11	11/16	6	466	1500	4.266	-		2	39	-	99	Same as run 4	Nozzle start and inlet start obtained Cell pressure = 1.2 psia. Wedge nozzle pressure changed from 50 to 60 psia. No improvement in cell pressure.
6	12	11/21	6	466	2250	3.962	-	B1	-	-	-	-	Same as run 4	TAFP
	13	11/21	6	466	2250	3.962	-		1	07	-	-	Same as run 4	Wedge nozzle pressure 55 to 90 psig. No tunnel nozzle start. Nozzle started when inlet closed for shutdown.
7	14	11/21	6	466	2950	3.962	-	B1	-	34	-	-	Same as run 4	TAFP
8	15	12/8/72	6	466	2950	4.266	-		-	16	-	-	Same as run 4	TAFP
9	16	1/18/73	6	466	2800	4.266	1C, 4	B1	-	35	-	-	Same as run 4	First combustion attempt. TAFP
	17	"	"	"	"	"	1C, 4		1	06	-	-	Same as run 4	Nozzle start not obtained. TAFP
	18	"	"	"	"	"	1C, 4		1	00	-	-	Same as run 4	Nozzle start obtained by cycling inlet spike open and closed. Inlet start obtained. Fuel ramped to equivalence ratio = .25 prior to tunnel unstart and TAFP.
10	19	2/2	6	466	2950	0.99/ 4.00	-	B1	-	13	-	-	Same as run 4	Nozzle start with inlet partially open. ($\Delta x = 0.99$). TAFP. No fuel injected.
11	20	2/2	6	466	2950	0.99/ 4.00	1C, 4	B1	1	02	-	-	Same as run 4	No start at $\Delta X = 0.99$. Nozzle started by cycling inlet spike. Combustor lit causing tunnel unstart.
12	21	2/15/73	6	750	3000	0.99/ 4.00	-	C1	-	-	-	-	Establish facility operational procedure	Jet pump installed. Test aborted due to freezing of coolant supply system.
13	22	2/21	6	750	3000	0.99/ 4.00	-	C1	-	22	-	-	Same as run 12 above	Jet pump used for this test. Nozzle start obtained. Unstart experienced when inlet was opened. Test aborted manually. Nozzle restart noted during shutdown.
14	23	2/21	6	750	3000	0.99/ 4.00	-	C1	-	58	-	-	Same as run 12 above	Jet pump and wedge nozzle inlet pressure varied. Nozzle start was not obtained. Use of jet pump did not affect test chamber pressure. Seals between AIM support struts and facility shroud blown out.
15	24	2/23	6	750	3000	0.99/ 4.00	-	C2	-	-	-	-	Same as run 12 above	Jet pump inactivated. TAFP
	25	2/23	6	750	3000	0.99/ 4.00	-	C2	-	-	-	-	Same as run 12 above	TAFP
	26	2/23	6	750	3000	0.99/ 4.00	1A, 1B	C2	-	49	-	-	Same as run 12 above	Nozzle start and engine start obtained. Fuel injected for 4 seconds prior to nozzle unstart. Unstart attributed to excessive fuel injected caused by facility valve malfunction.
16	27	3/1	6	930	3100	0.99/ 4.00	-	C2	1	42	-	-	Same as run 12 above	Nozzle start and inlet start obtained. Jet pump inactivated. Fuel was injected engine inlet unstart experienced 12 seconds later. Inlet start reestablished and fuel again injected. Inlet unstart experienced 9 seconds later. Test was manually aborted. Cowl leading edge assembly separated from the outer body. Failure of the separation was attributed to failure of the screw heads. The failure was caused by overheating of the screw heads resulting from ingesting the hot tunnel environment into this area. Ingestion of tunnel ambient was the result of a shock standing on the AIM cowl. Additional diagnostic instrumentation was installed in the facility shroud diffuser.
17	28	3/16	6	930	3100	0.99/ 4.00	1A, 1B	C2	1	11	-	-	Establish facility operational procedure to obtain hypersonic airflow.	Tunnel nozzle start and inlet start obtained. Fuel injected same as run 16 except washer inside diameter changed to 44.5 inches. Tunnel unstart observed 19 seconds after fuel introduced. Start reestablished. Test manually aborted 3 seconds later when excessive heating of AIM-A11 cowl leading edge assembly mount flange was noted. Excessive heating of the external skin of the AIM was noted.

TABLE 5-2 (Continued)

Run No.	Test No.	Date	Inlet Conditions: Mach No.	P_{T_2}	T_{T_2}	Inlet Spike Position, δ_s	Fuel Injector Used	Tunnel Config.	Time: Run Min	Run Sec	Useful Min	Useful Sec	Objective of Test	Comments
17	29	3/22	-	960	3100	0.99/ 4.00	1A, 1B	C1	-	36	-	-	Same as run 17 above	Repeat of reading 28 with seal repaired. Inlet purge did not improve tunnel start.
18	30	3/27	6	750	2000	0.99/ 4.00	Fuel injec. not planned	D	1	16	-	-	Same as run 17 above	Shroud inlet washer replaced with conical cylinder and 15° conical diffuser inlet contraction replaced with 7° cone, tunnel nozzle did not start.
20	31	4/30	6	750	2000	0.99/ 4.00	Fuel injec. not planned	E	-	51	-	-	Establish operational procedure	First run with fully started tunnel. Shroud inlet cone cylinder replaced with original 46 in. diameter washer. Tunnel start obtained when inlet spike was cycled twice, supersonic flow in diffuser. Test terminated when target conditions achieved due to limited supply of nitrogen. Test cell pressure was 1.2 psia.
21	32	4/30	6	750	2000	0.99/ 4.00	Fuel injec. not planned	E	1	42	-	-	Determine effect of varying wedge nozzle flow	Tunnel config. identical to run 20. Tunnel start obtained when inlet spike cycled twice. Test cell pressure of 1.0 psia obtained. Wedge nozzle has negligible effect on cell pressure.
22	33	5/4	6	750		0.99/ 4.00	1B, 2B	E	1	25	-	-	Investigate inlet unstart limit with first stage combustion	First successful supersonic combustion run. Intentional inlet unstart when first stage equivalence ratio reached 0.34. No second stage fuel added. O-ring between the outerbody and the cowl leading edge extruded.
23	34	5/15/73	6	750/ 930	3000	0.99/ 4.00	1A,1B,2A, 3A	E	2	08	-	-	Checkout AIM and facility. Fuel rich at P_{T_0} = 750 psia ϕ= 1.0 at P_{T_0} = 930 psia	Tunnel start and inlet start obtained. ϕ of 1.35 set at P_{T_0} = 150 psia and ϕ of 1.00 set at P_{T_0} = 930 psia. Facility fuel control valve for injector 1B oscillated. Run proved AIM and tunnel can operate at $\phi > 1.0$. Erosion of zirconium oxide coating on outer cowl body crossover manifold noted. Erosion caused by carbon dust in tunnel flow.
24	35	5/16/73	6	750	3000	0.99/ 4.00	1A,1B,2A,2C	E	-	25	-	-	Checkout AIM and facility. Design injector locations	Test was aborted when engine inlet unstart was observed three seconds after initiation of fuel injection. The engine unstart was result of injecting excessive fuel, caused by malfunction of facility control valve. Inspection of AIM unit revealed that the coolant leak on the spike assembly had progressed, and repair was necessary.
25	36	5/24	6	750	3000	0.99/ 4.00	1A,1B,2A,2C	E	2	19	1	38	Demonstrate operation with design injector location and determine auto ignition limit	First good run with design injector locations. Auto ignition obtained at ϕ = 0.55; first stage did not light until second stage fuel added. Overall ϕ ramped to 1.0 with first stage ϕ held at 0.24.
26	37	5/30/73	6	750	3000	0.99/ 4.00	-	E	-	-	-	-	Determine effect of first stage ϕ on combustor performance	Test aborted due to malfunction of the steam ejector system
	38	5/30	6	750	3000	0.99/ 4.00	1A,1B,2A,2C	E	-	47	-	26	Determine effect of first stage ϕ on combustor performance	Test aborted when inlet unstarted. Malfunction of the facility fuel control valve resulted in injecting excessive fuel into injector 2C. 3 small cracks in spike skin in region of igniters found in post run inspection. Cracks repaired to prevent water leak into combustor.
	39 thru 48	-	-	-	-	-	-	F	-	-	-	-	Purge system calibration test	
27	49	10/4/73	6	750	3000	-	-	E	-	-	-	-	Combustor optimization	TAFP
	50	10/5/73	6	750	3000	-	-						Combustor optimization	TAFP
	51	10/5/73	6	750	3000	0.99/ 4.00	1A,1B,2A,2C	E	2	39	2	09	Combustor optimization	Fuel control problems encountered.
28	52	10/10/73	6	750	3000	0.99/ 4.00	1A,1B,2C,4	E	1	21	-	50	Combustor optimization	Investigating performance improvement due to injecting fuel closer to inlet. Inlet unstarted at overall ϕ of .83.
	53	10/10	-	-	-	-	-	E	-	-	-	-	Purge system calibration test. Evacuated test cell.	
29	54	10/11/73	6	750	3000	0.99/ 4.00	1A,1B,2A,2C	E	3	04	2	13	Combustor optimization	Attempt to determine effect of first stage ϕ and thrust on performance. Auto ignition obtained at ϕ = .54. Data taken with igniters on and off to determine effect on performance. Inspection of unit revealed excessive coolant leak at spike/ igniter body interface. Repair necessary. Tunnel operating procedure modified to reduce water ingestion into AIM wall pressure taps.
	55	10/17/74	-	-	-	-	-	E	-	-	-	-	Purge system calibration test. Evacuated test cell.	
30	56	11/2/73	6	750	3000	-	-	E	-	-	-	-	Combustor optimization	Effect of first stage ϕ and second stage injectors at overall ϕ = 1.0 investigated. Also all second stage fuel added first, and then first stage ϕ. Fuel staging promoted off wall pressure distortion. Combustor wall pressure distortion was not affected by thermal expansion of fuel manifold. Inlet unstarted at overall ϕ of 1.0 with first stage ϕ = 0.34. Cowl pressure tap PA2 repaired for this run. Combined fuel to injectors 1A, 1B, 2A, 2C.

ORIGINAL PAGE IS OF POOR QUALITY

TABLE 5-2 (Continued)

Run No.	Reading No.	Date	Inlet Condition: Mach No.	Inlet Condition: P_{T_2}, Psia	Inlet Condition: T_{T_2}, °R	Inlet Spike Position, in.	Fuel Injectors Used	Tunnel Config.	Time: Run Min	Time: Run Sec	Time: Useful Min	Time: Useful Sec	Objective of Test	Comments
	57	11/2/73	6	750	3000	0.99/ 4.00	1A,1B,2A 2C	E	-	-	-	-		
	58	11/7/74	-	-	-	-	-	E	-	-	-	-	Purge system calibration	Determine effect of thermal expansion of fuel manifold 1B.
31	59	11/8/73	6	750	3000	-	-		-	-	-	-	Combustor optimization	TAFP
	60	11/8/73	6	750	3000	0.99/ 4.00	1A,1B,2A, 2C	E	2	34	2	04	Combustor optimization	Overall ϕ held constant while amount of fuel from innerbod and outerbody injectors varied. Fuel temperature compensation added to fuel control
32	61	11/13/73	6	750	3000	0.99/ 1.72/ 2.52	1A,1B,2A, 2C	E	2	50	2	21	Determine effect of spike position on engine performance	Inlet massflow ratios of 0.51 and 0.58 ran by varying the inlet spike position. Aft wall pressure distribution measured with fuel line purge flow shut off. Reworked section of the innerbod assembly burned and damaged during combustion; damaged section was removed. Operational procedure modified to prevent further damage.
33	62	11/20/73	6	930/ 466	3000			E					Performance test	TAFP
	63	11/21/73	6	930/ 466	3000	0.99/ 4.00	1A,1B,2A, 2C		2	59	1	52	Performance test	Tunnel total pressure varied to determine effect of altitude on performance.
34	64	11/28/73	6	750	3000	0.99/ 4.00	1B,2A,2C, 3A,3B	E	3	38	2	35	Subsonic-supersonic combustor mode transition	Transition from subsonic to supersonic combustion mode demonstrated. Inspection of unit revealed coolant was flowing into the 1B fuel manifold and a nickel plated section of the innerbody had blistered. Separation at the spike skirt-spike body has progressed to approximately 1.0 inches. Forward facing step at the interface of the cowl leading edge assembly and the outerbody had progressed to approximately .065 inches. Larger fuel metering venturi installed in fuel system E.
35	65	12/11/73	6	750	3000	4.00	1A,1B,2A, 2C	E	2	52	1	44	Supersonic combustion with instrumentation rig	Instrumentation rake installed. Rake caused tunnel to unstart at ϕ = 1.25. Exhaust gas sampling data taken.
	66	12/14	-	-	-	-	-	E	-	-	-	-	Purge system calibration	TAFP
	67	12/14	-	-	-	-	-		-	-	-	-	Purge system calibration	N_2 purge force calibration with cell evacuated.
36	68	12/14/73	6	750	3000	-	-		-	-	-	-		Time of steady state fuel flow increased to 20 seconds to allow gas sampling data to stabilize.
	69	12/14/73	6	750	3000	4.00	1A,1B,2A, 2C	E	3	20	2	17	Supersonic combustion	One tunnel unstart experienced near end of run. Several tunnel unstarts prevented by shutting off fuel. Incipient unstart detected by monitoring luminescent normal shock position in T.V. view of tunnel.
37	70	12/19/73	6	750	3000	-	-	E	-	-	-	-	Determine effects of angle of attack	Test terminated prematurely due to frozen vent valve.
	71	12/19/73	6	750	3000	4.00	1A,1B,2A, 2C		3	56	2	29		Cowl leading edge assembly removed after this run to remove facing step noted after reading 6m.
	72												Purge system calibration	Calibration with 1B fuel injector manifold heated test cell evacuated.
47	73 74,75	02/74	7	1000	3100	-	-	E	-	-	-	-	Mach 7 facility checkout	Test terminated due to failure of primary [illegible] (TAFP
	76	1/23/74	7	1000	3100	-	-	E	-	-	-	-	Mach 7 facility checkout	TAFP
	77	1/23/74	7	1000	3100	2.27	-	E	2	-	-	-	Mach 7 facility checkout	Attempt to start tunnel at Mach 7 unsuccessful. Secondary steam ejector inadequate; nozzle pressure varied; inlet spike assembly modified.
48	78	1/26/74	7	1000	3100	2.27	-		4	-	-	-	Mach 7 facility checkout	Test aborted after attempted tunnel start. TAFP [illegible] and [illegible]
49	79	1/26/74	7	1000	3100	-	-		-	-	-	-	Facility checkout	Aft wall pressure measurements.
50	80	1/28/74	7	1000	3100	2.27	-		2	-	-	-		TAFP. Model water system failure.
	81	1/28/74	7	1000	3100	2.27	-		2	-	-	-		[illegible]
	82	1/28/74	7	1000	3100	2.27	-		2	-	-	-		[illegible]
	83	1/28/74	7	1000	3100	2.27	-		2	-	-	-		[illegible]
51	84	1/30/74	7	1000	3100	2.27	-		2	-	-	-		[illegible]
	85	1/30/74	7	1000	3100	2.27	-		2	-	-	-		[illegible]
	86	1/30/74	7	1000	3100	2.27	-		2	-	-	-		[illegible]
	87	1/30/74	7	1000	3100	2.27	-		2	-	-	-		[illegible]
52	88	1/31/74	7	1000	3100	2.27	-		2	-	-	-		[illegible]
	89	1/31/74	7	1000	3100	2.27	-		2	-	-	-		[illegible]
	90	1/31/74	7	1000	3100	2.27	-		2	-	-	-		[illegible]
	91	1/31/74	7	1000	3100	2.27	-		2	-	-	-		[illegible]

ORIGINAL PAGE IS OF POOR QUALITY

ORIGINAL PAGE IS OF POOR QUALITY

TABLE 5-2 (Continued)

Run No.	Reading No.	Date	Inlet Condition			Inlet Spike Position, In.	Fuel Injectors Used	Tunnel Config.	Time				Objective of Test	Comments
			Mach No.	P_{T0}, Psia	T_{T0}, °R				Run		Useful			
									Min	Sec	Min	Sec		
52	88	3/28	7	1000	3100	2.57	1A,1B,2A, 2C	F	2	45	1	31	Combustion evaluation	First successful Mach 7 run. Tunnel closure removed. Diffuser seal repaired. Effect of fuel injection location investigated. Row 2 igniters on. Outer cowl body support damaged by carbon particles in tunnel flow due to failure of carbon part in facility heater. Shroud inlet pressure rake hit and damaged. Repaired outer cowl body support and water cooled protective wedge installed. Coolant leak at the interface of spike skirt and spike body noted at angular location 270° in addition to leak at 180 degrees noted in Rdg 64. Leak at 180° progressed to approximately 1.25 inches. Cowl leading edge tip radius and spike tip damaged by particles. Damaged areas reworked.
53	89	3/15/74	7	1000	3000	2.57	1A,1B,2A, 2C,4	F	3	-	2	02	Combustor optimization	Performance measured with various fuel injection schemes. T_{T0} varied during run. Igniters on. Test terminated prematurely due to failure of transducer in fuel control causing fuel control valve to fully open. Abnormal amount of carbon dust observed in tunnel flow. Cowl leading edge tip radius and spike tip again damaged. Tip section repaired.
54	90	3/[illegible]/75	7	1000	3000	2.57	1A,1B,1C, 4	F	3	09	1	16	Combustor optimization	Second stage fuel injection closer to inlet (injectors 1C, 4). Inlet unstarts encountered.
55	91	3/[illegible]/74	7	1000	3000	2.57	1A,1B,2C, 4	F	2	52	1	32	Effect of angle of attack	Tunnel start improved at angle of attack. Tunnel started at P_{T0} = 850 psia. 3 inlet unstarts encountered due to excessive 1st stage fuel. Total coolant leak into combustor estimated to be 5.0 gpm.
56	92	3/19/74	7	1000	2900	2.57	1A,1B,2C, 4	F	3	50	2	30	Combustor performance with instrumentation rake installed.	Instrumentation rake blockage had adverse effect on tunnel start. Inlet spike stroked twice to start tunnel. Oxygen content of tunnel flow varied while AIM exhaust gas sampling data taken.
57	93	3/27/74	5	415	2210	4.0	1A,1B,2A, 3A,3B	-	0	85	-	-	Facility check-out	First Mach 5 run. Subsonic combustion data obtained. Run terminated prematurely (TAFP).
58	94	3/28/74	5	(a) 415 (b) 300 (c) 206	2210 3000 2210	4.00 4.00 4.00	1A,1B,2A, 3A,3B 1A,1B,2A, 3A,3B 1A,1B,2A, 3A,3B	F	2	25	2	01	Combustor optimization	Subsonic and supersonic combustion and transition demonstrated. Four unstarts experienced, three unstarts attributed to high cell pressure, one to injecting excessive fuel intentionally into the AIM. More carbon in tunnel flow. Cowl leading edge and spike tip damaged. Both reworked.
59	95	3/29/74	5	415 300 206	2210 3000 2210	4.00 4.00 4.00	1A,1B,2A, 2C 1A,1B,2A, 2C 1A,1B,2A, 2C	F	3	+1	3	20	Combustor optimization	All comments made for Rdg 94 applicable for this run, except combustion was limited to supersonic combustion mode. Four engine unstarts experienced. Three unstarts were attributed to facility conditions and the other to programmed to determine inlet unstart limit.
60	96	4/[illegible]	5	415 300 206	2210 3000 2210	4.00 4.00 4.00	1A,1B,2A, 3A,3B	F					Evaluate effects of angle of attack	Subsonic and supersonic combustion and transition demonstrated at angle of attack. Intentional engine unstart obtained when excessive fuel was injected in supersonic combustion mode.
61	97	4/22	5	206 / 415	2210	4.00	1A, 3A, 3B	F					Combustor performance with instrumentation rake installed	Combustor exit flow conditions surveyed. Gas sampling data taken. Blockage of instrumentation rake had adverse effect on tunnel operation.

was available. To assist in determining the success of the test, and to plan the following tests, a limited amount of data reduction was performed at the test site.

Although 400 channels of recordings could be made on the tape, limited signal-conditioning equipment resulted in recording only 150 pressure-sensing channels from the AIM. The scan rate of each channel was five per second. Difficulties encountered in obtaining good data further decreased the number of usable recorded channels. The inability to record all desired pressure data on the AIM affected some of the analyses, as well.

6. DATA REDUCTION AND METHOD OF CALCULATION

A computer program was used in reducing the data from the AIM tests. The computer program was a cooperative effort by personnel from NASA-LeRC and AiResearch. NASA-LeRC was responsible for formulating that portion of the program that converted the test data to engineering units and also the computed surface-pressure integrals and the skin friction coefficients. AiResearch personnel were responsible for the performance section of the computer program. The chemical equilibria of the synthetic air and fuel-air mixtures were claculated by using subroutines in the computer program, described in Reference 6.0-1.

6.1 SUMMARY DESCRIPTION OF PERFORMANCE PROGRAM

Several methods were used to establish validity of critical parameters, such as the wind tunnel Mach number. The first method used curves generated from instrumentation rakes installed upstream of the engine during calibration of the wind tunnel. The second method used measured values of wind tunnel total pressure and temperature, and pitot pressure at the spike tip along with real-gas normal-shock solution to calculate the wind tunnel Mach number. The third method used measured values of wind tunnel total temperature, spike-tip pitot pressure, and spike-cone surface pressure, along with the real-gas normal- and conical-shock solutions, to calculate the wind tunnel Mach number. Calculations made utilizing each of the three methods indicated good agreement. After confidence was established in the three methods, the use of the third method was discontinued, since it required excessive computer time.

The conditions at the inlet throat were determined by computing the momentum and total enthalpy considering losses incurred on the inlet spike and the internal surfaces. The inlet mass flow ratio and additive drag were determined from theoretical calculations. Pressures used in these calculations were obtained as follows: For conditions where inlet start was obtained ($M_i > 1$) the calculated mass-momentum-average static pressure was used, and the measured static pressures at the throat were not used. For conditions where inlet unstart was experienced ($M_i = 1$) the average of the measured static pressures at the throat was used, with the Mach number constrained to unity to calculate spillage and additive drag. In both cases the flow was expanded to the free-stream static pressure to obtain kinetic energy and process efficiencies. Total conditions were obtained by compressing the flow isentropically until the calculated enthalpy matched the known total enthalpy. When the inlet was started, a side calculation was made by isentropically expanding the flow to an area 10 percent larger than the throat area. At this point, they flow was passed through a normal shock. The limiting inlet pressure recovery and the kinetic energy and process efficiencies were determined from conditions downstream of the normal shock.

PRECEDING PAGE BLANK NOT FILMED

Two methods were used to calculate conditions at the combustor stations. Up to the first station where fuel was injected, the mass-momentum-averaged static pressure that satisfied the state, continuity, momentum and energy equations was calculated. After fuel was injected, the average of the measured inner- and outerbody pressures was used, and the combustor efficiency was calculated to satisfy the conservation equations. The concept of real and inert hydrogen was used to define combustor efficiency equal to the weight-fraction of real hydrogen. The inert hydrogen was permitted neither to dissociate nor to react with other species.

The combustor throat was defined as the point of minimum-flow area between the struts in subsonic combustion, and at the strut exit plane in supersonic combustion. When the Mach number at the combustor throat was less than 0.95, a side calculation was made of the combustor efficiency required to produce sonic velocity at the throat.

The regeneratively-cooled combustor performance was simulated by recalculating the total enthalpy at the combustor exit as the sum of the freestream enthalpy of the synthetic air, the enthalpy of the hydrogen fuel at 50^0 Rankine, and the absolute value of the heat loss through the nozzle surfaces.

Nozzle performance was obtained by isentropically expanding the flow from the actual and regeneratively-cooled combustor exits, both to the nozzle exit area and to ambient pressure. The flow was then isentropically expanded from the actual combustor throat to those nozzle stations representing the locations of pressure taps, and the local skin friction coefficients were calculated. The nozzle vacuum stream thrust coefficient was obtained from the surface-pressure integrals on the nozzle walls, the nozzle friction drag, and the stream thrust (momentum) at the combustor and nozzle exits.

Side calculations were made of a fictitious constant-pressure zero-velocity combustor at 100 percent combustor efficiency with isentropic expansion to ambient pressure to obtain the combustor effectiveness, and of a fictitious nozzle to determine the static and total conditions required to match the actual vacuum specific impulse at the nozzle exit.

6.2 CALCULATION OF COOLING LOAD DISTRIBUTION

In AIM testing, it was originally planned to measure the water temperature rise at many points in the engine in determining its cooling load distribution and overall heat loss. However, because of faulty thermocouple readings, reliable water temperature rise was not obtained. Therefore, the heat loss distribution was determined from the differences between the skin thermocouples imbedded in the engine surfaces and the cooling water temperatures. Standard heat transfer equations were used to obtain local heat losses. These losses were then adjusted linearly with the overall heat loss as measured by the overall water temperature rise. This method was considered to be more reliable because the temperature differential between the skin and water was large, thus, small variation of water temperature would not seriously affect the heat transfer rate. The detailed equations and procedures used for computation are presented in Appendix B.

6.3 CORRELATION OF CAVITY FORCES

The purge nitrogen in the AIM cavity between the shroud and the outer-body produced a large tare force which was of the same order of magnitude as the engine net thrust. Since the thrust is considered the most important measurement in evaluating the engine performance, this tare force was calibrated and correlated in order to determine the correction for the measured thrust.

A sketch of the AIM cavity is shown in Figure 6.3-1. The cavity is divided into two compartments, the forward (A) and aft (B) cavities, separated by a sliding seal. Without this seal, the entire cavity would have to operate at a higher pressure dictated by the higher external surface pressure near the forward purge slot resulting in higher purge flow and cavity forces.

The nitrogen was fed into the forward cavity through an injection ring in the rear compartment of cavity A. Most of the purge flow is discharged through the forward purge slot. Some of the nitrogen leaks through the seal to pressurize the aft cavity. During the tests, it was noted that the leakage rate was sufficient to maintain the aft cavity pressure and the nitrogen line for the aft cavity was not used. The nitrogen flow was controlled by setting the forward cavity discharge pressure (P_{A1}) at a desired value.

There were two static pressure taps located in the front and back of each cavity (P_{A1}, P_{A2} and P_{B1}, P_{B2}). It was observed during the tests that the pressure ratio P_{A2}/P_{A1} increased with increasing hydrogen manifold temperature, resulting from the thermal expansion of the manifold, thus restricting the flow of the purge gas between the manifold insulation and the shroud. The cavity force was also affected when a load was applied to the engine. Varying the load on the engine resulted in change of the width of the slot from which the purge gas escaped from the forward purge cavity.

The flow path in the aft cavity was less restrictive. However, since the projected area was large, the net change in the cavity force was sensitive to the pressure changes in the aft purge cavity.

In view of the limited instrumentation and very complex flow paths, accurate calculation of cavity force from direct integration of pressure forces is not possible. Other attempts such as that presented in Reference 6.3-1 did not yield any useful results. A statistical approach was, therefore, used to correlate the measured cavity pressures.

This correlation used a multiple curvilinear regression which assumed the cavity force was a function of the combinations of the five measured pressures (P_{A1}, P_{A2}, P_{B1}, P_{B2} and P_{amb}). Among numerous combinations examined, the following equation gave the most satisfactory results.

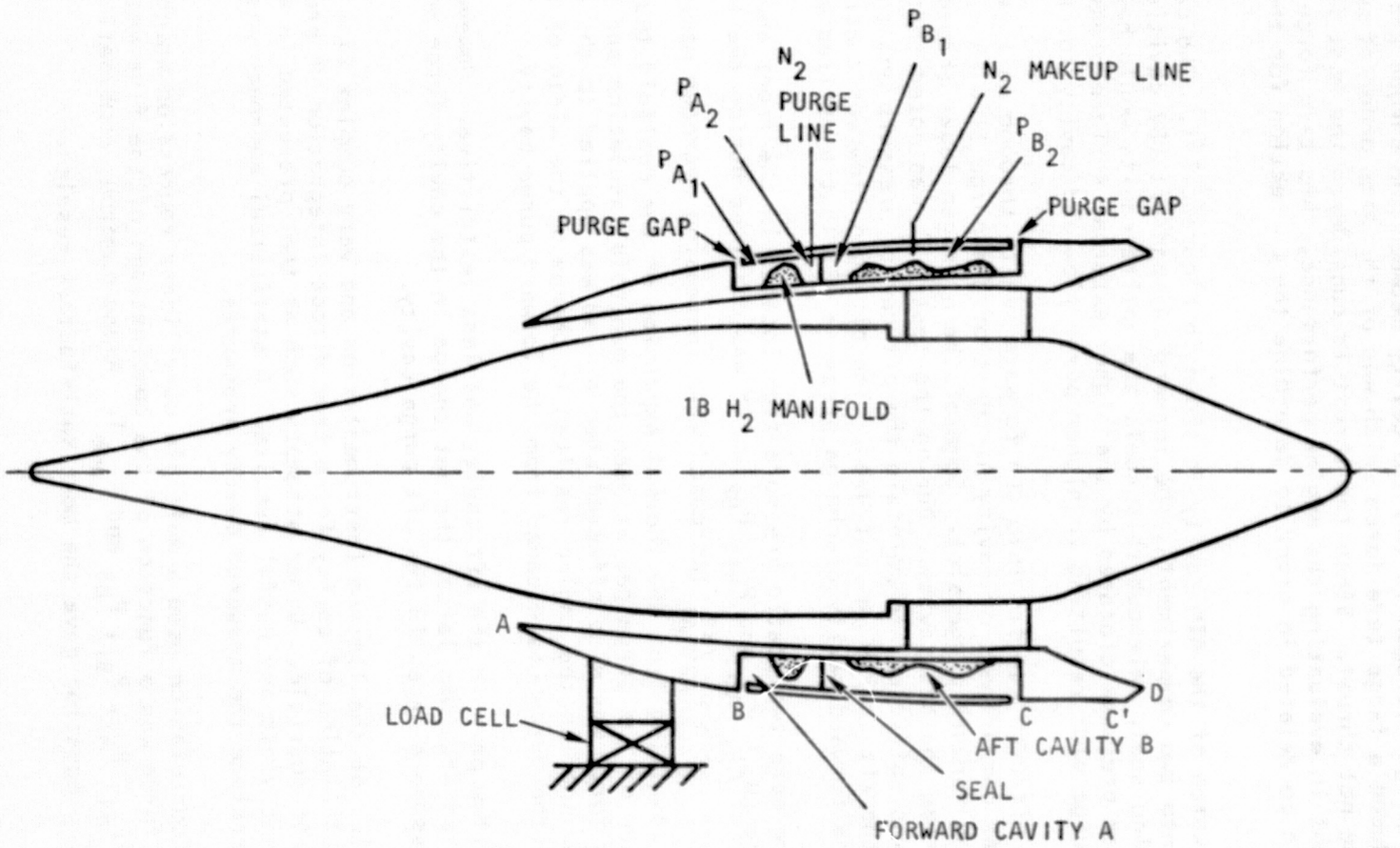

Figure 6.3-1. AIM Cavity

$$F_{cavity} = A_1(P_{A1} - P_{amb}) + A_2(P_{A2} - P_{amb}) + A_3(P_{B1} - P_{amb})$$
$$+ A_4(P_{B2} - P_{amb}) + A_5(P_{A2} - P_{amb})\left(\frac{P_{A2}}{P_{A1}}\right)$$
$$+ A_6(P_{A2} - P_{amb})\left(\frac{P_{A2}}{P_{B1}}\right) + A_7(P_{A1} - P_{amb})\left(\frac{P_{A1}}{P_{amb}}\right)$$
$$+ A_8(P_{B2} - P_{amb})\left(\frac{P_{B2}}{P_{amb}}\right) + A_9(P_{B1} - P_{amb})\left(\frac{P_{B1}}{P_{B2}}\right) + A_{10} \quad (6.3\text{-}1)$$

$$(F_{cavity})_{abs} = F_{cavity} - 130(P_{amb}) \quad (6.3\text{-}2)$$

where the first four terms in Eq. 6.3-1 represent the effect of measured pressures, and the next five terms account for the effects of pressure ratios along various flow paths. The last term is a constant which represents an extraneous unknown force and also provides a check of correctness of the correlation and data. $(F_{cavity})_{abs}$ is the absolute force acting on the internal surfaces of the cavity.

Data used for this correlation was obtained from readings 99, 101, and 105, with B cavity valve closed. Reading 99 was the calibration run without the preload, reading 101 with a drag preload of 217 lb (reduced forward slot width), and reading 105 was the run with hot-hydrogen manifold. These three runs encompass the effects of cavity pressures, purge slot width (preload), and manifold temperatures. A total of 88 data points was used.

AiResearch computer program COR528 was used to calculate the coefficients in Equation 6.3-1. This program calculates the coefficients to yield the minimum error between the measured and calculated values by the method of least squares. The following are the coefficients determined from this program:

$A_1 = -142.492$, $A_2 = 94.017$, $A_3 = 122.484$, $A_4 = -29.125$,

$A_5 = -68.743$, $A_6 = 21.333$, $A_7 = 2.409$, $A_8 = -12.084$,

$A_9 = -105.094$, $A_{10} = -4.686$

The standard error, defined below, is 21 lb.

$$\text{Standard error} = \sqrt{\frac{\sum_{1}^{N}(F_{calculated} - F_{measured})^2}{N}}$$

Figure 6.3-2 contains a plot of the correlated forces.

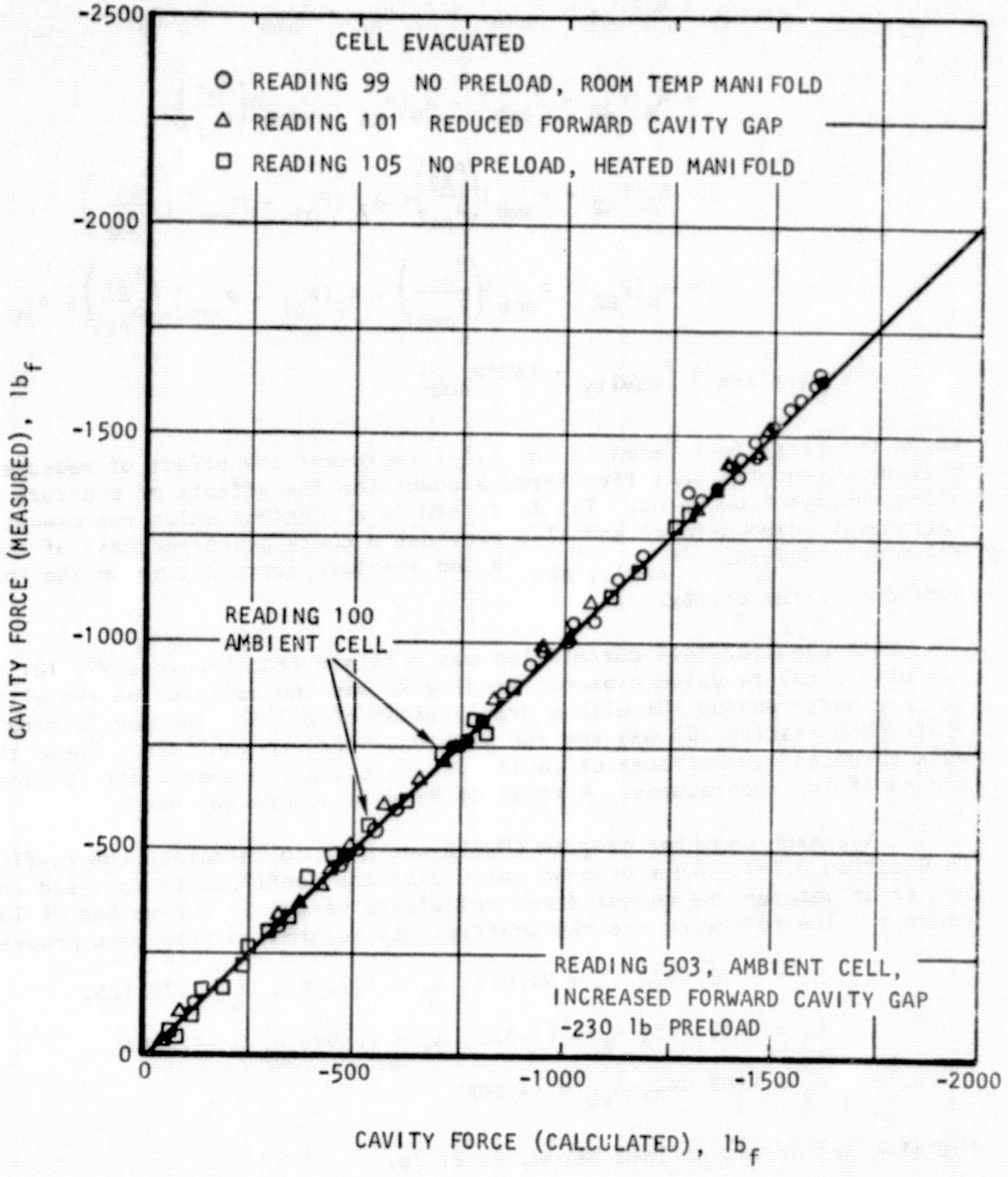

Figure 6.3-2. Correlation of Cavity Forces

An interesting check was made for readings 100 and 503 from which data were not used in the correlation. Both runs were made at ambient pressure; reading 503 was preloaded in the thrust direction, increasing the forward purge slot gap. The results are tabulated below:

	Time	$F_{measured}$	$F_{calculated}$	% Error
Reading 100	2005	-556.1	-545.85	1.84
	1758.39	-735.54	-702	4.56
Reading 503	1222.19	-336.07	-328.83	2.15

6.4 DETERMINATION OF EXTERNAL DRAG

The external drag was calculated from the summation of pressure and friction forces acting on the external metric surfaces of AIM. The calculation began from Station A to B and from C to D as shown in Figure 6.3-1.

(a) Pressure Forces

The calculation of pressure force from A to B was divided into three sections, and C to D into two sections:

$$\int_{ext.} PdA = \left[\int_{X_{CL}-.036}^{X_{CL}+.553} PdA_1 + \int_{X_{CL}+.553}^{X_{CL}+4.116} PdA_2 + \int_{X_{CL}+4.116}^{X_{CL}+6.366} PdA_3 \right]_{A-B}$$

$$+ \left[\int_{X_{CL}+32.096}^{X_{CL}+35.214} PdA_4 + \int_{X_{CL}+35.214}^{X_{CL}+38.34} PdA_5 \right]_{C-D}$$

The first term, from X_{CL}-0.036 to X_{CL}+0.553, was determined theoretically because there were no pressure measurements forward of Station X_{CL}+0.616 as:

$$\int PdA_1 = C_D \cdot q_o \cdot A_{ref}$$

where $C_D = 0.11$, $A_{ref} = 256.13$ in.^{2}, q_o = freestream dynamic pressure, psia. The second term, $\int PdA_2$, was calculated from averaged measured pressures and their corresponding projected areas as:

$$\int PdA_2 = \sum P_{ave.} \Delta A$$

The third term, $\int PdA_3$, was handled differently because the surface pressures in this region were influenced by the non-uniform nitrogen purge from the slot at Station X_{CL}+6.366. Test results indicated that high pressures were limited to

two narrow regions, one between the support pylons and the other at 0-deg position as shown in Figure 6.4-1; therefore, an area-weighted average was used for this region:

$$\int PdA_3 = 55.821 \times \left[\frac{1}{6}\left(\frac{P_{14} + P_{16} + P_{22} + P_{23} + P_{24} + P_{25}}{6}\right) + \frac{5}{6}\left(\frac{2 \times P_{13} + P_{17} + P_{18} + P_{20} + P_{21}}{6}\right)\right]$$

The pressure integral of the fourth term, $\int PdA_4$, was assumed zero in all cases, because there was no projected area change in this region. Even at 3 deg angle of attack, the estimated force was about 0.1 percent of the total external force, therefore,

$$\int PdA_4 = 0$$

The forces acting on the aft portion of the outer cowl were calculated from circumferential sectors of the aft annulus. The extent of the sector was estimated as that portion on which the outer cowl measured-pressures were acting.

$$\int PdA_5 = 75.76 \left(\frac{X}{360}\right) P_{measured}$$

where 75.76 $in.^2$ is the total projected area, and X's are as defined below:

P_{meas}	X
$P_{21\text{-}NO}$	6
$1/5\ (P_{26\text{-}NO} + P_{18\text{-}NO} + P_{19\text{-}NO} + P_{34\text{-}NO} + P_{20\text{-}NO})$	28
$P_{24\text{-}NO}$	14
$P_{25\text{-}NO}$	14
$P_{27\text{-}NO}$	14
$P_{28\text{-}NO}$	14
$P_{32\text{-}NO}$	14
$1/3\ (P_{22\text{-}NO} + P_{16\text{-}NO} + P_{23\text{-}NO})$	18
$1/3\ (P_{29\text{-}NO} + P_{30\text{-}NO} + P_{17\text{-}NO})$	208
$P_{31\text{-}NO}$	18
$P_{33\text{-}NO}$	12
$\Sigma =$	360

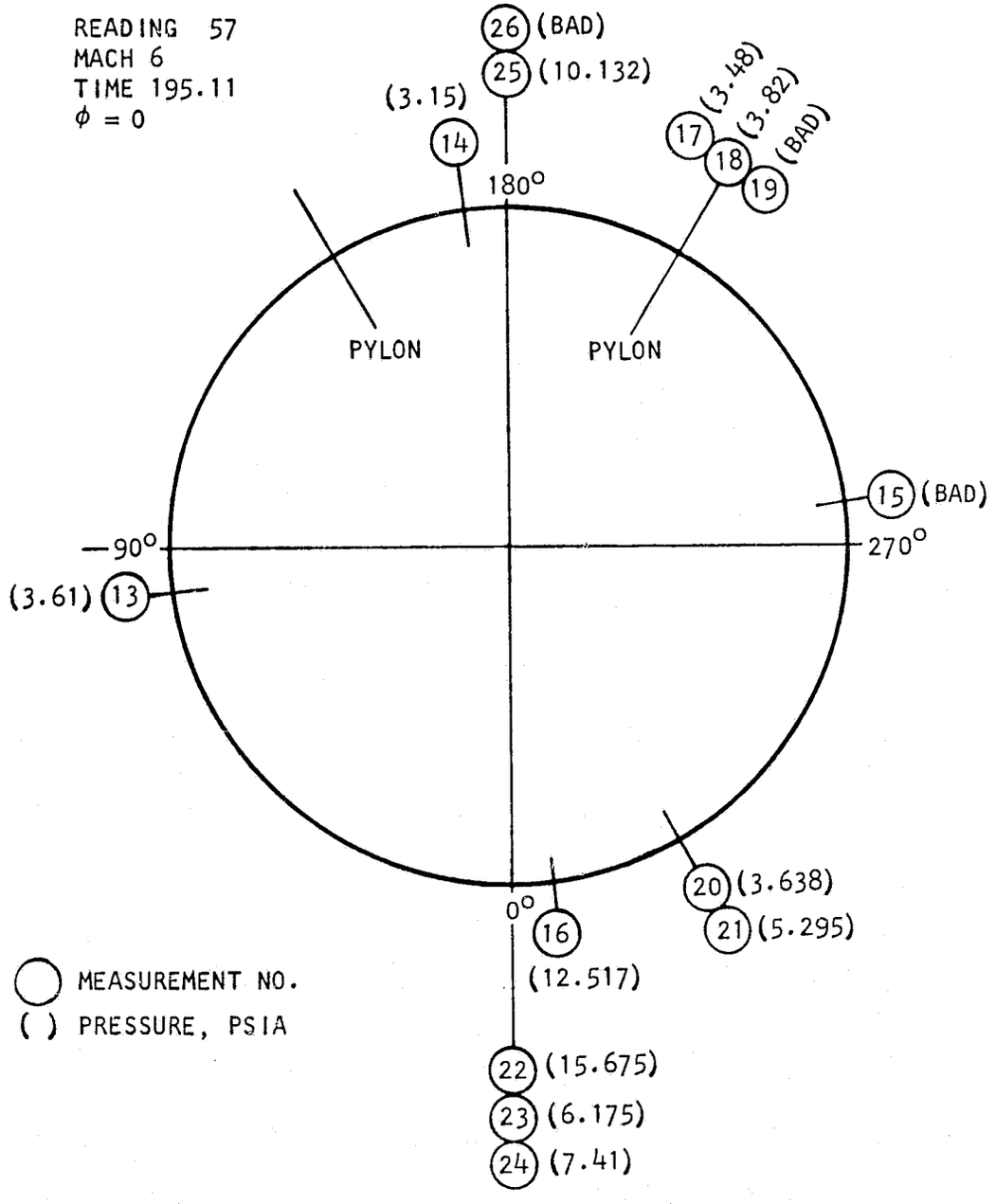

Figure 6.4-1. Typical External Surface Pressure Distribution Between X_{CL}+4.116 to X_{CL}+6.366

(b) Friction Drag

The calculation of friction drag was based on Spalding and Chi's analysis; detailed calculation procedure was presented in Reference 6.0-1.

$$\sum \text{Friction force} = \sum C_{f_{local}} \, q_L \, A_{wetted}$$

where $C_{f_{local}}$ = local friction coefficient obtained from Spalding and Chi's analysis

q_L = local dynamic pressure

A_{wetted} = wetted surface area

(c) External Drag

In reading 65, 69, 88, 92, and 97, special calculations of external drag were necessary because instrumentation channels for external surface pressures were used for other purposes. Therefore, a correlation was made to determine the external drag coefficient against test cell pressure as shown in Figure 6.4-2. It indicated that at Mach 5 and 7, the external drag coefficient was approximately 0.5 but increased with increased cell pressure for Mach 6 tests. This was attributed to a high pressure (Reference 6.4-1) donut-shaped ring existing between AIM and the facility shroud which moved forward, exerting the high pressure on the external metric surface when backpressure was increased, and simultaneously caused the cell pressure to increase. Figure 6.4-3 shows this phenomenon more clearly at Mach 6.

6.5 STRUT FORCE CALCULATION

The performance program was originally programmed to calculate strut force based on a theoretical calculation, assuming uniform flow ahead of the strut. This force would calculate as a drag term since, theoretically, pressures downstream of the maximum strut blockage should be lower than upstream.

However, test data indicate that the above is only true with subsonic combustion. For supersonic combustion, pressures downstream of the maximum strut blockage (measured between struts) were actually higher than upstream. In fact, data indicated significant combustion occurring between struts for the supersonic case.

Thus, the assumption that the strut force would always be a drag term was not correct. In some cases, it actually produced a thrust.

Examining test data, it appeared that measured static pressures between struts (there were no measurements along the strut surfaces) on both the inner and outer wall could be used to represent the forces occurring on the strut surface. Thus, a pressure integral was used to determine strut force, and a calculation was also made for strut base pressure, since the measurements between struts were not indicative of this lower value.

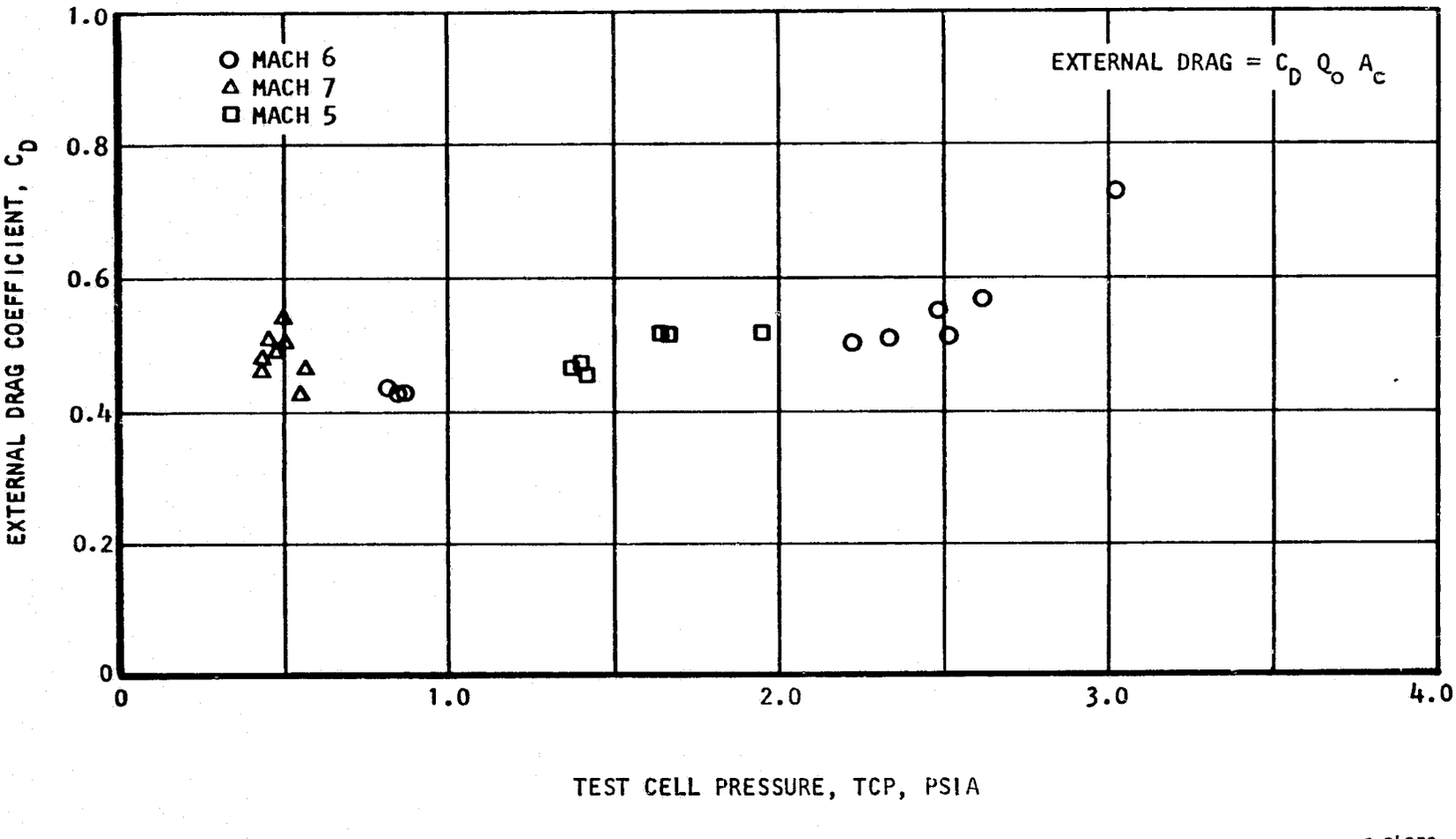

Figure 6.4-2. AIM External Drag

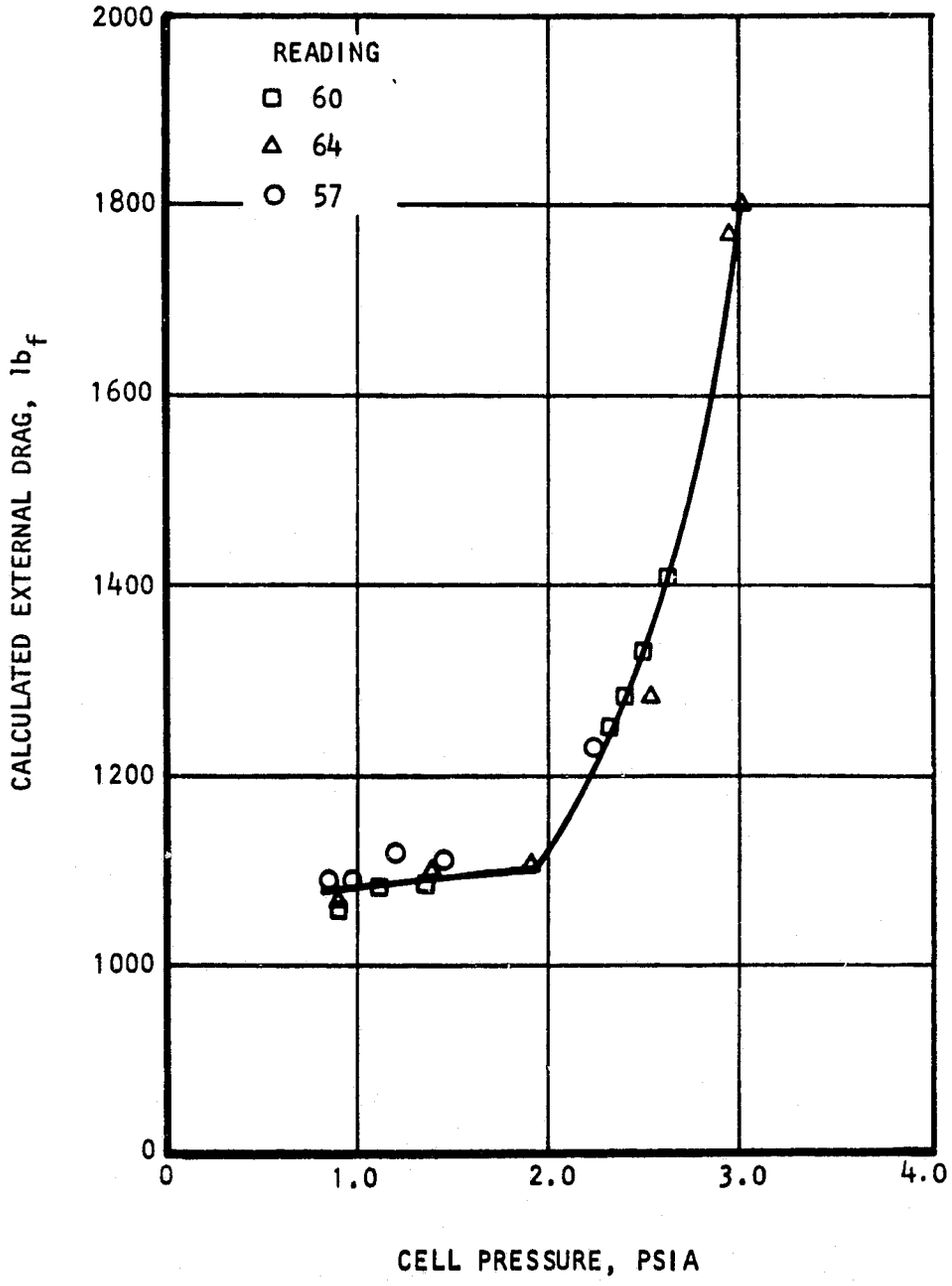

S-94971

Figure 6.4-3. Correlation of External Drag at Mach 6

The strut force obtained from the pressure integral was then linearly distributed over the strut length to obtain flow momentum at any station along the strut. The method devised was applied to all test data at an equivalence ratio of zero, and for both subsonic and supersonic combustion.

The base pressure correlation is presented in Figure 6.5-1.

6.6 PERFORMANCE CORRECTION FOR REGENERATIVELY COOLED SYSTEM

The AIM incorporated a water-cooled jacket in which heat was rejected and not recovered. In order to compensate for this heat loss, hydrogen fuel was heated up to 1500°R to simulate a regeneratively-cooled system. The differences between the heat added to fuel and the internal cooling loss are presented in Table 6.6-1 for several tests. The deficiency of energy in the system in terms of theoretical energy release was less than 10 percent in all cases.

In order to correct this deficiency, the one-dimensional data reduction computer program incorporated a side calculation in which the energy deficiency and the heat loss through nozzle surfaces was added to the stream at the combustor exit with no total pressure change. The flow was then expanded to the nozzle exit with measured nozzle efficiency.

TABLE 6.6-1

HEAT ADDED TO FUEL VS INTERNAL COOLING LOSSES

Reading Number	Time	Mach No.	f/a	Total Enthalpy for Regeneratively-Cooled System, H_{reg}, Btu/lb mix	Total Enthalpy at Test, H_{test}, Btu/lb mix	$\frac{H_{reg}-H_{test}}{H_{comb}}$, Percent
54	191.56	6	0.0164	624.4	557.2	8.07
64	293.81	6	0.0311	590.7	536.7	3.4
93	142.13	5.1	0.0126	374.8	340.6	5.33
93	150.23	5.2	0.0246	361.5	301.6	4.83
88	261.6	7.2	0.013	716.4	638.2	8.46
88	305.7	7.2	0.0283	632.6	492.1	9.88

H_{comb} = Theoretical heat release

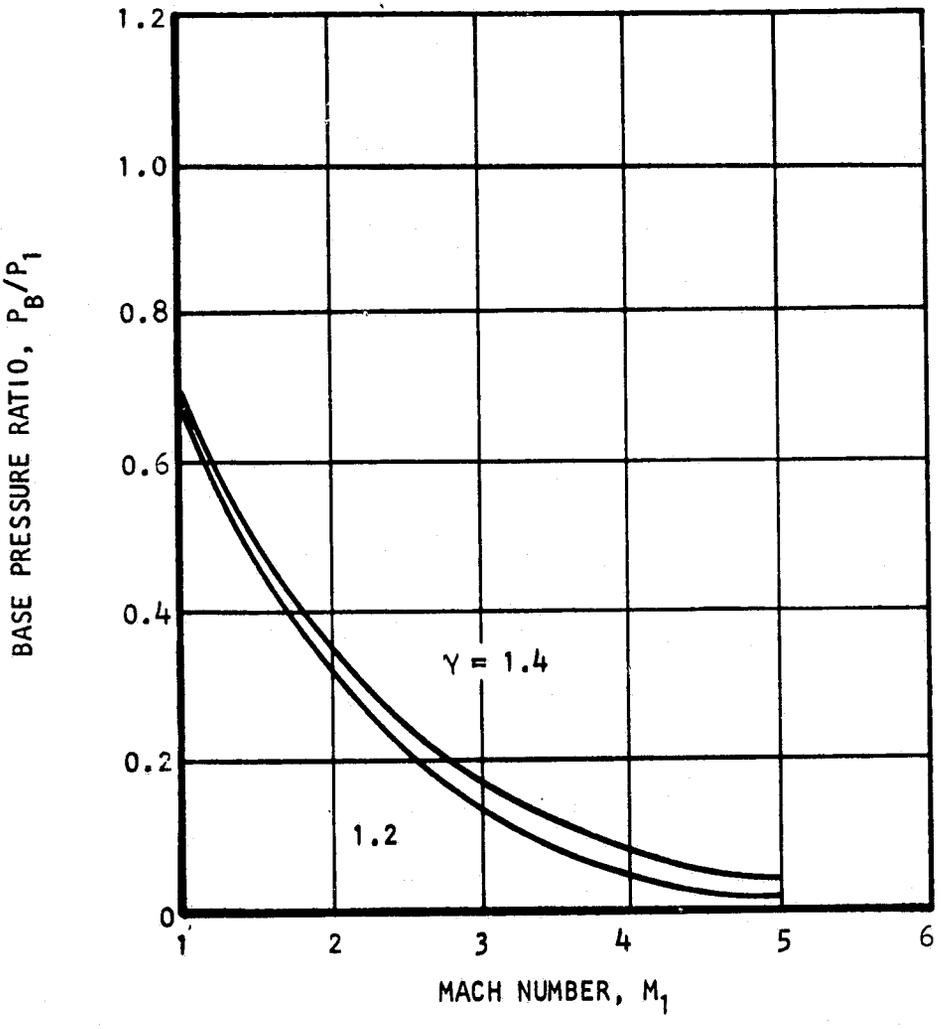

1. BASED ON KORST - A THEORY FOR BASE PRESSURES IN TRANSONIC AND SUPERSONIC FLOW
2. γ EFFECTS, AIAA PAPER NO. 67-446

S-94974

Figure 6.5-1. Strut Base Pressure Estimate

6.7 PERFORMANCE CORRECTION FOR INLET TOTAL TEMPERATURE

Because of the facility heater deficiency, the true temperature simulation of 3700°R at Mach 7 was not achieved. It is known that the effect of decreasing total temperature is to increase the engine performance. Therefore, it is necessary to correct the measured performance to properly account for deviations in test conditions. Theoretical calculations indicate that at Mach 7, a decrease of 100°F would increase the thrust coefficient by 5 percent and the specific impulse by 3.5 percent.

The correction of inlet total temperature may be accomplished by the following: The thrust coefficient is defined approximately as

$$C_T = \frac{T}{\frac{1}{2} \rho V_o^2 A_c} = \frac{M(V_4 - V_o)}{\frac{1}{2} W_a V_o / g}$$

The thermodynamic cycle efficiency is defined as

$$\eta_{cy} = \frac{M\left(V_4^2 - V_o^2\right)}{2Q}$$

and the propulsive efficiency is defined as

$$\eta_p = \frac{M\ (V_4 - V_o)\ V_o}{M\ \left(V_4^2 - V_o^2\right)/2}$$

which is the ratio of propulsive work to the increase in kinetic energy derived from fuel. From these three equations, it can be shown that

$$C_T = \frac{\eta_{cy}\ \eta_p\ Q}{W_a\ V_o^2/2} = \frac{2\eta_{cy}\eta_p g(HV)\ f/a}{V_o^2}$$

For small perturbations, η_{cy}, η_p, and heating value of the fuel may be considered as constants, and kinetic energy of the air, V_o^2, may be approximated by the total enthalpy of the air (or the total temperature). Therefore,

$$C_T \approx K \frac{f/a}{T_{T_o}}$$

The thrust coefficient is a function of the ratio of heat release to the inlet total temperature. The effect of inlet temperature variation on thrust coefficient may be simulated by the same percentage change of fuel-air ratio (or ϕ).

$$\phi_{flight} = \phi_{test} \frac{T_{T_{test}}}{T_{T_{flight}}}$$

Thus, the corrected thrust coefficient versus equivalence ratio curve may be obtained by shifting the tested thrust coefficient to a new equivalence ratio determined by the above equation. The specific impulse can then be determined at the new corrected conditions by:

$$I_{sp} = \frac{1}{2} C_T V_o \frac{A_c}{A_o} \Big/ (f/a)$$

6.8 DETERMINATION OF TUNNEL MACH NUMBERS

Calibration of Lewis Hypersonic Tunnel Facility at Mach 5, 6, and 7 was performed prior to AIM testing. Results were published in Reference 6.8-1. The calibrated average tunnel Mach number as a function of freestream total temperature is presented in Figure 6.8-1. The Mach 6 nozzle was calibrated at several temperature conditions, the Mach 7 nozzle at four different conditions, and Mach 5 at about 2000°R only.

These results yielded tunnel Mach number trends very well defined at Mach 6, less defined at 7, and undefined at 5.

Since AIM was tested at various temperatures, the tunnel Mach numbers corresponding to these temperatures may be determined from calibration data for Mach 6 and 7 as shown by the solid lines. At Mach 5, the pressure ratio of AIM spike tip and freestream total pressure was used to calculate the Mach number. In order to substantiate this approach, the Mach numbers determined from this method were compared with the calibration data. The agreement was very good for Mach 6, but the calculated tunnel Mach numbers were lower for Mach 7. At Mach 5, the agreement was also good for a single point at 2000°R where data was available. Therefore, decision was made to use spike-pitot/total-pressure ratio to calculate the tunnel Mach numbers for all Mach 5 runs.

6.9 DETERMINATION OF TUNNEL GAS COMPOSITION

The test facility used an induction-heated drilled-core graphite storage bed to raise the temperature of nitrogen to a nominal 4500°F at a maximum design pressure of 1200 psia. The nitrogen was mixed with ambient-temperature oxygen to produce synthetic air. Diluent nitrogen was added with the oxygen in the mixture at tunnel Mach numbers below 7 to control freestream total temperature and to supply the correct weight flow.

The oxygen to nitrogen ratio was determined from the flow measurements of oxygen, diluent nitrogen, and nitrogen entering the storage heater, and checked by gas samples taken through the aspirating thermocouple probes at the north and south sides of facility nozzle entrance prior to each run. The samples were collected in high-pressure bottles and later analyzed on a mass-spectrometer. Table 6.8-1 shows the measured composition for each run. The values of the last two columns were used in the one-dimensional data reduction computer program in which only N_2 and O_2 were considered.

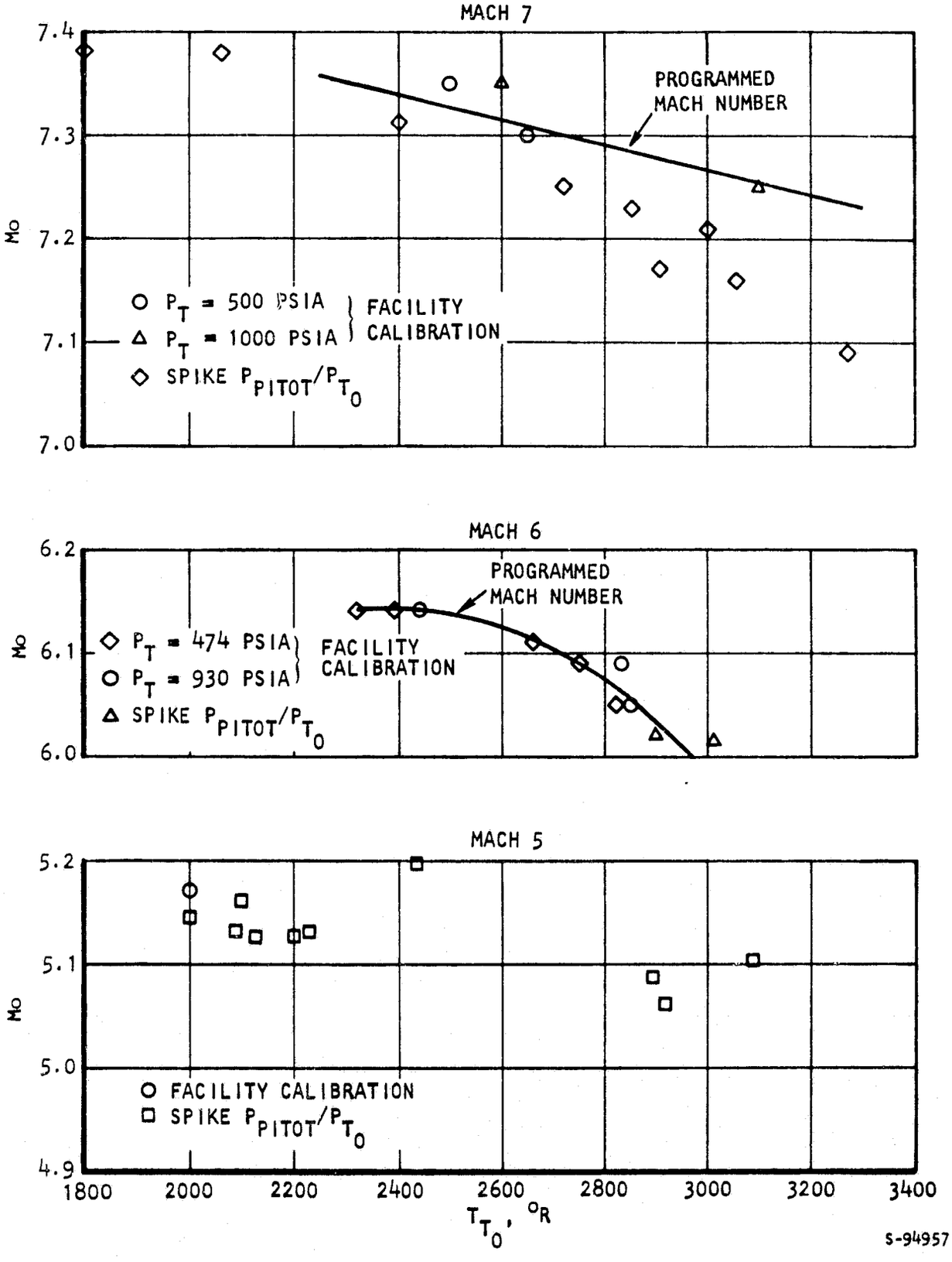

Figure 6.8-1. Mach Number Calibration

TABLE 6.8-1

FACILITY NOZZLE INLET SAMPLE ANALYSIS

Sample Side	Reading No.	N_2	O_2	H_2	CH_4	CO	CO_2	A	NO	Nox Analysis PPM	Average N_2 Weight	Average O_2 Weight
N	54	74.33	23.60	0.012	NA	0.254	0.037	0.026				
S		74.61	23.53	0.009	NA	0.253	0.035	0.027			0.7345	0.2655
N	57	73.21	22.77	0.000	0.012	0.303	0.042	0.033		42		
S		73.75	23.35	0.004	0.000	0.253	0.041	0.026		22	0.7361	0.2639
N	61	77.35	22.52	0.013	0.133	0.365	0.059	0.037		42		
S		74.86	24.47	0.021	0.014	0.297	0.043	0.037		42	0.7393	0.2607
N	63	78.25	20.02	0.009	0.014	0.195	0.034	0.027		26		
S		77.10	20.05	0.004	0.022	0.196	0.036	0.026		45	0.7724	0.2276
N	64	76.34	19.69	0.012	NA	0.2073	0.044	0.027		58		
S		75.31	20.53	0.000	NA	0.188	0.032	0.026		48	0.7675	0.2347
N	69	77.80	20.71	0.008	0.011	0.119	0.032	0.031				
S		76.69	20.88	0.012	0.011	0.090	0.036	0.029			0.7648	0.2352
N	71	76.36	21.79	0.020	0.014	0.1255	0.035	0.026				
S		75.16	21.36	0.016	0.013	0.1523	0.037	0.027			0.7545	0.2455
N	81	78.69	20.92	0.012	0.014	0.148	0.082	0.026				
S		76.15	23.47	0.004	NA	0.148	0.066	0.028			0.7533	0.2467
N	89	73.09	22.78	0.008	0.012	0.092	0.037	0.026				
S		76.25	20.46	0.008	0.012	0.215	0.038	0.021			0.7515	0.2482
N	90	73.69	21.45	0.000	0.012	0.186	0.040	0.022				
S		70.77	23.22	0.000	0.011	0.184	0.045	0.024			0.7389	0.2611
N	92	Variation of O_2 content										
S		See Figure 6.8-1										
N	93	68.20	31.22	0.012	0.012	0.090	0.036	0.042				
S		68.21	33.15	0.009	NA	0.150	0.040	0.039			0.6557	0.3443
N	94	78.38	21.46	0.016	0.012	0.123	0.022	0.028				
S		77.75	21.04	0.012	0.012	0.123	0.030	0.030			0.7628	0.2372
N	95	79.63	23.33	0.017	0.013	0.128	0.030	0.039				
S		77.24	22.78	0.008	0.013	0.093	0.035	0.027			0.7486	0.2514
N	96	78.24	20.56	0.008	0.013	0.403	NA	0.026	0.016			
S		77.29	21.30	0.008	0.014	0.389	0.155	0.032	0.007		0.7649	0.2351
N	97	76.06	19.46	0.008	0.012	0.121	0.045	0.024	0.005			
S		76.63	20.28	0.012	0.012	0.121	0.038	0.024	0.005		0.7709	0.2291

NA - Not Analyzed

ORIGINAL PAGE IS
OF POOR QUALITY

For readings when no gas sample was taken, the composition of previous reading was used. In reading 92, an investigation of the effects of inlet gas composition was conducted, the variation of oxygen constant versus time in that run is shown in Figure 6.9-1.

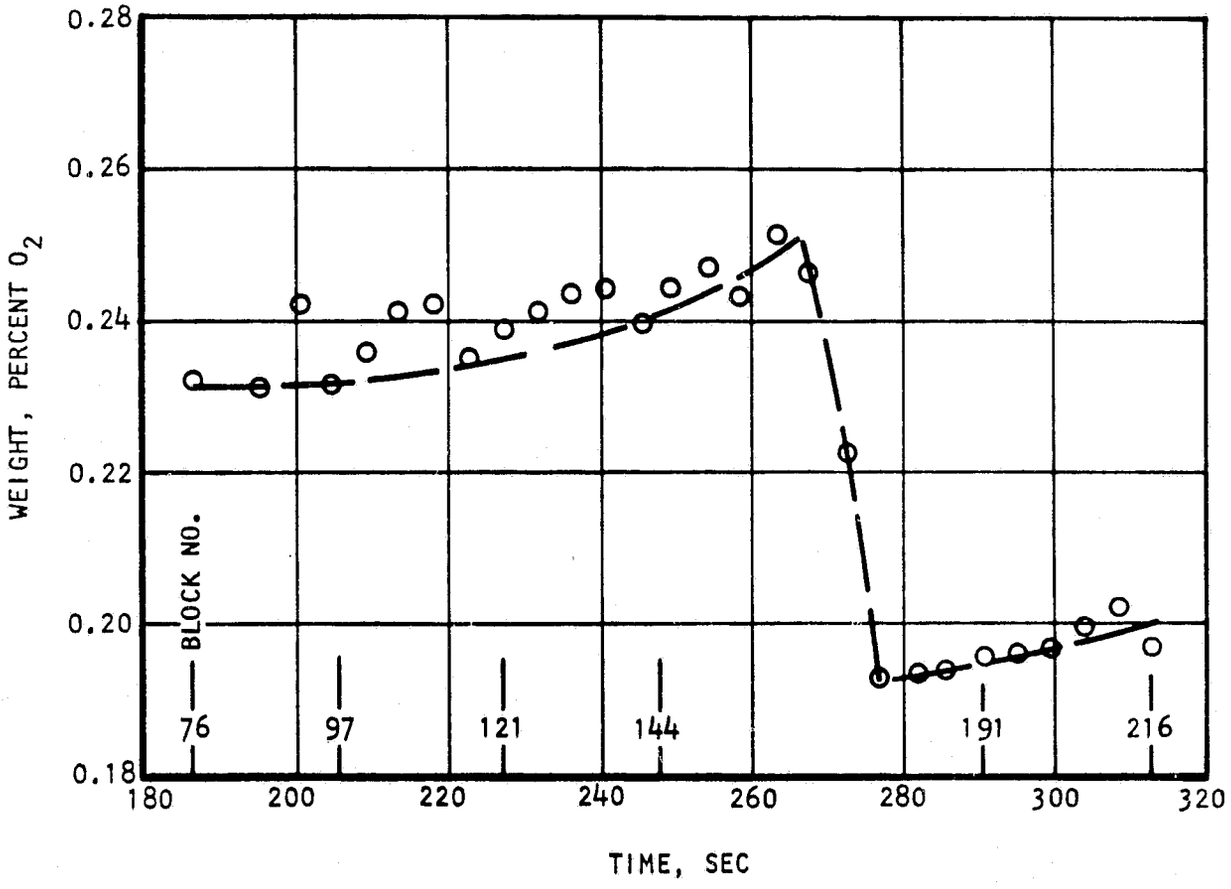

S-94975

Figure 6.9-1. Variation of Inlet Gas Composition in Reading 92

7. TEST DATA AND ANALYSES

The AIM test program was started 31 October 1973 and completed 22 April 1974. A total of 52 runs was made during this period, of which 36 were conducted at Mach 6, 11 at Mach 7, and 5 at Mach 5. In addition to these, several calibration runs were made. The engine was exposed to true hypersonic stream environment for 111 min. and 44 sec, with 41.5 min. of combustor operation. A summary of test points used in the data analyses is presented in Table 7.0-1. Many runs were aborted because of facility problems.

Test results are presented in the following seven subsections; i.e., inlet, combustor, nozzle, engine component interaction, instrumentation rig, cooling load, and overall engine performance. Engine component performance was obtained from a one-dimensional data reduction program (Reference 6.4-1). Overall engine internal thrust was obtained from both surface pressure integrals and thrust measurements.

Near the end of Mach 6 testing, insulation was lost around part of the graphite core in the facility heater. The time schedule did not permit complete repair, consequently, all Mach 7 testing was conducted at Mach 6 temperatures (3000°F to 3300°F) to avoid further deterioration. As a result, the test Mach number was higher (7.25) than design (7.00).

Examination of the data indicate good correlation was obtained for tests performed at Mach 6. The measured thrust was within 150 lb of those calculated. During Mach 7 tests, difficulties were encountered in obtaining good recorded data; consequently pressure integrals were not as accurate as those observed for Mach 6 tests. In some Mach 7 tests, the measured thrust was higher by as much as 800 lb than those calculated. Hence, an accurate analyses of the combustor and the nozzle performance could not be obtained.

Typical pressure distribution expressed in terms of the ratio of the surface static pressure to the wind tunnel total pressure is presented in Figures 7.0-1, 7.0-2 and 7.0-3 for Mach 5, 6, and 7 respectively.

7.1 INLET SECTION

The general configuration of the AIM is shown in Figure 7.1-1. The contour of the inlet section selected is presented in Table 7.1-1, and the air flow anticipated is shown schematically in Figure 7.1-2. This design permits obtaining the optimum contraction schedule and provides capability to close the inlet to reduce the drag and the aerodynamic heating of the engine when the engine is not operating, by translation of the centerbody sector.

The design was selected after extensive analysis and tests, including tests performed on 1/3- and 2/3-scale models. The results of these tests are shown in References 7.1-1, 7.1-2, 7.1-3 and 7.1-4.

PRECEDING PAGE BLANK NOT FILMED

TABLE 7.0-1

SUMMARY OF TEST POINTS USED FOR ANALYSES

Reading Number	Time	M_o	P_{T_o}, psia	T_{T_o}, °R	X_{CL}, in.	α	Inj.1/ϕ_1	Inj.2/ϕ_2	Inj.3/ϕ_3	ϕ_T	Ignitors 1, 2, 3	Purpose
33	126.95	6.0	750	3000	35.2	0°	0	0	0	0	No	No fuel injection
	161.15	↓	↓	↓	↓	↓	1A,1B/.24	0	0	0.24	1,2	1st stage only
	168.0	↓	↓	↓	↓	↓	1A,1B/.3	0	0	0.30	↓	1st stage only
	174.65	↓	↓	↓	↓	↓	1A,1B/.36	0	0	0.36	↓	Max. ϕ, engine unstart
34	98.15	6.0	750	3000	35.2	0°	0	0	0	0	1,2	
	104.45	↓	↓	↓	↓	↓	1A,1B/.20	0	0	0.20	↓	1st stage only
	148.55	↓	↓	↓	↓	↓	1A,1B/.23	2A/.58	0	0.81	↓	1st and 2nd stages
	181.85	↓	↓	↓	↓	↓	1A,1B/.21	2A/.56	3A/.39	1.16	↓	Max. ϕ, 3 stages
	196.25	↓	940	↓	↓	↓	1A,1B/.15	2A/.44	3A/.32	0.91	↓	Max. ϕ, 3 stages
36	119.18	6.0	750	3000	35.2	0°	0	0	0	0	No	Auto ignition
	124.58	↓	↓	↓	↓	↓	1A,1B/.26	0	0	0.26	↓	↓
	132.68	↓	↓	↓	↓	↓	1A,1B/.25	2A,2C/.34	0	0.59	↓	↓
	144.38	↓	↓	↓	↓	↓	1A,1B/.24	2A,2C/.49	0	0.73	↓	↓
	158.78	↓	↓	↓	↓	↓	1A,1B/.23	2A,2C/.69	0	0.92	↓	↓
	173.18	↓	↓	↓	↓	↓	1A,1B/.22	2A,2C/.75	0	0.97	↓	↓
38	96.24	6.0	750	3000	35.2	0°	0	0	0	0	No	
	107.05	↓	↓	↓	↓	↓	1A,1B/.33	0	0	0.33	↓	1st stage only
	113.35	↓	↓	↓	↓	↓	0	2C/.38	0	0.38	↓	2nd stage only
	116.95	↓	↓	↓	↓	↓	1A,1B/.18	2C/.67		0.85	↓	
52	165.93	6.0	750	3000	35.2	0°	0	0	0	0	No	ϕ1A,1B and ϕ4,2C
	172.23	↓	↓	↓	↓	↓	1A,1B/.24	4,2C/.26	0	0.50	↓	↓
	180.33	↓	↓	↓	↓	↓	1A,1B/.20	4,2C/.41	0	0.61	↓	↓
	189.33	↓	↓	↓	↓	↓	1A,1B/.20	4,2C/.53	0	0.73	↓	↓
54	156.46	6.0	750	3000	35.2	0°	0	0	0	0	No	Constant ϕ1A,1B, ϕ2A,2C
	185.26	↓	↓	↓	↓	↓	1A,1B/.21	2A,2C/.64	0	0.85	↓	ramped up 3 times
	200.56	↓	↓	↓	↓	↓	1A,1B/.23	2A,2C/.43	0	0.66	↓	↓
	222.16	↓	↓	↓	↓	↓	1A,1B/.24	2A,2C/.25	0	0.49	↓	↓
	235.66	↓	↓	↓	↓	↓	1A,1B/.24	2A,2C/.52	0	0.76	↓	↓
	253.66	↓	↓	↓	↓	↓	1A,1B/.18	2A,2C/.60	0	0.78	1.2	↓
	280.66	↓	↓	↓	↓	↓	1A,1B/.20	2A,2C/.61	0	0.81	No	↓
57	195.11	6.0	750	3000	35.2	0°	0	0	0	0	No	Optimized performance
	207.71	↓	↓	↓	↓	↓	1A,1B/.21	2A,2C/.73	0	0.94	↓	↓
	234.71	↓	↓	↓	↓	↓	1A,1B/.32	2A,2C/.60	0	0.92	↓	↓
	265.31	↓	↓	↓	↓	↓	1A,1B/.21	2A,2C/.36	0	0.57	↓	↓
	287.81	↓	↓	↓	↓	↓	1A,1B/.20	2A,2C/.54	0	0.74	↓	↓
60	155.69	6.0	750	3000	35.2	0°	0	0	0	0	No	Variation of fuel schedule
	178.19	↓	↓	↓	↓	↓	1A,1B/.21	2A,2C/.64	0	0.85	↓	↓
	186.29	↓	↓	↓	↓	↓	1A,1B/.22	2A,2C/.65	0	0.87	↓	↓
	202.49	↓	↓	↓	↓	↓	1A,1B/.21	2A,2C/.65	0	0.86	↓	↓
	223.19	↓	↓	↓	↓	↓	1A/.21	2A,2C/.66	0	0.87	↓	↓
	230.39	↓	↓	↓	↓	↓	1A,1B/.21	2A,2C/.67	0	0.88	↓	↓
	241.19	↓	↓	↓	↓	↓	1B/.19	2A,2C/.68	0	0.87	↓	↓
	249.29	↓	↓	↓	↓	↓	1B/.24	2A,2C/.68	0	0.92	↓	↓
	258.29	↓	↓	↓	↓	↓	0	2A,2C/.76	0	0.76	↓	↓
	264.59	↓	↓	↓	↓	↓	0	2A,2C/.80	0	0.80	↓	↓

ORIGINAL PAGE IS
OF POOR QUALITY

TABLE 7.0-1 (Cont.)

Reading Number	Time	M_o	P_{T_o}, psia	T_{T_o}, °R	X_{CL}, in.	α	Inj.1/ϕ_1	Inj.2/ϕ_2	Inj.3/ϕ_3	ϕ_T	Ignitors 1, 2, 3	Purpose
61	178.86	6.0	750	3000	36.7	0°	0	0	0	0	No	Effect of spike position
	198.66						1A,1B/.13	2A,2C/.36	0	0.49		
	205.86						1A,1B/.15	2A,2C/.49	0	0.64		
	212.16						1A,1B/.15	2A,2C/.61	0	0.76		
	222.06						1A,1B/.14	2A,2C/.73	0	0.87		
	231.06				37.5	0°	0	0	0	0	No	Effect of spike position
	243.66						1A,1B/.30	0	0	0.30		
	246.36						1A,1B/.30	2A,2C/.47	0	0.77		
	251.76						1A,1B/.29	2A,2C/.65	0	0.94		
	262.56						1A,1B/.27	2A,2C/.96	0	1.13		
	273.36						1A,1B/.26	2A,2C/1.15	0	1.41		
63	186.15	6.0	930	3000	35.2	0°	0	0	0		No	Effect of altitude
	192.45						1A,1B/.24	2A,2C/.56	0	0.80		
	216.75						1A,1B/.24	2A,2C/.76	0	1.00		
	249.15		470				0	0	0	0		
	275.25		470				1A,1B/.26	2A,2C/.73	0	0.99		
64	156.11	6.0	750	3000	35.2	0°	0	0	0	0	No	Subsonic-supersonic
	167.81						1B/.24	2A,2C/.77	0	1.01		transition
	202.01						0	0	3A,3B/.85	0.85		
	239.81						1B/.23	2A,2C/1.11	0	1.34		
	261.41						1B/.24	0	3A,3B/.8	1.04		
	293.81						1B/.26	2A,2C/.8	0	1.06		
65	164.03	6.0	750	3000	35.2	0°	0	0	0	0	No	Supersonic combustion
	174.83						1A,1B/.23	0	0	0.23		with instrumentation rig,
	180.23						1A,1B/.24	2A,2C/.34	0	0.58		gas sampling
	196.43						1A,1B/.24	2A,2C/.59	0	0.83		
	201.83						1A,1B/.24	2A,2C/.80	0	1.04		
	218.03						1A,1B/.27	2A,2C/.76	0	1.03		
	235.13						1A,1B/.25	2A,2C/.79	0	1.04		
69	177.00	6.0	750	3000	35.2	0°	0	0	0	0	No	Supersonic combustion
	198.60						1A,1B/.22	0	0	0.22		with instrumentation rig,
	212.10						1A,1B/.23	2A,2C/.48	0	0.48		gas sampling
	226.50						1A,1B/.23	2A,2C/.59	0	0.82		
	256.20						1A,1B/.22	2A,2C/.69	0	0.91		
	265.20						1A,1B/.23	2A,2C/.79	0	1.02		
71	160.54	6.0	750	3000	35.2	3°	0	0	0	0	No	Angle of attack perform-
	171.39						1A,1B/.22	0	0	0.22		ance
	174.94						1A,1B/.22	2A,2C/.31	0	0.53		
	193.84						1A,1B/.24	2A,2C/.59	0	0.83		
	207.34						1A,1B/.24	2A,2C/.81	0	1.05		
	248.74						0	2A,2C/1.33	0	1.33		
	266.74						0	2A,2C/.87	0	0.87		
	270.34						0	2A,2C/.87	0	0.87		
	284.74						0	2A,2C/.66	0	0.66		
	285.64						0	2A,2C/.66	0	0.66		

ORIGINAL PAGE IS OF POOR QUALITY

TABLE 7.0-1 (Cont.)

Reading Number	Time	M_o	P_{T_o}, psia	T_{T_o}, °R	X_{CL}, in.	α	Inj.1/ϕ_1	Inj.2/ϕ_2	Inj.3/ϕ_3	ϕ_T	Ignitors 1, 2, 3	Purpose
88	236.40	7.25	1000	3160	36.6	0°	0	0	0	0	2	Exploratory run
	245.40			3170			1A,1B/.30	0	0	0.30		
	261.60			3250			1A,1B/.42	0	0	0.42		
	269.70			3280			1A,1B/.55	0	0	0.55		
	270.60			3270			1A,1B/.57	0	0	0.57		
	271.50			3270			1A,1B/.58	0	0	0.58		
	278.70			3270			1A,4/.16	2A,2C/.70	0	0.86		
	285.90			3250			1A,4/.31	2A,2C/.60	0	0.91		
	294.00			3200			1A,4/.28	2A,2C/.57	0	0.85		
	299.40			3150			1A,4/.45	2A,2C/.46	0	0.91		
	305.70	↓	↓	3090	↓		1A,4/.49	2A,2C/.41	0	0.90	↓	↓
89	250.77	7.4	1000	1790	36.6	0°	0	0	0	0	No	Effect of low T_{T_O}
	272.37	7.25		3180			1A,1B/.32	2A,2C/.47	0	0.79	2	
	283.17			3270			1A,1B/.34	2A,2C/.55	0	0.89		
	290.37			3270			0	2A,2C/.75	0	0.75		
	294.87			3310			0	2A,2C/.92	0	0.92		
	304.77			3290			0	2A,2C/.59	0	0.59		
	310.17	↓		3060			1A,1B/.32	2A,2C/.57	0	0.89		
	316.47	7.30		2720			1A,1B/.29	2A,2C/.54	0	0.83		
	327.27	7.34		2410			1A,1B/.28	2A,2C/.54	0	0.82		
	352.47	7.25	↓	3300	↓		1A,1B/.36	2A,2C/.57	0	0.93	↓	↓
90	197.22	7.25	1000	3000	36.6	0°	0	0	0	0	No	Optimization
	206.22						1A,1B/.48	0	0	0.48	2	
	212.52						1A,1B/.49	4/.05	0	0.54		
	217.02						1A,1B/.48	1C,4/.34	0	0.82		
	230.52						1A,1B/.26	1C,4/.51	0	0.77		
	235.02						1A,1B/.79	1C,4/1.19	0	1.98		
	246.72						1A/.51	0	0	0.51		
	247.62	↓	↓	↓	↓		1A/.55	0	0	0.55	↓	↓
91	175.65	7.25	1000	3100	36.6	3°	1A,1B/.39	0	0	0.39	2	Angle of attack
	180.15						1A,1B/.47	0	0	0.47	2	
	186.45						0	0	0	0	No	
	190.05						1A,1B/.51	4/.13	0	0.64	2	
	203.55						1A,1B/.52	0	0	0.52		
	216.15						1B/.27	4,2C/.34	0	0.61		
	224.25						1B/.28	4,2C/.50	0	0.78		
	226.95						1B/.28	4,2C/.45	0	0.73		
	229.65						1B/.33	4,2C/.39	0	0.72		
	235.95	↓	↓	↓	↓		1B/.29	2C/.41	0	0.70	↓	↓
92	186.87	7.38	1000	2050	36.6	0°	0	0	0	0	No	Supersonic combustion with instrumentation rig, gas sampling and O_2 content effect
	205.77	7.29		2850			1A,1B/.48	4,2C/.34	0	0.72	2	
	227.37						1A,1B/.50	4,2C/.43	0	0.93		
	248.07	↓		↓			1B/.33	4,2C/.58	0	0.91		
	290.37	7.25		3000			1A,1b/.47	4,2C/.55	0	1.12		
	312.87	7.25	↓	3000	↓		1A,1B/.36	4,2C/.49	0	0.85	↓	↓

TABLE 7.0-1 (Cont.)

Reading Number	Time	M_o	P_{T_o}, psia	P_{T_o}, °R	X_{CL}, in.	α	Inj.1/ϕ_1	Inj.2/ϕ_2	Inj.3/ϕ_3	ϕ_T	Ignitors 1, 2, 3	Purpose
93	134.03	5.1	420	2100	35.2	0°	0	0	0	0	No	No fuel injection
	142.13						0	2A/.29	0	0.29	2	2nd stage only
	150.23						0	2A/.31	3A,3B/.25	0.56		Subsonic combustion
	158.33						0	0	3A,3B/.60	0.60		and O_2 content effect
	162.83						0	0	3A,3B/.71	0.71		
	174.53						0	0	3A,3B/.49	0.49		
	183.63						0	0	3A,3B/.35	0.35		
94	134.14	5.1	420	2230	35.2	0°	0	0	0	0	No	Subsonic combustion
	140.44						0	2A/.49	0	0.49	2	
	150.34						0	2A/.49	3A,3B/.47	0.96		
	157.54						0	0	3A,3B/1.03	1.03		
	163.84						0	0	3A,3B/1.19	1.19		
	180.04						0	0	3A,3B/.59	0.59		
	214.24		300	2940			0	2A/.53	0	0.53		Effect of T_{TO}
	215.14						0	2A/.53	0	0.53		
	218.74						0	2A/.54	3A,3B/.5	1.04		
	231.34						1A,1B/.15	0	0	0.15		
	233.14						1A,1B/.25	0	0	0.25		
	234.04						1A,1B/.27	0	0	0.27		
95	129.55	5.2	300	2430	35.2	0°	0	0	0	0	No	Supersonic combustion
	140.35	5.1		3080			1A,1B/.16	0	0	0.16	2	
	160.15			2940			1A,1B/.18	2A,2C/.68	0	0.86		
	169.15						1A,1B/.19	2A,2C/.83	0	1.02		
	189.85						0	2A,2C/.99	0	0.99		
	196.15						0	2A,2C/.86	0	0.86		
	204.25						0	2A,2C/.71	0	0.71		
	211.45						0	2A,2C/.58	0	0.58		
	217.75						0	2A,2C/.70	0	0.70		
	228.55						1A,1B/.22	2A,2C/.63	0	0.85		
	241.15						0	0	0	0	No	
	252.85		320	2800			1A,1B/.18	2A,2C/.70	0	0.88	2	
	289.75		310	2890			0	2A,2C/.86	0	0.86		
	310.45		420	2230			0	2A,2C/.66	0	0.66		Effect of T_{TO}
	317.65		420	2230			0	2A,2C/.51	0	0.51		
96	134.44	5.1	420	2230	35.2	3°	0	0	0	0	No	Angle of attack performance
	141.64						0	2A/.38	0	0.38	2	
	150.64						0	2A/.45	3A,3B/.38	0.83		
	165.94						0	0	3A,3B/.87	0.87		
	172.24						0	0	3A,3B/.59	0.59		
	180.34						0	0	3A,3B/.43	0.43		
	244.24		300	2925			0	0	0	0	No	
	264.04		420	2230			1A,1B/.10	0	0	0.10	2	
	274.84						1A,1B/.21	0	0	0.21	2	
	275.74						1A,1B/.20	0	0	0.20	2	
	294.64						0	0	0	0	No	
	313.54						0	0	3A,3B/.77	0.77	2	

TABLE 7.0-1 (Cont.)

Reading Number	Time	M_o	P_{T_o}, psia	P_{T_o}, °R	X_{CL}, in.	α	Inj.1/ϕ_1	Inj.2/ϕ_2	Inj.3/ϕ_3	ϕ_T	Ignitors 1, 2, 3	Purpose
97	135.71	5.1	210	2100	35.2	0°	0	0	0	0	No	Subsonic combustion with
	156.41			2200			0	2A/.51	3A,3B/.49	0.90	2	instrumentation rig and
	160.91						0	2A/.32	3A,3B/.24	0.56		gas sampling probes
	182.51						0	0	3A,3B/.50	0.50		
	201.41						0	0	3A,3B/.67	0.67		
	224.81						0	0	3A,3B/.86	0.86		
	252.71		420				0	2A/.50	3A,3B/.43	0.93		
	271.61						0	2A/.43	3A,3B/.34	0.77		
	295.91						0	0	3A,3B/.74	0.74		
	317.51						0	0	3A,3B/.90	0.90		
	322.01						0	0	3A,3B/1.07	1.07		
	325.61						0	0	3A,3B/1.08	1.08		

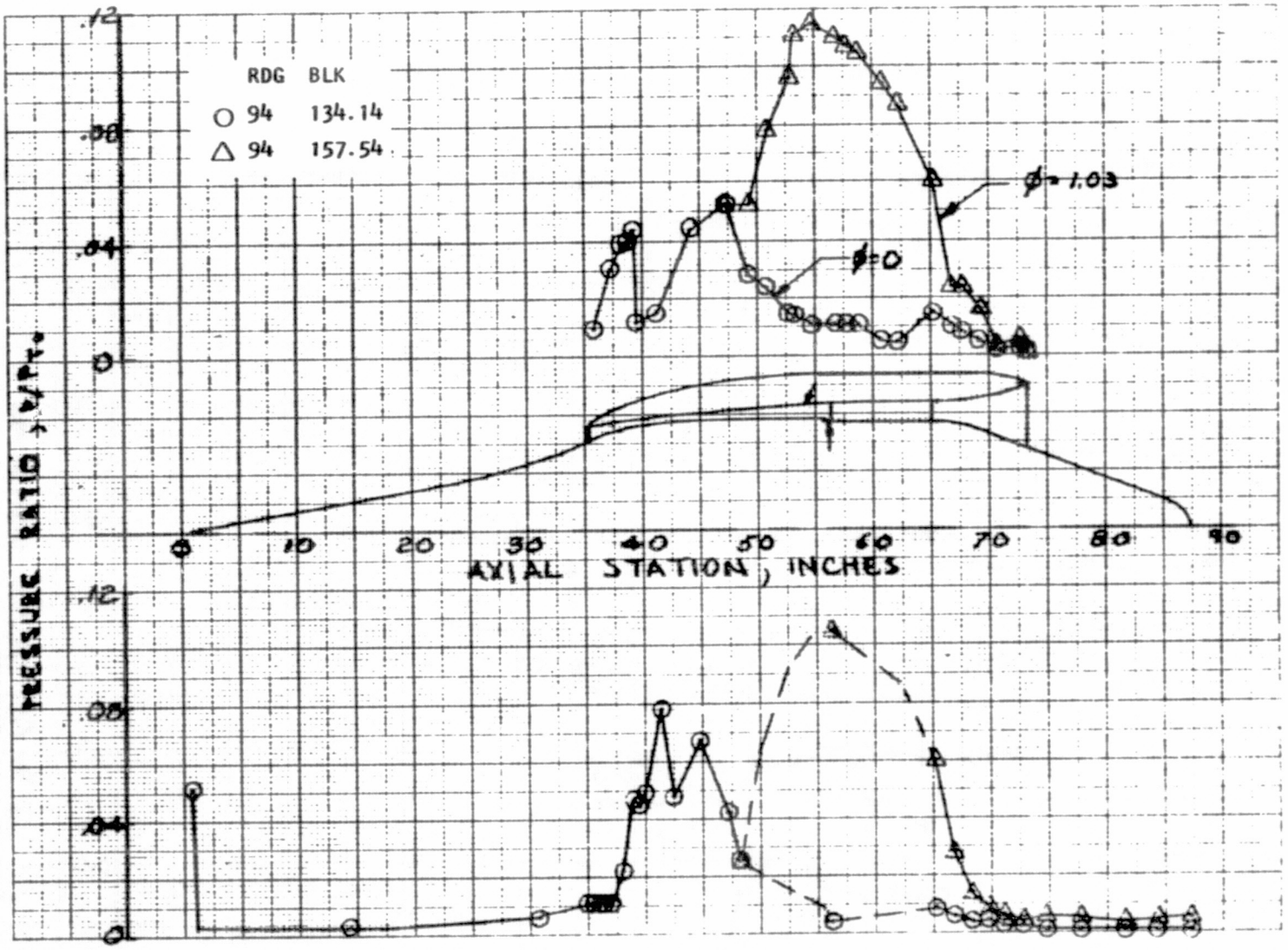

Figure 7.0-1. Mach 5 Pressure Distribution

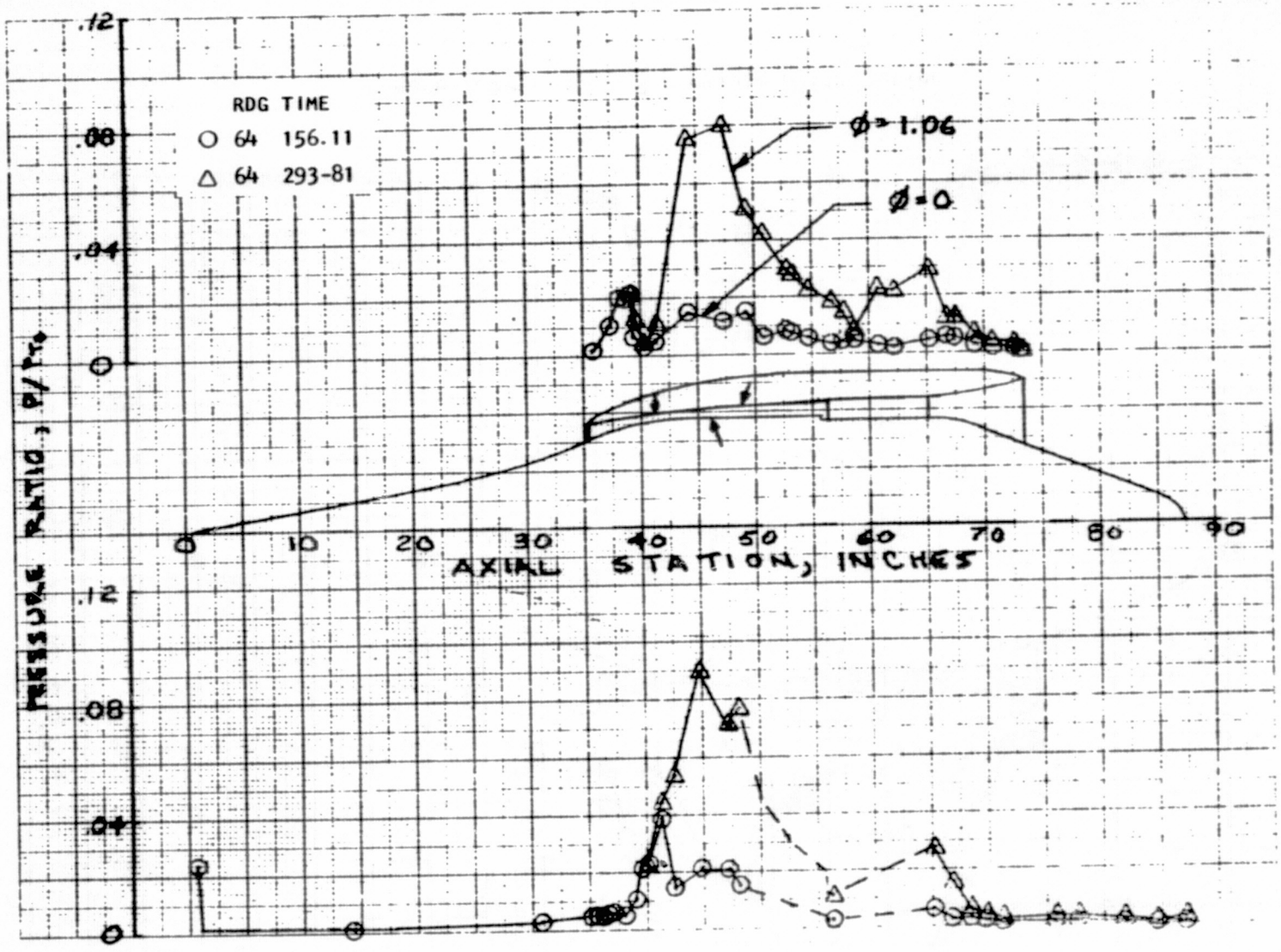

Figure 7.0-2. Mach 6 Pressure Distribution

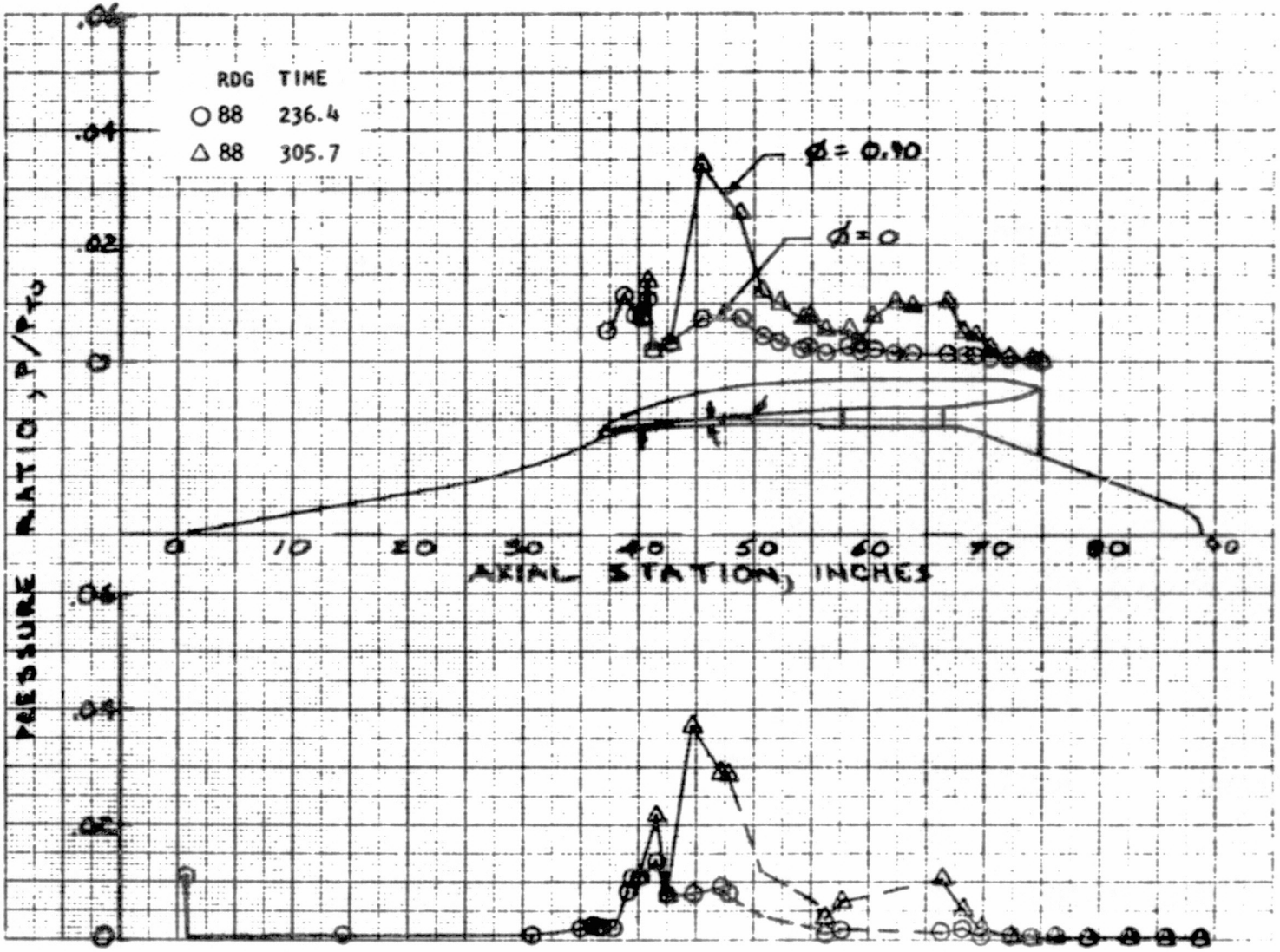

Figure 7.0-3. Mach 7 Pressure Distribution

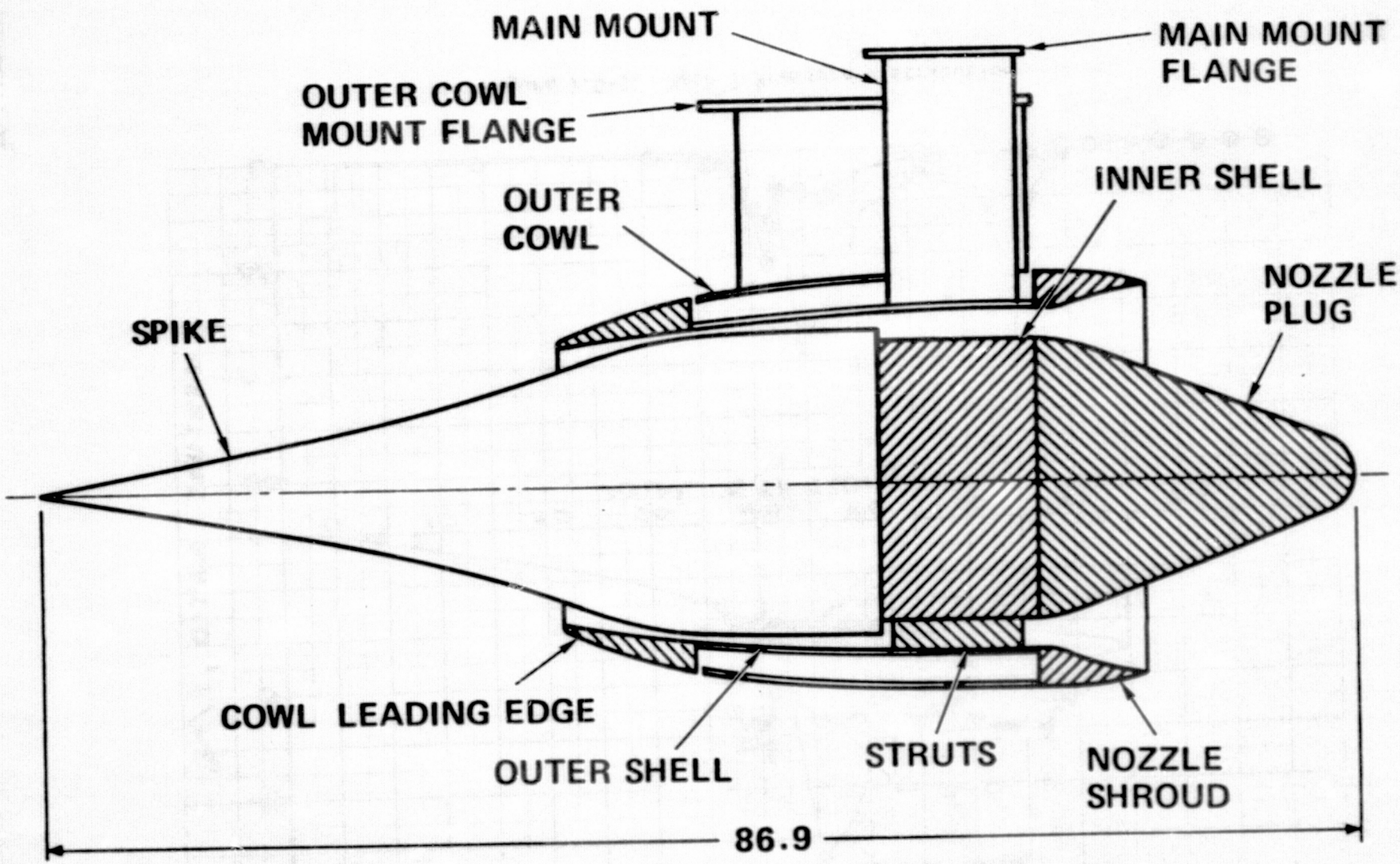

Figure 7.1-1. General Configuration of the AIM

TABLE 7.1-1

HRE-AIM INLET COORDINATES
(Mach 6.0 Cowl Design Position)

(a) Spike			(b) Cowl		
X, in.	R, in.		R, in.	R, in.	
0.5948	0.0		34.8478	9.0293	-90°
0.6981	0.1231	Straight Line	34.8840	9.0000	12°
18.3600	3.2374	10.0°	35.3970	9.1035	
19.3041	3.4112		35.8740	9.1922	10°
20.4426	3.6328		36.1710	9.2412	
21.6907	3.8850		36.4140	9.2776	8°
22.8296	4.1215		36.7650	9.3222	
23.8500	4.3380		37.4940	9.3981	
25.8753	4.7820		40.5000	9.6952	5.64535°
26.7661	4.9851				
27.9000	5.2560				
28.9037	5.5178				
29.6546	5.7260				
30.3600	5.9259	15.819°			
32.7600	6.6600				
34.0800	7.1400				
37.7100	8.6066	22.0°			
38.0700	8.7345				
38.5380	8.8740				
38.8260	8.9415				
39.1320	9.0000				
39.7800	9.0963				
40.5000	9.1800	5.645°			

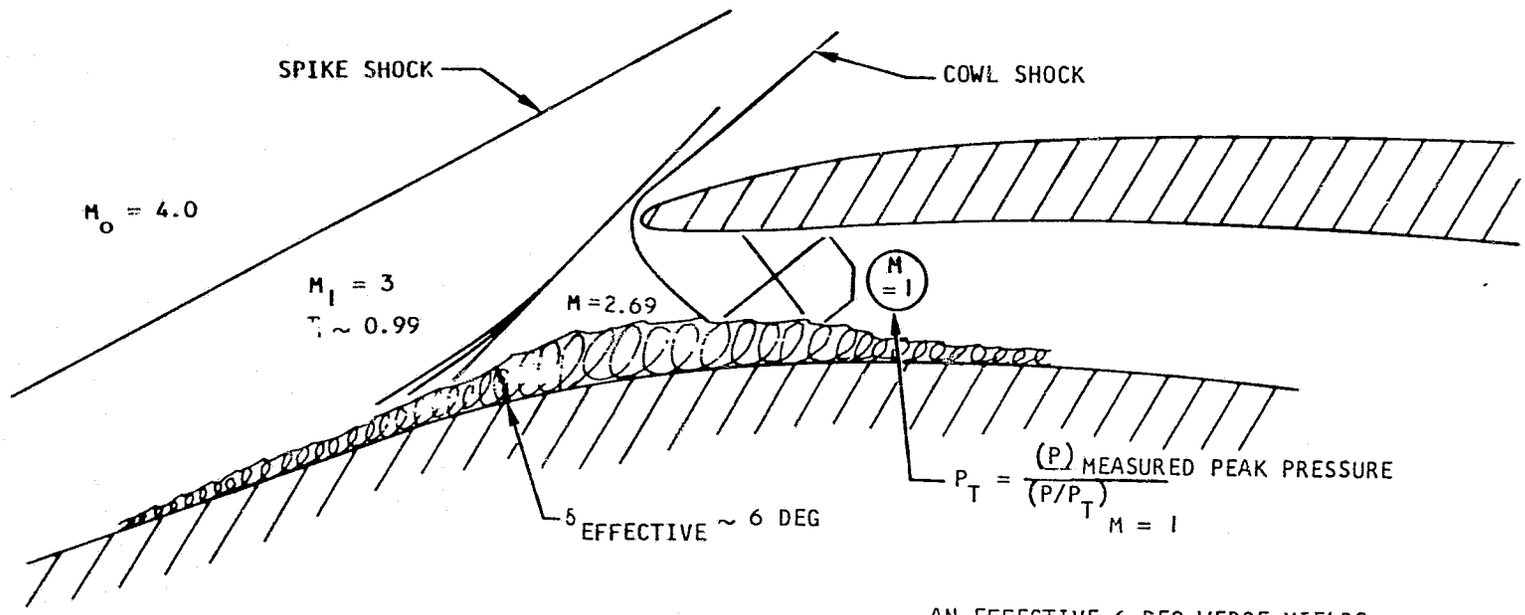

Figure 7.1-2. Flow Field Postulated for Inlet Starting

The inlet section can be described as an axisymetric external-internal compression design. The centerbody section consisted of a 10-deg half-angle cone with the apex blunted by a 1/8-in. radius tip section. The cone was followed by a 5.82-deg isentropic compression and by further external turning to a maximum angle of 22 deg. A large radius turn then reduces the flow direction to its value of 5.645 deg at the nominal throat. The outer section, with a blunted lip of 0.030 in. radius, had an initial internal angle of 12 deg, then decreased gradually to 5.645 deg as the internal wall approached the inlet throat.

Details of spike tip and cowl lip blunting for cooling purposes are given in Figure 7.1-3, along with a definition of a reference station on the cowl, X_{CL}. It is the position of this station on the cowl, relative to the spike vertex, which is used in the ensuing discussion to identify the spike position. Figure 7.1-4 presents several nominal spike positions in terms of X_{CL} as well as X_C^I. The relationship is $X_C^I \equiv X_{CL} - 0.631$ in.

7.1.1 Instrumentation

Pressure-sensing taps were installed on the inlet section to record the general pressure profile along the inlet section and to determine the effects of operating at an angle of attack.

Fifty-two pressure taps (29 on the spike and 23 on the cowl) were provided along the horizontal and vertical centerline of the inlet. Difficulties encountered in recording the desired pressure taps reduced the number of useful static pressure recordings to no more than 31. Table 7.1-2 shows the selected and the recorded static pressure taps on the spike and cowl section.

7.1.2 Data Reduction

The data obtained during the wind tunnel tests were recorded on tape in a digital form. This tape was processed thru a computer, and printouts were obtained in engineering units. The output of the computer was also retained in the computer and was used in processing the performance analysis program. The engineering units printout was used to select the specific points of interest, and the performance program, described elsewhere in this report, was used to compute the necessary aerodynamic parameters, heat transfer parameters, cycle, and component performances. One-dimensional force-momentum balance equations, combined with equations related to laws of conservation and thermodynamic properties for equilibrium air, were used for the analysis of the inlet section.

The momentum equation used to determine conditions at the inlet throat, or combustor entrance, is expressed as follows.

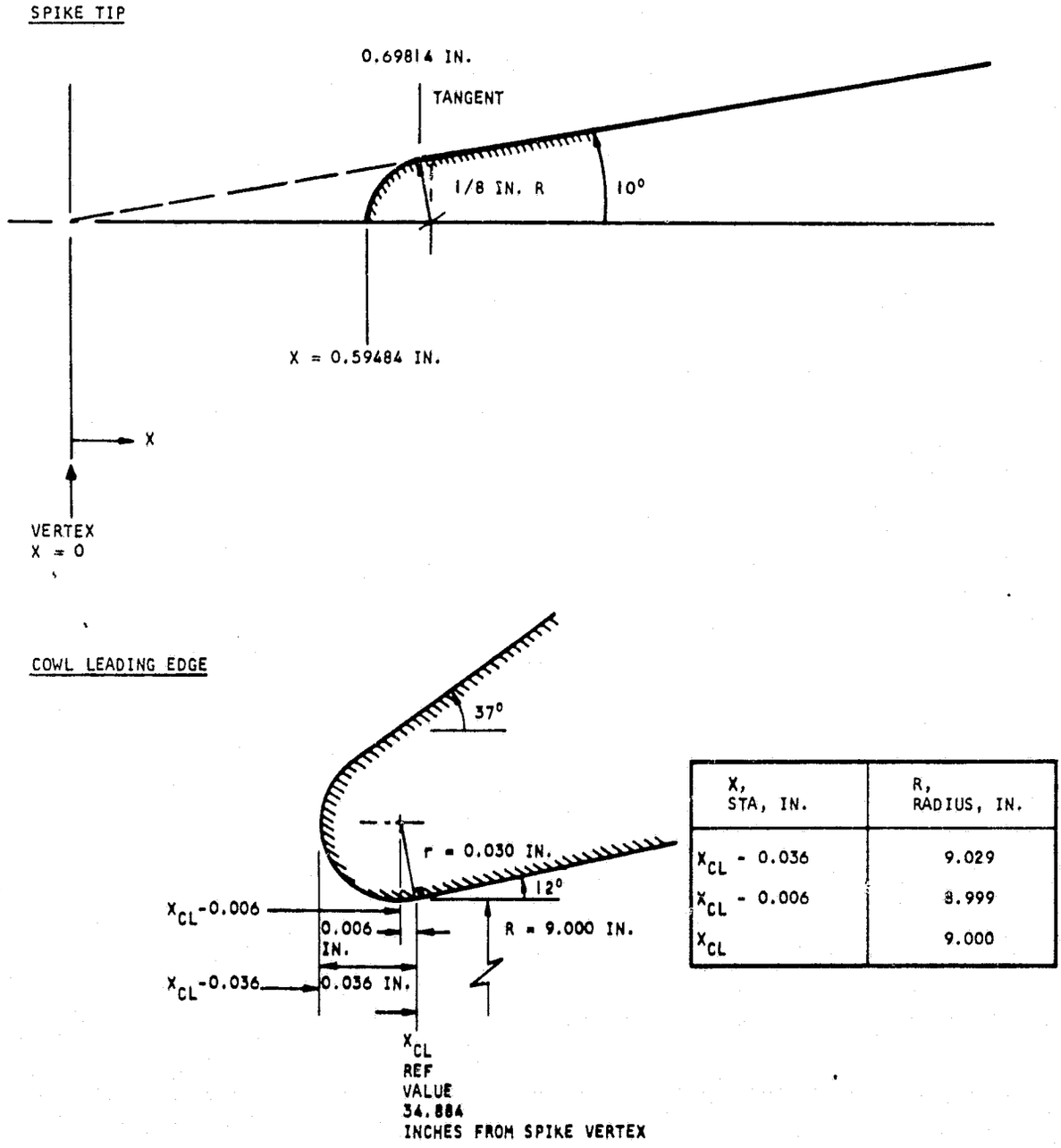

X, STA, IN.	R, RADIUS, IN.
X_{CL} - 0.036	9.029
X_{CL} - 0.006	8.999
X_{CL}	9.000

Figure 7.1-3. AIM Spike Tip and Cowl Leading Edge

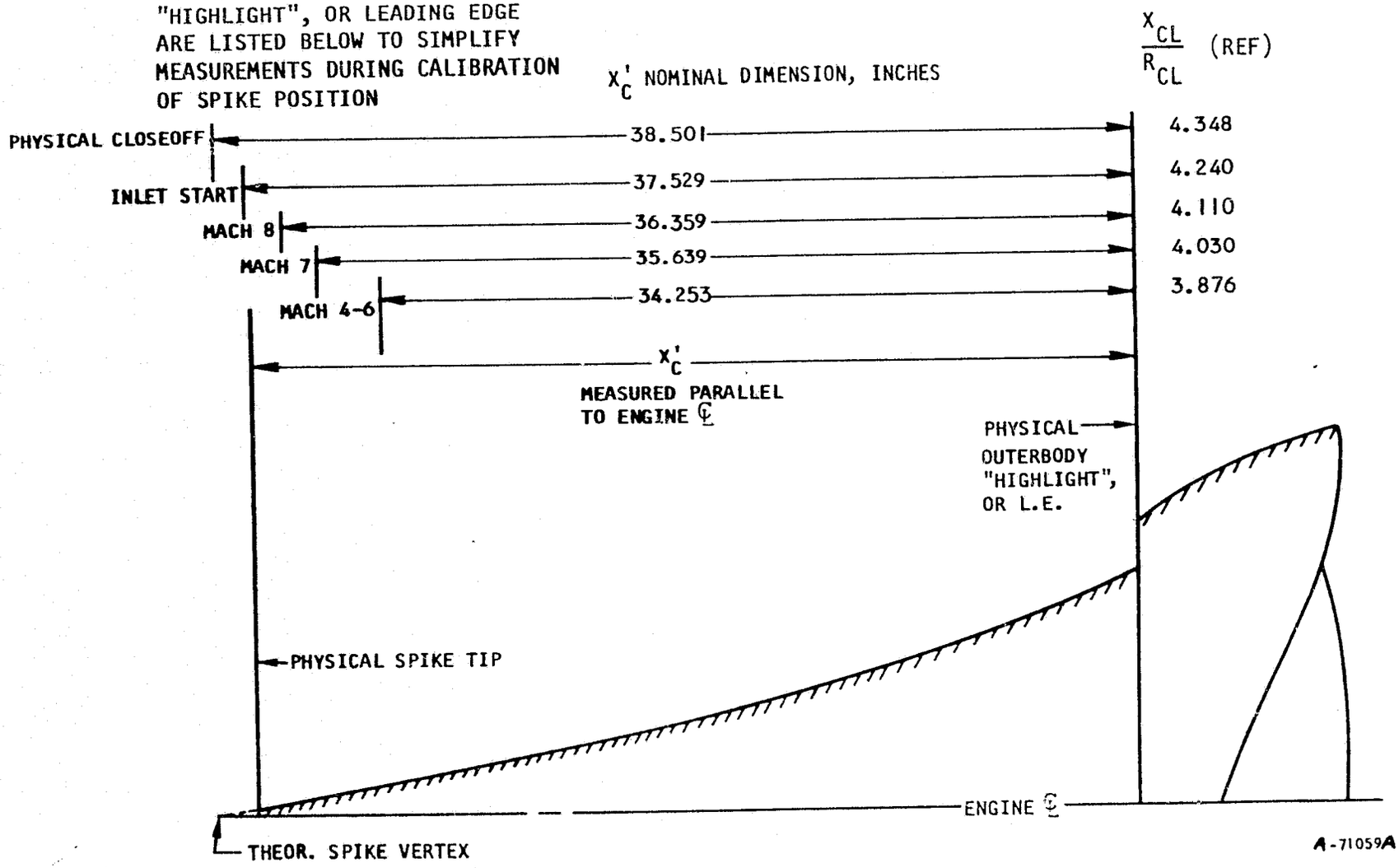

Figure 7.1-4. AIM Spike Tip Positions

TABLE 7.1-2

STATIC PRESSURE TAP DISTRIBUTION FOR INLET ANALYSIS

SPIKE

Quadrant	Included Angle, Deg	Station										
		14.4	30.6	35.0	35.5	36.0	36.5	37.0	38.0	39.0	39.5	40.0
		Tap Number										
I	315-45		6-S	7-S	11-S	12-S	13-S	17-S		24-S	28-S	29-S
II	45-135	3-S		8-S			14-S		20-S			30-S
III	135-225			9-S			15-S					31-S
IV	225-315			10-S			16-S					32-S

NOTE: Pressure tap No. 1-S is located at the center of the spike tip. It is used independently to determine the drag coefficient of the hemispherical tip, and to determine or check wind tunnel Mach number.

COWL

Quadrant	Included Angle, Deg	Station									
		35.5	36.0	36.5	37.0	37.5	38.0	38.5	39.0	39.5	40.0
		Tap Number									
I	315-45	31-C			35-C		40-C	44-C	45-C	49-C	50-C
II	45-135				36-C		41-C		46-C		
III	135-225										
IV	225-315										

$$F_2 = \frac{W_a V_2}{g} + p_2 A_2 = \frac{W_a V_o}{g} + p_o A_o + \int_{\substack{pdA \\ spike \\ \& cowl}} + \int_{\substack{pdA \\ spillage \\ streamline}}$$

$$- \int C_f q \, dA_s \cos \delta_s - C_{D_{\substack{spike \\ tip}}} q_o A_{\substack{spike \\ tip}} - C_{D_{\substack{cowl \\ lip}}} q_o A_{\substack{cowl \\ lip}}$$

where:

$$W_a = g \, p_o V_o A_c \left(\frac{A_o}{A_c} \right)$$

All the parameters involved in the above equation, with the exception of spillage drag and drag coefficients for the spike tip and cowl lip, were intended to be products of direct measurements or derivations thereof. As indicated before, airflow calibration tests were cancelled, leaving the determination of inlet mass flow ratios to theoretical means. The satisfactory correlations obtained between theory and experiment with the 2/3-scale model substantiates this approach. Mass-flow ratios versus cowl position for constant freestream Mach numbers have been estimated for the full-scale AIM and are presented in Reference 7.1-2; they were later supplemented by a more thorough analysis done by NASA (Reference 7.1-5). Inlet airflow was thus calculated from the theoretical mass flow ratio (a function of spike position and wind tunnel Mach number), and the value of mass flow per unit area in the wind tunnel.

Calibration of the LeRC tunnel facility nozzles (Reference 7.1-6) was available for Mach numbers in the inviscid core of 6.05 ±0.02 and 7.25 ±0.08. Due to the lack of full calibration information for the Mach 5 nozzle, the tunnel stagnation conditions, combined with the pressure readings at the spike tip (1-S), were employed to determine the tunnel flow characteristics for the Mach 5 testing.

Integrated wall forces in the momentum equation were based on linear interpolation in the axial direction of measured static pressures. Where more than one pressure reading was available at a given station, an arithmetic average was used.

The spillage streamline area integral was calculated from

$$\int_{streamline} PdA = q_o A_c C_{D_A} + P_o A_c \left(1 - \frac{A_o}{A_c} \right)$$

using theoretical values of A_o/A_c and C_{D_A}, the additive drag coefficient, a function of A_o/A_c. Angle-of-attack corrections were effected by a mass flow ratio correlation given in Reference 7.1-2.

The drag coefficients for the blunted portions of the spike tip and cowl lip were obtained by numerical pressure integration. The pressure distributions were taken from typical Mach 6 cases computed by the computer program noted in Reference 7.1-5.

The friction coefficient is calculated by the method of Reference 7.1-7 for a turbulent boundary layer. For this analysis the engine walls are divided into three distinct groups:

1. Flat plate analysis--This analysis is used for all engine external surfaces, and all nozzle and cowl internal surfaces.

2. Flat plate analysis corrected for conical surface--This is used for the inlet spike only. The correction is to reduce the flat-plate Reynolds number by 1/2.

3. Duct flow analysis--This covers all surfaces of the combustor. In This region the boundary layer is assumed to have a fully established turbulent profile,with the boundary layer thickness equal to 1/2 the duct height.

Once the inlet throat thrust function is determined, an effective Mach number and related effective static pressure across the throat area are derived, simultaneously satisfying the total energy, mass flow, and momentum at that station. An effective total pressure is then obtained by isentropic calculation for equilibrium air to stagnation conditions.

The flow characteristics derived this way are those that may be obtained if the actual non-uniform flow could be mixed and converted into a uniform flow in a constant-area duct without wall friction losses. Thus mixing losses are inherently contained in these average values. This fact must be kept in mind when comparing these results with other tests or theoretical analyses, where other weighting methods of averaging have been used.

7.1.2.1 Selection of Test Points for Inlet Analysis

To avoid any question of combustor/inlet interaction, the steady state inlet data to be presented are taken from tests without fuel injection for comparison with the 2/3-scale model or theoretical results. Table 7.1-3 presents the reading numbers and specific times chosen for this purpose, together with wind tunnel parameters, spike position, and related estimated performance. The effect of fuel injection on wall pressures, including inlet unstarting conditions, will be discussed in a later section of this report.

ORIGINAL PAGE IS
OF POOR QUALITY

TABLE 7.1-3

TEST POINTS SELECTED FOR INLET ANALYSIS (NO FUEL INJECTION)

Rdg No.	Time	M_o	$\left(\frac{X}{R}\right)_{CL}$	P_{t_o}, psia	T_{t_o}, °R	$Re_d \times 10^{-6}$	M_T	$\frac{P_{t_{TH}}}{P_{to}}$	$\left(\frac{P_{t_2}}{P_{to}}\right)_{sub}$	η_{KE} Super.	η_{KE} Subsonic	K_D Super.	K_D Subsonic	α
60	155.69	6.013	3.902	747.2	2950	2.38	2.457	.3658	.1633	.9444	.8972	.8873	.9033	0°
61	178.86	5.989	4.066	745.2	2998	2.33	2.429	.4123	.1885	.9469	.9026	.9052	.9130	0°
63	186.15	5.977	3.897	924.5	3019	2.89	2.496	.3853	.1659	.9461	.8967	.8903	.9035	0°
63	249.15	5.994	3.898	473.0	2988	1.50	2.546	.4011	.1654	.9363	.8856	.8980	.9059	0°
64	156.11	6.010	3.899	748.0	2956	2.40	2.494	.3805	.1644	.9456	.8968	.8900	.9039	0°
65	164.03	5.968	3.900	749.0	3035	2.33	2.530	.4005	.1673	.9455	.8946	.8940	.9042	0°
69	175.20	5.987	3.897	749.5	3001	2.35	2.467	.3715	.1642	.9418	.8939	.8887	.9035	0°
71	160.54	6.037	3.898	742.7	2897	2.44	2.149	.2500	.1450	.9194	.8856	.8642	.8958	3°
88	236.40	7.249	4.056	999.5	3157	1.64	2.816	.3215	.1027	.9398	.8904	.9008	.9121	0°
89	250.77	7.325	4.054	989.5	1793	4.75	2.833	.3228	.1081	.9396	.8947	.9016	.9179	0°
90	197.22	7.270	4.053	996.2	2992	1.81	2.820	.3230	.1032	.9413	.8922	.9008	.9127	0°
91	186.45	7.260	4.052	995.5	3069	1.80	2.560	.2204	.0896	.9073	.8665	.8817	.9068	3°
92	186.87	7.383	4.052	993.2	2053	3.63	2.807	.3203	.1081	.9475	.9021	.8992	.9165	0°
93	134.03	5.146	3.895	415.3	2026	3.93	2.038	.4356	.2820	.9315	.9005	.9004	.9162	0°
94	134.14	5.128	3.894	427.0	2200	3.62	2.051	.4370	.2831	.9323	.9011	.8991	.9158	0°
96	134.44	5.059	3.906	423.7	2216	3.67	1.999	.3984	.2796	.9217	.8953	.8867	.9127	3°
96	294.64	5.073	3.906	417.5	2228	3.57	1.981	.3910	.2755	.9172	.8911	.8874	.9127	3°
97	135.71	5.161	3.896	210.8	2097	1.91	2.022	.4308	.2795	.9270	.8963	.9020	.9168	0°

7.1-3 Inlet Static Pressure Distributions

The fundamental measurement used in evaluation of the inlet performance consisted of wall static pressure. These static pressures are presented in this section followed by a discussion of derived inlet performance parameters. Freestream static pressure is used to non-dimensionalize these measurements for evaluation of "altitude" effects and for comparison with other data.

Freestream static pressure is available from wind tunnel calibrations of Mach number vs total temperature for each nozzle. This calibration thus determines the test section Mach number, which is used with tunnel stagnation conditions to calculate test section static pressure (and all gas properties) by equilibrium expansion.

Static pressure readings which did not follow the wind tunnel evacuation pressures preceding each run, or failed to reach equilibrium following a run, were eliminated by inspection prior to performance calculations. The computer then averaged the remaining pressures and integrated the wall forces by linear interpolation. The resulting average pressures vs station are shown in the accompanying graphs as data points, because these are the bases for the quoted performance. Theoretical static pressure distributions for similar test conditions, where available, are superimposed for comparison.

7.1.3.1 Mach 6

Static pressures for a typical case for this Mach number are presented in Figures 7.1-5 and 7.1-6 for the spike and cowl, respectively. Corresponding theoretical distributions are superimposed as solid lines. Quite acceptable agreement between theory and test is exhibited on the cowl surface. On the spike, however, the predicted decrease in static pressure beginning at Station 4.21 does not materialize. Interaction of the cowl shock with the spike boundary layer is apparently responsible for this discrepancy.

Reynolds number changes were found to have a negligible effect on inlet static pressures at this Mach number. This is demonstrated by Figures 7.1-7 and 7.1-8 which correspond to a 48-percent decrease in Reynolds number from that of Figures 7.1-5 and 7.1-6.

Figures 7.1-9 and 7.1-10 present the effect of a spike position change on the inlet static pressures. Spike position for these two figures lies between the Mach 7 and Mach 8 design values. In spite of the resulting increased spillage, the higher contraction ratio results in increased cowl pressures over those of Figure 7.1-6 in which the spike is approximately in the Mach 6 design position. No appreciable difference is observed in spike pressures in Figure 7.1-9 vs Figure 7.1-5.

Reading 71 (see Table 7.1-3), plotted in Figures 7.1-11 and 7.1-12, was run with the model pitched to 3-deg angle of attack. Spike position is the same as for Figures 7.1-7 and 7.1-8. Comparing the raw data for these figures showed a spread of windward and leeward pressures as expected; however, the average pressure levels shown in Figures 7.1-11 and 7.1-12 are increased

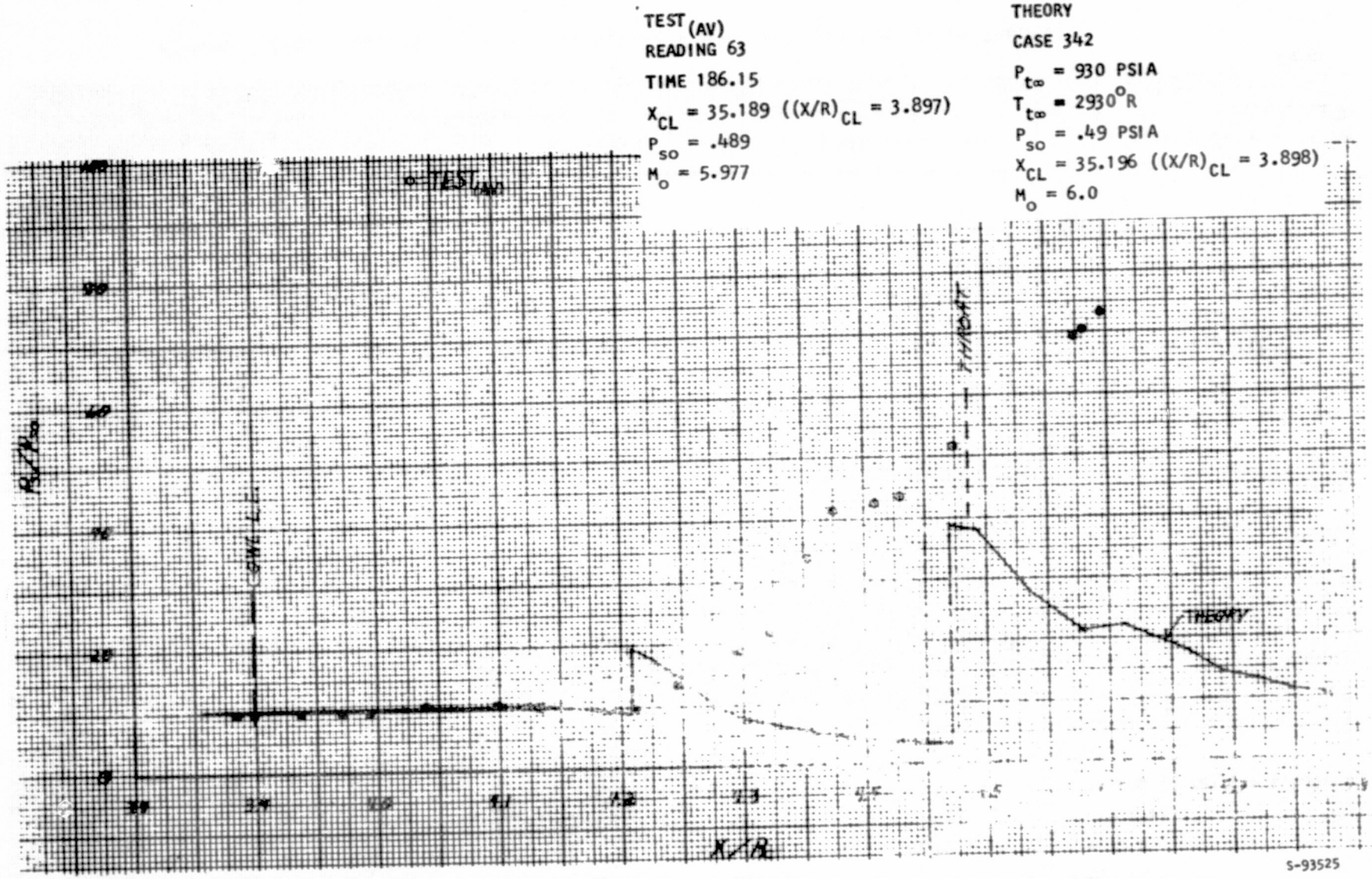

Figure 7.1-5. Mach 6 Typical Spike Static Pressure Distribution vs Theory

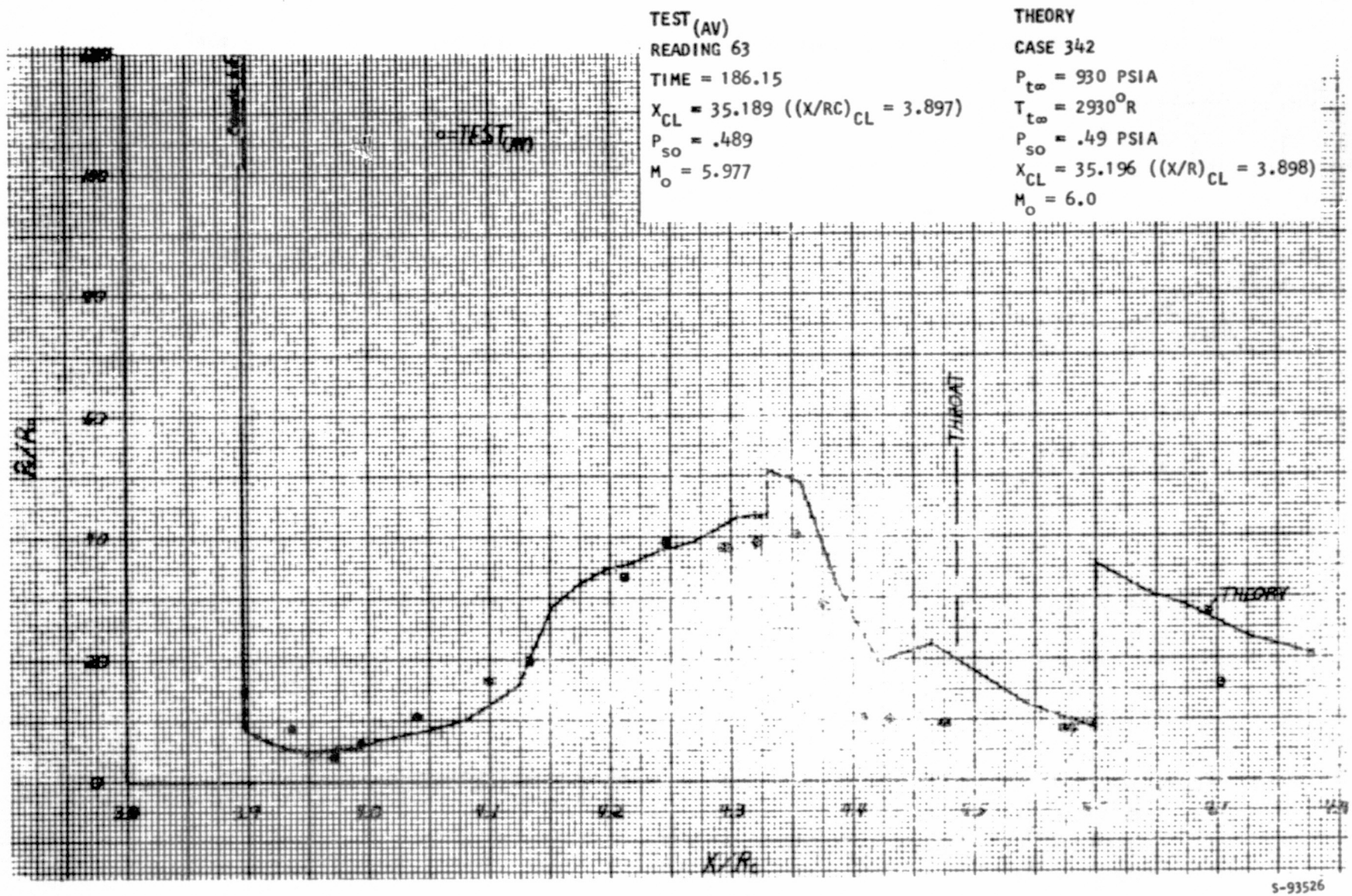

Figure 7.1-6. Mach 6 Typical Cowl Static Pressure Distribution vs Theory

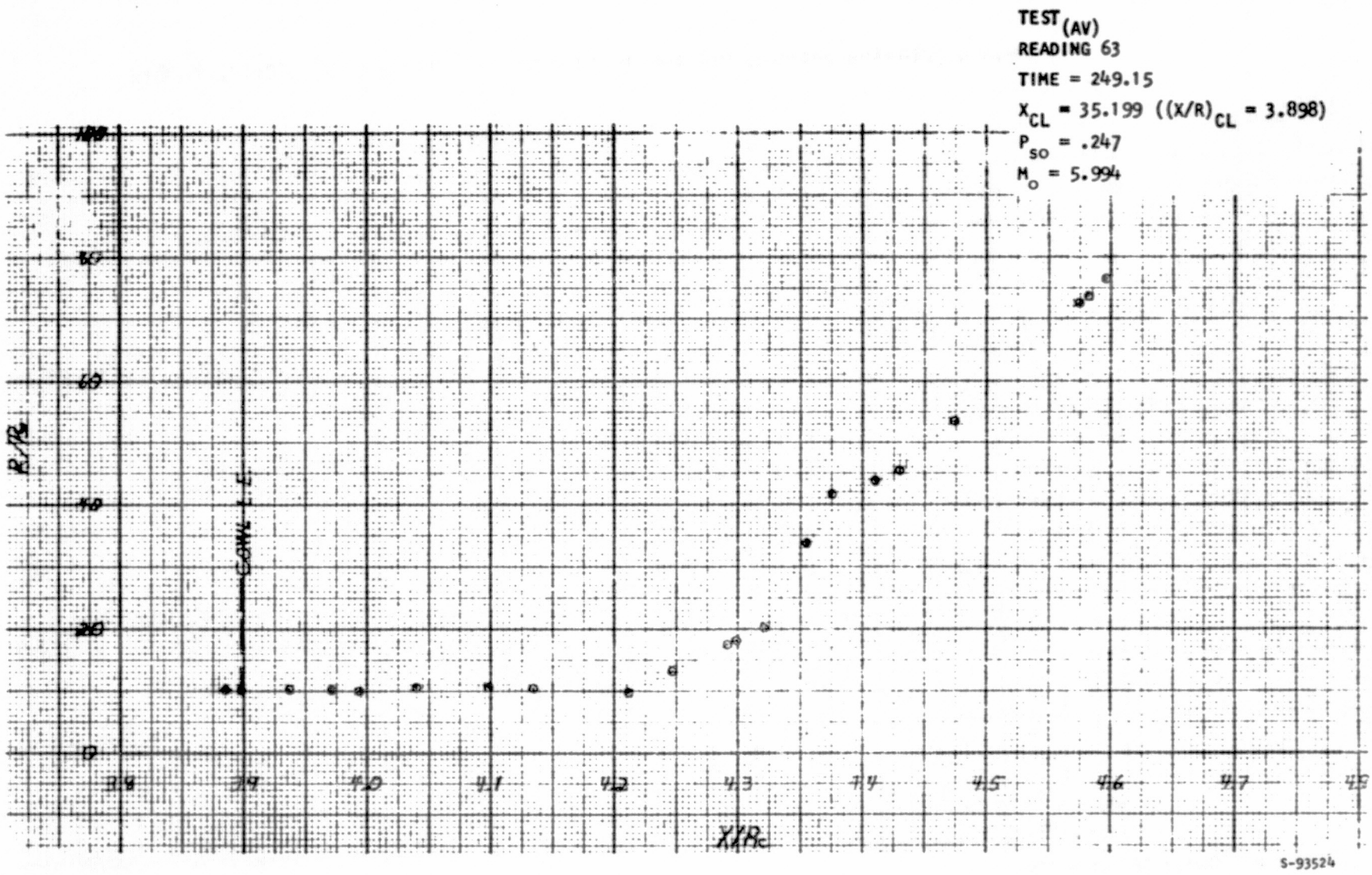

Figure 7.1-7. Mach 6 Spike Pressure Distribution; Reduced Reynolds Number

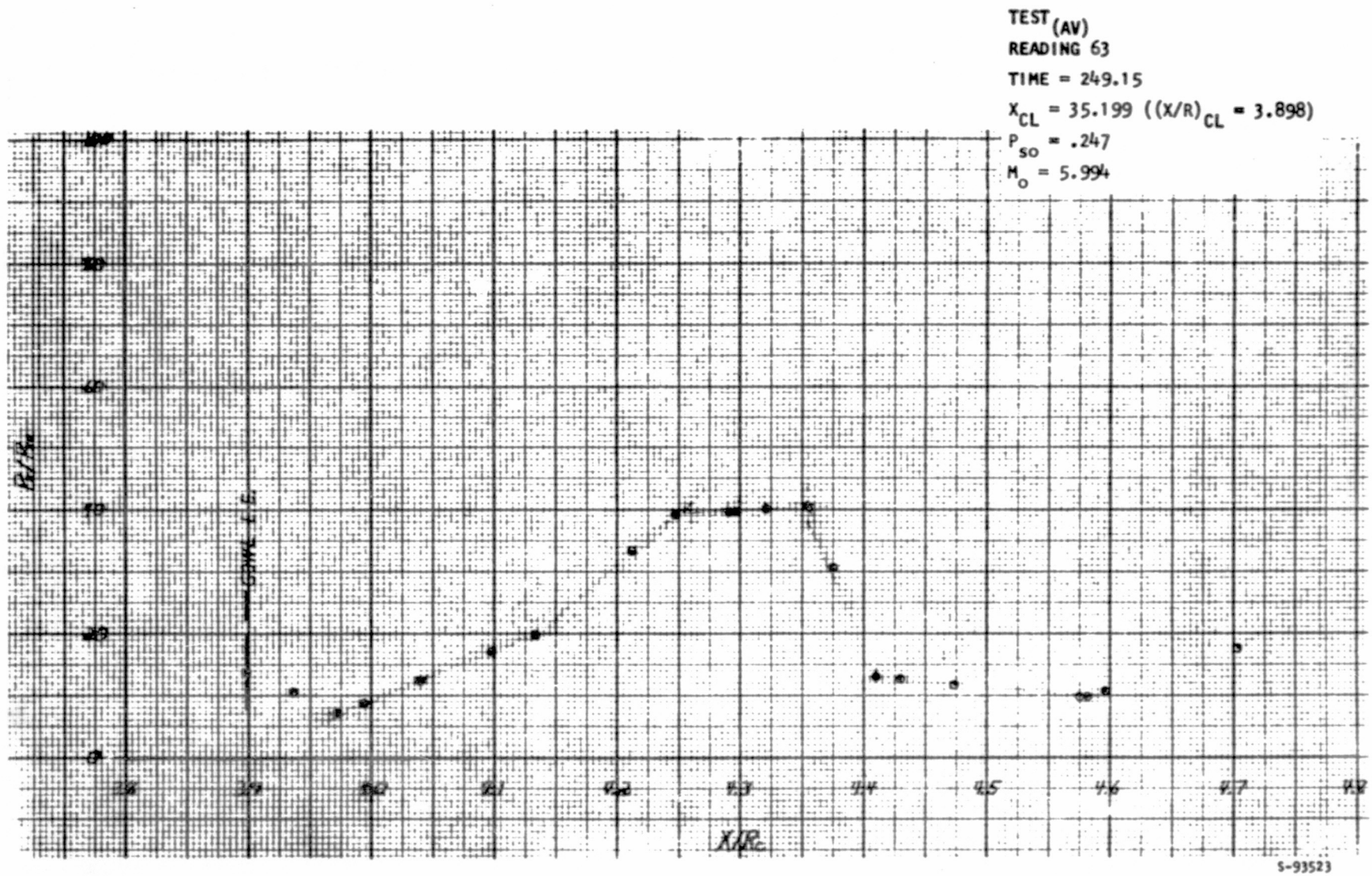

Figure 7.1-8. Mach 6 Cowl Pressure Distribution; Reduced Reynolds Number

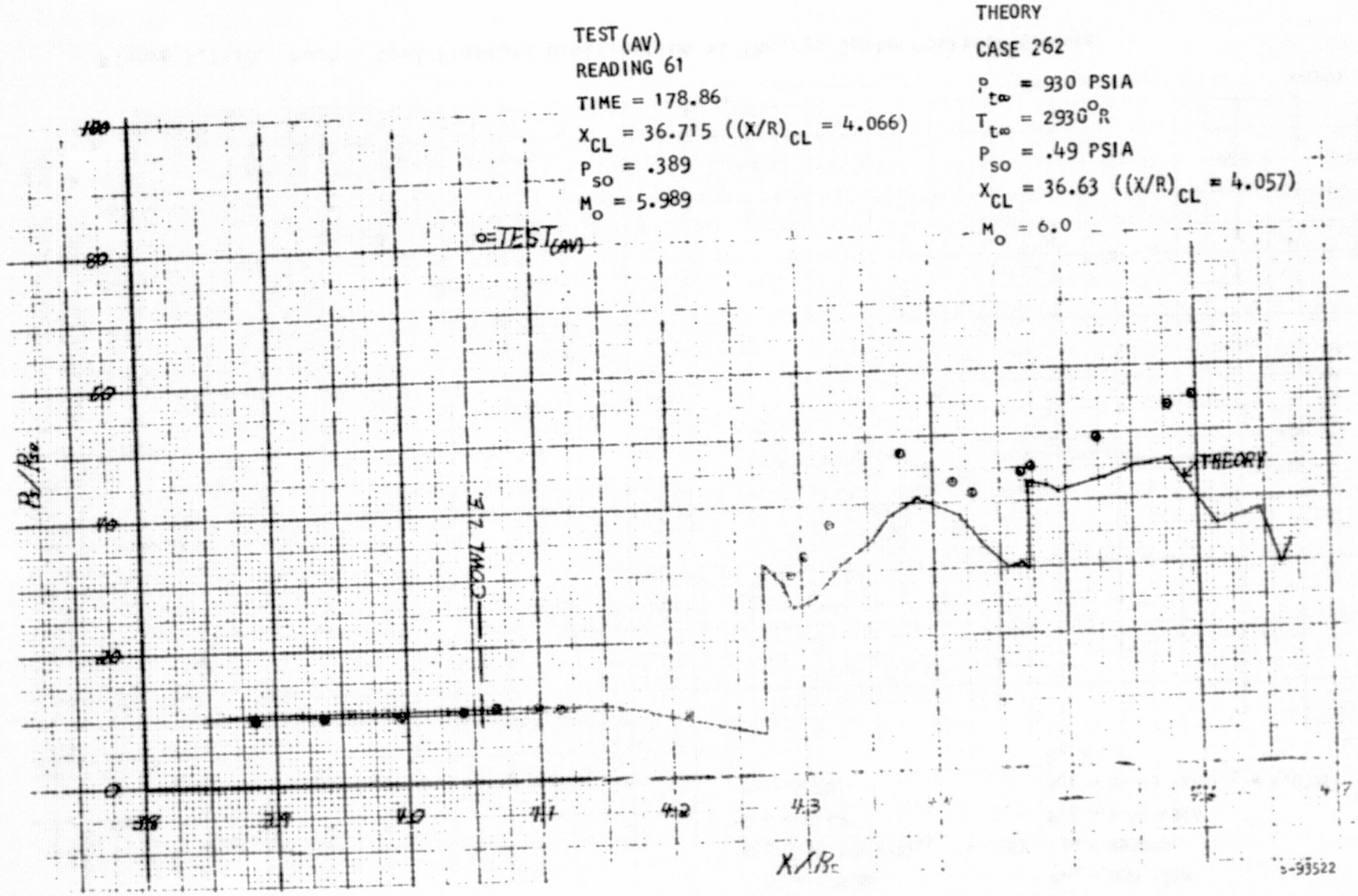

Figure 7.1-9. Mach 6 Spike Pressure Distribution vs Theory; Spike Position Change

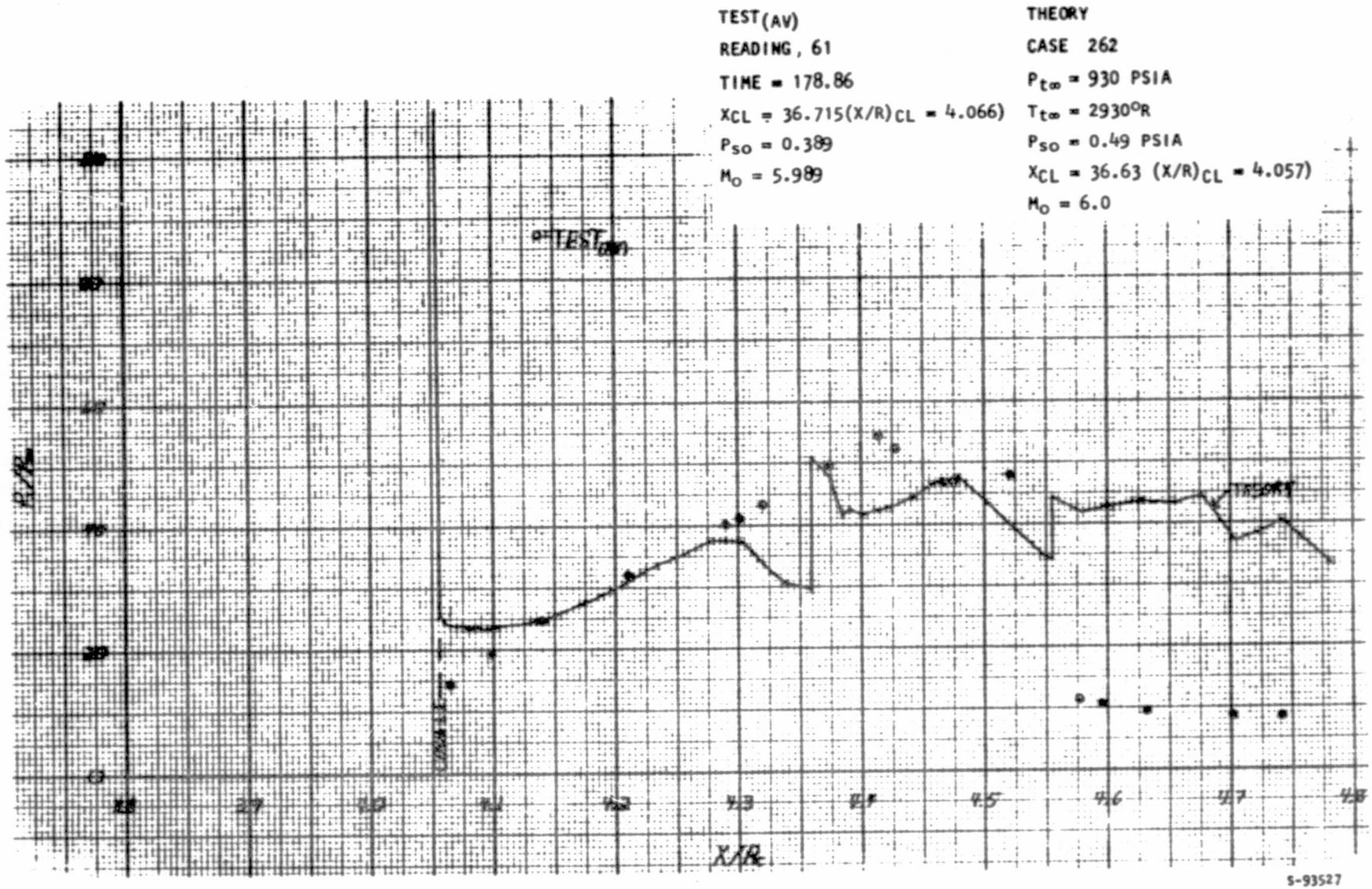

Figure 7.1-10. Mach 6 Cowl Pressure Distribution vs Theory; Spike Position Change

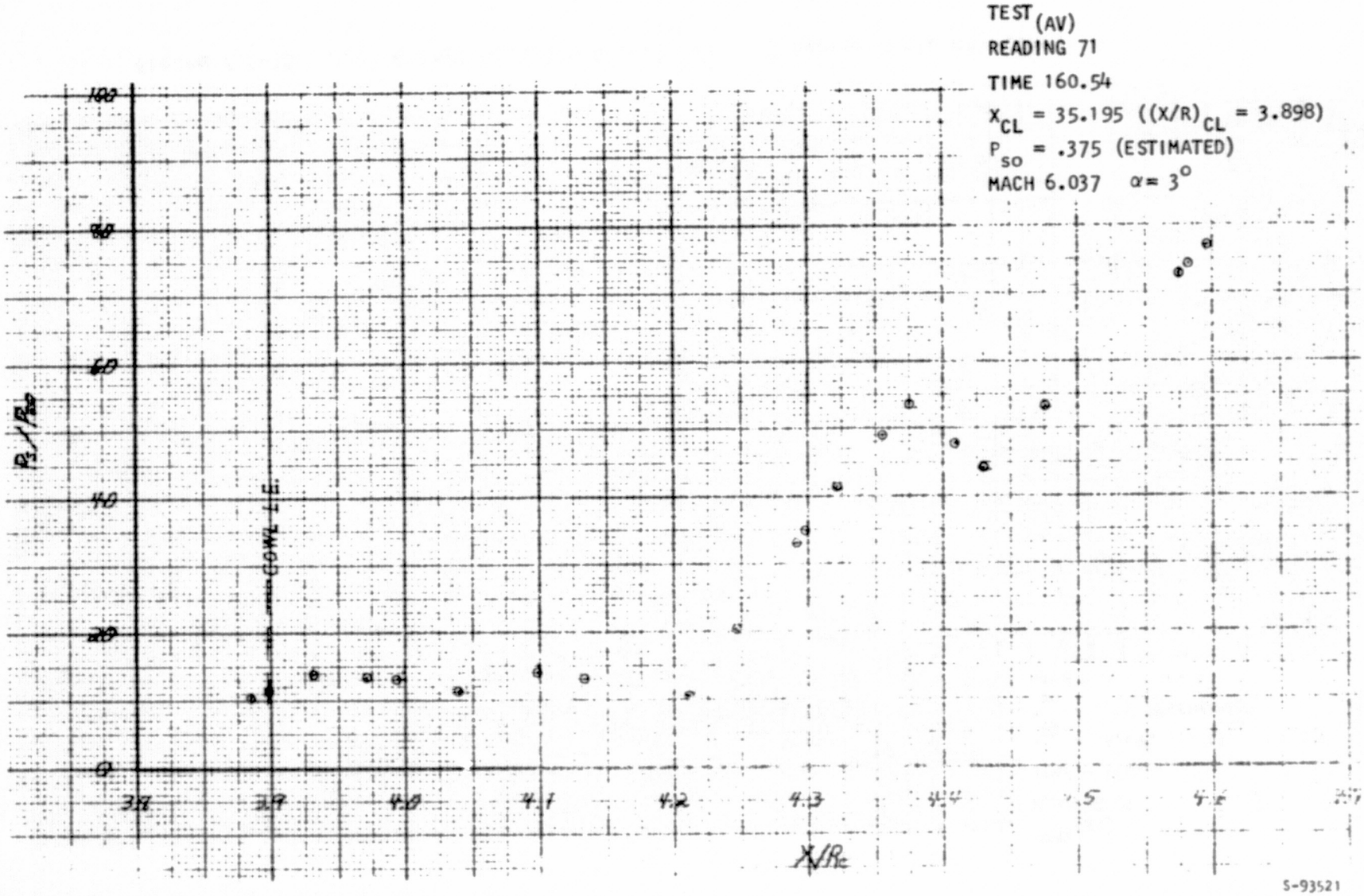

Figure 7.1-11. Mach 6 Spike Pressure Distribution; 3 Degree Angle of Attack

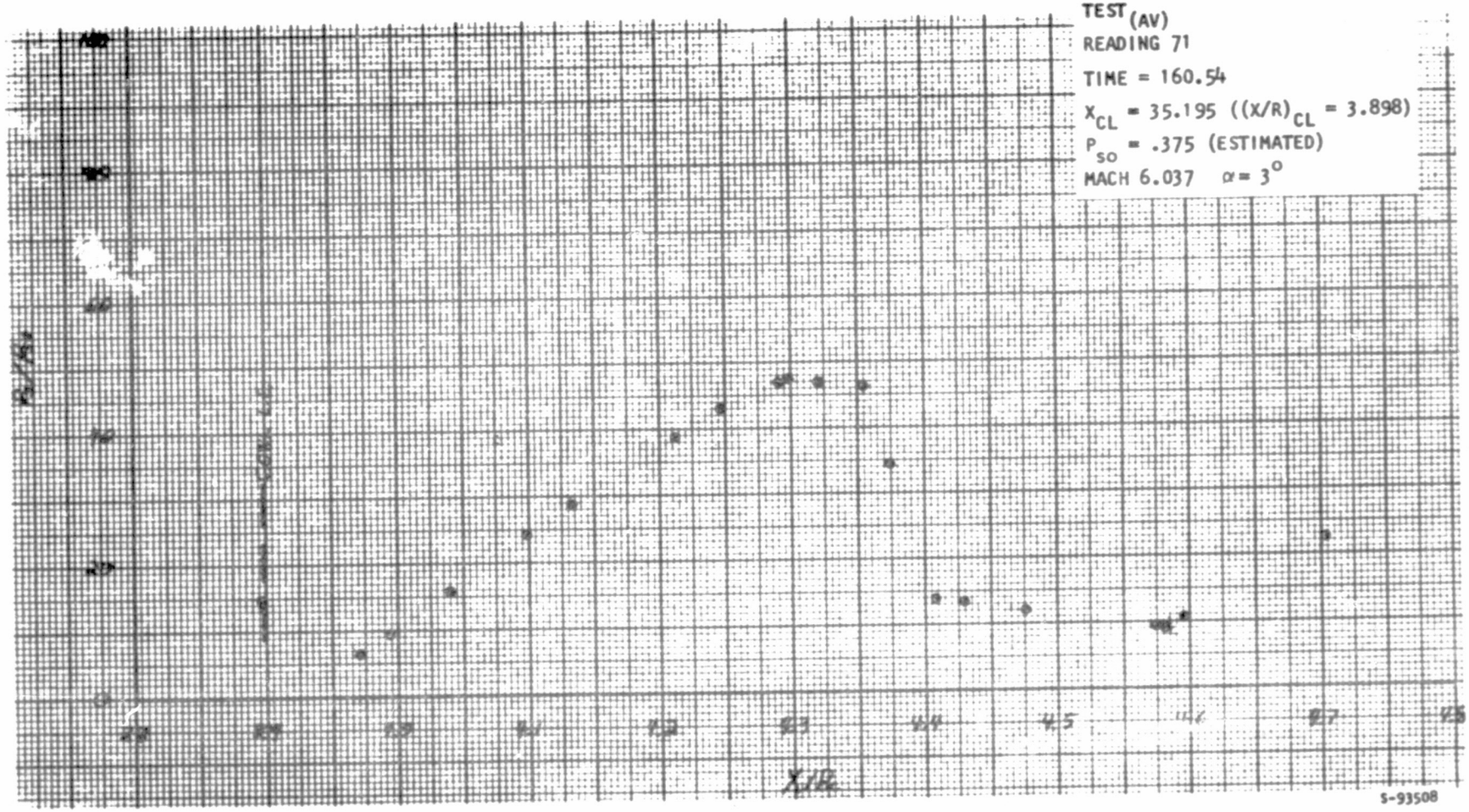

Figure 7.1-12. Mach 6 Cowl Pressure Distribution; 3 Degree Angle of Attack

slightly on both the spike and cowl. Although the unstart limit was not investigated with the AIM engine, angles of attack to 5 deg on the 2/3-scale model were tested without unstart.

7.1.3.2 Mach 7

Experimental effort at Mach 7 was concentrated on fuel injection schedules at the design spike position. Reynolds number variations and angle of attack effects on inlet performance were investigated. Figures 7.1-13 and 7.1-14 present typical Mach 7 pressure distributions compared with theory. Again, as with Mach 6, the spike pressure was dominated by the cowl shock/boundary layer interaction and did not exhibit the sharp pressure peaks predicted. Cowl pressure predictions correlate well with the measured pressures except for a distinct shock/expansion predicted near $X/R_C = 4.41$.

The effects of pitching the engine to 3-deg angle of attack, Figures 7.1-15 and 7.1-16, appear small. These slight changes in static pressure, however, are responsible for most of the 10-point drop in total pressure recovery, compared with reading 88 noted in Table 7.1-3. That is, the net wall pressure forces increased by 51 lb, or 16 percent, while the friction increase amounted to 8 lb, or 9 percent, due to the 3-deg angle of attack.

Figures 7.1-17 and 7.1-18 show the pressure distribution resulting from a three-to-one increase in Reynolds number over that of Figures 7.1-13 and 7.1-14. Resulting changes in wall friction are well within the experimental errors, producing virtually no change in inlet recovery.

7.1.3.3 Mach 5

The Mach 5 cases listed in Table 7.1-3 are for the design spike position with variations in Reynolds number and angle of attack. Typical pressure distributions are presented in Figures 7.1-19 and 7.1-20. As in all previous comparisons, the internal spike surface pressures are dominated by the cowl shock-boundary layer interaction,and a predicted expansion process does not materialize. The cowl pressure is adequately predicted to Station 4.40, where a low pressure is encountered in the test data. Some of the pressure readings, which had been eliminated in this region, registered higher than the "average" point shown.

Reading 97 (Table 7.1-3) was run at approximately 1/2 the Reynolds number of that for the data shown in Figures 7.1-19 and 7.1-20. The static pressure distribution was relatively unchanged on the spike, Figure 7.1-21, and slightly higher on the cowl, Figure 7.1-22.

Figures 7.1-23 and 7.1-24 present the average static pressure distributions on the spike and centerbody, respectively, for 3-deg angle of attack. The slight differences in static pressure and accompanying spillage (6 percent reduction in mass flow ratio) resulting from angle of attack, reduced the subsonic pressure recovery by 2.7 percent.

TEST$_{(AV)}$
READING 88
TIME 236.4
X_{CL} = 36.619 ($(X/R)_{CL}$ = 4.056)
P_{so} = .154
M_o = 7.249

THEORY
CASE 1080A
$P_{t\infty}$ = 1,000 PSIA
$T_{t\infty}$ = 3,000°R
P_{so} = .159776 PSIA
X_{CL} = 36.558 ($(X/R)_{CL}$ = 4.049)
M_o = 7.25

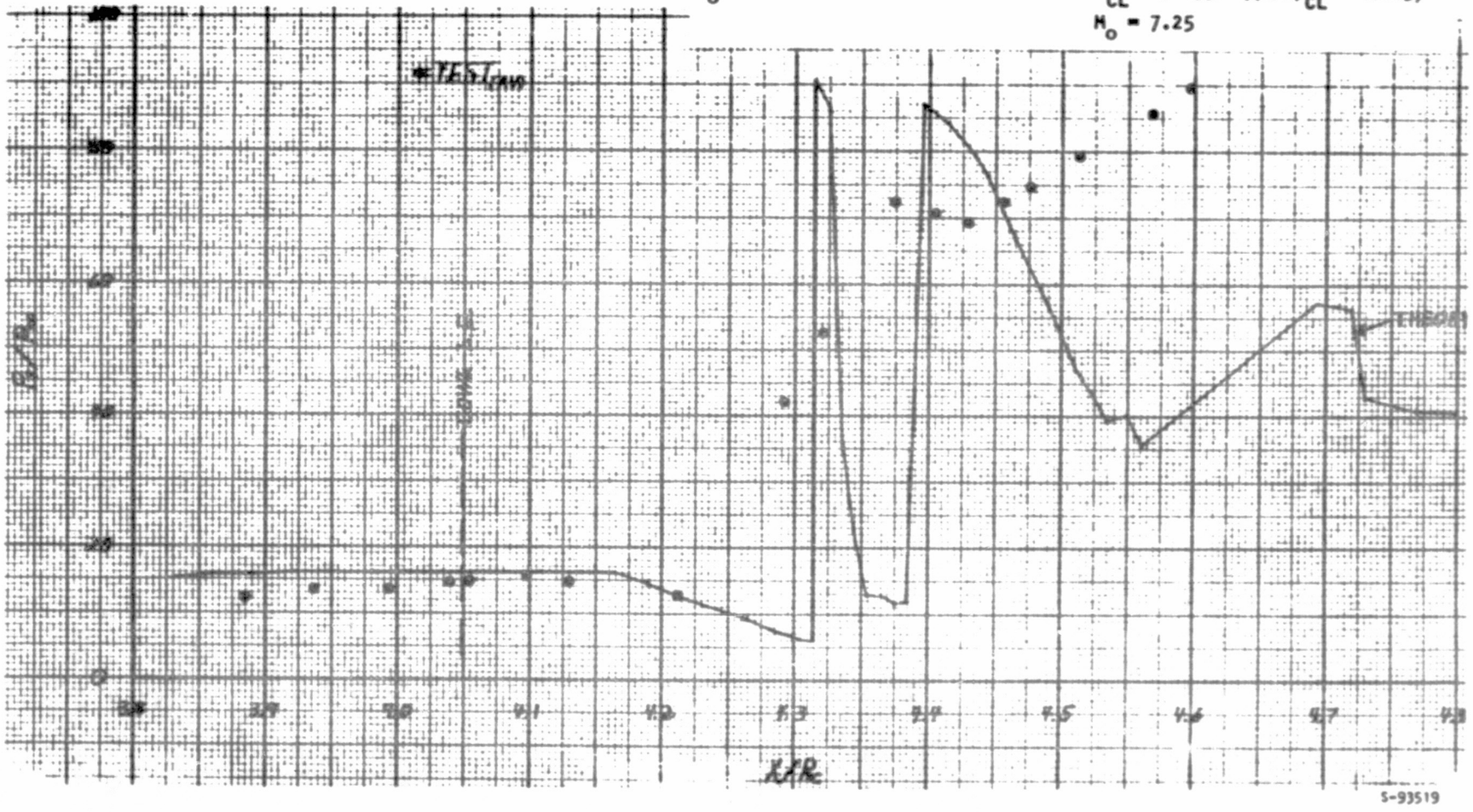

Figure 7.1-13. Mach 7 Typical Spike Static Pressure Distribution vs Theory

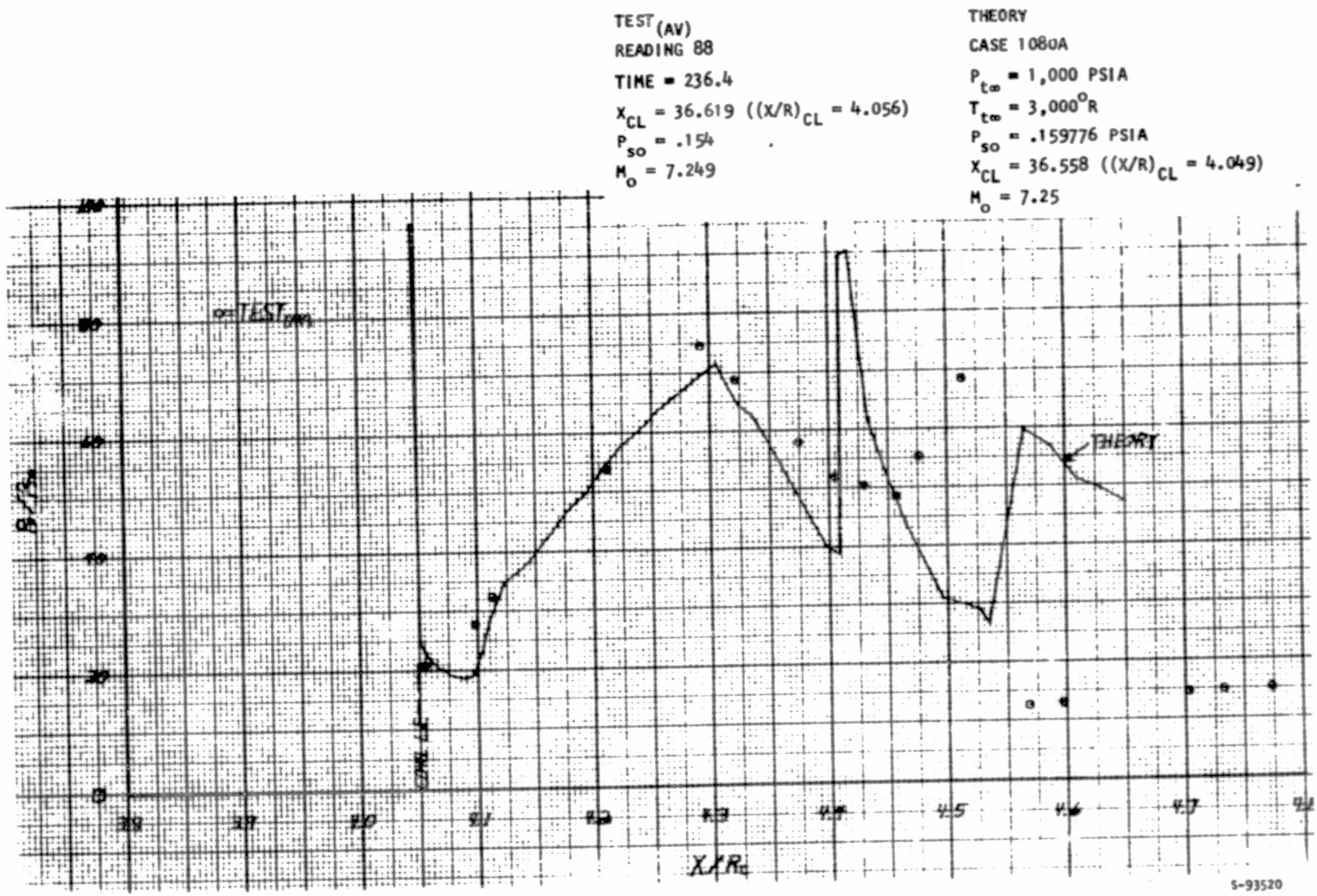

Figure 7.1-14. Mach 7 Typical Cowl Static Pressure Distribution vs Theory

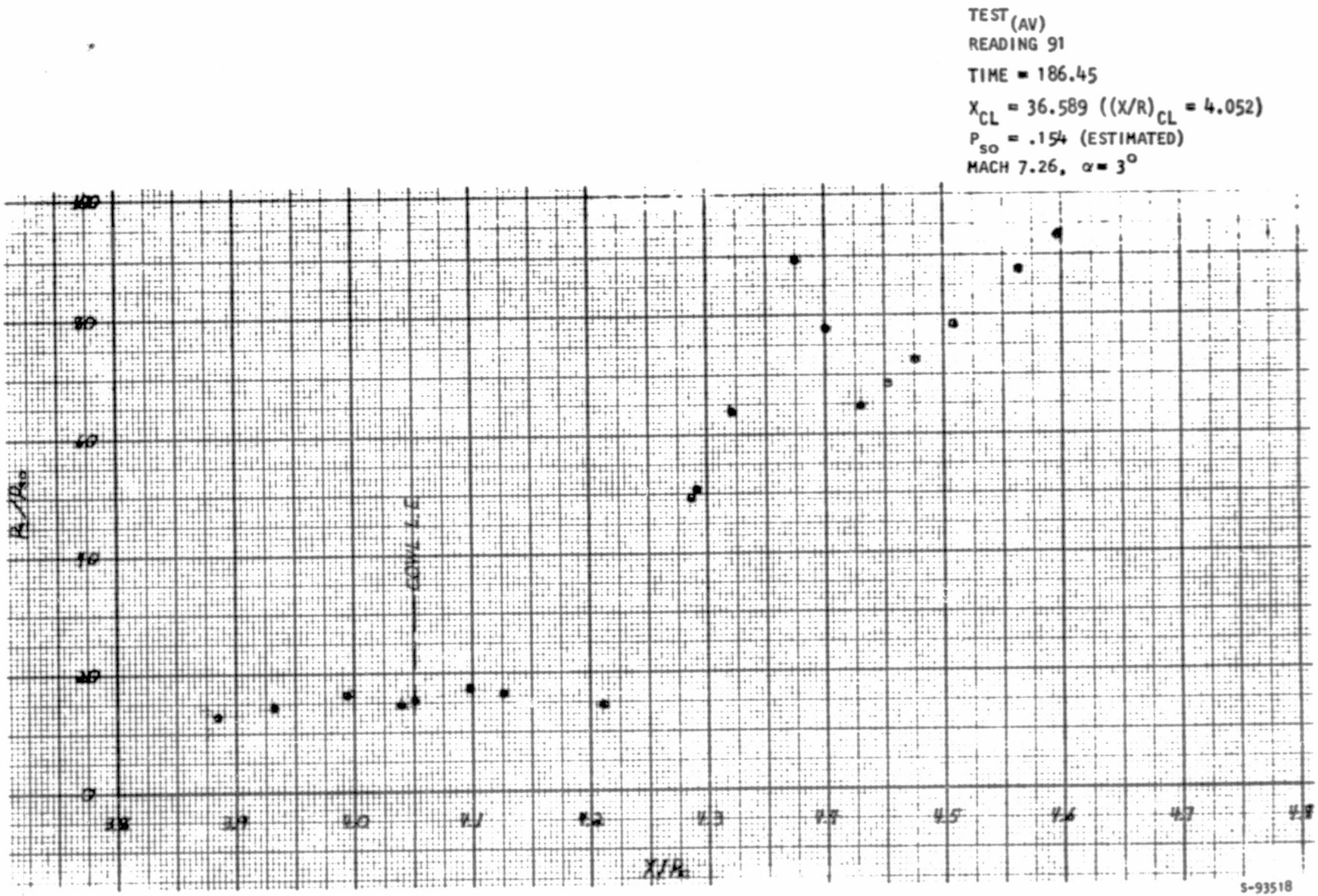

Figure 7.1-15. Mach 7 Spike Pressure Distribution; 3 Degree Angle of Attack

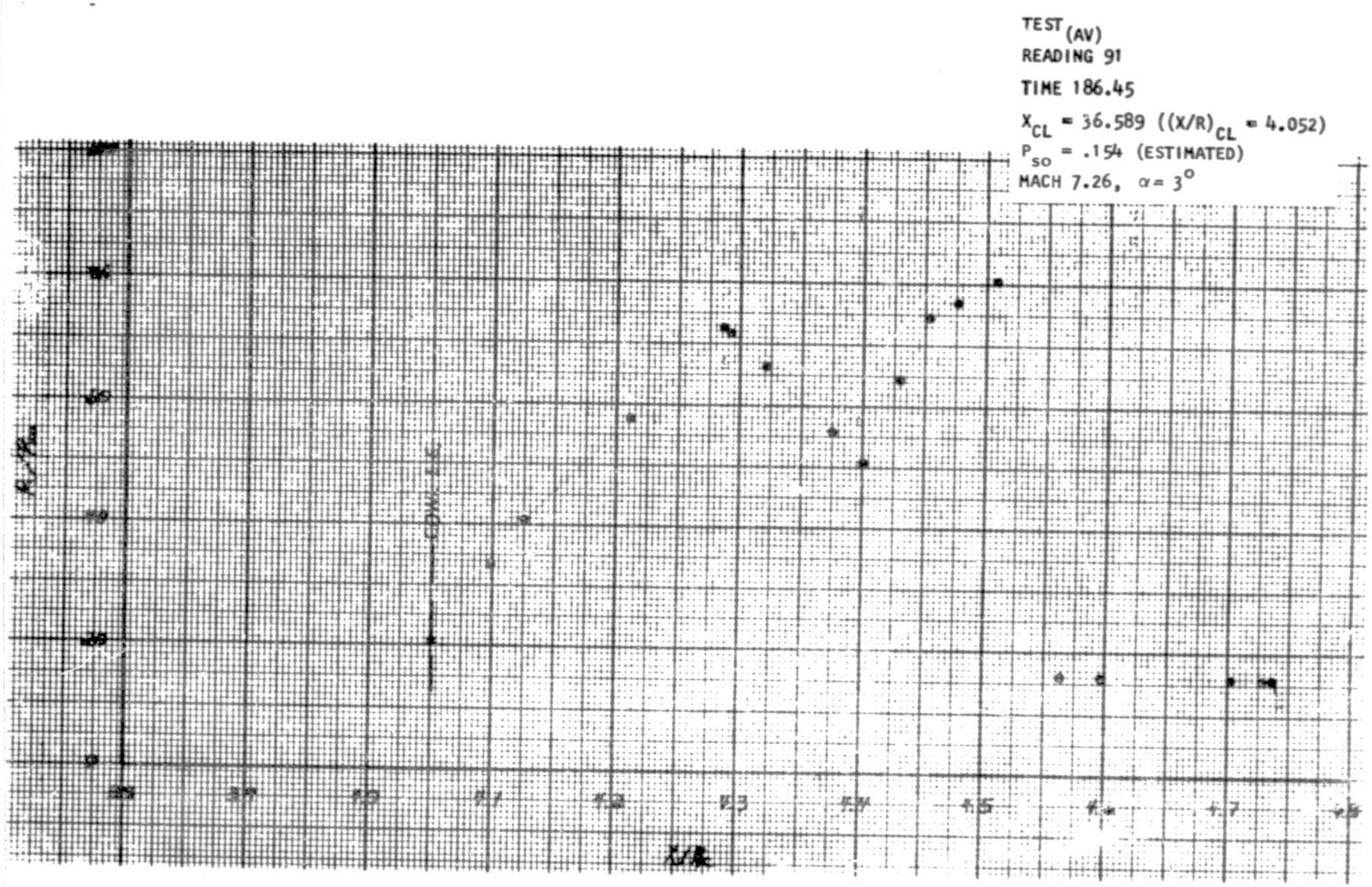

Figure 7.1-16. Mach 7 Cowl Pressure Distribution; 3 Degree Angle of Attack

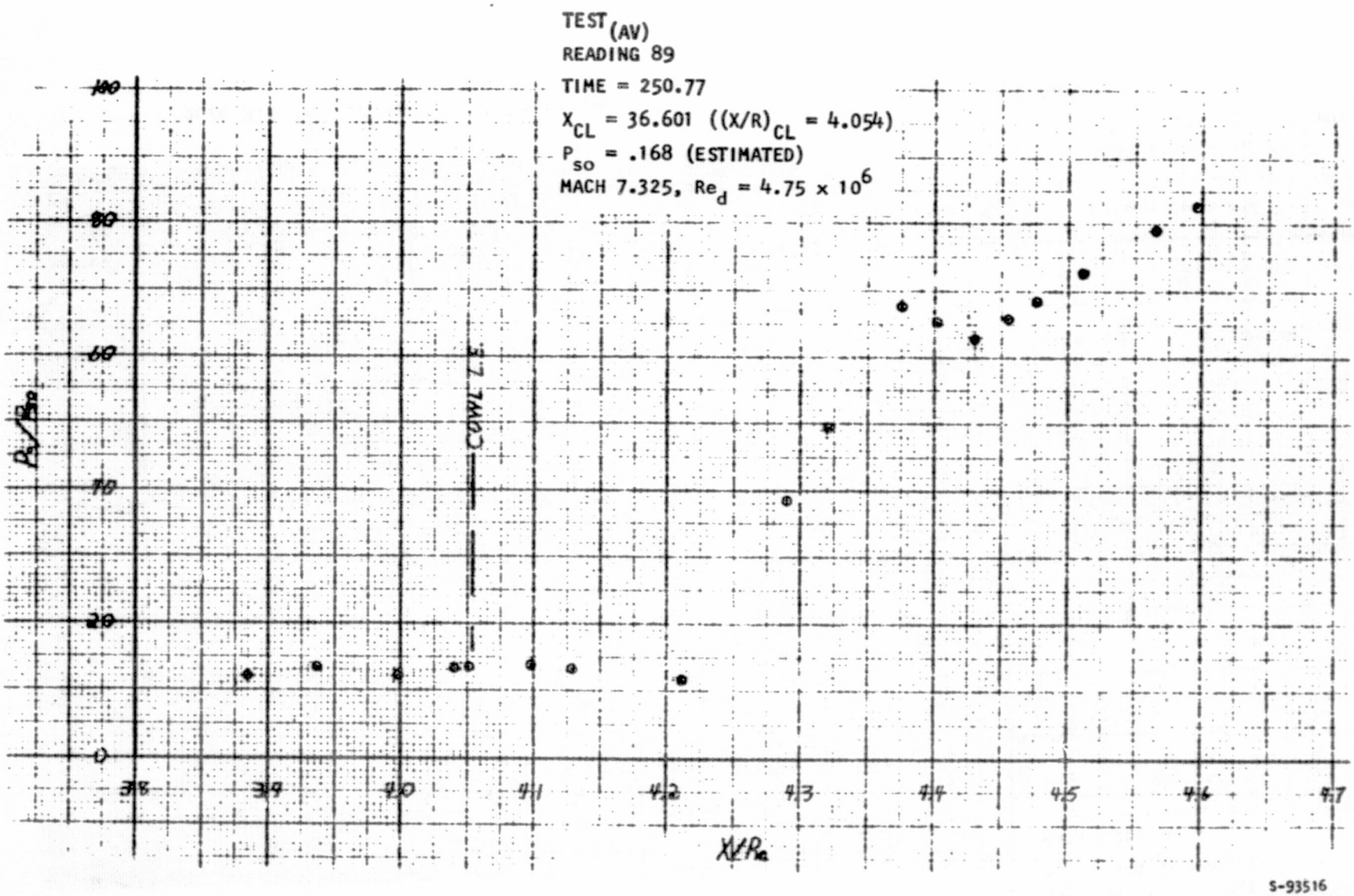

Figure 7.1-17. Mach 7 Spike Pressure Distribution; Increased Reynolds Number

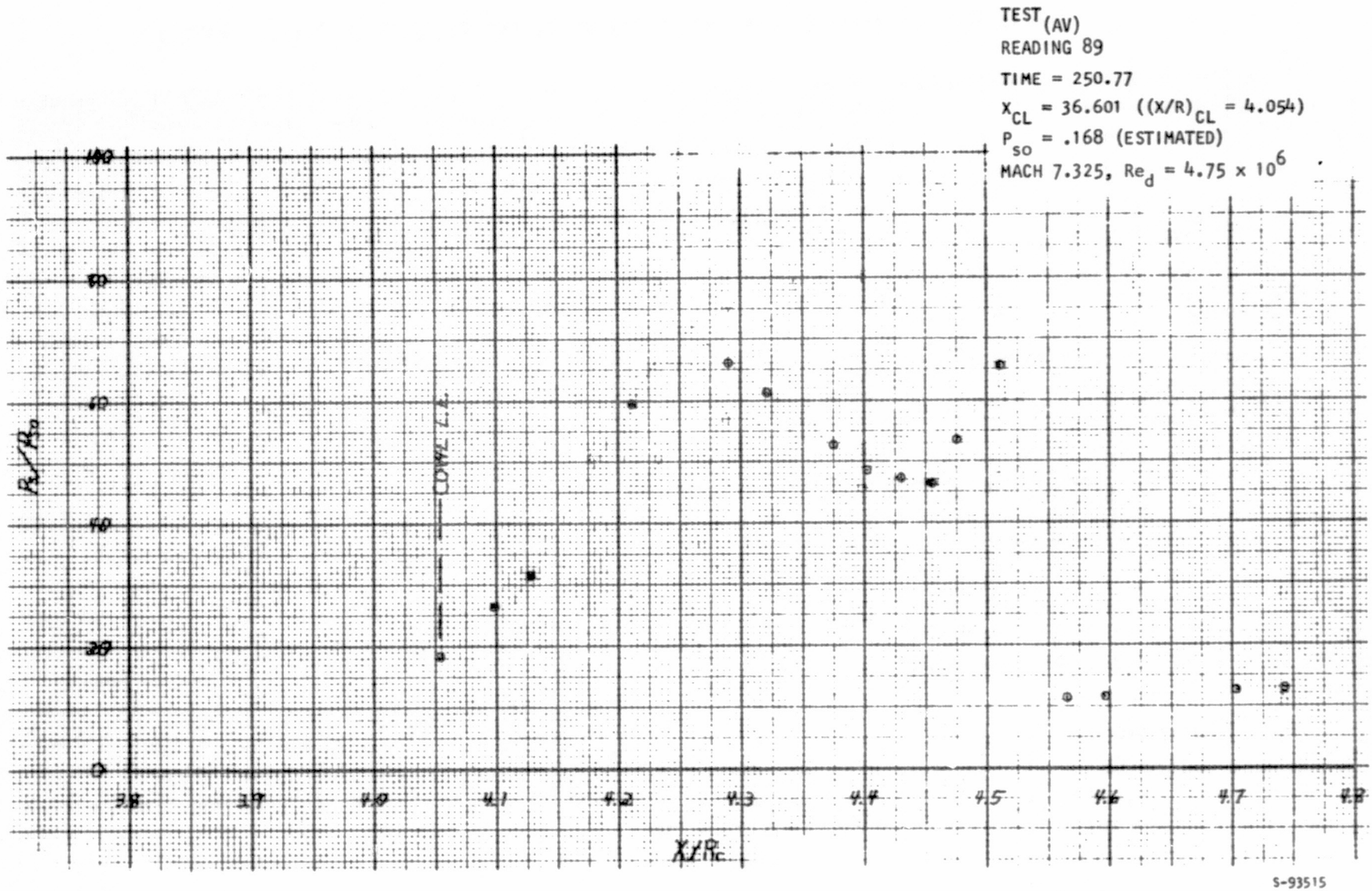

Figure 7.1-18. Mach 7 Cowl Pressure Distribution; Increased Reynolds Number

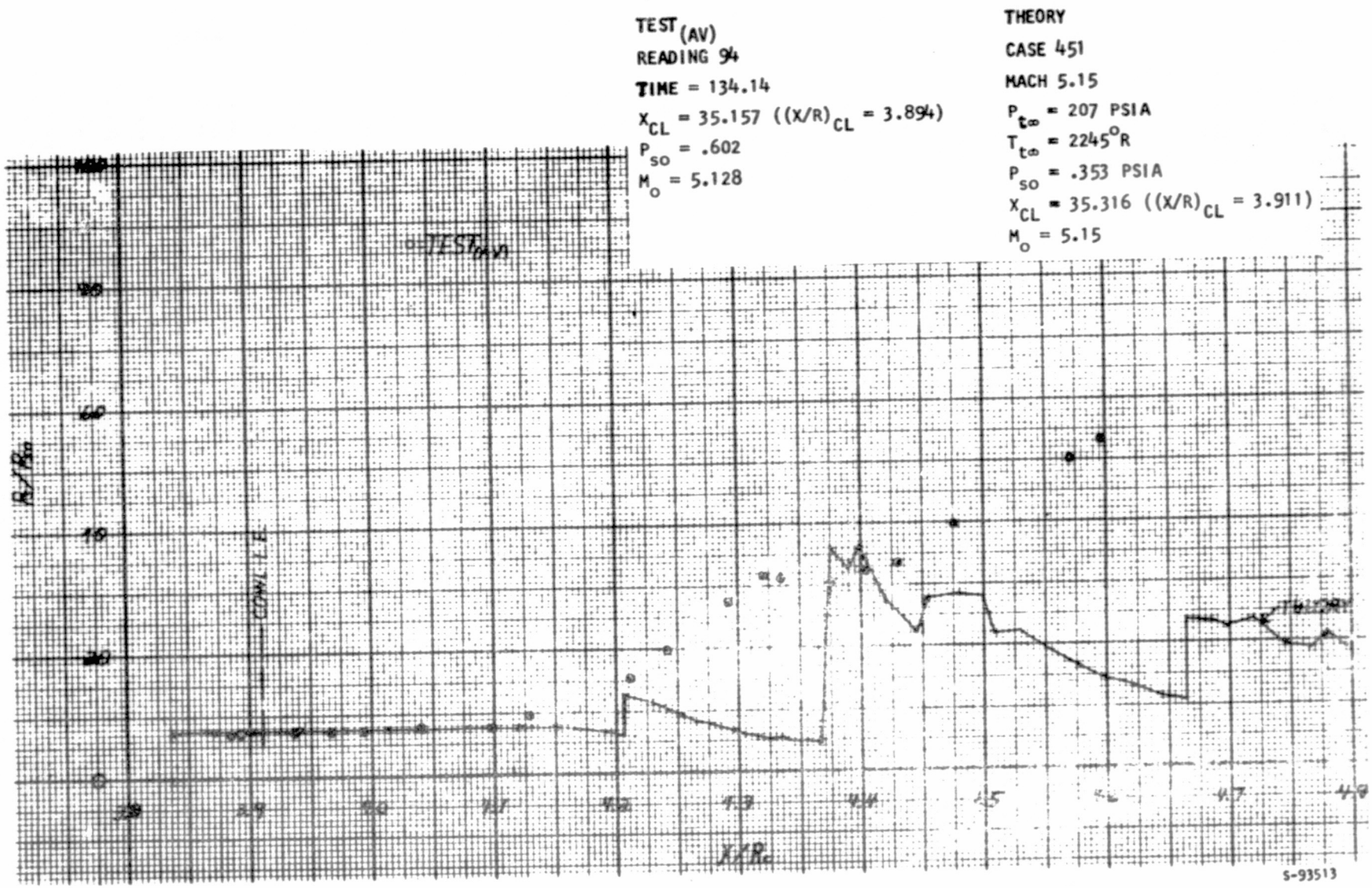

Figure 7.1-19. Mach 5 Typical Spike Static Pressure Distribution vs Theory

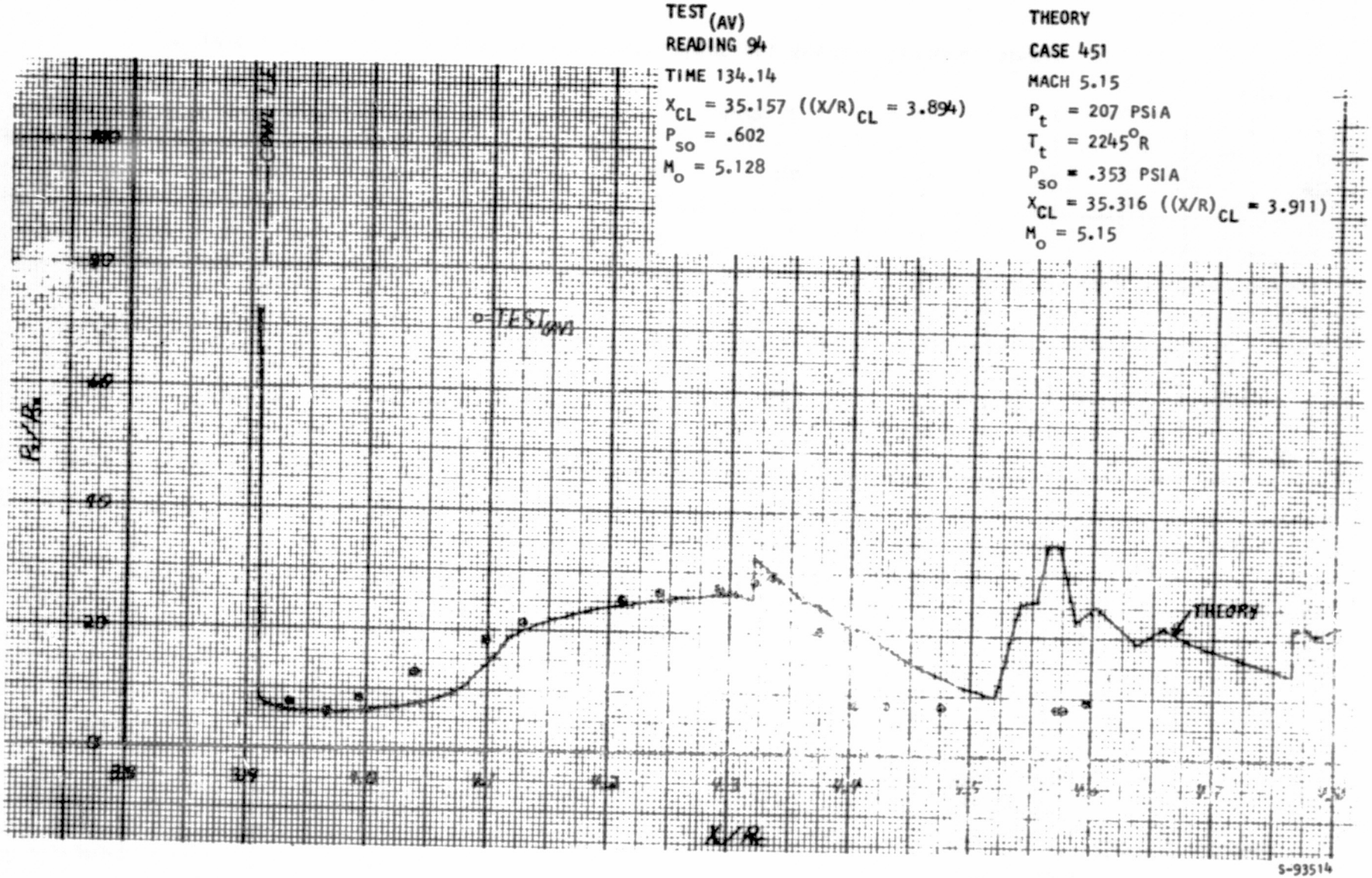

Figure 7.1-20. Mach 5 Typical Cowl Static Pressure Distribution vs Theory

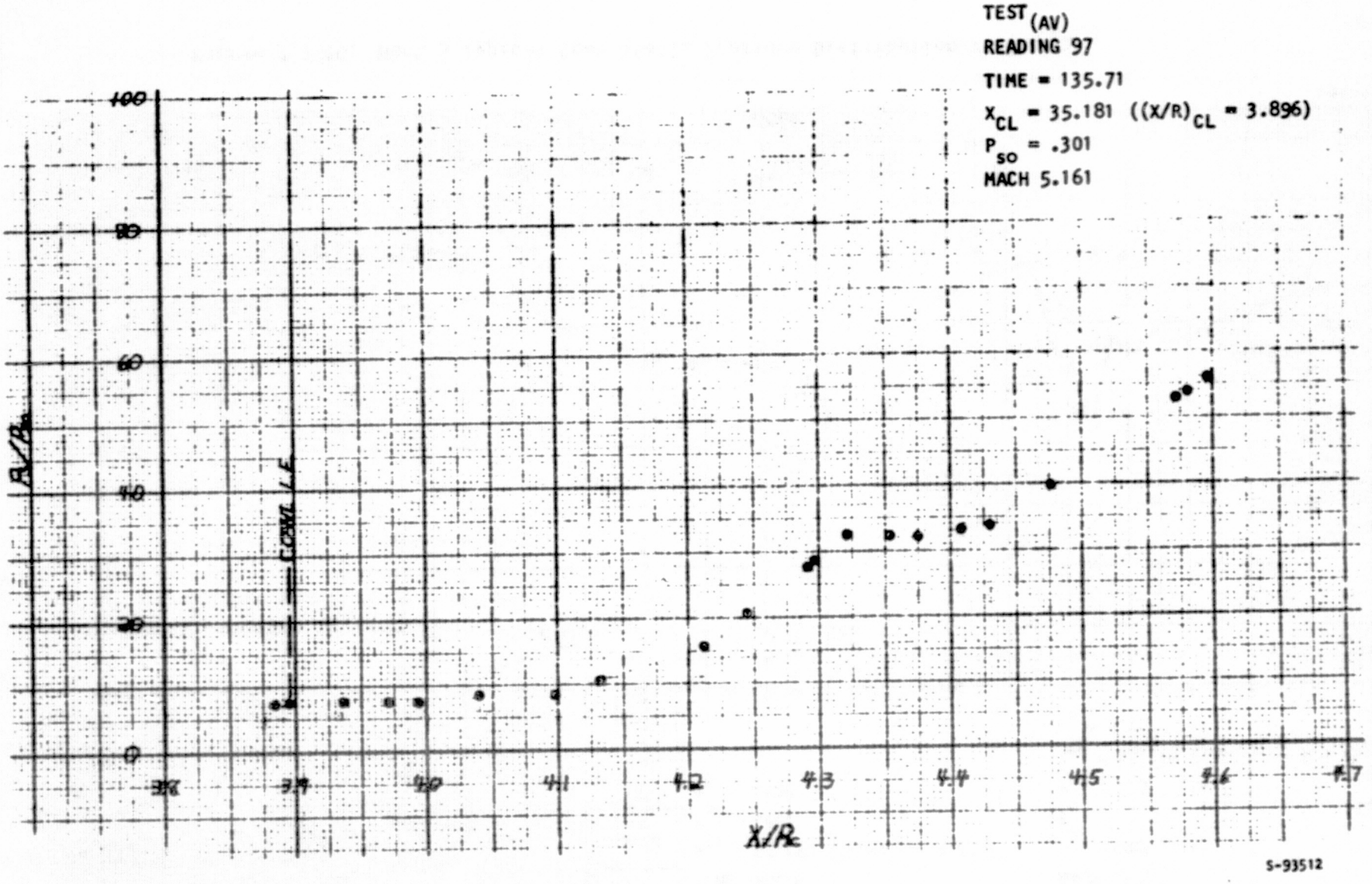

Figure 7.1-21. Mach 5 Spike Pressure Distribution; Reduced Reynolds Number

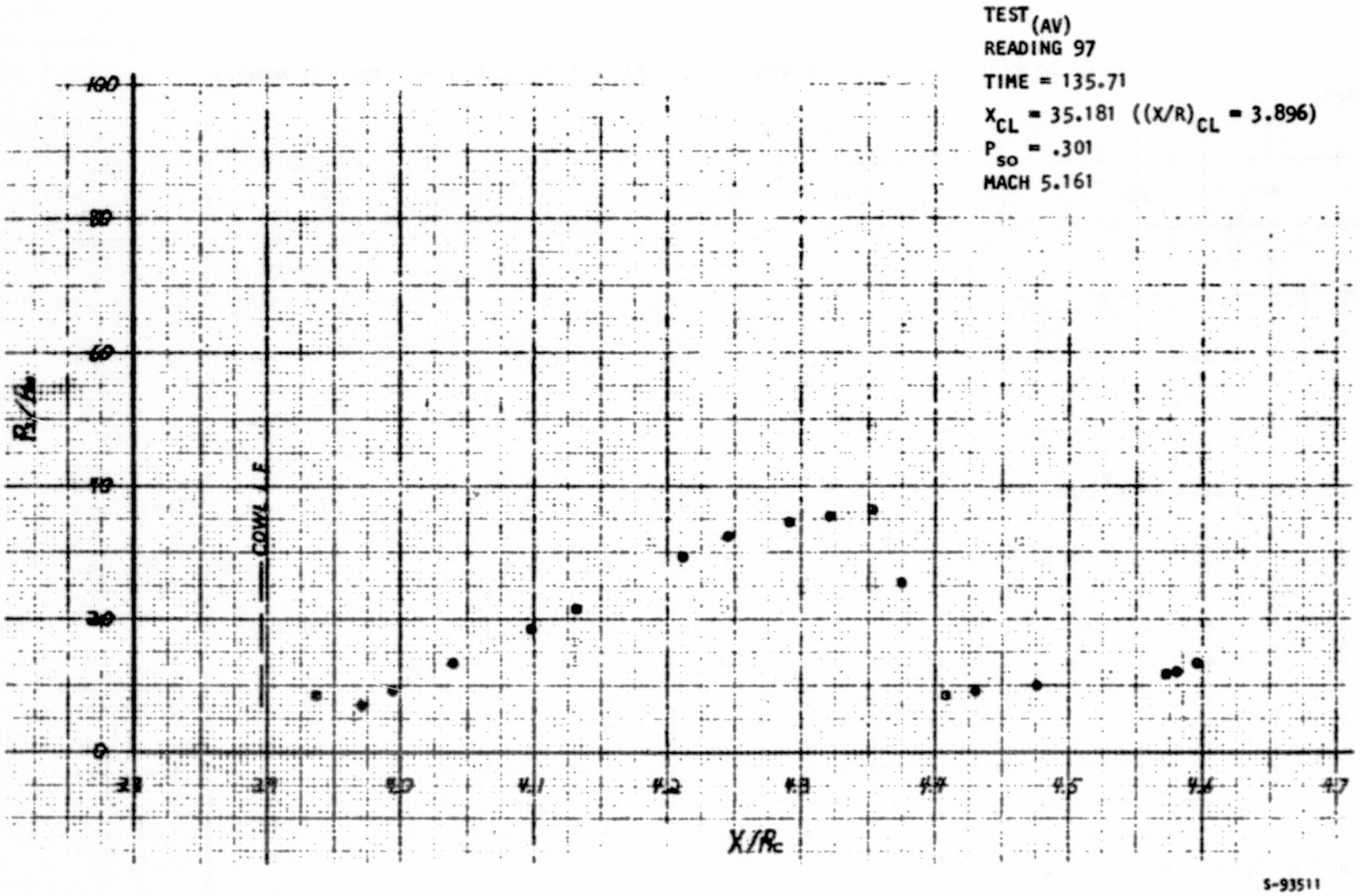

Figure 7.1-22. Mach 5 Cowl Pressure Distribution; Reduced Reynolds Number

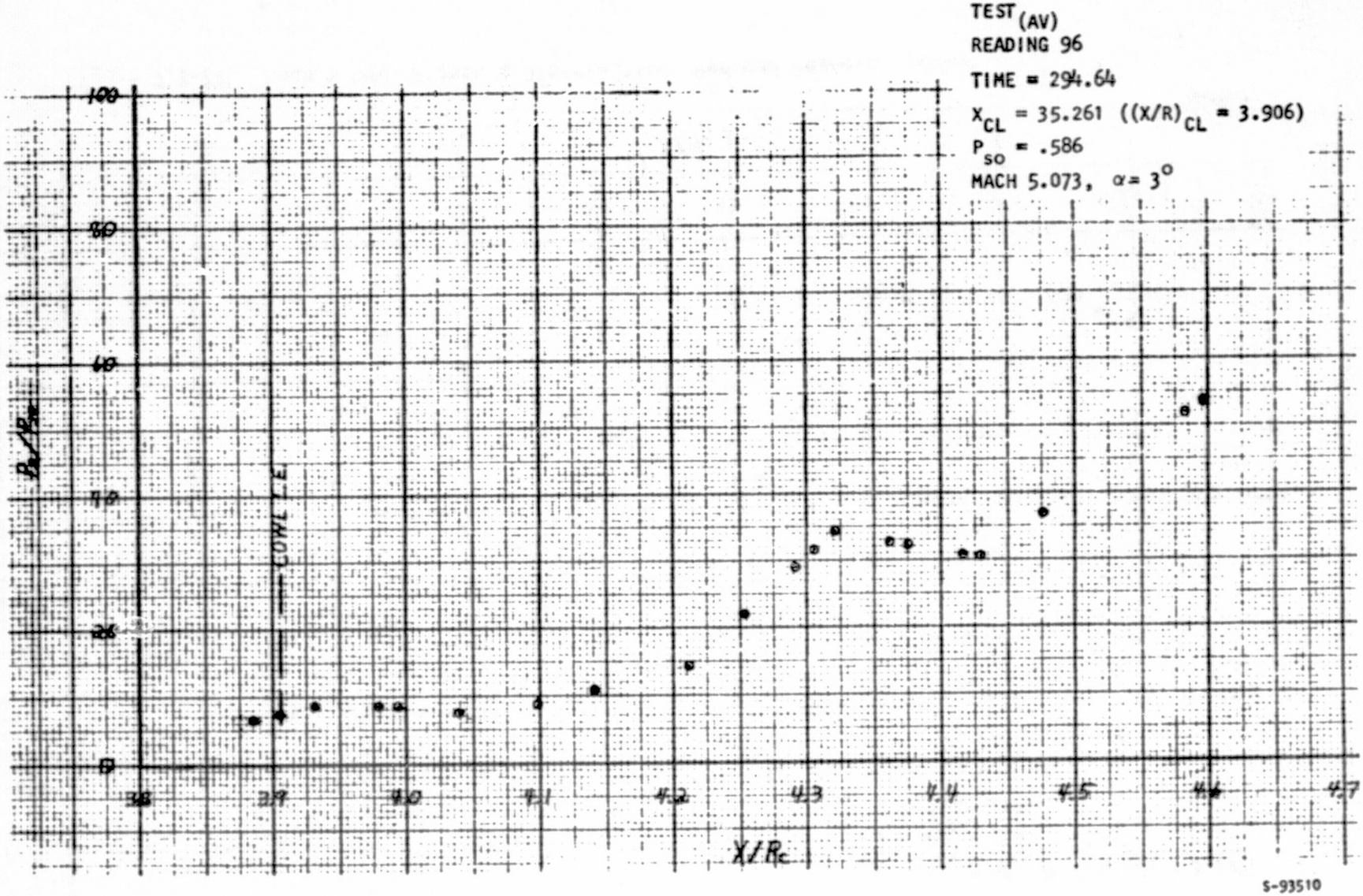

Figure 7.1-23. Mach 5 Spike Pressure Distribution; 3 Degree Angle of Attack

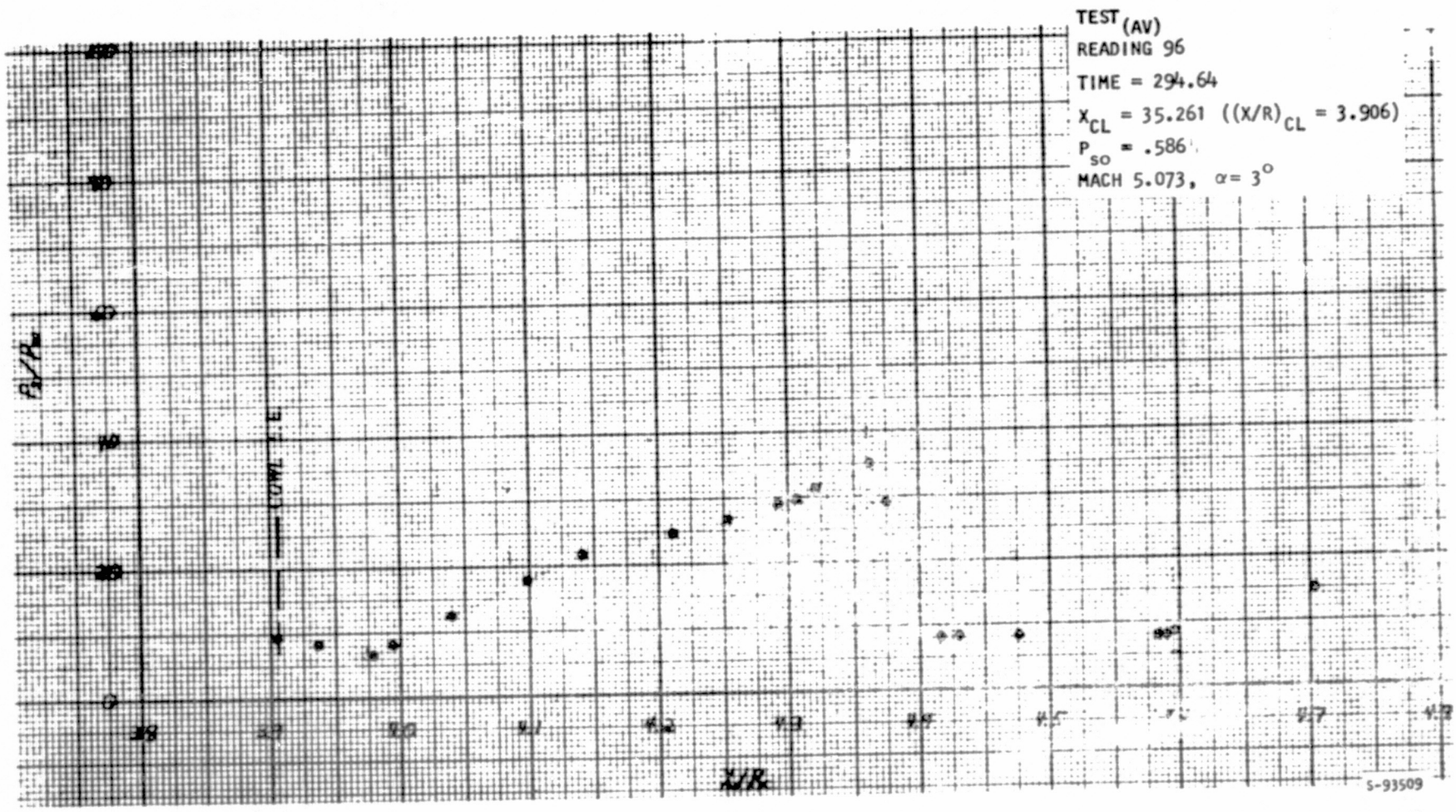

Figure 7.1-24. Mach 5 Cowl Pressure Distribution; 3 Degree Angle of Attack

7.1.4 Calculated Inlet Performance

Representative inlet performance values are listed in Table 7.1-3. Sources of errors in calculated results, together with correlating parameters and comparative data will be discussed in this section.

7.1.4.1 Potential Errors

The momentum equation outlined under "Data Reduction Procedures" identifies the quantities necessary for determining inlet performance in these tests. These include wind tunnel parameters, (1) velocity, (2) static and dynamic pressures and airflow per unit area; and inlet parameters, (1) mass flow ratio, (2) wall pressure distribution, and (3) friction calculations, together with leading edge bluntness and spillage drag correlations. Some of the potential errors will be outlined prior to a discussion of the test results.

Since determination of the wind tunnel operating conditions is basic to the engine analysis to follow, these properties have been calculated by several methods to establish the resulting differences. The experimental readings and calculation results are presented in Table 7.1-4 for a typical case. Relatively close agreement is found between the wind tunnel calibration values of all properties and the three calculation methods. The results presented in this report use the wind tunnel nozzle calibration results for the Mach 6 and 7 tests, and the spike pitot reading for the Mach 5 tests, where a wind tunnel nozzle calibration is not available.

Reference 7.1-8 analyzes the probable errors in determining inlet performance with the following results:

M_o	$\left(\frac{\Delta F_2}{F_2}\right)$, %	$\left(\frac{\Delta \eta_P}{\eta_P}\right)$, %	$\left(\frac{\Delta \eta_{KE}}{\eta_{KE}}\right)$, %
5	3.84	±26.5	±2.0
6	3.48	±27.9	±1.6
7	3.46	±30.5	±1.3

These calculations assume knowledge of the wall forces within 2-1/2 to 3 percent of the throat-stream thrust. Although an "absolute" measure of these accuracies is not available, the magnitudes of the forces involved is helpful in visualizing their importance. Figure 7.1-25 presents the terms in the momentum equation, approximately as distributed in the inlet for a case including spillage drag. From this figure it can be seen that the wall forces are approximately 25 percent of the throat-stream thrust. The above accuracies thus correspond to a requirement for measuring wall forces with an accuracy on the order of 10 percent. This objective appears easily attainable with existing pressure transducers.

TABLE 7.1-4

COMPARISON OF ESTIMATED WIND TUNNEL CHARACTERISTICS DERIVED FROM SPECIFIC MEASUREMENTS BUT USING DIFFERENT METHODS

Experimental Readings (Reference Reading No. 63, 186.15 sec)

P_{to} = 924.5 psia (62.9085 atm) T_{to} = 3018.65°R (1677.03°K)

$P_{t_{2\,(spike)}}$ = 22.437 psia (1.5267 atm) $P_{s_{o_m}}$ = 0.446 psia (0.03037 atm)

Parameters Used and Means of Correlation	P_{to}, T_{to} Synthetic Air Tunnel Nozzle Calibration	P_{to}, T_{to}, P'_t Synthetic Air AIM Performance Program	P_{to}, T_{to}, P_{so} Corrected Ideal Gas Tables OAL Memo 147-1	P_{to}, T_{to}, P_{so} Low Pressure Real Air Keenan & Kaye Tables
Flow velocity, V_o, ft/sec	5949	5953	5954	5928
Speed of sound, a_o, ft/sec	995.3	990.5	976.7	975.3
Tunnel Mach No., M_o	5.977	6.010	6.096	6.078
Tunnel static temperature, T_{s_o}, °R	411.0	407.0	396.6	395.6
Tunnel static pressure, P_{s_o}, psia	0.489	0.473	0.446	0.446

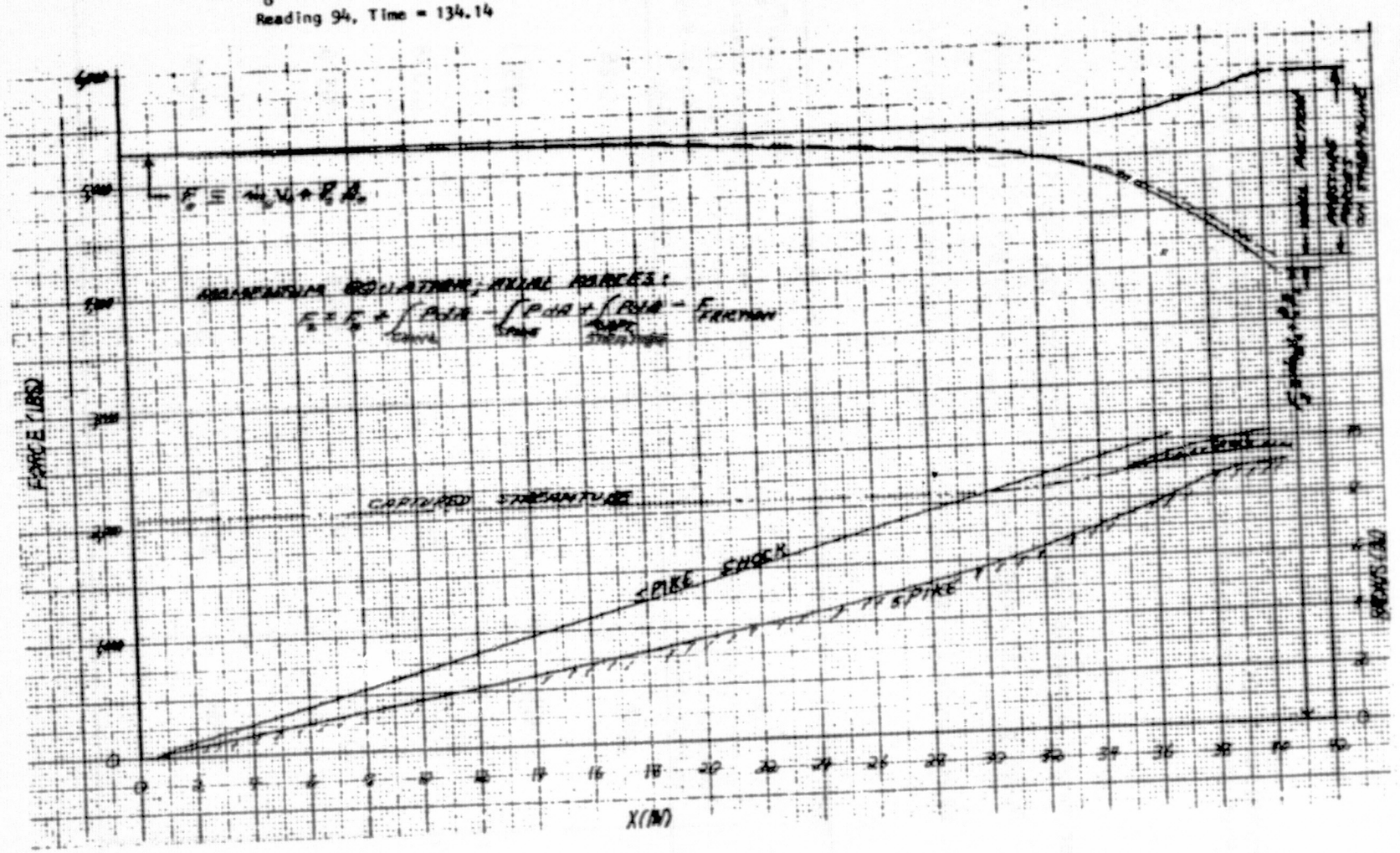

Figure 7.1-25. Typical Inlet Control Volume Force Distribution

Comparison of the AIM inlet total pressure recovery with that previously published (References 7.1-1 and 7.1-2) for the 2/3-scale development model raises a second issue--the mixing loss inherent in the present results. The pressure recovery quoted in those references for the 2/3-scale model were calculated using mass-flow weighting of the measured total pressure. Calculations for a typical pitot profile measured at the inlet throat during a Mach 6 test on this model yielded the following:

2/3-SCALE MODEL PRESSURE RECOVERY COMPARISON

Calculation	Pressure Recovery, percent
Mass-weight	50
Area-weight	38
Mass-momentum	35

Thus it is anticipated that the AIM inlet recovery as calculated by mass-momentum conservation will "appear" to be lower than that reported for the 2/3-scale model.

7.1.4.2 AIM Inlet Efficiency - Supersonic Flow

The momentum theorem employed in the AIM data analysis is applied to the inlet supersonic flow to the inlet throat. Results are presented in this section. Subsonic inlet performance values are inferred from these data as discussed in a subsequent section of this report.

The effects of wall-cooling on inlet efficiency are thought to be similar in magnitude to those encountered in the 2/3-scale model. That is, approximately 2 to 4 percent of the entering enthalpy was removed by wall-cooling in the inlet in both models. No experiments were conducted to specifically investigate the effect of varying the coolant flow rates, thus precluding derivation from the data of an influence coefficient for wall-cooling.

The relative magnitudes of the various terms in the momentum equation are presented in Figure 7.1-25 for a typical case as background information. The friction loss is seen to be relatively small; approximately 2.3 percent of the vacuum stream thrust (F_o) of the captured stream-tube. For these data, the force on the spillage streamline is 1 percent of F_o, as is the combined drag of the blunted tip and lip, while the cowl force is 6.6 percent of F_o and the spike force amounts to 23.4 percent of F_o. The vacuum stream thrust remaining at the inlet throat is 74.5 percent of F_o, resulting in a total pressure recovery of 43.7 percent.

A summary plot of the throat pressure recovery data of Table 7.1-3 for zero angle of attack is presented in Figure 7.1-26. Development model data from Reference 7.1-2 is included on the graph for comparison. The difference in recovery level between these two data sets is thought to be principally the result of (1) integrating surface static pressures rather than throat total pressures, and (2) mass-weighting versus mass-momentum weighting the flow

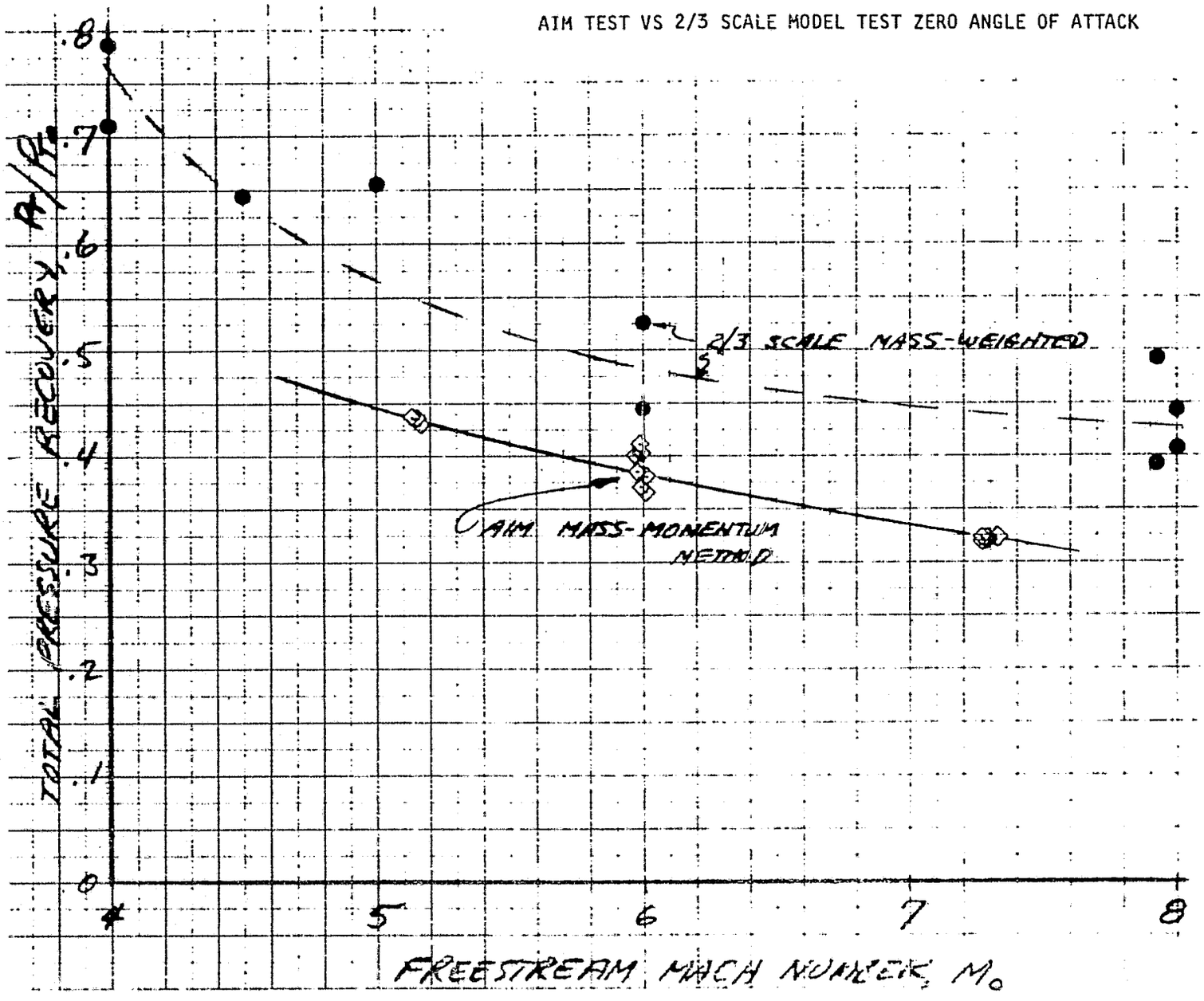

Figure 7.1-26. Inlet Throat (Supersonic) Pressure Recovery

properties. Differences in pressure recovery resulting from these calculation techniques is best evaluated by analysis of theoretical solutions, where both surface static pressures and throat total pressure profiles are available. Table 7.1-5 lists a number of comparative cases. The AIM data are repeated in Figure 7.1-27. From these examples it can be seen that the percent difference introduced by the various calculation methods to obtain pressure recovery can be substantial.

The AIM throat pressure recovery appears to correlate with Mach number as indicated in Figure 7.1-28. A hypersonic similarity parameter also may be useful in establishing inlet performance trends; Figures 7.1-29, 7.1-30 and 7.1-31.

7.1.4.3 AIM Inlet Efficiency - Subsonic Flow

The subsonic pressure recovery, kinetic energy efficiency, and diffuser efficiency values listed in Table 7.1-3 were calculated in the following way: the supersonic flow in the inlet throat was isentropically expanded to an area 10 percent greater than the throat area, at which conditions a normal shock was calculated for equilibrium air. The artifice of expanding to a larger area is an arbitrary correction to the indicated pressure recovery for the fact that in the subsonic combustion mode, stable inlet operation calls for a slightly supercritical inlet operating point.

The subsonic pressure recovery data of Table 7.1-3 are compared with other data in Figure 7.1-32, correlated with aerodynamic contraction ratio. The AIM inlet contraction is seen to be somewhat modest by comparison. The AIM pressure recovery values follow the general data trends established by this correlation. Measured 2/3-scale subsonic pressure recovery is somewhat less than the values determined from the AIM tests; Figure 7.1-33. The subsonic recovery values for the 2/3-scale model tests are considered conservative, however, because the engine combustor area distribution was not simulated in the scaled model subsonic diffuser.

7.1.5 Inlet Unstart

Transient pressure data were recorded during certain inlet unstart tests. Although attenuation of the peak pressures is suspected, due to the remote transducer mounting employed (tube length > 25 ft, tube diameter = 0.043 in.) the recorded traces are reproduced herein to indicate typical waveforms. Figure 7.1-34 presents a time history of recorded fuel flows in the various manifolds. An increase in three fuel flows, beginning at time 213.5 sec triggered the first inlet unstart.

Pressure-time histories measured on the centerbody 0.4 in. forward of the inlet throat are reproduced in Figure 7.1-35. A pressure spike at time 200 sec was caused by the initial fuel injection ramp of Figure 7.1-34, peaking at than time. The question of whether inlet unstart accompanied the pressure pulse at centerbody Station 40.0 at time 200 sec, can be answered by observing the cowl pressures at approximately the same station, Figure 7.1-36; the

TABLE 7.1-5

RESULTS OF THREE METHODS OF PRESSURE RECOVERY CALCULATION

M_o	Calculation Method	Throat Total Pressure Recovery			
		2/3 Scale Model		AIM, Full Scale	
		Theory	Test	Theory	Test
6.00	Mass-weight	0.53			
	Mass-momentum weight	0.474			
6.01	Mass-weight		0.445		
	Mass-momentum weight		0.362		
6.05	Mass-weight		0.526		
	Mass-momentum weight		0.435		
5.15	Mass-weight			0.618	
	Control volume mass-momentum			0.473	0.436
5.13	Control volume mass-momentum				0.437
6.01	Mass-weight			0.588	
5.98	Control volume mass-momentum				0.385
7.25	Mass-weight			0.443	
	Control volume mass-momentum			0.261	0.322

C-3

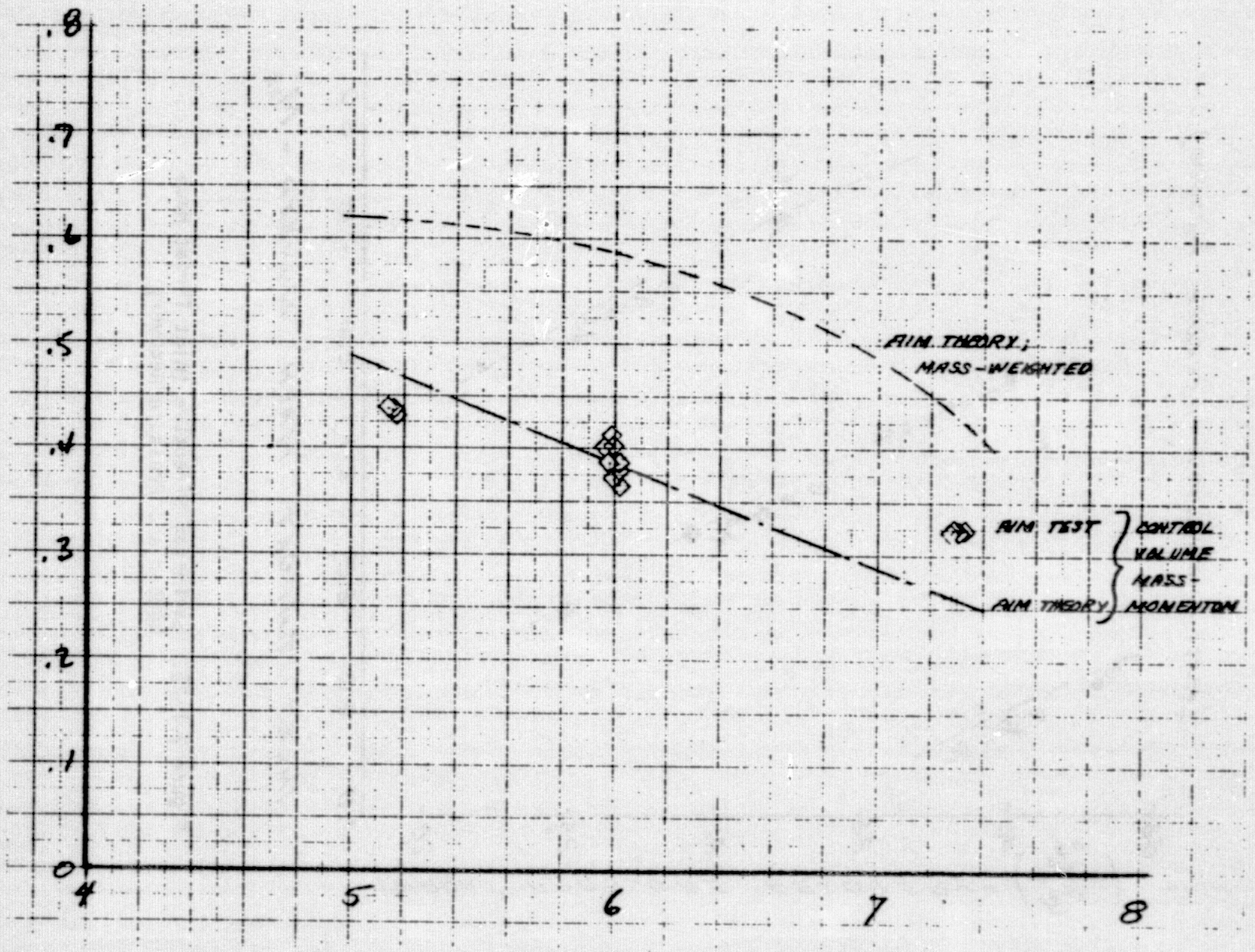

Figure 7.1-27. AIM Supersonic Pressure Recovery Test Vs. Theory

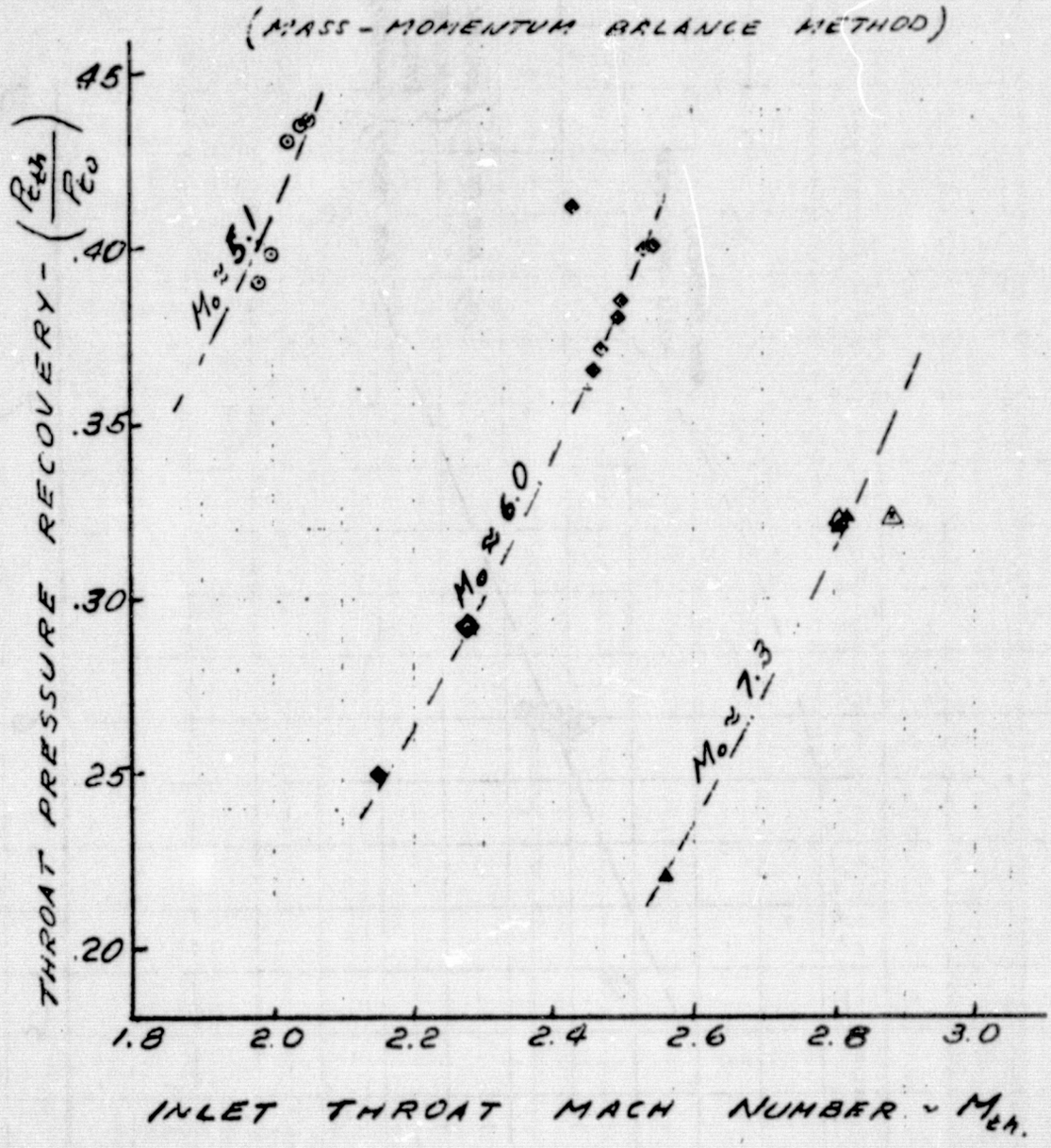

Figure 7.1-28. Estimated Effective Inlet Throat Mach Number and Pressure Recovery

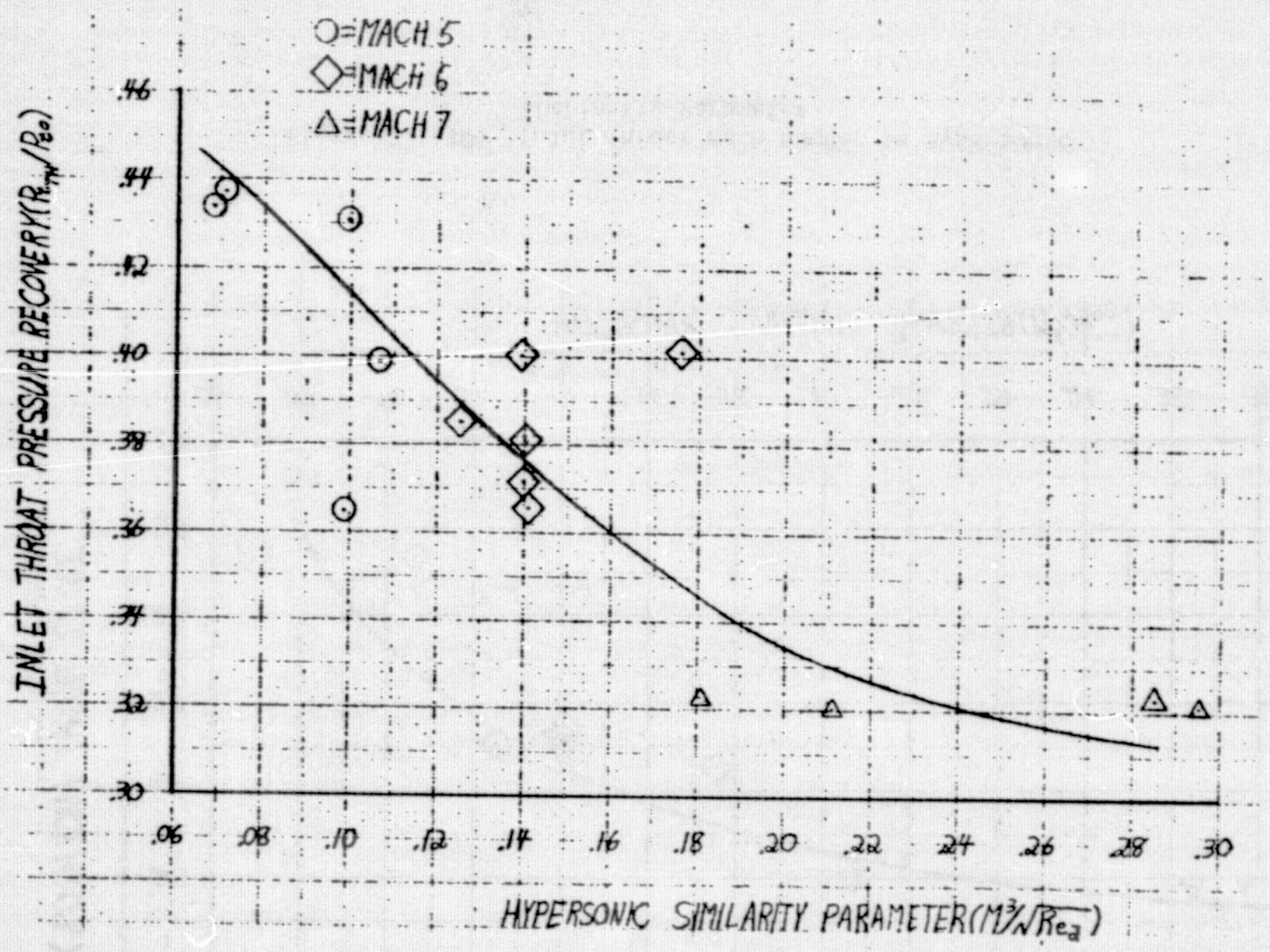

Figure 7.1-29. Inlet Throat Pressure Recovery Vs Hypersonic Similarity Parameter

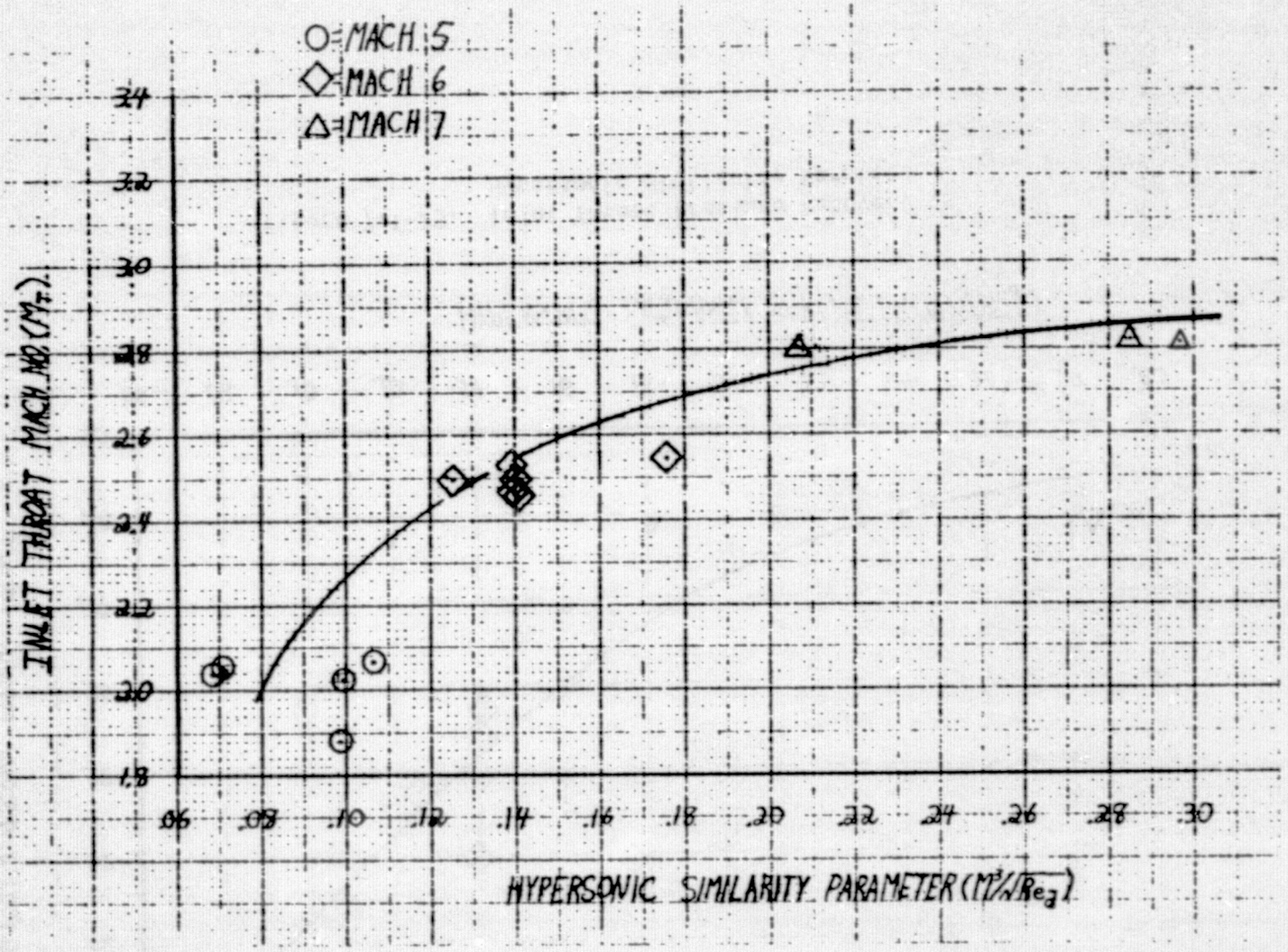

Figure 7.1-30. Inlet Throat Mach Number vs Hypersonic Similarity Parameter

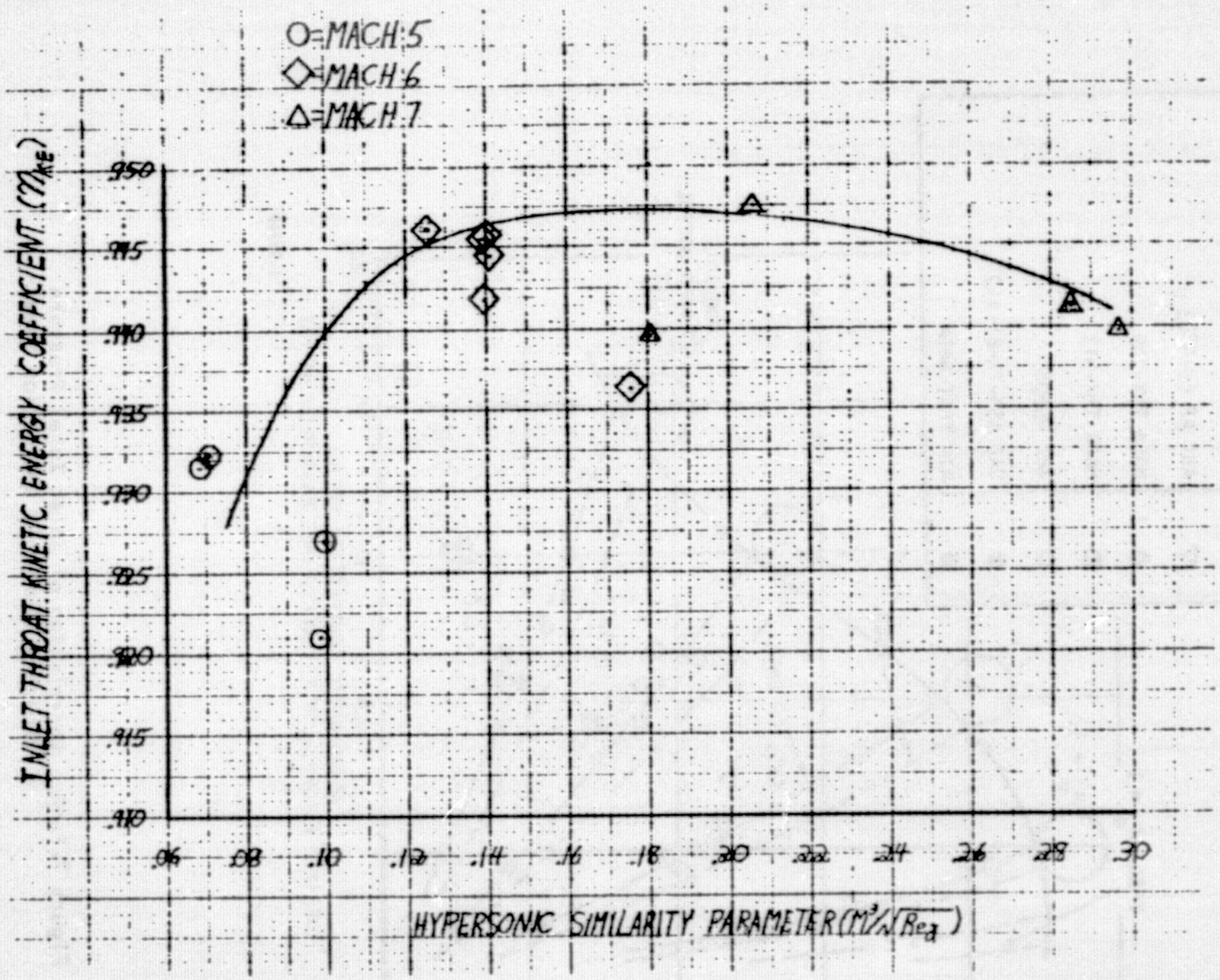

Figure 7.1-31. Inlet Throat Kinetic Energy Efficiency Vs Hypersonic Similarity Parameter

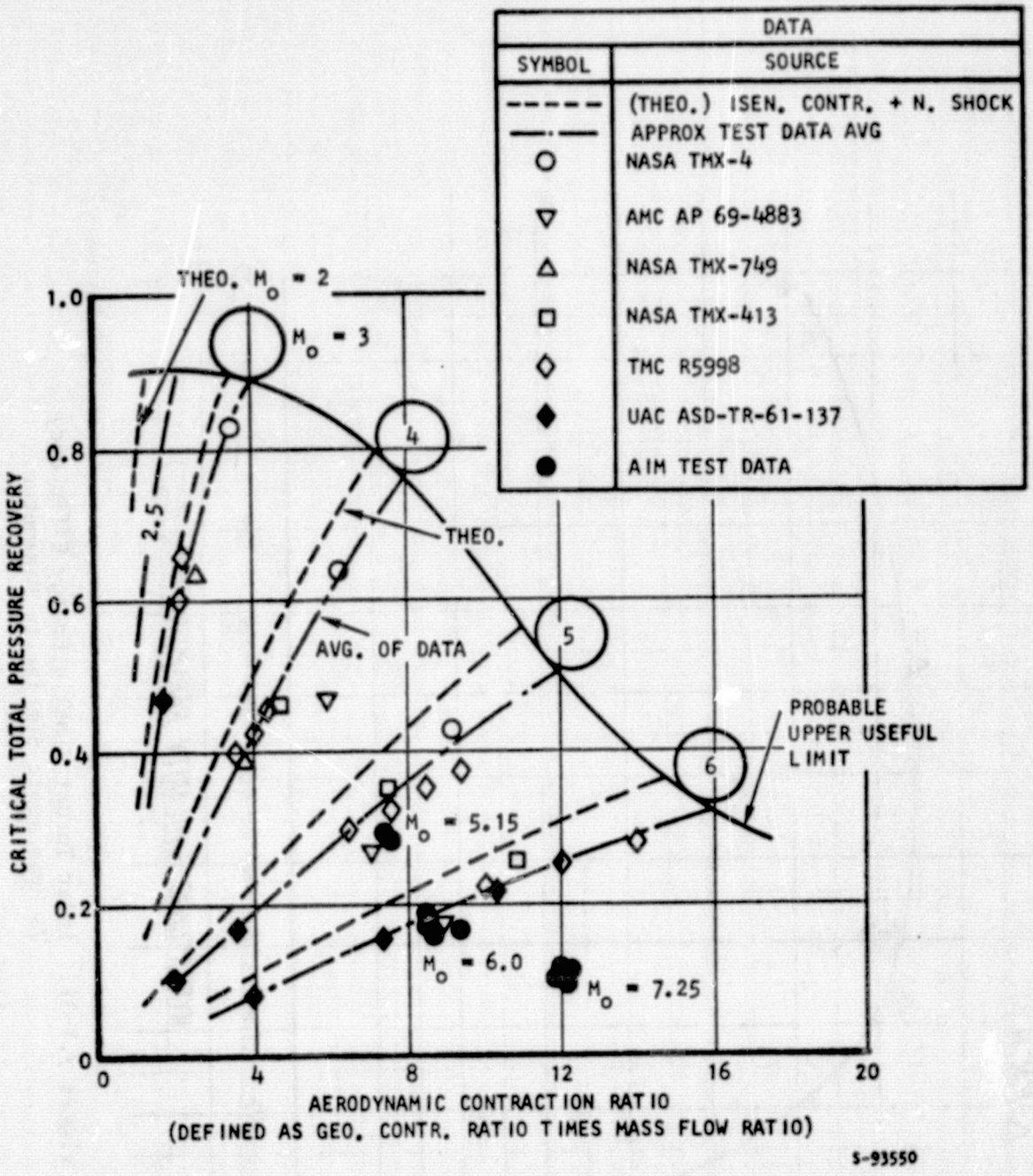

Figure 7.1-32. Correlation of Inlet Total Pressure Recovery (Subsonic Combustion Mode)

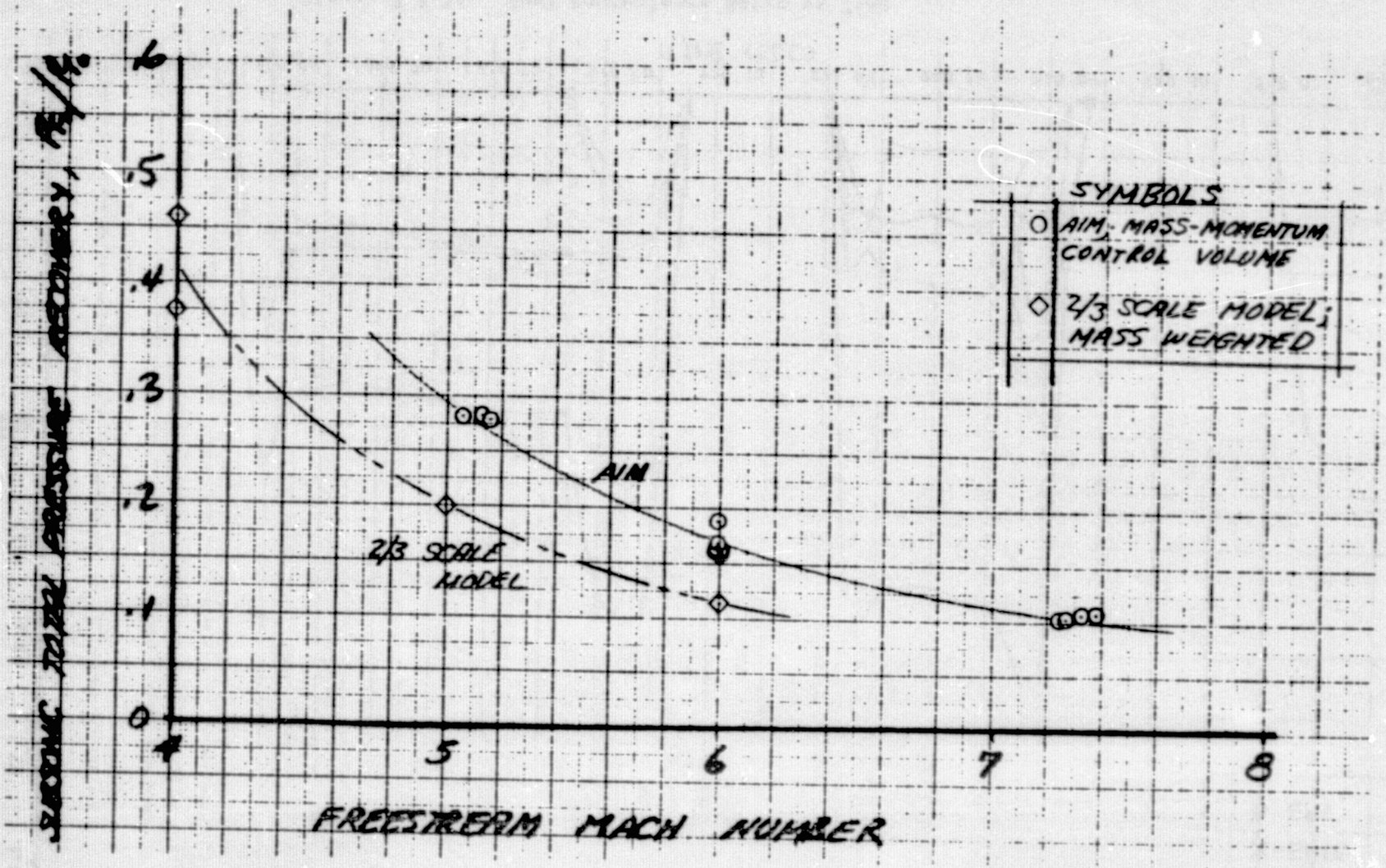

Figure 7.1-33. Subsonic Pressure Recovery AIM Vs. 2/3-Scale Development Model

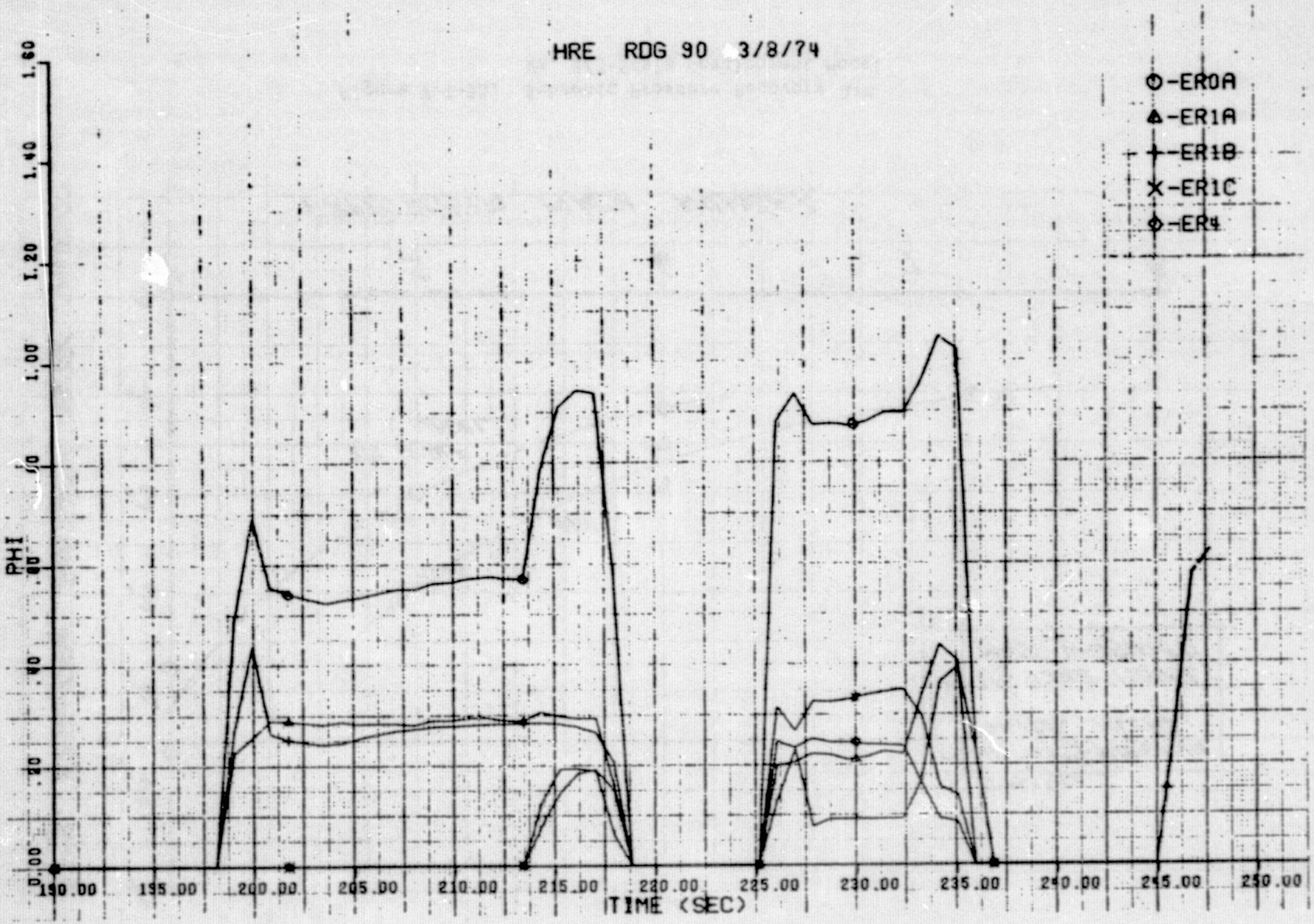

Figure 7.1-34. Fuel Equivalence Ratio vs Time

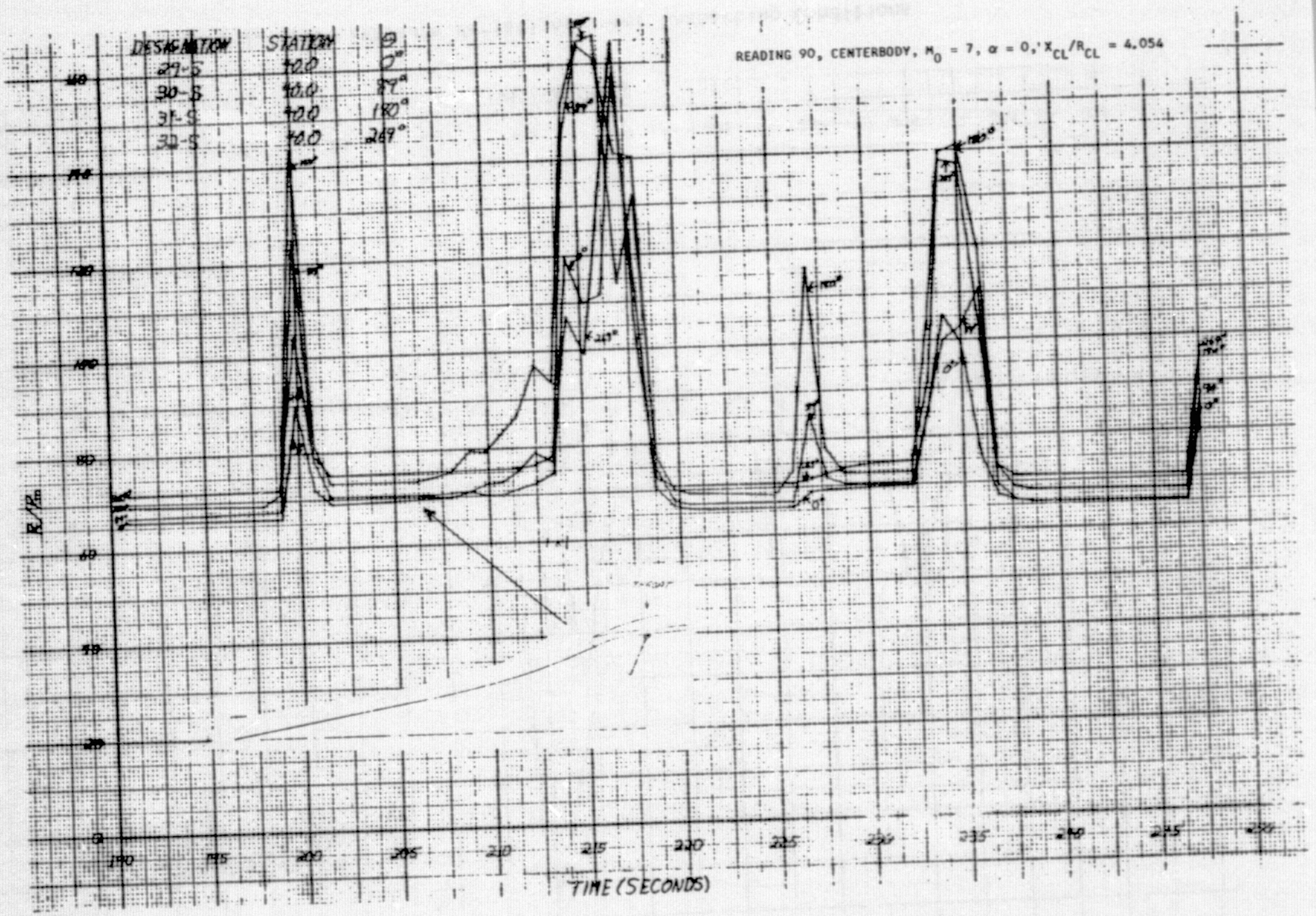

Figure 7.1-35. Pressure Variations Under Unstarting Conditions

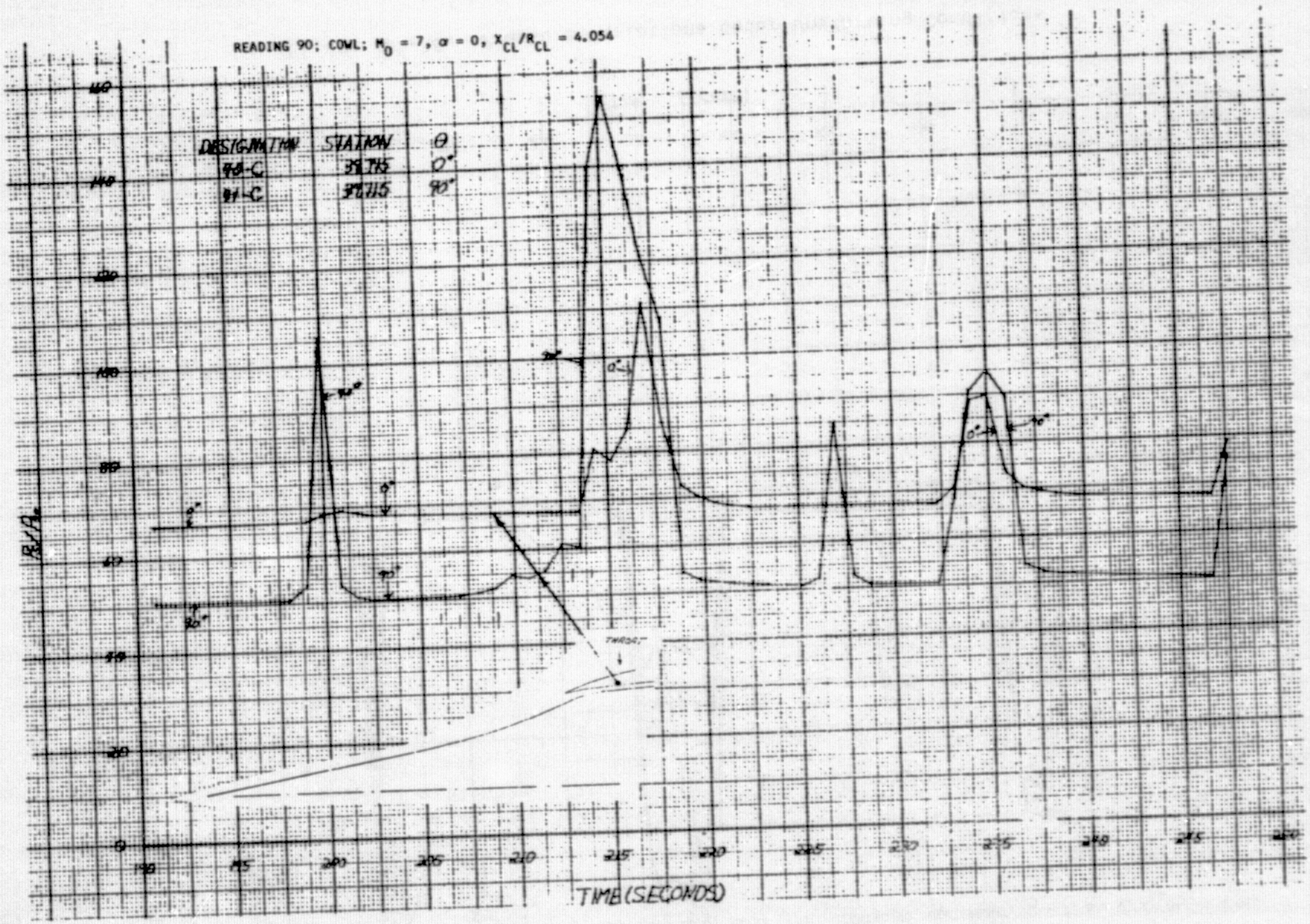

Figure 7.1-36. Pressure Va-iations Under Unstarting Conditions

pressure tap at $\theta = 0^{o}$ shows only a slight disturbance. Pressures on the spike at approximately the cowl lip station at the same time (200 sec) show no disturbance; Figure 7.1-37.

A major disturbance can be seen on all traces between times 214 and 220 sec as well as at time 235 sec. The pressure disturbance propagates forward at least as far as Station 30.7, but not as far as Station 14.4 (the next instrumented station) during this test. Cut-off of the fuel flow permitted the inlet to self-start at this Mach number without spike translation.

An inlet unstart sequence at Mach 6, where the internal contraction of the inlet precludes self-starting, showed the pressure distrubance advancing to at least Station 14.4. The pressure increase observed at this station was slight, however, being of the order of 12 percent.

7.1.6 Conclusions

Tests of a full scale Aerothermodynamic Integration Model (AIM) have been successfully completed in the NASA Plum Brook hypersonic test facility. Inlet static pressures were measured and have been used in conjunction with correlations of other parameters to obtain estimates of the inlet performance. Conclusions reached on the basis of these data are presented below.

1. Static pressures measured on the AIM inlet surfaces show reasonable agreement with theoretical predictions, except in regions where the theory predicts large pressure discontinuities. Boundary layer interactions are thought to explain this discrepancy.

2. Reynolds number variations from 1.5×10^{6} to 4.8×10^{6} showed no appreciable effect on inlet performance.

3. Engine angle of attack increases the average inlet wall pressures on both the spike and cowl surfaces.

4. Calculated inlet wall friction in the configuration tested is a small fraction of the momentum change from freestream to the inlet throat. Wall forces dominate the momentum loss.

5. Supersonic pressure recovery levels calculated from these tests are lower than the levels previously reported for a 2/3-scale inlet development model. However, the present results include an inherent mixing loss due to the calculation procedures not present in the subscale model data.

6. A correlation of inlet supersonic pressure recovery with freestream Mach number and inlet throat Mach number is observed in the data.

7. Calculated AIM inlet subsonic pressure recovery shows a consistent correlation with other data in the literature.

8. Inlet unstart can be caused by excessive fuel injection in the supersonic condition.

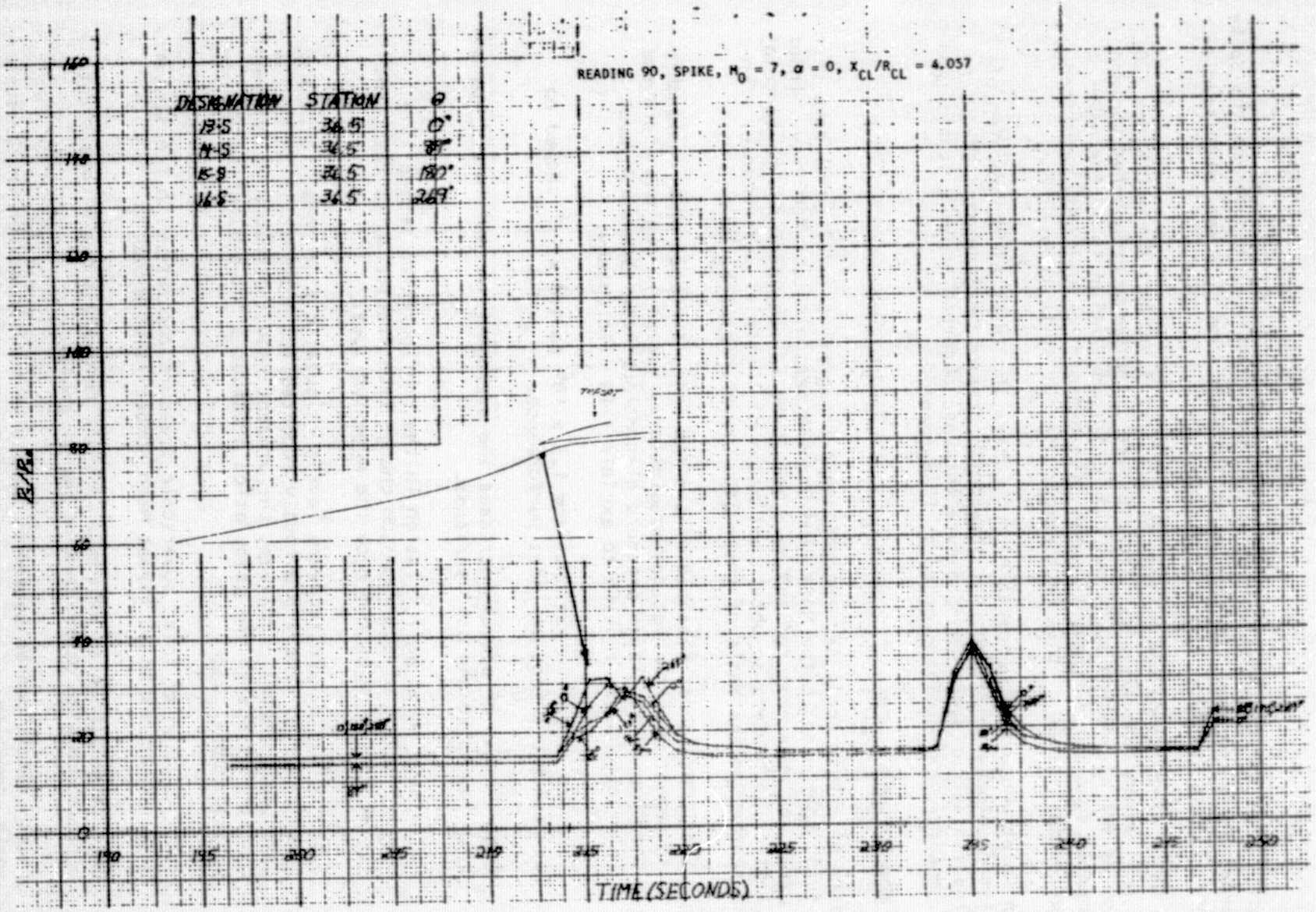

Figure 7.1-37. Pressure Variations Under Unstarting Conditions

9. The present inlet configuration can be restarted in the design Mach 7.3 position by fuel flow reductions without spike translation.

10. Pressure disturbances move farther forward on the inlet centerbody during inlet unstart at Mach 6, than at Mach 7.3 due to differences in internal contraction.

7.1.7 Recommendations

The following recommendations for future hypersonic inlet development are based on the AIM tests reported herein.

1. Explore the lack of correlation of theory with AIM data in regions of large pressure discontinuities and recommend appropriate corrective measures.

2. Establish the overall accuracy of the method of inlet performance calculation used herein, by analysis of data from a model having appropriate instrumentation for measuring wall force, momentum, heat transfer, and airflow rate. Measurement and correlation of wall friction are important elements of such an effort.

3. In conjunction with recommendation (2), explore the feasibility of inlet performance determination by force balance measurements. As hypersonic inlet configuration complexity increases, the force-balance technique may become the only practical method for measuring inlet performance.

4. Experimentally explore the net effect of inlet heat transfer on inlet momentum recovery, to identify optimum wall cooling objectives for hypersonic vehicle application.

7.2 COMBUSTOR DESIGN

The AIM combustor area ratio distributions are shown in Figure 7.2-1 for operating conditions of Mach 5, 6, and 7. The area ratio is defined as the combustor area divided by the inlet throat area. The useful overall combustor length for operation at Mach 5 and 6 is 25.5 in. with an area ratio of 3.6, and 26.2 in. with an area ratio of 5.1 for Mach 7. The combustor zone was divided into three stages. The first stage was defined as the region downstream of fuel injectors 1a and 1b. The second stage was downstream of fuel injectors 2a and 2c. The third stage was defined as downstream of fuel injectors 3a and 3b. The first two stages were used for supersonic combustion at higher flight Mach numbers and were also used for the subsonic diffusion during subsonic combustion. The third stage was used for subsonic combustion.

The combustor was designed so that fuel equivalence ratio of unity could be injected into the first stage (using fuel injectors 1a, 1b) for operation at Mach 8. The translating spike was to be positioned such that combustion would occur in the constant-area section for Mach 8, thereby achieving maximum performance. For operation below Mach 8, supersonic combustion, fuel was to be injected into the combustor in two stages (utilizing fuel injectors 1a, 1b, 2a, 2c) in order to prevent thermal choking and resultant inlet unstart.

2-D combustor tests had indicated a need for alternate fuel injector locations, hence fuel injectors 1c and 4 were provided.

Three sets of ignitors were provided to assist initiating combustion if required. The first and the last set of ignitors consisted of six equally spaced hydrogen-oxygen torch-type ignitors. The second set consisted of five torch-type ignitors. The first two sets were used for supersonic combustion and the third for subsonic combustion.

The step formed by the end of the spike assembly and the innerbody was used as a flame stabilizer for subsonic combustion.

The location of the maximum width of the struts formed the geometric throat of the combustor for subsonic combustion. Reduction of area resulting from the struts was 5 percent. This throat area was selected to provide the best performance, considering the supersonic and subsonic combustion.

For subsonic combustion at Mach 4, the combustor was designed to stabilize the normal shock near the inlet throat, while at Mach 6, the shock would move downstream near the step. Because of the small restriction at the geometric throat, subsonic combustion occurred at high subsonic Mach numbers. The overall subsonic combustor length was 8 in., of which 2 in. extend upstream into the second stage.

The size and location of fuel injectors were selected to obtain desired mixing by optimizing the fuel penetration and jet spreading. The detailed injector design procedures were reported in Reference 7.2-1. As shown in Figure 7.2-1, the flows from injectors 1c, 2c, 2a, and 3a were directed

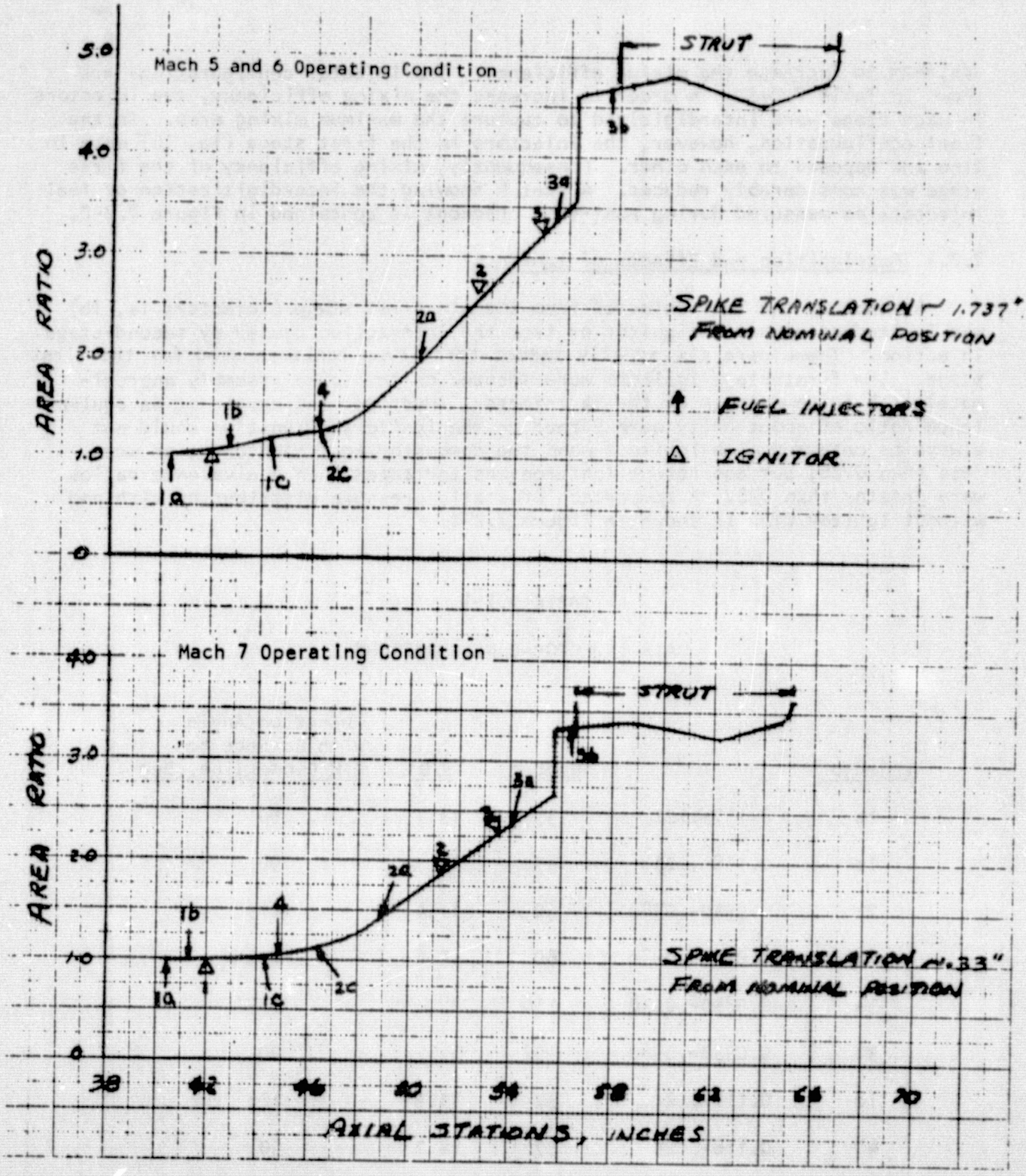

Figure 7.2-1. Combustor Area Ratio

upstream to increase the mixing efficiency. The injector configurations are shown in Table 7.2-1. In order to increase the mixing efficiency, the injectors in each stage were interdigitized to capture the maximum mixing area. In the final configuration, however, the injectors in the first stage (1a, 1b) were in line and opposed to each other. Consequently, mixing efficiency of the first stage was considerably reduced. A sketch showing the interdigitization of fuel injectors as measured during post-test checkout is contained in Figure 7.2-2.

7.2.1 Autoignition and Effects of Ignitors

At Mach 6, the fuel injected from the AIM first stage (injectors 1a, 1b) was ignited at either an ignitor or from the interaction caused by second-stage injection. There were six equally spaced torch-type ignitors used for the first stage. The first-stage ignitors were located on the spike assembly approximately 1.5 in downstream of the 1a injector. Hydrogen and oxygen at an equivalence ratio of about unity were burned in the ignitors. Ignition could not always be obtained with ignitors when the combustor equivalence ratios were less than 0.25, but consistent ignition was indicated when equivalence ratios were greater than 0.3. A comparison of static pressure distribution with and without ignitor flow is shown in Figure 7.2-3.

TABLE 7.2-1

AIM INJECTOR CONFIGURATIONS

Injector		Number	S/D	Injection Angle With Respect to AIM Centerline, Deg
1a	0.117-.121	37	13.1	90
1b	0.118-.123	37	13.9	90
2a	0.0930-.0980	60	11.4	113
2c	0.0930-.0980	60	10.6	119
3a	0.0890-.0930	114	7.0	115
3b	0.0930-.0980	102	6.3	90
1c	0.117-.121	37	13.5	106
4	0.118-.123	37	14.2	90

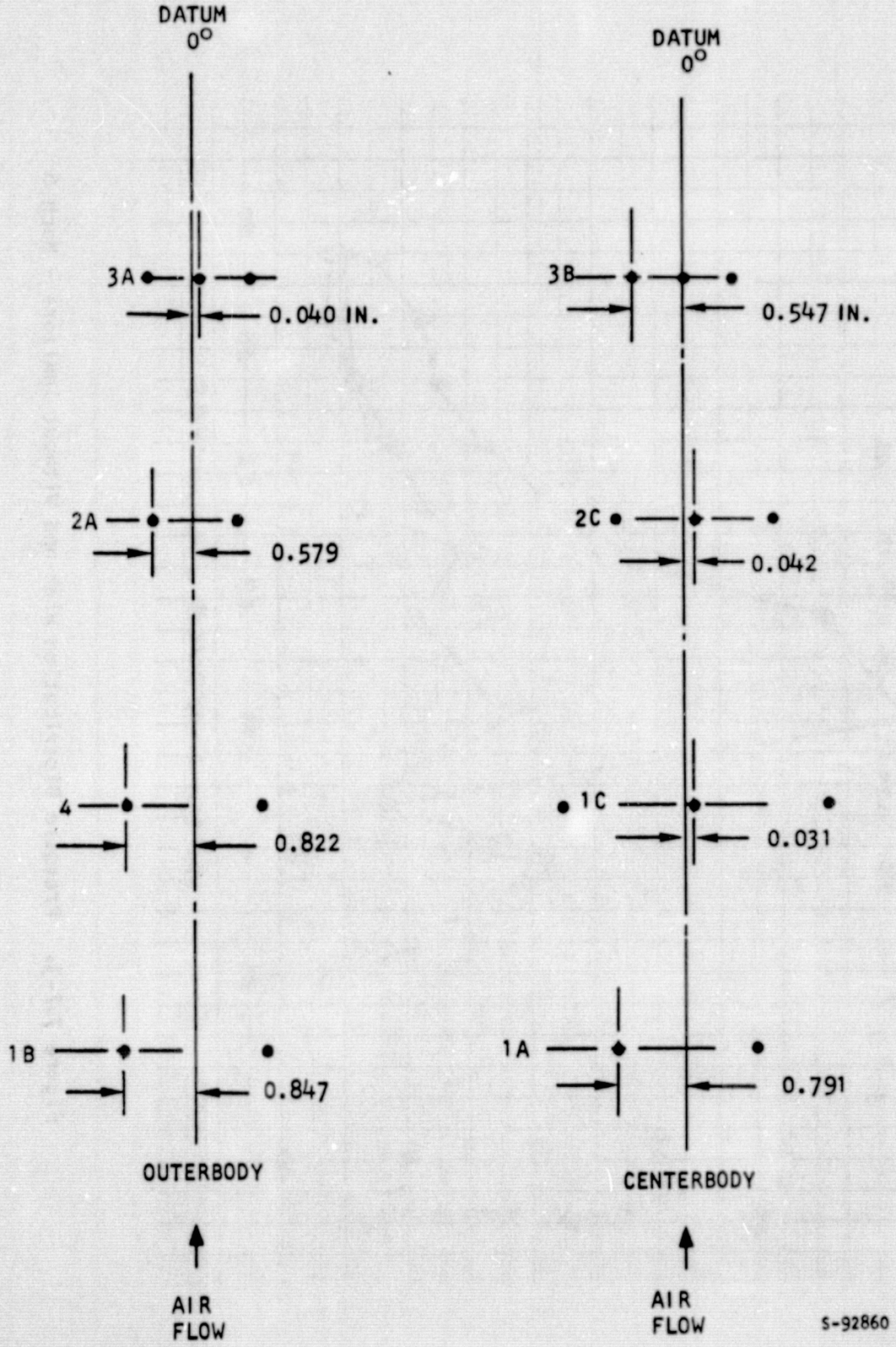

Figure 7.2-2. Interdigitization of Fuel Injectors

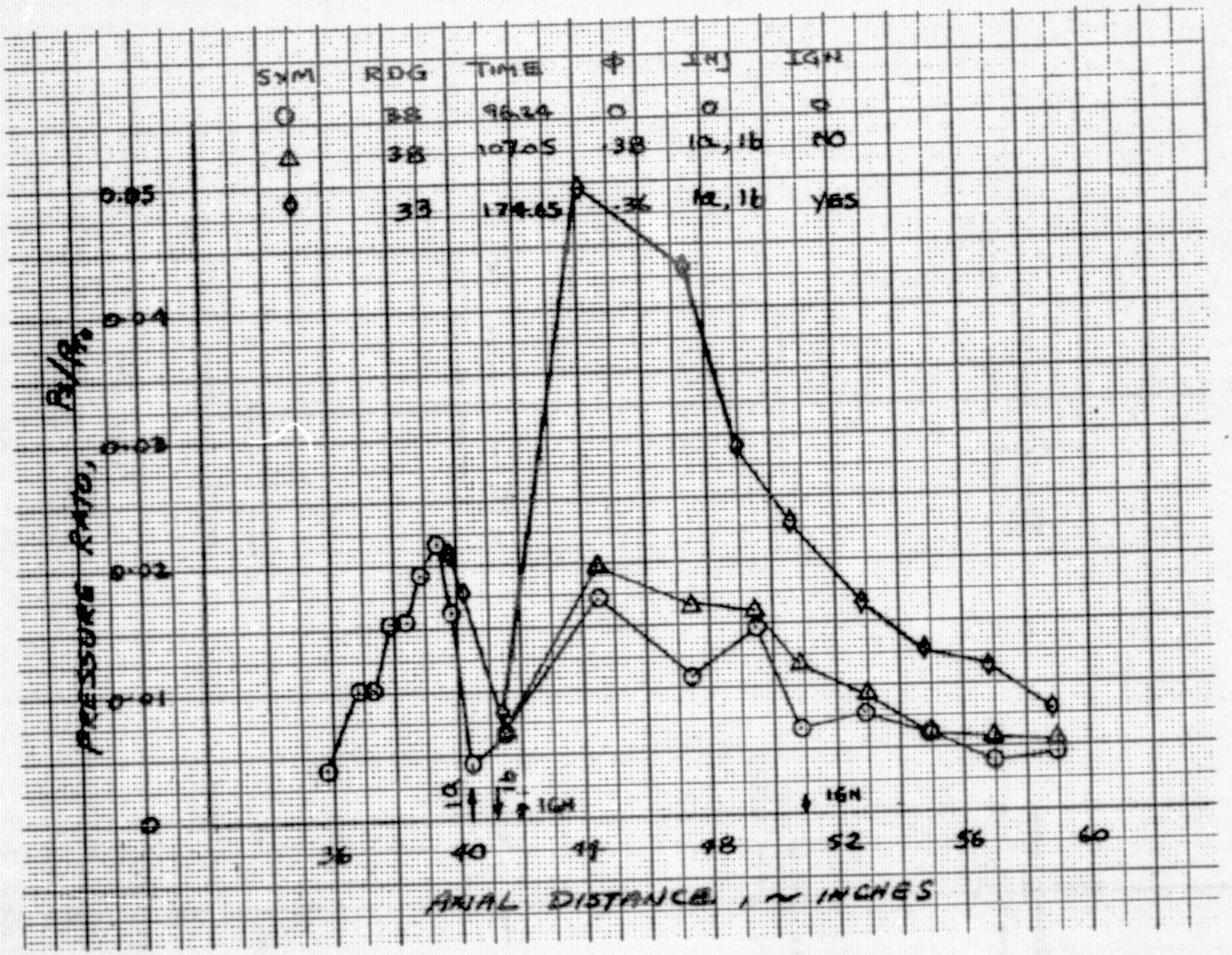

Figure 7.2-3. Pressure Distribution With and Without Ignitors - Mach 6

The most successful method used to auto-ignite the first-stage flow was the interactive effect of second-stage injection. This method was repeatable and reliable. The second stage injector (2c) was located approximately 5 inches downstream of the first stage. It is interesting to note that auto-ignition for subsonic combustion was accomplished by first injecting fuel from 1b, 2a, and 2c to ignite the first and second-stage fuel, and then injecting fuel from 3a, 3b (subsonic combustion fuel injectors) while simultaneously reducing fuel flow from 1b, 2a, and 2c, to zero. Subsonic combustion could be sustained by the recirculation zone downstream of the centerbody step which acted as a flame holder.

Because of the reduced windtunnel total temperature ($\sim 3000^{\circ}R$) during Mach 7 tests, the first stage fuel would not auto-ignite below an equivalence ratio of 0.42. The calculated static temperature and Mach number at the inlet throat where the fuel was first introduced were $1215^{\circ}R$ and 3.5, respectively. Although ignitor sets 2 and 3 were used during all Mach 7 tests, they were probably too far downstream to be effective in igniting the first-stage fuel. When fuel was injected in the second stage only, it could not be ignited with an equivalence ratio as high as 0.92. Interaction between first and second stage combustion was not as strong as that experienced during the Mach 5 and Mach 6 tests. It is interesting to note from time plot as shown in Figure 7.2-4, that the ignition points appeared to occur when a slight surge of fuel flow took place. This led to believe that ignition was triggered by change of local flow conditions.

In Mach 5 true temperature tests at $2250^{\circ}R$, ignitor sets 2 and 3 were used during all runs. Ignitor set 2 was located on the outerbody at Station 50.9 pointing upstream to ignite second stage fuel, while set 3 was also on the outerbody at Station 53.28 pointing downstream to ignite the third stage.

Tests indicated that ignition was not achieved using injector 2a alone to equivalence ratio of 0.55, however, positive ignition was obtained as soon as fuel was injected from 3a, 3b. In the subsonic combustion mode, ignition was obtained when equivalence ratio from 3a, 3b reached approximately 0.6.

The auto-ignition characteristics of hydrogen-air mixture is important in determining the operational Mach numbers and altitudes of a scramjet without any assistance of other ignition techniques. Theoretically, auto-ignition of hydrogen in a reasonable time and length may be calculated from kinetic studies. Empirical correlations of induction time have also developed. A typical example is shown below from shock-tube tests (Reference 7.2-2) applicable for temperature range of $1800^{\circ}R$ to $1450^{\circ}F$ and fuel equivalence ratio from 0.5 to 1.0.

$$t_i = \frac{2.32 \times 10^{-7} \, e^{15950/T}}{(P)^{.4} \, \phi}$$

where (t) is the induction period in milliseconds, (p) is the pressure in psia, (T) is the temperature in deg K, and (ϕ) is the equivalence ratio. Unfortunately, most studies were based on premixed streams with uniform temperature and

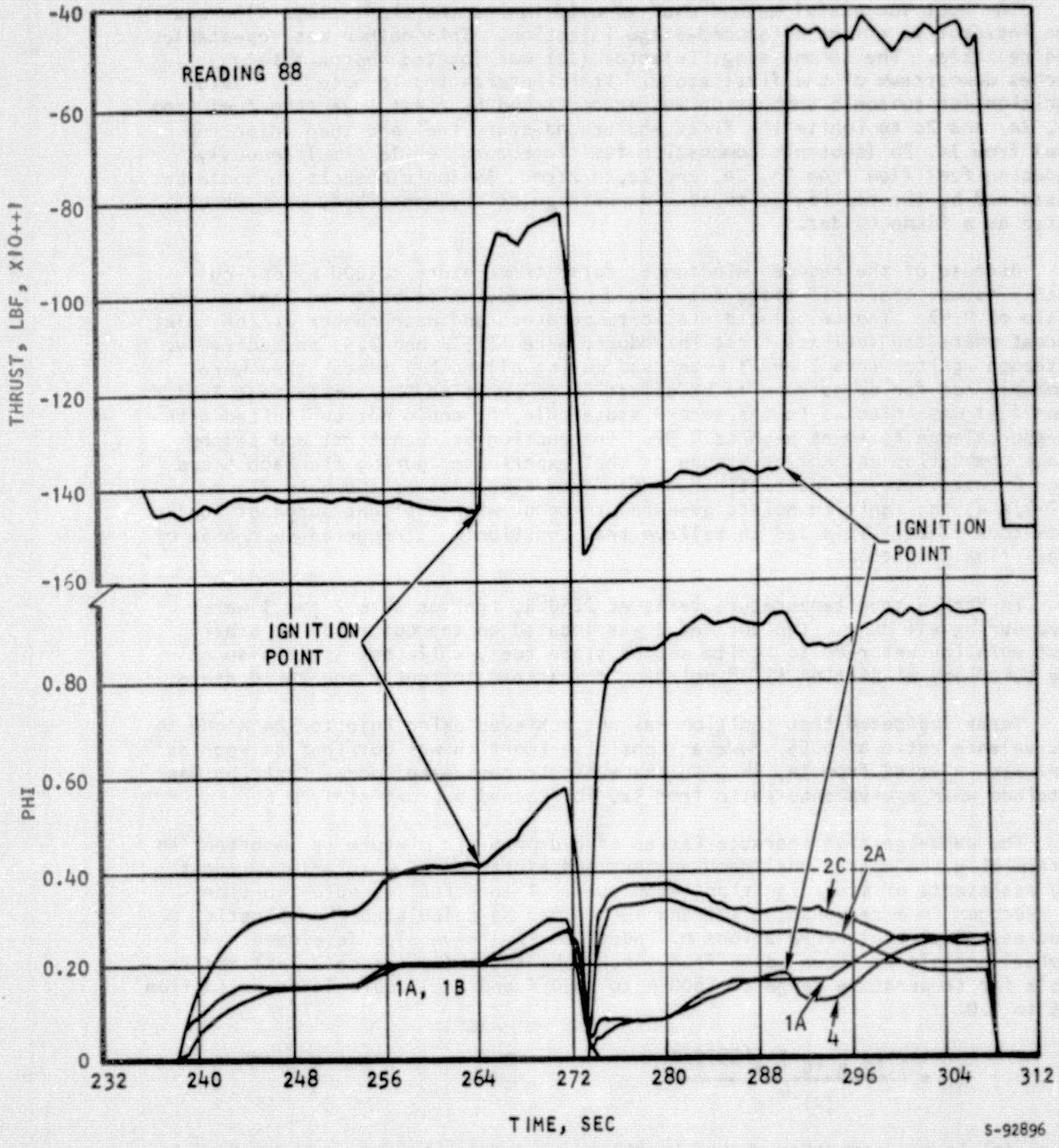

Figure 7.2-4. Time Plots of Equivalence Ratio and Measured Thrust

pressure. According to these calculations, it was recognized that at Mach 6 combustor inlet condition (T_s = 1450°R, P_s = 16 psia, V = 4580 ft/sec, $\phi \sim 0.3$) autoignition would not occur. However, cross-stream injection of fuel was expected to increase local temperature and pressure at the leading edge of the jet, and the recirculation region behind the jet would also provide a low-velocity zone to retain the ignition source. It was anticipated that sufficient recovery of temperature and pressure and strong shock-boundary layer interaction from the fuel injection process would result in ignition as previously experienced in the 2-dimensional combustor tests (Reference 7.2-3).

Autoignition characteristics of AIM at Mach 6 proved to be quite different from that in the 2-dimensional combustor model test, even though the combustor inlet conditions were about the same. In the 2-dimensional test, autoignition repeatedly occurred when the equivalence ratio greater than 0.2 was injected. (Reference 7.2-4).

In the AIM, autoignition could not be achieved even with equivalence ratio as high as 0.38 injected from the first stage as shown in Figure 7.2-3. A comparison of flow parameters and geometry between the 2-D model and AIM is shown below.

	Surface Material	Method of Cooling	Flow Profile	Composition	Injector	Combustor Config.
AIM	Nickel	Water	Nonuniform	Clean air	In line	Annular
2-D Model	STL	Water	Uniform	Vitiated	Inter-digitized	2D

The flow parameter in AIM at the combustor entrance was even slightly more favorable for autoignition than that in 2-D model. The lask of autoignition in AIM may have been caused by an inline fuel injector arrangement of 1a and 1b which would have less flow blockage. The induced shock-boundary layer interaction may not have been strong enough to initiate the combustion. Also, the gas composition in 2-D model tests may have contained radicals which would accelerate the chain reaction and lower the autoignition temperature. On the other hand, the presence of water vapor in the vitiated stream also tends to act as a very efficient third body, causing a quenching of chain-branching reaction to increase the ignition delay time (Reference 7.2-5). The net effect is uncertain (the controversy between clean and vitiated air is still not clearly understood). Another factor may have been end-wall effects; the 2-D model end walls may have influenced the ignition process, but the effect is difficult to evaluate quantitatively.

7.2.2 Effects of Altitude

The effect of altitude on measured wall static pressures on the inner cowl and centerbody at Mach 6 is shown in Figures 7.2-5 and 7.2-6. The freestream total pressures of 925, 750 and 470 psia correspond to 76,000, 81,000, and 91,000 feet of altitude simulation, respectively. At total pressures of 925 and 750 psia, the pressure distribution and calculated combustor

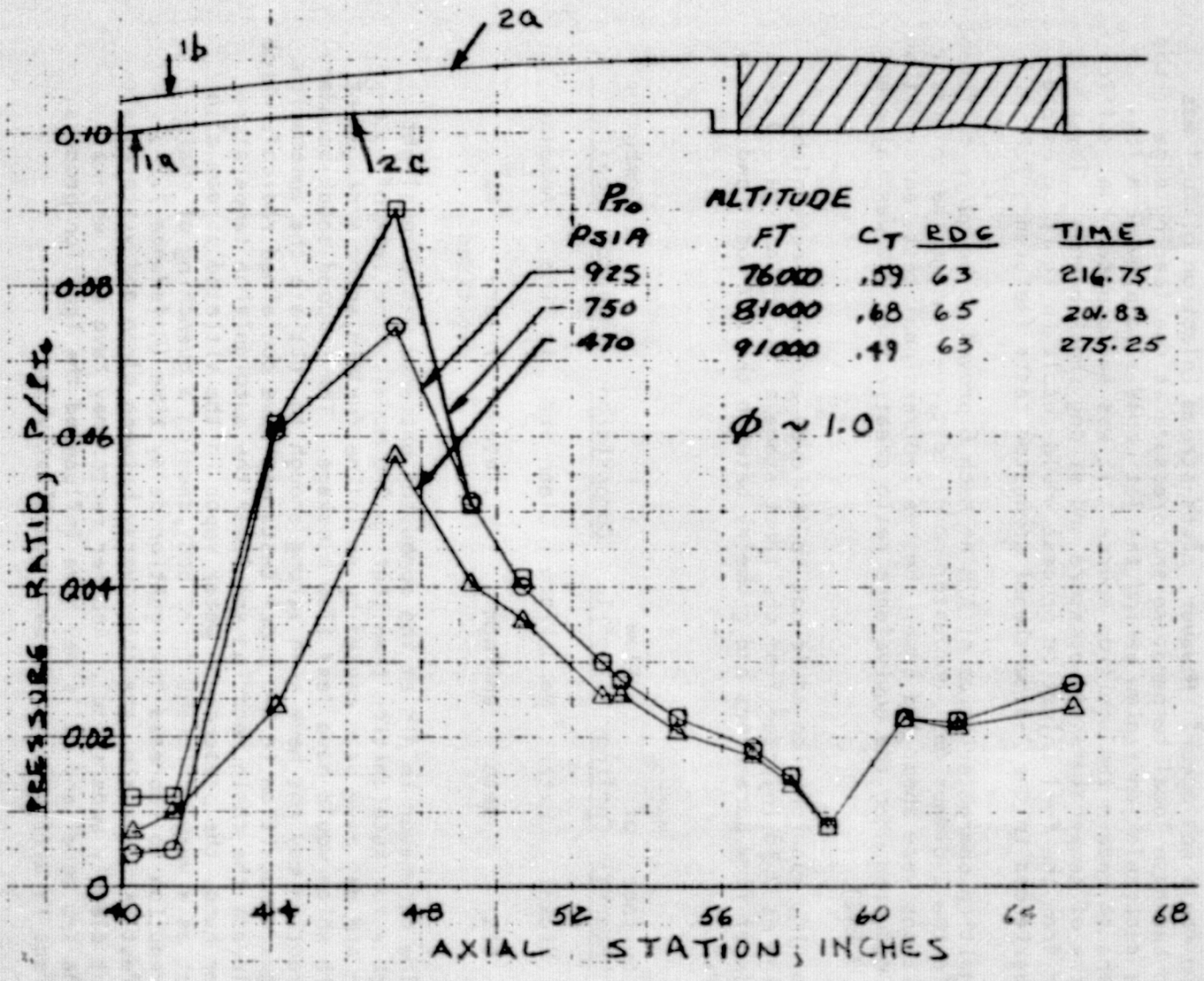

Figure 7.2-5. Effects of Altitude - Inner Cowl Pressure

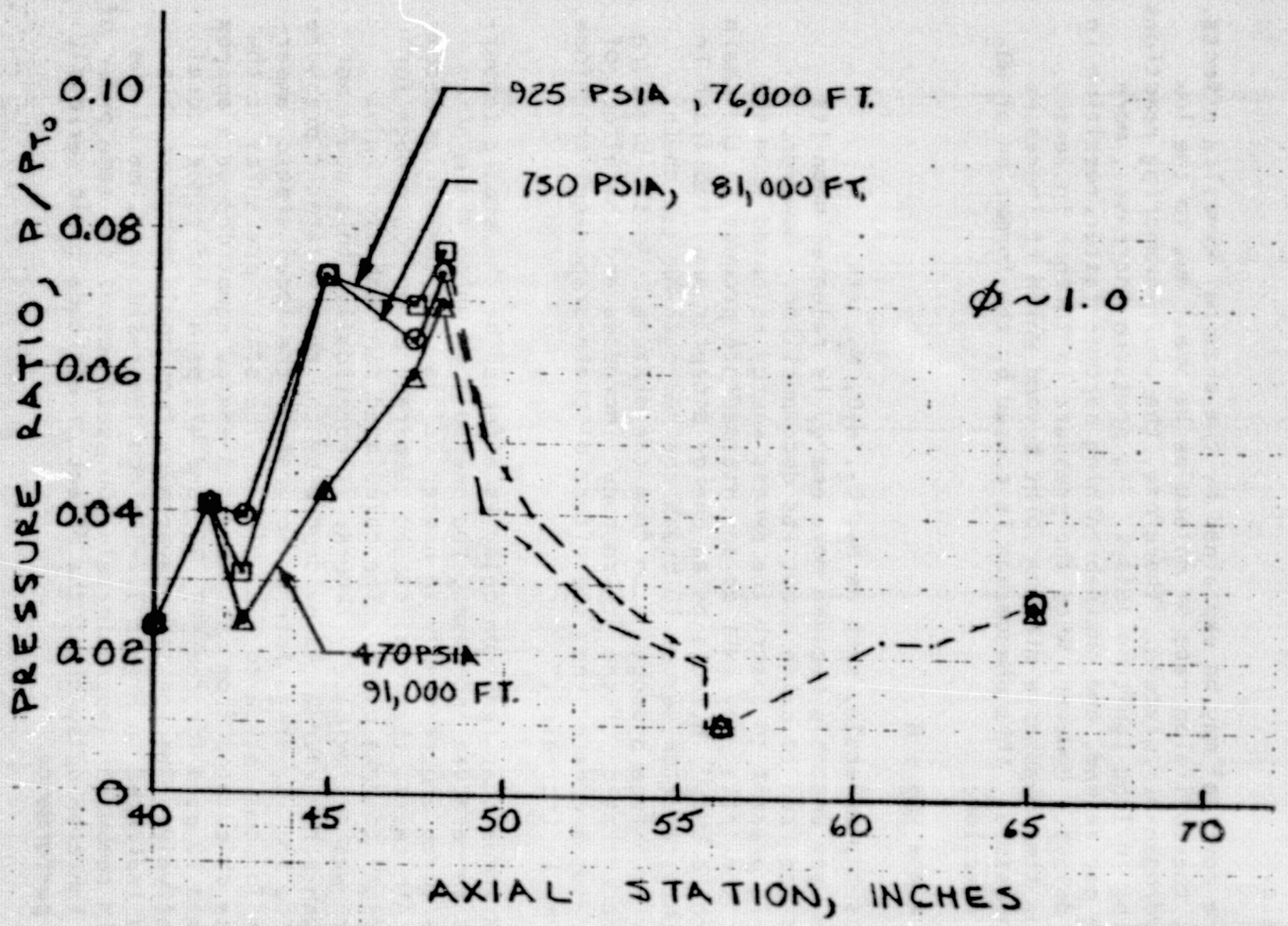

Figure 7.2-6. Effects of Altitude - Centerbody

efficiency (90-100 percent) were about the same with a higher rise at 750 psia between injectors 2a and 2c. At 470 psia both the pressure distribution and calculated combustor efficiency (66 percent) were significantly lower. Also, as shown in Figure 7.2-5 overall performance in terms of thrust coefficient was highest at 750 psia.

This pressure reversal may be explained by the chemical kinetics effects. At low pressures, the collision rate of molecules is small due to the low density of the hydrogen-air mixture. Therefore, the chain-branching reactions are slow, resulting in long ignition delays. As pressure increases, more molecules collide per second, and chain-branching becomes faster, resulting in shorter ignition delays. However, when the pressure is further increased, the ignition delay time reaches a minimum point beyond which it increases with increasing pressure. This phenomenon is caused by the formation of HO_2 in the following reaction:

$$H + O_2 + M = HO_2 + M$$

where M represents any molecule, such as H_2, O_2, H_2O, N_2, etc. Ordinarily HO_2 is very unstable because more energy is released upon its formation than is required to bring about its decomposition. However, if another molecule is present to absorb the excess energy released from the formation of HO_2, the latter may exit as an intermediate product in the chain reaction. The "third body", M, acts as an energy acceptor and stabilizer in this reaction. This reaction serves to break the hydrogen-oxygen chain reaction by removing a free hydrogen atom from the mixture. As the pressure increases, the concentration of the "third body" increases and the effect of chain-breaking becomes greater than the effect of chain-branching; therefore, ignition delay time is increased.

Figure 7.2-7 shows that ignition delay is affected by the static temperature. As static temperature increases, the pressure at which the minimum delay time occurs moves progressively to higher values, and the curves become steeper. In the AIM tests, the local static temperature was low enough for the "reversal effect" to take place. The calculated AIM combustor inlet static temperature was approximately 1400°R. Theoretically, this could not ignite the hydrogen-air mixture. As evidenced by the rise in static pressures aft of injectors 1a and 1b, stage interaction raised the local static temperature high enough for combustion to take place. The static pressures at the combustor entrance calculated from mass-momentum-energy equations were approximately 20, 15, and 10 psia for the 925, 750, and 470 psia wind tunnel total pressures, respectively. The ignition reversal effect could occur in this pressure range as indicated in Figure 7.2-3, since the residence time of the mixture in the AIM combustor (approximately 500 μsec) was of the same order of magnitude as the ignition delay time; the effect of altitude could seriously impair combustor performance.

7.2.3 Supersonic and Subsonic Combustion

The pressure distribution on the combustor centerbody and inner cowl surfaces are shown in Figures 7.2-8 and 7.2-9, respectively, for supersonic and subsonic combustion at Mach 6 with the same equivalence ratio. The

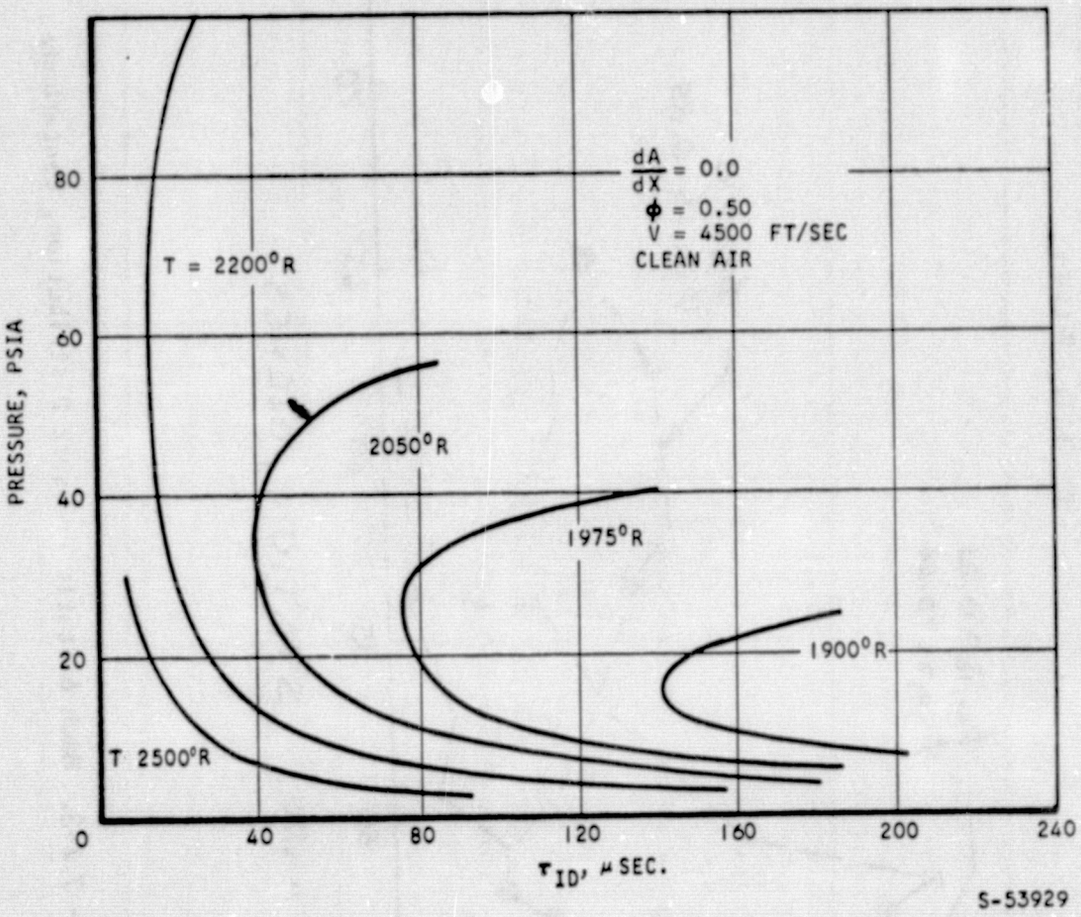

Figure 7.2-7. Effect of Initial Static Pressure and Temperature on Ignition Delay

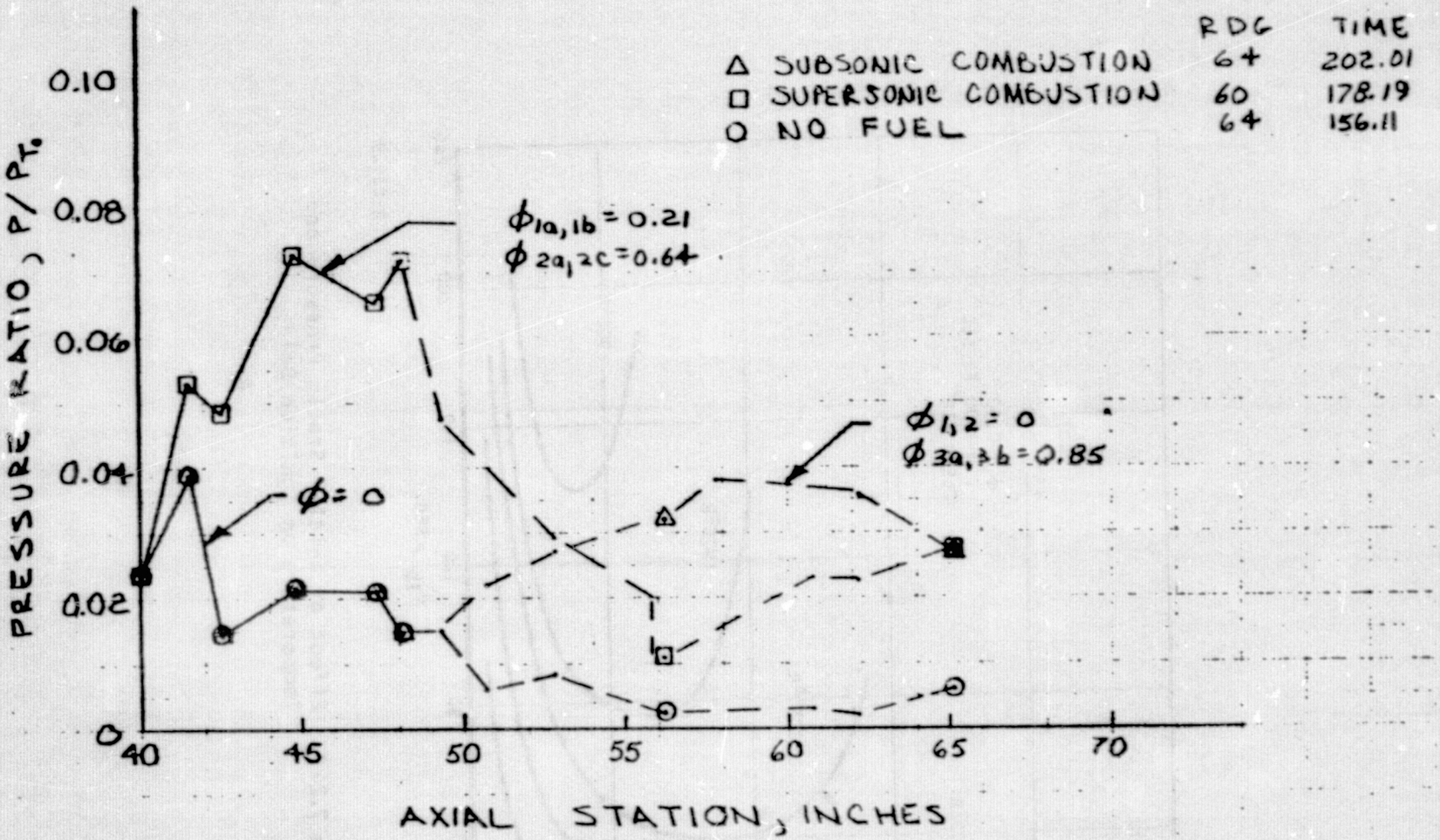

Figure 7.2-8. Mach 6 Static Pressure Distribution, Centerbody

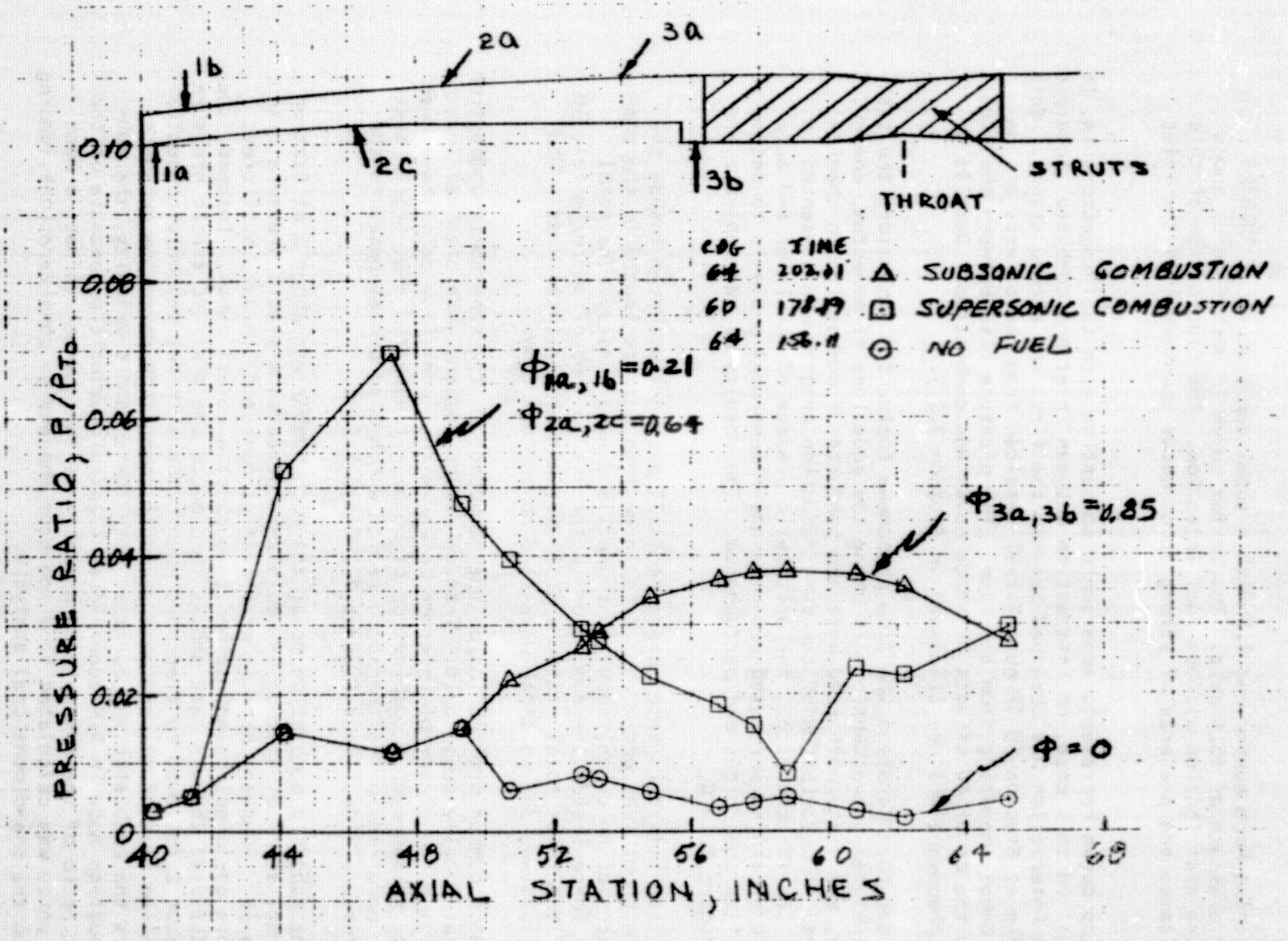

Figure 7.2-9. Mach 6 Static Pressure Distribution, Inner Cowl

combustor inlet Mach number was 2.5 with a total temperature of 3000°R and static pressure of 15.6 psia. The bottom curve in both figures shows the pressure distribution without fuel injection. The fluctuation of this curve indicates the presence of strong shock waves downstream of the inlet throat.

The top curve represents supersonic combustion with fuel injectors 1a, 1b and 2a, 2c. In this case, no interaction between inlet and combusto occurred. But strong interaction was observed between the first and second stages. The pressure dip at Station 59 (Figure 7.2-9) resulted from the effects of the expansion waves emanating from the step. The pressure rise between the struts was due to the combined effects of shock waves and combustion. Details of this wave phenomena will be discussed in Section 7.2.7.

In order to understand the flow phenomena inside the combustor, the test data was analyzed one-dimensionally using the equations of momentum, energy, continuity, and state,with reactants and products of combustion in chemical equilibrium. A description of the data reduction program was presented in Section 6. In the combustor, the arithmetic average of the inner and outer wall static pressures were used with the one-dimensional analysis to determine the local flow conditions and performance. The results of the analysis are shown in Figure 7.2-10.

Significant loss in total pressure (~75 percent) occurred inside the combustor without fuel addition. This large loss was attributed to the combined effects of friction, shocks,and profile mixing losses. The total frictional force inside the combustor contributed a loss of approximately 38 percent of the inlet total pressure,or 53 percent of the total loss. The remaining loss was due to shock waves and nonuniform flow.

The Mach number profile inside the combustor in the supersonic combustion mode was not totally supersonic. Transonic Mach numbers were attained (one-dimensionally) downstream of injector 2c where the local flow could have been supersonic, subsonic,or a combination of both. It appeared that significant combustion occurred in the transonic region,which also corresponded to the highest pressure rise. (see Figures 7.2-8 and 7.2-9).

In the subsonic combustion mode, the Mach number was about 2 at Station 49. A normal shock at Station 49 would have produced a static pressure rise of about 4.30. However, because of the large combustor throat, sufficient backpressure could not be maintained to support a normal shock. Instead, the flow was diffused through weak shocks to produce the observed static pressure rise of about 2,followed by transonic Mach numbers in the subsonic combustor stage. Unlike that of conventional subsonic combustion where low subsonic flow enters the combustor and burns at very low subsonic velocity, the subsonic combustion mode in AIM occurred at transonic velocities because of the small area ratio of the subsonic combustor. At the thermal throat, a Mach number of unity was calculated from momentum and energy considerations, lending credence to the one-dimensional analysis.

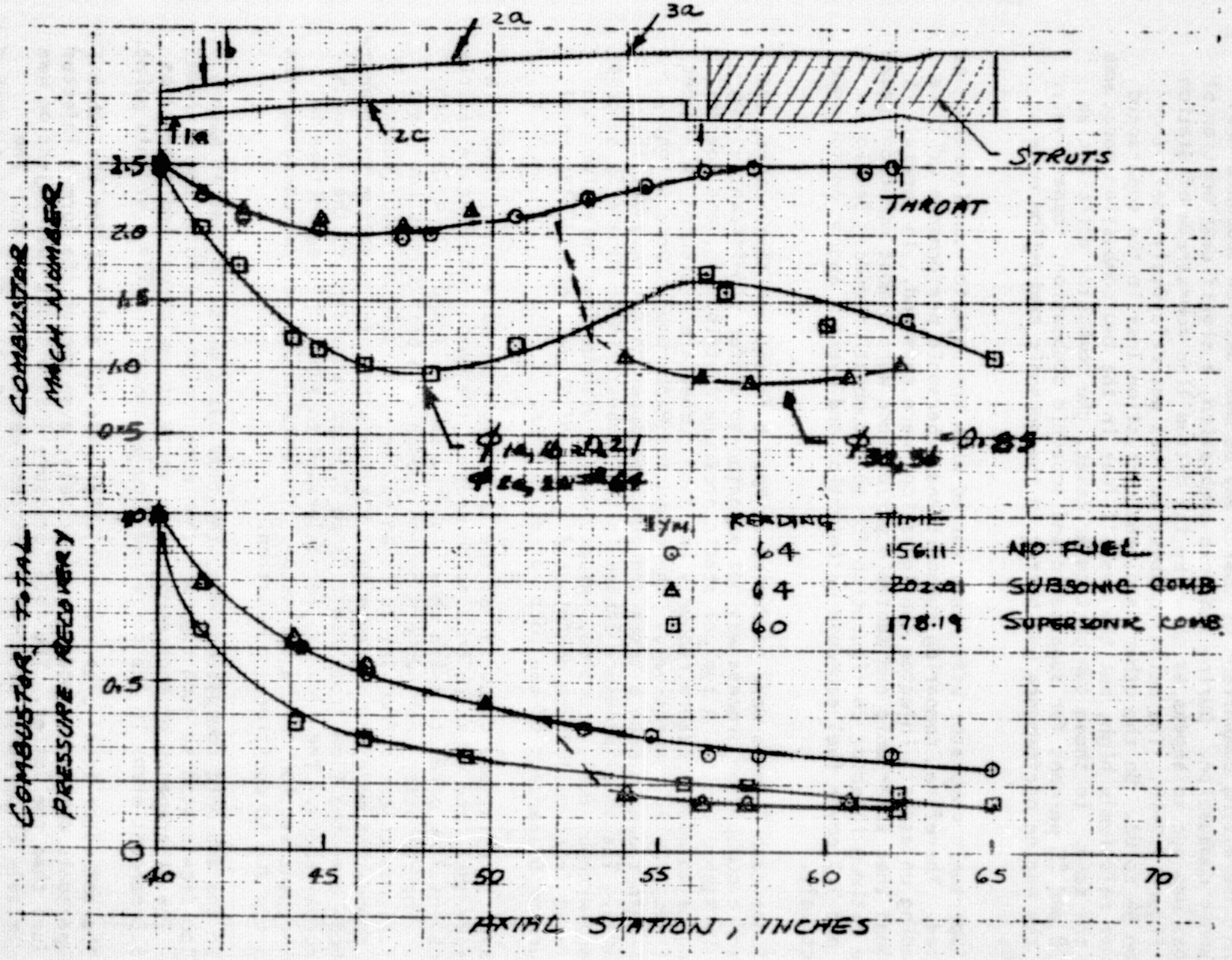

Figure 7.2-10. Combustor Flow Parameters - Mach 6

An interesting comparison of losses may be made between subsonic and supersonic combustion. During subsonic combustion, a significant portion of the loss was due to shocks, as shown by the dotted line downstream of Station 51 in Figure 7.2-10. The actual combustion loss was relatively small from Station 54 to 62. On the other hand, the combustion loss in the supersonic case was relatively high, but the overall loss in the two combustion modes was about the same. In these two particular cases, the combustor efficiencies were 78 and 88 percent for supersonic and subsonic combustion, respectively. Thus, the engine performance was better in the subsonic combustion mode at Mach 6.

Supersonic combustor efficiency varied with the injector configuration as expected. Therefore, comparing subsonic and supersonic performance would be misleading unless all injector configurations were examined. In general, it was found that supersonic and subsonic performance were almost identical based on the optimum injector configuration for each combustion mode. Sections 7.2.5 and 7.7 cover fuel schedule optimization and overall engine performance, respectively.

Since Mach 7 tests were conducted at Mach 6 freestream temperature, the supersonic combustion process was not expected to differ significantly from those in Mach 6 tests. A typical static pressure distribution, and corresponding calculated pressure recovery and Mach number are presented in Figures 7.2-11 and 7.2-12, respectively. The combustor Mach numbers were slightly higher than those in Mach 6 tests and remained supersonic throughout the combustor. The total pressure losses in the combustor were 93 and 84 percent with and without fuel injection, respectively. Without fuel injection, the calculated frictional force contributed a loss of 51 percent of inlet total pressure or 61 percent of the total pressure loss.

Mach 5 tests were conducted at the true flight temperature of 2200°R in both supersonic and subsonic combustion modes. The combustor pressure distributions and flow parameters are shown in Figures 7.2-13 and 7.2-14 for both modes. The combustor Mach numbers became subsonic in both combustion modes. When fuel was injected from 2a, 2c at an equivalence ratio of 0.66 (supersonic combustion mode), a pressure perturbation propagated upstream to separate and shock down the flow from Mach 1.53 to 0.68 corresponding to the strength of a normal shock. The flow was reaccelerated to supersonic velocities in the divergent section of the combustor. The Mach number was decreased between the struts due to additional combustion.

In the subsonic combustion mode, the flow was similar to that at Mach 6. The flow decelerated to Mach 0.55 and then accelerated to 0.88 at the minimum area. The discrepancy of Mach number from unity at the throat indicated less than 1.5 percent error in the corrected flow parameter, $W\sqrt{T}/P_T$, at this point.

The combustor total pressure recoveries were 0.3 and 0.27 for the subsonic and supersonic combustion modes, respectively, even though the former injected more fuel than the latter. The total pressure loss without fuel injection was approximately 61 percent, of which 26 percent was due to friction. The functional loss was reduced to 26 percent at Mach 5, from 51 percent at Mach 7.

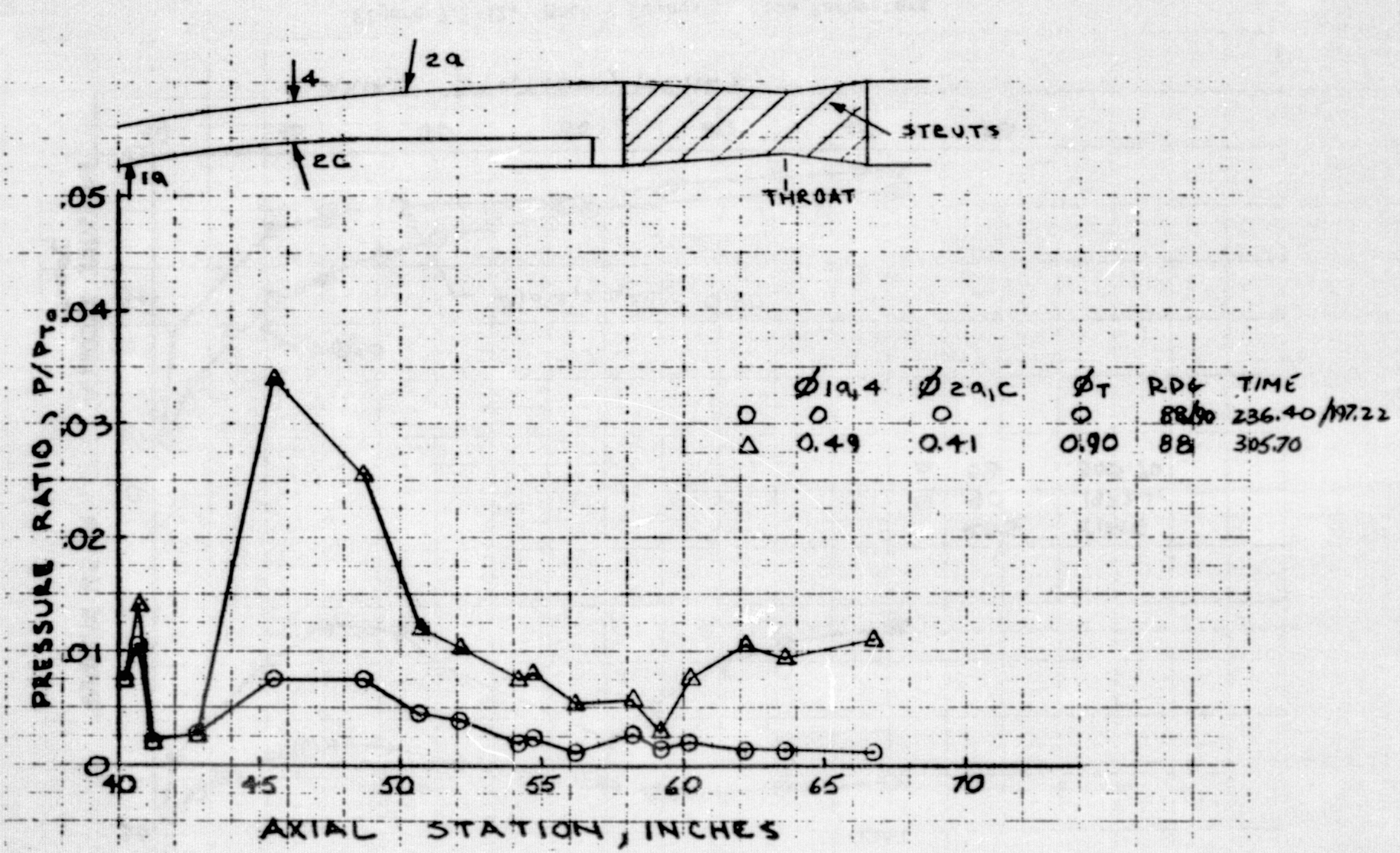

Figure 7.2-11. Mach 7 Static Pressure Distribution, Inner Cowl

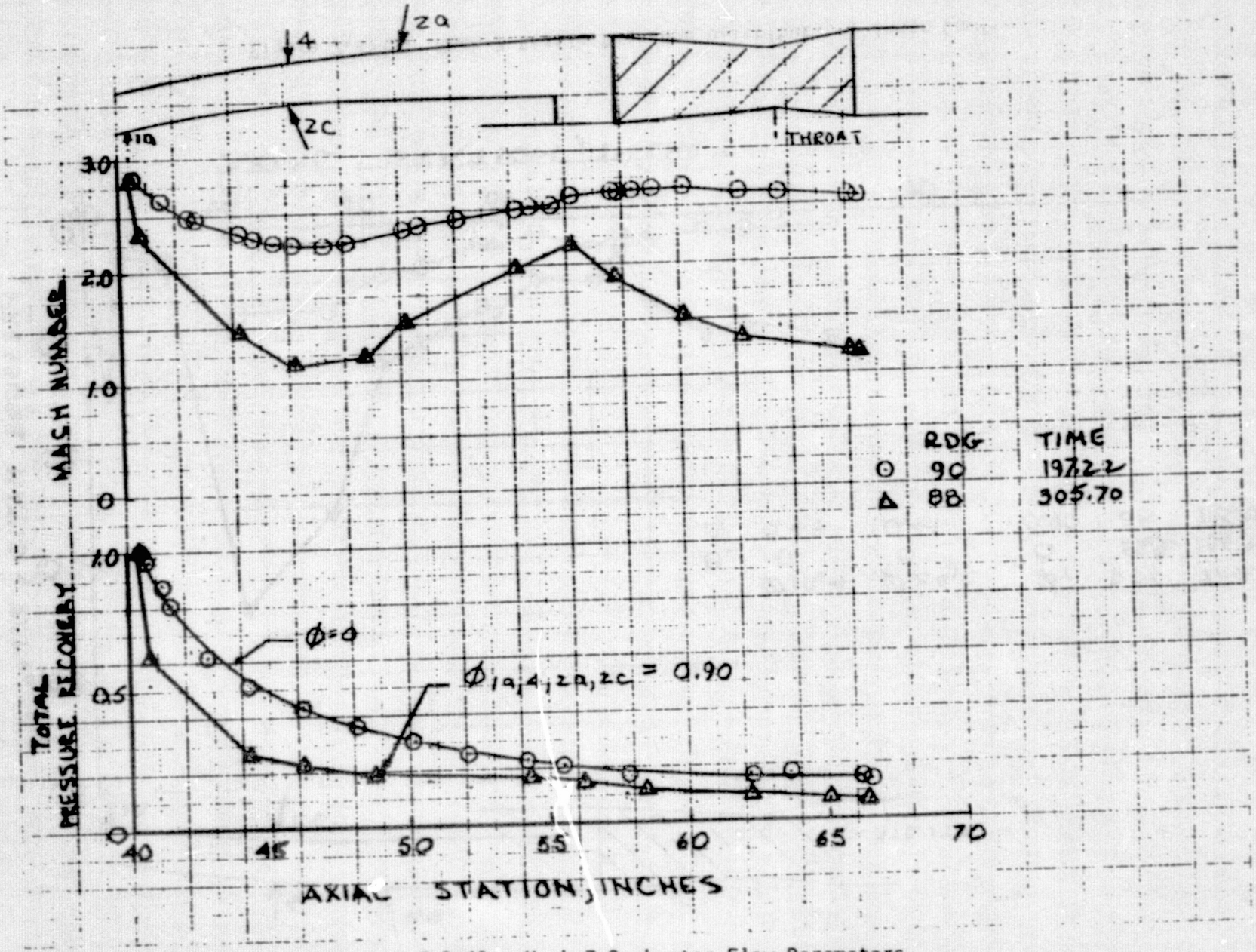

Figure 7.2-12. Mach 7 Combustor Flow Parameters

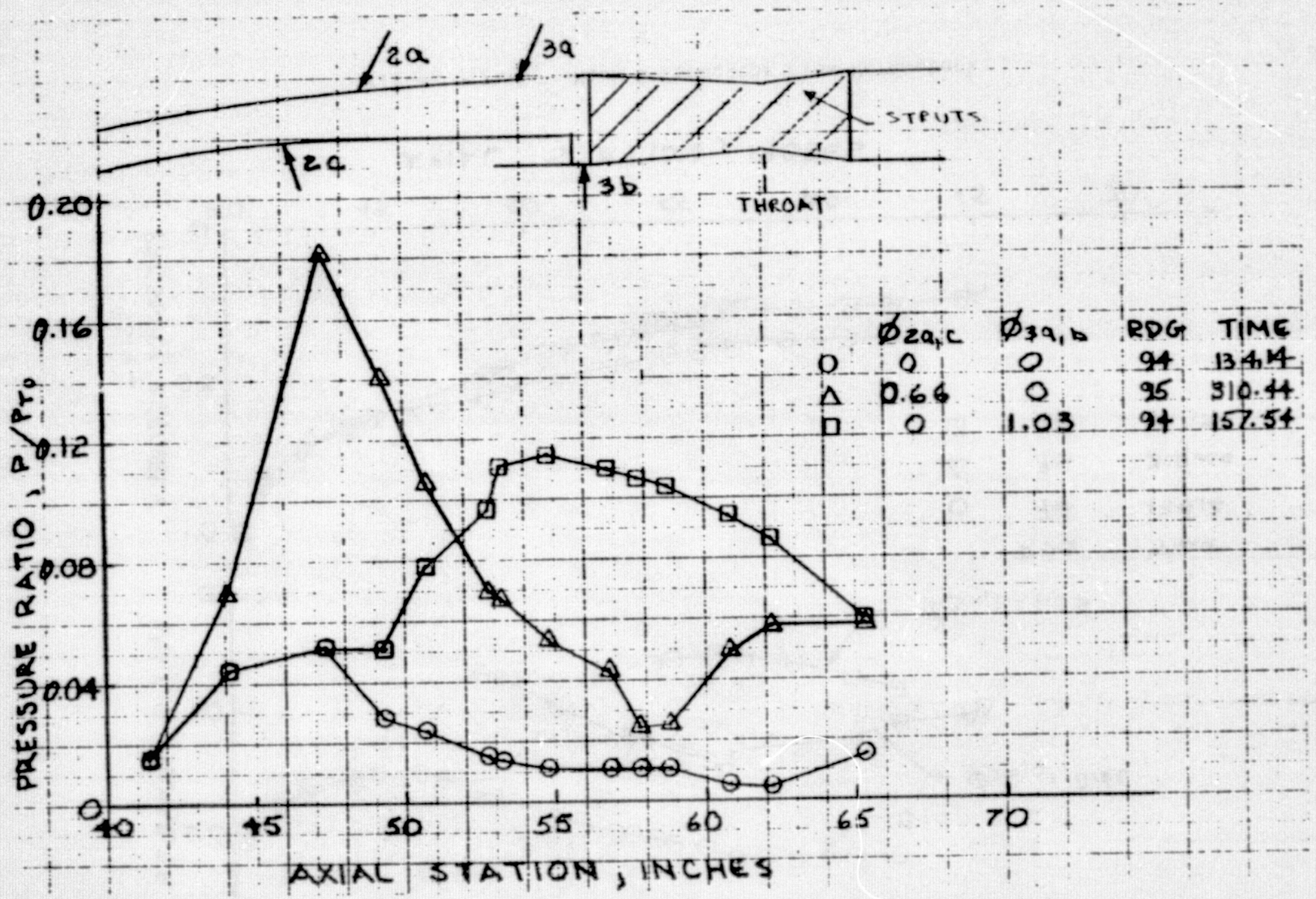

Figure 7.2-13. Mach 6 Static Pressure Distribution, Inner Cowl

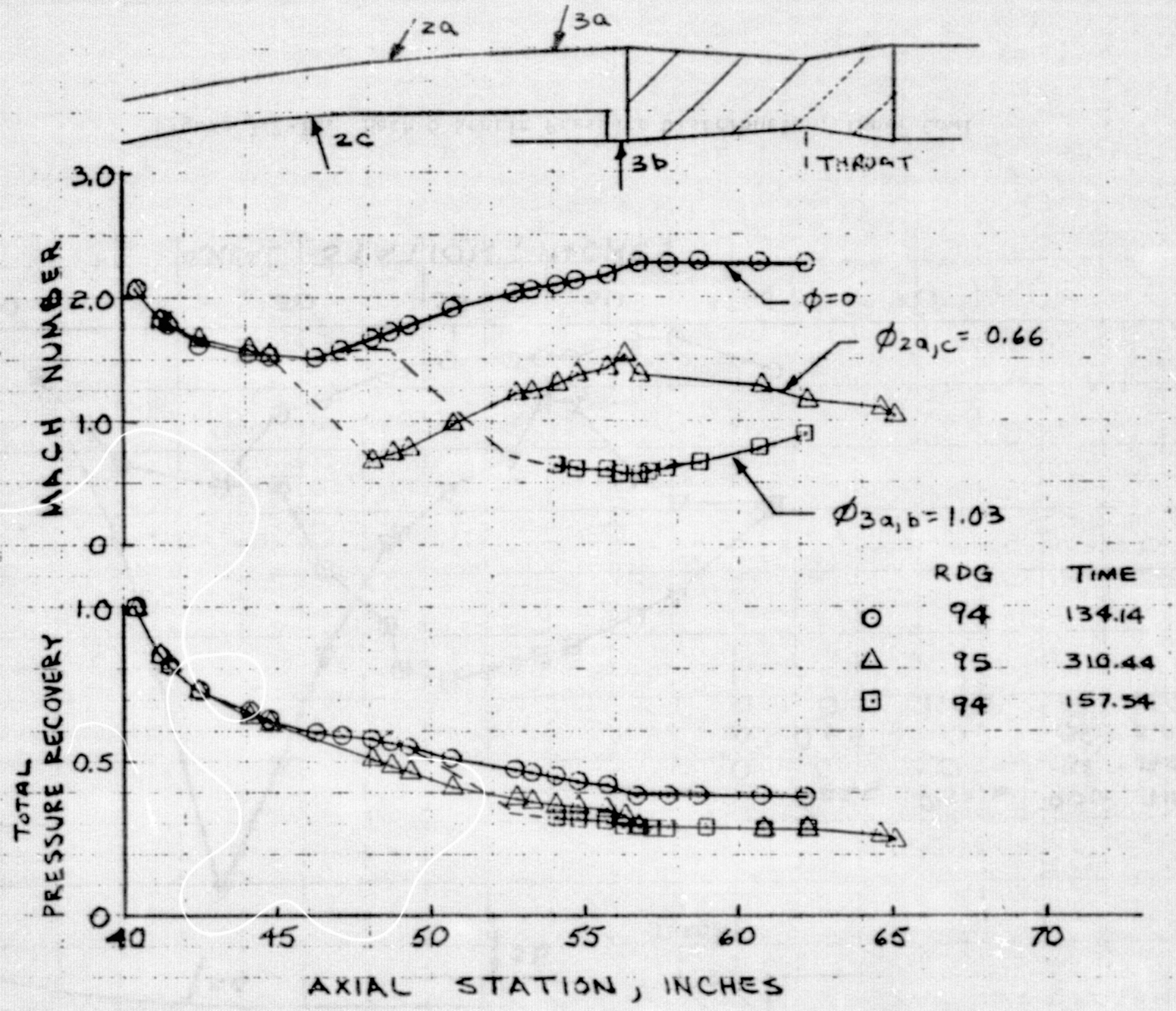

Figure 7.2-14. Mach 5 Combustor Flow Parameters

7.2.4 Effects of Spike Translation

In the Mach 6 design, the nominal cowl leading edge (X_{CL}) was positioned at 34.884 in. from the spike tip. During the Mach 6 tests, it was necessary to translate the spike forward approximately 0.3 in. ($X_{CL}/R = 3.91$) to attain a mass flow ratio of 0.98 and an inlet contraction ratio of 8.97. In addition to this nominal Mach 6 operating position, two different spike positions X_{CL}/R = 4.08 and 4.17, were investigated in Reading 61. The purpose of this test was to investigate the inlet and combustor performance at the maximum aerodynamic contraction ratio, and at the same aerodynamic contraction ratio but at different spike positions. These two positions resulted in appreciable spillage; however, the aerodynamic contraction ratios (mass flow ratio x contraction ratio) were maintained at 10.24 (maximum) and 8.5, respectively, as compared with 8.8 for the nominal case. Table 7.2-2 shows a comparison of three spike positions with and without fuel injection. The combustor total pressure recovery and efficiency were decreased with forward spike translation even though the combustor inlet Mach number did not change significantly. The increase in total pressure loss in the combustor was attributed both to the increased friction per unit mass flow and to the increased area ratio in the combustor. The calculated friction force for each of the three cases ($X_{CL}/R = 3.91$, 4.08, and 4.17) was 10.05, 11.54, and 12.38 (lbf/lb_m-air) with corresponding area ratios of 3.62, 5.27 and 6.88, respectively. The higher combustor area ratios produced high Mach numbers, resulting in increased total pressure loss in the combustor.

The lower combustor efficiencies may be explained from static pressure distribution plots as shown in Figure 7.2-15, in which inner cowl surface pressures were plotted for two different spike positions. In reading 61 (Symbol □), because the spike was translated forward 2.8 in. from nominal position (reading 57, Symbol ○), the spacing between injectors 1a and 1b and 2a and 2c, and that between step and struts were increased by the same amount. Consequently, the interaction between them was significantly reduced, as indicated by much smaller pressure rise downstream of injector 2a.

7.2.5 Optimization of Fuel Schedules

In the supersonic combustion mode, the fuel injection system consisted of six injector rows: three on the inner surface (1a, 1c, and 2c), and three on the outer surface (1b, 4 and 2c). Because of time limitation, injector 1c was not used in Mach 6 tests. In order to evaluate the combustor performance, ten different fuel injector combinations were tested. However, due to a large number of plugged static pressure taps on the combustor surfaces, and uncertainty in thrust measurements prior to reading 52, tests using six different injector combinations were selected for performance comparison. These test points and relevant information are listed in Table 7.2-3.

The axial momentum change in the combustor, ΔF_c, was employed to evaluate the overall combustor performance, because it represents the true thrust-producing capability of the combustor for the same inlet conditions. This parameter was an algebraic summation of the wall pressure integrals, fuel momentum, and the frictional losses. Considerable data scatter was observed when this value was plotted versus fuel-air ratio as shown in Figure 7.2-16. The flow momentum change was noticeably lower when fuel injectors 1a, 1b, 2a, and 2c were used, as indicated by the Δ symbols.

TABLE 7.2-2

EFFECTS OF SPIKE TRANSLATION

Reading Number	Time	ϕ	W_a	MFR	CR	MFR X CR	$P_{R_{inlet}}$	M_{throat}	$P_{R_{comb}}$	η_c	$\frac{A_{comb}}{A_{in.}}$	$\frac{X_{CL}}{R}$
57	195.113	0	26.712	.981	8.97	8.8	.386	2.5	.2788	-	3.62	3.91
61	178.86	0	21.29	.782	13.1	10.24	.41	2.43	.1811	-	5.27	4.08
61	231.062	0	13.5	.497	17.1	8.5	.292	2.286	.2518	-	6.89	4.17
57	207.713	.94	26.608	.978	9.02	8.82	.386	2.5	.1441	.78	3.64	3.91
61	222.062	.869	21.29	.784	13.06	10.24	.4096	2.433	.1023	.71	5.27	4.08
61	251.762	.939	13.526	.498	17.05	8.49	.34	2.437	.0707	.434	6.88	4.17

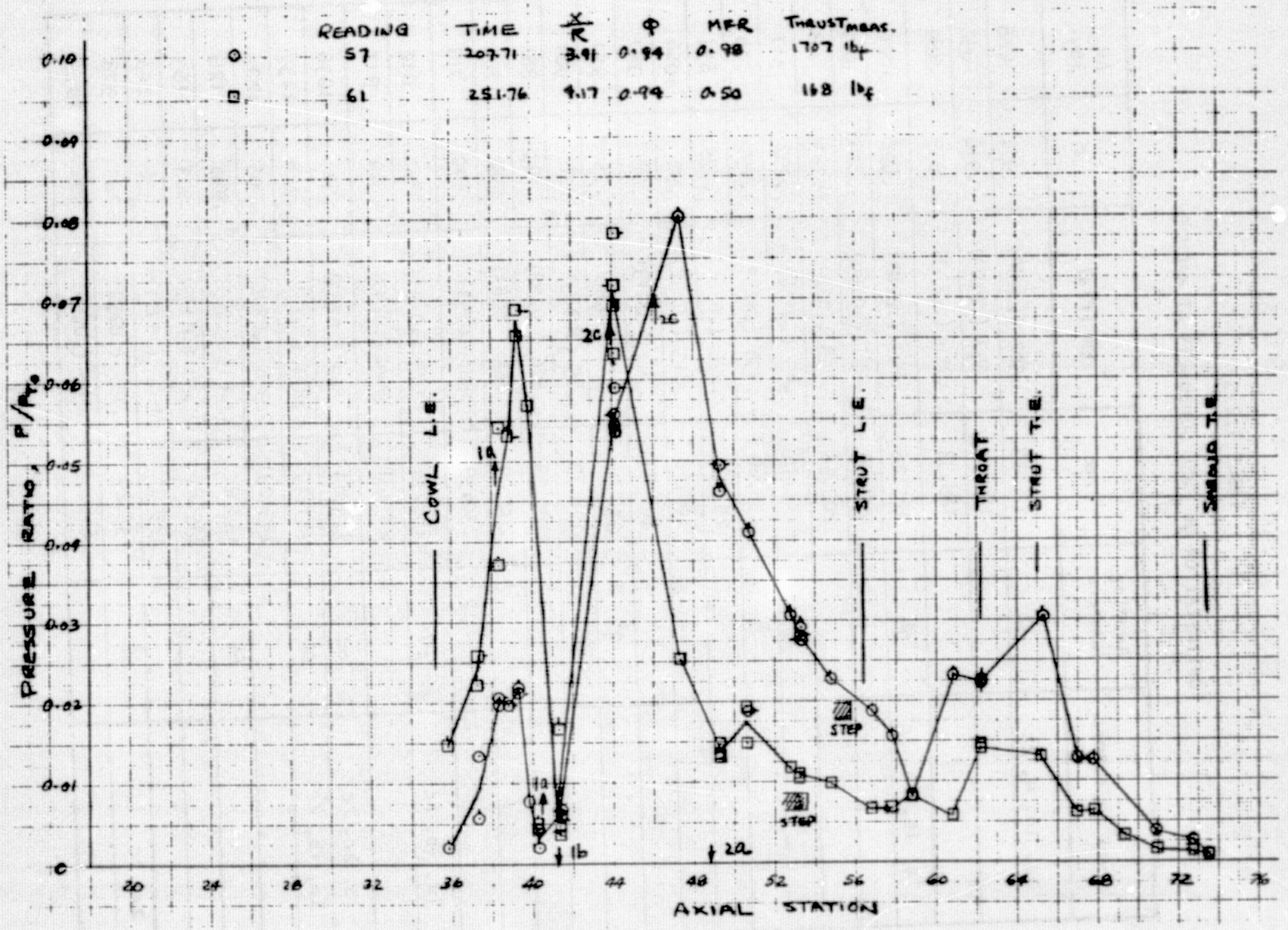

Figure 7.2-15. Static Pressure Distribution, Inner Cowl

TABLE 7.2-3

OPTIMIZATION OF FUEL SCHEDULES AT MACH 6

Fuel Injectors	Reading Numbers	Time	ER (f/a)	η_c	ΔF_c, lb_f
1a, 1b, 4, 2c	52	172.23	.502 (.0168)	.912	428
		180.33	.607 (.0203)	.916	632
		189.33	.726 (.0243)	.959	889
1a, 1b, 2a, 2c	54	185.26	.847 (.0283)	.898	1026
		191.56	.491 (.0164)	.874	383
		200.56	.658 (.022)	.783	548
		222.16	.49 (.0164)	.792	311
		235.66	.756 (.0253)	.759	714
		253.66	.776 (.0265)	.775	851
		280.66	.813 (.0272)	.92	1044
	57	207.71	.942 (.0313)	.78	987
		234.71	.923 (.0307)	.73	951
	60	178.19	.85 (.0283)	.78	901
		186.29	.866 (.0288)	.743	881
		202.49	.864 (.0287)	.682	795
		230.39	.88 (.0292)	.690	839
1a, 1b, 2c	57	265.31	.575 (.0191)	.891	612
		287.81	.744 (.0247)	.894	912
1a, 2a, 2c	60	223.19	.869 (.0289)	.87	1036
2a, 1b, 2c	60	241.19	.871 (.029)	.958	1137
		249.29	.916 (.0305)	.965	1209
	64	167.81	1.011 (.0297)	.995	1126
		239.81	1.34 (.0393)	.603	1163
		293.81	1.06 (.0311)	.956	1216
2a, 2c	60	258.29	.757 (.0252)	.965	978
		264.59	.795 (.0264)	.934	1013

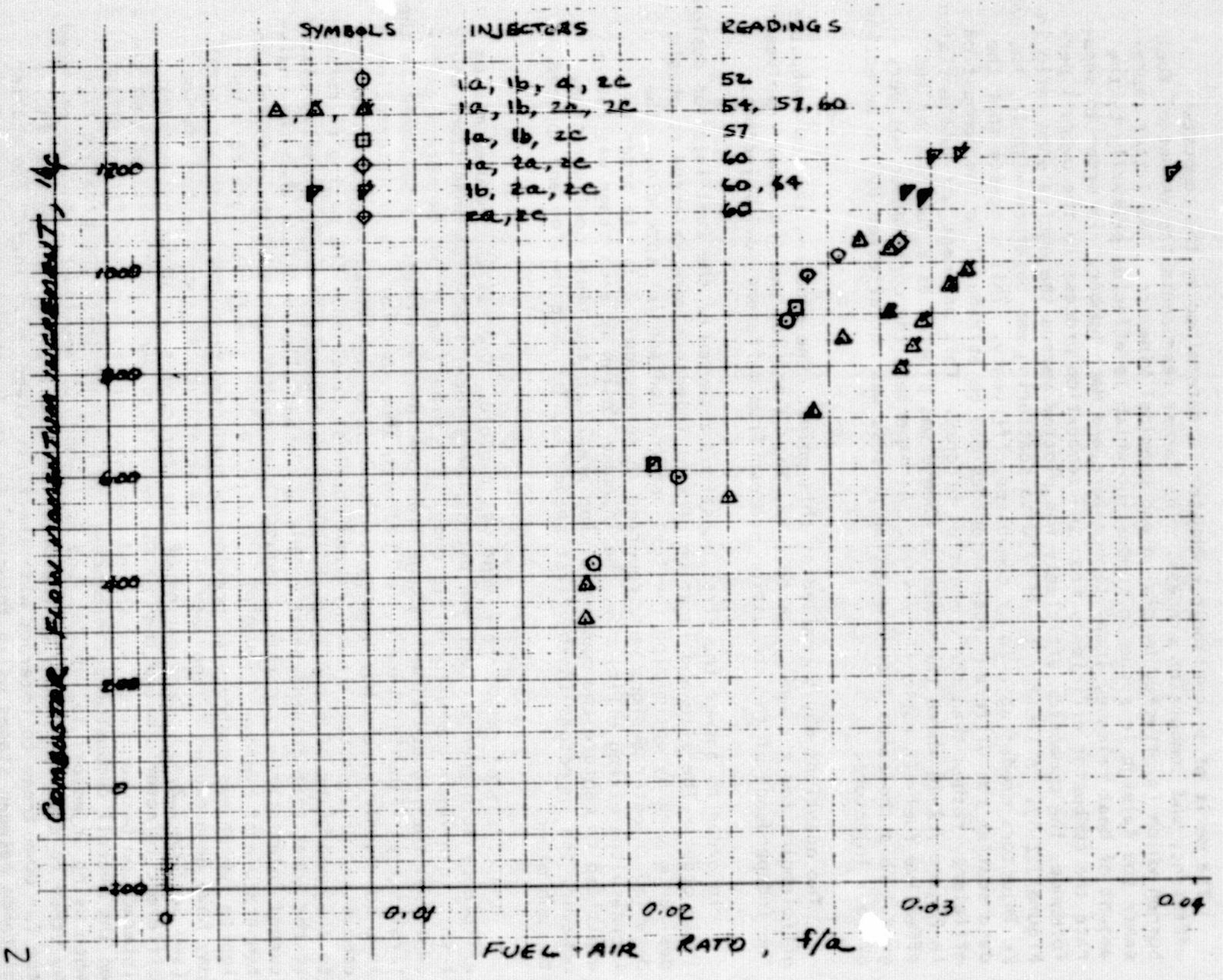

Figure 7.2-16. Mach 6 Correlation of Combustor Flow Momentum

The merit of a supersonic combustor is determined by the combustor efficiency and combustion process. The former represents the amount of fuel burned which is affected by mixing and chemical kinetics. The latter represents the Raleigh loss due to combustion which is affected primarily by the amount of heat release, local temperature, and Mach number. In order to separate the combustor efficiency from the combustion process in the overall performance, the combustor efficiency was plotted versus the equivalence ratio in Figure 7.2-17. A similar trend of data scattering was observed with 1a, 1b, 2a, 2c injectors producing a lower combustor efficiency. This suggests that the data scatter for different fuel injectors may be attributed to the combustion efficiency rather than the combustion process. This argument was substantiated in Figure 7.2-18 where the momentum change was plotted as a function of the effective fuel-air ratio (η_c x f/a). As expected, the correlation was very good. This indicates that combustion process was not affected by the selection of fuel injectors.

Two questions may be raised at this point. One concerns the low combustor efficiencies for the fuel injectors 1a, 1b, 2a and 2c, and the other involves the independence of the combustion process from different fuel injectors.

In order to answer the first question, a review of the fuel injector design is in order. The size and location of fuel injectors were selected to obtain desired mixing by optimizing the fuel penetration and jet spreading. The detailed injector designs were reported in Reference 7.2-1. In order to increase the mixing efficiency, the injector design in each stage was interdigitized to capture the maximum mixing area. In the final configuration, however, the injectors in the first stage (1a, 1b) were in-line and opposed to each other.

The effect of this arrangement was twofold. One was the reduced mixing efficiency at higher equivalence ratios, where local fuel-rich conditions would result in a lower combustor efficiency. The other, which may be more significant, was the reduced flow blockage from the in-line injector arrangement in the first stage. Flow blockage associated with shock-boundary layer interaction in a supersonic stream has been proven to have a significant influence on the combustion process, both in mixing and chemical reaction. The mixing is related to the generation of turbulence, while chemical reaction time is closely related to the local static temperature. This was especially important when the undisturbed inlet static temperature (≈1475°R) at Mach 6 was below the autoignition temperature of hydrogen (≈1800°F). The failure of the first stage to autoignite (which was contrary to previously conducted combustor component tests) may have been caused by the lack of flow separation at the injector station (see Section 7.2.1). Examination of the static pressure distributions for different injector combinations of Figures 7.2-19 and 7.2-20 revealed that the interaction between first and second combustor stages had significant effects on the overall combustor performances. In Figure 7.2-19, the pressure rise when using injectors 1a, 1b, 2a, and 2c (symbol Δ) was lower than that produced by other injectors. It may be reasoned that the location of injector 2a was too far downstream to interact with the first stage (≈7.5 in.). The shorter distance between stages using injectors 1a, 1b, 4, and 2c, or a larger disturbance generated by a single-sided injection from the second stage using injectors 1a, 1b, 2c appeared to have enhanced the combustion process. The same

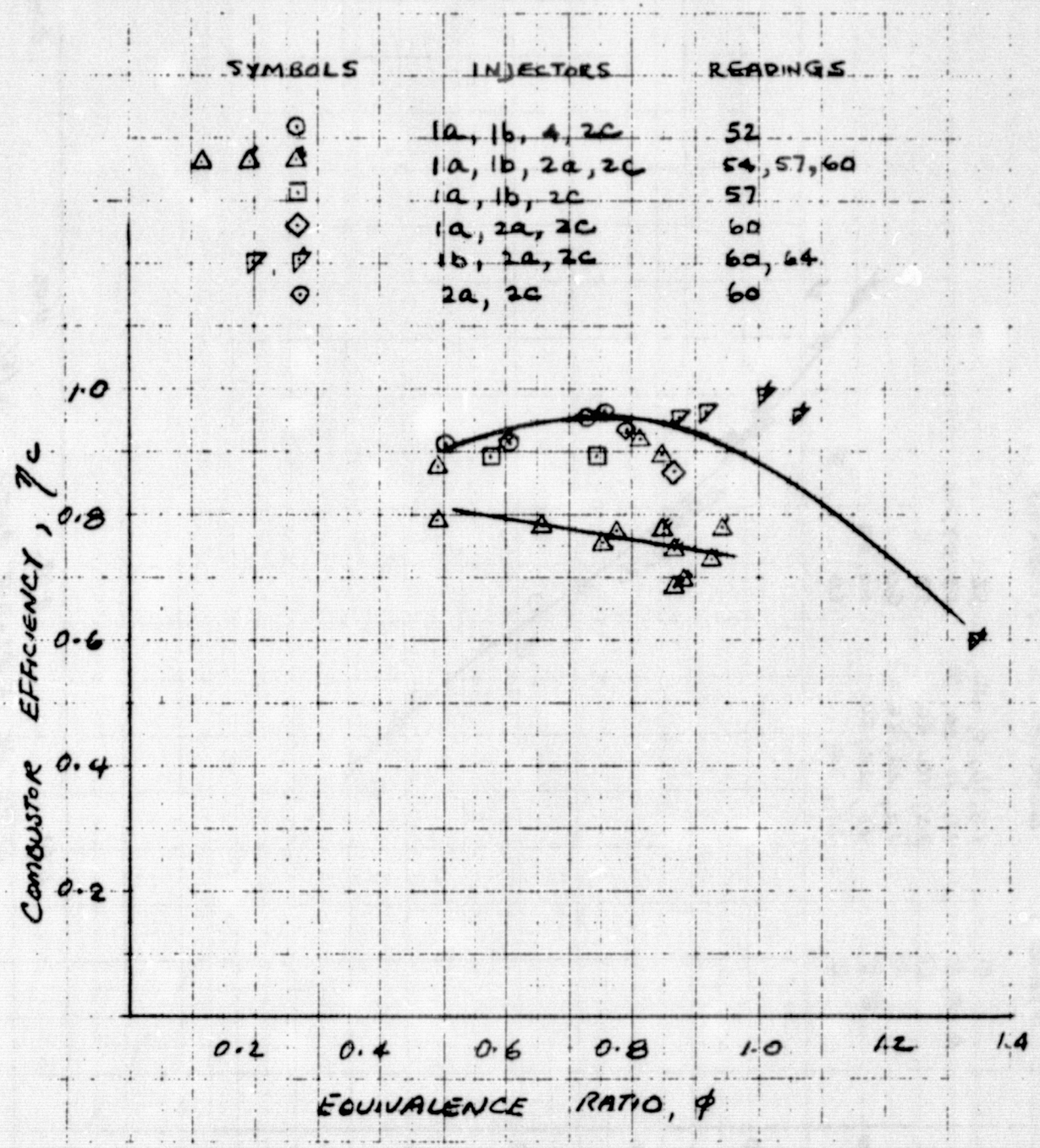

Figure 7.2-17. Mach 6 Combustor Efficiency

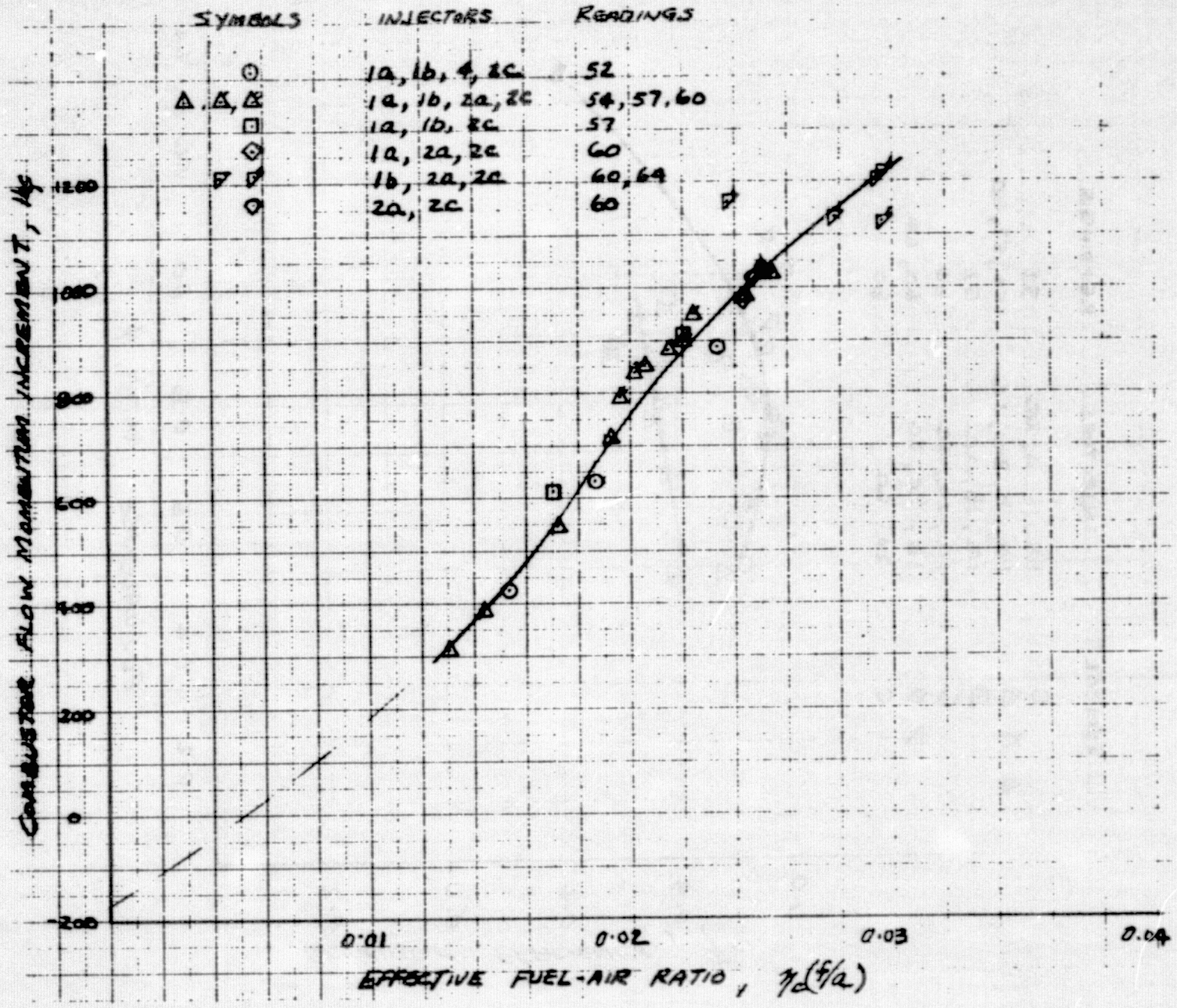

Figure 7.2-18. Mach 6 Correlation of Combustor Flow Momentum

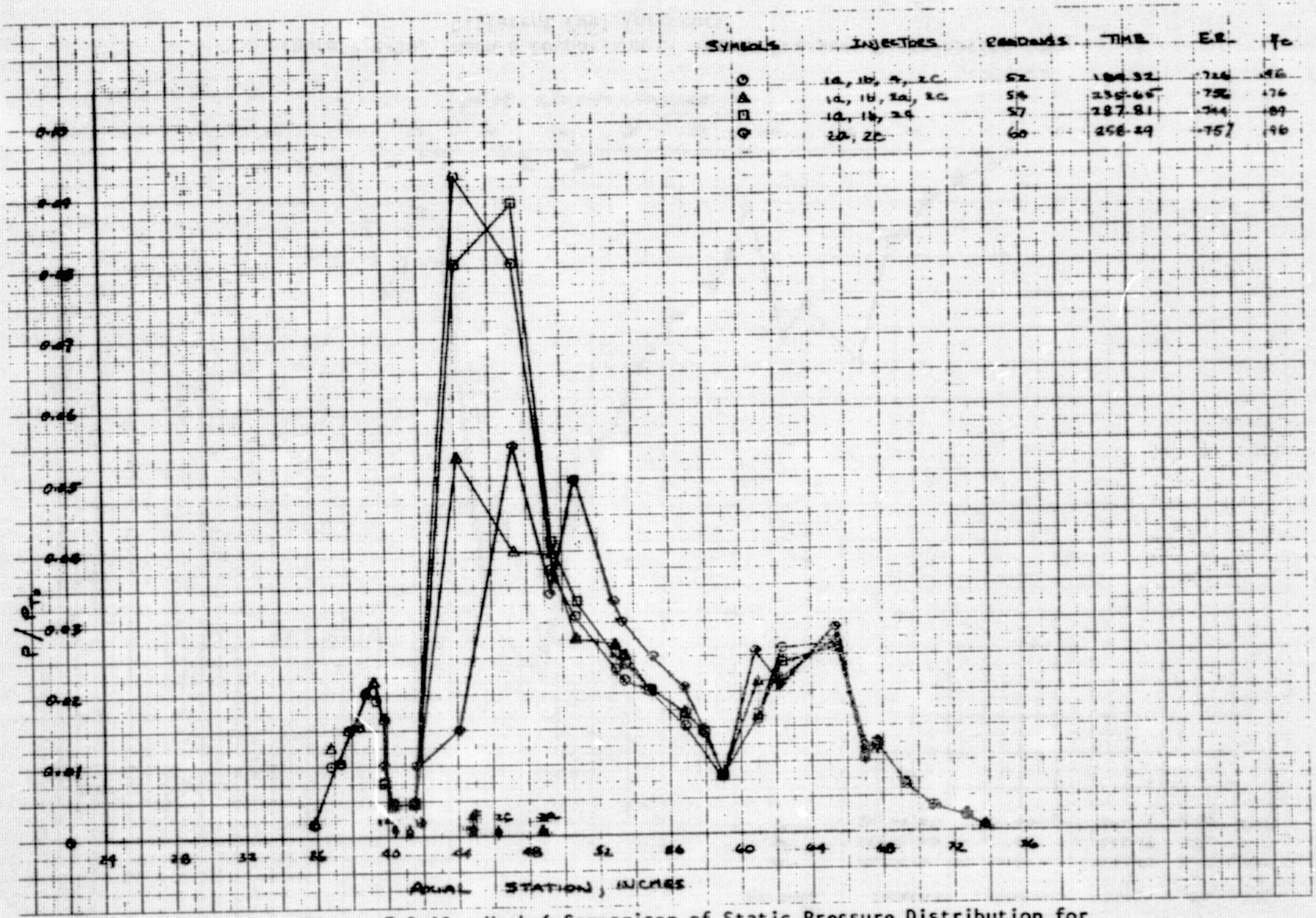

Figure 7.2-19. Mach 6 Comparison of Static Pressure Distribution for Different Fuel Injectors

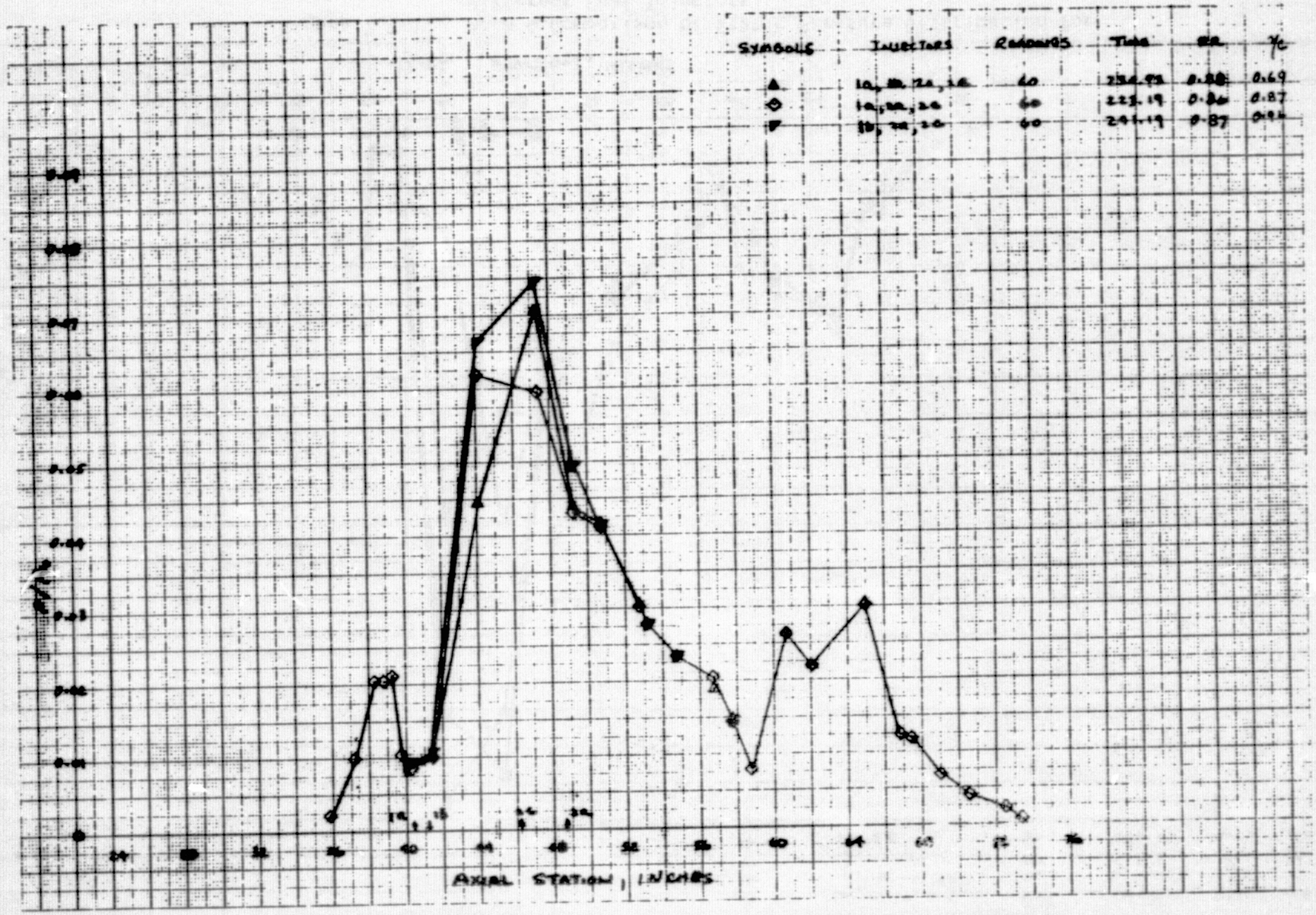

Figure 7.2-20. Mach 6 Comparison of Static Pressure Distribution for Different Fuel Injectors

reasoning may be applied in explaining the pressure distribution shown in Figure 7.2-20 where the best performance (highest pressure) was obtained using injector 1b alone for the first stage and injectors 2a, 2c for the second stage.

In order to investigate the combustion process, two typical cases were selected for comparison. The first case (reading 52, time 189.32) used injectors 1a, 1b, 4, and 2c to produce combustion nearest the inlet throat at a small area ratio, while the second case (reading 60, time 258.29) used injectors 2a and 2c to produce a delayed supersonic combustion at a larger area ratio. The computed one-dimensional Mach number and total pressure recovery were plotted, versus combustor length, in Figure 7.2-21. Total temperature and combustor efficiency were plotted in Figure 7.2-22. In Figure 7.2-21, the first case (Symbol O) produced a significant total pressure loss ($P_T/P_{T_2} = 0.44$) and corresponding drop in Mach number prior to significant temperature rise near Station 42. This loss may be attributed to the duct loss, the first stage fuel injection, induced shock and mixing losses, and disturbance caused by the interaction between stages. The Mach number decreased to 1.6 from the combustor inlet Mach number of 2.55. Combustion took place at Mach numbers between 0.75 and 1.75. The second case (injectors 2a and 2c, Symbol ◇) also produced a significant pressure drop prior to temperature rise (Station 46). It is interesting to note that a significant portion of this loss is due to the duct loss (0.5) without fuel injection, indicated by the diamond symbols. The fuel injection caused an additional loss, reducing the pressure recovery to 0.4 and the Mach number to 1.5. Thus, the anticipated high Mach number at a larger flow area in the second case was not attained. The combustion process occurred at flow Mach numbers ranging from 1 to 1.5. Therefore, both the Raleigh loss due to the heat release and pressure loss prior to heat release, for these two cases, were about the same as indicated by the similar total pressure recovery at the combustor exit.

It is also interesting to note that the flow in reading 52 was decelerated from supersonic to subsonic Mach numbers and then accelerated from subsonic to supersonic Mach numbers. This mixed mode of operation appeared to be stable and attained high combustor efficiencies. The choke point (M = 1) would move upstream if more heat was released, and would eventually unstart the inlet.

In Figure 7.2-17, for injectors other than 1a, 1b, 2a, 2c, the combustor efficiency increased with equivalence ratio as long as the equivalence ratio was less than unity. It appeared that turbulence and stage interaction was enhanced by increased fuel flow, resulting in more efficient combustion.

The best combustor performance was achieved by using injectors 1b, 2a, and 2c near equivalence ratio of unity.

Because of limited testing time, investigation of fuel optimization at Mach 7 was less extensive than that at Mach 6. At Mach 7, only three injector configurations with two-stage combustion were investigated, as shown in Table 7.2-4. Unfortunately, equivalence ratios and testing conditions for these three cases were not identical, making the comparison more difficult. Furthermore, as discussed in Section 7.7.2, the combustor pressure integrals were

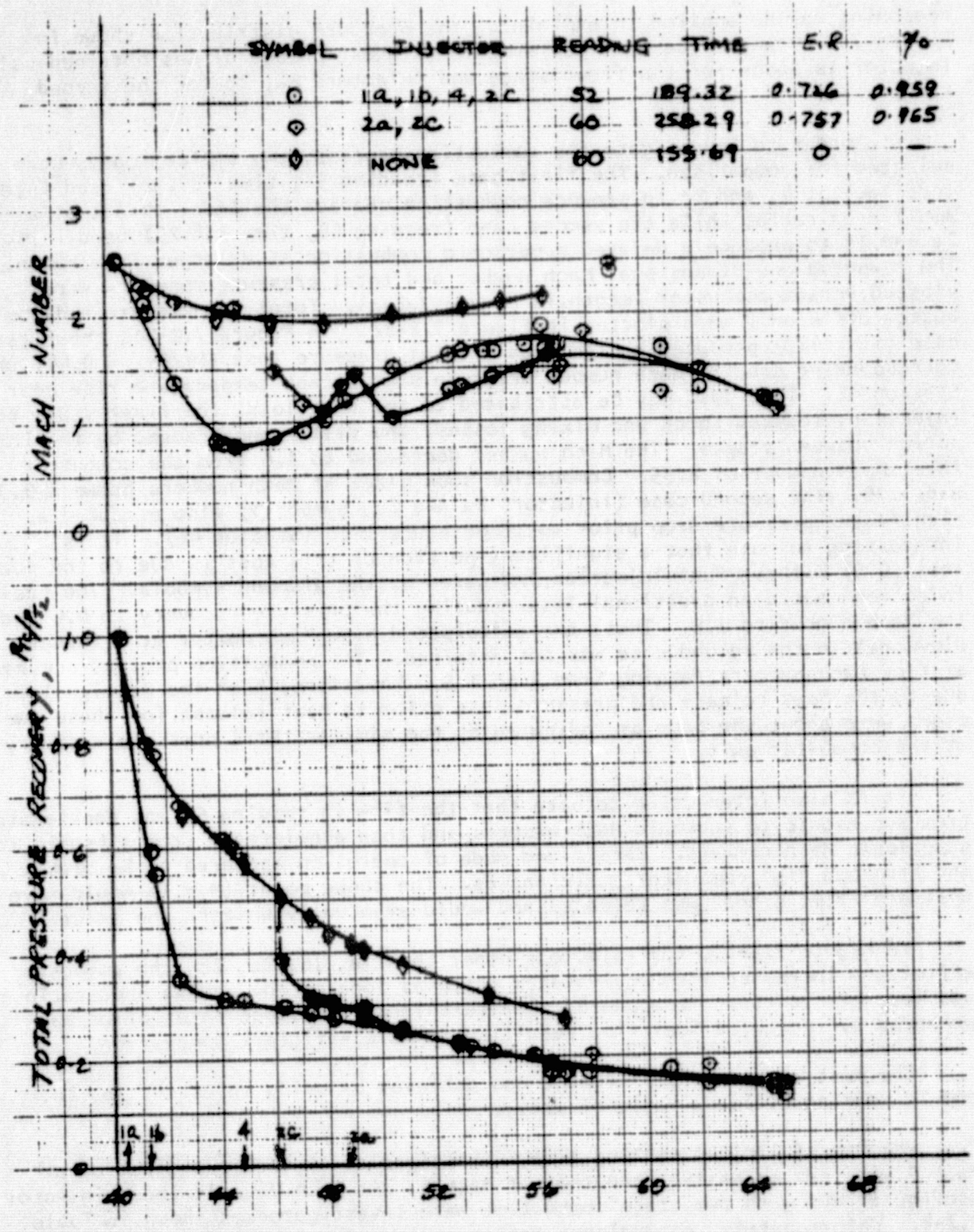

Figure 7.2-2i. Mach 6 Combustor Flow Parameters

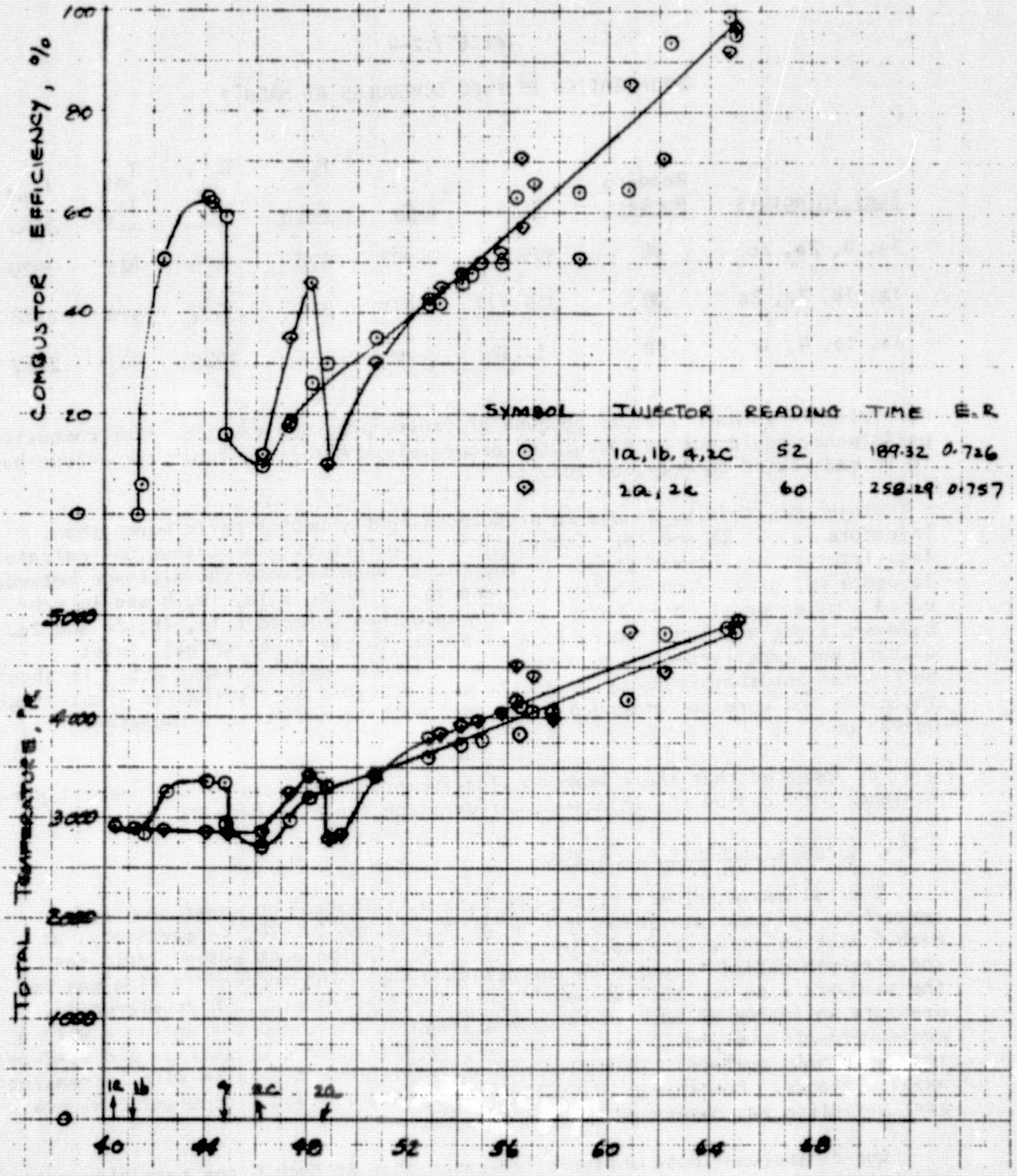

Figure 7.2-22. Mach 6 Combustor Flow Parameters

TABLE 7.2-4

OPTIMIZATION OF FUEL SCHEDULES AT MACH 7

Fuel Injectors	Reading Number	Time	E.R.	P_{T_o}, psia	T_{T_o}, ^oR	T_m, lb_f	I_{sp}, sec
1a, 4, 2a, 2c	88	305.70	0.903	998	3086	826	1929
1a, 1b, 2a, 2c	89	310.173	0.891	998	3057	976	2286
1a, 1b, 4, 1c	90	230.52	0.769	995	2925	907	2267

not reliable in Mach 7 tests because of faulty pressure taps, so that combustor performance could not be calculated accurately. A more reliable comparison had to be made based on measured thrust.

Injectors 1a, 1b, 2a and 2c produced slightly better performance than injectors 1a, 4, 2a and 2c. Examination of the pressure distribution indicated less interaction between stages in the latter case because the distance between 1a and 4 was greater than between 1a and 1b. Injectors 1a, 1b, 4 and 1c produced similar or slightly better performance than injectors 1a, 1b, 2a and 2c. However, since the latter were located closer to the inlet throat, inlet unstart was experienced at an overall equivalence ratio of about 0.8. It should be pointed out that injectors 4 and 1c were designed as alternative first-stage injectors and were not intended to be used with 1a and 1b in a two-stage operation.

It appeared that there were no significant differences in the overall performance produced by the injector configuration tests at Mach 7.

7.2.6 Effects of Angle of Attack

Typical measured wall static pressure distribution on inner cowl and on centerbody surfaces are shown in Figures 7.2-23 and 7.2-24, respectively, at Mach 6 with an angle of attack of 3 deg. The flag on each symbol indicates the circumferential location of the pressure tap. The zero-angle flag was on the windward side and the 180-deg flag on the leeward side. Circumferential pressure variation on both surfaces was large at the combustor entrance with a maximum-to-minimum pressure ratio of 1.63 on the inner cowl surface and 1.42 on the centerbody surface. This flow non-uniformity was decreased with increasing axial distance. Downstream of Station 50, no significant circumferential pressure variation was observed.

One-dimensional data analysis indicates that at Mach 6 the mass flow ratio and inlet pressure recovery were decreased to 93 and 25 percent, respectively, from 98 and 38 percent at the zero angle-of-attack case. The combustor efficiency was also decreased to approximately 68 percent from 95 percent. The low

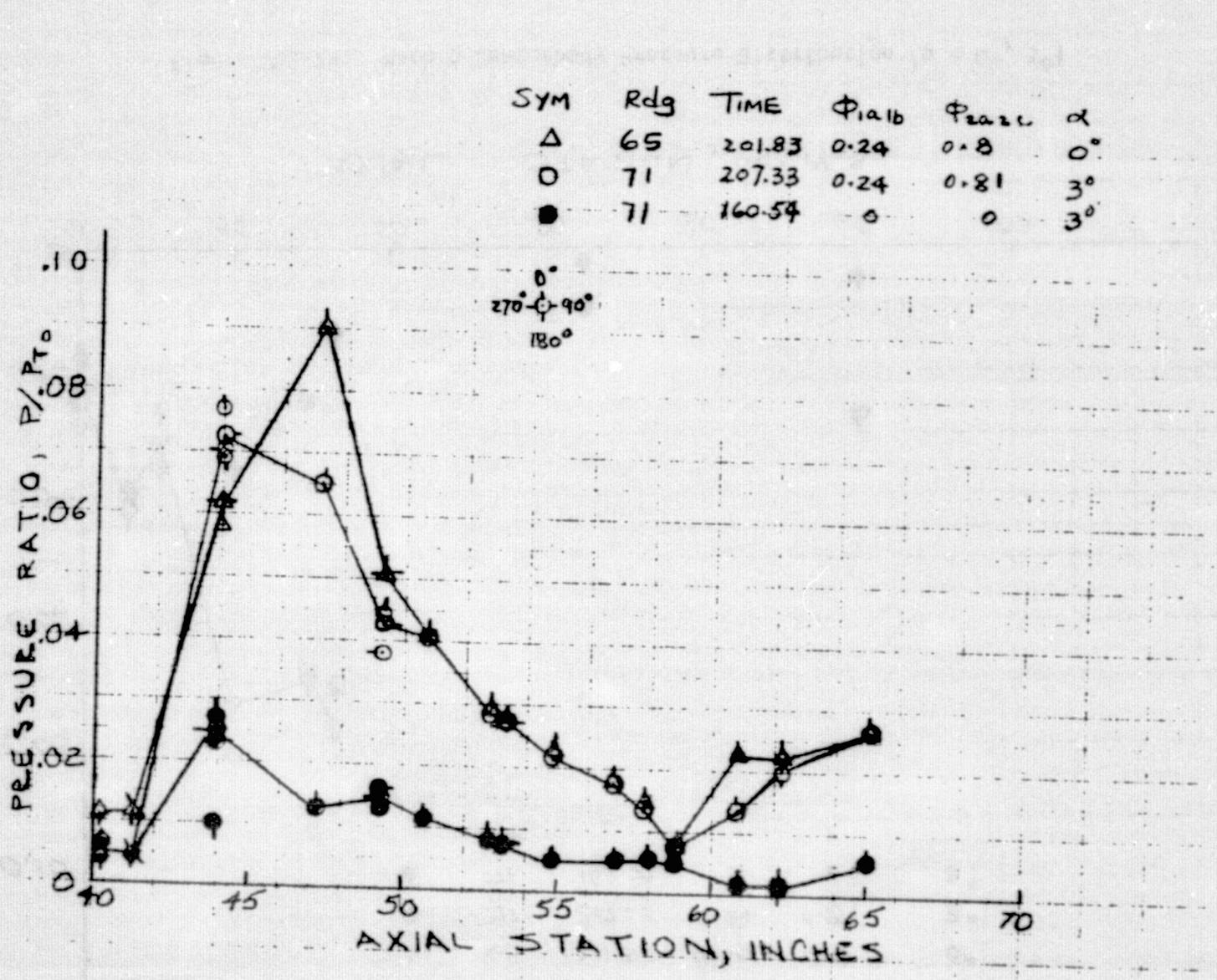

Figure 7.2-23. Mach 6 Inner Cowl Pressure Distribution (α = 0°, 3°)

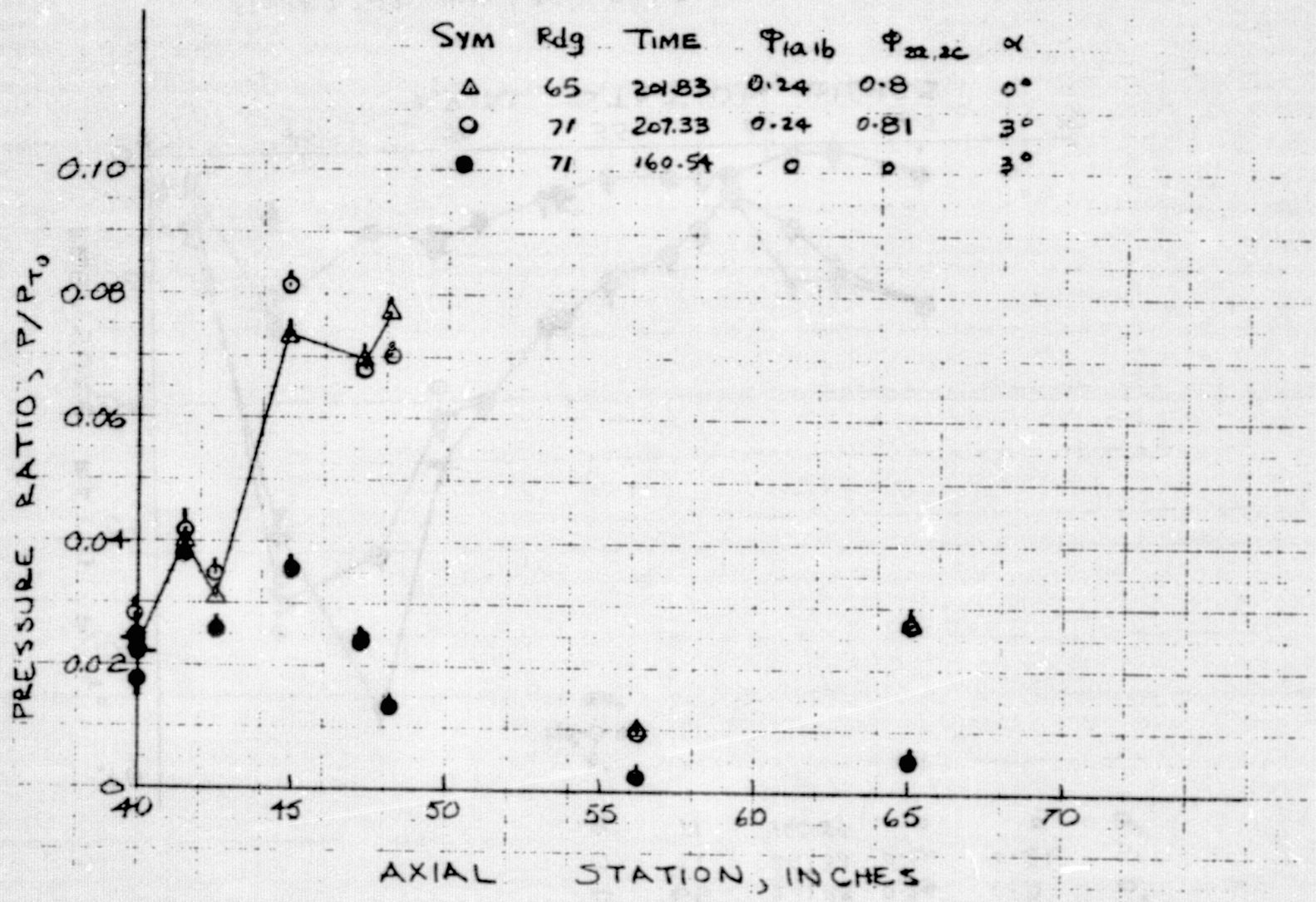

Figure 7.2-24. Mach 6 Centerbody Pressure Distribution ($\alpha = 0^\circ, 3^\circ$)

combustor efficiency was probably the result of non-uniform distribution of inlet flow. With choked fuel flow injectors, the fuel-air mixture might be lean on the windward side and rich on the leeward side, resulting in poor mixing and low combustor efficiency. The measured engine performance was a function of injector configuration and decreased approximately 15 to 30 percent from the zero angle-of-attack case as indicated in Section 7.7.

A similar trend was observed at Mach 7 and Mach 5. At Mach 7 the supersonic inlet pressure recovery was decreased to 22 percent, at Mach 5 it decreased to 39 percent. The overall engine performance was decreased approximately 15 percent from the zero angle-of-attack case. The static pressure distribution at Mach 7 is shown in Figure 7.2-25. A typical static pressure distribution at Mach 5 is shown on Figure 7.2-26.

7.2.7 Flow Field Between Struts

The static pressure drop on the inner cowl surface downstream of the centerbody step may be explained by the expansion waves emanating from the step. This is shown in Figures 7.2-27 and 7.2-28 with and without fuel addition, respectively, for three different spike positions. The average static pressures are normalized with respect to the inner cowl average pressure at Station 53. In both figures, it demonstrates that the location of the low-pressure region shifts with the spike translation. The low pressure region is much closer to the step for fuel injection cases indicating steeper expansion waves due to lower Mach number from upstream heat addition. The existence of a recompression shock is evidenced by the pressure rise downstream of the step on the centerbody surface, as shown in bottom two sketches in Figure 7.2-27, where the centerbody has uncovered one set of the static pressure taps. The pressure rise downstream of the low pressure point on the inner cowl surface for the fuel addition case is steeper than the no-fuel-addition case, which led to believe that the flow from the second stage combustor might have been quenched locally by the expansion waves and again ignited by the recompression shock. This type of combustion is very similar to a shock-induced combustion process which would cause the recompression shock to assume a steeper angle due to increased back pressures. This is possible if the flow normal-component downstream of the shock is subsonic. Unfortunately, the number of static pressure taps was not sufficient to formulate a complete flow field. However, indication of the increased wall temperature in this region as discussed in Section 7.6 further substantiates the observations made above.

The strut leading edge shock from the observed heat patterns on the centerbody skin is shown in Figure 7.2-29. It indicated that the shock was close to the strut body and did not interfere with the static pressure measurements which were used for previous analysis located on the centerline between the struts.

7.2.8 Effects of Inlet Gas Composition

Because of the facility heater deficiency, the Mach 7 true temperature of 3770°R was not achieved. The tests were conducted, instead, at a reduced temperature (3000°R approximately). In order to determine whether the combustion process was chemical-kinetics-limited or mixing-controlled at the reduced temperature, an attempt was made to vary the freestream oxygen contents from 23.5 percent to

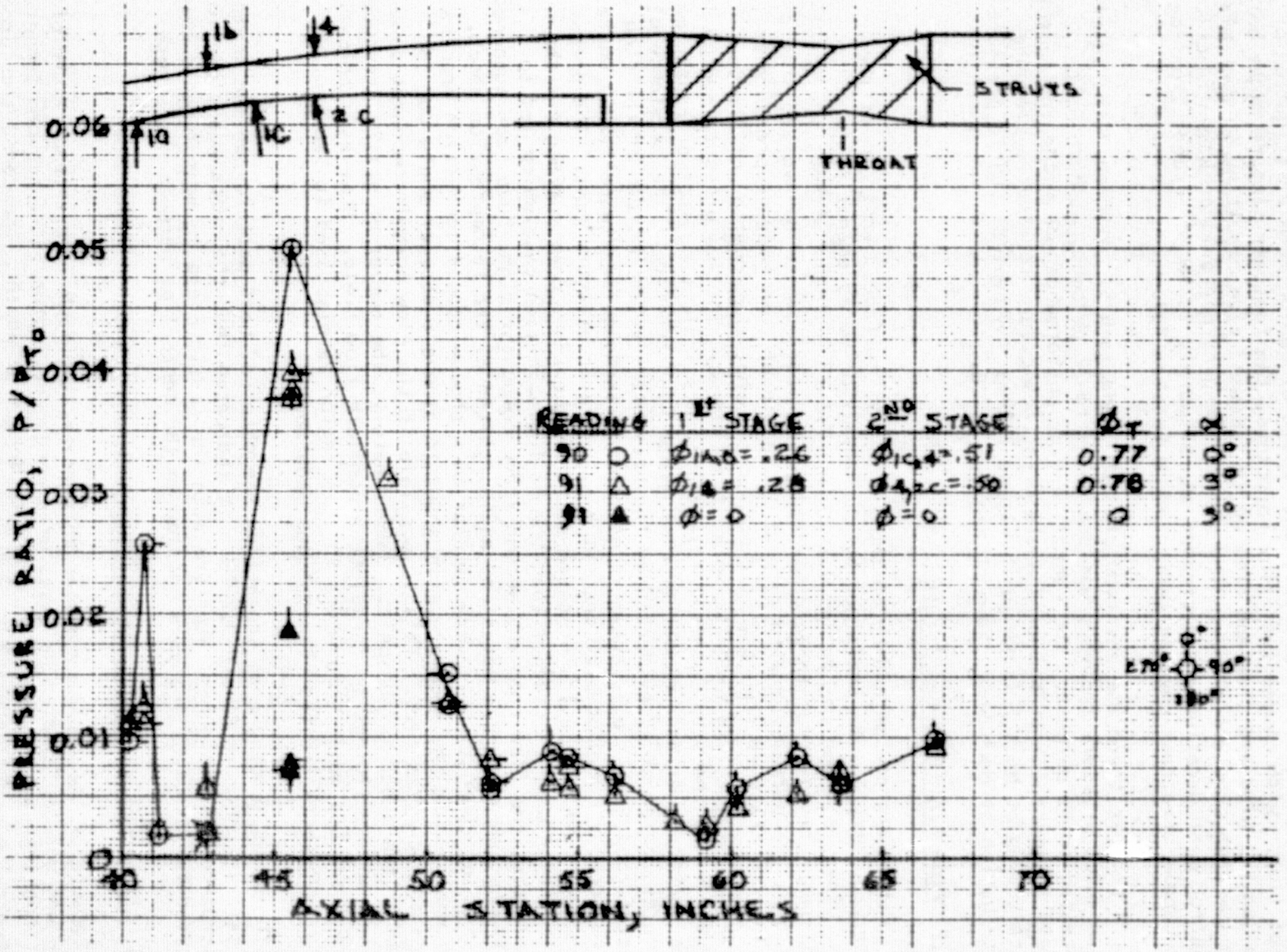

Figure 7.2-25. Mach 7 Inner Cowl Pressure Distribution (α = 0°, 3°)

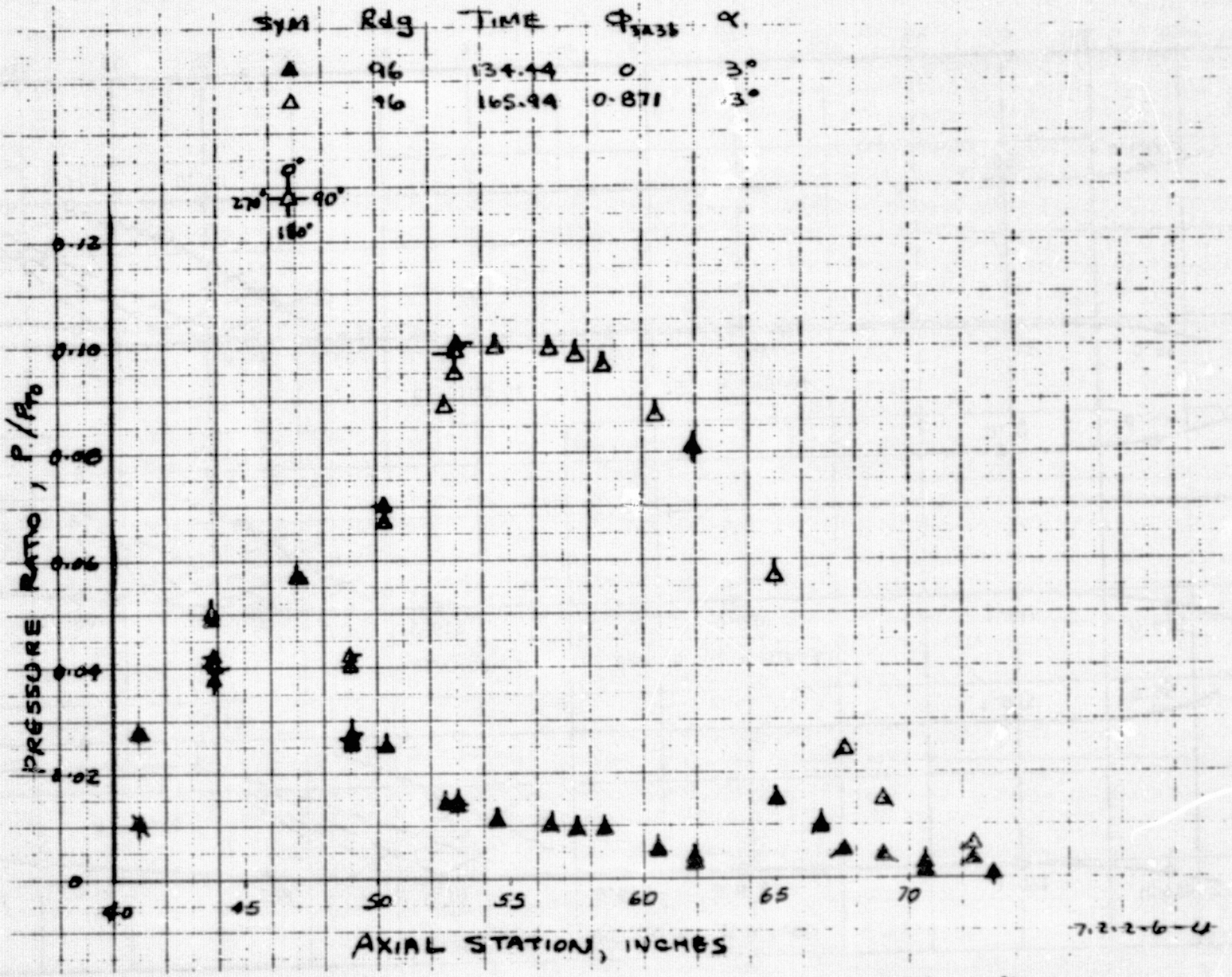

Figure 7.2-26. Mach 5 Inner Cowl Pressure Distribution (α = 3°)

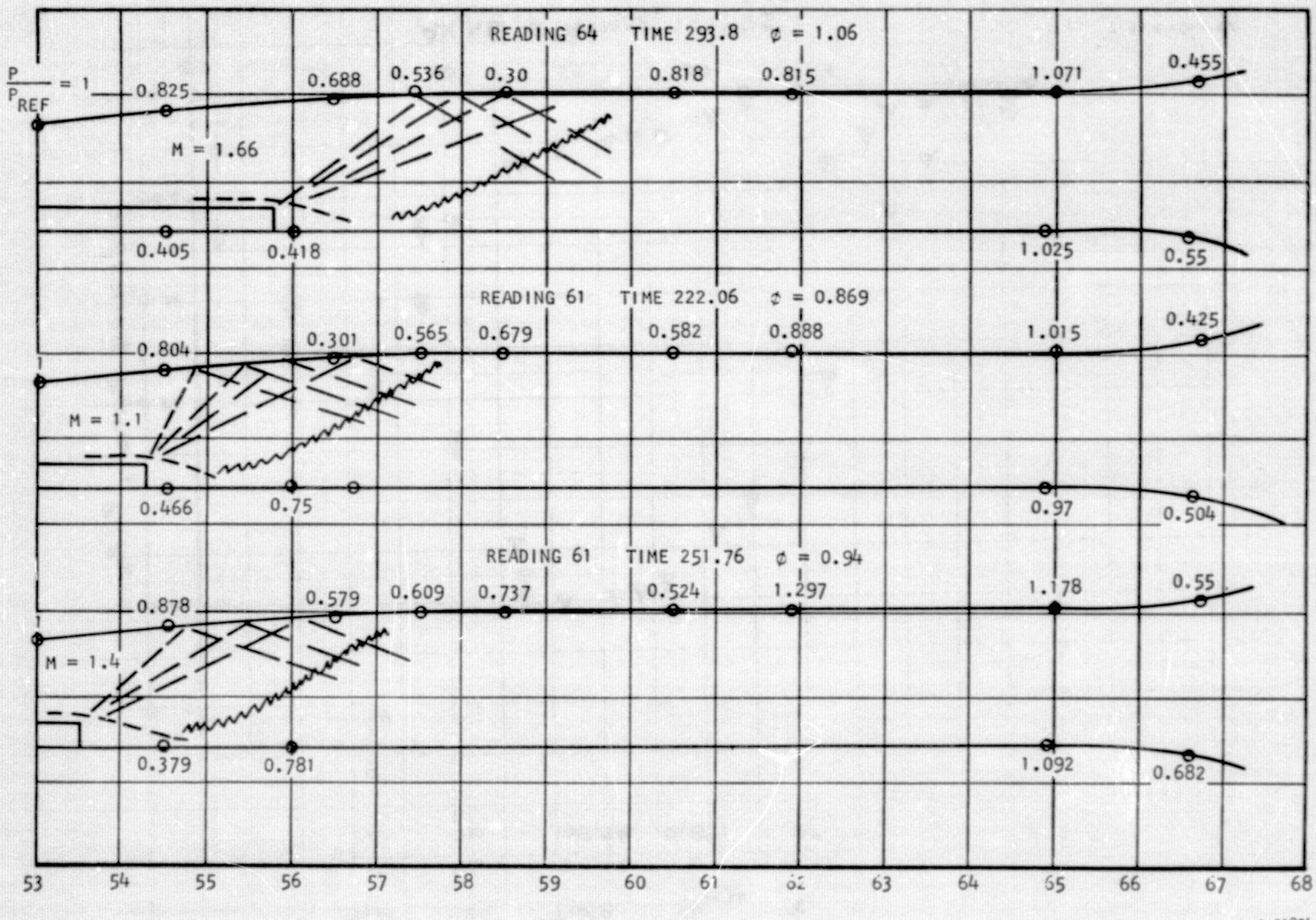

Figure 7.2-27. Flow Field Between Struts

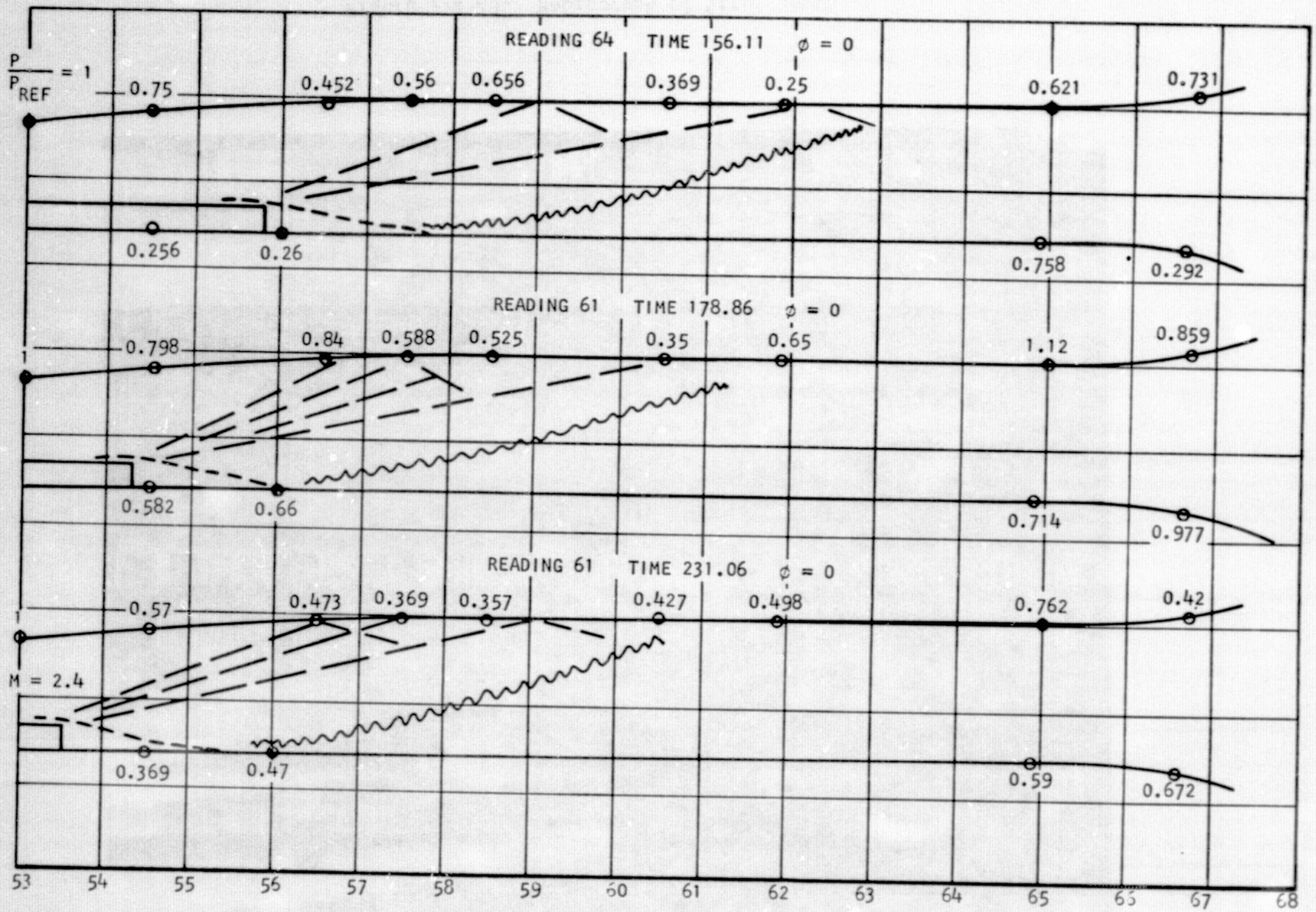

Figure 7.2-28. Flow Field Between Struts

S-92893

ORIGINAL PAGE IS
OF POOR QUALITY

Figure 7.2-29. Photograph of Strut Shock

19.5 percent by weight in reading 92. It was suggested that if the combustion were kinetic limited, the combustor performance would not be varied with the same amount of fuel injection, provided the fuel-air ratios do not exceed the stoichiometric value.

A typical comparison of pressure distribution on the centerbody surface is presented in Figure 7.2-30. As expected, the static pressure and the measured load cell force were lower with decreased oxygen content. Unfortunately, the overall equivalence ratio exceeded unity, which makes the argument less certain for lack of oxygen. It indicated, however, that lower pressure was observed prior to the second-stage injection, where equivalence ratio was about 0.5 indicating mixing limited flow existed up to Station 46. Overall combustor performance could not be assessed in this run because a large number of surface static pressure taps were missing.

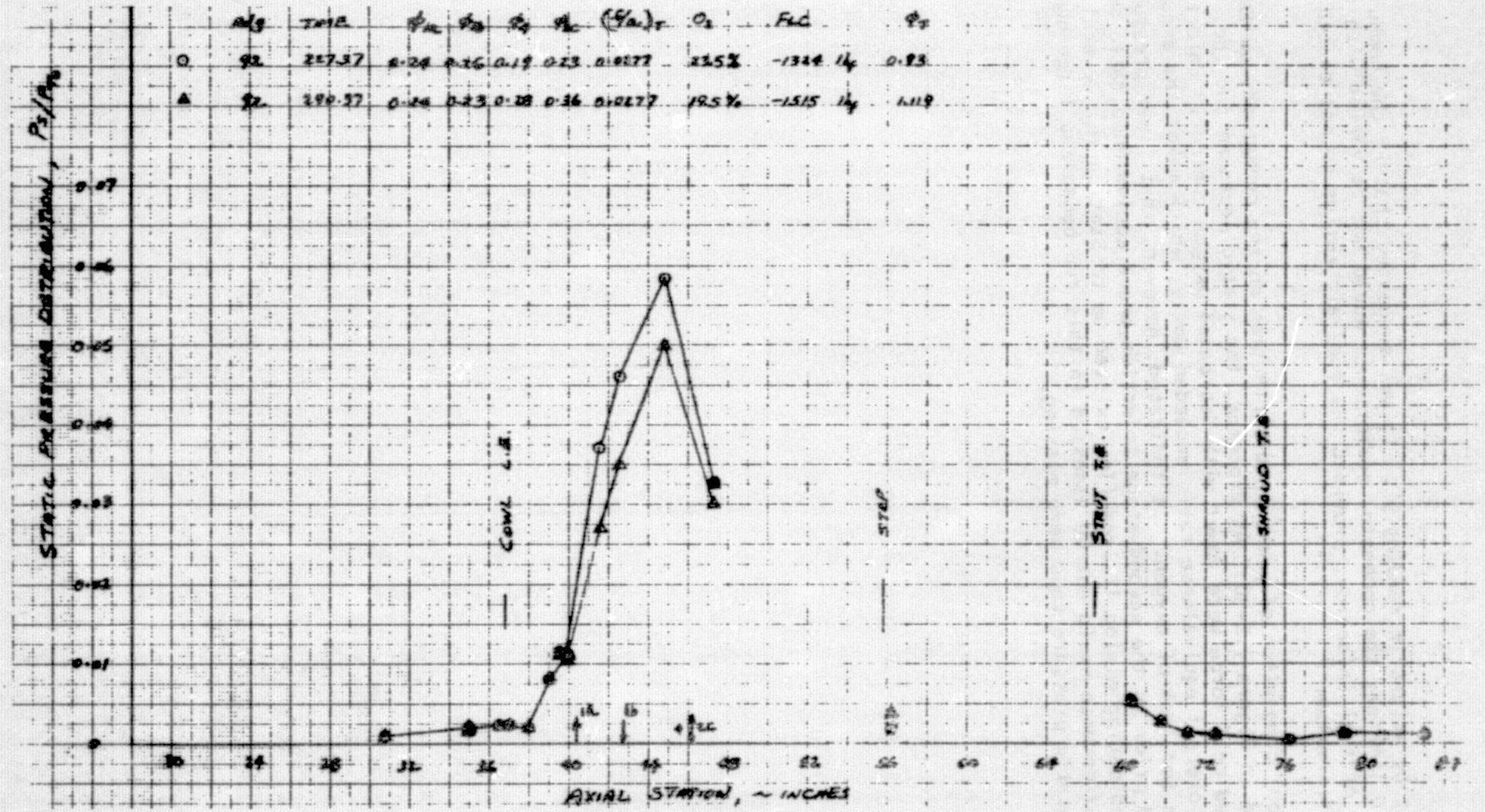

Figure 7.2-30. Mach 7 Effects of Inlet Gas Composition

7.2.9 Effects of Inlet Total Temperature

In reading 89 Mach 7 test, total temperature was reduced to determine its effect on combustor and engine performance. Fuel was injected from 1a, 1b, 2a, 2c at equivalence ratios less than unity. The only steady state data available with this configuration that indicated significant combustion was at freestream total temperatures of 2720°R and 2410°R. To get a larger spread in total temperature, data from reading 88 with injector combination 1a, 4, 2a, and 2c tested at 3090°R was also used. The pressure distributions on the combustor outer surface for these runs are shown in Figure 7.2-31 as the ratio of measured wall static pressure divided by freestream total pressure.

The static pressure upstream of the combustor step increased with decreasing temperature. At injector 1a there was a sharp peak pressure rise similar to the case in Mach 6 tests when the spike was translated forward. It was pointed out in Section 7.2.4 that injectors were spaced too far apart for strong interaction to take place and that the observed pressure peaks were due to local disturbance near individual injectors.

Downstream of the centerbody step the pressures at 3090°R and 2720°R behaved similar to those Mach 6 supersonic combustion mode, but at 2410°R the pressures were similar to the Mach 6 subsonic combustion mode, where pressure increased steadily to a peak value just ahead of the thermal throat and then decreased. Since static pressure rise ratio is directly proportional to the ratio of temperature rise to stream total temperature,

$$\frac{\Delta P}{p} \propto \frac{\Delta T}{T_T}$$

At 2410°R freestream total temperature, the pressure rise in the strut region must have been high enough to choke the combustor exit and create a subsonic region ahead of the thermal throat.

Reliable combustor parameters could not be obtained in reading 89 because of faulty pressure taps as discussed in Section 7.7.2. An attempt was made to insert two pressure points between Stations 45.5 and 50.7, as shown by the dotted line in Figure 7.2-31, in order to obtain some estimation of flow parameters. Figure 7.2-32 shows the results of this adjustment. As expected from pressure distributions, the combustor was choked at 2410°R.

The total temperature plot in Figure 7.2-32 (symbol Δ) showed that no significant combustion occurred between injector 2c and the strut leading edge, where the flow area increased very rapidly. This indicated that good combustion in a diverging duct was difficult to achieve as previously experienced in two-dimensional combustor tests.

For all cases, large total temperature rises occurred in the strut region. This was similar to what occurred at Mach 6. The exit total temperatures were, however, 300°R lower than at Mach 6 even though the tests were conducted at Mach 6 freestream temperature.

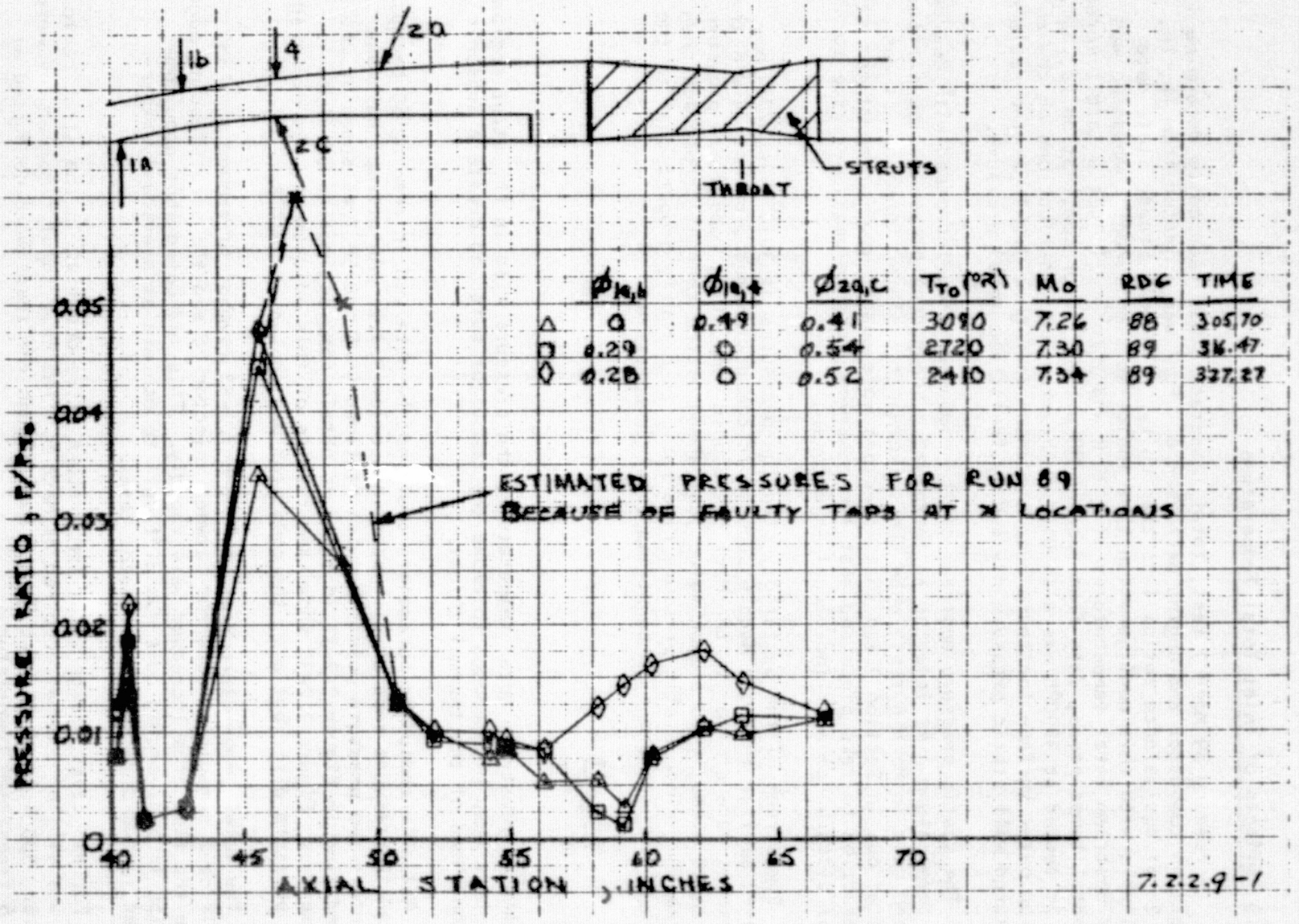

Figure 7.2-31. Mach 7 Effect of Inlet Total Temperature (Pressure Distribution)

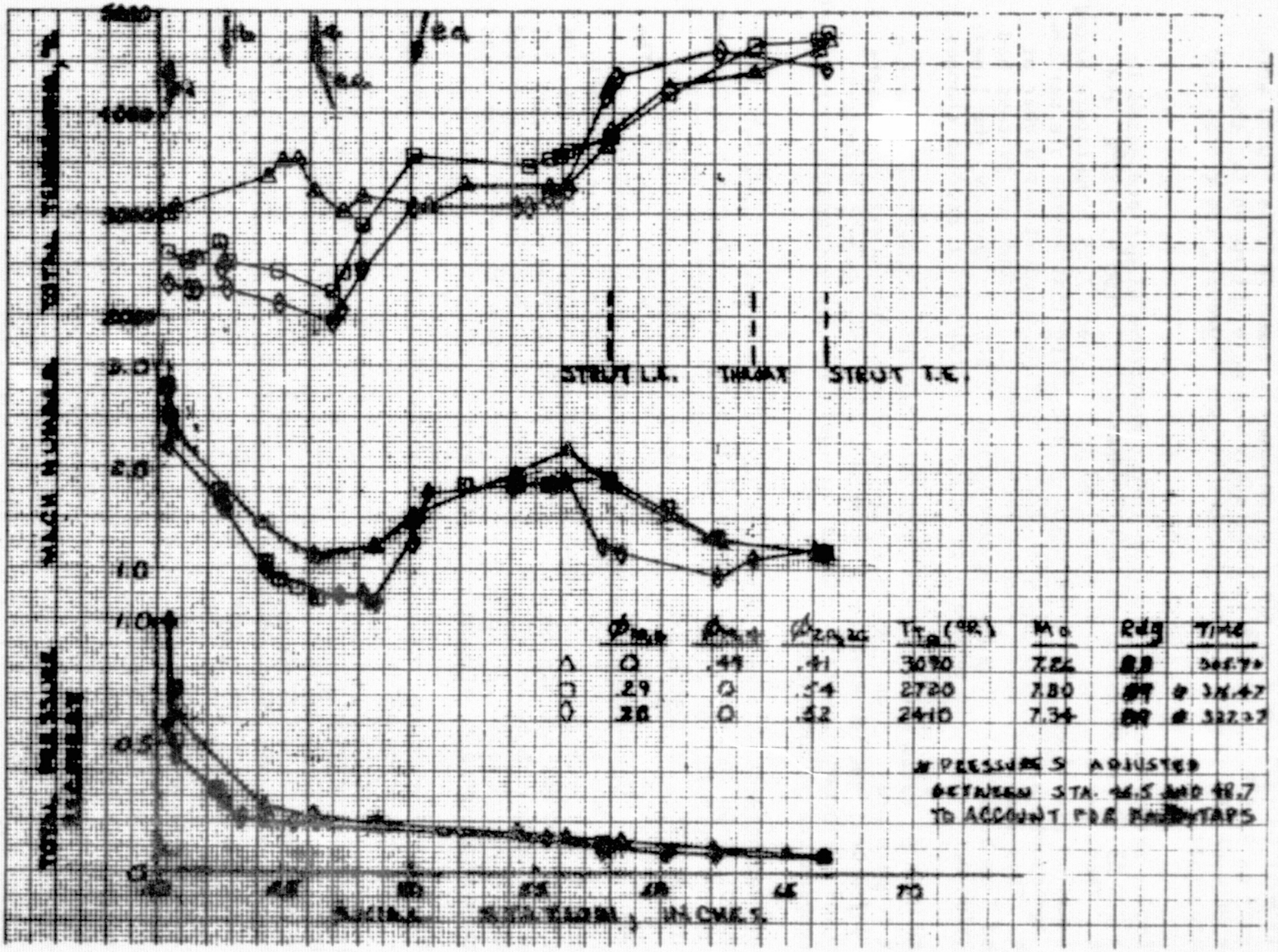

Figure 7.2-32. Mach 7 Effect of Inlet Total Temperature (Flow Parameters)

It must be realized that the flow parameters shown in this figure were not exact at 2720°R and 2410°R because pressures were estimated for the region between the second stage injectors 2a, 2c. However, the trends are probably realistic.

Engine performance obtained from thrust measurements are presented in Figure 7.2-33 for three different total temperatures, 3100°R, 2720°R, and 2400°R. These performances were corrected to true mach 7.25 temperature based on discussion presented in Section 6.7. It indicated that reasonable performance agreement was obtained between 2720°R and 3100°R, but it was higher at 2400°R. This supports the early observation that the combustion process had changed from supersonic to subsonic combustion at 2400°R, thereby, the linear correction method was not adequate to account for combustion process changes.

At Mach 5, tests were conducted at both true temperatures and at Mach 6 flight temperatures. High-temperature tests were conducted with the supersonic injectors, low temperature tests mostly with the subsonic injectors. The engine performances were presented in Figure 7.2-34, as compared with Mach 5 true-temperature performances.

In reading 95, tests with injectors 2a, 2c (supersonic injectors) were made at both high and low freestream total temperatures. Figures 7.2-35 shows the pressure distribution along the outer combustor surface at freestream total temperatures of 2230°R and 2940°R at lean equivalence ratios of 0.66 and 0.70 respectively. The pressure distributions are vastly different. The one-dimensional flow parameters presented in Figure 7.2-36 showed that at 2940°R the flow was slightly supersonic past 2a. The Mach number gradually decreased due to heat release, and became transonic in between the struts. At 2230°R, the flow was rapidly decelerated just ahead of the first injector 2c and became subsonic between injectors 2c and 2a. The flow was re-accelerated past Mach 1 to supersonic. Further heat release between the struts decreased the Mach number to near unity at combustor exit.

As expected, when the measured thrust at 2940°R was corrected to 2230°R, it was lower by approximately 25 percent.

It may be concluded that for small temperature excursions and for similar combustion process, performance obtained at one test temperature may be extrapolated to another using the method outlined in Section 6.7. For large temperature excursions and/or different combustion process, corrected performance using this method is not recommended.

7.2.10 Combustor Performance

The combustor efficiency (η_c) is defined as the mass fraction of injected fuel reacted in chemical equilibrium required to satisfy the one-dimensional conservation equations and to match the measured wall static pressures.

$$\eta_c = \frac{W_{H_2 \text{ reacted}}}{W_{H_2 \text{ injected}}}$$

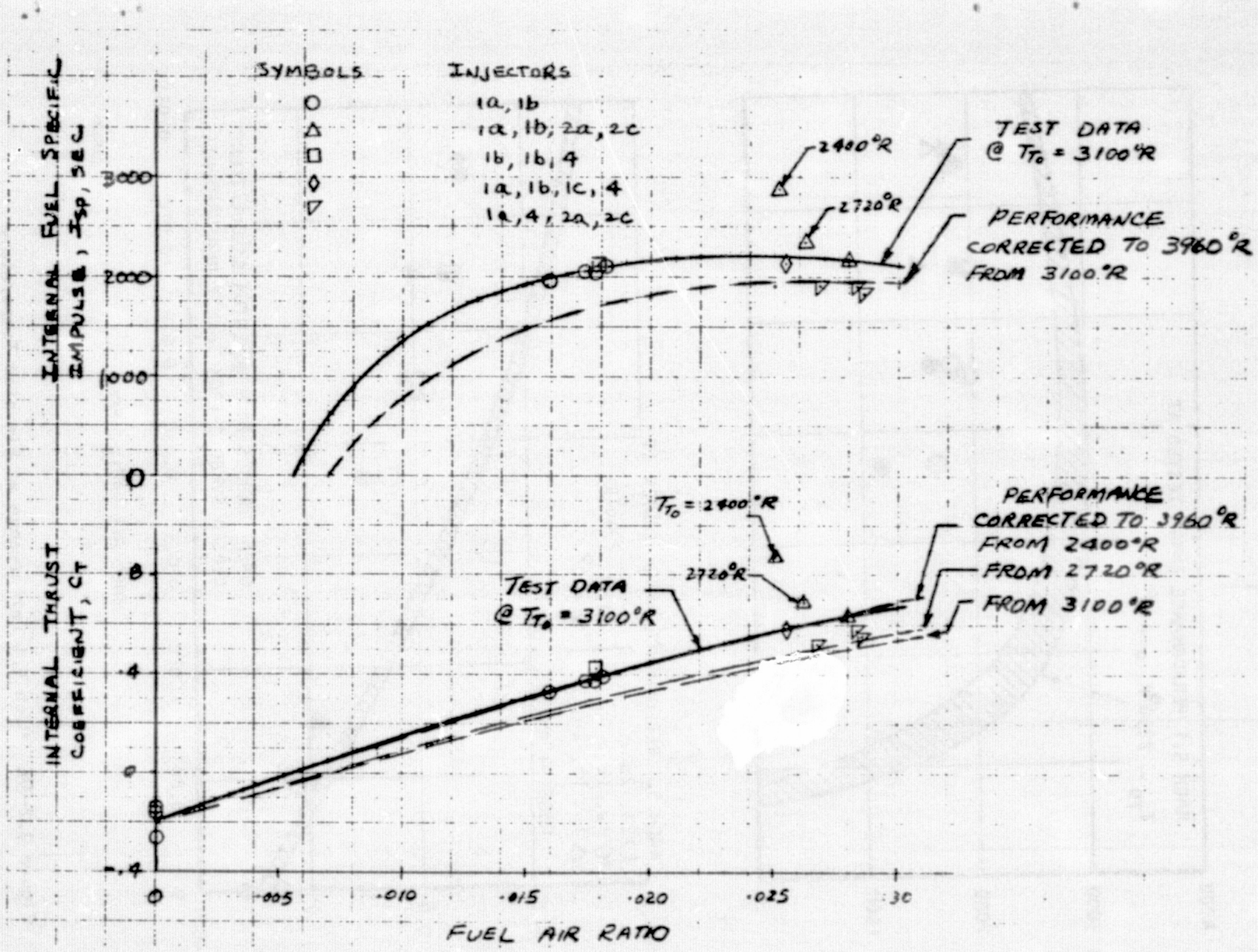

Figure 7.2-33. Corrected and Uncorrected Mach 7.25 Internal Performance

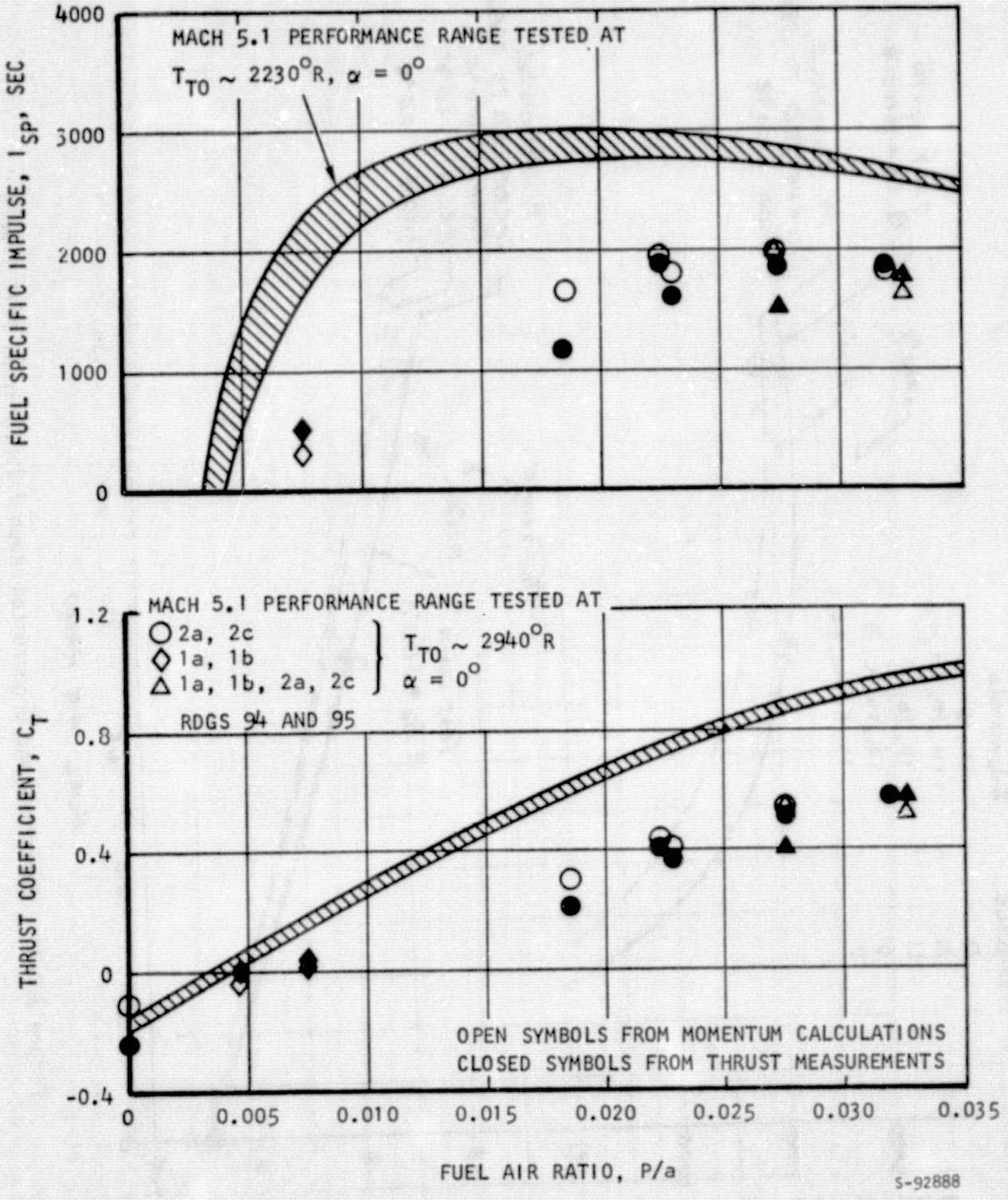

Figure 7.2-34. Mach 5.1 Performance at Elevated Temperature

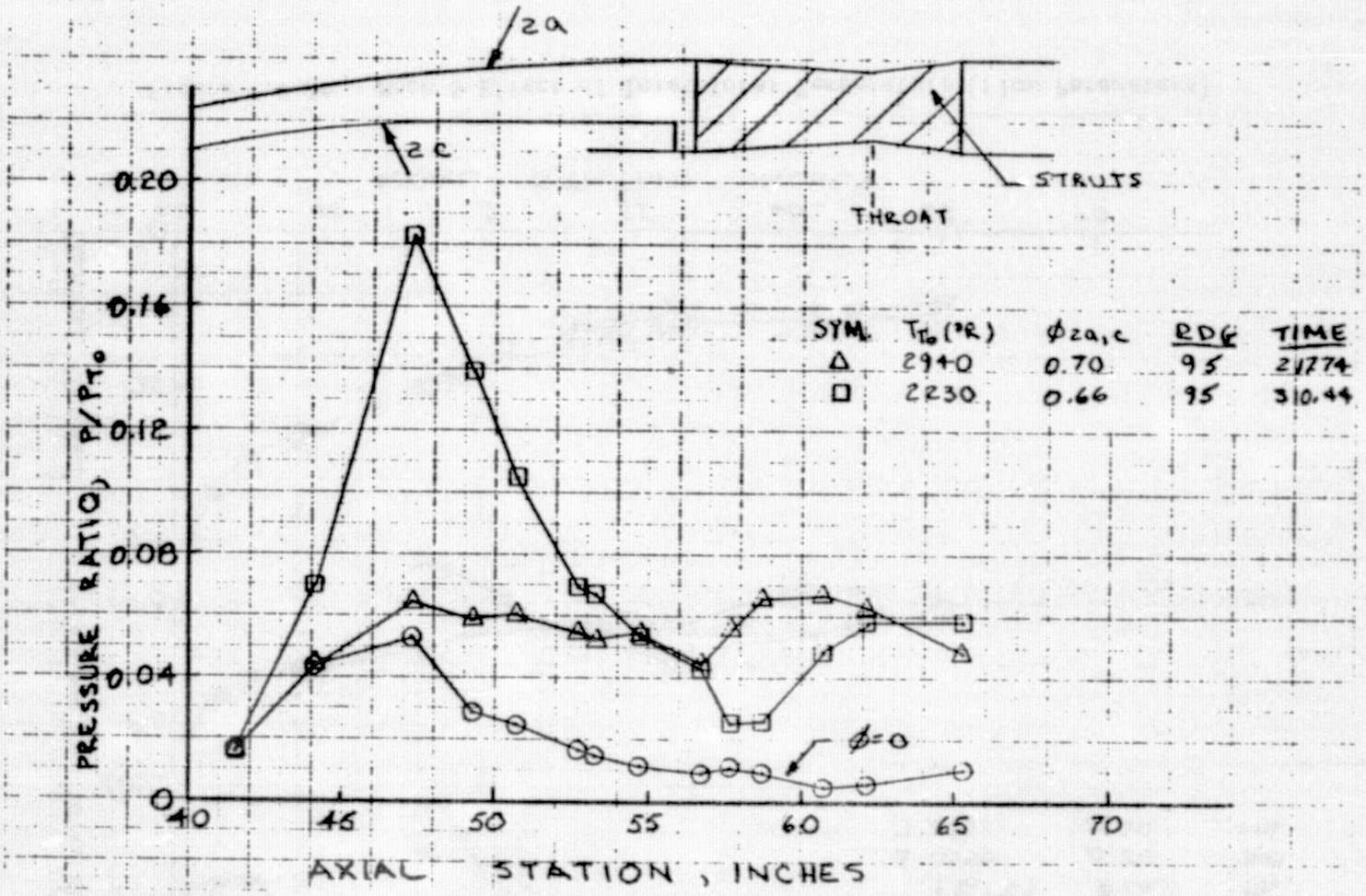

Figure 7.2-35. Mach 5 Effect of Inlet Total Temperature (Pressure Distribution)

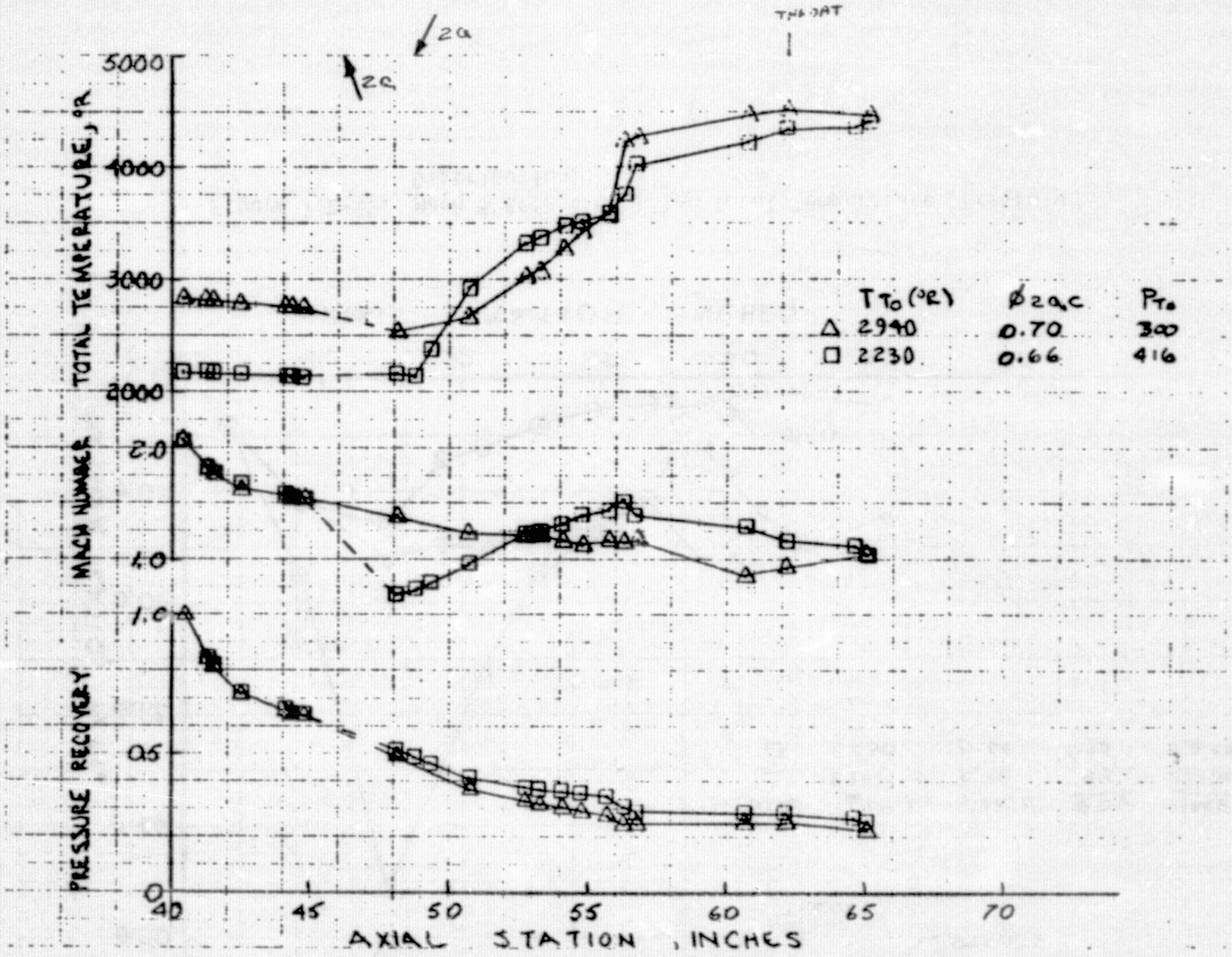

Figure 7.2-36. Mach 5 Effect of Inlet Total Temperature (Flow Parameters)

At Mach 6 the overall efficiency was high, and as anticipated, varied with the particular injectors used. Maximum efficiency up to 95 percent was obtained. A typical plot of combustor efficiency versus axial station is shown in Figure 7.2-37 for a case (Case 1) of supersonic combustion with fuel injection from 1b, 2a, and 2c at an equivalence ratio of 1.06. The fuel from injector 1b mixed and burned rapidly, reaching 74 percent efficiency in 4 inches. The overall efficiency decreased when additional fuel was injected from 2c and 2a. The efficiency plot in the region between injectors 1b and 2a is shown dashed because the flow was not truly one-dimensional, as evidenced by wide variations in lower and upper wall pressures. Once past this region, the flow was more uniform and thus the one-dimensional calculations were more representative. Combustor efficiencies with other injector configurations were presented in Section 7.2.5.

An error band is shown around the mean of the efficiency calculations. This band was based on an error analysis which included the inaccuracies of measured flow, wall static pressures, and heat loss, along with errors in calculating the combustor pressure integral.

It should be noted that there is a large scatter in the calculations in the strut region because of the method of calculating the strut force. For lack of measured pressures on the strut itself, the strut force was calculated from measured wall static pressures between struts and was linearly distributed along its length.

The combustion efficiency distribution for another case (Case 2) with fuel injection from 1b, 3a, and 3b is given in Figure 7.2-38. Note that the slope of combustion efficiency of fuel from 1b is not as steep as in Case 1. Also, there was a delay of about an inch before any combustion occurred.

7.2.10.1 Combustor Performance Parameters. Combustion efficiency alone is not sufficient to completely define the performance of supersonic combustor. The availability of energy to produce thrust must also be defined. The combustor total perssure loss in conventional subsonic combustion ramjets is not high, with most of the loss occurring in the inlet. In supersonic combustion a considerable total pressure loss occurs during combustion.

The sensitivity of combustor total pressure recovery with effective equivalence ratio is shown in Figure 7.2-39. Examination of the data shows a small variation in total pressure recovery with wide variations in effective equivalent ratio and injector configuration. However, small changes in combustion exit total pressure can produce large changes in engine thrust. Combustor exit total pressure is also difficult to measure directly. Therefore, the use of measured or calculated total pressure recovery to define a combustion process was assumed impractical. This figure indicated that the Mach 6 combustion process was better than the constant-pressure process with equivalence ratio greater than 0.5.

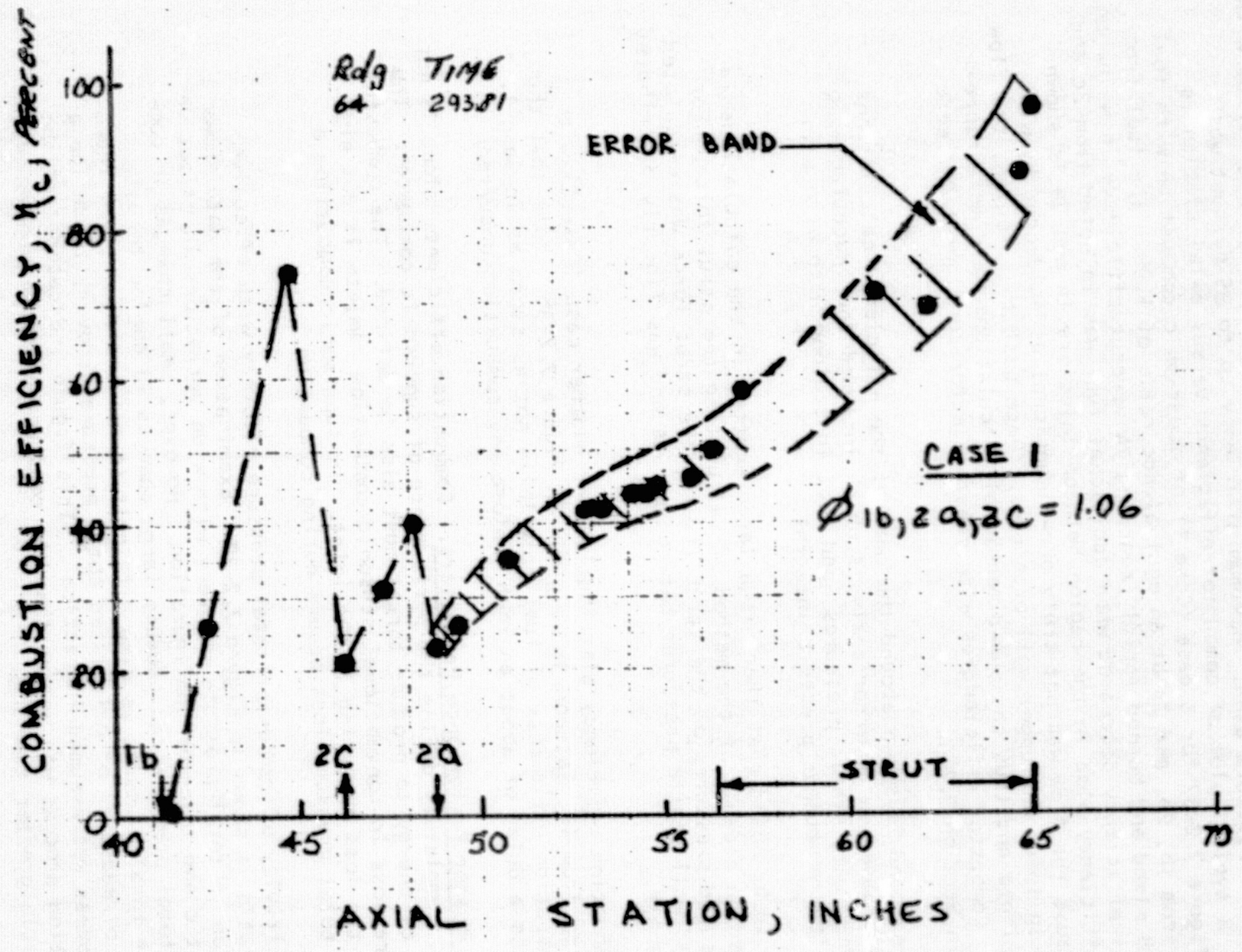

Figure 7.2-37. Mach 6 Supersonic Combustor Efficiency

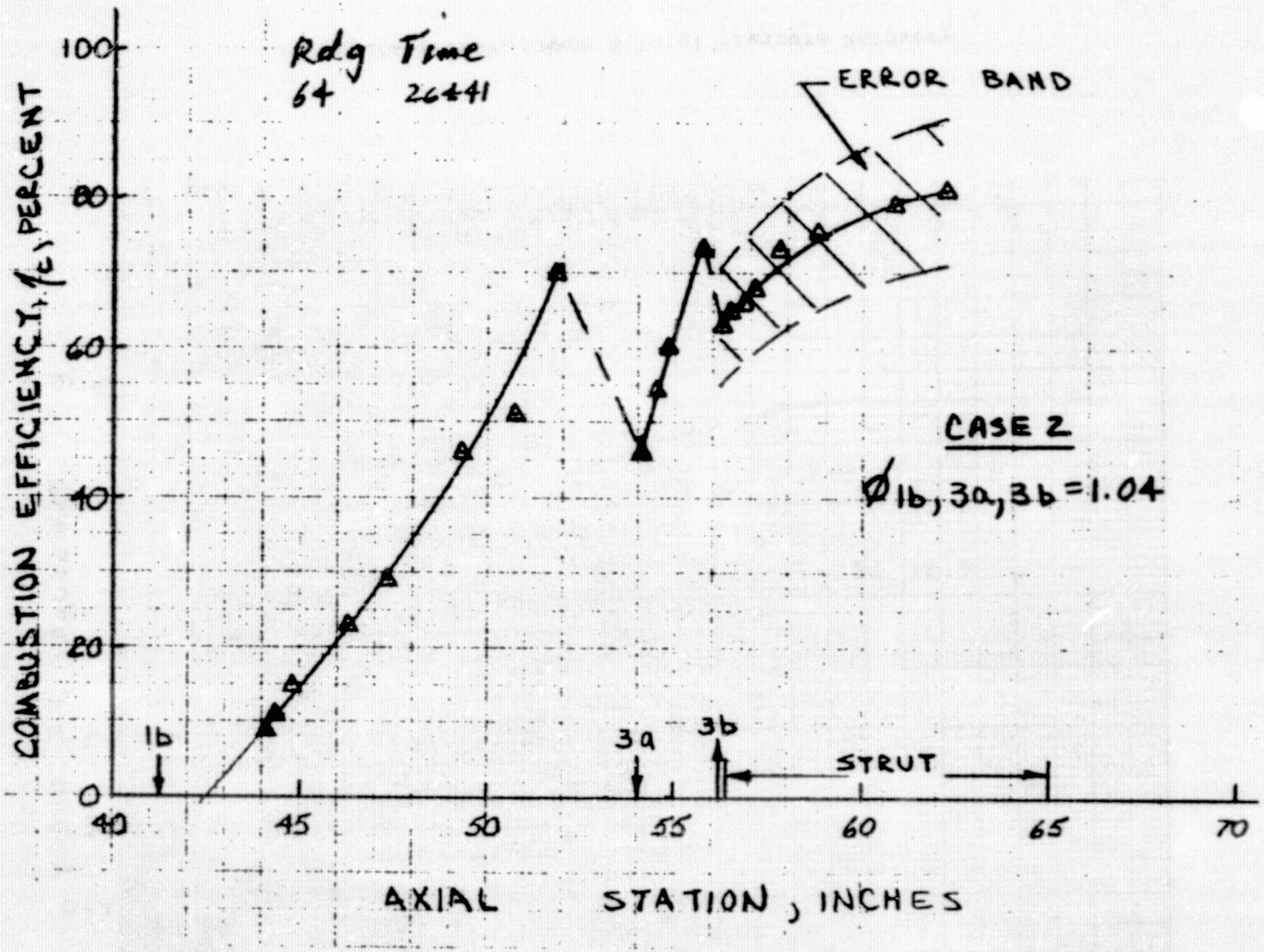

Figure 7.2-38. Mach 6 Super/Subsonic Combustor Efficiency

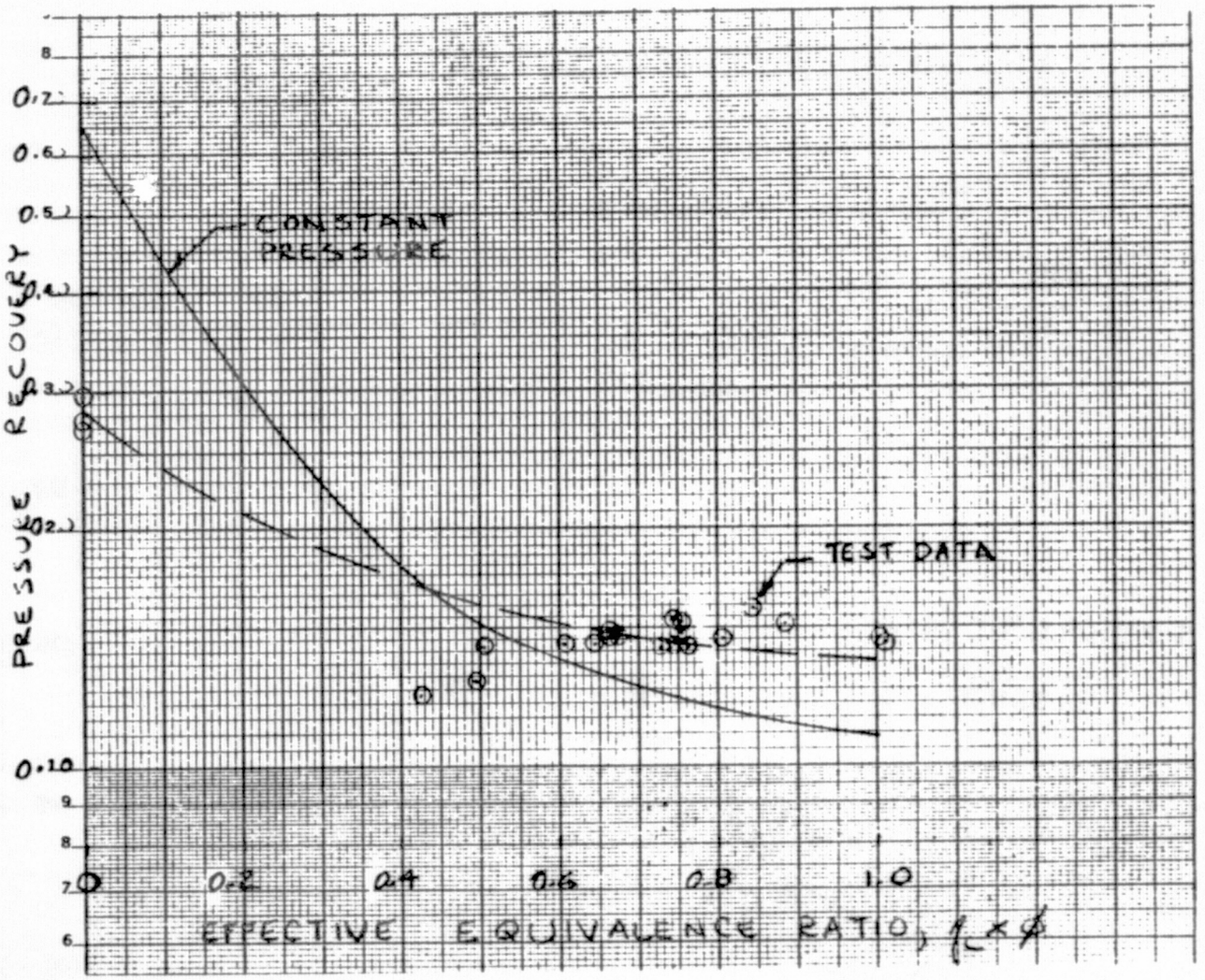

Figure 7.2-39. Mach 6 Total Pressure Recovery

The Crocco pressure-area relationship assumes that combustor pressure varies exponentially with area. The equation is

$$PA^{\frac{\epsilon}{\epsilon-1}} = \text{constant}$$

$$\text{with } \int PdA = (1 - \epsilon)(P_{exit}A_{exit} - P_{inlet}A_{inlet})$$

where $\epsilon = 0$ = constant pressure process

$\epsilon = 1$ = constant-area process

$\epsilon = -\gamma M^2$ = constant Mach number process

Once ϵ is defined, both combustor exit static pressure and the pressure integral $\int PdA$ are also defined. The problem with this correlation is that the pressure varies monotonically with the area. It implies that the area ratio alone will determine the pressure distribution. In an actual combustor, the pressure distribution is strongly affected by the injection, mixing, and chemistry process as well as the combustion geometry.

The actual combustion process in a diverging combustor could not be expressed by this simple equation. In fact, two different values of ϵ are required to represent the actual combustion process--one to match the value of $\int PdA$ and the other to match the static pressure at the combustor exit. For a typical example, to match the value of $\int PdA$ in AIM data required an ϵ of 0.07, whereas combustor exit static pressure was matched at an ϵ of 0.2. Therefore, the assessment of combustor process using a single value of ϵ is not practical.

Another parameter used to determine the combustion process is the pressure-area integral factor, K, defined as

$$K = \frac{\int PdA}{\frac{1}{2}(P_{exit} + P_{inlet})\Delta A}$$

Unlike the Crocco relationship, a single value of K would be able to match the thrust and pressure from test data and completely define the combustor exit condition.

The K-factor was calculated from several of the AIM tests having different injector configurations, and presented in Figure 7.2-40 as a function of effective equivalence ratio. Very good correlation was obtained for these Mach 6 tests because overall combustor losses did not vary significantly with injector configuration.

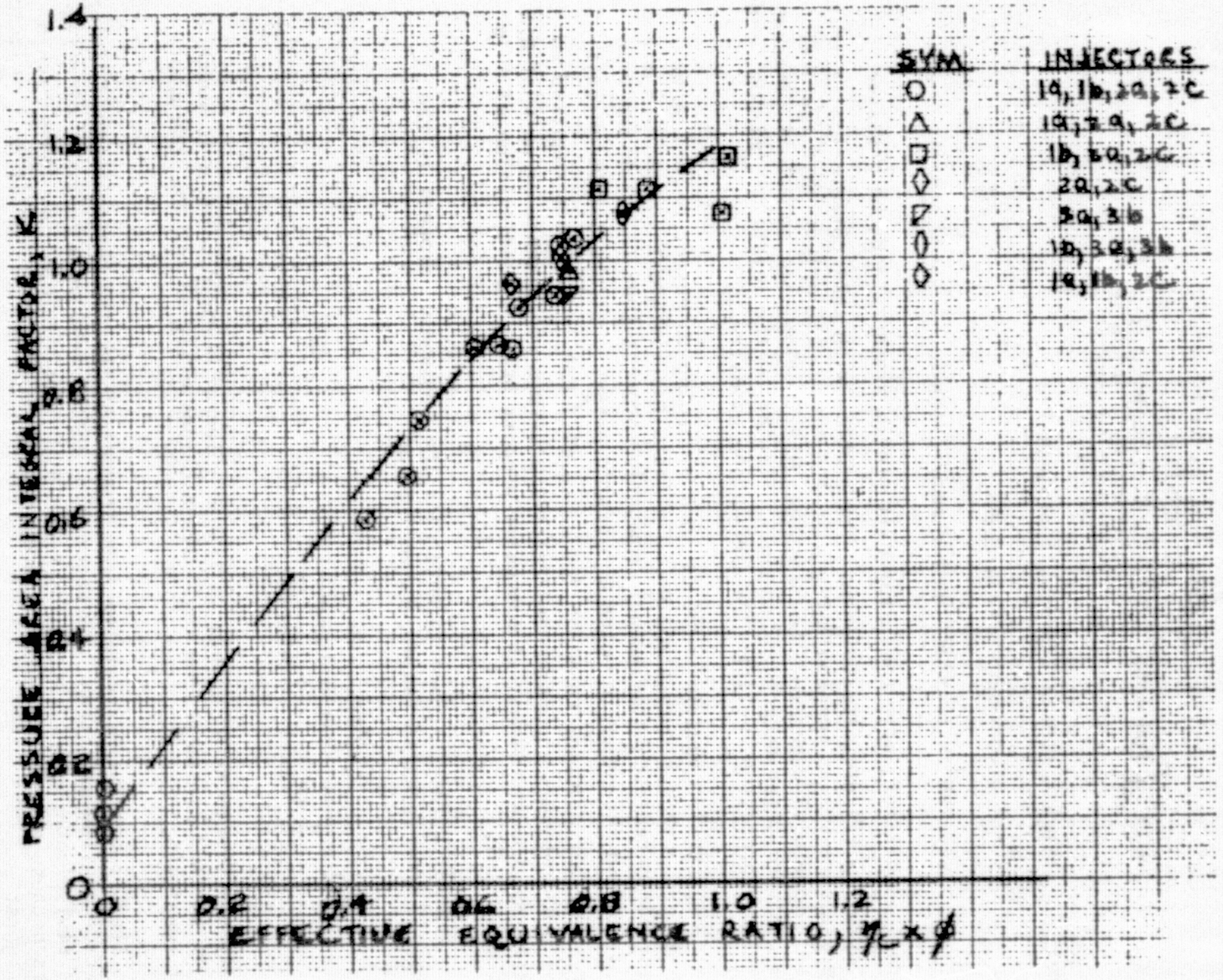

Figure 7.2-40. Mach 6 Combustor Pressure Area Integral Factor

Finally, a single parameter which may be used to indicate the performance of a supersonic combustor is the Combustor Effectiveness. It is defined as:

$$\eta_{ce} = \frac{(1 + f/a) I_{vac_{am}} - I_{vac_2}}{(1 + f/a) I'_{vac_{am}} - I_{vac_2}}$$

Where I_{vac_2} = combustor entrance vacuum specific impulse

$I_{vac_{am}}$ = actual combustor exit vacuum specific impulse expanded isentropically to ambient pressure

$I'_{vac_{am}}$ = combustor exit vacuum specific impulse for constant pressure, zero velocity-combustion expanded isentropically to ambient pressure

Of course, 100 percent ideal combustor effectiveness will never be reached, because the heat addition loss (Raleigh loss) is assumed to be zero for the ideal thrust calculation.

The Combustor Effectiveness was calculated and plotted as a function of equivalence ratio and presented in Figure 7.2-41. It appears that for all of the various injector configurations used, η_{ce} varies between 0.7 and 0.9. It has the advantage of using a single parameter to indicate the thrust-producing potential of the combustor. The highest combustor effectiveness in Figure 7.2-41 corresponds to the maximum measured thrust.

At Mach 7 exact combustor performance values were difficult to ascertain because of the poor agreement between calculated and measured thrust. The plot of combustor efficiency shown in Figure 7.2-42 is the most representative of the few points where there was good agreement in the engine net thrust. The calculations are for reading 88 tested at 3090°R freestream total temperature and with injector configuration 1a, 4, 2a, 2c.

Fuel was injected from 1a at an equivalence ratio of 0.24 and burned fairly rapidly, reaching approximately 70-percent efficiency in about five inches downstream of injection. The remaining fuel injected from 2c, 4, and 2a, raised the total equivalence ratio to 0.90. It appeared that flow was quenched by second stage fuel injection and did not burn until it reached strut section. The mass averaged static temperature was computed to be 2400°R downstream of injectors 2c and 4 and decreased to 1950°R at the step. These low static temperatures coupled with decreasing pressure gradient (Figure 7.2-11) and lack of stage interaction probably caused the no-burning condition prior to the step.

Most of the combustion occurred in the strut region with the overall combustor efficiency reaching 84 percent.

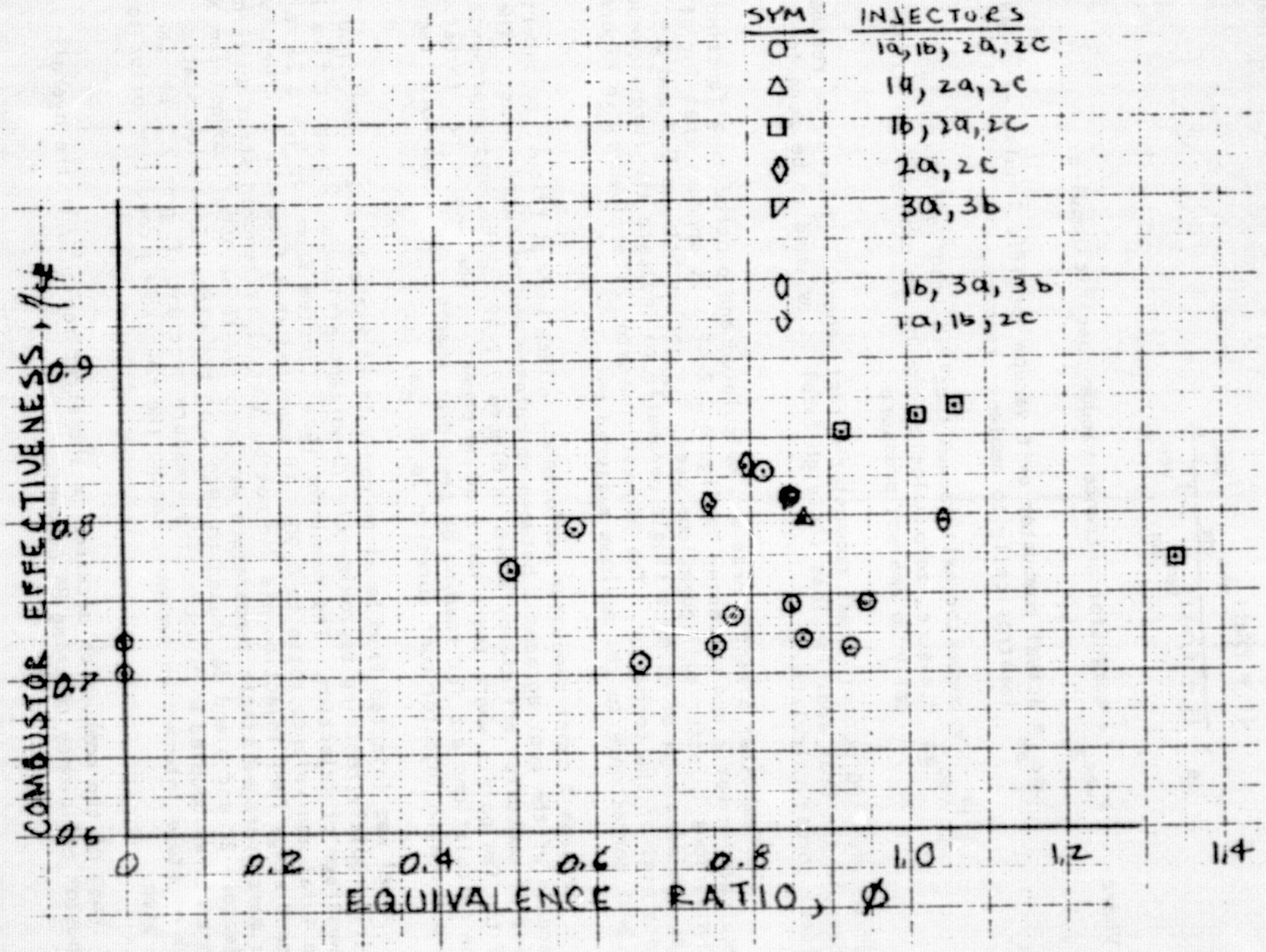

Figure 7.2-41. Mach 6 Combustor Effectiveness

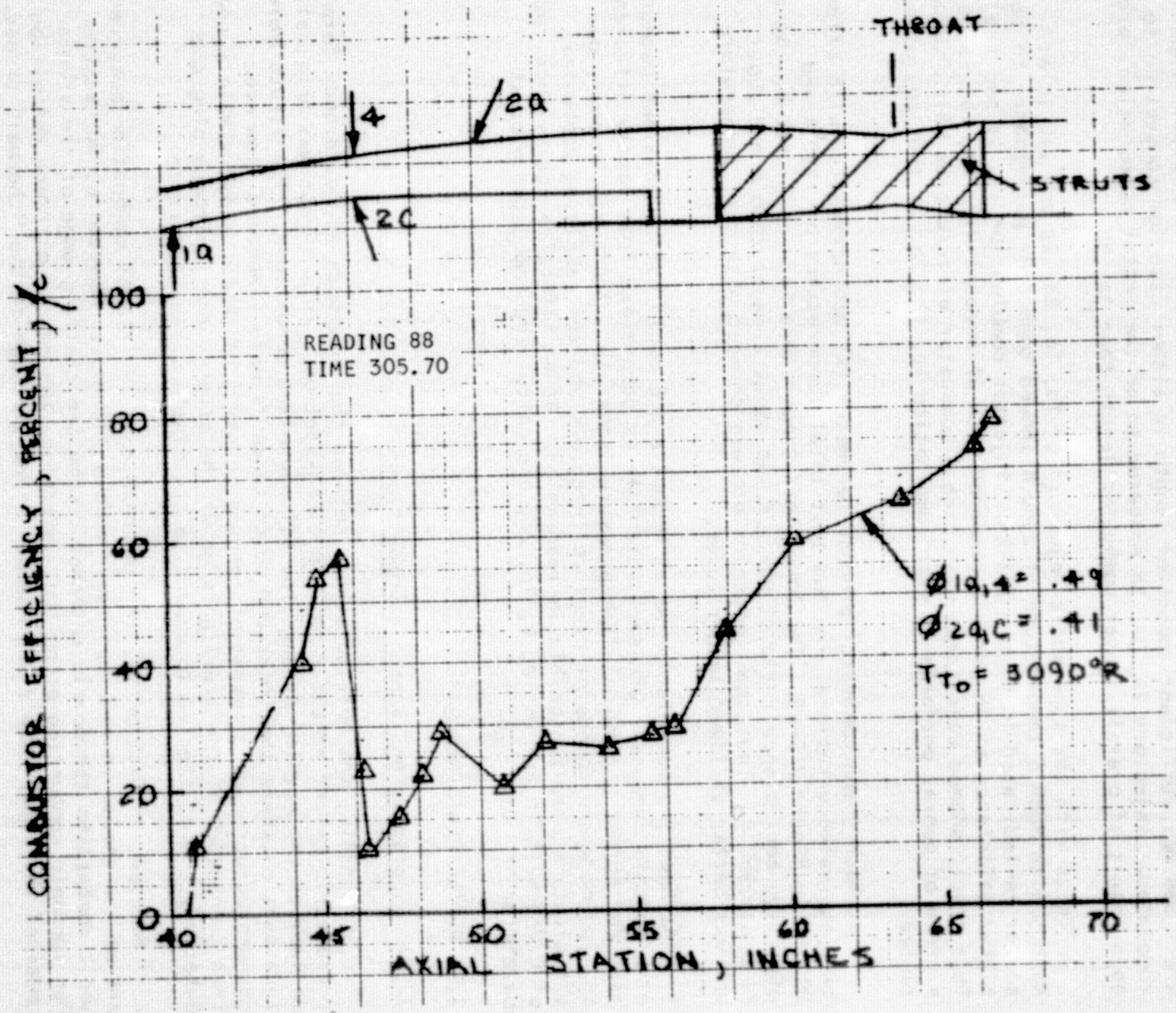

Figure 7.2-42. Mach 7 Combustor Efficiency

At Mach 5, the combustor efficiency of subsonic combustion at an equivalence ratio of unity is shown in Figure 7.2-43 using injectors 3a, 3b and also the combination 2a, 3a, 3b. A maximum efficiency of 74 percent was obtained with the former and 90 percent with the latter. It appears that there was not sufficient combustor length in either case for combustion to be completed. Injectors 2a, 3a, 3b appeared to be the better combination, probably as a result of overall longer combustor length than 3a, 3b.

Tests with the supersonic injectors of 1a, 1b, 2a, 2c and 2a, 2c at Mach 5,with Mach 6 temperature of 2940°R showed combustor performance to be poorer as indicated in Figure 7.2-44. Injector combination 2a, 2c had the higher efficiency at 74 percent compared with 61 percent with 1a, 1b, 2a, 2c. This result seemed consistent with Mach 6 combustor efficiencies which showed a trend of poorer performance with combination 1a, 1b, 2a, 2c than any other tested.

At Mach 5 the combustor process parameter (K) was correlated with effective equivalence ratio at the two test total temperatures of 2230°R and 2940°R in Figure 7.2-45. The lower test temperature had the higher K. At an effective equivalence ratio of unity,K was about 1.64 at 2230°R and about 1.36 at 2940°R. Thus the combustion process changed with test temperature and was better at lower temperatures.

At Mach 7 a correlation as at Mach 5 and 6 could not be obtained because of uncertain combustor pressure integrals as determined from vastly different measured thrust and thrust from pressure integrals. There was however, one test point where combustor pressure integrals and the resulting combustor efficiency seemed reasonable in reading 88. At an effective equivalence ratio of 0.755 with injectors 1a, 4, 2a, 2c, the calculated combustor process parameter, K, was 0.76.

7.3 NOZZLE PERFORMANCE

7.3.1 Supersonic and Subsonic Combustion

In the AIM, the holding struts between the innerbody and outerbody form a geometric throat at their maximum cross-section. This throat was originally defined as the nozzle entrance for all operating conditions. The struts were in a section where the inner and outer contours were fixed,and flow area changes occurred as a result of changes in strut blockage. Approximately one inch downstream of the trailing edge of the struts, the innerbody plug and outerbody shroud started to expand to the final nozzle area ratio.

However, in Section 7.2 it was shown that additional combustion occurred aft of the throat in the supersonic combustion mode. Therefore, for supersonic combustion the nozzle entrance became the trailing edge of the struts. For subsonic combustion or no fuel injection, the nozzle entrance definition remained the same, namely the maximum strut blockage or the "thermal" throat.

The nozzle area ratio was 5.45 from the thermal throat and 4.80 from the strut trailing edge. Without fuel injection the nozzle pressure ratio at Mach 5, 6, and 7 was 110, 210, and 300 respectively. At nominal operating

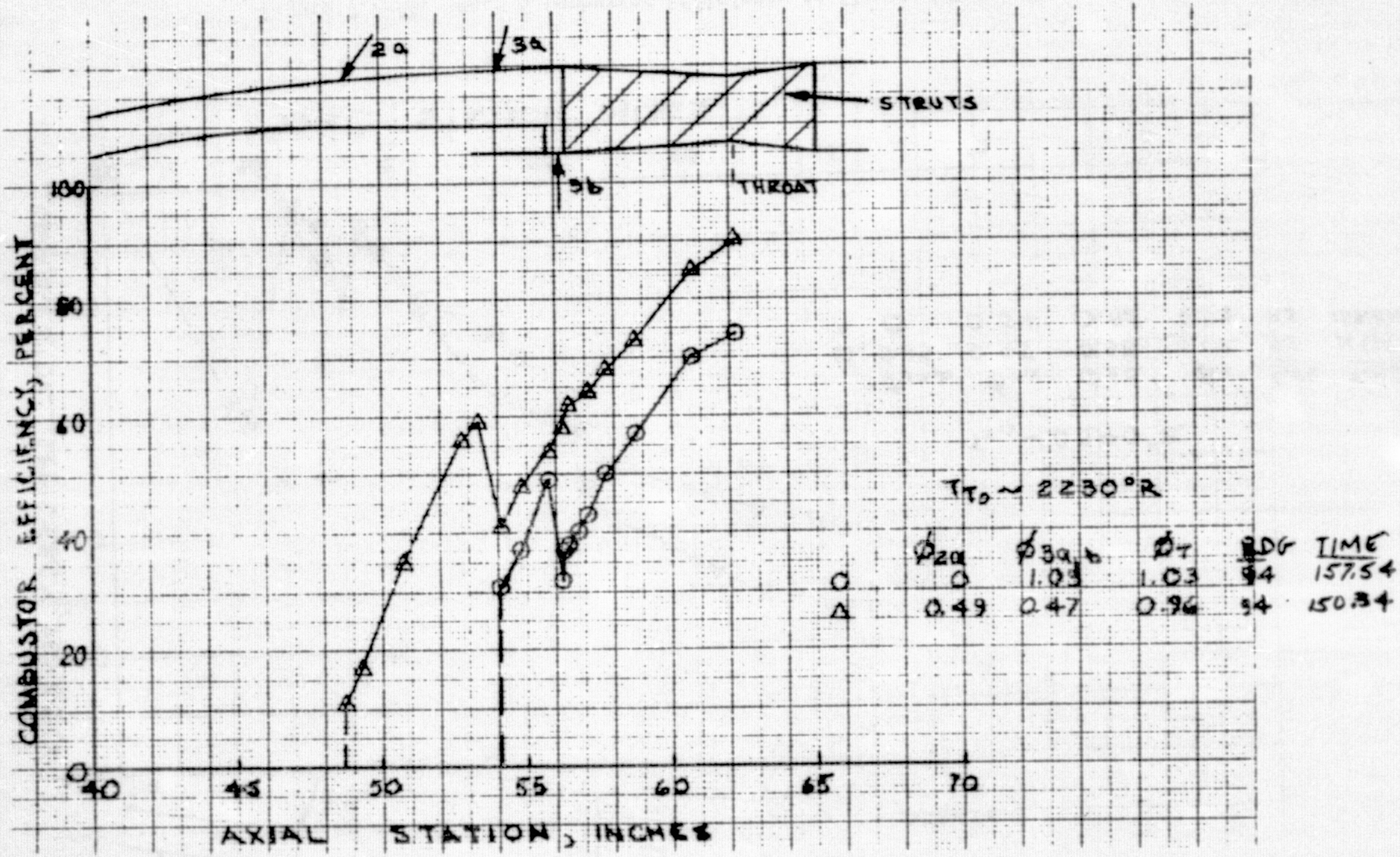

Figure 7.2-43. Mach 5 Combustor Efficiency

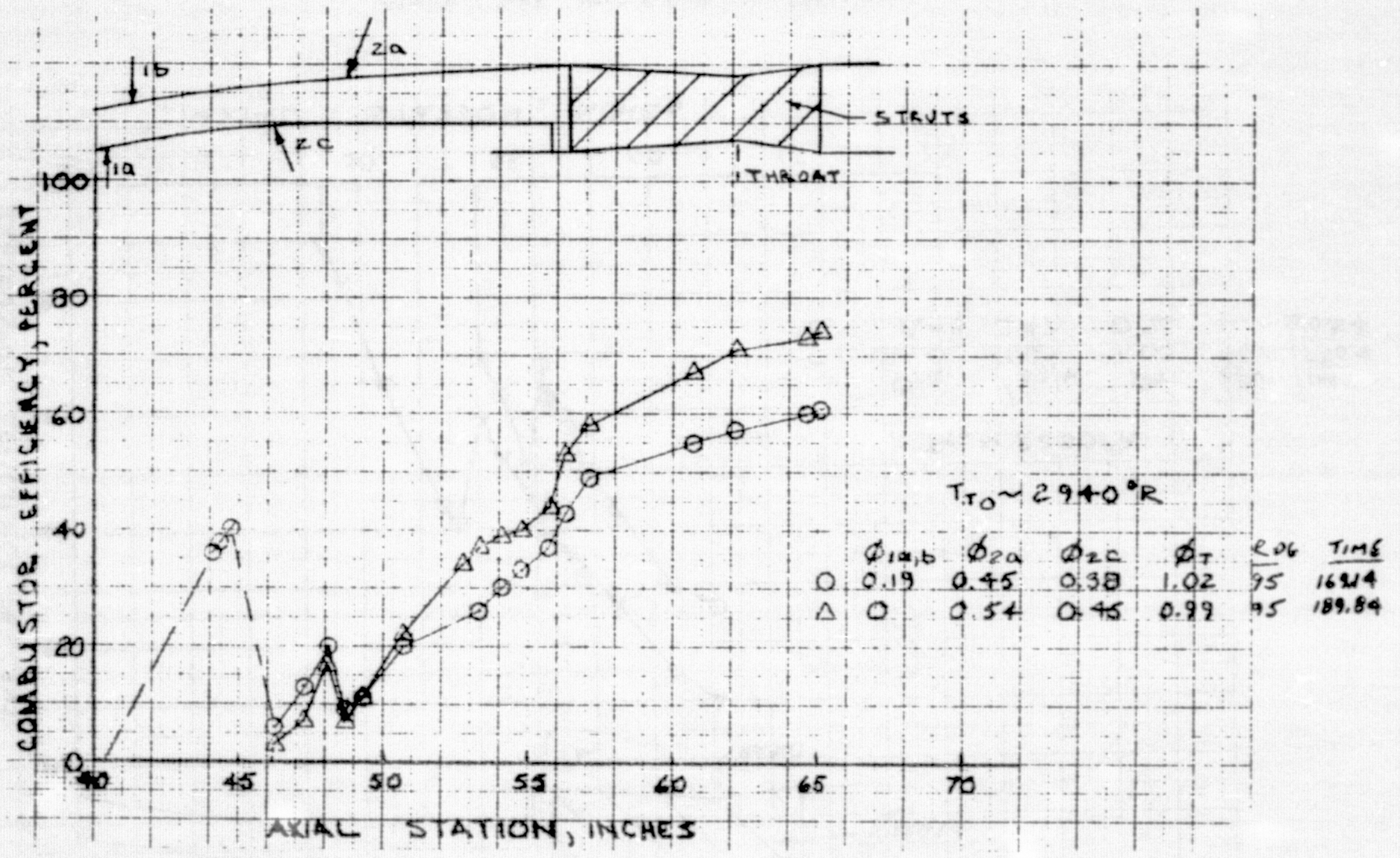

Figure 7.2-44. Mach 5 Combustor Efficiency at Elevated Temperature

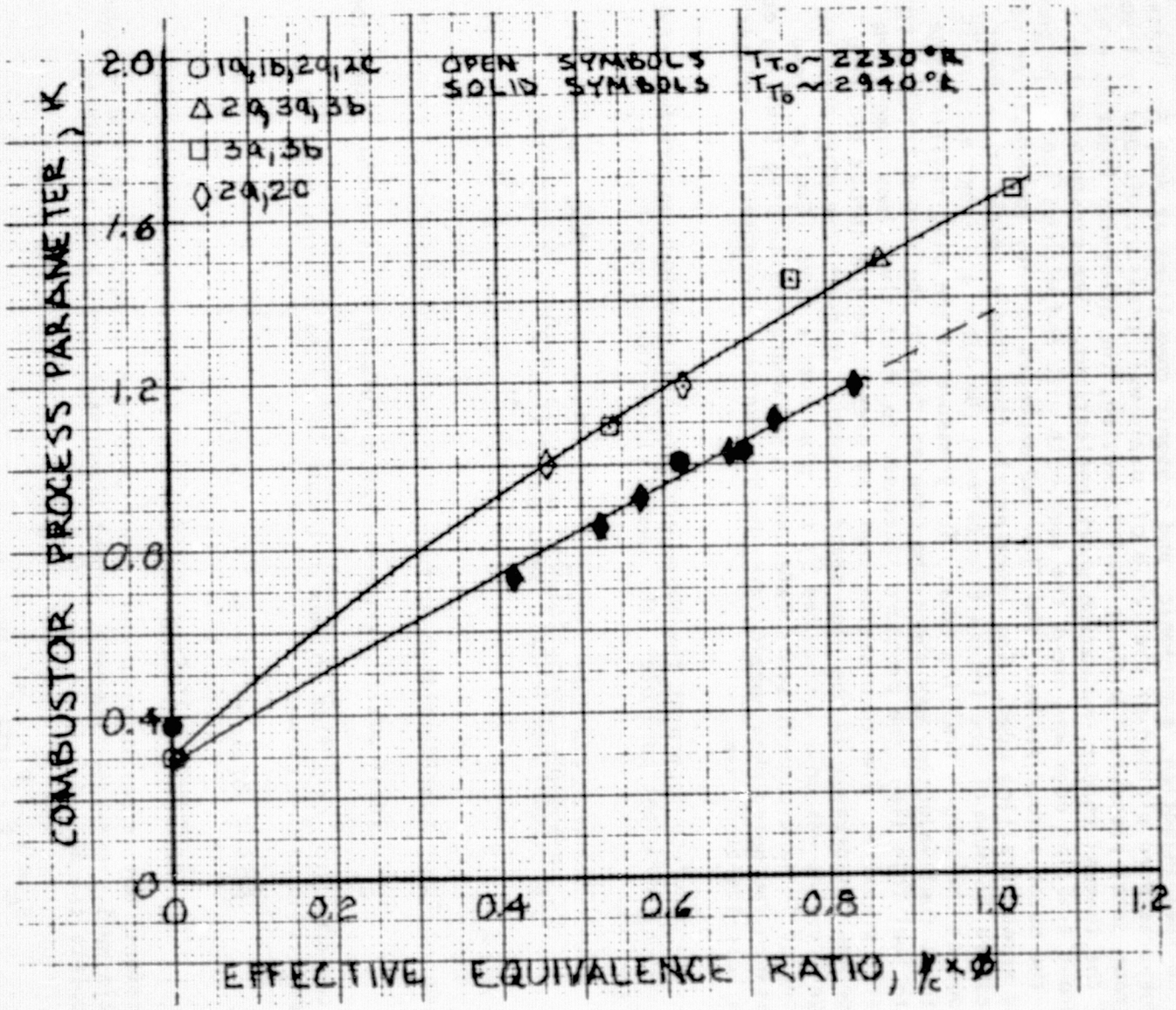

Figure 7.2-45. Mach 5 Combustor Pressure Area Integral Factor

conditions near an equivalence ratio of unity at Mach 5, 6, and 7, the pressure ratio was 90, 110, and 150 respectively.

Figure 7.3-1 shows AIM nozzle pressure distributions for the conditions of no fuel injection, supersonic, and subsonic combustion at Mach 6. These pressures were plotted as the ratio of nozzle wall pressure divided by free-stream total pressure. Without fuel injection, the pressures fluctuated aft of the thermal throat, indicating shock reflections. The pressure at the shroud trailing edge was about the same, both with and without fuel injections. On the outer shroud surface, the flow had expanded to very low pressures near the shroud trailing edge. The inner nozzle flow thus expanded to a lower pressure because of the interaction between the outer and inner supersonic flows at the shroud trailing edge. The pressure at the plug trailing edge without fuel injection was about the same as that on the shroud trailing edge. With fuel injection, the pressure increased to about five-times freestream static pressure. The interaction that was present at the shroud trailing edge was not present at the plug trailing edge. Instead, the plug trailing edge pressure was only influenced by the plug nozzle flow. Similar trend occurred in nozzle model tests Reference 7.3-1 where nozzle plug trailing edge pressure increased when nozzle inlet Mach number was decreased in simulating the heat-addition case.

In order to interpret the above pressure distributions on nozzle performance, a convenient parameter, the vacuum stream thrust coefficient, C_s, defined as:

$$C_s = \frac{\text{Actual Nozzle Exit Momentum}}{\text{Ideal Nozzle Exit Momentum}} = \frac{F_4}{F_{4_i}} = \frac{F_3}{F_{4_i}} + \frac{\int PdA - F_f}{F_{4_i}}$$

was used.

Where F_3 = nozzle inlet momentum

F_{4_i} = ideal nozzle exit momentum calculated by isentropic expansion of the combustor exit flow in chemical equilibrium to an area equal to the geometric nozzle exit area.

$\int PdA$ = nozzle wall pressure integral

F_f = nozzle friction force

Therefore, nozzle performance can be obtained from integration of the measured nozzle wall pressures. However, thrust measurements can also be used to calculate the actual exit momentum (F_4) as:

$$F_4 = F_c + F_{ext.} + F_{cav} + F_o$$

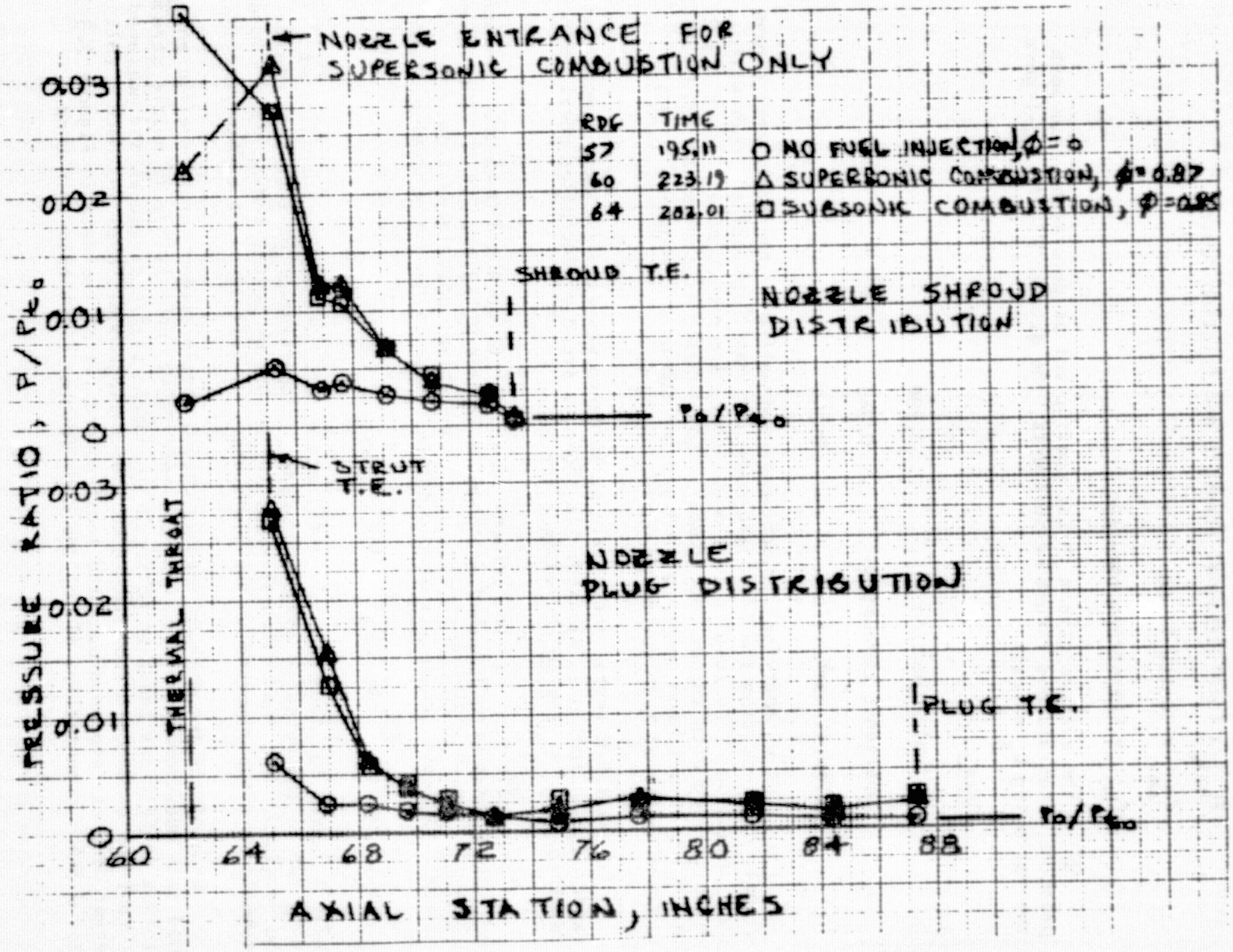

Figure 7.3-1. Mach 6 AIM Nozzle Pressure Distribution

Where F_c = Corrected load cell force

F_{ext} = Total external pressure and friction forces

F_{cav} = Cavity force

F_o = Freestream momentum

Using the average stream thrust coefficient as determined from both pressure integrals and thrust measurements, the data in Figure 7.3-1 gave the following C_s values:

Case	C_s
No fuel injection	0.990
Supersonic combustion	0.949
Subsonic combustion	0.944

The value without fuel injection agreed well with the test results previously obtained from the 1/3-scale model but was three points lower with fuel injection. The results from model tests are presented in Figure 7.3-2 as correlated with throat Mach number. For supersonic combustion, the C_s was 0.97 with throat Mach number of 1.3, and for subsonic combustion C_s was 0.975 with throat Mach number of unity.

From all AIM tests, the nozzle performance was significantly lower than expected when fuel was injected. It showed a trend of decreased nozzle performance with increasing equivalence ratio.

Correlations of nozzle performance at Mach 6 for the AIM in the supersonic combustion mode were obtained as shown in Figures 7.3-3 and 7.3-4. There was a large scatter in nozzle stream thrust coefficient calculated from both methods. A least-square fit of the data was made using the general equation

$$y = C_1 + C_2X + C_3X^2 + C_4X^3 + \ldots\ldots\ldots$$

with a linear fit found to have the least error. Due to the insufficient data run in the subsonic combustion modes, no correlation of that data could be obtained. The two available subsonic combustion points shown by the closed symbols were superimposed on the plots, and they fell within the data scatter.

Each of the two methods used to obtain nozzle stream thrust coefficients had data measurement errors. In Reference 7.3-2, uncertainty in nozzle stream thrust coefficient based on measured AIM nozzle static pressures and measured thrust was determined from Mach 5 to 7 operating conditions. At Mach 6 this error band was placed around the least-square fit of the data in Figures 7.3-3 and 7.3-4. Essentially, all of the data scatter fit within this band.

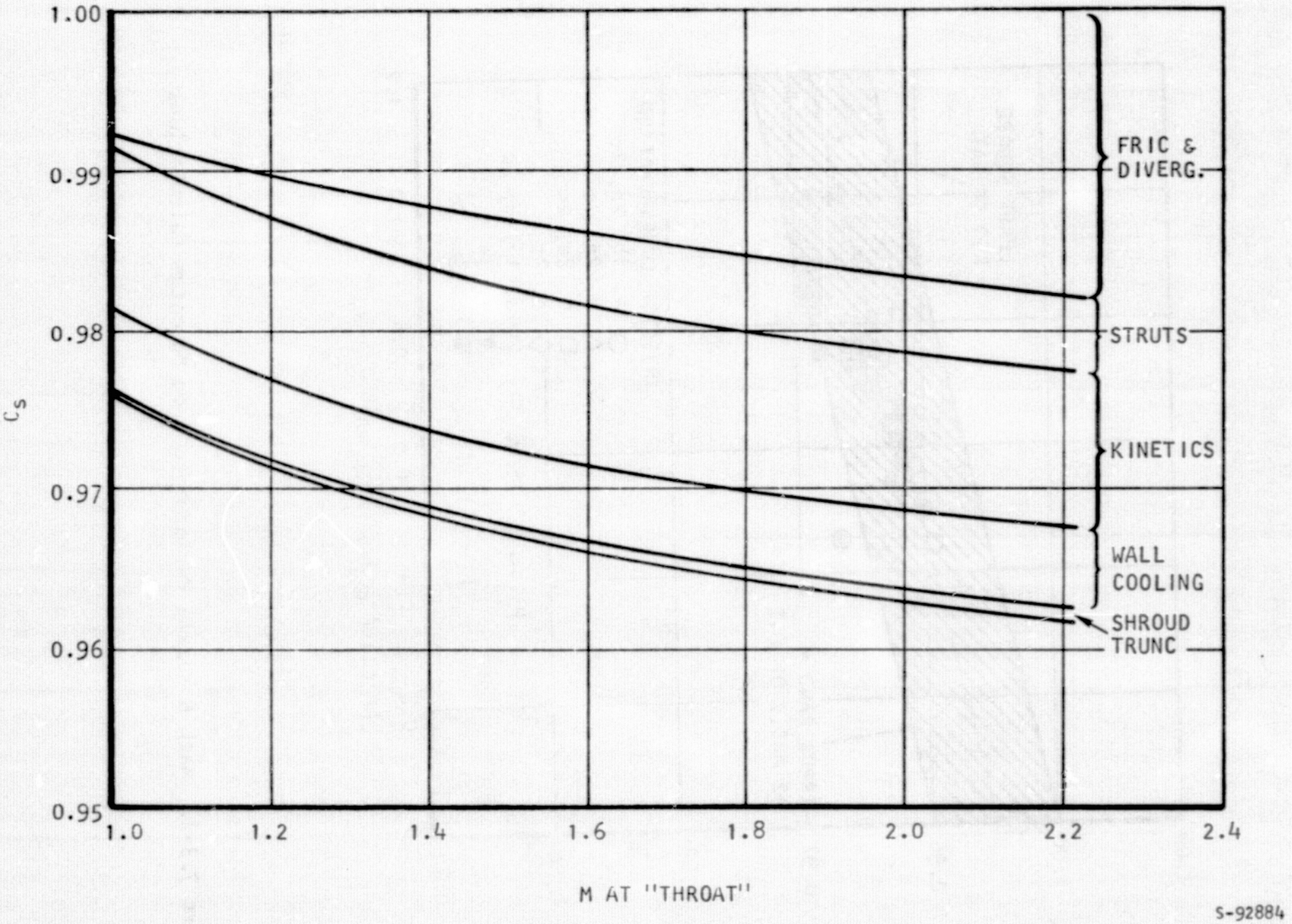

Figure 7.3-2. One-Third-Scale Nozzle Performance

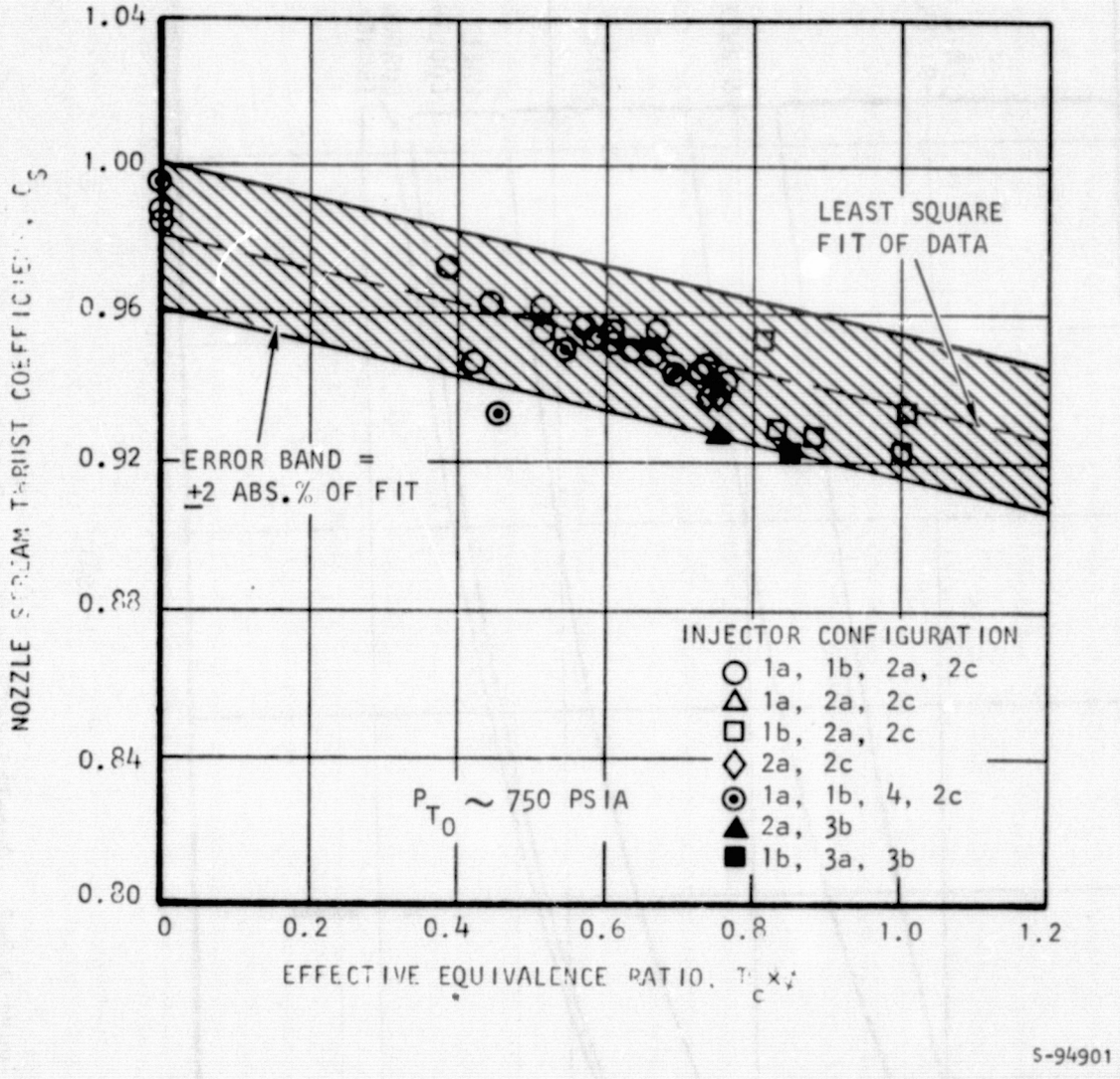

Figure 7.3-3. Mach 6 Nozzle Performance From Momentum Calculations

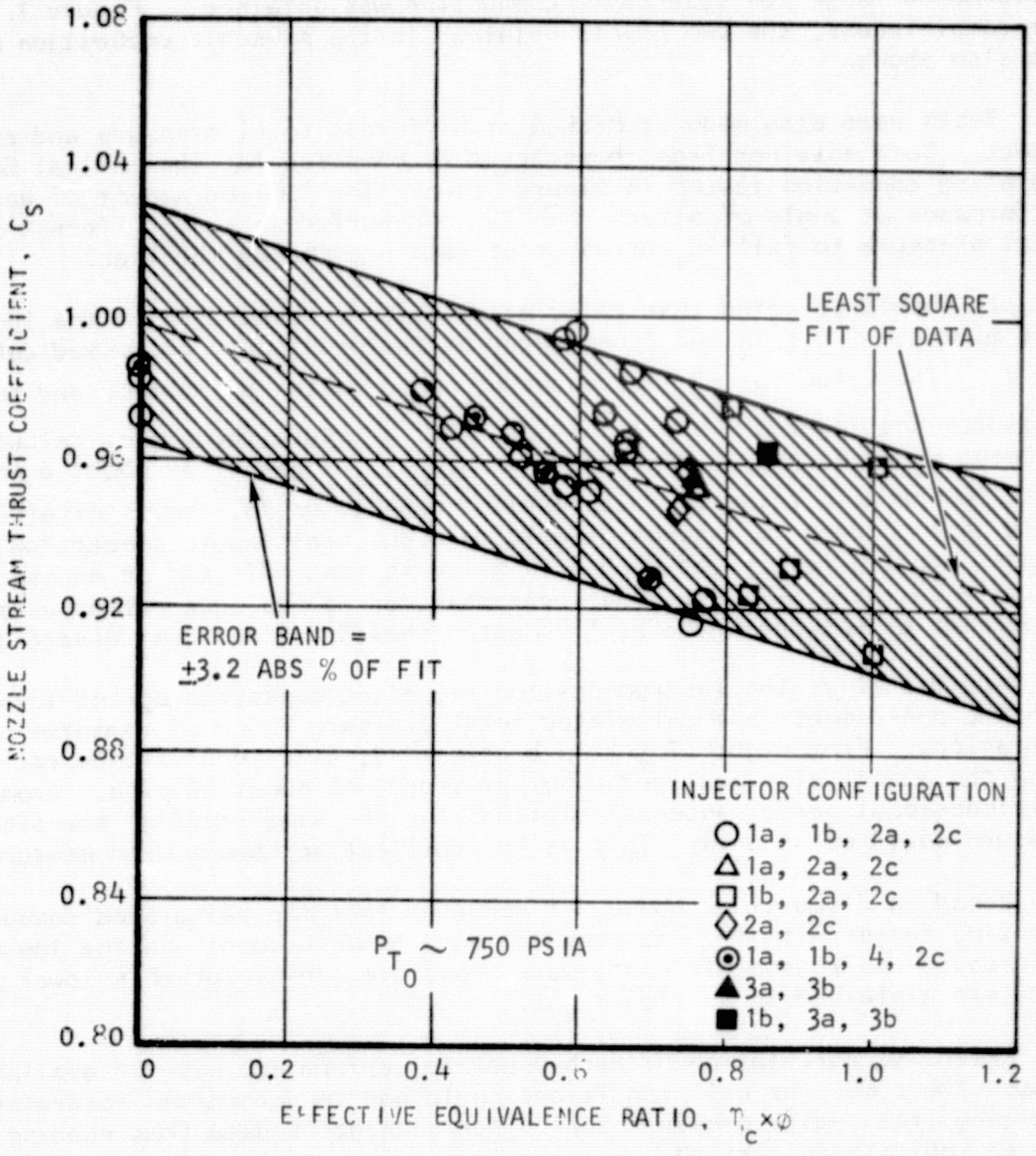

S-94900

Figure 7.3-4. Mach 6 Nozzle Performance From Thrust Measurements

The overlapping of the error bands from the two different methods was considered to be the most probable nozzle stream thrust. The probable nozzle performance range for supersonic combustion was obtained in Figure 7.3-5. For completeness, the two points obtained in the subsonic combustion mode are also shown.

Tests were also made at Mach 6 at different total pressure and angle of attack. Data obtained from those tests is compared for the nominal Mach 6 operating condition tested in Figure 7.3-6. The limited amount of data showed performance at angle of attack ($\alpha = 3^{0}$) and performance at different operating total pressure to fall in the range of data previously obtained.

It should be noted that calculation of C_s is dependent on the ideal nozzle exit momentum (F_{4_i}) in the denominator of the previously discussed definition for C_s. The value for F_{4_i} is dependent on combustor efficiency and total pressure--the lower the efficiency or total pressure the higher calculated C_s. A change of 5 percent in combustor efficiency changes C_s by about a point. Thus, in order to raise C_s to a level of 0.97 to 0.975, combustor efficiency would have to drop to a range of 0.70 to 0.80. This would appear low, based on gas sampling results at Mach 6 in which it was indicated at an overall equivalence ratio of 1.02. The local measured equivalence ratios were within ±5 percent except one probe at 170^{0}, which showed a 15-percent discrepancy.

Additionally, the instrumentation rig pitot pressures agreed favorably with the one-dimensional calculated total pressure based on momentum considerations. From Figure 7.5-3 in Section 7.5, at an equivalence ratio of unity the numerically averaged pitot pressure was about 42 psia. From the one-dimensional performance calculations for the same reading, the pitot pressure would be 45 psia. This is in excellent agreement with measured values.

Based on discussions above, it appeared that the calculated combustor exit condition agreed with the instrumentation rig measurement and the low nozzle performance was reasonably confirmed. Possible causes for this lower performance are explained in Section 7.3.2.

Extensive correlation of Mach 7 nozzle performance was not available because the combustor exit conditions could not be determined accurately, resulting from faulty pressure taps. Representative data from reading 88 with an equivalence ratio 0.9 was obtained. The nozzle thrust coefficient computed from momentum considerations was 0.937, and that computed from measured thrust was 0.976. These values fell within the error bands of the Mach 6 data (Figures 7.3-3 and 7.3-4) at an effective equivalence ratio of 0.75. Comparing the nozzle pressure distribution with Mach 6 data showed there was practically no difference, with the exception of a few pressure readings. It was felt that the curve of nozzle thrust coefficient versus effective equivalence ratio obtained from Mach 6 data was representative of Mach 7 nozzle performance.

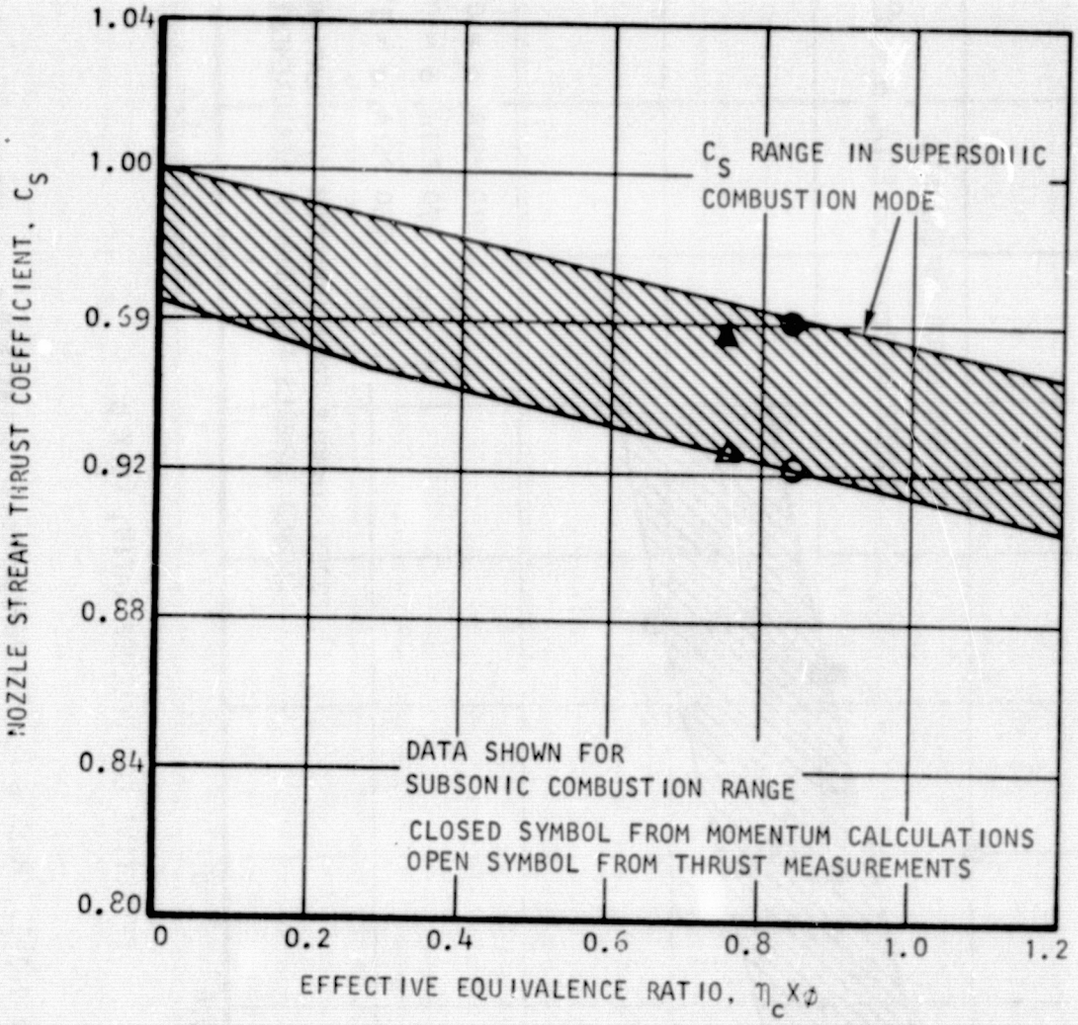

S-94898

Figure 7.3-5. Mach 6 Probable Nozzle Performance

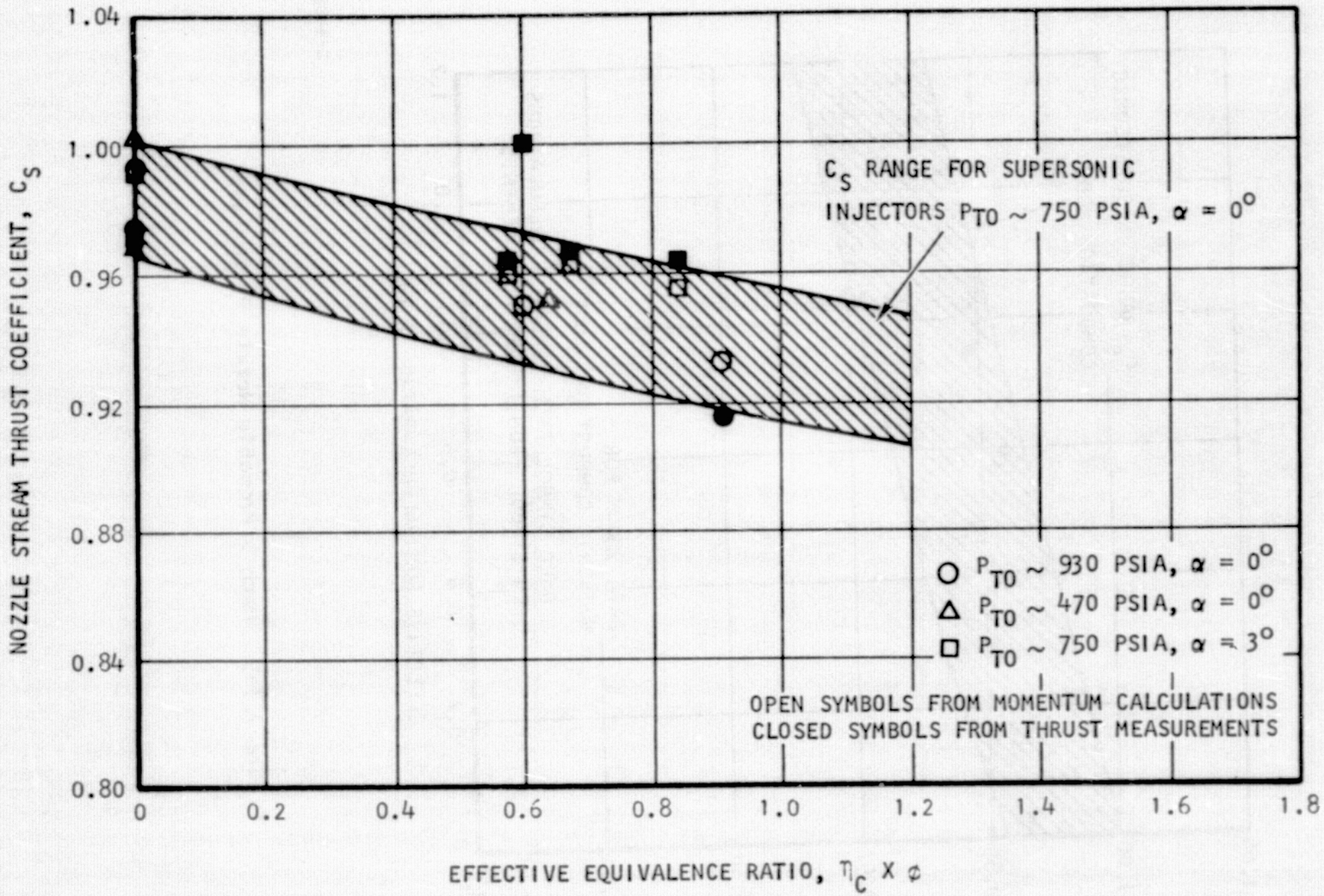

Figure 7.3-6. Mach 6 Nozzle Performance Comparison

At Mach 5 there was fairly good agreement between measured thrust and that calculated from surface pressure integrals. The data at Mach 5 nominal operating conditions was not extensive. In Figure 7.3-7 nozzle performance obtained at Mach 5 was compared with that at Mach 6. The data at Mach 5 agreed fairly well with Mach 6 and showed the same trend of decreasing nozzle performance with increasing effective equivalence ratio. When temperature was increased to 2940°R, the nozzle performance was also in fair agreement with Mach 6 results as shown in Figure 7.3-8. At three degrees angle of attack there was larger disagreeement between measured thrust and that calculated from pressure integrals. As a result, the nozzle coefficients in Figure 7.3-9 show a larger scatter, but also in good agreement with the Mach 6 range of performance.

In summary, it appears that nozzle performance correlates with effective equivalence ratio. The nozzle stream thrust coefficient decreases as this ratio increases. Mach 5, 6, and 7 appear to have similar nozzle performance, even at angle of attack. The performance with combustion was about three points lower than that obtained from 1/3-scale model tests.

7.3.2 Correlation of Nozzle Performance

In Section 7.3.1 it was shown that nozzle performance correlated with effective equivalence ratio and that is decreased as this ratio increased. At an effective equivalence ratio of unity, the nozzle stream thrust coefficient (C_s) was about 0.935 (Mid-C_s range Figure 7.3-5) for both supersonic and subsonic combustion. Without fuel injection, the C_s was 0.982.

It was pointed out in the previous section that the nozzle performance was dependent on the computation of combustor exit conditions. However, it was also shown that the computation of combustor exit conditions was supported by the gas sampling and pitot pressure measurements.

Therefore, the AIM test data was further examined to determine the cause of the unexpected high losses. The AIM nozzle losses would normally include friction, divergence, kinetics, cooling, and configurational losses. Model tests generated data covering all of those losses except those due to chemical kinetics. The kinetics losses were estimated by a computer program (Reference 7.3-3). Table 7.3-1 gives a loss breakdown of the AIM nozzle, compared with that predicted and that obtained during tests.

For the AIM loss breakdown, divergence and kinetics losses were based on calculations in References 7.3-1 and 7.3-3 while friction and heat losses were obtained from the test data. At an equivalence ratio of zero, the measured C_s of 0.982 is slightly higher than the calculated value of 0.978 from the nozzle loss breakdown and predicted value of 0.972. At an equivalence ratio of unity, both the predicted C_s and that calculated from a loss breakdown are much higher than the measured value of 0.935.

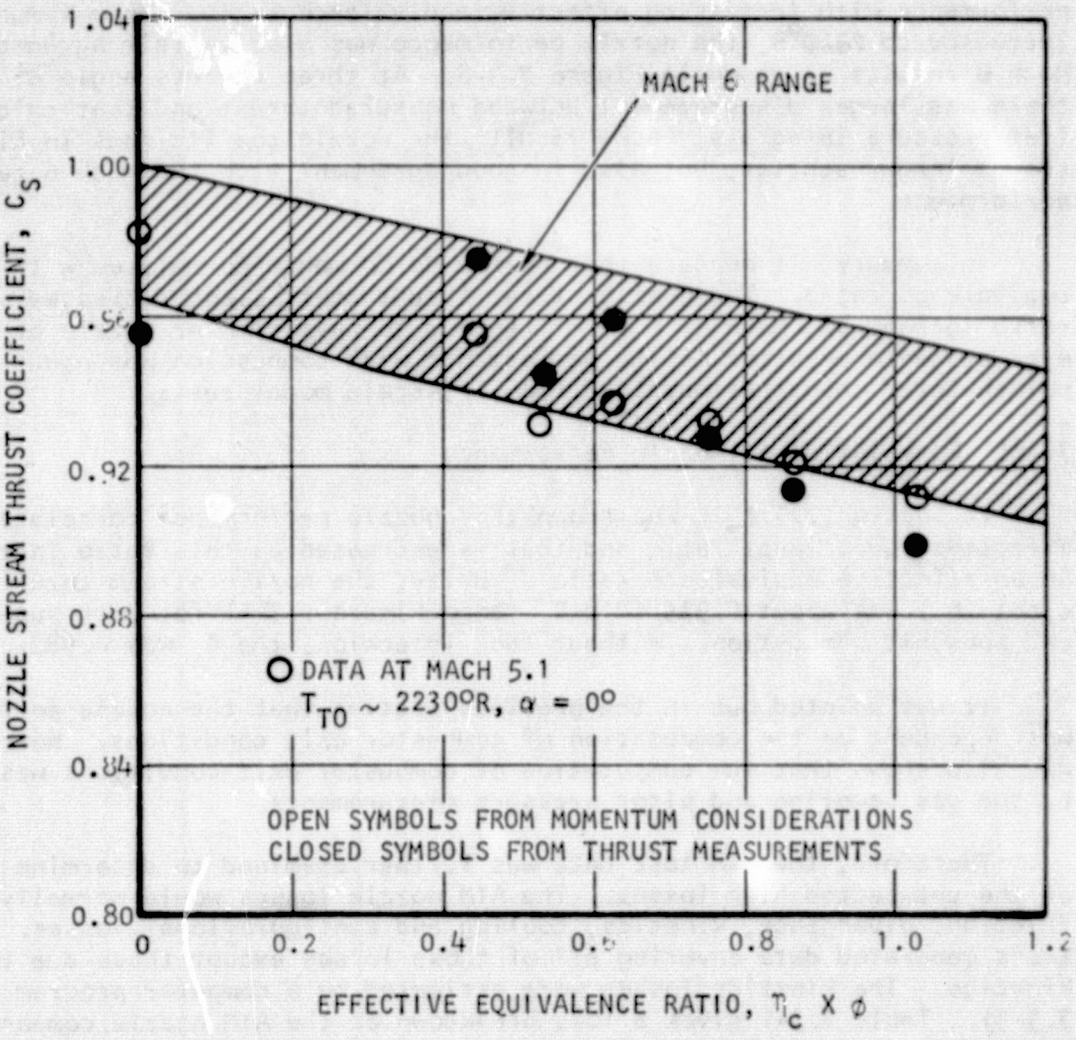

Figure 7.3-7. Mach 5 Nozzle Performance

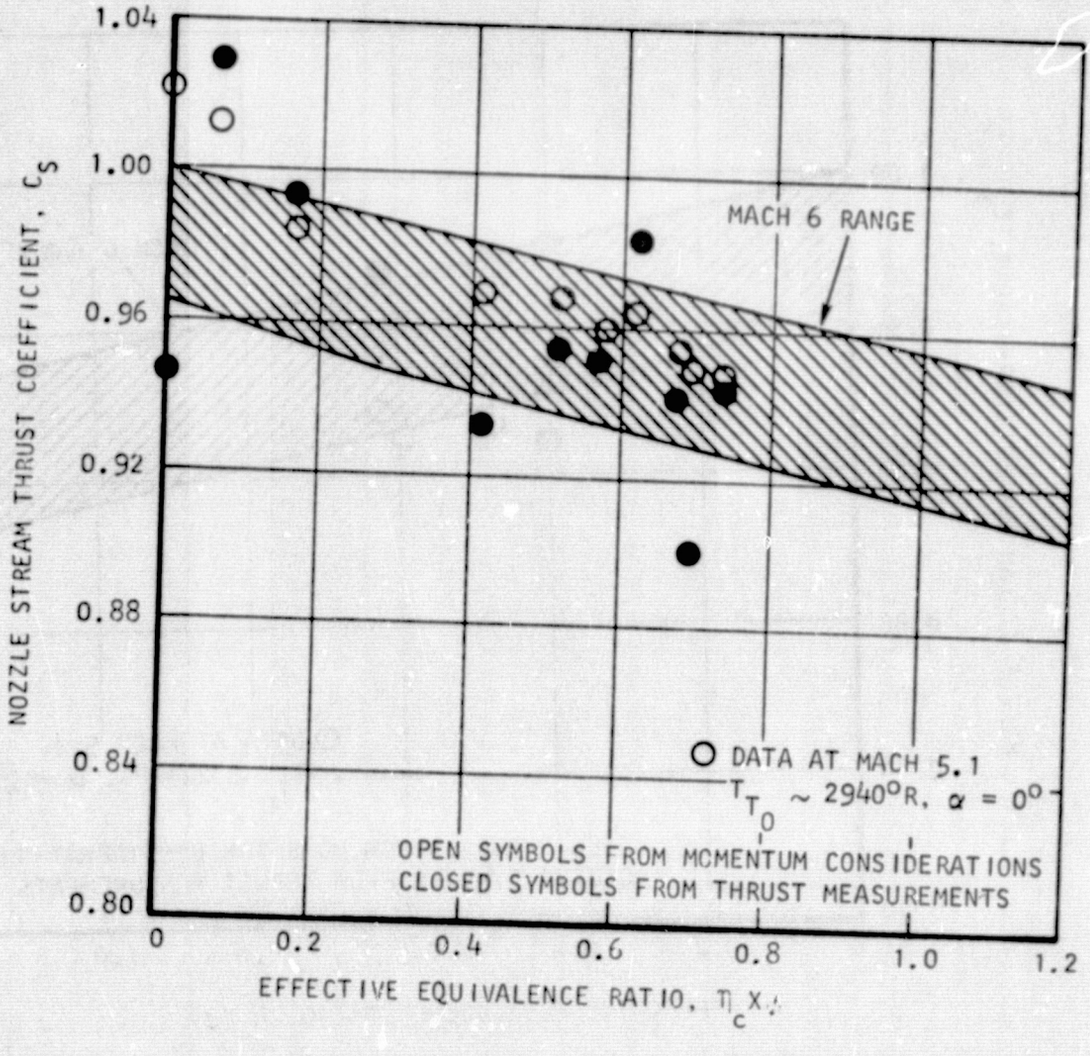

Figure 7.3-8. Effect of Temperature on Mach 5 Nozzle Performance

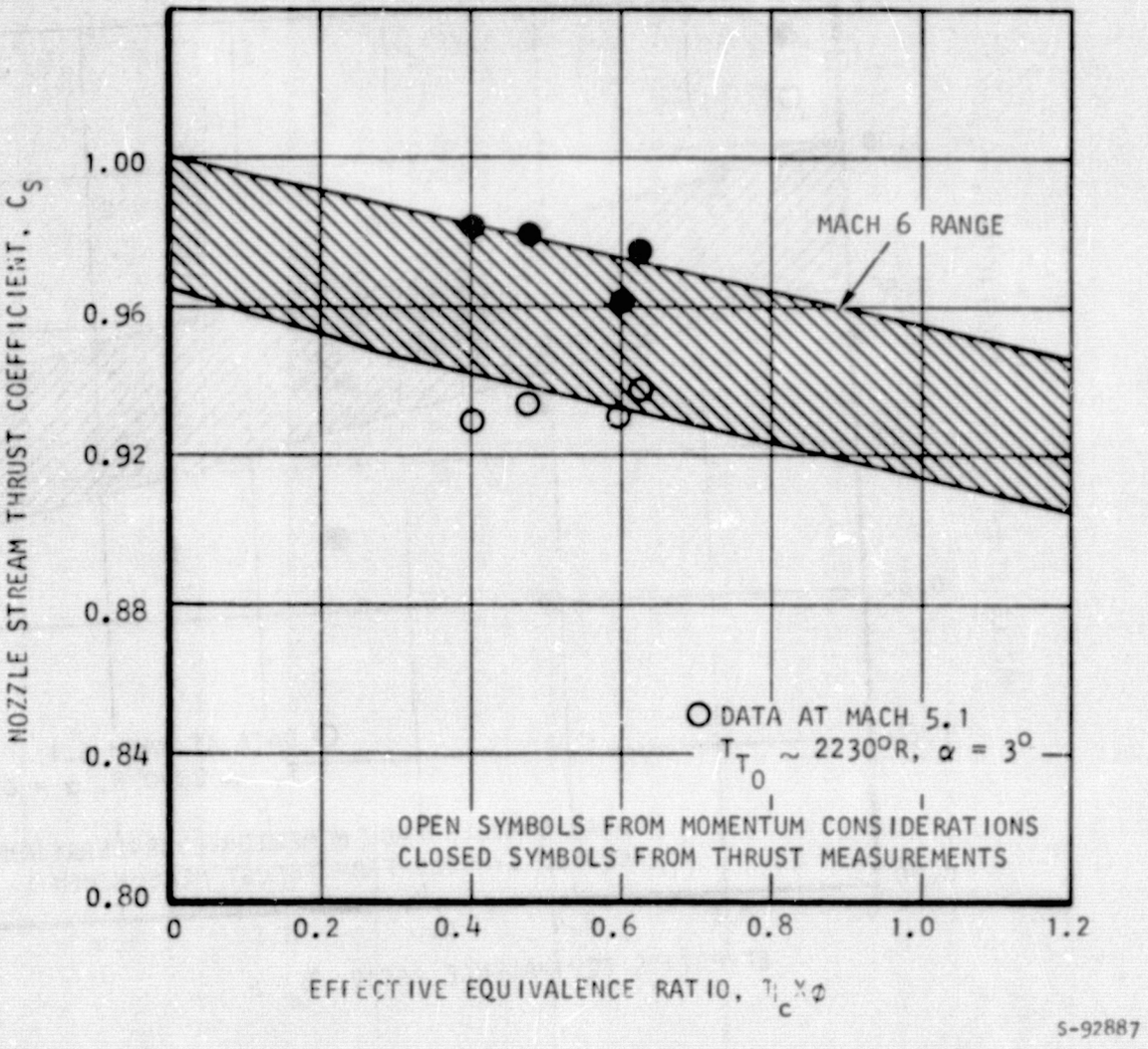

Figure 7.3-9. Effect of Angle of Attack on Mach 5 Nozzle Performance

TABLE 7.3-1

NOZZLE LOSSES (PERCENT)

	Measured		Predicted	
	Ø = 0	Ø = 1	Ø = 0	Ø = 1
C_s	0.982	0.935	0.972	0.970
Loss breakdown:				
Divergence and friction	0.012	0.012	0.018	0.010
Configuration	0.005	0.005	0.005	0.005
Heat loss	0.005	0.012	0.005	0.005
Kinetics effects	----	0.010	----	0.010
Total loss	0.022	0.039	0.028	0.030
C_s (from breakdown)	0.978	0.961	0.972	0.970

The difference in performance between an equivalence ratio of zero and unity could not be accounted for in the loss breakdown. For kinetics effects on additional loss of 1 percent could be added if the flow were assumed frozen at the nozzle entrance. This would still leave about 2 percent loss unaccounted for. The additional nozzle loss may have been caused by combustor exit flow conditions not simulated in the subscale tests.

As pointed out in Section 7.5, for at least 60 percent of the flow area between struts, there was significant yaw which increased with equivalence ratio as determined from pitot static cone probes. This yaw angle could have caused severe loss in nozzle performance because nozzle exit momentum is directly proportional to the cosine of yaw angle. For example, an effective yaw angle for the entire combustor exit of 14 deg would have decreased nozzle thrust coefficient 3 percent, or the magnitude of performance difference between an equivalence ratio of unity and zero that could not be accounted for in Table 7.3-1. Also, there could have been combustor flow turbulence which was not dissipated prior to entering the nozzle. This loss in energy due to turbulence would not have been recovered in the nozzle and would have resulted in lower nozzle gross thrust produced.

Therefore, the low nozzle performance may have been caused by a combination of increased heat loss, chemical kinetics effects, combustor flow angularity, or flow turbulence. Further work is recommended to verify the level of nozzle performance, since it was much lower than expected.

7.4 ENGINE COMPONENT INTERACTIONS

7.4.1 Inlet-Combustor Interaction

One of the major concerns in the AIM design was the interaction between inlet and combustor as to whether stable combustion could be achieved with fuel injection at the inlet throat and what the maximum amount of fuel might be that could be injected without causing inlet unstart.

Observations from tests have demonstrated that stable operations were obtained during all phases of testing, which includes change of fuel schedules, transition from subsonic combustion to supersonic combustion mode and vice versa, change of inlet total pressure, and angle-of-attack runs. Even during inlet unstart, no chugging or oscillation was observed; however, reverse flame expelled from the inlet was noticeable from a TV screen, but this was quickly extinguished after fuel shut-down.

The maximum equivalence ratio that could be injected from the first stage injectors 1a and 1b was as high as 0.36 in reading 33 Mach 6 test. In this run, ignitors were used and no fuel was injected from the second stage. Examination of the pressure distribution just prior to inlet unstart indicates that there was only a very small upstream disturbance on the spike surface, as shown in Figure 7.4-1. The disturbance was plotted as the ratio of unstart pressure to the undisturbed pressure without fuel injection. The disturbance, however, was much stronger on the inner cowl surface, but it occurred only locally at Station 40 with a pressure ratio of 2.9 in the 180-deg position, and no disturbance was observed at the 0-deg position. This localized disturbance is believed to have caused the inlet unstart. It appeared that the five ignitors located downstream of ignitor 1a were not sufficient to ignite the mixture uniformly in this run. The distrubed pressure ratio at Station 40 (about 0.4 in. upstream of injector 1a) versus equivalence ratio is plotted on the top of Figure 7.4-2. The inlet unstart equivalence ratio was 0.08 higher than the predicted value obtained from 2-D combustor test and 2/3-scale inlet tests. The unstart pressure ratio was 2.9, as compared with a predicted value of 2.5. These differences may be accountable considering the fact that the combustion in this run was localized.

Similar plots with two-stage combustion from Reading 57 are plotted in Figure 7.4-3 and 7.4-2. Again, it showed no visible disturbance on the centerbody at Station 40. The disturbance on the inner cowl was more uniform both on Station 40 and 41.1. It may be noted that combustion in this run was initiated from the second stage fuel injection which interacted with the first stage. Consequently, the combustion was more uniform. The unstart pressure ratio compares very well with the unstart limit from 2/3-scale model test as shown in Figure 7.4-2.

The lack of disturbance on the centerbody surface upstream of fuel injection point may be attributable to higher local Mach number, ranging from 3 to 3.5 (Reference 7.4-1) as compared to 1.8 to 2.9 on the inner cowl surface. The higher Mach number, combined with a more favorable pressure gradient could withstand a higher pressure ratio without flow separation.

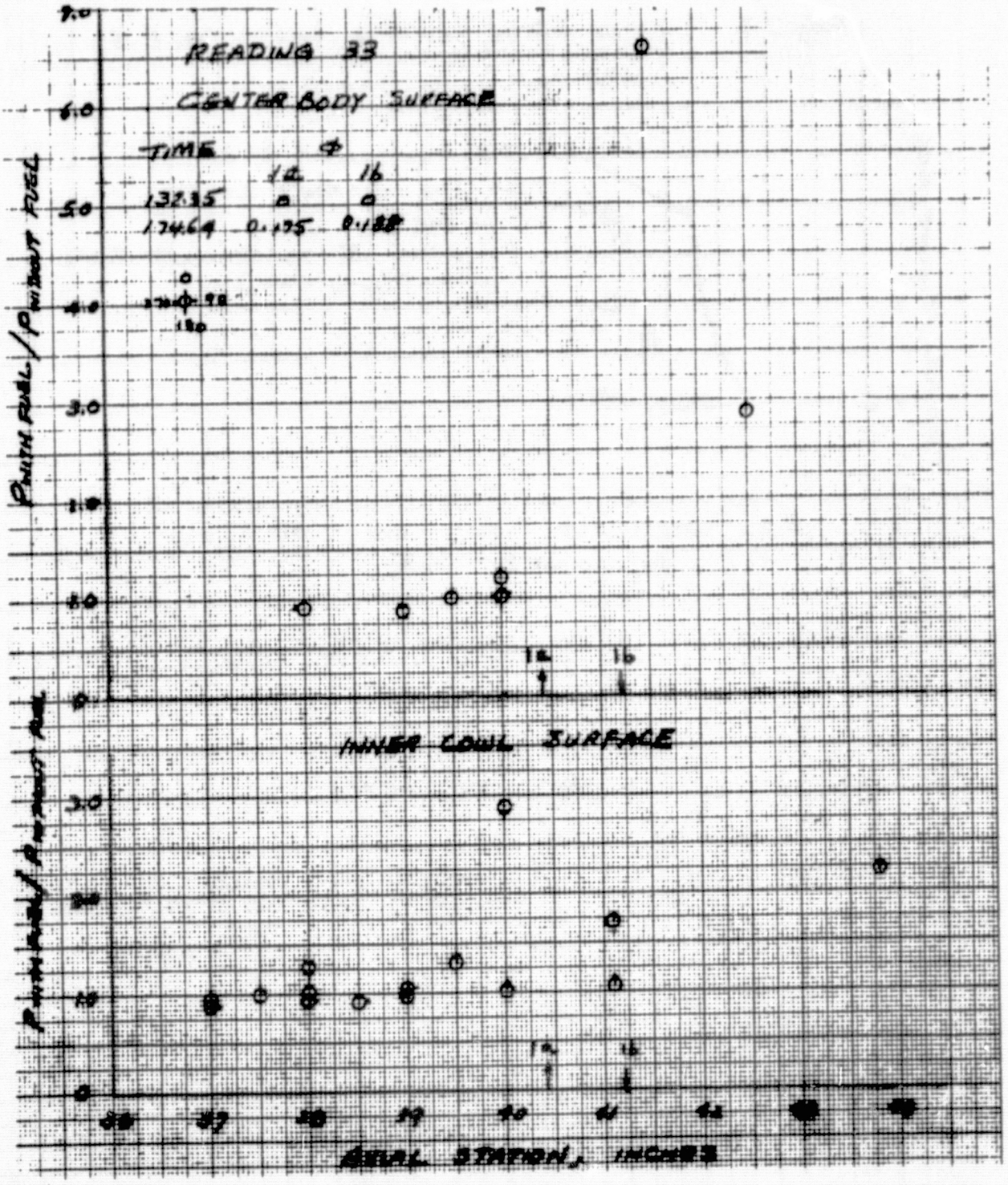

Figure 7.4-1. Mach 6 Inlet-Combustor Interaction (P vs X)

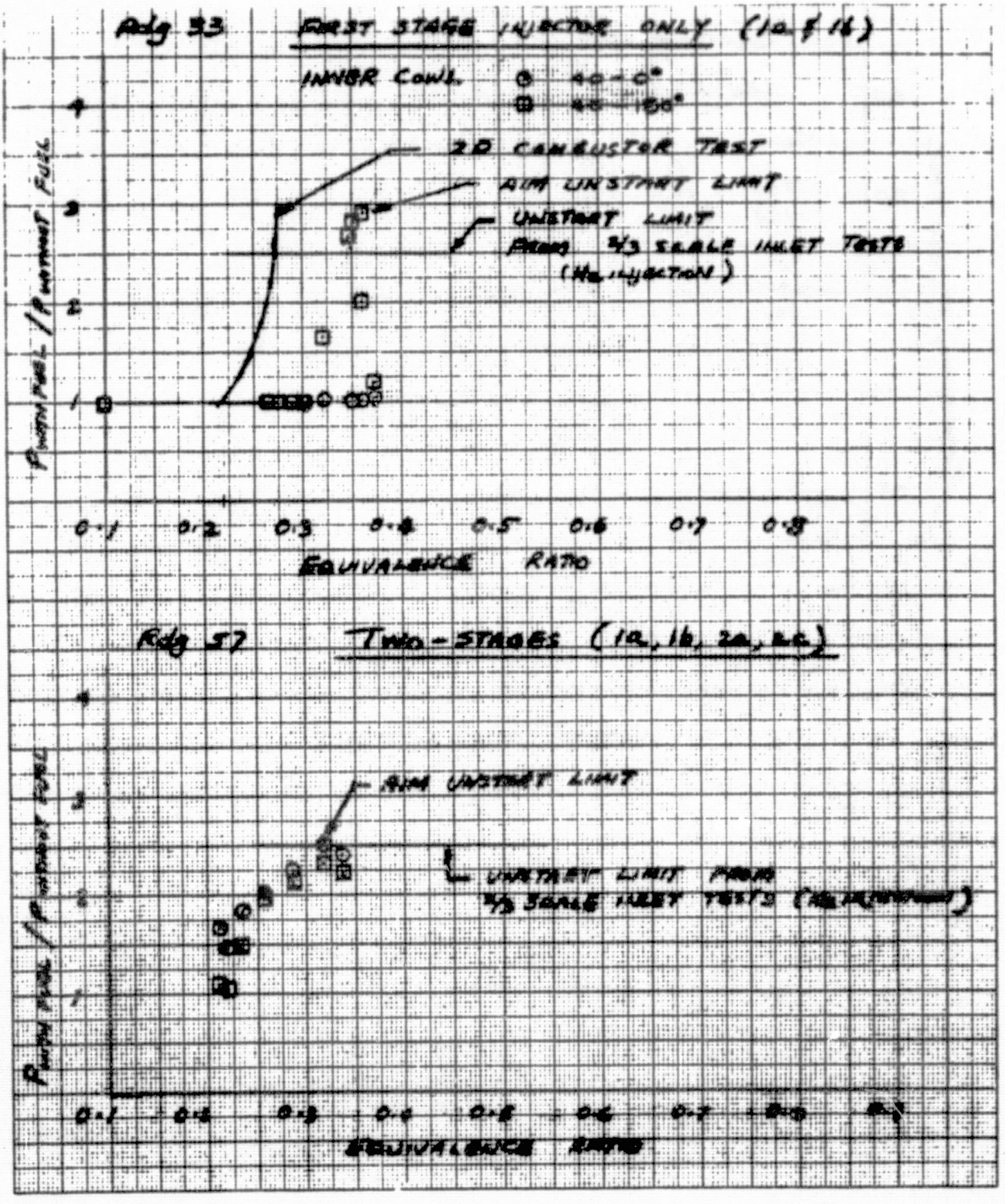

Figure 7.4-2. Mach 6 Inlet-Combustor Interaction (P vs ϕ)

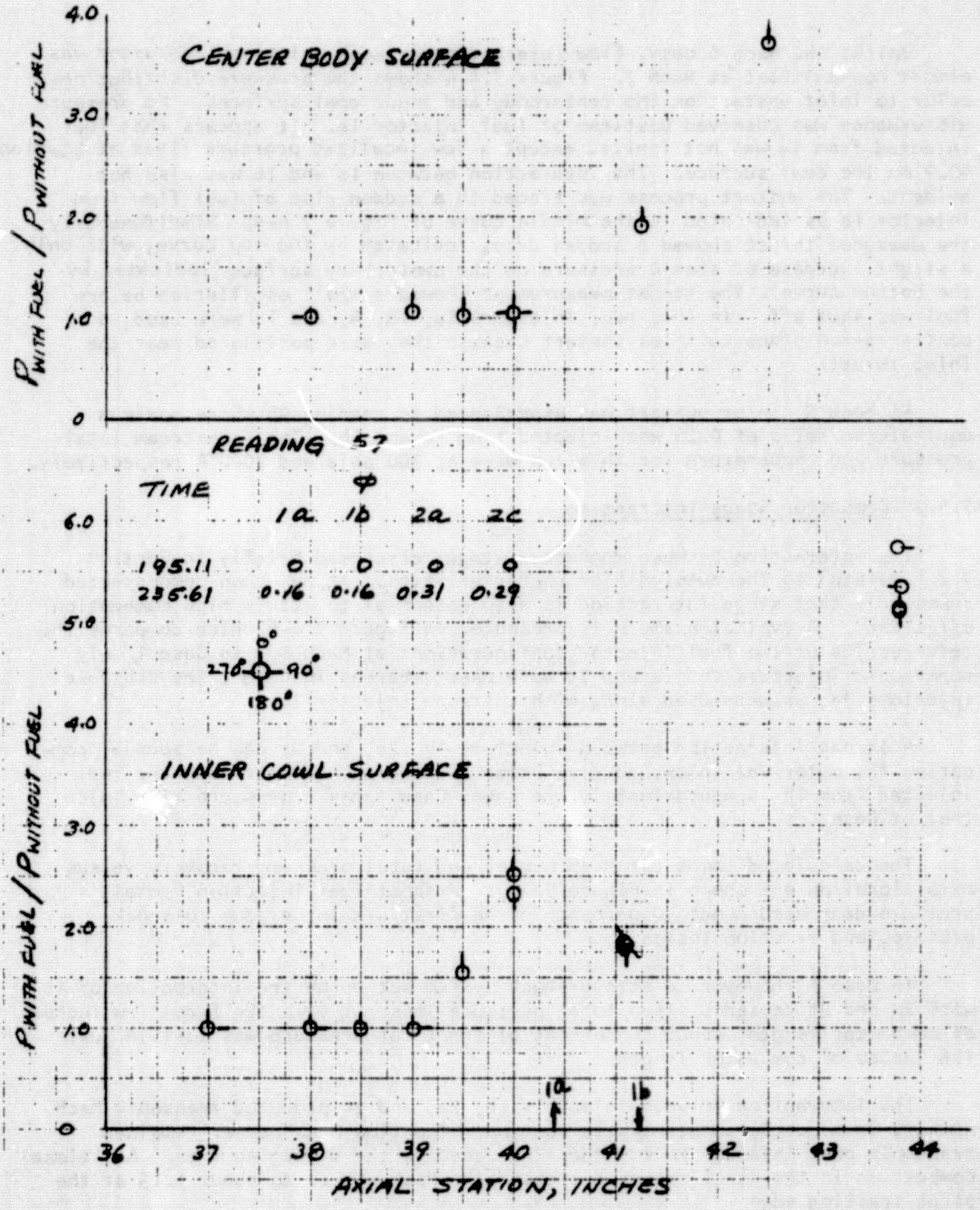

Figure 7.4-3. Mach 6 Inlet Combustor Interaction (P vs X two stages)

Unlike the Mach 6 case, flow interaction between inlet and combustor was almost non-existent at Mach 7. Figure 7.4-4 shows the pressure distributions prior to inlet unstart on the centerbody and inner cowl surfaces. No pressure disturbance was observed upstream of fuel injector 1a. It appears that fuel injected from 1a was not ignited except a few localized pressure rises at Station 40.7 on the cowl surface. The interaction between 1a and 1b was also not evident. The unstart process was traced to a sudden rise of fuel flow from injector 1a as indicated in the middle curve of Figure 7.4-5. Simultaneously, the measured thrust showed a sudden drop, indicated by the top curve, with only a slight increase of static pressure on the centerbody surface (indicated by the bottom curve). The thrust measurement showed a small oscillation before fuel was shut off. In this run, injectors 1a, 1b, 4, and 1c were used, a configuration prone to inlet unstart because they were positioned near the inlet throat.

At Mach 5, inlet unstart was experienced in reading 94 where maximum equivalence ratio of 0.26 was injected from 1a and 1b. The freestream total pressure and temperature for this run were at 300 psia and 3000^{o}R respectively.

7.4.2 Combustor Stage Interaction

The interaction between combustor stages discussed briefly in Section 7.2.1, related to the autoignition characteristics. It has been demonstrated repeatedly that stage interaction is also essential to attain high combustion efficiency. A typical example is presented in Figure 7.4-6, which compares the test results of two fuel injector configurations at Mach 6. In Case 1, only supersonic injectors 1b, 2a and 2c were used, whereas in Case 2 the subsonic injectors 3a, 3b were used, along with upstream injector 1b.

A strong interaction between injectors 1b, 2a, and 2c can be seen by comparing the outer wall pressure rise prior to Station 46. Although the fuel injected from 1b is approximately the same, Case 1 has a pressure rise twice that of Case 2.

The calculated combustor Mach number and total pressure recovery versus axial location are shown in Figure 7.4-7. Without fuel injection, total pressure decreased about 50 percent in the first six inches due to shock, profile, and friction losses.

In Case 1, however, a strong shock system set up by the interaction of 1b with 2a and 2c caused a steep total pressure loss curve in the first few inches of combustor length, about 50 percent of the total pressure was lost in just 1.6 inches of combustor length.

The interaction between injectors 1b, 2a, and 2c produced transonic Mach numbers in a nearly constant-area section. The flow Mach number remained transonic past injector 2c and then increased in the diverging area. Additional combustion in the strut region decreased the Mach number to about 1.15 at the strut trailing edge.

Without strong injector interaction in Case 2, the combustion in the first stage was not as complete as in Case 1. The Mach number remained supersonic

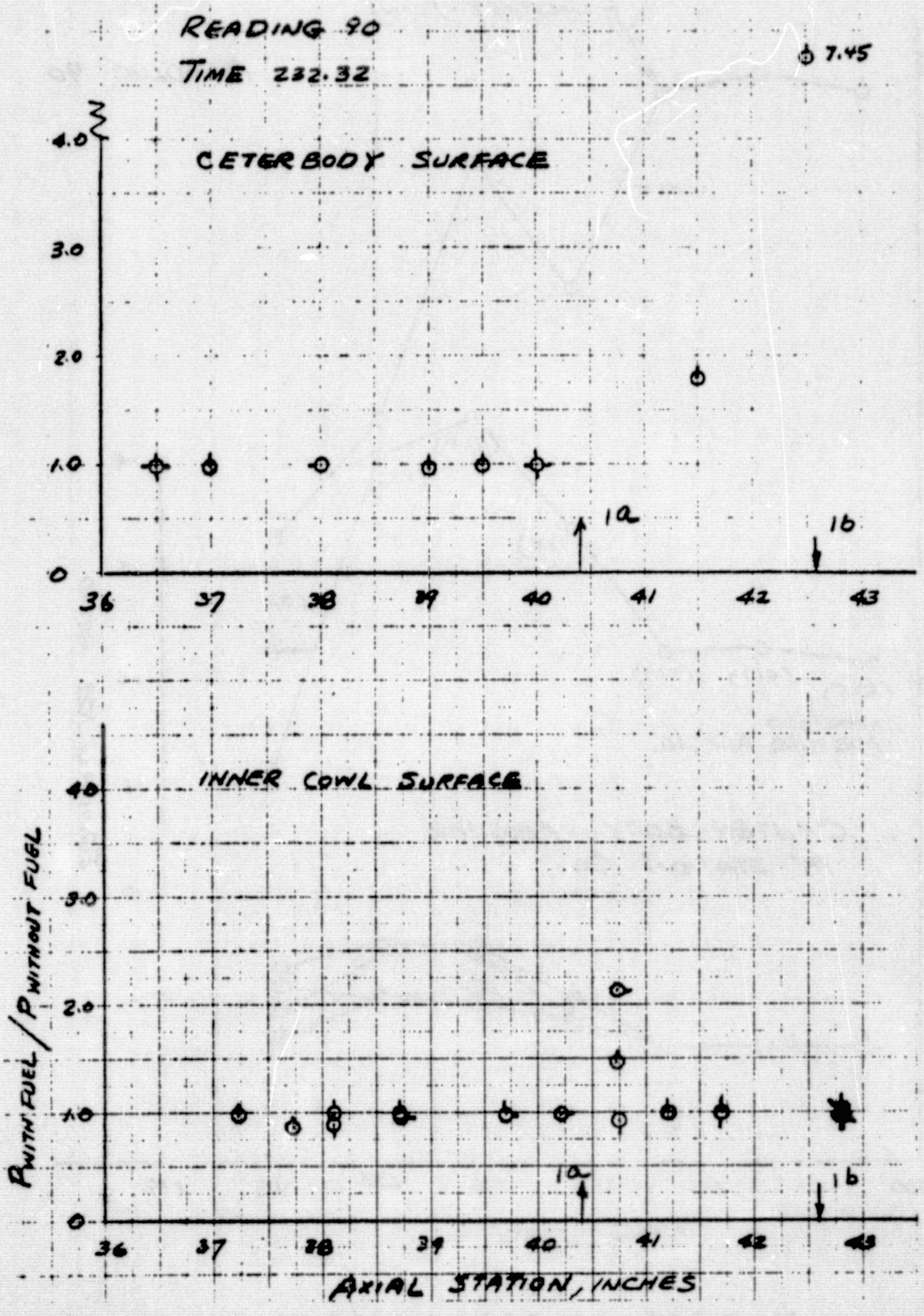

Figure 7.4-4. Mach 7 Inlet Combustor Interaction (P vs X)

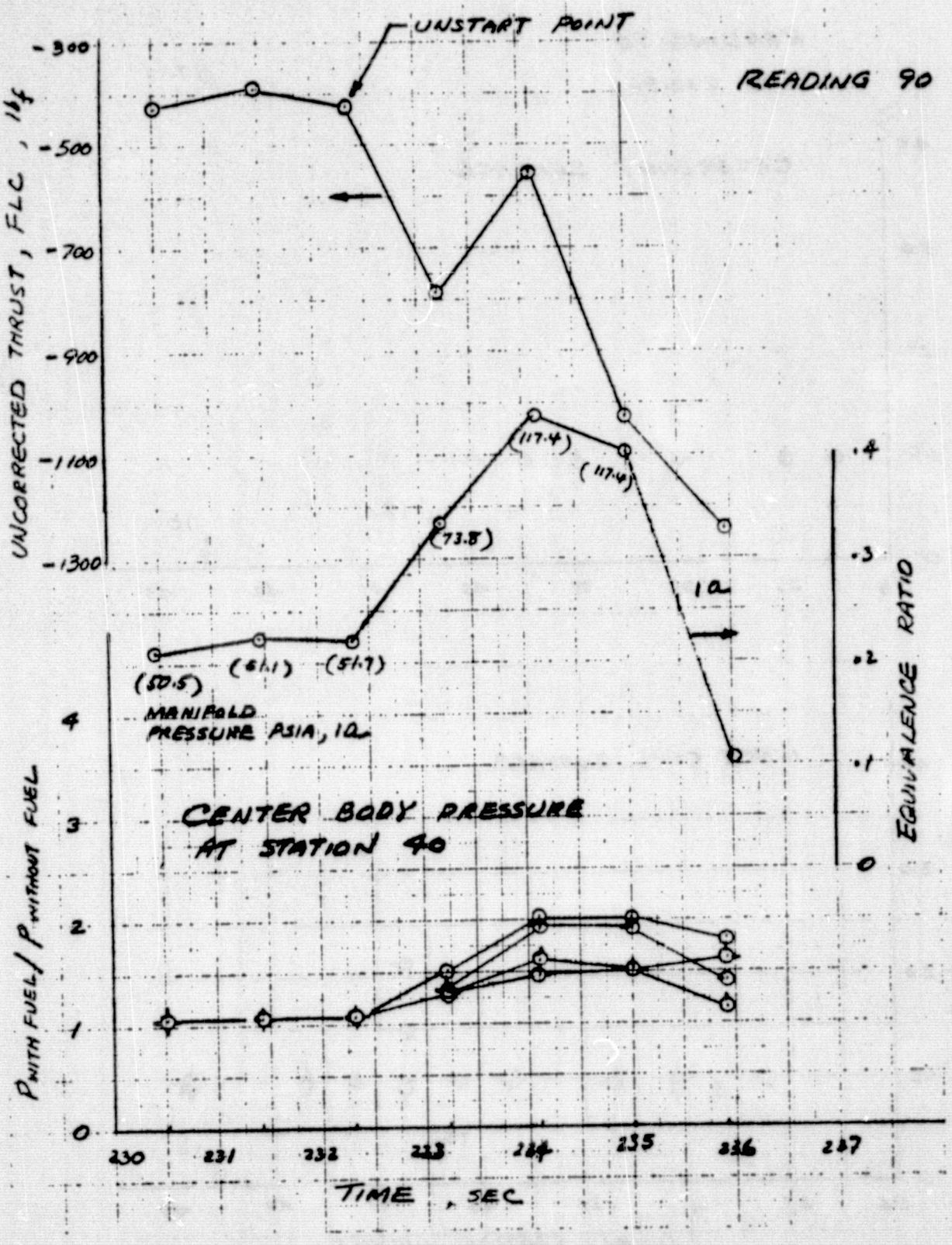

Figure 7.4-5. Mach 7 Inlet Unstart Point

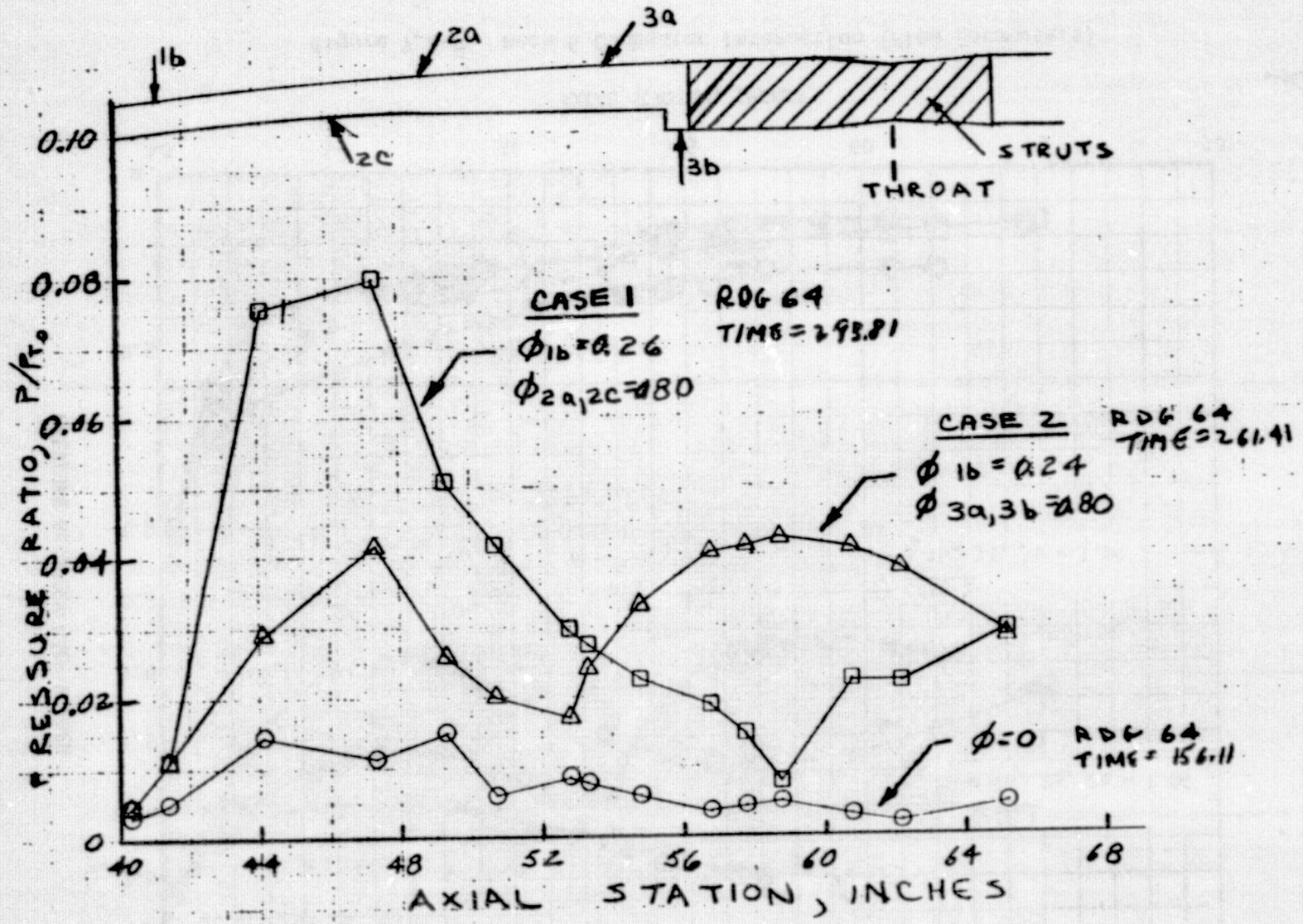

Figure 7.4-6. Mach 6 Combustor Interaction (Pressure Distribution)

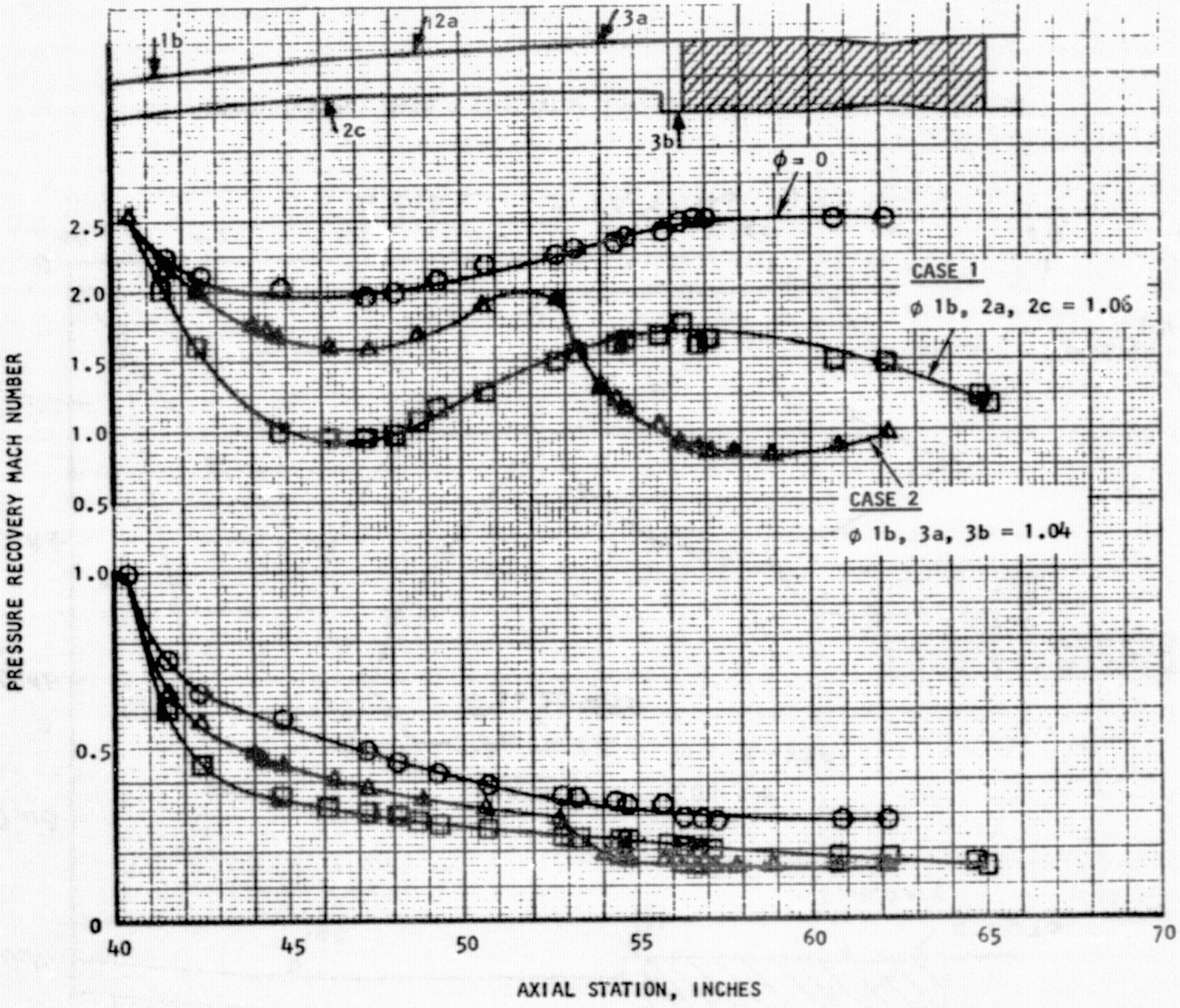

Figure 7.4-7. Mach 6 Combustor Interaction (Flow Parameters)

the constant-area section and then accelerated as the flow area increased. Because of the combustion of fuel from injectors 3a and 3b, the flow was reduced to subsonic, then accelerated to Mach 1 at the throat.

With stage interaction in Case 1, fuel from 1b was burned to an efficiency of 75 percent within 3.8 inches, while in Case 2, only about 10 percent was burned (Figures 7.2-37 and 7.2-38).

The pressure disturbance produced by the second stage injection propagated upstream to ignite the first stage and drove the Mach number down to transonic mixed-flow range. In this mixed-flow range where both supersonic and subsonic flow existed, good combustion efficiency was achieved. Interaction is difficult to assess quantitatively. It depends on local flow condition and combustor geometry. Interaction between 1b and 2c was strong in a nearly constant-area duct but interaction was weak between 2a and 2c in a diverging duct. No significant burning was observed downstream of injector 2a until the strut was reached. In the pressure and temperature range tested, high supersonic combustion efficiency was difficult to achieve in a diverging duct, as previously experienced in 2-D combustor tests (Reference 7.2-3).

Case 2 has an overall combustion efficiency of only 81 percent, compared with 96 percent in Case 1. Mixing near an equivalence ratio of one is difficult and required 24 inches of combustor length to almost completely burn, in a supersonic combustion mode in Case 1. Apparently the 8-in. length provided for subsonic combustion was too short for fuel to mix and completely burn in Case 2.

A calculation of flow residence time in the combustor indicates that there is only 500 μsec available for the fuel to mix, ignite, and react. During subsonic combustion in Case 2, the combustor residence time is reduced by one-half, even though average velocities are lower, since the total combustor length is 8 inches, compared with 24 inches, in Case 1.

7.4.3 Combustor-Nozzle Interaction

In Section 7.3.2, it was explained that from pitot-static probe measurements a significant flow yaw angle existed downstream of the struts. Flow yaw was also observed from heat patterns on the leading edge of the struts, from shock patterns ahead of probe stems on the instrumentation rig, and also from the wake behind several struts.

Figure 7.4-8 shows the heat pattern observed on the struts after a Mach 7 test. The hot gas from the combustor appears to have flowed in a clockwise direction, looking forward from the aft end as indicated by the shaded areas on Side "a" on 5-, 7-, 9-, and 11-O'clock struts. Flow ahead of 1- and 3-o'clock struts showed a reversed direction. A similar evidence of flow rotation was observed from the shock patterns on the instrumentation rig just upstream of the conical probe stems (Figure 7.4-9). The shock patterns are not symmetrical about the centerline of the probes, with most of them being displaced more to the left than to the right. This would indicate that flow was coming from the right toward the left, or in a clockwise direction viewing from aft.

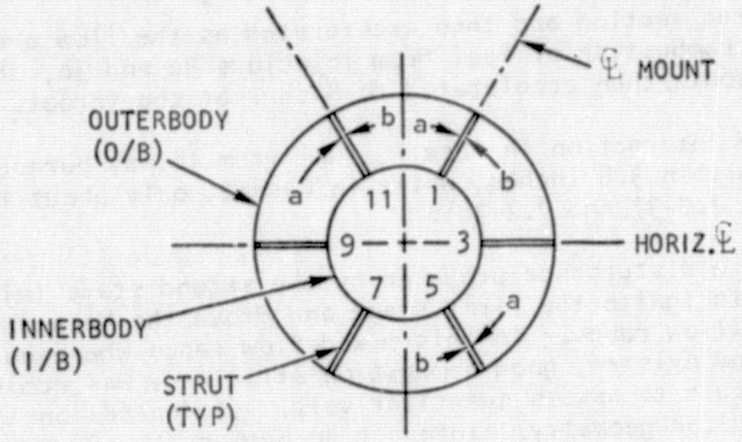

(LOOKING FORWARD FROM AFT)

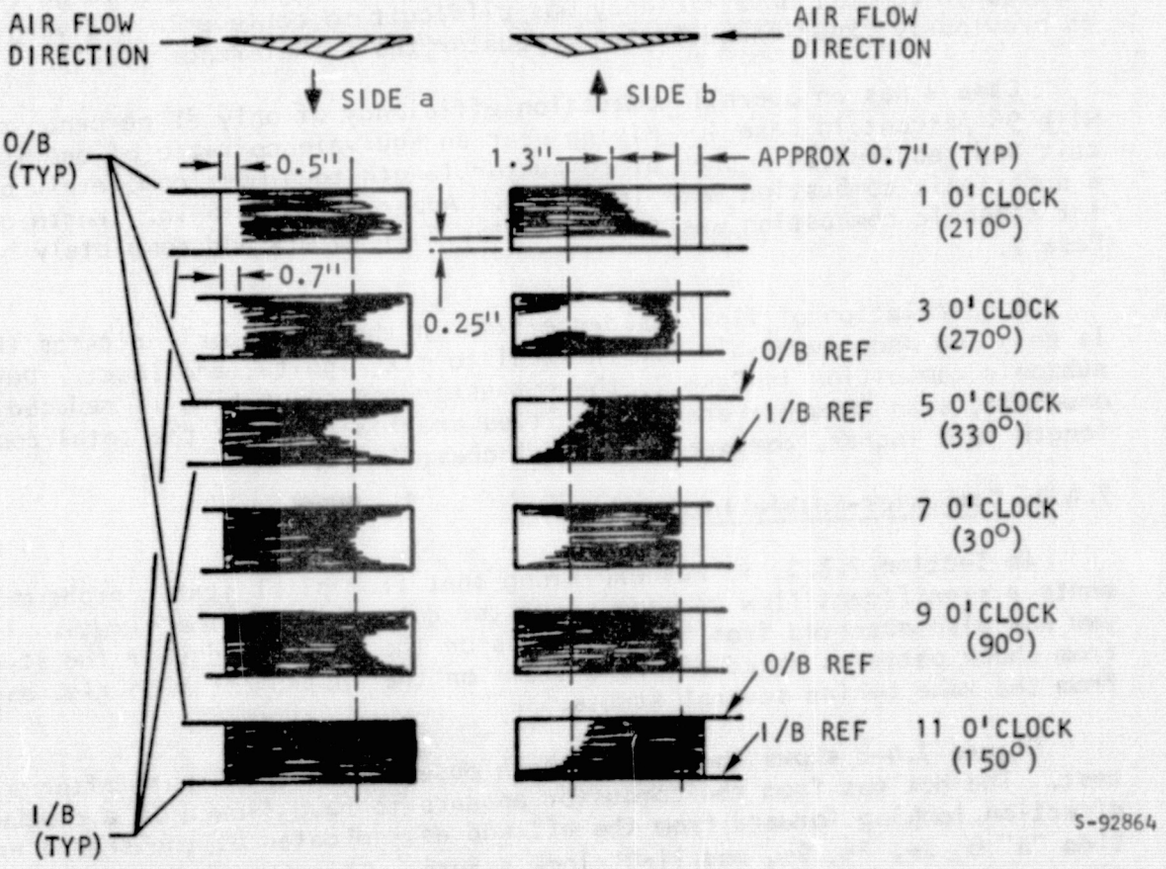

Figure 7.4-8. Heated Pattern on Strut

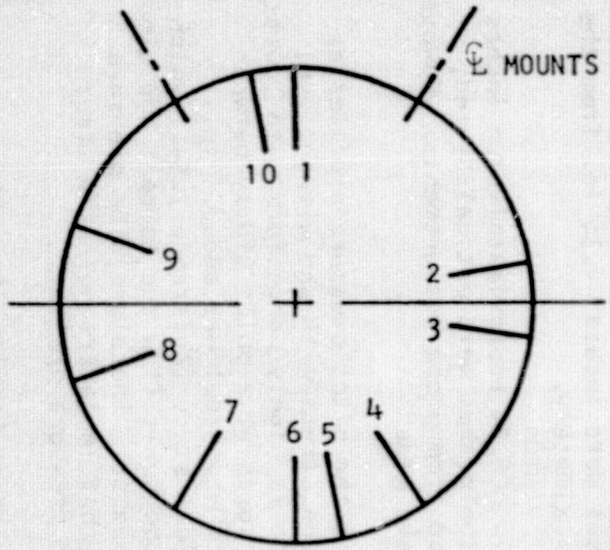

LOOKING FORWARD FROM AFT

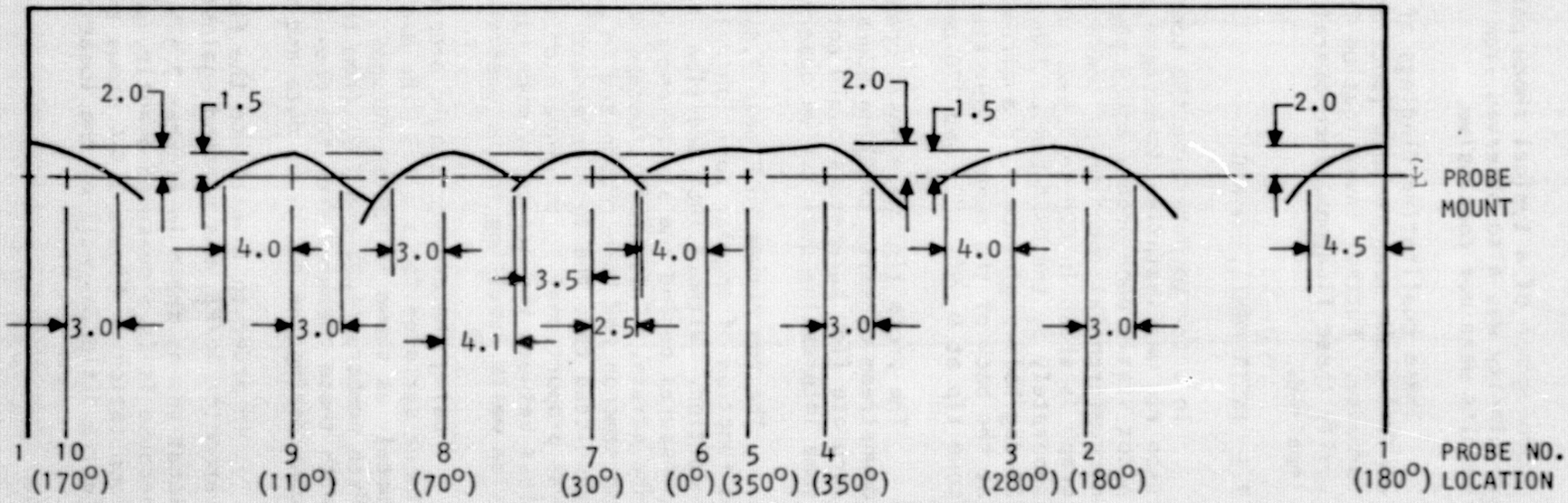

DEVELOPED VIEW OF HEAT-AFFECTED ZONE

S-92895

Figure 7.4-9. Bow Shock Pattern on Instrumentation

A photograph of a typical shock pattern is shown in Figure 7.4-10. Flow angularity was also observed from the wakes downstream of several struts but results were not conclusive.

These qualitative findings of flow angularities and those observed from conical probe measurements (Section 7.3.2) may explain the low nozzle performance. Further investigation into this problem is needed in order to verify these findings, since overall engine performance can be seriously impaired.

7.5 INSTRUMENTATION RIG

In order to determine the combustor exit flow conditions, an instrumentation rig was installed downstream of the engine. This rig consisted of 5 pitot static cone probes and 5 gas sampling-total temperature probes. The circumferential location of these probes is shown in Figure 7.5-1. A photograph is shown in Figure 7.5-2. The results of gas sampling will be reported separately by the NASA-LeRC. The cone-static probes had a blunt nose, a 25-deg half-angle cone and a circumferential slot for coolant water ejection at the back of the cone. Four static orifices were located 0.36 in. from the cone tip at 0, 90, 180, and 270 degrees approximately.

The probe tips were positioned at Station 66.74 approximately two inches downstream of strut trailing edges. Since the probes were not calibrated, accurate flow parameters could not be deduced from probe measurements. However, some interesting qualitative observations were made.

The top curves in Figure 7.5-3 represent the pitot pressure profiles as a function of angular position relative to the struts, with and without fuel addition. Without fuel addition, the profile is highly nonuniform, with lowest pressures behind the struts and highest pressures at a point midway between the struts. This profile became more uniform when fuel was added. This phenomenon had been recognized in a theoretical study (Reference 7.5-1) which predicted that the total pressure loss in supersonic flow due to heat addition was proportional to the square of the Mach number. Therefore, the pressure loss between the struts is much higher than that in layers near the strut side walls, resulting in the observed uniform pressure profile.

Using the average static pressure measured at Station 65 on the outer and inner surfaces for $\gamma = 1.3$, the Mach number profiles may be calculated approximately as shown in bottom curves. It is interesting to note that the average Mach numbers (1.08 and 2.9) from these curves appear to agree reasonably well with those computed from the one-dimensional performance program (1.2 and 2.55), considering the different data and methods used in the calculations.

In order to investigate the flow angularity at the combustor exit, a parameter $\Delta p/P_T'$, was plotted against equivalence ratios for different probe locations as shown in Figures 7.5-4 and 7.5-5. This parameter was selected because it is a measured quantity and does not involve parameters from other computations. Figure 7.5-4 shows that the flow yaw angle was affected by the fuel addition, as well as the location of the probe.

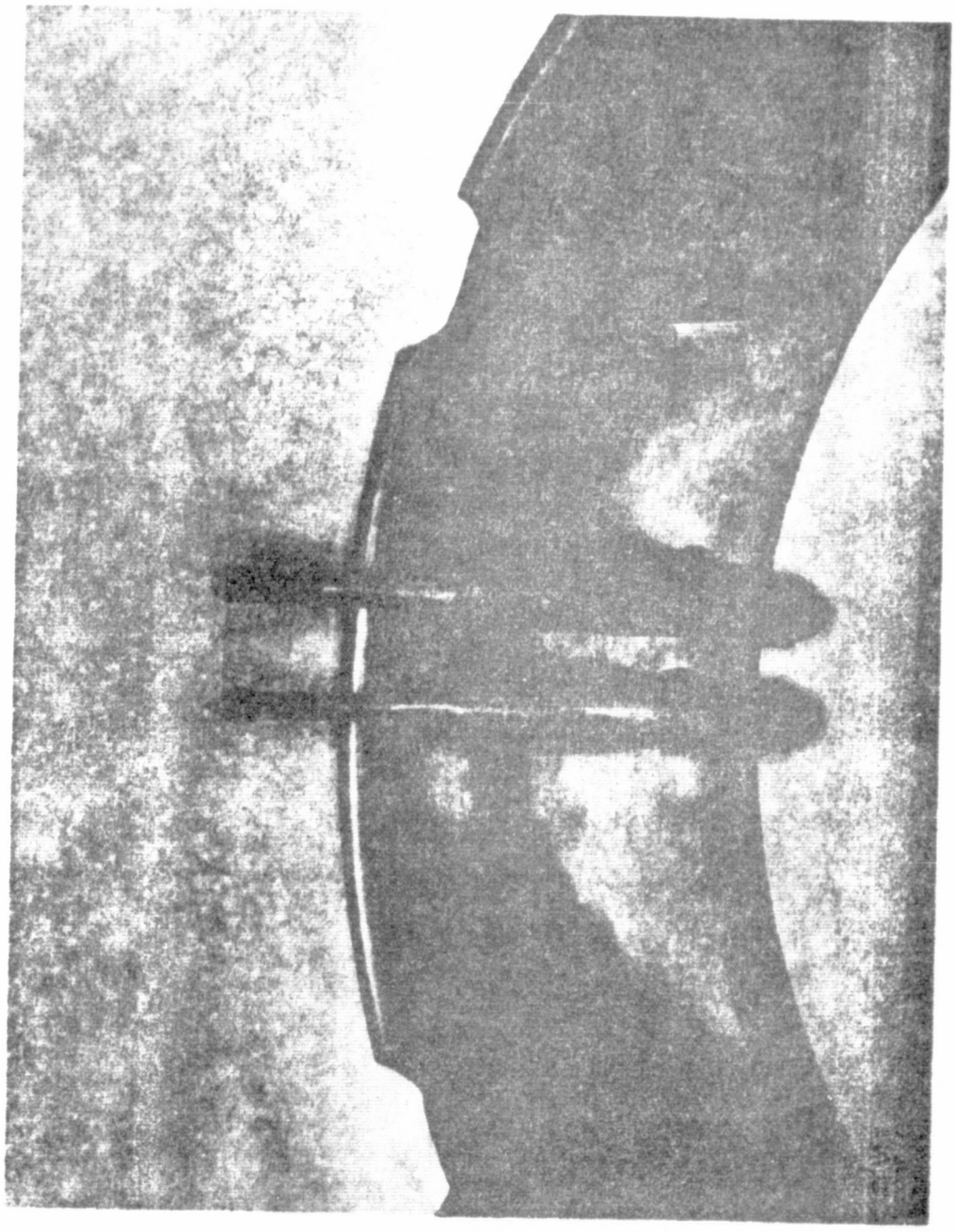

F-21072

Figure 7.4-10. Photograph of Shock Pattern

ORIGINAL PAGE IS
OF POOR QUALITY

PROBE LOCATION
VIEW FROM REAR

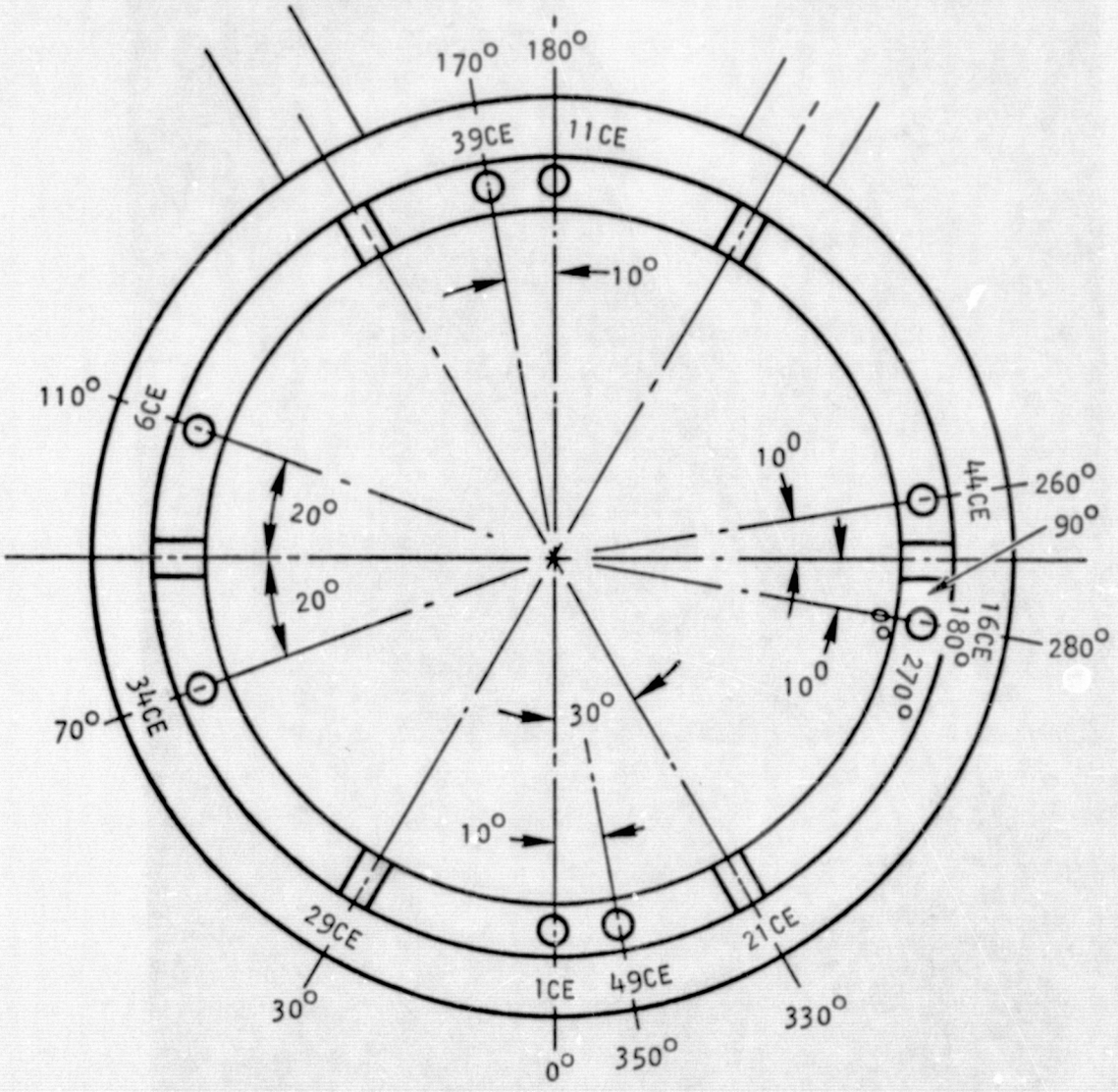

PROBE TIP AT 20.42 IN. DIA., STATION 66.74 IN.

PITOT STATIC PROBES
1CE, 6CE, 11CE, 16CE, 21CE

GAS SAMPLING-TEMP PROBES
29CE, 34CE, 39CE, 44CE, 49CE

S-92863

Figure 7.5-1. Probe Location, View from Rear

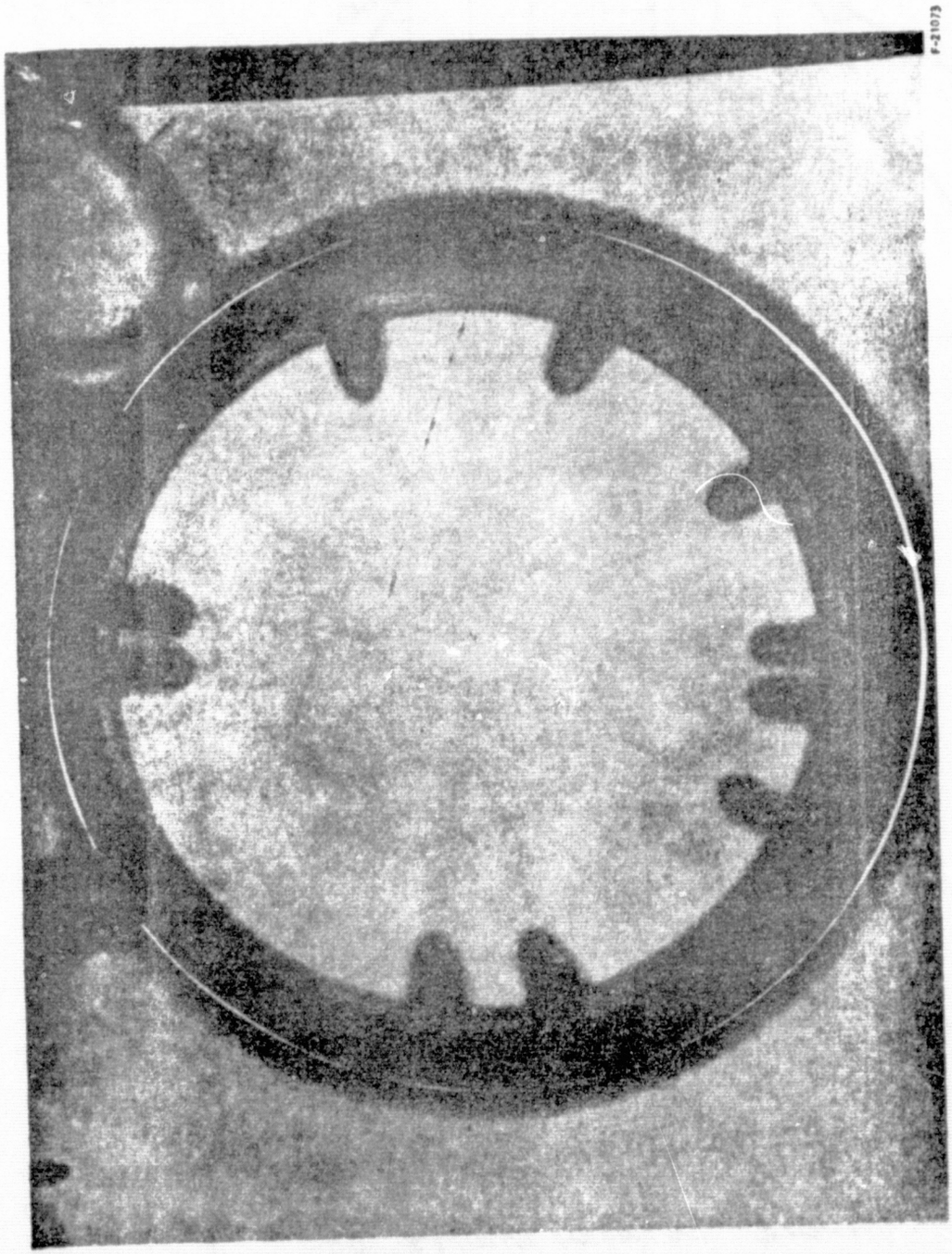

Figure 7.5-2. Instrumentation Rig Probes

ORIGINAL PAGE IS
OF POOR QUALITY

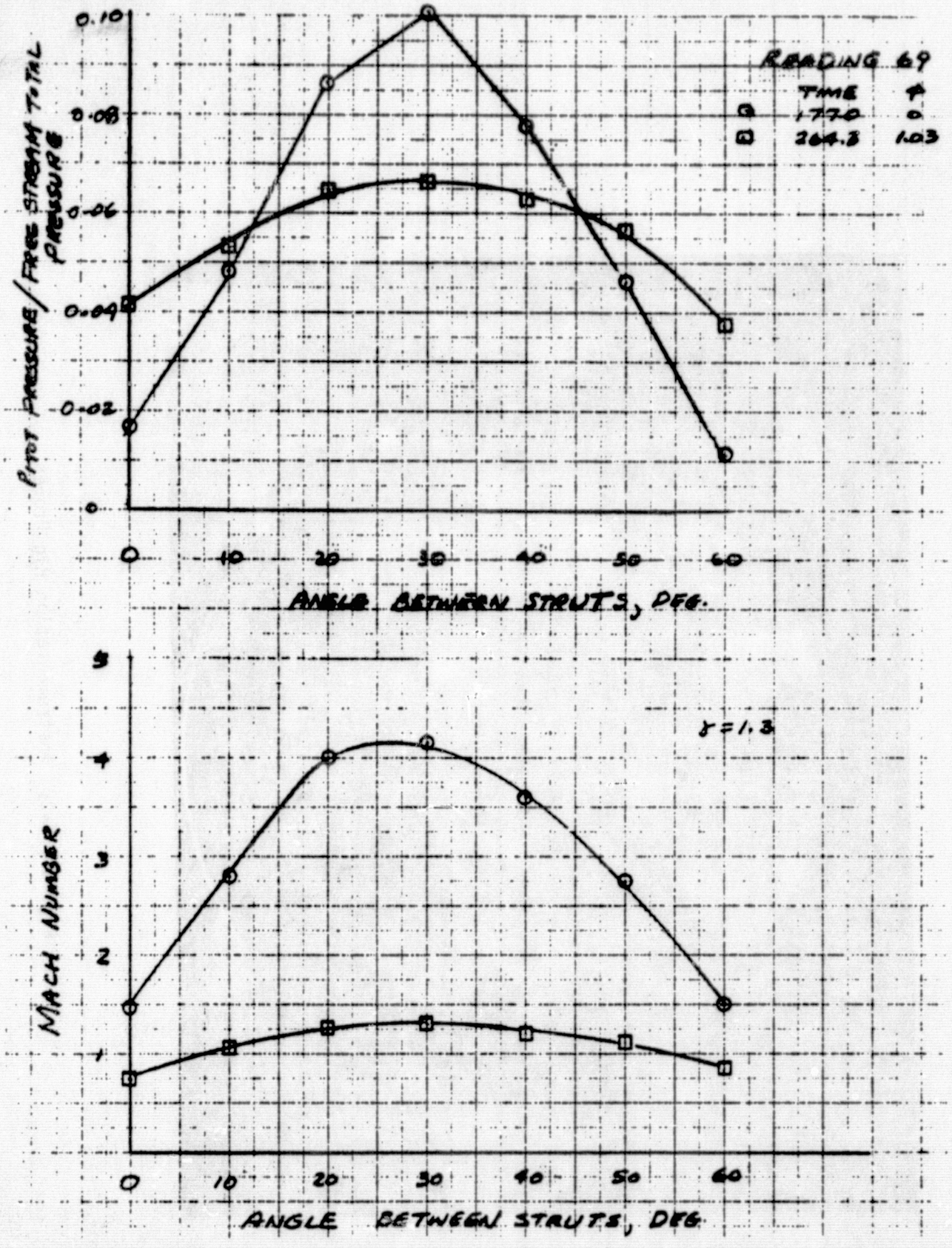

Figure 7.5-3. Mach ' Flow Parameters at Combustor Exit

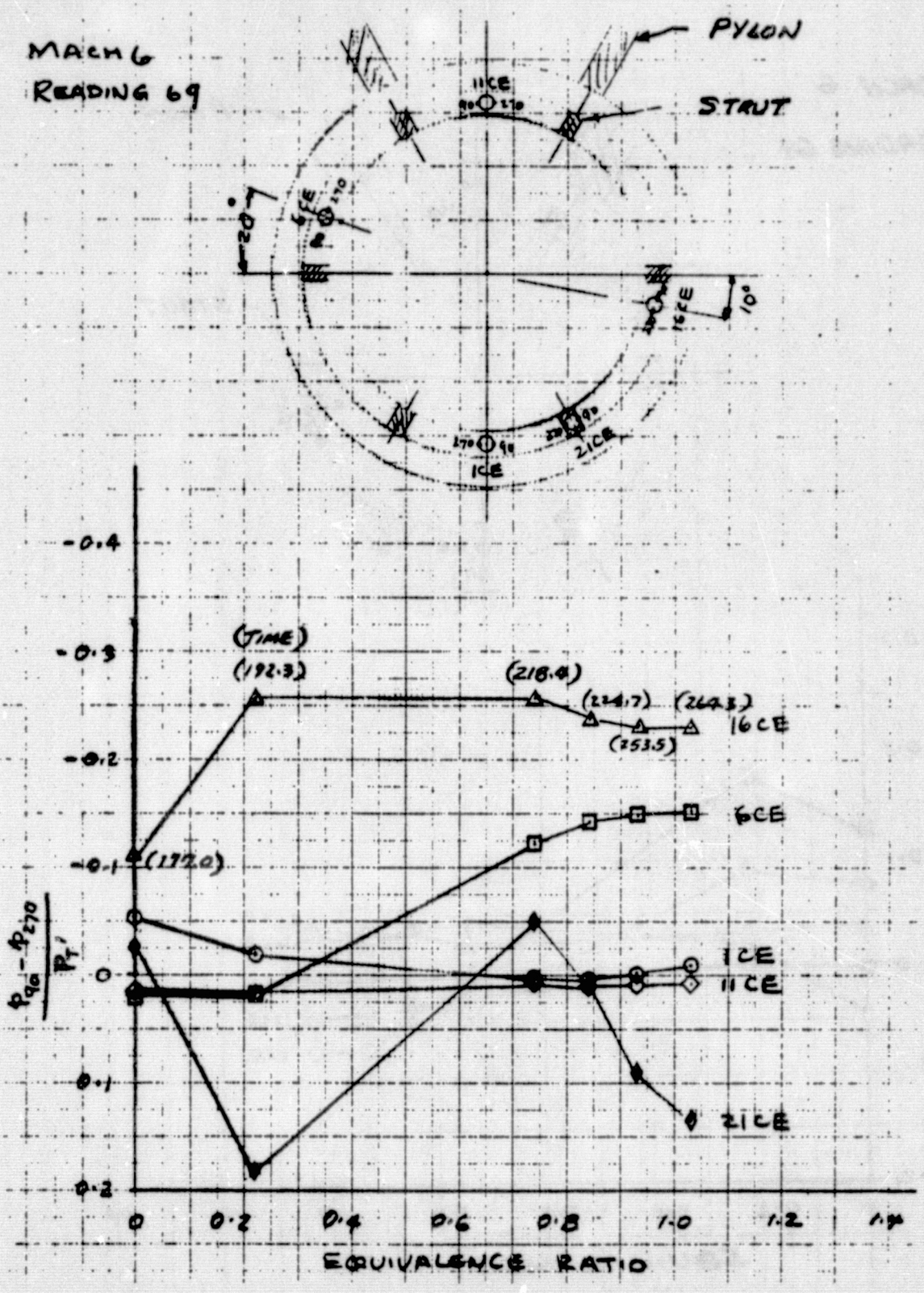

Figure 7.5-4. Mach 6 Flow Field (Yaw) at Combustor Exit

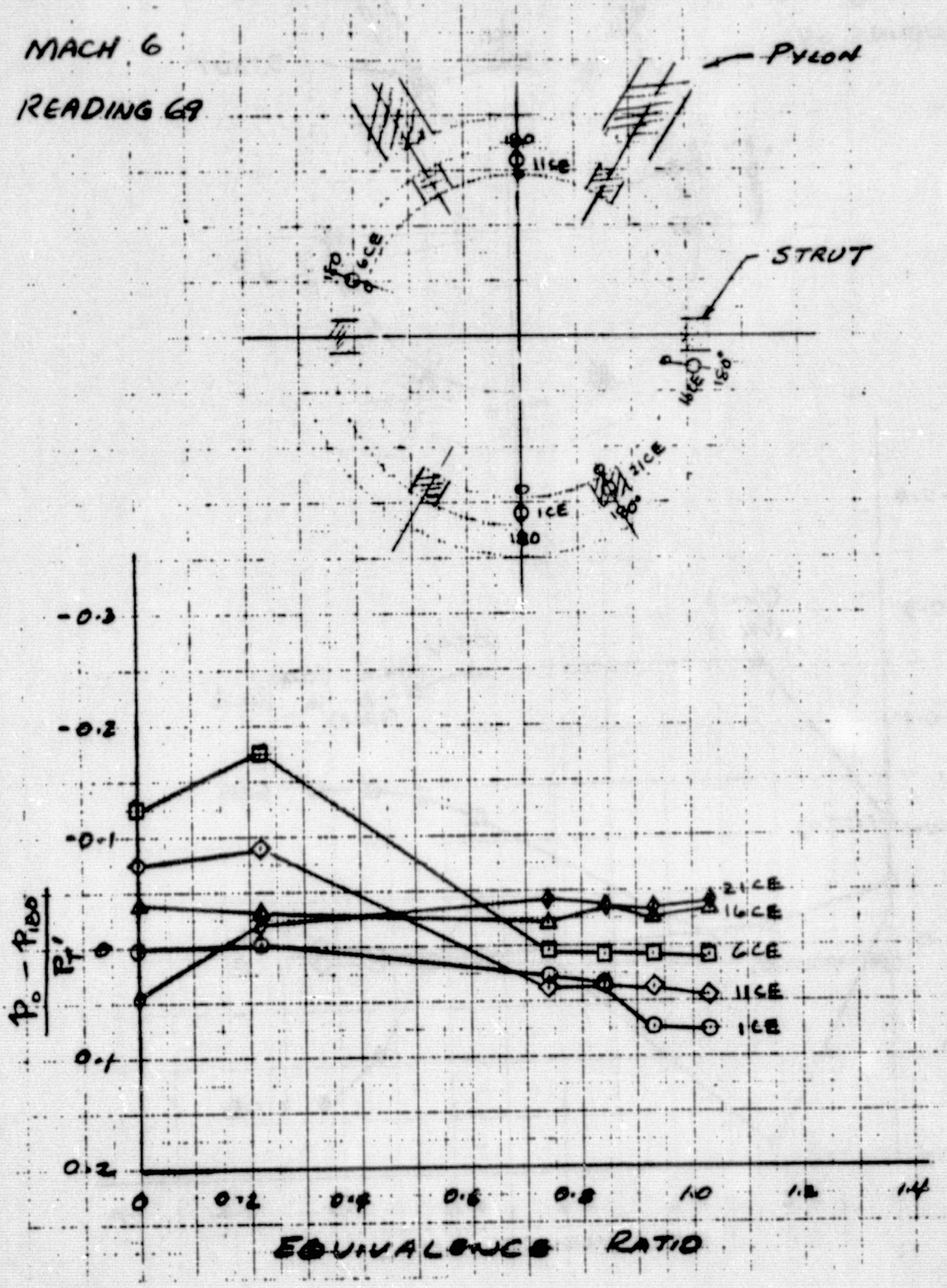

Figure 7.5-5. Mach 6 Flow Field (Pitch) at Combustor Exit

Probes 1CE and 11CE,which were located midway between the struts,exhibit no significant yaw,while probes 16CE which were located 10 and 20 degrees clockwise, respectively, from the centerline of the struts,indicate an increase of yaw as the probes approach the strut centerline. The magnitide of yaw increased with fuel addition. Probe 21CE, which is located at the strut centerline, showed the inconsistent behavior expected from base flow. Based on these observations, the flow tended to move toward the low-pressure region at the strut centerline. The pressure difference between main flow stream and strut base became greater as more fuel was added to the stream,and therefore the yaw became more pronounced. It may be assumed that the flow would have a yaw angle in an opposite direction in the other half of the strut span. However, this could not be substantiated because no probe was installed in that region. This yaw angle can cause severe loss in nozzle performance because the nozzle exit momentum is directly proportional to the cosine of yaw angle.

The flow pitch is represented by a similar parameter in Figure 7.5-5. The magnitude of the pitch was relatively small. The flow exhibited a tendency to move inward toward the nozzle plug with no fuel addition, but the trend was reversed with fuel addition.

Similar plots are presented for Mach 7 and 5 in Figures 7.5-6, 7.5-7, 7.5-8, and 7.5-9 respectively. The combustor exit Mach number profile became progressively nonuniform as the freestream Mach number was increased. The effect was more pronounced without fuel addition. As expected, the combustor exit-pitot-pressure-to-freestream-total-pressure ratio decreased with increased freestream Mach number. It is interesting to note that at the Mach 5 subsonic combustion mode, the calculated combustor exit Mach number was near unity for all probes in Figure 7.5-8.

Examination of Figures 7.5-4 and 7.5-7, shows that the combustor exit flow yaw existed at Mach 7 and 5. It also appears that degree of yaw increased with increasing freestream Mach number.

7.6 COOLING LOAD AND SURFACE TEMPERATURE DISTRIBUTION

The AIM overall cooling load was calculated from water temperature rises and flow rates for the inner and outer surfaces. The cooling load varied with inlet total pressures as well as the injector locations as shown in Figure 7.6-1 for Mach 6 tests; the former was due to change of heat transfer coefficients with increased airflow rate, while the latter was due to changes of combustor length with different injectors.

The maximum cooling load for two-stage combustion at Mach 6 was approximately 5500 Btu/sec at equivalence ratio of unity with P_T = 750 psia and T_T = 3000°R. This energy loss equals approximately 13 percent of total heat release. This heat loss was partially compensated for by heating the fuel before injection up to 1500°R in order to simulate the regeneratively cooled system. At a 3-deg angle of attack, the cooling load up to 6500 Btu/sec was noted.

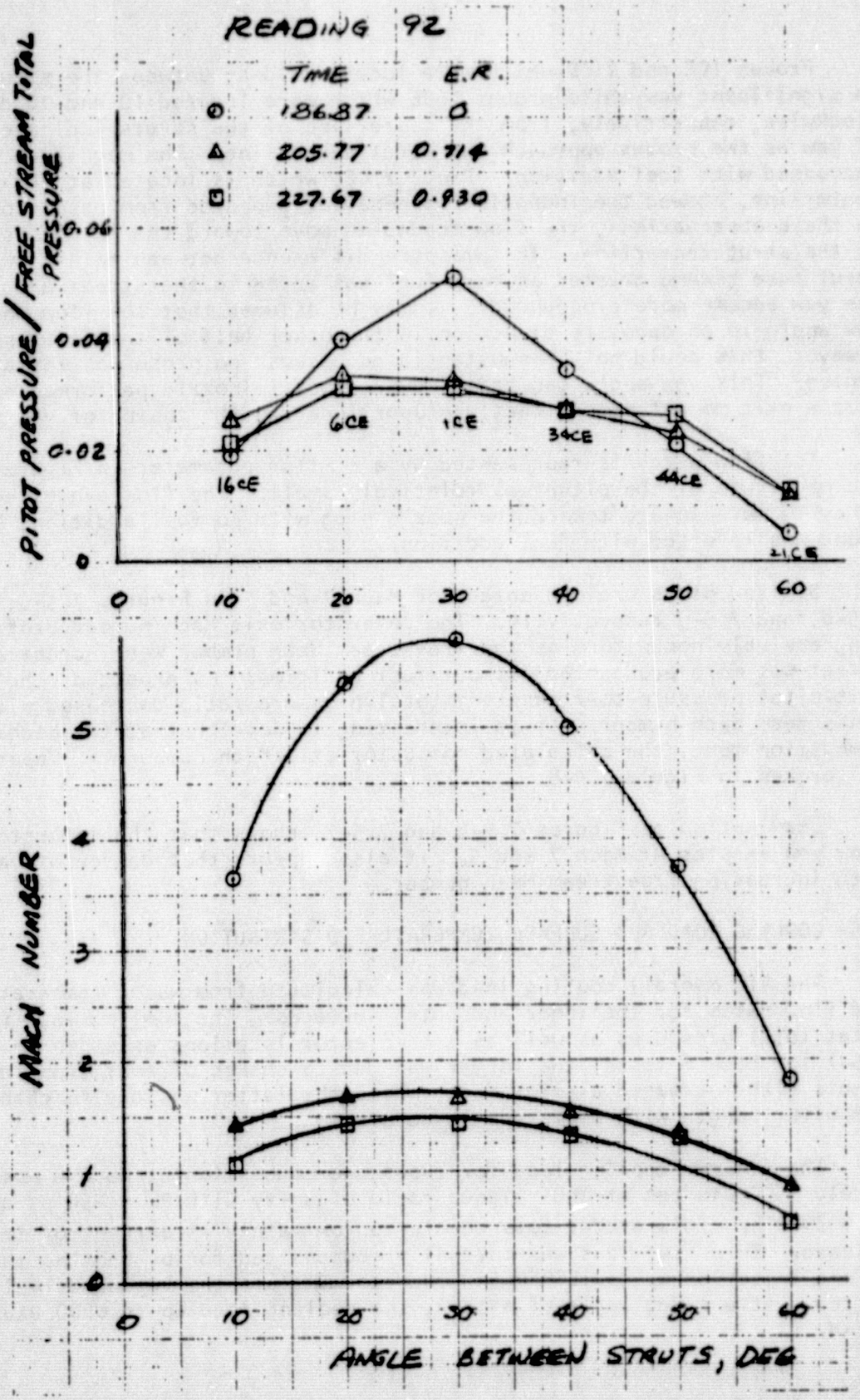

Figure 7.5-6. Mach 7 Flow Parameters at Combustor Exit

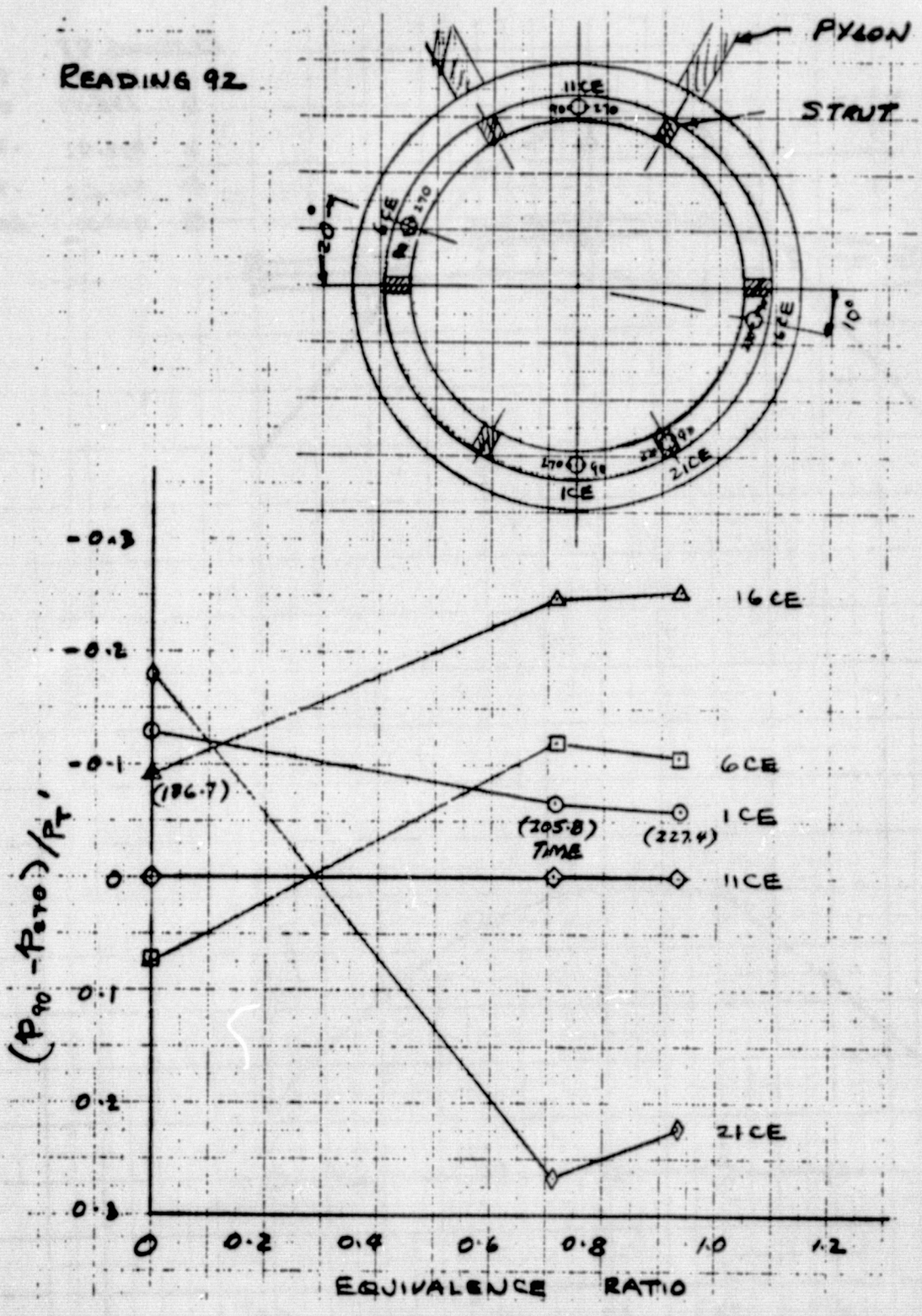

Figure 7.5-7. Mach 7 Flow Field (Yaw) at Combustor Exit

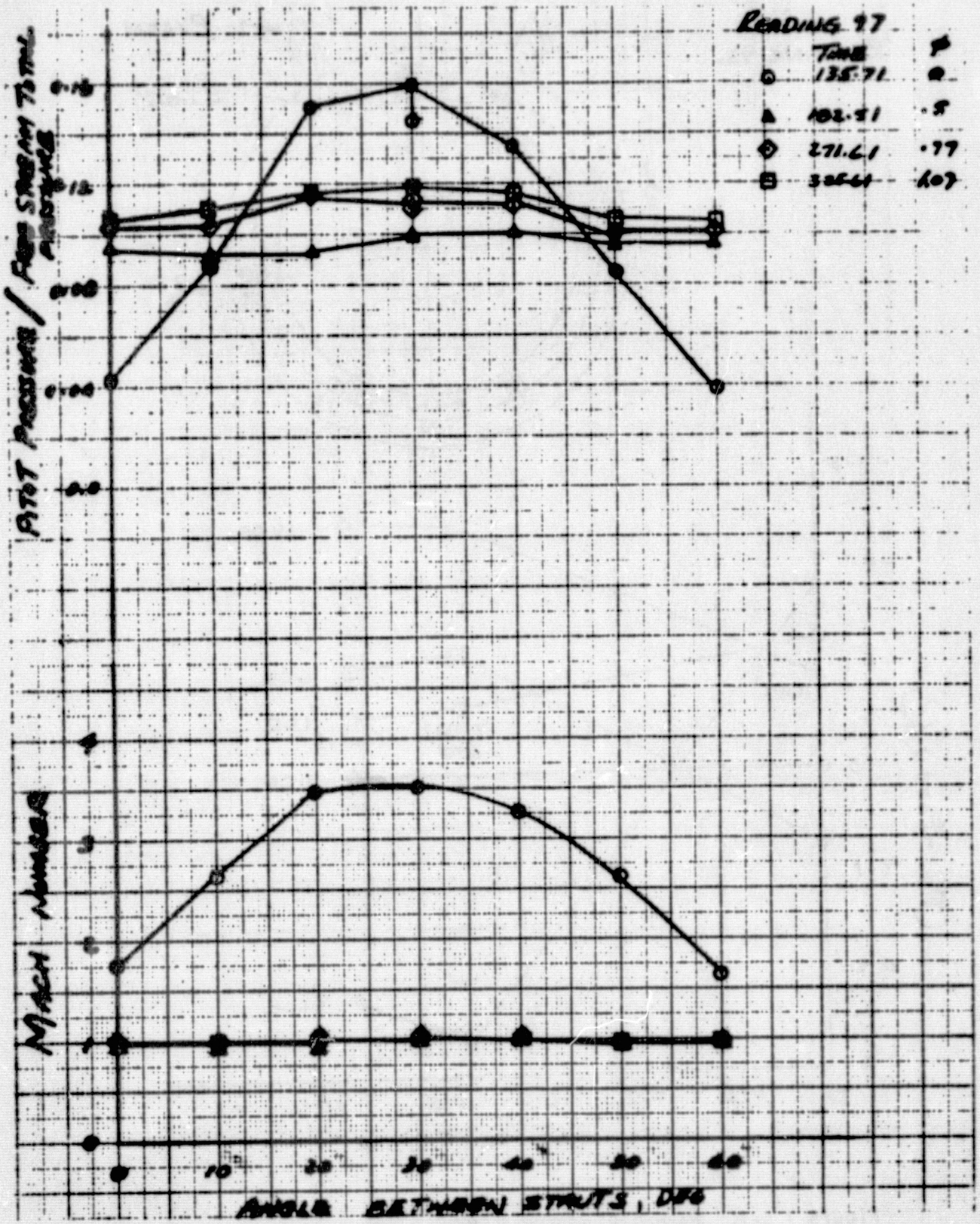

Figure 7.5-8. Mach 5 Flow Parameters at Combustor Exit

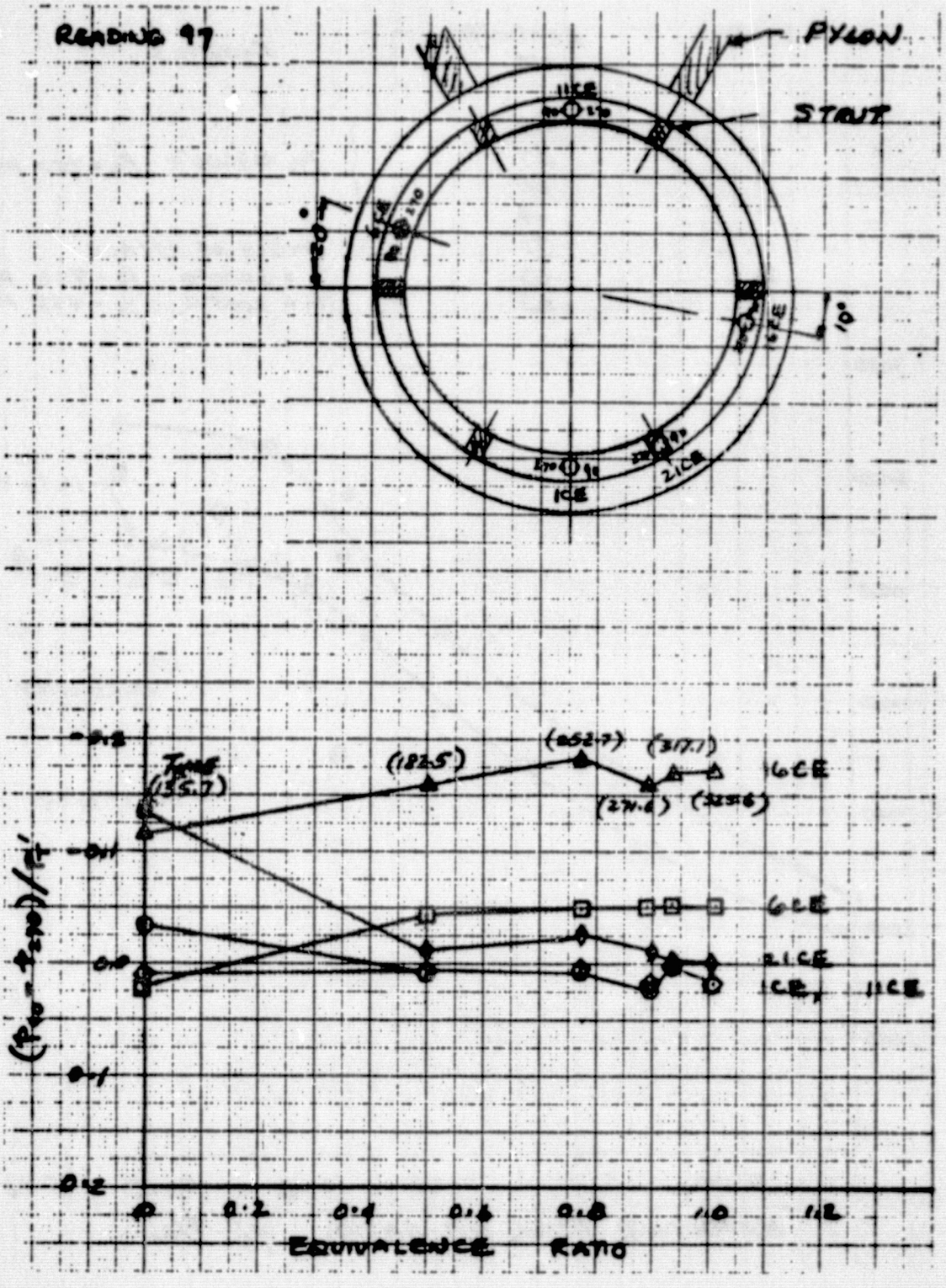

Figure 7.5-9. Mach 5 Flow Field (Yaw) at Combustor Exit

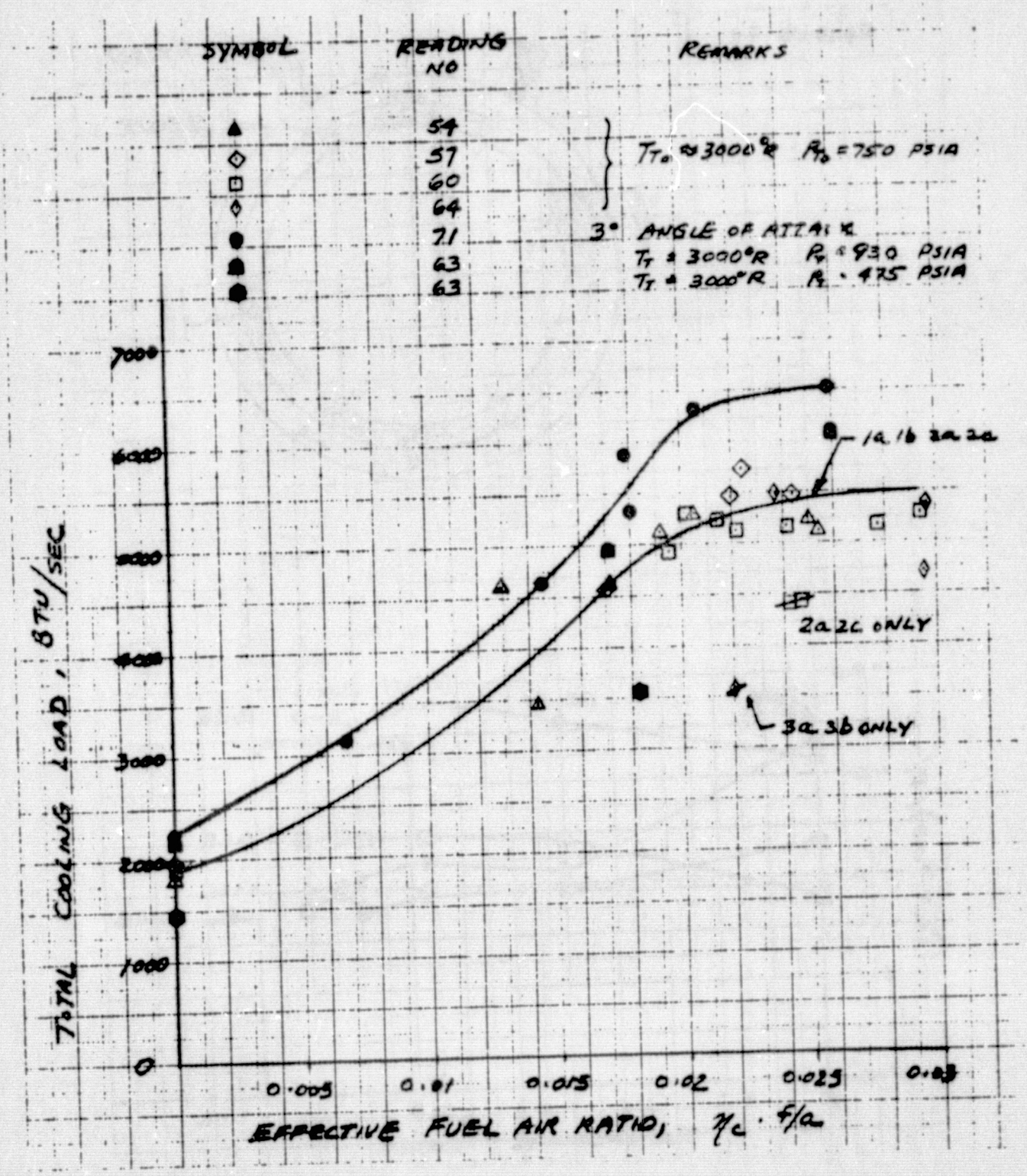

Figure 7.6-1. Mach 6 Overall Cooling Load

The estimated skin temperature is shown in Figure 7.6-2. This temperature was calculated based on a linear temperature gradient between the water temperature and the thermocouple temperature which was imbedded approximately 0.03-0.04 in. under the skin surface. The average skin thickness was 0.150 in. The maximum calculated surface temperature of 1450°R occurred at the second-stage injector station corresponding to the peak-pressure rise point. The increase of surface temperature both on the outerbody and on the inner body downstream of Station 60 further substantiate the combustion phenomenon between struts as discussed in Section 7.2-7. This temperature rise between struts was not observed without fuel injection.

The one-dimensional calculated total gas temperature in the combustor is also shown in Figure 7.6-2. The close agreement between the calculated and the theoretical adiabatic temperature indicates that good combustion was achieved and that the combustor heat loss and the energy gain by heating up the fuel was about the same, which is necessary in simulating a regeneratively cooled system.

Figure 7.6-3 shows the theoretically calculated engine cooling load distribution as compared with the measured heat loss. The measured heat loss distribution was determined from overall cooling water temperature rise and the skin thermocouple temperature as discussed in Section 6-2. This method was considered to be more reliable than measuring the water temperature rise at many points in the engine as originally planned,because of numerous faulty water thermocouple readings. The maximum local averaged heat flux was 355 Btu/sec-ft^2 at the second-stage fuel injection station. The average heat flux for the combustor was 200 Btu/sec-ft^2. The stagnation heat flux for the strut leading edge was 1711 Btu/sec-ft^2 as compared with a theoretical design value of 1890 Btu/sec-ft^2 (Reference 7.6-1) calculated at a slightly different operating condition. The calculated overall heat load is in good agreement with average experimental data.

The cooling loads were significantly reduced in Mach 7 tests, primarily due to reduced airflow rate to 15 lb/sec from 26.8 lb/sec in Mach 6. Cooling loads of 4000 and 1500 Btu/sec with equivalence ratio of one and without fuel injection, respectively, were obtained,as compared to 5500 and 1800 Btu/sec in Mach 6. Figure 7.6-4 shows the overall cooling load versus fuel-air ratio. The effective fuel-air ratio was not used because the combustor efficiency cannot be accurately determined in Mach 7 tests. It indicated from the heat loss calculation that no combustion occurred prior to fuel-air ratio of 0.015 ($\phi \approx 0.5$). The cooling load distribution for typical cases is presented in Figure 7.6-5. The skin thermocouple temperatures were approximately 150°R to 200°R below the Mach 6 temperatures as shown in Figure 7.6-6. The calculated theoretical temperature indicated no significant burning downstream of injector 2a where the area is diverging. A large temperature rise occurred downstream of the step between the strut sections.

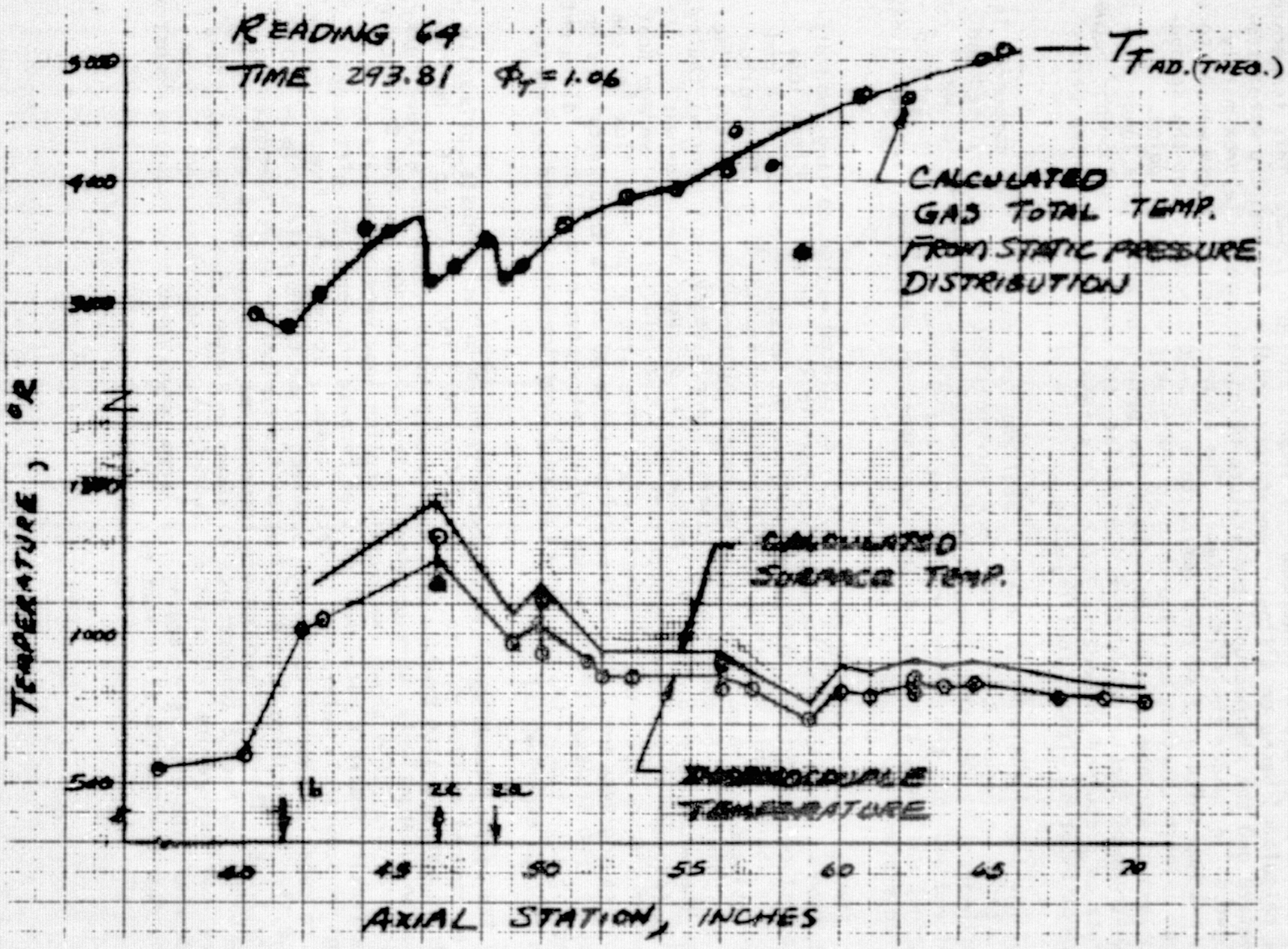

Figure 7.6-2. Temperature Distribution

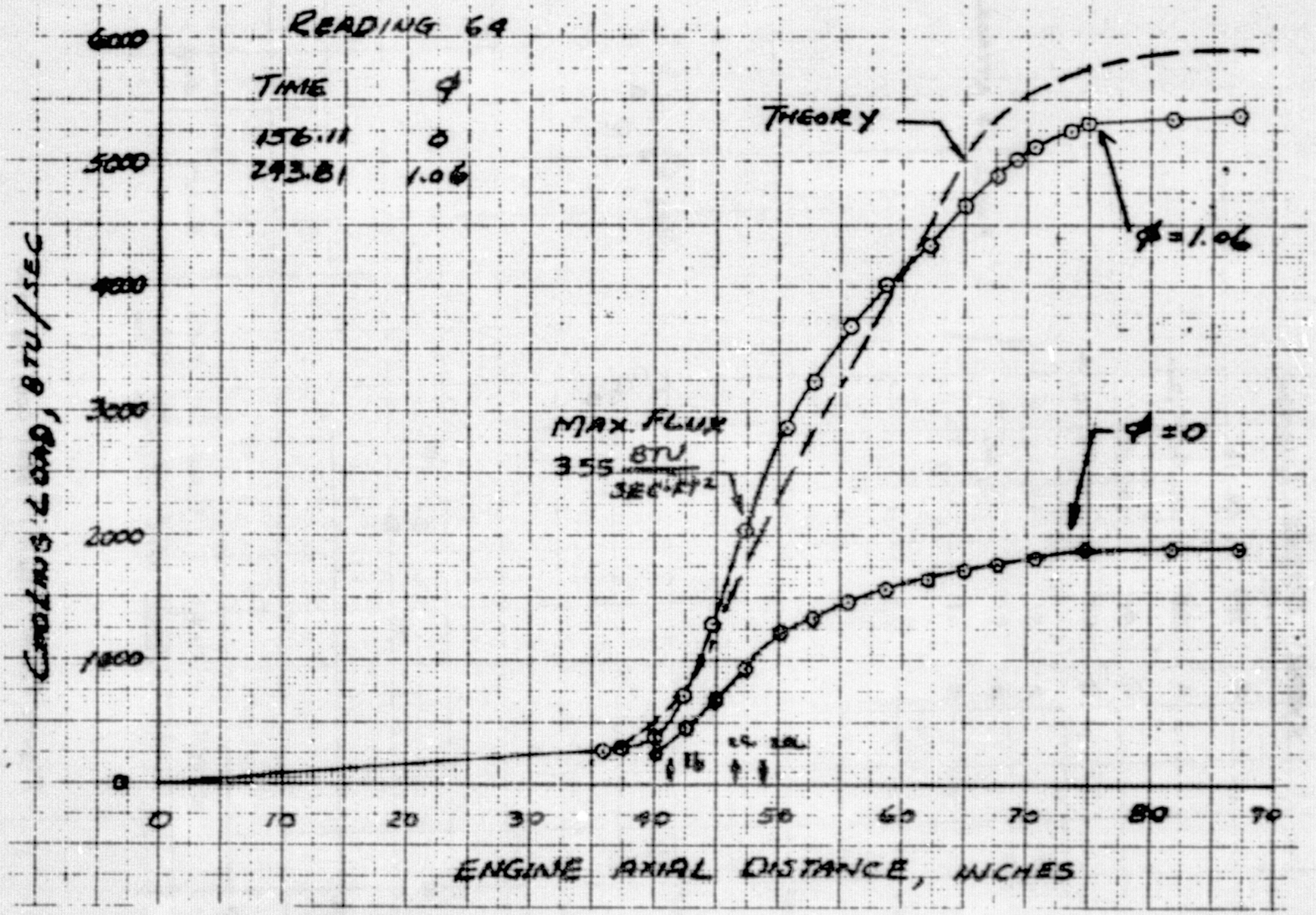

Figure 7.6-3. Mach 6 Accumulative Cooling Load Distribution

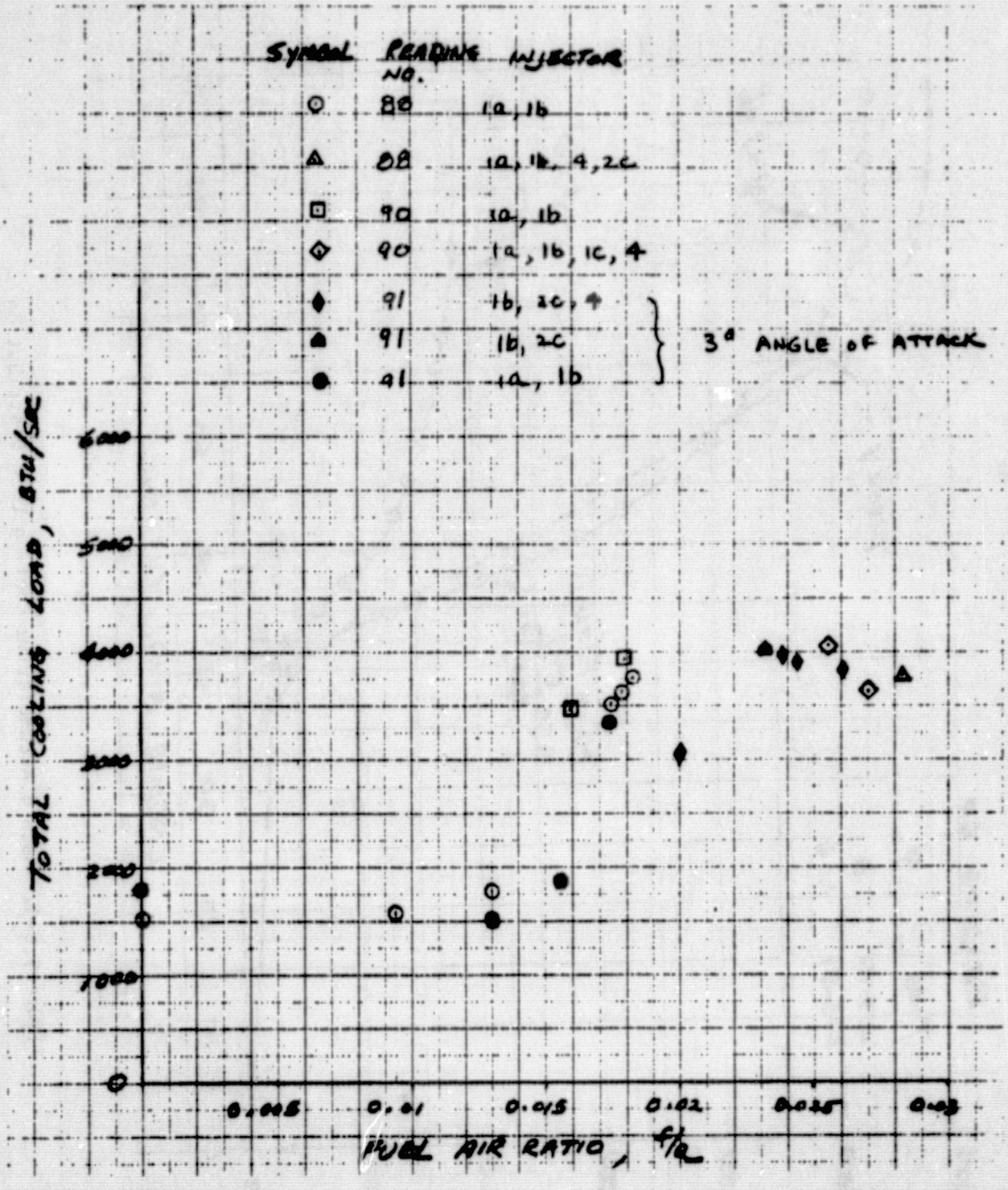

Figure 7.6-4. Mach 7 Total Cooling Load

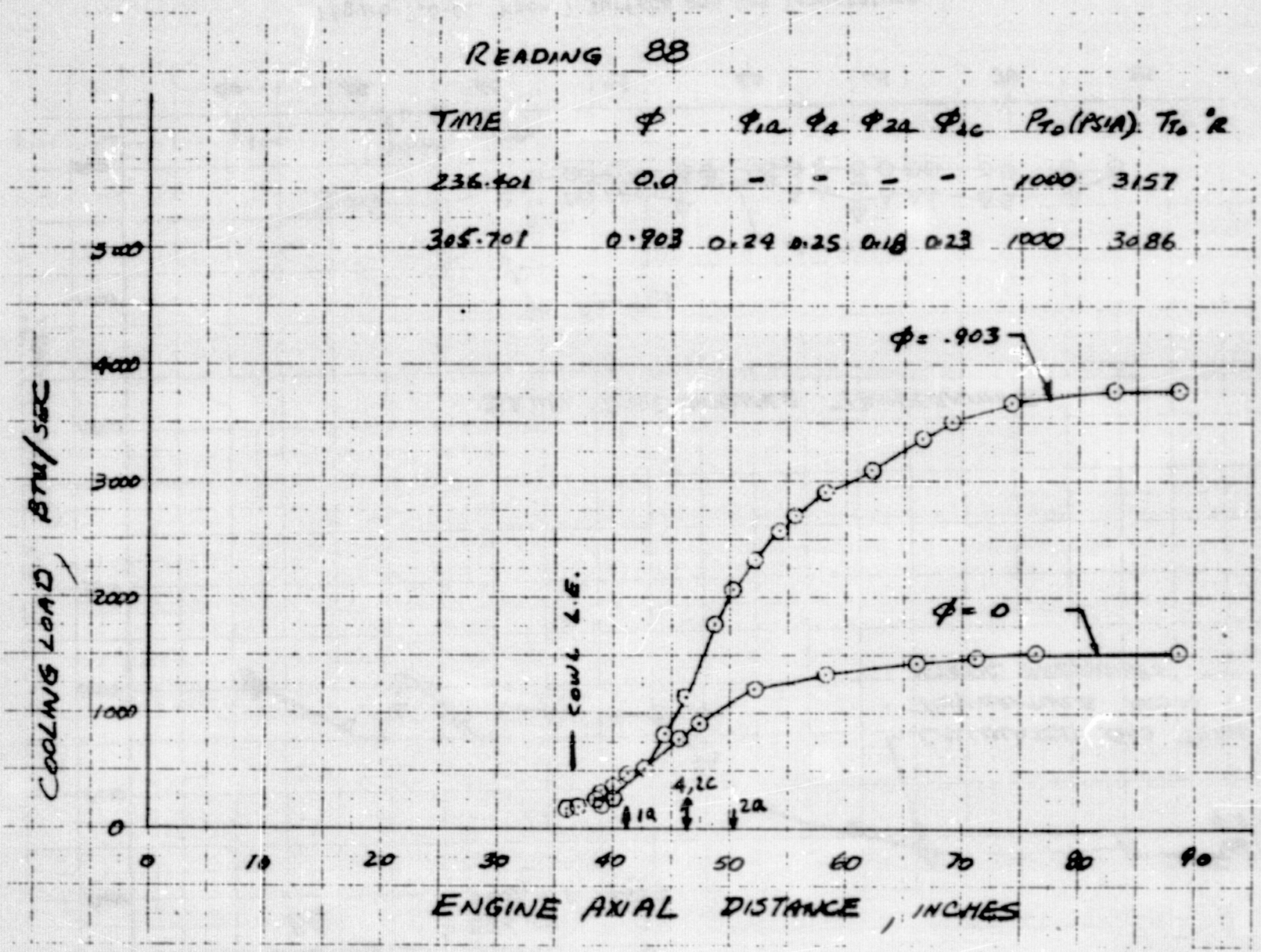

Figure 7.6-5. Mach 7 Accumulative Cooling Load Distribution

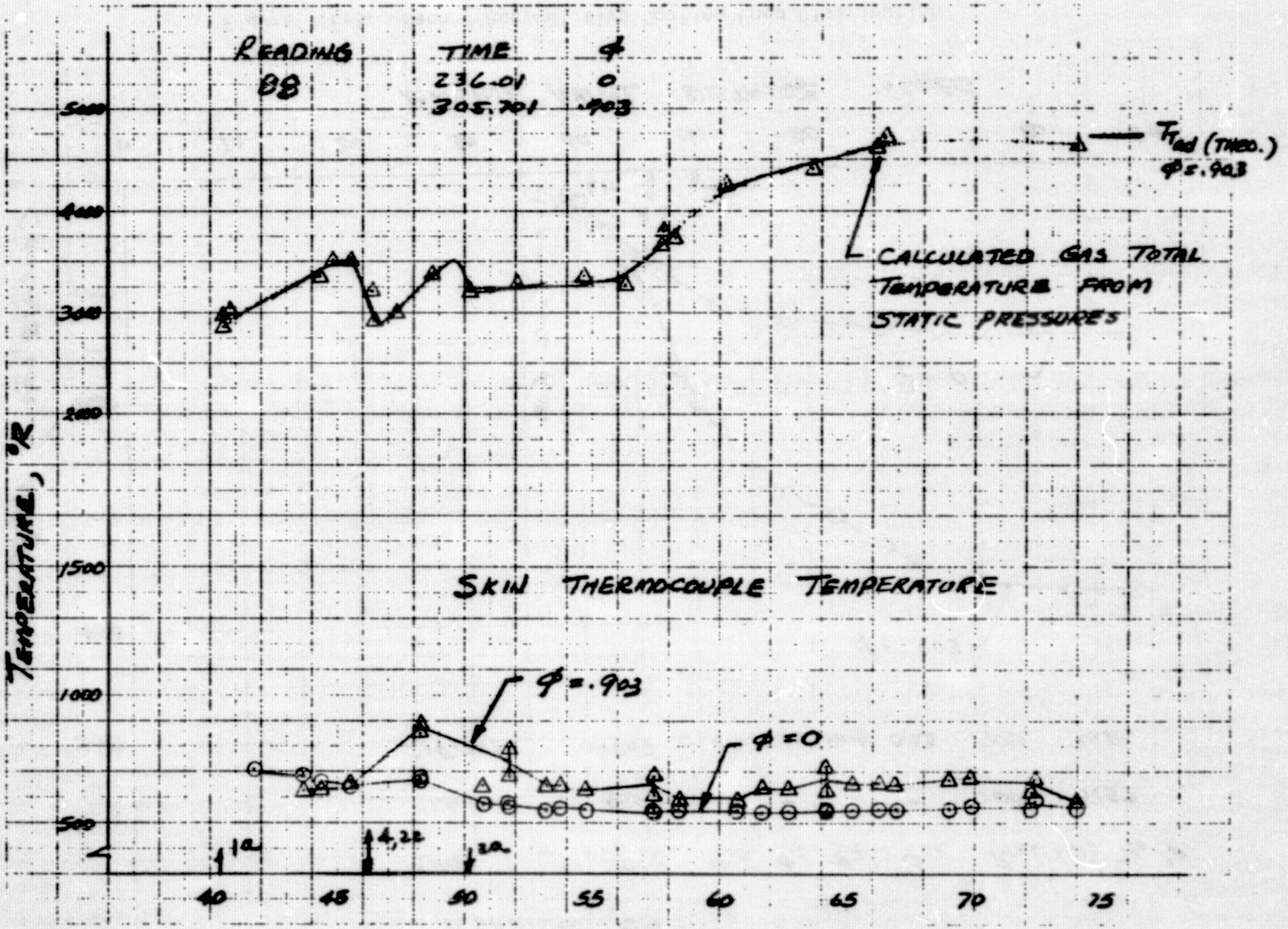

Figure 7.6-6. Mach 7 Surface and Gas Temperature

The maximum cooling load at Mach 5 subsonic combustion mode was approximately 4500 Btu/sec at an equivalence ratio of 1.19 as shown in Figure 7.6-7. In supersonic combustion mode and in 30 deg angle of attack, the overall cooling load was slightly higher. The typical cooling load distribution along the engine axial distance for both subsonic and supersonic combustion mode are presented in Figure 7.6-8. It should be pointed out that the difference in cooling load ahead of fuel injection station with and without fuel addition was probably due to the method of calculation rather than actual cooling load. Significant skin temperature rise was observed in subsonic combustion as shown in Figure 7.6-9. In this case, fuel was heated up to 1260°R with a gain of approximately 4200 Btu/sec, calculated from 50°R fuel, simulating a regeneratively cooled system. This gain of energy was about equal to the heat loss of 4300 Btu/sec. Thus, the difference of the adiabatic gas temperature of 4760°R to the calculated gas temperature of 4500°R was attributable to incomplete combustion. This re-affirmed the one-dimensional calculated combustor efficiency for this case of only 74 percent.

An interesting comparison of overall cooling load for unit inlet air flow near equivalence ratio of unity for three different Mach numbers is shown below.

Mach number	P_T, psia	T_T, °R	ϕ_T	η_C	Heat Loss/W_{air}, Btu/lb_m
5	417	2229	1.03	0.74	129.9
6	750	3000	1.06	0.95	203.12
7	1000	3085	0.9	0.84	250.86

7.7 OVERALL ENGINE PERFORMANCE

The internal thrust, T_i, is defined as the net sum (in a direction parallel with and opposed to the entering airstream) of the absolute pressure and friction imposed by the fluids passing through the engine on the physical parts of the engine (Reference 7.7-1). The engine net internal thrust was determined by two independent methods. The first method used the thrust measurements corrected with the external drag force and cavity force. Both of these forces were in the same order of magnitude as the net thrust force. The external drag force was large, due to the steep outer cowl angle and the high pressures produced between the outer cowl and the tunnel shroud when fuel was injected. The cavity force was caused by the unbalanced forces from purge nitrogen flow in the AIM.

The second method used a direct calculation from measured pressures on the engine surface ($\int PdA$), the calculated friction force (Reference 6.4-1), and fuel momentum.

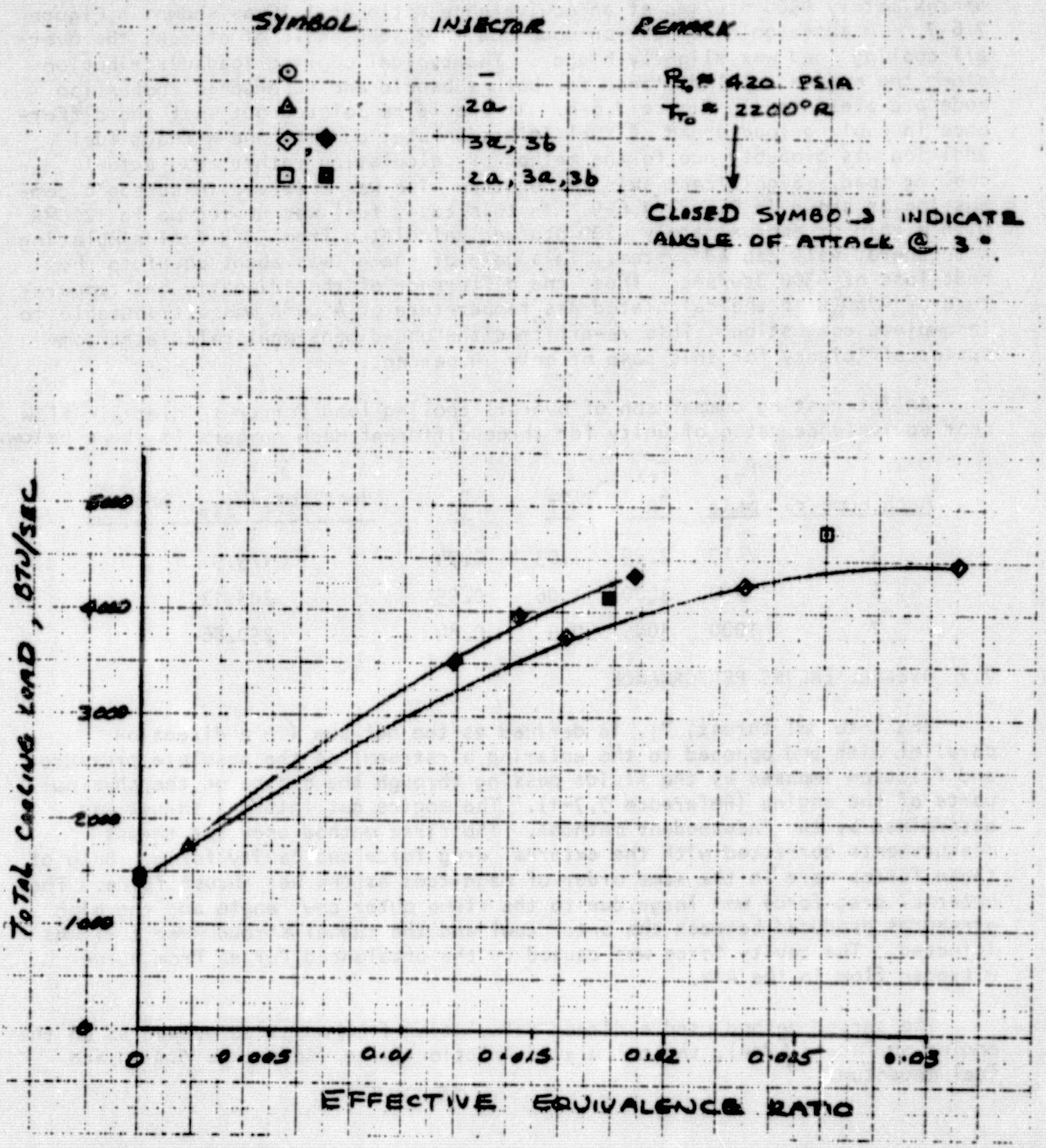

Figure 7.6-7. Mach 5 Total Cooling Load

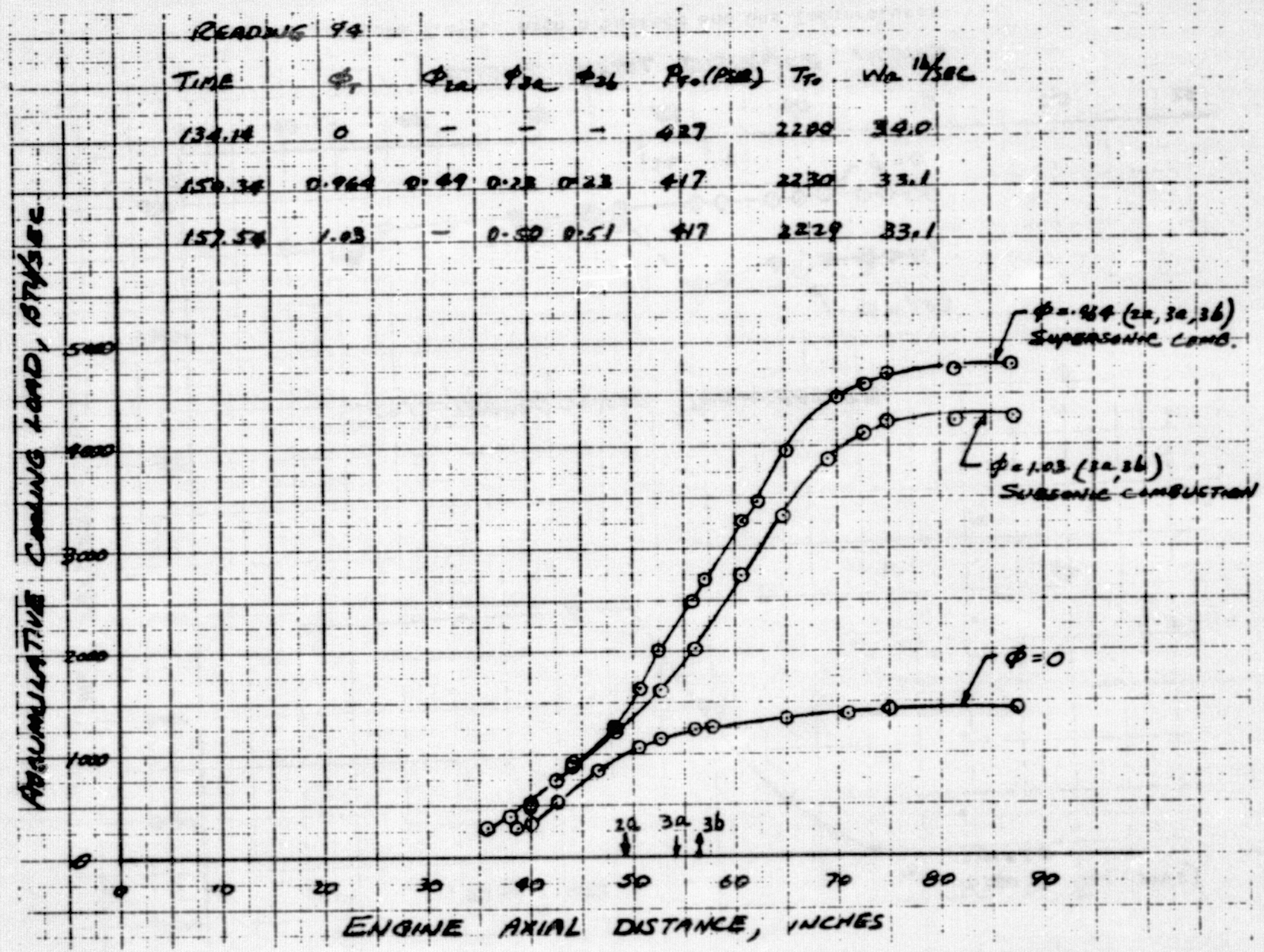

Figure 7.6-8. Mach 5 Accumulative Cooling Load

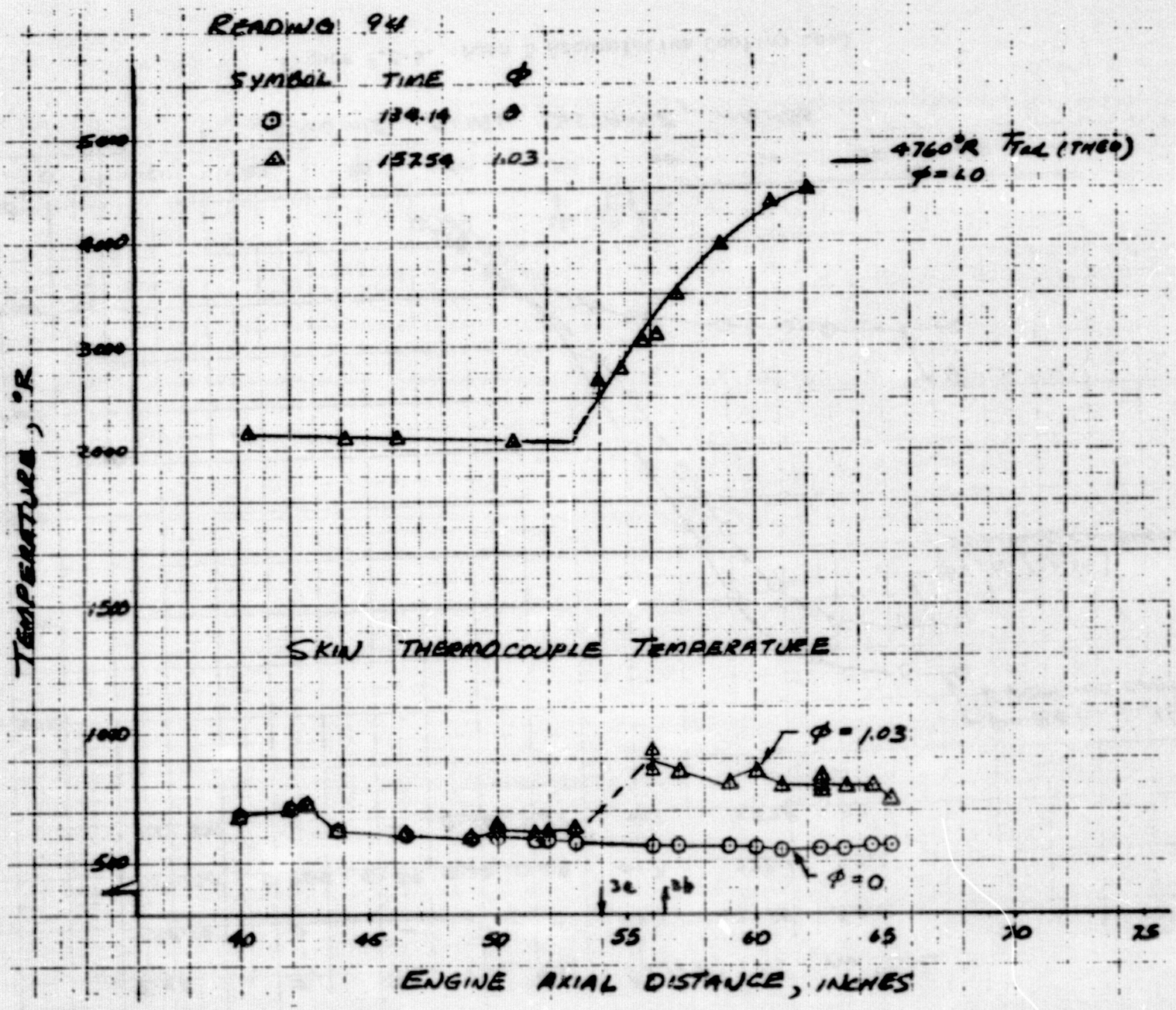

Figure 7.6-9. Mach 5 Surface and Gas Temperatures

The equations used for these two methods were:

(1) $T_i = F_c + F_{ext} + F_{cav}$

and

(2) $T_i = \int PdA - F_{fuel} - F_{friction}$

where

T_i = internal thrust

F_c = corrected load cell force

F_{ext} = total pressure and friction external force (See Section 6.4)

F_{cav} = cavity force (See Section 6.3)

$\int PdA$ = internal engine surface pressure integral

F_{fuel} = fuel momentum

$F_{friction}$ = internal friction force

The commonly used thrust differential method which determines the thrust increment between hot and cold runs was not employed. This method assumes that the external forces are invarient and would have caused serious errors if not carefully examined.

The internal performance of the AIM engine was defined as follows:

$$\text{Thrust Coefficient } (C_T) = \frac{\text{Internal Thrust}}{q_o \quad A_c}$$

$$\text{Fuel Specific Impulse } (I_{sp}) = \frac{\text{Internal Thrust}}{\text{Fuel Flow}}$$

where

q_o = freestream dynamic pressure, psia

and

A_c = engine cowl area, 256.13 in.^{2}

The dynamic pressure was calculated from wind tunnel conditions and the fuel flow was measured during tests.

7.7.1 Mach 6 Performance

The comparison of internal thrust calculated from the two methods discussed above for typical Mach 6 tests is shown in Figure 7.7-1. The calculated total internal friction force was 440 lb--about 25 percent of the internal thrust. Fuel injected at angles greater than 90 deg, to increase mixing efficiency, caused a loss in engine thrust of about 100 lb, or 5 percent of the internal thrust. For the data shown in Figure 7.7-1, the internal thrust calculated by the two methods agreed within 10 percent.

In Figure 7.7-2, the contribution of forces from the AIM inlet, combustor, and nozzle, to engine thrust is illustrated at an equivalence ratio near unity. The diverging area in the combustor contributed about the same thrust as the nozzle. Since engine internal thrust was determined from the difference between two large values--freestream and nozzle exit momentum--small errors in either of these values can produce large errors in the internal thrust. At Mach 6, gross thrust is approximately four-times the internal thrust.

The thrust coefficient and specific impulse were plotted in Figure 7.7-3 over the range of fuel-air ratios tested. Thrust coefficient was plotted versus fuel-air ratio rather than equivalence ratio because the composition of synthetic air was varied from run to run. For the majority of tests, the internal thrust calculated from the thrust measurements agreed with that from surface pressure integrals within 10 percent.

Considering the errors involved in calculating performance from each of the two methods, the AIM performance is expected to be more reliable using the averaged value. Thus, at an equivalence ratio of unity (f/a = 0.0293) the AIM thrust coefficient was 0.695 and specific impulse was 2235 sec.

Note that in Figure 7.7-3, the performance with the supersonic injectors 1b, 2a, 2c near an equivalence ratio of unity was almost identical to that with injector 1b and the subsonic injectors 3a, 3b. This was as expected because of the sizing of the thermal throat. The thermal throat was not optimized for subsonic combustion, but was instead made larger as a compromise for supersonic combustion. This caused the normal shock to move downstream from the inlet throat during subsonic combustion. Therefore, the increased shock losses reduced the engine performance to approximately the same as those in supersonic combustion. The detailed matching procedure and performance were discussed in Reference 6.4-1.

Tests were also conducted at Mach 6 with freestream total pressures, spike translations, and angles of attack other than the nominal Mach 6 operating conditions (750 psia freestream total pressure, zero degree angle of attack, and the cowl leading edge (X_{CL}) at 35.2 in. from the spike tip). Performance data from these tests were compared with the nominal Mach 6 performance previously shown in Figure 7.7-3.

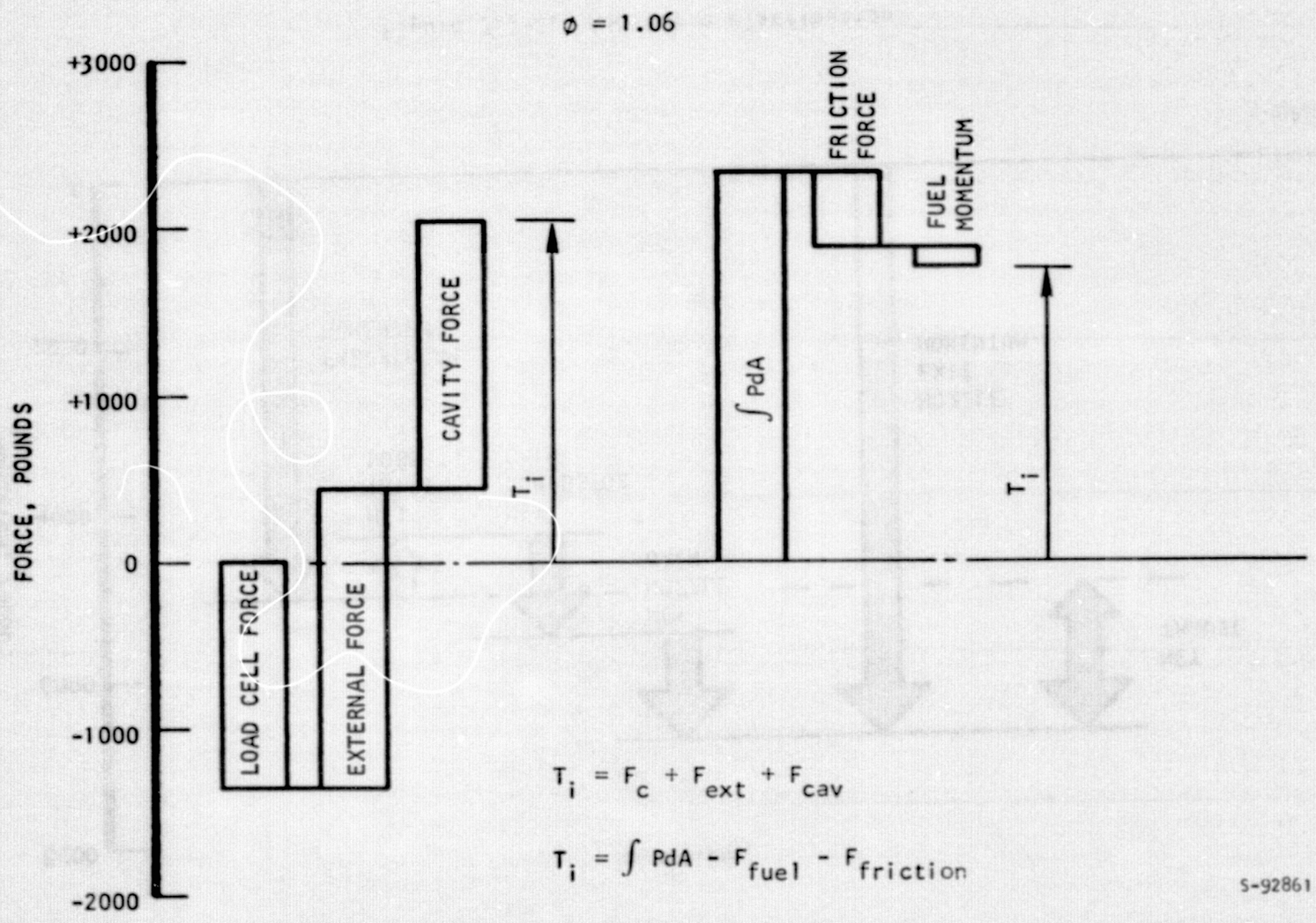

Figure 7.7-1. Comparison of Thrust Calculations

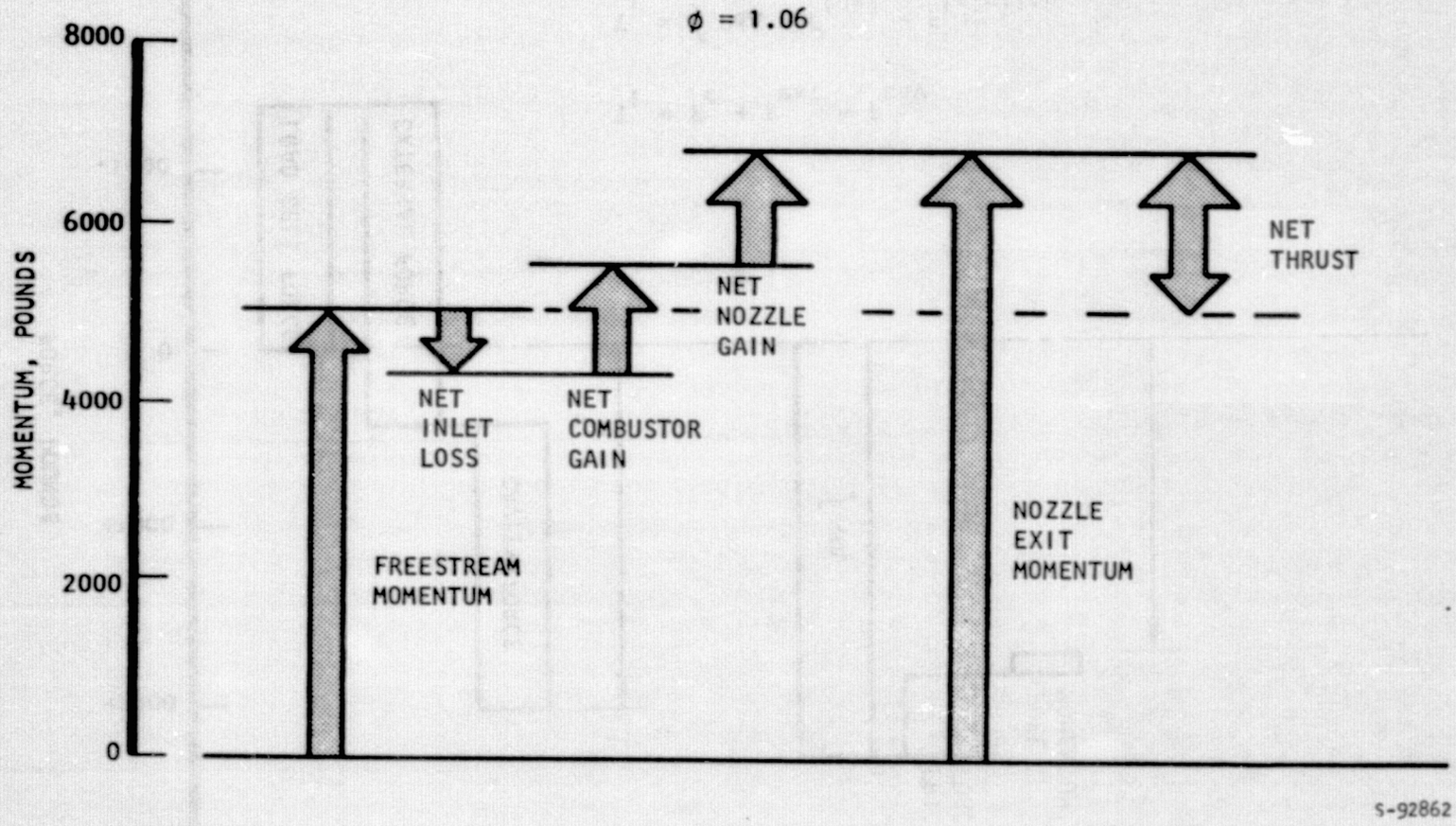

Figure 7.7-2. AIM Force Distribution

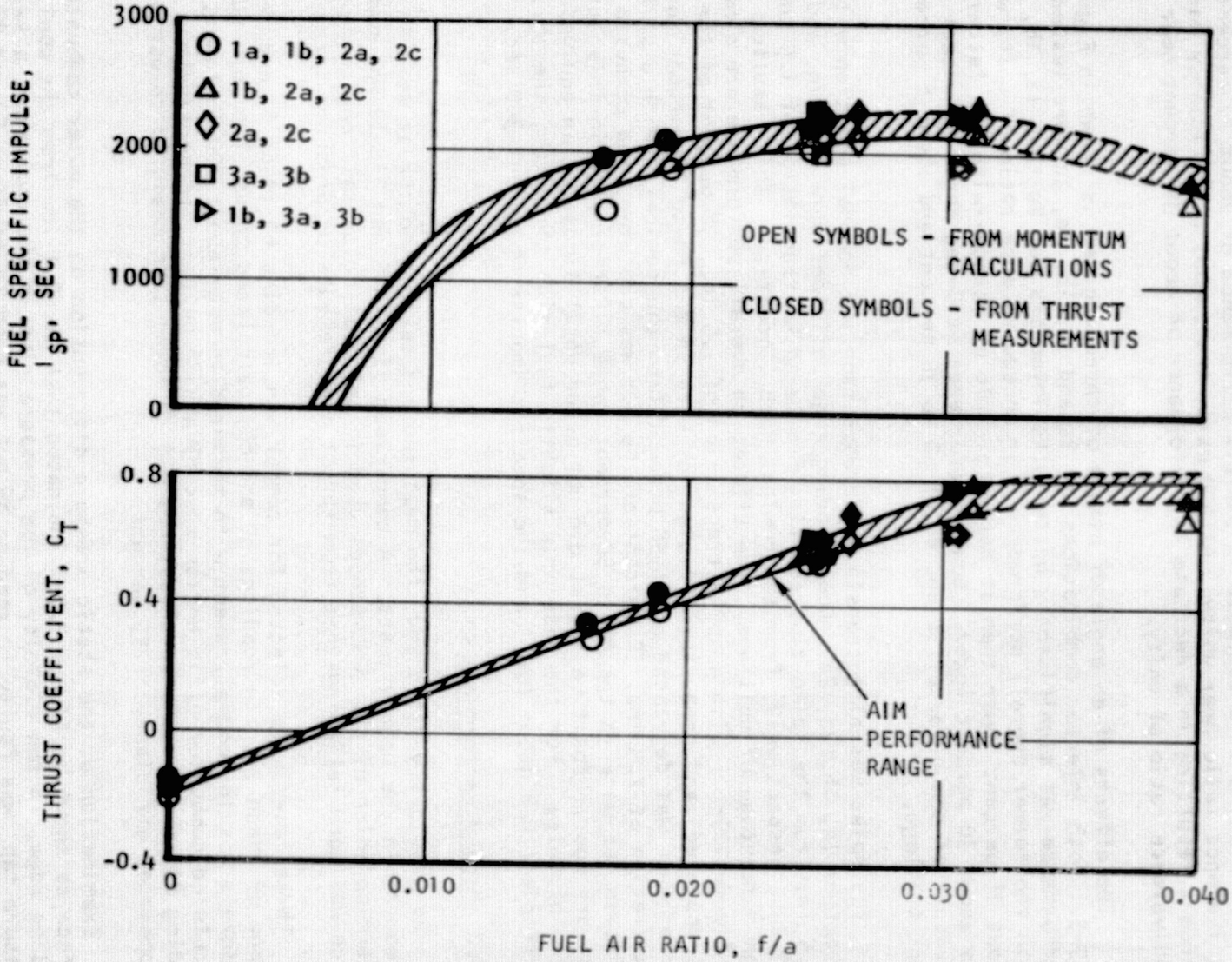

Figure 7.7-3. AIM Internal Performance

Figure 7.7-4 shows the effect of freestream total pressure on overall engine performance. Injectors 1a, 1b, 2a, 2c were used with freestream total pressures of 930 psia and 470 psia. At 930 psia, the component efficiencies were similar to those at 750 psia, but the combustor efficiency was slightly lower, resulting in a decrease in overall performance of about 12 percent at an equivalence ratio near unity. At 470 psia, the combustor efficiency was 66 percent, resulting in a decrease in performance of about 30 percent near an equivalence ratio of unity.

The effects of an angle of attack of three degrees is shown in Figure 7.7-5. Both injector combinations 2a, 2c and 1a, 1b, 2a, 2c were tested. Performance was significantly better with injectors 2a, 2c than 1a, 1b, 2a, 2c. With the former, overall performance near an equivalence ratio of unity was about 15 percent lower than at zero-deg angle of attack--with the latter it was about 30 percent lower. Lower performance at 3-deg angle of attack was a result of combustor efficiencies of 60 to 70 percent and about 6 percent more spillage.

The spike was also translated forward from the nominal position with the injectors 1a, 1b, 2a, 2c. Cowl leading edge positions were 36.7 in. and 37.5 in. from the spike tip, resulting from a spike translation of 1.5 and 2.3 in., respectively, from the nominal Mach 6 position. This resulted in a high percentage of spillage. The effects on overall performance are shown in Figure 7.7-6. With a spike translation of 1.5 in., 78 percent of the air was captured, and combustor efficiencies were in the 60- to 70-percent range. Performance was decreased about 50 percent from the nominal. With a spike translation of 2.3 in., 50 percent of the air was captured, and combustor efficiencies were in the 40- to 50-percent range. Performance in this case was very poor. Positive thrust did not occur until almost at an equivalence ratio of unity. For the case of a slightly fuel-rich combustor, the thrust coefficient was about 0.05, and the specific impulse was about 300 sec.

7.7.2 Mach 7 Performance

As previously discussed, the measured and calculated thrust were in poor agreement in the Mach 7 tests. A comparison of Mach 6 and 7 data was made to determine which of the two methods used in calculating overall engine performance was more reliable--that from thrust measurements or pressure integrals.

Three cases were selected for comparison, reading 60 (Mach 6) and readings 88 and 89 (Mach 7). In readings 60 and 88, calculated thrust from pressure integrals was in good agreement with measured thrust--about 100 lb lower. The calculated combustor efficiencies were 87 and 84 percent, respectively. In reading 89, the calculated thrust was 630 lb lower than measured thrust with a combustor efficiency of 55 percent.

Examination of the static pressure distribution on the outer combustor surface, as shown in Figure 7.7-7, indicated that at 12.1 in. from the cowl leading edge, in the vicinity of the pressure rise in the combustor, a key pressure tap was faulty in reading 89 but was good in readings 60 and 88. It should be noted that the pressure tap on the outer combustor surface--10.4 in. from the cowl leading edge--was faulty for all tests. This caused

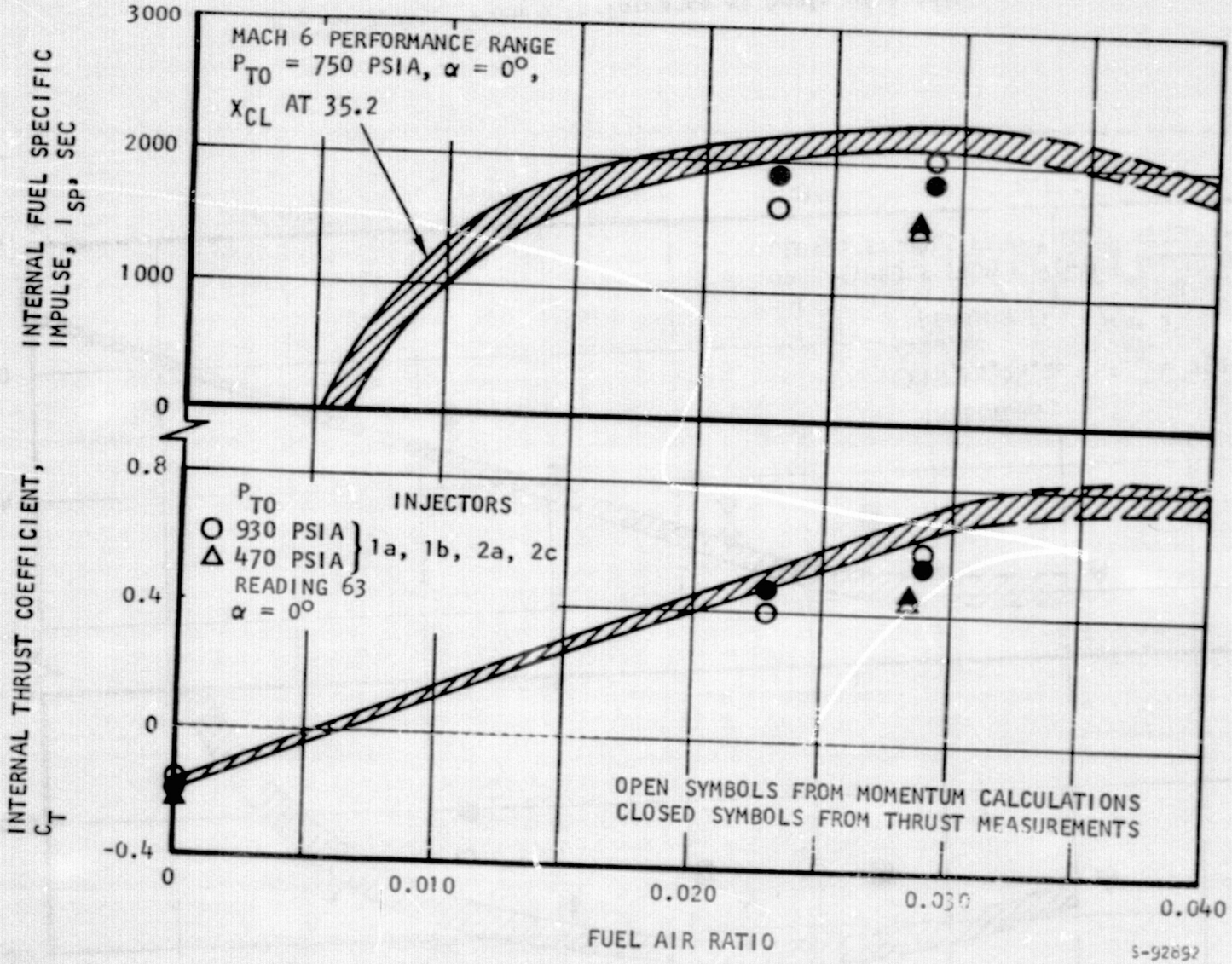

Figure 7.7-4. Mach 6 Performance at Different Freestream Total Pressures

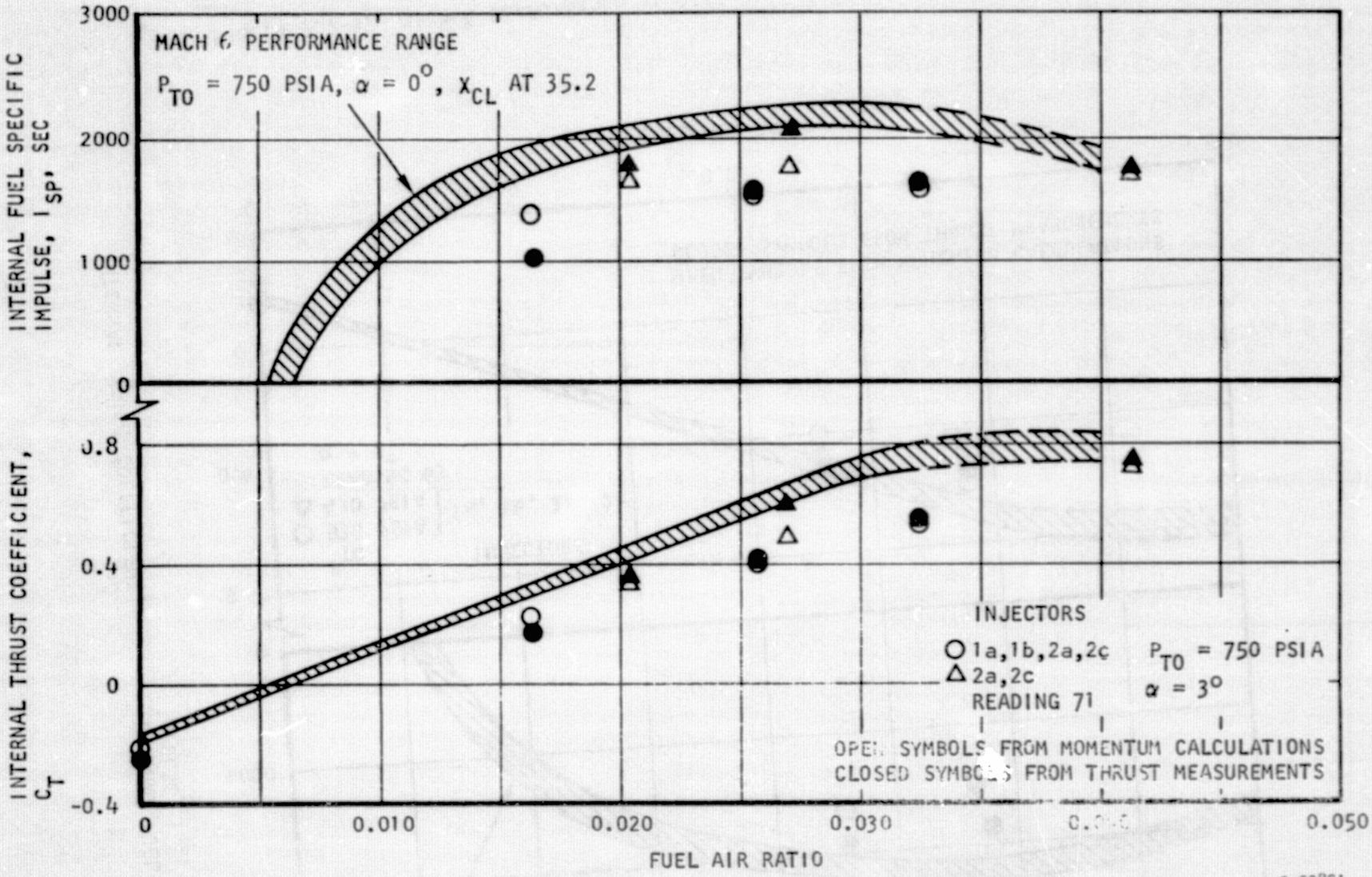

Figure 7.7-5. Mach 6 Performance at Angle of Attack

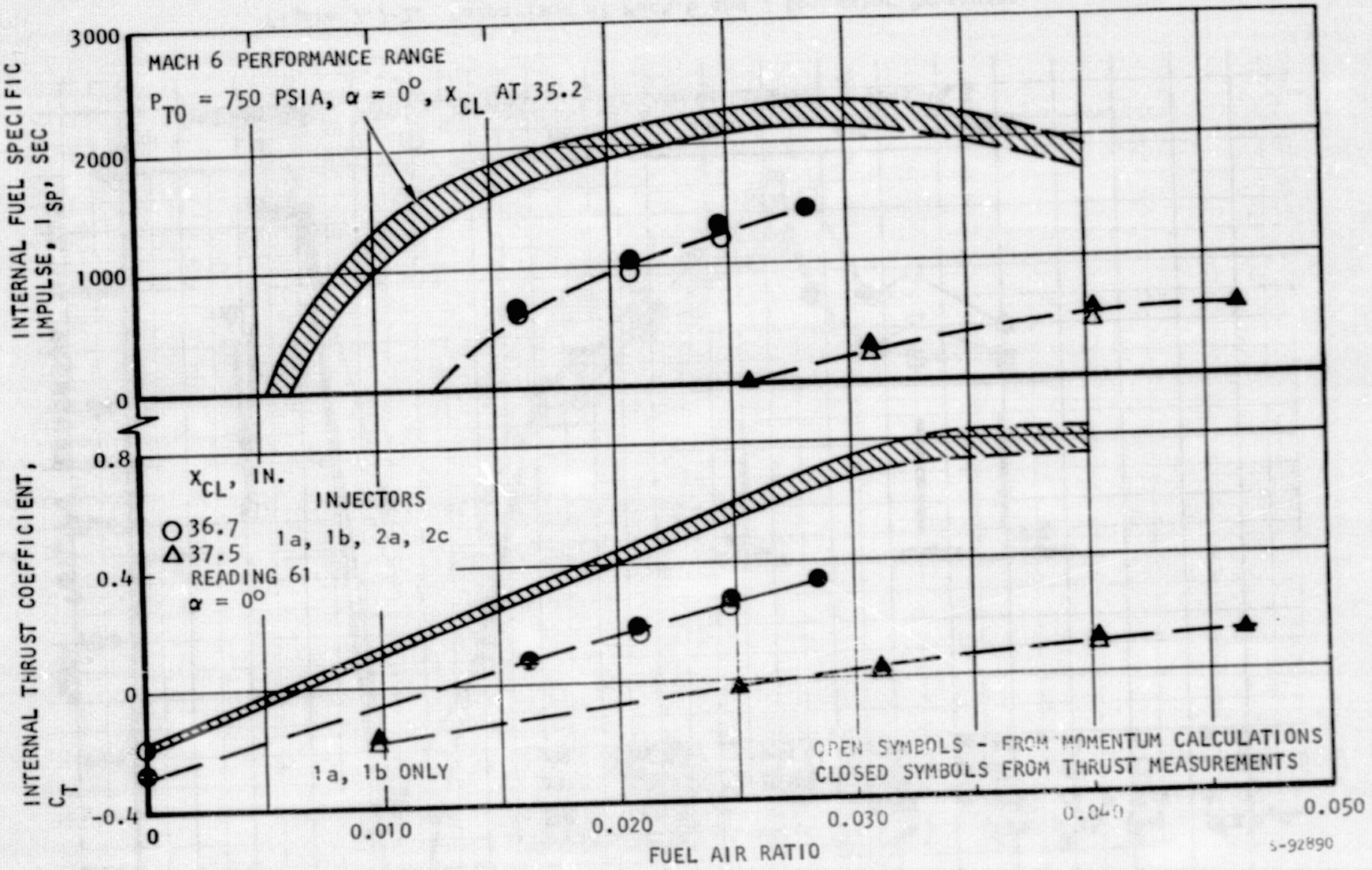

Figure 7.7-6. Mach 6 Performance at Different Cowl Leading Edge Locations

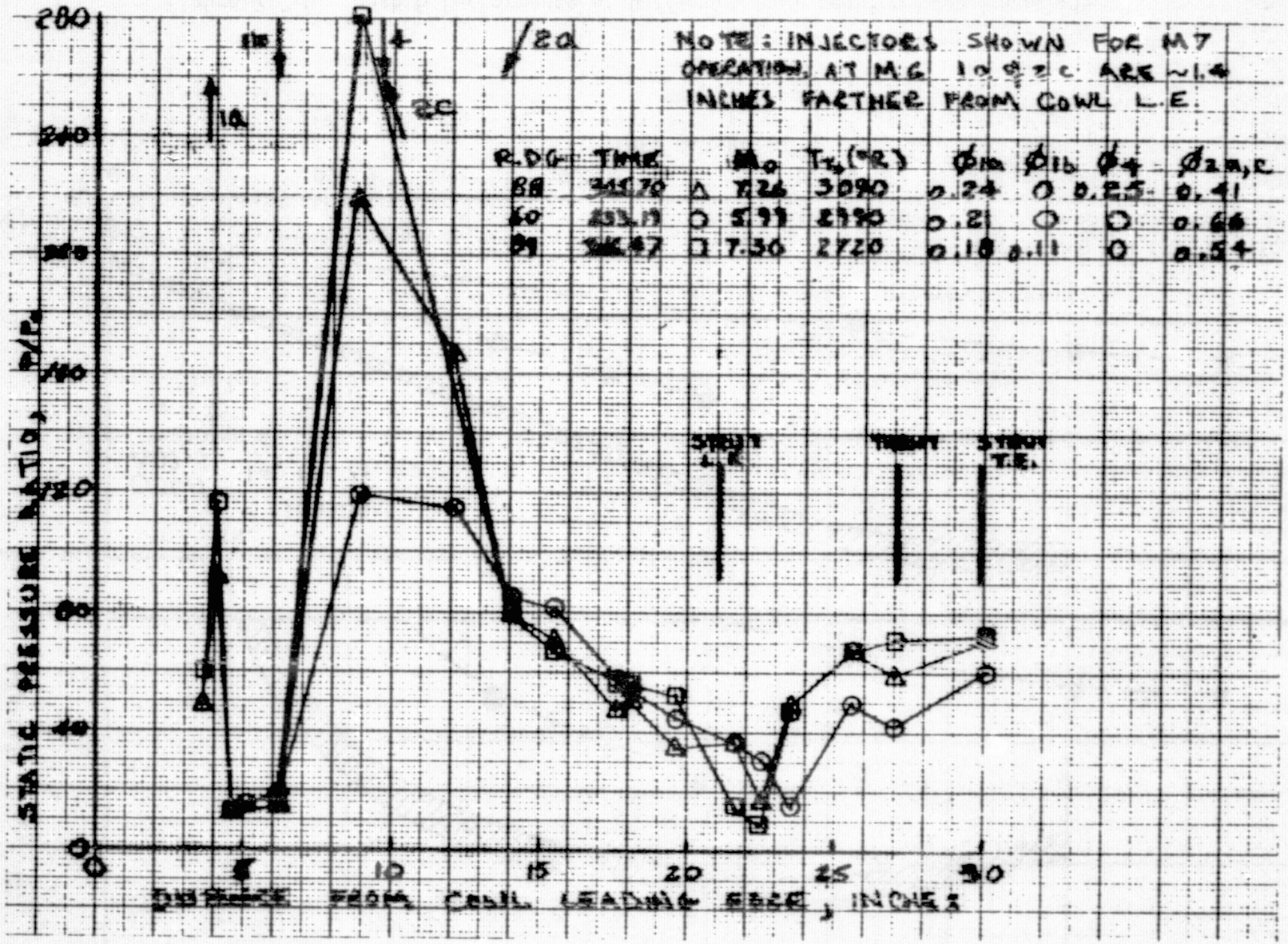

Figure 7.7-7. Comparison of Mach 6 and 7 Combustor Pressures

an appreciable discrepancy in combustor thrust, since a linear fit of the pressures was used to calculate the pressure integrals. From 8.9 to 14.1 in. from the cowl leading edge (the region between good pressure taps in reading 89), the outer combustor surface projected area is about 23.5 sq in. Therefore, a force between 300 to 400 lb could be missing in the thrust calculation due to the faulty pressure taps in reading 89. The pressure tap at 10.4 in. and other pressure integral errors could be responsible for the discrepancy between calculated and measured thrust in readings 60 and 88.

In view of the above discussion, the thrust measurement was used to determine the Mach 7 performance shown in Figure 7.7-8. The total temperature in all of the Mach 7 tests was below that of a true flight simulation. The measured thrust was corrected to true flight conditions using the procedure outlined in Section 6.6, where the ratio of test total temperature to reference temperature was used to obtain the flight fuel-air ratio. Test thrust and impulse were then plotted versus flight fuel-air ratio. Since the flight simulation was nominally Mach 7.25 rather than Mach 7, the reference temperature used was 3960°R rather than 3770°R which occurs at Mach 7. The corrected performance shown in Figure 7.7-9 should be used with caution, since the theoretical calculations were based on linear theory which is good for small temperature differences, but of questionable accuracy for very large differences because the corrections to higher temperatures were based on the premise that the combustion process would not change at the test and reference temperatures. As was discussed in Section 7.2.5, the test temperature did have an effect on the combustion process when it was lowered to 2400°R. One would assume that the combustion process would have been different had the AIM been tested at Mach 7 total temperatures of 3770°R. In fact, in all probability the combustion process would have produced higher combustor efficiencies at higher test temperatures. Without any corrections for a regeneratively cooled system, and at zero-degree angle of attack, a thrust coefficient of about 0.495 and a specific impulse of about 1885 sec was obtained at an equivalence ratio of unity. Based on the data in Figure 7.7-9, 3-deg angle of attack resulted in about 12 percent lower performance. This was similar to the least Mach 6 performance degradation at 3 deg angle of attack.

7.7.3 Mach 5 Performance

At Mach 5 there was excellent agreement between overall performance calculated from surface pressure integrals and with that from measured thrust, as shown in Figure 7.7-10. All of the data agreed within 10 percent, and in some cases, the agreement between thrust measurements and pressure integrals was within one percent. At an equivalence ratio of unity the thrust coefficient was 0.905 and specific impulse was 2730 sec.

The performance from tests conducted at 3 deg angle of attack is shown in Figure 7.7-11. The larger differences between calculated and measured performance was probably due to limited number of pressure taps to accurately measure the non-uniform pressure distribution at angle of attack tests. The data near an equivalence ratio of unity was about 15 percent lower than the average performance at zero angle of attack, or about the same as at Mach 6 and 7.

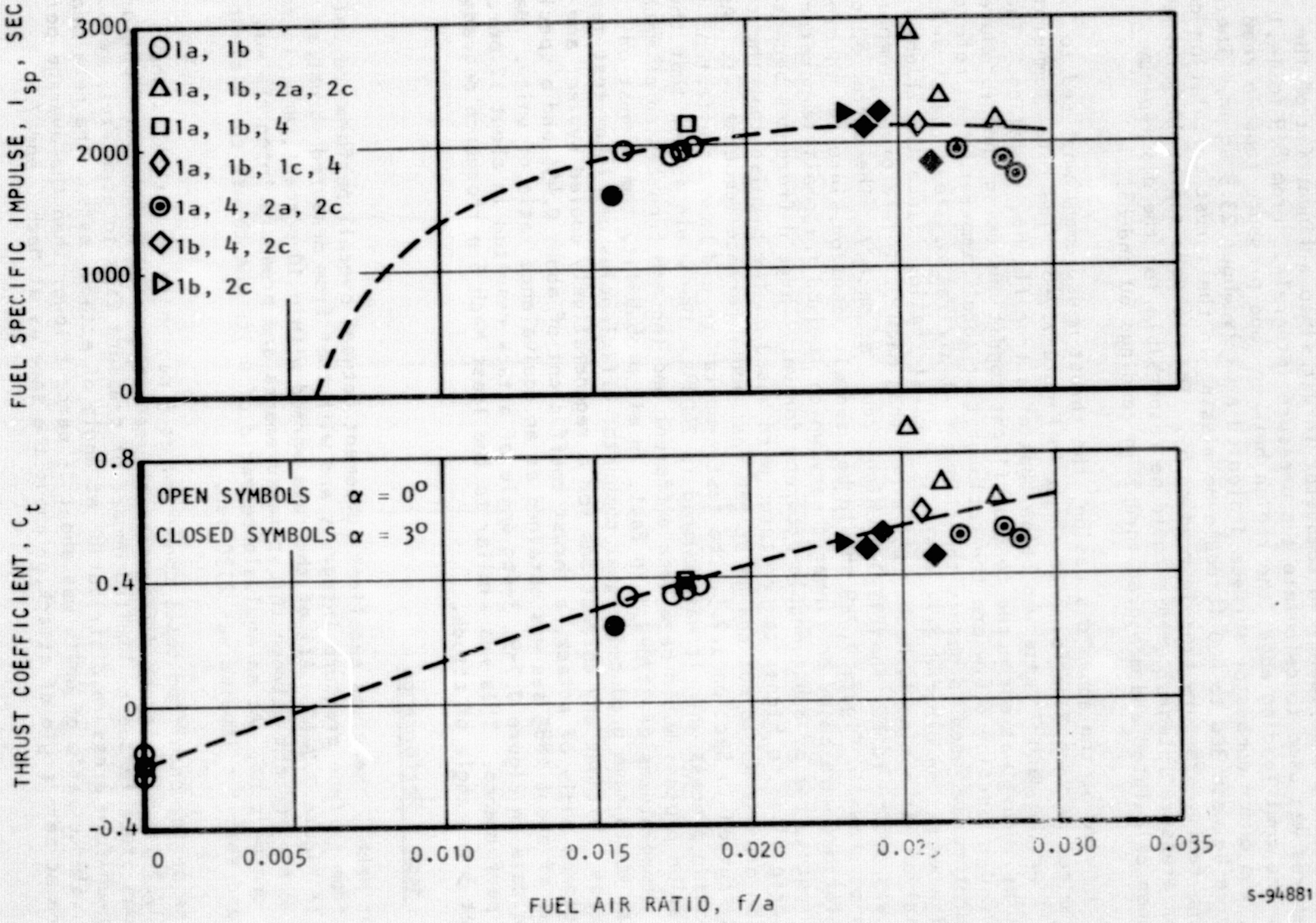

Figure 7.7-8. Uncorrected Mach 7.25 Internal Performance

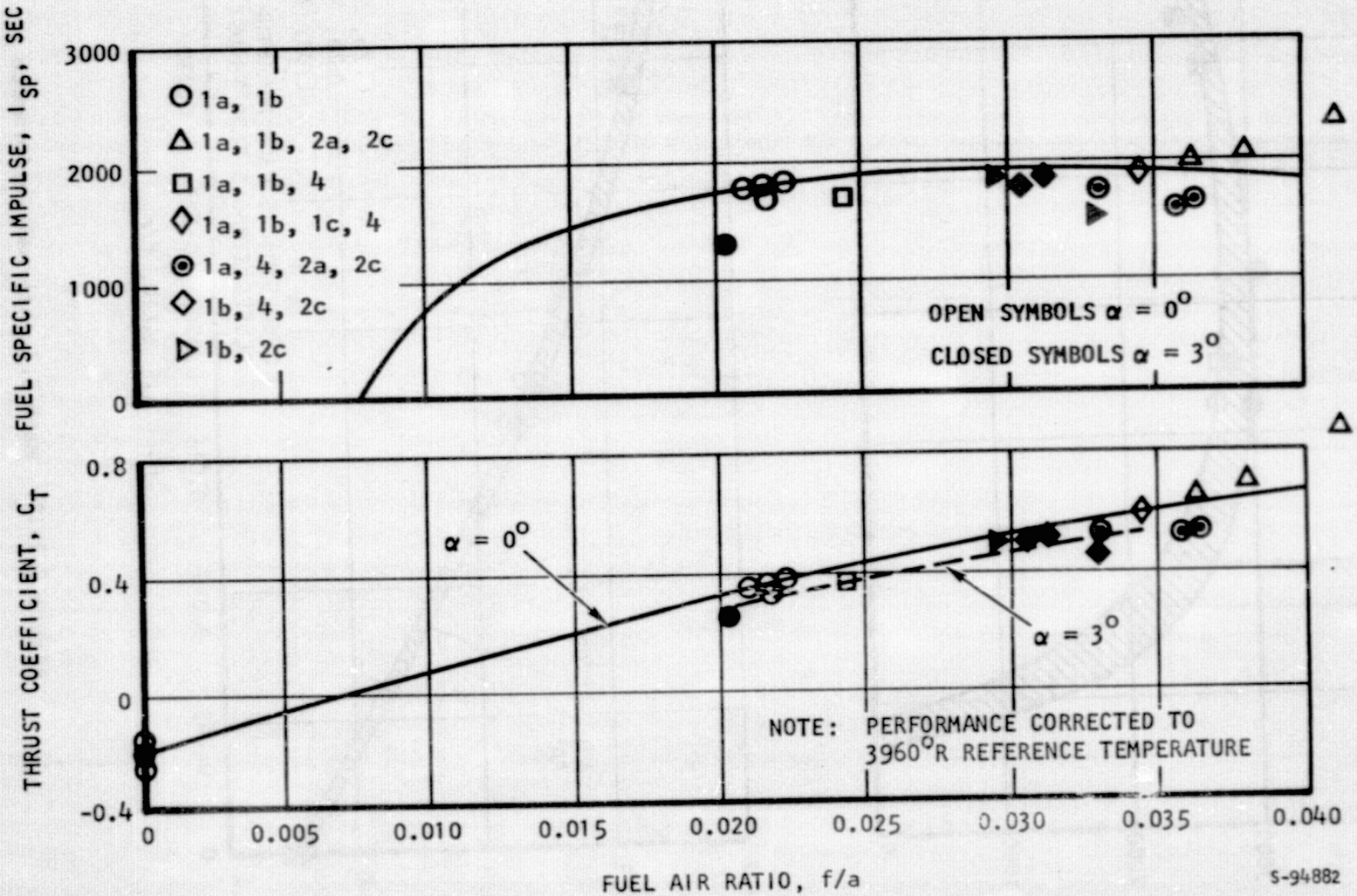

Figure 7.7-9. Corrected Mach 7.25 Internal Performance

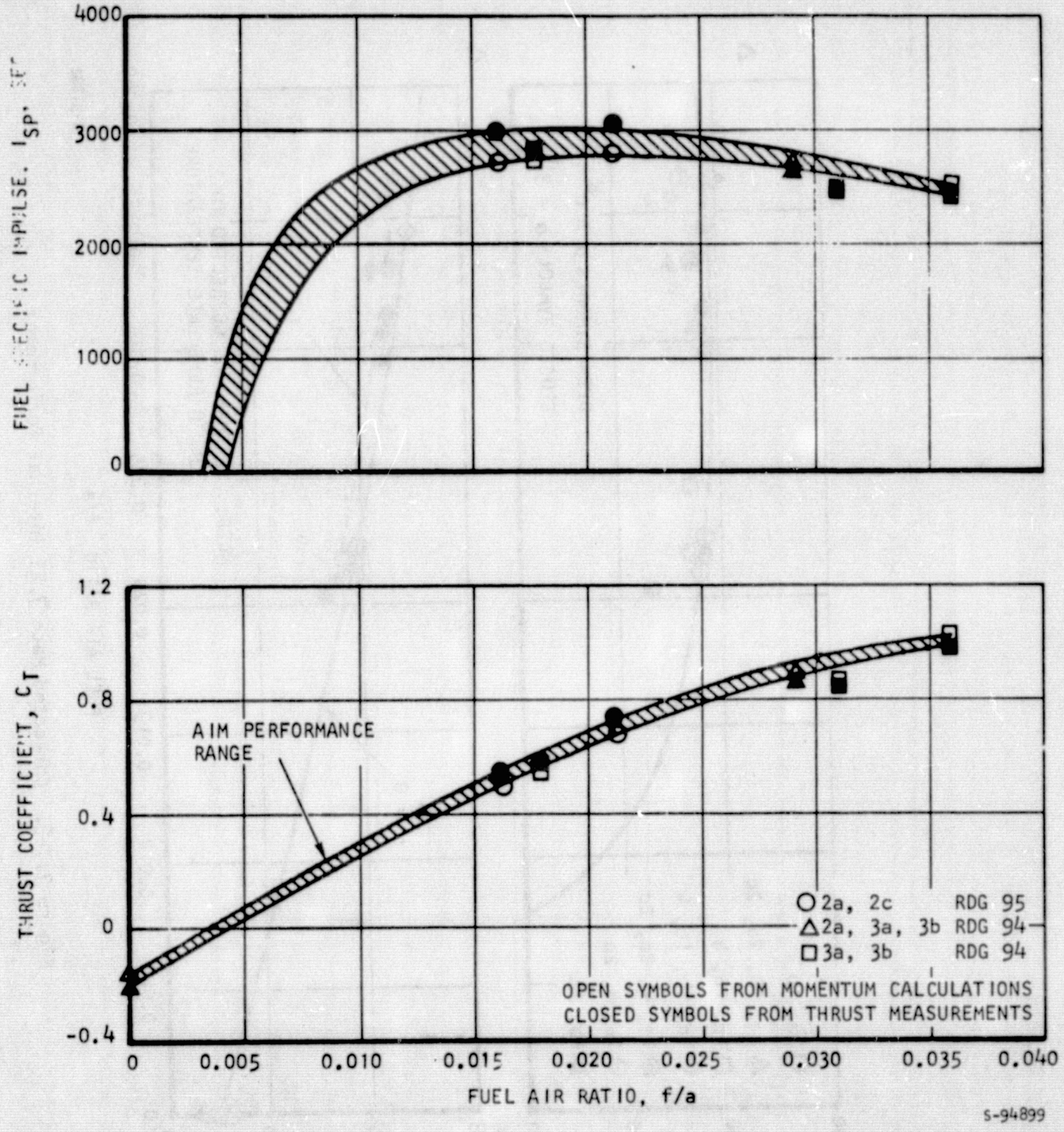

Figure 7.7-10. Mach 5.1 Internal Performance

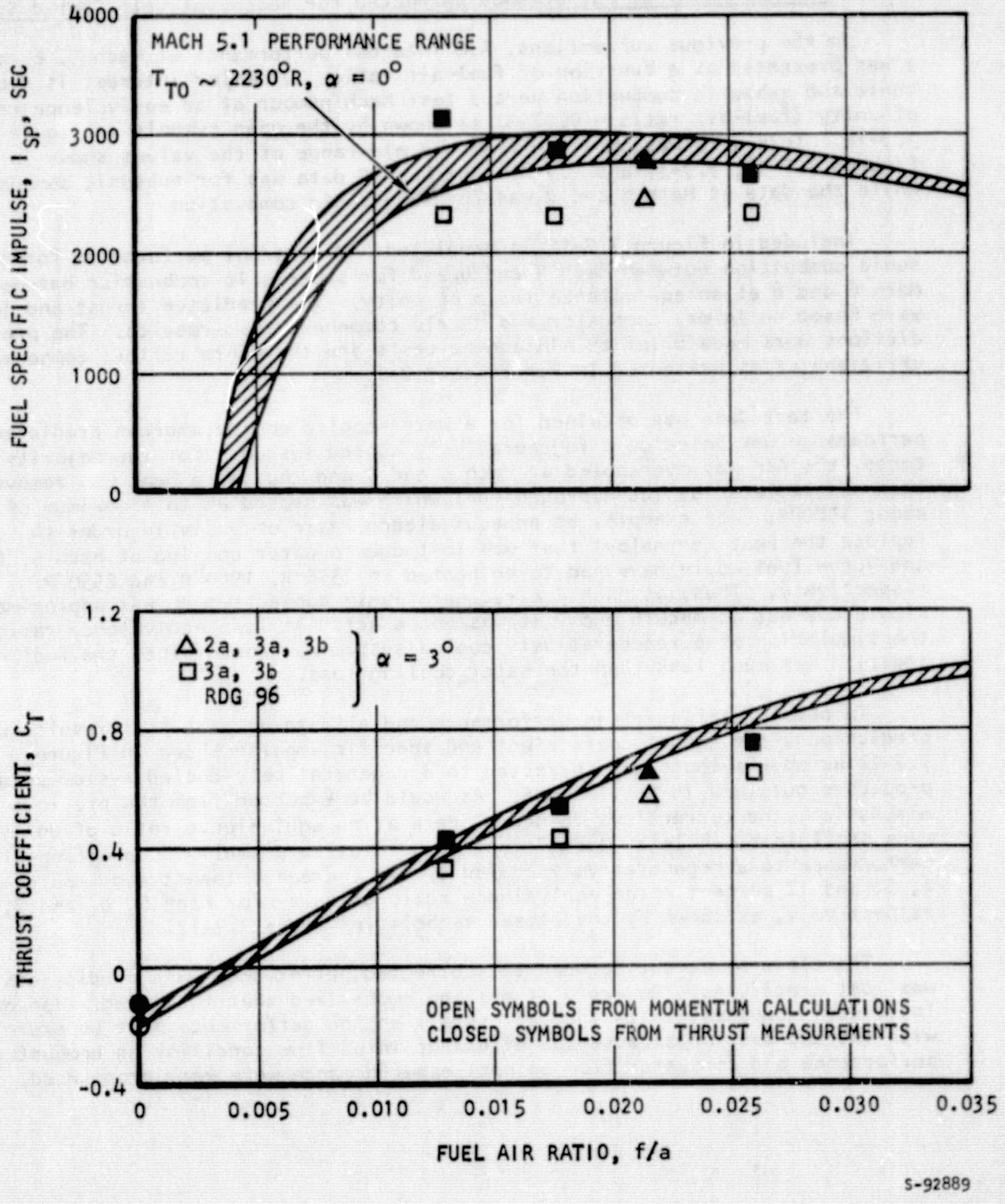

Figure 7.7-11. Mach 5.1 Performance at Angle of Attack

7.7.4 Overall Internal Performance Corrected for Regeneratively Cooled System

In the previous subsections, AIM internal performance at Mach 5, 6, and 7 was presented as a function of fuel-air ratio. Of major interest is supersonic and subsonic combustion versus test Mach number at an equivalence ratio of unity (fuel-air ratio = 0.0293), as shown by the open symbols in Figure 7.7-12. This data was obtained from the mid-range of the values shown in Figures 7.7-10, 7.7-3, and 7.7-8. The Mach 5 data was for subsonic combustion, while the data at Mach 6 and 7 was for supersonic combustion.

Included in Figure 7.7-12 is predicted AIM internal performance for subsonic combustion between Mach 4 and 6, and for supersonic combustion between Mach 6 and 8 at an equivalence ratio of unity. The predicted thrust and impulse were based on inlet, combustor, and nozzle component test results. The predictions were made prior to AIM engine tests and therefore reflect component efficiencies as presented in Reference 7.2-1.

The test data was obtained for a water-cooled engine, whereas predicted performance was based on a regeneratively cooled system. For the majority of tests, the AIM was overcooled at Mach 6 and 7 and thus more heat was removed than was replaced by the hydrogen fuel, which was heated up to a maximum of about 1500°R. For example, at an equivalence ratio of unity, in order to replace the heat (enthalpy) that was lost due to water cooling at Mach 5, 6, and 7, the fuel would have had to be heated to 1350°R, 1900°R, and 2550°R, respectively. Thus, at Mach 5 a regeneratively cooled system was approximately simulated, but at Mach 6 and 7 it was not exact. At lean equivalence ratios, the simulation of a regeneratively cooled system was worse, since the fuel heat addition was much less than the water cooling loss.

To obtain realistic AIM performance and also to compare test results with predictions, the thrust coefficient and specific impulse shown in Figure 7.7-12 as open symbols was corrected to a regeneratively cooled system using the procedure outlined in Section 6.5. As would be expected from the previous discussion, the corrections to Mach 5 data at an equivalence ratio of unity were negligible, while at Mach 7 they were relatively small. Correcting AIM performance to a regeneratively cooled system increased thrust and impulse by 2, 5, and 12 percent at an equivalence ratio of unity for Mach 5, 6, and 7, respectively, as shown by the closed symbols in Figure 7.7-12.

The close agreement between the corrected performance with predictions was most gratifying. However, it must be emphasized that the integration of individual component tests into an overall engine performance must be exercised with extreme caution, because the effect of inlet flow condition on combustor performance and combustor flow on nozzle performance were very pronounced.

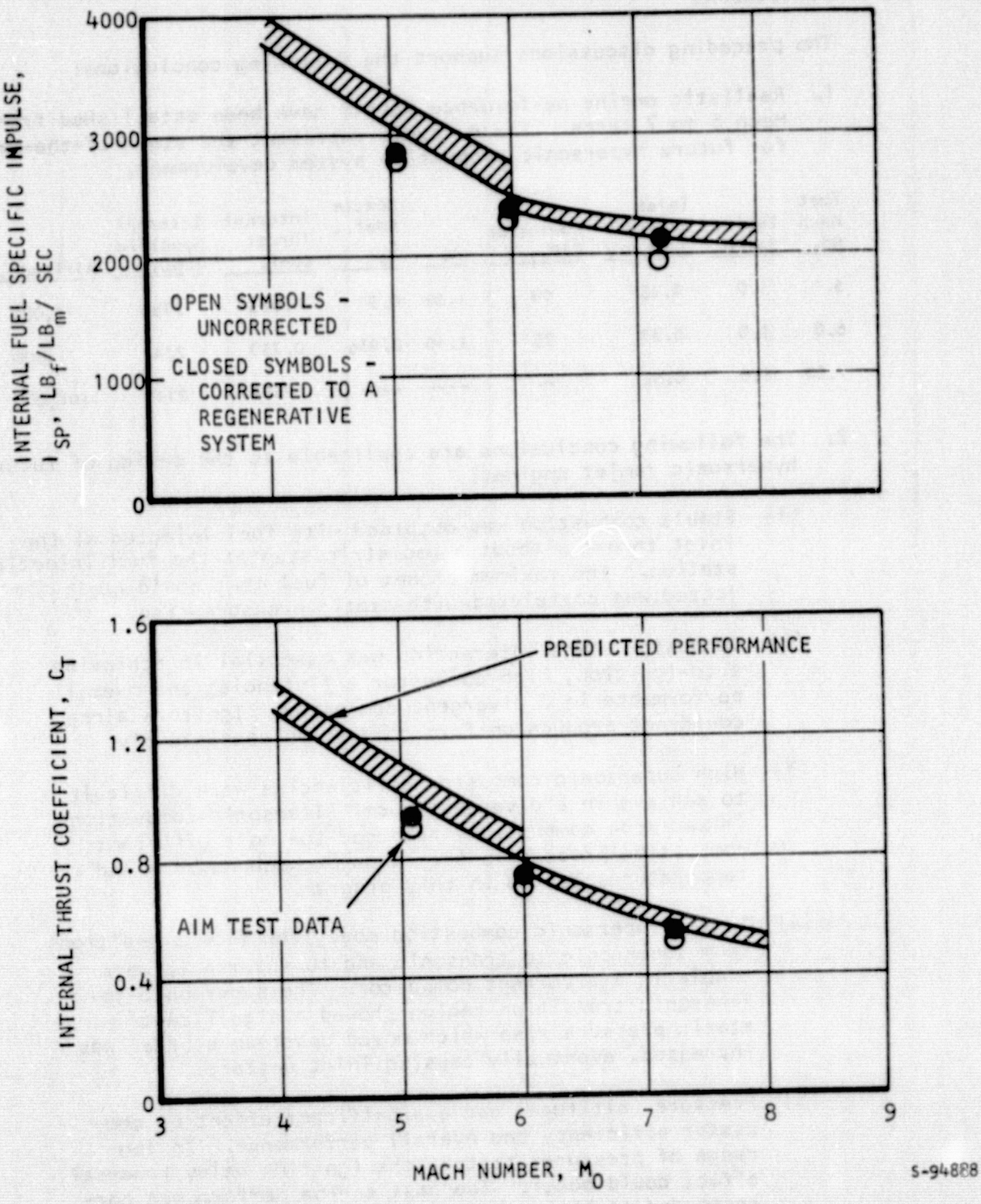

Figure 7.7-12. AIM Internal Performance

7.8 CONCLUSIONS

The preceding discussions support the following conclusions:

1. Realistic engine performance levels have been established from Mach 5 to 7 tests. These levels represent the state-of-the-art for future hypersonic propulsion system development.

Test Mach No.	Equiv. Ratio	Inlet Pressure Recovery	Combustor Eff., %	K	Nozzle Coef., C_s	Internal Thrust Coef.	Internal Specific Impulse	Altitude, ft
5.1	1.0	0.43	90	1.52	0.94	0.923	2785	72,000
6.0	1.0	0.39	95	1.15	0.936	0.730	2346	81,000
7.25	1.0	0.32	--	----	----	0.554	2110	101,000

2. The following conclusions are applicable to the design of future hypersonic ramjet engines:

   (1) Stable combustion was obtained with fuel injected at the inlet throat without a geometric step at the fuel injection station. The maximum amount of fuel that could be injected was correlated with static pressure rise.

   (2) Combustor stage interaction was essential in achieving auto-ignition, high combustor efficiencies and overall performance in a divergent combustor. Ignitors alone could not produce uniform combustion consistently.

   (3) High supersonic combustor efficiencies were difficult to achieve in a divergent duct. Transonic combustion (mixed mode combustion) produced the most efficient combustion process in the range of Mach numbers and temperatures tested in this program.

   (4) In the supersonic combustion mode, the flow transitions from supersonic to transonic and to supersonic were stable in a divergent combustor. The supersonic-to-transonic transition region showed a significant static pressure rise which moved upstream as fuel was increased, eventually causing inlet unstart.

   (5) Pressure (altitude) had a significant effect on combustor efficiency and overall performance. In the range of pressures tested, the ignition delay reversal effect could occur. The best engine performance corresponded to the combustor inlet pressure that could produce the minimum ignition delay time.

(6) The effect of inlet flow on combustor performance and combustor flow on nozzle performance were very pronounced. Therefore, engine performance obtained from integration of results from individual component tests should be used with caution.

(7) Engine performance may be corrected for small freestream temperature variations. For large temperature variations, the correlation was not accurate because of the change in the combustion process.

(8) The theoretical overall heat loss was in good agreement with experimental data, providing increased confidence in future engine designs.

3. The following conclusions are applicable to the AIM design:

(1) Non-uniform flow with shock waves delivered to the combustor caused significant losses both with and without fuel injection.

(2) The annular combustor was sensitive to angle of attack at flight Mach numbers 5, 6, and 7. At 3 degrees, the performance degradation was approximately 15 percent.

(3) The eight-inch subsonic combustor length designed for operation at high subsonic velocities was too short to achieve good combustor efficiencies.

(4) The step formed by the sliding centerbody was successfully employed as a flame holder for subsonic combustion. The expansion waves from the step during supersonic combustion apparently inhibited the combustion; however, the recompression shock further downstream enhanced combustion between the struts.

(5) The low nozzle performance may be partially attributed to the flow angularity or possible flow turbulence at the combustor exit. Further investigation into the causes is recommended.

4. The one-dimensional real-gas data reduction program using surface-static pressure measurements proved to be a useful tool in determining component performance and flow parameters.

REFERENCES

2-1. Burbank, P. B., R. A. Newlander, and I. K. Collins, "Heat Transfer Measurements on a Flat-Plate Surface and Heat Transfer Measurements on Attached Protuberances in a Supersonic Turbulent Boundary Layer at Mach Numbers of 2.65, 3.51, and 4.44," NASA TND-1372, December 1962.

2-2. Vinson, P. W., J. L. Amick, H. P. Liepman, "Interaction Effects Produced by Jet Exhausting Laterally Near Base of Ogive-Cylinder Model in Supersonic Main Stream," NASA Memo 11-5-58W, February 1959.

2-3. Kaufman, L. G. II, "Hypersonic Flows Past Transverse Jets," AIAA Paper No. 67-190, January 23-26, 1967.

2-4. Fay, J. A., and Riddell, F. R., "Theory of Stagnation Point Heat Transfer in Dissociated Air," J. of Aeronautical Sciences, Vol. 25, No. 2, February 1958, pp. 73 to 85.

2-5. Lees, L., "Laminar Heat Transfer Over Blunt-Nosed Bodies at Hypersonic Flight Speeds," Journal of Jet Propulsion, April 1956, pp. 259 to 269.

2-6. Kestin, J., "The Effect of Free Stream Turbulence on Heat Transfer Rates," Advances in Heat Transfer, Vol. 3, Edited by T. F. Irvine Jr., and J. P. Hartnett, Academic Press, 1966, pp. 1 to 32.

2-7. Edney, B. E., "Effects of Shock Impingement on the Heat Transfer Around Blunt Bodies," AIAA Journal, Vol. 6, No. 1, January 1968, pp. 15 to 21.

2-8. Wuerer, J. E., and F. I. Clayton, "Flow Separation in High Speed Flight," Douglas Report SM -46429, April, 1965.

2-9. Charwat, A. F., C. F. Dewey, Jr., J. N. Roos, and J. A. Hitz, "An Investigation of Separated Flows - Part II: Flow in the Cavity and Heat Transfer," Journal of the Aerospace Sciences, Vol. 28, No. 7, July 1961, pp. 513-527.

2-10. Smith, H. E., "The Flow Field and Heat Transfer Downstream of a Rearward Facing Step in Supersonic Flow," ARL 67-0056, U.S. Air Force.

2-11. Hiers, R. S. and Loubsky, W. J., "Effects of Shock-Wave Impingement on the Heat Transfer on a Cylindrical Leading Edge," NASA TN D-3859, Ames Research Center, February 1967.

2-12. Mori, Y., and Nakayama, W., "Study on Forced Convective Heat Transfer in Curved Pipes," International Journal of Heat and Mass Transfer, Vol. 10, 1967, pp. 37-59.

2-13. Chupp, R. E., et al, "Evaluation of Internal Heat Transfer Coefficients for Impingement Cooled Turbine Aerofoils," AIAA 4th Propulsion Joint Specialist Conference, Paper No. 68-564, Cleveland, Ohio, June 1968.

PRECEDING PAGE BLANK NOT FILMED

2-14. Cassanto, J. M., and R. S. Mendelson, "Local Flow Effects on Base Pressure," AIAA Journal, Vol. 6, No. 6, June 1968, pp. 1182-1185.

2-15. Love, E. S., "A Re-examination of the Use of Simple Concepts for Predicting the Shape and Location of Detached Shock Waves," NASA TN 4170, December 1957.

4-1. Johnson, L. D., "Some Observations on the Electron Beam Welding of Copper", Welding Journal, Vol. 49, No. 2, February 1970, Research Supplement 55s-60s.

6.0-1. Gordon, Sanford and McBride, Bonnie J., "Computer Program for Calculation of Complex Chemical Equilibrium Compositions, Rocket Performance, Incident and Reflected Shocks, and Chapman-Jouget Detonations, NASA SP-273, 1971.

6.3-1. AiResearch Memo EWLA-1071-0303, "AIM Thrust Correlation Due to Nitrogen Purge", L. Andersen to E. Harris, 3 March 1974.

6.4-1. Engineering Staff, Hypersonic Research Engine Project - Phase II, Aerothermodynamic Integration Model Test Plan, AiResearch Document No. AP-71-7877, Rev. 1, Data Item No. 2-2.02, 15 August 1972.

6.8-1. Cullom, Richard R. and Erwin A. Lezberg, "Calibration of Lewis Hypersonic Tunnel Facility at Mach 5, 6, and 7", NASA TND-7100.

7.1-1. "Development of Hypersonic Ramjet Research Engine Inlet Phase IIA - Final Test Summary Report," Lockheed Report No. LR22071 and Appendix, 13 December 1968. (Declassified)

7.1-2. "Hypersonic Research Engine Project - Phase IIA, Inlet Program Final Technical Data Report (U), AiResearch Report No. AP-69-4883, 27 March 1969 (CONFIDENTIAL). (Available as NASA CR-66797).

7.1-3. "Tests of a One-Third Scale NASA Hypersonic Research Engine Inlet at Mach Numbers 6 and 8." (U) Arnold Engineering Development Center Report No. AEDC-TR-68-28, March 1968 (Declassified)

7.1-4. "Wind Tunnel Tests of a Two-Thirds Scale NASA HRE Inlet at Mach Numbers 4, 5, 6 and 8." (U) Arnold Engineering Development Center Report No. AEDC-TR-69-9, February 1969 (Confidential).

7.1-5. "An Inlet Analysis for the NASA Hypersonic Research Engine Aerothermodynamic Integration Model," NASA Technical Memorandum No. TM X-3038, November 1974 (Unclassified)

7.1-6. "Calibration of Lewis Hypersonic Tunnel Facility at Mach 5, 6, and 7", NASA Technical Note No. TN-D-7100, November, 1972.

7.1-7. Spalding and Chi, "The Drag of a Compressible Turbulent Boundary Layer on a Smooth Flat Plate with and without Heat Transfer". Journal of Fluid Mechanics, Vol. 18, Pt. 1, Jan. 1964, pp. 117-143.

7.1-8. "Hypersonic Research Engine Project - Phase II Aerothermodynamic Integration Model Measurement Plan (U)" AiResearch Manufacturing Co. Document No. AP-70-6216, 9 June 1970 (Confidential)

7.2-1. Engineering Staff, Hypersonic Research Engine Project - Phase II, Aerothermodynamic Integration Model Development, Seventh Interim Technical Data Report, AiResearch Document AP-69-5899, Data Item 55-4.07, 22 January 1970.

7.2-2. Snyder, A. D., Robertson, J., Zanders, D. L., and Skinner, G. B., "Shock Tube Studies of Fuel-Air Ignition Characteristics," Monsanto Research Corp., AFAPL-TR-65-93, August, 1965.

7.2-3. Engineering Staff - Hypersonic Research Engine Project - Phase II Combustor Program, Final Technical Data Report (U), Data Item No. 55 - 2.11, AiResearch Document No. AP-70-6054, 2 March 1970, (Confidential)

7.2-4. Engineering Staff, Hypersonic Research Engine Project - Phase II, Combustor Program, Tenth Interim Technical Data Report (U), Data Item No. 55 - 2.10, AiResearch Document No. AP-69-5405, 22 August 1969, Confidential

7.2-5. Engineering Staff, Hypersonic Research Engine Project - Phase II, Chemical Kinetics Study for the Supersonic Combustor Model (U), Data Item No. 54.10, AiResearch Document No. AP-70-6319, 13 April 1970, Confidential

7.3-1. Engineering Staff, Hypersonic Research Engine Project - Phase II, Nozzle Program, Terminal Summary Report, Data Item No. 55 - 3.05, AiResearch Document AP-68-4451, 2 December 1968, Confidential

7.3-2. Engineering Staff, Hypersonic Research Engine Project - Phase II, AIM Measurement Plan, Data Item No. 2 - 1.01, AiResearch Document AP-70-6216, 4 June 1970, Confidential

7.3-3. Moretti, G., "A New Technique for the Numerical Analysis of Non-Equilibrium Flows", AIAA Journal 3, 2, February 1965, pp. 223-229

7.4-1. Andrews, Earl H., Jr., James W. Russell, Ernest A. Mackley, and Ann L. Simmonds, "An Inlet Analysis for the NASA Hypersonic Research Engine AIM, NASA TM X-3038.

7.5-1. Engineering Staff, Hypersonic Research Engine Project, Phase II, Combustor Program, Second Interim Technical Data Report, Data Item No. 55 - 2.02, AiResearch Document No. AP-67-2535, 1 Sept. 1967.

7.6-1. Engineering Staff, Hypersonic Research Engine Project - Phase II, Boilerplate Engine Development, Second Interim Technical Data Report, Data Item No. 55 - 4.02, AiResearch Document AP-68-4285, 11 October 1968, Confidential

7.7-1. Hypersonic Research Engine Project, Statement of Work for Phase II, Document No. L-4947B (Revised) 3 September 1968, Langley Research Center, Langley Station, Hampton, Va.

APPENDIX A

DESCRIPTION OF PERFORMANCE OUTPUT

PRECEDING PAGE BLANK NOT FILMED

APPENDIX A

DESCRIPTION OF PERFORMANCE OUTPUT

Each page of the performance output has a standard heading with Reading number (Test number), Block number (numbered sequentially and corresponding to recorded times of test data), Time (of data recording from start of test in seconds), Mach number, PT (total pressure in wind tunnel in psia), TT (total temperature in wind tunnel in ^{0}R), and Page number. Pages 1, 2 and 3 contain a summary of flow parameters at each calculation station in the AIM. Each station is headed by a station designator (i.e., wind tunnel, inlet throat, combustor, etc.) followed by three integers (the additional zero following the combustor designator is meaningless). The first integer denotes the station number, the second denotes the combustor station number and the third denotes the number of iterations required to converge on a solution. The third integer may assume values between 0-21, 100-121 and 200-221. A value of the third integer equal to 21 denotes that the mass flow was too great (or the flow area too small) to obtain a solution, 121 denotes that the solution for total conditions did not converge in 21 iterations and 200-221 denotes that the mass flow was too small (or the flow area too large) to obtain a solution. When both solutions for static and total conditions have converged, the third integer may assume the values 1-20 or 101-120 depending on which solution (static or total) required the larger number of iterations.

Most of the station designators are self-explanatory. The first appearance of the designators "Wind tunnel" and "Spike Tip NS" (NS = NORMAL SHOCK) reports conditions in wind tunnel and upstream of the spike tip based on a wind tunnel Mach number determined from calibration runs. The second appearance of these designators reports these conditions based on a wind tunnel Mach number calculated from the wind tunnel total and spike tip pitot pressures and the total temperature of the synthetic air in the wind tunnel applied to the normal shock equations. The designators "INLET UPNRSK" and "INLET DNNRSK" denote conditions upstream and downstream of a normal shock positioned at a fictitious flow area 1.10 times the flow area at the inlet throat. The designator "COMBUSTOR REGEN" denotes conditions at the combustor throat simulating a regeneratively cooled ramjet. "NOZZLE AE" and "NOZZLE PO" report conditions when the flow is expanded isentropically to the nozzle exit area and to the wind tunnel static pressure, respectively. "FICTIVE COMBUSTR" denotes conditions in a zero velocity, constant pressure combustor with combustor efficiency equal to unity. "FICTIVE NOZZLE" reports conditions required to match the actual momentum and nozzle exit area.

Definition and units of parameters in the SUMMARY REPORT (pp 1-3) are listed below:

P	-	pressure, psia
T	-	temperature, ^{0}R
H	-	enthalpy, Btu/lbm
GAMMA	-	Specific heat ratio

MOLWT	-	molecular weight
SONV	-	sonic velocity, ft/sec
MACH	-	Mach number
VEL	-	flow velocity, ft/sec
S	-	entropy, Btu/lb_m-^0R
W/A	-	flow rate per unit area, lbm/sq in.
W	-	flow rate, lbm/sec
A/A_C	-	local area ratio
MOMTM	-	flow momentum, lb_f
Q	-	dynamic pressure, lb_f/sq in.
I_{VAC}	-	vacuum specific impulse, lb_f-sec/lb_m
PHI	-	equivalence ratio
ETAC	-	combustor efficiency

Definitions and units of parameters on pages 4 and 5 follow:

X_{ABS}	-	axial distance from vertical spike tip, inches
P-IB	-	surface pressure on innerbody, psia
P-ØB	-	surface pressure on inner cowl, psia
PDA	-	pressure integral, $\int_0^{XABS} PdA$, lb_f
QOX	-	cumulative internal heat loss from spike tip to Station X, Btu/sec
Q-IB	-	cumulative internal heat loss from innerbody, Btu/sec
CAWALL	-	cumulative surface area, sq in.
P-IB/PSO	-	innerbody static to wind tunnel static pressure ratio
P-IB/PTO	-	innerbody static to wind tunnel total pressure ratio
PØB/PSO	-	outerbody static to wind tunnel static pressure ratio
PØB/PTO	-	outerbody static to wind tunnel total pressure ratio

Definition and units of parameters on page 6 follow:

X	-	axial distance from spike virtual tip
DDRAG	-	incremental frictional drag force, lb_f
CDRAG	-	cumulative frictional drag force, lb_f
CF	-	skin friction coefficient
HC	-	heat transfer coefficient, Btu/(sec-sq ft-^{0}R)

1-17-75
Reg. corrected

REACTING = PURE PLUG = 54 TT = 197.542 ALT = 5.2 PT = 217.249 TT = 2220.9
TARGET PERFORMANCE

S U M M A R Y R E P O R T

	P	T		GAMMA	THRUST SPEC	MACH	VEL	S	F/A	W	A/AP	NOZZ	G	ISAC	PHI	ETAP
MIAD TUNNEL		1														
0.000	417.249	2229	1.3164	28.886	2250											
0.000	0.585	375	1.3983	28.886	951	5.170	4916	1.781	0.10331	31.783	0.8659	4986	11.446	156.9		
SPIKE TIP NS		2														
0.000	21.342	2229	1.3165	28.886	2250											
0.000	19.370	2177	1.3263	28.886	2225	0.388	862	1.985	0.10331	31.783	0.8659	5147	1.923	156.7		
MIAD TUNNEL		3														
0.000	417.249	2229	1.3161	28.886	2251											
0.000	0.621	382	1.3984	28.886	959	5.123	4908	1.781	0.10912	33.073	0.8659	5183	11.374	156.7		
SPIKE TIP NS		4														
0.000	21.342	2229	1.3165	28.886	2250											
0.000	19.180	2177	1.3269	28.886	2222	0.407	904	1.985	0.10912	33.073	0.8659	5183	2.095	156.7		
INLET THROAT		5														
40.400	190.976	2171	1.32	28.886	2222											
40.400	20.270	1224	1.3852	28.886	1498	2.110	3583	1.827	1.10652	33.073	0.1191	4265	44.112	129.0		
INLET THROAT		6														
40.400	190.976	2171	1.3218	28.886	2222											
40.400	18.398	1195	1.3871	28.886	1477	2.170	3639	1.827	1.08675	33.073	0.1234	4322	54.198	130.7		
INLET THROAT		7														
40.400	117.487	2171	1.3215	28.886	2222											
40.400	98.343	2172	1.3239	28.886	2170	0.583	1180	1.886	1.08475	33.073	0.1234	4322	14.661	130.7		
COMBUSTOR	0	8	1	4												
40.810	190.843	2171	1.3204	28.886	2222											
40.810	21.752	1250	1.3837	28.886	1713	2.188	3590	1.827	1.15128	33.073	0.1122	4204	43.361	128.9		
COMBUSTOR	0	9	2	4												
41.274	190.648	2165	1.3217	28.886	2218											
41.276	25.238	1356	1.3571	28.886	1780	1.888	3322	1.838	1.15422	33.073	0.1119	4137	54.582	125.1		
COMBUSTOR	0	10	3	4												
41.301	158.056	2162	1.3217	28.886	2218											
41.301	25.538	1365	1.3564	28.886	1786	1.858	3304	1.839	1.15489	33.073	0.1118	4127	59.694	124.8		
COMBUSTOR	0	11	4	4												
41.500	155.438	2161	1.3218	28.886	2217											
41.500	26.317	1385	1.3554	28.886	1798	1.813	3254	1.841	1.15688	33.073	0.1116	4103	57.598	124.1		
COMBUSTOR	0	12	5	4												
42.860	136.319	2150	1.3212	28.886	2212											
42.860	28.498	1454	1.3512	28.886	1841	1.677	3087	1.898	1.14982	33.073	0.1126	4019	50.929	121.2		
COMBUSTOR	0	13	6	4												
44.041	124.868	2131	1.3214	28.886	2213											
44.041	29.506	1485	1.3444	28.886	1858	1.614	2992	1.851	1.14705	33.073	0.1144	3947	51.367	119.5		
COMBUSTOR	0	14	7	4												
44.310	123.586	2129	1.3214	28.886	2211											
44.310	29.728	1489	1.3443	28.886	1859	1.594	2965	1.852	1.14548	33.073	0.1145	3937	5 .936	119.1		
COMBUSTOR	0	15	8	4												
44.776	120.799	2124	1.3221	28.886	2199											
44.776	30.204	1501	1.3427	28.886	1867	1.569	2928	1.852	1.14123	33.073	0.1171	3917	50.115	118.4		
COMBUSTOR	0	16	9	4												
44.800	120.550	2124	1.3221	28.886	2199											
44.800	30.209	1501	1.3427	28.886	1867	1.569	2927	1.853	1.14055	33.073	0.1173	3918	47.459	118.4		
COMBUSTOR	0	17	10	4												
46.260	113.574	2111	1.3225	28.886	2193											
46.260	29.239	1449	1.3444	28.886	1858	1.573	2925	1.855	1.03640	33.073	0.1246	3908	47.121	118.2		
COMBUSTOR	0	18	11	4												
47.301	111.542	2106	1.3228	28.886	2189											
47.301	29.542	1438	1.3529	28.886	1829	1.653	3023	1.855	0.96484	33.073	0.1338	3949	45.525	119.4		

GARRETT AIRESEARCH MANUFACTURING COMPANY OF CALIFORNIA

ORIGINAL PAGE IS OF POOR QUALITY

READING = 0096 BLOCK = 59 TT-4 = 157.592 MACH 5.2 PT = 417.249 TT = 2228.9

	P	T															
COMBUSTOR	0	19	12	4													
47.310	111.556	2133	460.4(	547)	1.3264	28.866	2184										
47.310	24.535	1836	225.7(	355)	1.3524	28.866	1829	1.653	3023	1.855	0.966878	33.173	0.1339	5969	45.321	119.9	
COMBUSTOR	0	20	13	4													
48.110	112.144	2097	464.7(	536)	1.3230	28.866	2186										
48.110	21.928	1573	204.1(	334)	1.3561	28.866	1791	1.755	3198	1.854	0.899424	33.173	0.1436	6005	43.431	121.1	
COMBUSTOR	0	21	14	4													
48.751	112.985	2092	465.2(	540)	1.3232	28.866	2184										
48.751	17.844	1339	192.4(	322)	1.3516	28.866	1751	1.864	3263	1.853	0.853096	33.173	0.1554	6065	44.140	122.4	
COMBUSTOR	0	22	15	5													
49.281	114.703	2088	474.1(	533)	1.3253	28.866	2182										
49.281	15.495	1253	177.4(	307)	1.3635	28.866	1715	1.981	3364	1.851	0.777709	33.173	0.1682	6118	41.829	124.5	
COMBUSTOR	0	23	16	11													
50.691	137.408	2076	476.7(	530)	1.3258	28.866	2176										
50.691	10.159	1058	124.1(	257)	1.3757	28.866	1583	2.332	3693	1.837	0.684230	33.173	0.1951	6303	38.098	130.1	
COMBUSTOR	0	24	17	202													
52.791	76.823	2135	393.7(	504)	1.3224	28.798	2217										
52.791	88.400	1865	310.1(	473)	1.3318	28.798	2171	1.950	1945	1.893	0.504458	33.145	0.2379	6712	10.466	142.1	0.62 1.00
COMBUSTOR	0	25	18	203													
53.291	74.211	2130	392.4(	507)	1.3211	28.798	2214										
53.291	87.133	1935	329.2(	344)	1.3293	28.798	2192	1.850	1774	1.895	0.522402	33.185	0.2468	6828	10.437	145.5	0.62 1.00
COMBUSTOR	0	26	19	5													
54.031	61.822	2669	422.1(	423)	1.3019	28.833	2648										
54.031	47.539	2511	367.1(	369)	1.3172	28.833	2573	2.044	1857	2.256	0.570135	33.242	0.2824	6936	10.287	148.5	0.52 0.31
COMBUSTOR	0	27	20	2													
54.041	61.812	2670	422.1(	423)	1.3019	28.834	2649										
54.041	47.539	2512	367.1(	369)	1.3171	28.833	2579	2.044	1857	2.256	0.569997	33.242	0.2831	6939	10.276	148.6	0.52 0.31
COMBUSTOR	0	28	21	4													
54.801	61.098	2795	419.3(	444)	1.2980	28.785	2697										
54.801	47.950	2643	366.6(	412)	1.3111	28.788	2628	2.019	1824	2.247	0.472841	33.242	0.2942	7167	11.451	156.1	0.52 0.37
COMBUSTOR	0	29	22	4													
55.760	59.807	3063	415.1(	453)	1.2834	28.850	2793										
55.760	47.030	2904	358.3(	397)	1.2944	28.851	2765	2.019	1887	2.284	0.446284	33.242	0.2971	7344	11.013	157.4	0.52 0.39
COMBUSTOR	0	30	23	5													
56.216	58.653	3107	442.8(1111)		1.2755	21.873	3124										
56.216	46.592	2964	395.3(1054)		1.2859	21.874	2980	2.557	1854	2.574	0.358321	33.199	0.3674	8141	9.312	174.4	1.03 0.32
COMBUSTOR	0	31	24	2													
56.226	58.648	3105	442.6(1112)		1.2753	21.877	3125										
56.226	46.583	2972	395.1(1059)		1.2858	21.877	2985	2.557	1851	2.574	0.358372	33.199	0.3674	8144	9.314	174.4	1.03 0.32
COMBUSTOR	0	32	25	4													
56.281	58.679	3280	442.3(1144)		1.2744	21.838	3148										
56.281	45.215	3130	374.6(1149)		1.2861	21.837	3022	2.588	1773	2.573	0.358193	33.199	0.3684	8157	9.271	174.6	1.03 0.32
COMBUSTOR	0	33	26	5													
56.421	55.956	3310	441.7(1191)		1.2736	21.888	3198										
56.421	45.108	3167	378.6(1153)		1.2841	21.887	3053	2.588	1771	2.595	0.358427	33.199	0.3717	8184	9.221	174.8	1.03 0.38
COMBUSTOR	0	34	27	7													
56.501	56.401	3205	441.3(1174)		1.2774	21.923	3143										
56.501	46.319	3121	384.3(1114)		1.2862	21.922	3020	2.579	1775	2.598	0.358329	33.199	0.3725	8192	9.208	174.9	1.03 0.38
COMBUSTOR	0	35	28	6													
56.781	57.088	3390	446.4(1222)		1.2713	21.963	3185										
56.781	46.050	3238	378.2(1186)		1.2824	21.963	3061	2.588	1795	2.594	0.358226	33.199	0.3754	8252	9.165	175.4	1.03 0.40
COMBUSTOR	0	36	29	6													
57.007	57.274	3501	450.3(1245)		1.2657	22.004	3241										
57.007	45.765	3330	382.5(1199)		1.2775	22.003	3102	2.588	1801	2.595	0.358167	33.199	0.3762	8268	9.140	175.6	1.03 0.40
COMBUSTOR	0	37	30	6													
57.731	56.869	3761	450.1(1345)		1.2512	22.084	3359										
57.731	44.881	3584	382.2(1298)		1.2636	22.084	3217	2.624	1841	2.623	0.358134	33.199	0.3783	8314	9.067	176.2	1.03 0.41

GARRETT AIRESEARCH MANUFACTURING COMPANY OF CALIFORNIA

ORIGINAL PAGE IS OF POOR QUALITY

READING = 0094 BLOCK = 59 TIME = 157.542 MACH 5.2 PT = 417.249 TT = 2229.9 PAGE 3

	P	T	H		GAMMA	MOLWT	SONV	MACH	VEL	S	M/A		A/AC	NUMIN	C	IVAL	PMI	ETAC
COMBUSTOR	0	38	31	4														
58.751	56.350	3982	430.9	(1453)	1.2377	22.539	3297											
58.751	43.725	3790	392.8	(1373)	1.2460	22.550	3227	0.651	2100	2.634	0.35353	34.199	0.3777	6462	11.537	186.9	1.03	0.57
COMBUSTOR	0	39	32	5														
60.761	56.253	4396	422.4	(1416)	1.2078	22.988	3389											
60.761	38.962	4128	280.9	(1503)	1.2208	23.030	3298	0.788	2601	2.651	0.36584	34.199	0.3650	6407	14.785	187.3	1.03	0.70
COMBUSTOR	0	40	33	4														
62.181	56.583	4491	415.9	(1653)	1.1999	23.103	3405											
62.181	35.981	4165	247.7	(1515)	1.2159	23.165	3297	0.880	2902	2.653	0.37575	34.199	0.3553	6359	16.984	185.9	1.03	0.74
SONIC THROAT		41	34	205														
62.181	42.896	5011	415.9	(1842)	1.1563	23.651	3490											
62.181	35.981	4660	189.6	(1717)	1.1643	23.857	3370	0.999	3366	2.651	0.37575	34.199	0.3553	6852	19.653	200.4	1.03	1.00
COMBUSTOR REGEN		42	35	4														
62.181	56.583	4503	423.0	(1659)	1.1991	23.099	3409											
62.181	35.781	4173	251.8	(1519)	1.2153	23.163	3299	0.887	2927	2.654	0.37575	34.199	0.3553	6364	17.093	186.1	1.03	0.74
NOZZLE AE		43	36	4														
87.257	56.583	4491	415.9	(1651)	1.1999	23.103	3405											
87.257	1.303	2134	-81.4	695)	1.3069	23.235	2920	2.968	7182	2.653	0.00893	34.199	1.9372	8300	7.693	242.7	1.03	0.74
NOZZLE PO		44	37	4														
87.257	56.583	4491	415.9	(1651)	1.1999	23.103	3405											
87.257	0.821	1753	-741.8	568)	1.3168	23.235	2223	3.429	7611	2.653	0.00051	34.199	3.2943	8414	4.791	251.9	1.03	0.74
NOZZLE AE REGEN		45	38	4														
87.257	56.583	4503	423.0	(1659)	1.1991	23.099	3409											
87.257	1.307	2114	-81.4	699)	1.3105	23.235	2928	2.965	7192	2.654	0.00893	34.199	1.9372	8314	7.704	243.1	1.03	0.74
NOZZLE PO REGEN		46	39	4														
87.257	56.583	4503	423.0	(1659)	1.1991	23.099	3409											
87.257	0.821	1761	-734.2	571)	1.3184	23.235	2227	3.429	7625	2.654	0.00040	34.199	3.3047	8431	4.788	252.4	1.03	0.74
FICTIVE COMBUSTO		48	41															
62.181	190.976	5127	415.9	(1919)	1.1467	23.775	3537											
62.181	0.821	1767	-1133.1	534)	1.3017	24.226	2141	0.112	2414	2.584	0.05019	34.199	2.4605	4781	0.647	288.1	1.03	1.00
FICTIVE NOZZLE		49	42	4														
87.257	30.269	4393	374.7	(1621)	1.1978	23.170	3365											
87.257	1.691	2535	-453.7	855)	1.2948	23.235	2837	2.941	8439	2.697	0.00893	34.199	1.9371	7738	8.897	228.3	1.03	0.74

ORIGINAL PAGE IS OF POOR QUALITY

XABS	P=1P	P=P2	P=P3	P=P4	P=P5	P=P6	P=P7	P=P8	P=P9	P=P10
0.9F1F-01	1.0415E 00	[illegible]	-5.227[illegible]-01	[illegible]	0.000	0.000	2.0[illegible]E-02	[illegible]	[illegible]	0.000
1.836F 01	1.415E 00	[illegible]	-4.7[illegible] 01	[illegible]	0.000	0.000	1.838E 02	[illegible]	[illegible]	0.000
3.070F 01	2.555E 00	[illegible]	-2.[illegible]E 02	[illegible]	0.000	0.000	5.[illegible]93E 02	4.117E 01	[illegible]	0.000
3.50AF 01	4.204F 00	[illegible]	-0.2[illegible]E 02	[illegible]	0.000	0.000	[illegible]E-02	[illegible]F 01	[illegible]	0.000
3.516F 01	0.263E 00	0.[illegible]	-0.[illegible]E 02	[illegible]	0.000	0.000	6.[illegible]39E 02	6.[illegible]F 01	1.022E-02	9.740F 00
3.516F 01	0.265E 00	0.[illegible]	-0.[illegible]E 02	[illegible]	0.000	0.000	6.[illegible]92E 02	6.[illegible] 01	1.022E-02	9.715F 00
3.555F 01	0.300E 00	0.[illegible]	-0.[illegible] 02	[illegible]	0.000	0.000	7.22[illegible] 02	7.[illegible] 01	1.050E-02	7.592F 00
3.583F 01	0.3[illegible]E 00	5.[illegible]F 01	-5.137E 02	-2.757E 02	-2.757E 02	0.000	7.513E 02	7.[illegible] 01	1.050E-02	9.092F 00
3.606F 01	0.[illegible]E 00	5.[illegible]F 01	-5.23[illegible] 02	-2.795E 02	-2.793E 02	0.000	7.[illegible]E 02	7.[illegible] 01	1.055E-02	8.356F 00
3.64AF 01	0.815E 00	7.[illegible]E 01	-5.357E 02	-2.862E 02	-2.862E 02	0.000	8.185E 02	7.[illegible] 01	1.154E-02	1.280F 01
3.701F 01	0.635E 00	1.11 E 01	-5.[illegible]E 02	-3.31[illegible] 02	-2.953E 02	-3.[illegible] 01	8.745E 02	7.[illegible] 01	1.111E-02	1.795F 01
3.729F 01	5.945E 00	1.[illegible] 01	-5.573E 02	-3.[illegible] 02	-3.[illegible]E 02	-4.732E 01	9.[illegible] 02	9.574E 01	1.025E-02	2.[illegible] 01
3.803F 01	9.399E 00	1.[illegible] 01	-4.129E 02	-3.[illegible] 02	-3.142E 02	-7.510F 01	9.859E 02	1.515E 01	2.250E-02	2.487F 01
3.831F 01	1.229E 01	1.[illegible] 01	-4.[illegible] 02	-3.[illegible] 02	-3.200E 02	-8.540F 01	1.017E 03	1.981E 01	2.994E-02	2.604F 01
3.875F 01	1.[illegible]3E 01	1.[illegible] 01	-4.[illegible] 02	-3.[illegible] 02	-3.303E 02	-1.019F 02	1.[illegible] 03	2.711E 01	4.[illegible]E-02	2.8[illegible] 01
3.87[illegible] 01	1.715E 01	1.[illegible] 01	-4.[illegible] 02	-3.[illegible] 02	-3.[illegible] 02	-1.[illegible] 02	1.[illegible] 03	2.[illegible] 01	4.[illegible]E-02	2.[illegible] 01
3.901F 01	1.951E 01	1.[illegible] 01	-4.[illegible] 02	-3.[illegible] 02	-3.371E 02	-1.116F 02	1.[illegible]E 03	3.[illegible] 01	[illegible]E-02	2.[illegible] 01
3.929F 01	1.[illegible]E 01	1.[illegible] 01	-4.[illegible] 02	-3.[illegible] 02	-3.[illegible] 02	-1.[illegible] 02	1.[illegible] 03	3.[illegible] 01	[illegible]E-02	2.[illegible] 01
3.950F 01	1.[illegible] 01	1.[illegible] 01	-4.[illegible] 02	-3.[illegible] 02	-3.515E 02	-1.[illegible] 02	1.[illegible] 03	3.[illegible] 01	[illegible]E-02	2.[illegible] 01
3.97[illegible] 01	1.[illegible] 01	5.[illegible] 01	-7.[illegible] 02	-3.[illegible] 02	-3.[illegible] 02	-1.[illegible] 02	1.[illegible] 03	3.[illegible] 01	[illegible]E-02	2.[illegible] 00
4.000F 01	2.[illegible] 01	5.[illegible] 01	-8.[illegible] 02	-3.[illegible] 02	-3.[illegible] 02	-1.[illegible] 02	1.[illegible] 03	3.[illegible] 01	[illegible]E-02	2.[illegible] 00
4.040F 01	2.[illegible] 01	5.[illegible] 01	-8.[illegible] 02	-3.[illegible] 02	-3.[illegible] 02	-1.[illegible] 02	1.[illegible] 03	3.[illegible] 01	[illegible]E-02	2.[illegible] 00
4.081F 01	2.[illegible] 01	5.[illegible] 01	-8.[illegible] 02	-3.[illegible] 02	-3.[illegible] 02	-1.[illegible] 02	1.[illegible] 03	3.[illegible] 01	[illegible]E-02	2.[illegible] 00
4.12[illegible] 01	3.[illegible] 01	5.[illegible] 01	-9.[illegible] 02	-3.[illegible] 02	-3.[illegible] 02	-1.[illegible] 02	1.[illegible] 03	3.[illegible] 01	[illegible]E-02	2.[illegible] 00
4.150F 01	3.[illegible] 01	5.[illegible] 01	-9.[illegible] 02	-3.[illegible] 02	-3.[illegible] 02	-2.[illegible] 02	1.[illegible] 03	3.[illegible] 01	[illegible]E-02	2.[illegible] 00
4.2[illegible] 01	1.[illegible] 01	1.[illegible] 01	-1.[illegible] 03	-7.[illegible] 02	-4.[illegible] 02	-2.[illegible] 02	1.[illegible] 03	3.[illegible] 01	[illegible]E-02	1.[illegible] 01
4.[illegible] 01	2.[illegible] 01	1.[illegible] 01	-1.[illegible] 03	-9.[illegible] 02	-5.[illegible] 02	-3.[illegible] 02	1.[illegible] 03	4.[illegible] 01	[illegible]E-02	2.[illegible] 01
4.[illegible] 01	2.[illegible] 01	1.[illegible] 01	-1.[illegible] 03	-9.[illegible] 02	-5.[illegible] 02	-3.[illegible] 02	1.[illegible] 03	4.[illegible] 01	[illegible]E-02	3

READING = 0094 BLOCK = 59 TTAP = 157.542 MACH 5.2 PT = 417.249 TT = 2228.9

XABS	P=IB	P=OB	PDA	QDX	Q=IB	Q=OB	CAWALL	P=IB/PSO	P=IA/PTO	P=OB/PSO	P=OA/PTO
6.502E 01	2.470E 01	2.58CF 01	1.677E 03	-3.380E 03	-1.706E 03	-1.674F 03	4.337E 03	3.980F 01	5.920E-02	4.157E 01	6.183E-02
6.506F 01	2.470E 01	2.565F 01	1.677E 03	-3.387F 03	-1.709E 03	-1.678E 03	4.342E 03	3.980F 01	5.920E-02	4.134F 01	6.149E-02
6.526E 01	2.332E 01	2.494F 01	1.677E 03	-3.416E 03	-1.723E 03	-1.693E 03	4.368E 03	3.757E 01	5.588E-02	4.018E 01	5.977E-02
6.692E 01	1.184E 01	1.019F 01	1.672E 03	-3.632F 03	-1.829E 03	-1.803E 03	4.584E 03	1.907E 01	2.837E-02	1.642E 01	2.442E-02
6.759E 01	9.047E 00	1.061F 01	2.083E 03	-3.706E 03	-1.864E 03	-1.842F 03	4.665E 03	1.458E 01	2.168E-02	1.710F 01	2.543E-02
6.836E 01	5.840E 00	8.539F 00	2.316E 03	-3.769E 03	-1.900E 03	-1.889E 03	4.760E 03	9.410E 00	1.400E-02	1.376E 01	2.046E-02
6.908E 01	4.817E 00	6.800F 00	2.481E 03	-3.804E 03	-1.929E 03	-1.934F 03	4.84AE 03	7.761F 00	1.154E-02	1.063F 01	1.582E-02
6.969E 01	3.950E 00	4.504F 00	2.588E 03	-3.943E 03	-1.951E 03	-1.972F 03	4.922E 03	6.365F 00	9.467E-03	7.257F 00	1.079E-02
7.064E 01	3.031E 00	1.240F 00	2.692E 03	-4.000E 03	-1.980E 03	-2.020F 03	5.036E 03	4.884E 00	7.264E-03	1.998F 00	2.972E-03
7.107E 01	2.615E 00	1.564F 00	2.724E 03	-4.03CE 03	-1.992E 03	-2.038E 03	5.08AE 03	4.214E 00	6.267E-03	2.519F 00	3.747E-03
7.260E 01	1.795E 00	2.715F 00	2.828E 03	-4.116F 03	-2.028E 03	-2.090E 03	5.273E 03	2.893F 00	4.303E-03	4.375F 00	6.507E-03
7.275E 01	1.715E 00	2.375F 00	2.83AE 03	-4.126E 03	-2.031E 03	-2.095F 03	5.290E 03	2.763E 00	4.110E-03	3.827E 00	5.692E-03
7.350E 01	2.027E 00	A.750E-01	2.894E 03	-4.166F 03	-2.045E 03	-2.121E 03	5.374E 03	3.266E 00	4.858E-03	1.088F 00	1.618E-03
7.350F 01	2.029E 00	6.659E-01	2.895E 03	-4.166E 03	-2.045E 03	-2.121E 03	5.375E 03	3.269E 00	4.862E-03	1.073F 00	1.596E-03
7.483E 01	2.580E 00	0.000	2.944E 03	-4.242E 03	-2.066E 03	-2.176E 03	5.427E 03	4.157E 00	6.183E-03	0.000	0.000
7.768E 01	2.325E 00	0.000	3.042E 03	-4.275F 03	-2.100E 03	-2.176F 03	5.525E 03	3.746E 00	5.572E-03	0.000	0.000
8.158E 01	1.600E 00	0.000	3.126E 03	-4.304F 03	-2.128E 03	-2.176E 03	5.630E 03	2.578F 00	3.835E-03	0.000	0.000
8.439F 01	1.735E 00	0.000	3.163E 03	-4.325E 03	-2.149E 03	-2.176F 03	5.684E 03	2.796E 00	4.158E-03	0.000	0.000
8.725F 01	2.330E 00	0.000	3.212E 03	-4.361E 03	-2.186E 03	-2.176F 03	5.707E 03	3.754E 00	5.584E-03	0.000	0.000
8.726F 01	2.331E 00	0.000	3.212E 03	-4.361F 03	-2.186E 03	-2.176E 03	5.707E 03	3.756F 00	5.587E-03	0.000	0.000

ORIGINAL PAGE IS
OF POOR QUALITY

ORIGINAL PAGE IS OF POOR QUALITY

REACTNG = 0090 BLOCK = 59 TT-F = 157.502 MCL= 5.2 P1 = 417.249 TT = 2229.9

PAGE 4

X	CONRAD	CURVE	CF	MC
4.040F 01	1.175E 02	1.175E 02	2.224E-03	5.011E-02
4.091E 01	1.677E-01	1.177E 02	2.234E-03	5.251E-02
4.128F 01	1.441E 01	1.321E 02	2.304E-03	5.411E-02
4.138F 01	1.087E 00	1.332E 02	2.354E-03	5.651E-02
4.150F 01	2.600E 00	1.358E 02	2.375E-03	5.701E-02
4.200F 01	1.573E 01	1.515E 02	2.647E-03	5.807E-02
4.406F 01	2.537E 01	1.769E 02	2.888E-03	5.774E-02
4.431F 01	3.859E 00	1.808E 02	2.698E-03	5.795E-02
4.478F 01	7.194E 00	1.880E 02	2.513E-03	5.826E-02
4.480F 01	3.707E-01	1.884E 02	2.513E-03	5.826E-02
4.626E 01	2.195E 01	2.103E 02	2.521E-03	5.869E-02
4.730F 01	1.891E 01	2.292E 02	2.478E-03	4.991E-02
4.731F 01	1.312E-01	2.293E 02	2.478E-03	4.990E-02
4.811F 01	1.090E 01	2.402E 02	2.821E-03	4.511E-02
4.875F 01	8.252E 00	2.485E 02	2.860E-03	4.835E-02
4.928F 01	6.818E 00	2.553E 02	2.745E-03	5.690E-02
5.049F 01	1.535E 01	2.686E 02	2.091E-03	2.787E-02
5.279F 01	1.710E 01	2.857E 02	2.425E-03	5.050E-02
5.329F 01	2.413E 00	2.881E 02	2.883E-03	4.818E-02
5.403F 01	3.805E 00	2.919E 02	3.299E-03	5.881E-02
5.480F 01	5.141E-02	2.924E 02	3.033E-03	4.219E-02
5.880F 01	3.649E 00	2.960E 02	3.000E-03	4.142E-02
5.576F 01	8.361E 00	2.977E 02	2.999E-03	4.085E-02
5.622F 01	1.360E 00	2.990E 02	3.299E-03	5.814E-02
5.623F 01	3.800E-02	2.990E 02	3.095E-03	3.751E-02
5.628F 01	2.092E-01	2.990E 02	3.263E-03	3.885E-02
5.682F 01	5.862E-01	2.996E 02	3.117E-03	3.783E-02
5.659F 01	3.308E-01	3.000E 02	3.444E-03	3.200E-02
5.678F 01	1.158E 00	3.012E 02	3.088E-03	3.877E-02
5.701F 01	9.155E-01	3.022E 02	3.107E-03	3.803E-02
5.773F 01	3.067E 00	3.053E 02	3.094E-03	3.953E-02
5.875F 01	4.581E 00	3.101E 02	3.138E-03	3.949E-02
6.076F 01	1.195E 01	3.220E 02	3.095E-03	4.203E-02
6.218F 01	9.350E 00	3.297E 02	3.167E-03	4.115E-02
6.480F 01	1.928E 01	3.489E 02	3.194E-03	4.035E-02
6.502F 01	3.325E 00	3.522E 02	3.178E-03	3.947E-02
6.506F 01	3.579E-01	3.732E 02	3.178E-03	3.943E-02
6.526F 01	1.799E 00	3.751E 02	3.189E-03	3.865E-02
6.692F 01	1.651E 01	3.895E 02	3.020E-03	2.579E-02
6.759F 01	5.132E 00	3.948E 02	3.015E-03	2.349E-02
6.836F 01	5.878E 00	4.007E 02	2.955E-03	1.951E-02
6.908F 01	9.509E 00	4.097E 02	2.919E-03	1.882E-02
6.949F 01	3.331E 00	4.129E 02	2.847E-03	1.345E-02
7.040F 01	3.969E 00	4.129E 02	2.795E-03	8.089E-03
7.107F 01	1.848E 00	4.134E 02	2.781E-03	7.952E-03
7.280F 01	5.215E 00	4.178E 02	2.794E-03	8.413E-03
7.275F 01	8.448E-01	4.191E 02	2.775E-03	7.849E-03
7.350F 01	2.035E 00	4.211E 02	2.713E-03	5.688E-03
7.350F 01	3.390E-03	4.211E 02	2.713E-03	5.656E-03
7.483F 01	1.350E 00	4.225E 02	2.799E-03	9.270E-03
7.748F 01	2.972E 00	4.255E 02	2.773E-03	8.538E-03
8.158F 01	2.742E 00	4.296E 02	2.[illegible]E-03	8.373E-03
8.439F 01	1.289E 00	4.309E 02	2.[illegible]E-03	8.751E-03
8.725F 01	8.018E-01	4.317E 02	2.734E-03	8.418E-03
8.726F 01	0.000	4.317E 02	2.734E-03	8.462E-03

RAMJET PERFORMANCE

ENGINE PERFORMANCE

CALCULATED THRUST	2502.	(LBF)
MEASURED THRUST	2473.	(LBF)
CALCULATED SPECIFIC IMPULSE	2928.	(LBF-SEC/LBM)
MEASURED SPECIFIC IMPULSE	2900.	(LBF-SEC/LBM)
CALCULATED THRUST COEFFICIENT	0.8547	
MEASURED THRUST COEFFICIENT	0.8449	

REFRIGERATED-COOLED ENGINE PERFORMANCE

CALCULATED

STREAM THRUST	7751.	(LBF)
NET THRUST	2515.	(LBF)
SPECIFIC IMPULSE	2940.	(LBF-SEC/LBM)
THRUST COEFFICIENT	0.8631	

MOMENTUM AND FORCES

INLET FRICTION DRAG	117.5	(LBF)
INLET MOMENTUM CHANGE	-971.0	(LBF)
COMBUSTOR FRICTION DRAG	212.1	(LBF)
COMBUSTOR STRUT DRAG	155.39	(LBF)
COMBUSTOR MOMENTUM CHANGE	2090.	(LBF)
NOZZLE FRICTION DRAG	79.78	(LBF)
NOZZLE STRUT DRAG	76.62	(LBF)
NOZZLE MOMENTUM CHANGE	1379.	(LBF)
NOZZLE PRESSURE INTEGRAL	1555.	(LBF)
EXTERNAL FRICTION DRAG	52.01	(LBF)
EXTERNAL PRESSURE INTEGRAL	-1312.	(LBF)
TOTAL EXTERNAL DRAG	-1364.	(LBF)
TOTAL STRUT DRAG	232.01	(LBF)
CAVITY FORCE	-1318.	(LBF)
CALCULATED LOAD CELL FORCE	-188.	(LBF)
MEASURED LOAD CELL FORCE	-208.	(LBF)
FUEL VACUUM SPECIFIC IMPULSE	-155.5	0.0

STATIONS

NOMINAL COWL LEADING EDGE	50.884	(IN)
SPIKE TRANSLATION	0.2809	(IN)
INLET THROAT	40.400	(IN)
COWL LEADING EDGE	55.165	(IN)
NOZZLE SHROUD TRAILING EDGE	73.505	(IN)
NOZZLE PLUG TRAILING EDGE	87.257	(IN)
STRUT LEADING EDGE	56.421	(IN)
STRUT TRAILING EDGE	65.621	(IN)
COMBUSTOR EXIT	62.181	(IN)

INLET

ANGLE OF ATTACK	3.000	(DEGREES)
MASS FLOW RATIO	0.8459	
ADDITIVE DRAG COEFFICIENT	0.0110	
LIMITING PRESSURE RECOVERY EFFICIENCY	0.8803	
DELTA PT2	0.1466	(PSI)
TOTAL PRESSURE RECOVERY = SUPERSONIC	0.8577	
TOTAL PRESSURE RECOVERY = SUBSONIC	0.8953	
INLET PROCESS EFFICIENCY = SUPERSONIC	0.9865	
INLET PROCESS EFFICIENCY = SUBSONIC	0.9166	
KINETIC ENERGY EFFICIENCY = SUPERSONIC	0.9253	
KINETIC ENERGY EFFICIENCY = SUBSONIC	0.8918	
ENTHALPY AT P0 = SUPERSONIC	-17.98	(BTU/LBM)
ENTHALPY AT P0 = SUBSONIC	-1.888	(BTU/LBM)

COMBUSTOR

FUEL-AIR RATIO	0.0311	
EQUIVALENCE RATIO	1.030	
COMBUSTOR EFFICIENCY	0.734	
TOTAL PRESSURE RATIO	0.8963	
COMBUSTOR EFFECTIVENESS	0.7880	
INJECTOR DISCHARGE COEFFICIENTS	0.8600	0.7000

NOZZLE

VACUUM STREAM THRUST COEFFICIENT = CS	0.9323
NOZZLE COEFFICIENT = CI	0.8865
PROCESS EFFICIENCY	0.8883
KINETIC ENERGY EFFICIENCY	0.8888

FUEL INJECTORS

INJECTORS	STATION	VALVE
1A	49.845	
1B	61.266	
1C	48.300	
2A	48.741	
2C	64.255	
3A	54.131	E
3B	56.216	E
4	64.784	

AIRESEARCH MANUFACTURING COMPANY OF CALIFORNIA

ORIGINAL PAGE IS OF POOR QUALITY

SUMMARY REPORT

	P	T	M		GAMMA	MOLWT	SONV	MACH	VEL	S	A/A	A	A/AC	MDOTP	C	TVAC	PHI	ETAC
WIND TUNNEL		1	0	6														
0.000	998.749	3086	696.3(	821)	1.2904	28.903	2617											
0.000	0.155	208	-57.6(	72)	1.3964	28.901	866	7.358	6142	1.816	0.05999	15.080	0.9880	2918	5.688	193.5		
SPIKE TIP NS		2	0	7														
0.600	11.312	3086	696.3(	821)	1.2903	28.901	2617											
0.600	10.428	3029	679.2(	804)	1.2921	28.901	2595	0.357	926	2.124	0.05939	15.080	0.9880	3073	0.857	203.8		
WIND TUNNEL		3	0	0														
0.000	998.749	3086	696.3(	821)	1.2906	28.903	2617											
0.000	0.149	306	-55.7(	73)	1.3966	28.901	857	7.158	6135	1.816	0.06339	16.083	0.9880	3102	6.084	193.3		
SPIKE TIP NS		4	0	0														
0.600	11.312	3086	696.3(	821)	1.2903	28.901	2617											
0.600	10.297	3021	676.6(	802)	1.2924	28.901	2591	0.388	994	2.124	0.06339	16.083	0.9880	3107	0.980	193.3		
INLET THROAT		5	0	3														
40.400	320.771	2997	669.2(	795)	1.2934	28.902	2582											
40.400	10.582	1295	188.5(	319)	1.3606	28.901	1741	2.817	4905	1.885	0.78972	15.080	0.8785	2512	57.103	166.6		
INLET BRNRSK		6	0	3														
40.400	320.771	2997	669.2(	795)	1.2934	28.902	2582											
40.400	9.128	1245	175.6(	305)	1.3637	28.901	1709	2.908	4970	1.885	0.68156	15.080	0.8844	2531	52.691	167.9		
INLET BRNRSK		7	0	4														
40.400	102.558	2997	669.2(	795)	1.2934	28.902	2582											
40.400	89.311	2904	648.2(	767)	1.2963	28.902	2545	0.866	1185	1.984	0.68156	15.080	0.8844	2531	12.509	167.9		
COMBUSTOR	0	8	1	21														
40.410	216.194	2939	681.1(	808)	1.2977	26.340	2680											
40.410	11.712	1433	217.0(	387)	1.3547	26.340	1918	2.519	4819	2.057	0.75530	15.195	0.8785	2511	56.541	165.3	0.29	0.87
COMBUSTOR	0	9	2	3														
40.747	200.715	2972	679.1(	859)	1.2959	26.405	2693											
40.747	15.123	1584	247.3(	431)	1.3463	26.405	2008	2.320	4649	2.065	0.75808	15.195	0.8783	2498	50.745	166.0	0.29	0.11
COMBUSTOR	0	10	3	21														
41.237	202.497	2849	676.3(	822)	1.3018	26.285	2648											
41.237	10.776	1377	223.9(	372)	1.3588	26.285	1881	2.830	4758	2.053	0.75203	15.195	0.8789	2485	55.8[illegible]	162.2	0.29	0.[illegible]
COMBUSTOR	0	11	4	21														
41.500	187.875	2828	674.8(	815)	1.3024	26.267	2640											
41.500	11.742	1428	242.9(	386)	1.3561	26.267	1912	2.831	4849	2.057	0.74487	15.195	0.8796	2439	53.812	160.3	0.29	0.80
COMBUSTOR	0	12	5	21														
42.440	184.478	2804	668.4(	808)	1.3031	26.245	2631											
42.440	9.891	1367	210.2(	352)	1.3628	26.244	1836	2.808	4788	2.059	0.70251	15.195	0.8804	2367	52.277	155.[illegible]	0.29	0.[illegible]
COMBUSTOR	0	13	6	21														
42.732	117.028	2799	666.6(	806)	1.3038	26.244	2628											
42.732	6.641	1372	228.8(	371)	1.3591	26.244	1879	2.891	4879	2.089	0.69259	15.195	0.8857	2358	50.347	155.[illegible]	0.29	0.00
COMBUSTOR	0	14	7	21														
42.797	48.848	3290	665.9(	954)	1.2799	26.795	2795											
42.797	7.089	1934	233.0(	531)	1.3269	26.798	2187	2.131	4852	2.187	0.69002	15.195	0.8840	2352	49.[illegible]45	156.[illegible]	0.29	0.01
COMBUSTOR	0	15	8	2														
44.310	85.348	3245	653.1(	902)	1.2817	26.788	2779											
44.310	25.352	2461	397.0(	692)	1.3082	26.789	2448	1.463	3577	2.107	0.63874	15.195	0.8929	2297	35.503	150.9	0.29	0.00
COMBUSTOR	0	16	9	0														
44.800	77.527	3399	646.2(	893)	1.2738	26.977	2825											
44.800	31.275	2780	492.2(	799)	1.2952	26.981	2576	1.297	3211	2.142	0.63075	15.195	0.8941	2270	31.[illegible]76	149.[illegible]	0.29	0.50
COMBUSTOR	0	17	10	3														
45.517	74.824	3415	641.0(	888)	1.2726	27.019	2828											
45.517	30.412	2879	481.5(	820)	1.2913	27.023	2615	1.184	2996	2.145	0.62637	15.195	0.8907	2250	29.[illegible]46	148.1	0.28	0.57
COMBUSTOR	0	18	11	4														
46.222	73.395	3098	635.0(	879)	1.2847	28.581	2843											
46.222	32.516	2568	459.2(	788)	1.3078	28.582	2607	1.170	3099	2.294	0.[illegible]1547	15.311	0.[illegible]978	2282	26.[illegible]82	147.[illegible]	0.68	0.23

AIRESEARCH MANUFACTURING COMPANY OF CALIFORNIA

ORIGINAL PAGE IS OF POOR QUALITY

READING # 0088 BLOCK # 208 TIMP # 305.701 MACH 7.3 PT # 998.749 TT # 3085.7

	P	T	M		GAMMA	MOLWT	BONV	MACH	WFL	S	W/A	W	A/AC	NOMTP	Q	IVAC	PHI	ETAC
COMBUSTOR	0	19	12	0														
46.232	73.310	3094	688.9(970)		1.2897	24.541	2843											
46.232	32.449	2567	458.9(788)		1.3075	24.542	2607	1.170	3051	2.298	0.61368	15.811	0.0974	2262	29.095	197.8	0.89	0.23
COMBUSTOR	0	20	13	6														
46.250	72.428	2798	655.8(933)		1.3049	22.636	2832											
46.250	32.440	2310	475.8(755)		1.3214	22.636	2589	1.158	2998	2.399	0.61675	15.819	0.0976	2248	28.735	185.8	0.72	0.10
COMBUSTOR	0	21	14	2														
46.240	72.400	2798	655.3(933)		1.3049	22.637	2832											
46.240	32.419	2310	475.5(755)		1.3214	22.637	2589	1.158	2999	2.399	0.61681	15.819	0.0977	2248	28.728	185.8	0.72	0.10
COMBUSTOR	0	22	15	4														
47.310	69.015	2912	639.4(972)		1.2991	22.777	2873											
47.310	29.590	2385	488.2(779)		1.3169	22.777	2618	1.193	3125	2.412	0.57142	15.819	0.1093	2296	27.750	148.9	0.72	0.15
COMBUSTOR	0	23	16	4														
48.110	67.036	3077	626.0(1030)		1.2909	22.962	2933											
48.110	28.057	2538	422.8(830)		1.3093	22.963	2680	1.191	3192	2.431	0.52511	15.819	0.1106	2358	26.009	152.6	0.72	0.22
COMBUSTOR	0	24	17	4														
48.757	61.203	3272	615.4(1089)		1.2811	23.172	2999											
48.757	25.700	2691	398.1(883)		1.3011	23.175	2740	1.218	3328	2.450	0.47647	15.819	0.1263	2424	24.690	157.3	0.72	0.29
COMBUSTOR	0	25	18	5														
50.197	58.583	3127	594.4(1099)		1.2885	21.987	3021											
50.197	15.852	2308	285.0(784)		1.3144	21.988	2624	1.528	3998	2.581	0.38998	15.502	0.1552	2554	24.228	164.9	0.90	0.23
COMBUSTOR	0	26	19	2														
50.207	58.586	3125	604.3(1098)		1.2886	21.986	3021											
50.207	15.743	2304	282.0(782)		1.3168	21.987	2622	1.527	8003	2.580	0.38985	15.502	0.1550	2557	24.230	165.0	0.90	0.23
COMBUSTOR	0	27	20	6														
50.737	62.358	2995	594.2(1049)		1.2944	21.841	2971											
50.737	12.198	2030	229.2(693)		1.3284	21.842	2478	1.737	8303	2.523	0.34423	15.502	0.1662	2541	24.358	187.1	0.90	0.27
COMBUSTOR	0	28	21	6														
52.147	53.903	3208	587.3(1128)		1.2840	22.058	3047											
52.147	10.987	2219	201.8(748)		1.3188	22.060	2568	1.710	8392	2.553	0.31043	15.502	0.1990	2665	21.186	171.9	0.90	0.27
COMBUSTOR	0	29	22	6														
54.287	54.324	3132	589.7(1102)		1.2871	21.962	3021											
54.287	7.375	1954	116.4(654)		1.3289	21.964	2529	1.983	8742	2.598	0.25521	15.502	0.2379	2751	18.885	176.9	0.90	0.26
COMBUSTOR	0	30	23	6														
54.747	48.550	3281	566.5(1158)		1.2794	22.105	3073											
54.747	7.858	2155	126.8(725)		1.3192	22.108	2529	1.856	8693	2.572	0.29878	15.502	0.2480	2767	17.881	178.0	0.90	0.30
COMBUSTOR	0	31	24	6														
55.497	50.914	3202	582.1(1128)		1.2834	22.042	3048											
55.497	6.625	1986	92.1(664)		1.3264	22.045	2538	1.949	8850	2.581	0.23076	15.502	0.2631	2790	17.391	179.4	0.90	0.28
COMBUSTOR	0	32	25	6														
55.760	52.323	3164	580.6(1110)		1.2853	22.011	3031											
55.760	6.192	1913	79.4(638)		1.3300	22.013	2497	2.047	8907	2.595	0.22622	15.502	0.2684	2797	17.252	179.9	0.90	0.27
COMBUSTOR	0	33	26	6														
56.257	46.741	3223	557.9(1134)		1.2822	22.171	3051											
56.257	4.550	1863	54.8(610)		1.3313	22.173	2568	2.145	9117	2.570	0.17851	15.502	0.3001	2820	16.197	180.5	0.90	0.29
COMBUSTOR	0	34	27	5														
57.682	34.919	3418	550.9(1284)		1.2803	22.456	3174											
57.682	5.537	2409	65.2(812)		1.3053	22.457	2836	1.870	8930	2.622	0.18499	15.502	0.3079	2906	12.841	186.8	0.90	0.01
COMBUSTOR	0	35	28	6														
57.737	32.800	3738	551.7(1333)		1.2525	22.577	3211											
57.737	6.059	2599	84.9(884)		1.2947	22.595	2727	1.773	8928	2.638	0.18498	15.502	0.3289	2894	12.346	188.9	0.90	0.00
COMBUSTOR	0	36	29	3														
57.877	32.246	3754	550.1(1333)		1.2513	22.594	3216											
57.877	6.047	2621	85.0(891)		1.2954	22.615	2733	1.769	8824	2.637	0.18337	15.502	0.3716	2898	12.648	187.1	0.90	0.05
COMBUSTOR	0	37	30	6														
57.957	34.991	3433	549.7(1201)		1.2592	22.477	3141											
57.957	6.548	2423	92.0(819)		1.3048	22.479	2843	1.868	8938	2.623	0.18517	15.502	0.3675	2911	12.478	187.0	0.90	0.01

ORIGINAL PAGE IS OF POOR QUALITY

READING = 0098 BLOCK = 20A TTMP = 305.701 MACH 7.3 PT = 998.740 TT = 3085.7

	P	T	H		GAMMA	MOLWT	SONV	MACH	VEL	S	-/A	*	A/AP	MOMIN	C	TVAC	PHI	ETAC
COMBUSTOR	0	34	31	3														
58.237	58.419	3457	590.6f(1300)		1.2577	22.583	3168											
58.237	5.600	2938	80.6f 827)		1.3031	22.516	2858	1.862	8992	2.625	0.184A9	15.549	0.9688	2917	12.887	187.4	0.90	0.82
COMBUSTOR	0	39	32	0														
58.483	58.827	3500	587.7f(1280)		1.2671	22.353	3181											
58.483	4.892	2191	30.6f 734)		1.3146	22.340	2931	2.010	8087	2.685	0.18832	15.549	0.9695	2921	12.989	187.9	0.90	0.38
COMBUSTOR	0	40	33	7														
59.187	75.628	2928	585.2f(1023)		1.2963	21.832	2934											
59.187	2.835	1270	-47.8f 910)		1.3432	21.832	1985	2.790	5534	2.694	0.18177	15.549	0.9753	2929	13.523	188.4	0.90	0.22
COMBUSTOR	0	41	34	6														
60.207	27.938	4177	582.0f(1099)		1.2196	23.005	3315											
60.207	7.735	3258	131.3f(1128)		1.2687	23.109	2977	1.523	4533	2.670	0.18078	15.589	0.9777	2938	11.323	189.0	0.90	0.59
COMBUSTOR	0	42	35	5														
62.217	28.296	4522	535.7f(1432)		1.1887	23.431	3377											
62.217	10.487	3889	208.8f(1371)		1.2239	23.584	3169	1.274	4004	2.688	0.18833	15.549	0.9650	2935	11.054	188.6	0.90	0.73
COMBUSTOR	0	43	36	8														
63.637	28.187	4323	530.9f(1555)		1.2073	23.228	3342											
63.637	9.231	3526	157.1f(1230)		1.2892	23.317	3065	1.811	4325	2.670	0.17048	15.589	0.9553	2930	11.482	188.5	0.90	0.65
COMBUSTOR	0	44	37	8														
66.191	25.225	4540	521.2f(1438)		1.1858	23.487	3376											
66.191	10.698	3953	212.2f(1395)		1.2185	23.628	3180	1.235	3992	2.690	0.18196	15.589	0.9709	2923	9.898	188.0	0.90	0.74
COMBUSTOR	0	45	38	8														
66.477	23.112	4417	519.5f(1468)		1.1771	23.575	3385											
66.477	10.792	4117	280.1f(1960)		1.2981	23.735	3222	1.160	3739	2.699	0.15055	15.589	0.8092	2922	8.787	187.9	0.90	0.78
COMBUSTOR	WEGEA	46	39	21														
66.477	23.112	4809	459.9f(1750)		1.1885	23.436	3007											
66.477	17.680	4885	552.7f(1689)		1.1764	23.524	3390	0.683	2316	2.729	0.15055	15.589	0.8092	2965	5.818	189.4	0.90	0.78
NOZZLE AE		47	40	5														
68.713	23.112	4417	519.5f(1468)		1.1771	23.575	3385											
68.713	0.670	2358	-502.3f 771)		1.2961	23.837	2519	2.839	7150	2.699	0.03134	15.589	1.0371	3788	3.682	293.6	0.90	0.78
NOZZLE PU		48	41	5														
68.713	23.112	4417	519.5f(1468)		1.1771	23.575	3385											
68.713	0.155	1870	-796.7f 527)		1.3199	23.837	2107	3.708	7940	2.699	0.1134	15.589	0.9418	4059	1.473	241.	0.90	0.78
NOZZLE AE WEGEA		49	42	5														
68.713	23.112	4830	459.9f(1750)		1.1888	23.436	3007											
68.713	0.718	2592	-414.2f 858)		1.2813	23.836	2432	2.785	7331	2.729	0.03134	15.589	1.0371	3900	3.571	256.4	0.90	0.78
NOZZLE PU WEGEA		50	43	5														
68.713	23.112	4809	459.9f(1750)		1.1885	23.436	3007											
68.713	0.155	1828	-804.7f 579)		1.3125	23.837	2235	3.683	8233	2.729	0.11077	15.589	0.9377	4202	1.678	271.3	0.90	0.78
FICTIVE COMBUSTR		69	62	0														
66.477	320.771	5261	519.5f(1921)		1.1768	24.283	3551											
66.477	0.155	1097	-1250.9f 524)		1.3864	24.712	1724	5.858	8611	2.686	0.02121	15.589	2.8624	4842	3.182	299.4	0.90	1.00
FICTIVE NOZZLE		70	63	1														
68.713	15.133	4538	492.1f(1434)		1.1732	23.559	3352											
68.713	0.682	2794	-335.9f 935)		1.2733	23.835	2725	2.762	6437	2.791	0.03134	15.589	1.0371	3565	3.135	228.6	0.90	0.78

XABS	P=IP	P=OB	PPA	QOX	Q=IR	Q=OB	CA=ALL	P=TR/PSO	P=IR/PTO	P=OB/PSO	P=OR/PTO
6.981E-01	4.900E-01	0.000	-2.732E-01	0.000	0.000	0.000	2.470E-02	4.441E 00	4.909E-00	0.000	0.000
1.836E 01	6.700E-01	0.000	-2.294E 01	0.000	0.000	0.000	1.436E 02	4.441E 01	4.909E-04	0.000	0.000
3.070E 01	1.030E 00	0.000	-9.264E 01	0.000	0.000	0.000	5.053E 02	4.641E 00	1.031E-03	0.000	0.000
3.508E 01	1.899E 00	0.000	-1.876E 02	0.000	0.000	0.000	6.804E 02	1.228E 01	1.961E-03	0.000	0.000
3.555E 01	2.215E 00	0.000	-2.063E 02	0.000	0.000	0.000	7.013E 02	1.432E 01	2.218E-03	0.000	0.000
3.606E 01	2.870E 00	0.000	-2.281E 02	-1.813E 02	-1.813E 02	0.000	7.244E 02	1.338E 01	2.077E-03	0.000	0.000
3.648E 01	2.270E 00	0.000	-2.067E 02	-1.857E 02	-1.857E 02	0.000	7.143E 02	1.271E 01	2.278E-03	0.000	0.000
3.661E 01	2.310E 00	3.210E 00	-2.063E 02	-1.871E 02	-1.871E 02	0.000	7.507E 02	1.493E 01	2.313E-03	2.078E 01	3.218E-03
3.662E 01	2.311E 00	3.230E 00	-2.064E 02	-1.872E 02	-1.872E 02	0.000	7.509E 02	1.494E 01	2.310E-03	2.088E 01	3.234E-03
3.701E 01	2.410E 00	4.257E 00	-2.884E 02	-1.915E 02	-1.915E 02	0.000	7.913E 02	1.556E 01	2.413E-03	2.752E 01	4.262E-03
3.720E 01	2.301E 00	4.987E 00	-2.885E 02	-1.946E 02	-1.946E 02	0.000	8.204E 02	1.448E 01	2.300E-03	3.225E 01	4.994E-03
3.803E 01	2.010E 00	8.296E 00	-2.723E 02	-2.036E 02	-2.036E 02	0.000	9.008E 02	1.300E 01	2.013E-03	5.368E 01	8.308E-03
3.875E 01	4.677E 00	1.109E 01	-2.700E 02	-2.780E 02	-2.142E 02	-6.181E 01	9.809E 02	4.317E 01	4.448E-03	7.427E 01	1.150E-02
3.875E 01	4.497E 00	1.108E 01	-2.700E 02	-2.762E 02	-2.142E 02	-6.198E 01	9.804E 02	4.330E 01	4.704E-03	7.421E 01	1.149E-02
3.901E 01	8.390E 00	1.043E 01	-2.750E 02	-2.958E 02	-2.190E 02	-7.683E 01	1.010E 03	5.425E 01	8.691E-03	6.874E 01	1.065E-02
3.950E 01	1.106E 01	9.037E 00	-2.922E 02	-3.349E 02	-2.292E 02	-1.047E 02	1.086E 03	7.410E 01	1.147E-02	5.843E 01	9.049E-03
3.977E 01	1.105E 01	8.169E 00	-3.030E 02	-3.555E 02	-2.357E 02	-1.198E 02	1.097E 03	7.142E 01	1.104E-02	5.242E 01	8.119E-03
4.000E 01	1.068E 01	7.899E 00	-3.091E 02	-3.748E 02	-2.419E 02	-1.330E 02	1.120E 03	6.908E 01	1.070E-02	5.075E 01	7.859E-03
4.024E 01	1.240E 01	7.525E 00	-3.184E 02	-3.984E 02	-2.485E 02	-1.464E 02	1.151E 03	8.014E 01	1.241E-02	4.865E 01	7.534E-03
4.049E 01	1.357E 01	9.449E 00	-3.220E 02	-4.088E 02	-2.532E 02	-1.555E 02	1.179E 03	8.775E 01	1.359E-02	6.239E 01	9.661E-03
4.061E 01	1.368E 01	9.787E 00	-3.222E 02	-4.096E 02	-2.535E 02	-1.561E 02	1.172E 03	8.822E 01	1.366E-02	6.323E 01	9.792E-03
4.075E 01	1.460E 01	1.017E 01	-3.291E 02	-4.388E 02	-2.633E 02	-1.750E 02	1.211E 03	1.039E 02	1.610E-02	9.161E 01	1.419E-02
4.124E 01	1.961E 01	1.937E 00	-3.547E 02	-4.819E 02	-2.798E 02	-2.021E 02	1.269E 03	1.284E 02	1.988E-02	1.253E 01	1.940E-03
4.150E 01	2.151E 01	2.012E 00	-3.798E 02	-5.053E 02	-2.898E 02	-2.143E 02	1.300E 03	1.391E 02	2.150E-02	1.301E 01	2.018E-03
4.224E 01	7.500E 00	2.283E 00	-4.321E 02	-6.016E 02	-3.323E 02	-2.693E 02	1.410E 03	4.849E 01	7.510E-03	1.427E 01	2.284E-03
4.273E 01	1.092E 01	2.384E 00	-4.391E 02	-6.323E 02	-3.642E 02	-2.881E 02	1.444E 03	7.084E 01	1.098E-02	1.526E 01	2.363E-03
4.280E 01	1.170E 01	2.437E 00	-4.413E 02	-6.398E 02	-3.523E 02	-2.875E 02	1.459E 03	7.591E 01	1.174E-02	1.538E 01	2.381E-03
4.331E 01	3.078E 01	1.992E 01	-4.791E 02	-8.352E 02	-4.868E 02	-3.449E 02	1.434E 03	1.999E 02	3.092E-02	1.288E 02	1.998E-02
4.480E 01	3.695E 01	2.540E 01	-4.852E 02	-9.085E 02	-5.050E 02	-3.655E 02	1.494E 03	2.395E 02	3.706E-02	1.655E 02	2.563E-02
4.552E 01	3.891E 01	3.391E 01	-5.067E 02	-1.019E 03	-6.343E 02	-3.809E 02	1.787E 03	2.257E 02	3.494E-02	2.193E 02	3.395E-02
4.622E 01	3.891E 01	3.213E 01	-4.858E 02	-1.146E 03	-7.187E 02	-4.240E 02	1.870E 03	2.123E 02	3.285E-02	2.077E 02	3.217E-02
4.623E 01	3.894E 01	3.210E 01	-4.853E 02	-1.147E 03	-7.199E 02	-4.244E 02	1.871E 03	2.121E 02	3.282E-02	2.076E 02	3.214E-02
4.625E 01	3.903E 01	3.205E 01	-4.838E 02	-1.150E 03	-7.220E 02	-4.254E 02	1.873E 03	2.122E 02	3.287E-02	2.073E 02	3.209E-02
4.626E 01	3.900E 01	3.203E 01	-4.836E 02	-1.152E 03	-7.232E 02	-4.260E 02	1.874E 03	2.121E 02	3.284E-02	2.071E 02	3.207E-02
4.731E 01	2.981E 01	2.937E 01	-4.291E 02	-1.398E 03	-8.920E 02	-5.553E 02	2.304E 03	1.924E 02	2.995E-02	1.880E 02	2.908E-02
4.811E 01	2.977E 01	2.773E 01	-3.583E 02	-1.600E 03	-9.981E 02	-6.258E 02	2.103E 03	1.841E 02	2.864E-02	1.748E 02	2.737E-02
4.876E 01	2.570E 01	2.570E 01	-2.795E 02	-1.784E 03	-9.930E 02	-7.774E 02	2.140E 03	1.654E 02	2.573E-02	1.654E 02	2.573E-02
5.020E 01	1.585E 01	1.585E 01	-1.253E 02	-2.196E 03	-1.130E 03	-9.347E 02	2.363E 03	1.019E 02	1.587E-02	1.019E 02	1.587E-02
5.021E 01	1.578E 01	1.578E 01	-1.245E 02	-2.198E 03	-1.131E 03	-9.345E 02	2.365E 03	1.015E 02	1.580E-02	1.015E 02	1.580E-02
5.070E 01	1.216E 01	1.216E 01	-8.544E 01	-2.196E 03	-1.178E 03	-9.679E 02	2.431E 03	7.841E 01	1.217E-02	7.841E 01	1.217E-02
5.215E 01	1.099E 01	1.099E 01	-3.194E-01	-2.351E 03	-1.293E 03	-1.179E 03	2.631E 03	7.109E 01	1.103E-02	7.109E 01	1.103E-02
5.425E 01	7.375E 00	7.375E 00	1.008E 02	-2.577E 03	-1.438E 03	-1.439E 03	2.875E 03	4.764E 01	7.390E-03	4.764E 01	7.390E-03
5.475E 01	7.458E 00	7.458E 00	1.204E 02	-2.627E 03	-1.484E 03	-1.488E 03	2.939E 03	5.181E 01	7.884E-03	5.181E 01	7.884E-03
5.550E 01	6.625E 00	6.625E 00	1.494E 02	-2.695E 03	-1.511E 03	-1.544E 03	3.035E 03	4.603E 01	6.995E-03	4.603E 01	6.995E-03
5.576E 01	4.192E 00	4.192E 00	1.572E 02	-2.714E 03	-1.525E 03	-1.563E 03	3.060E 03	2.909E 01	4.422E-03	2.909E 01	4.422E-03
5.624E 01	3.725E 00	5.375E 00	2.510E 02	-2.760E 03	-1.551E 03	-1.609E 03	3.110E 03	2.609E 01	3.965E-03	3.767E 01	5.727E-03
5.768E 01	5.837E 00	5.537E 00	2.498E 02	-2.884E 03	-1.620E 03	-1.709E 03	3.249E 03	3.589E 01	5.455E-03	3.883E 01	5.904E-03
5.774E 01	6.575E 00	5.503E 00	2.710E 02	-2.873E 03	-1.620E 03	-1.705E 03	3.247E 03	3.584E 01	5.447E-03	3.845E 01	5.847E-03
5.778E 01	6.575E 00	5.559E 00	2.751E 02	-2.882E 03	-1.629E 03	-1.715E 03	3.260E 03	3.611E 01	5.488E-03	3.906E 01	5.940E-03
5.790E 01	5.568E 00	5.568E 00	2.773E 02	-2.883E 03	-1.631E 03	-1.715E 03	3.260E 03	3.611E 01	5.488E-03	3.906E 01	5.940E-03
5.824E 01	5.420E 00	5.420E 00	2.854E 02	-2.895E 03	-1.641E 03	-1.726E 03	3.281E 03	3.511E 01	5.337E-03	3.797E 01	5.774E-03
5.898E 01	4.892E 00	4.892E 00	2.897E 02	-2.919E 03	-1.653E 03	-1.746E 03	3.310E 03	3.143E 01	4.778E-03	3.143E 01	4.778E-03
5.919E 01	2.625E 00	2.625E 00	2.998E 02	-2.954E 03	-1.679E 03	-1.788E 03	3.360E 03	1.597E 01	2.428E-03	1.597E 01	2.428E-03
6.021E 01	7.725E 00	7.725E 00	3.111E 02	-3.000E 03	-1.700E 03	-1.805E 03	3.385E 03	4.695E 01	7.135E-03	4.695E 01	7.135E-03
6.222E 01	1.749E 01	1.749E 01	3.190E 02	-3.104E 03	-1.759E 03	-1.870E 03	3.490E 03	1.064E 02	1.617E-02	1.064E 02	1.617E-02
6.344E 01	9.231E 00	9.231E 00	3.190E 02	-3.164E 03	-1.794E 03	-1.907E 03	3.558E 03	5.614E 01	8.531E-03	5.614E 01	8.531E-03

AIRESEARCH MANUFACTURING COMPANY OF CALIFORNIA

ORIGINAL PAGE IS OF POOR QUALITY

READING = 3000 BLOCK = 200 TIME = 365.701 DEC 7.3 PT = 998.709 TT = 5085.7

XARS	PSTR	PSDA	PPS	PDS	SHIP	PSTH	CANAL	PSTH/PSD	SHIP/PTO	PSDP/PSL	PSDP/PTO
6.6105E 01	1.0065E 01	1.0 A5E 01	5.1434E 02	-5.5321E 03	-1.4527E 03	-1.5005E 03	0.2405E 02	6.0455E 01	1.0644E-02	0.0855E 01	1.0644E-02
6.6005E 01	1.0072E 01	1.0 P4E 01	5.1405E 02	-5.5554E 03	-1.5215E 03	-1.5175E 03	0.2537E 02	6.0331E 01	1.0735E-02	7.1258E 01	1.0995E-02
6.6525E 01	1.0072E 01	1.0C49E 01	5.1405E 02	-5.5015E 03	-1.5215E 03	-1.5195E 03	0.2502E 02	6.0331E 01	1.0735E-02	7.1258E 01	1.0995E-02
6.6725E 01	1.0016E 01	1.0108E 01	5.1405E 02	-5.5704E 03	-1.5476E 03	-1.5227E 03	0.2506E 02	6.0361E 01	1.0682E-02	7.1114E 01	1.1027E-02
6.8345E 01	5.5495E 00	5.4156E 00	5.0137E 02	-5.4005E 03	-1.4795E 03	-1.5015E 03	0.2506E 02	3.5855E 01	5.8529E-03	3.1116E 01	8.4186E-03
6.9055E 01	0.0725E 00	0.7045E 00	0.9875E 02	-5.5025E 03	-1.5898E 03	-1.6105E 03	0.2485E 02	2.4335E 01	1.0775E-03	5.0765E 01	0.7045E-03
6.9925E 01	2.5805E 00	5.5235E 00	5.0935E 02	-5.5545E 03	-1.5995E 03	-1.6005E 03	0.2505E 02	1.5395E 01	2.5251E-03	2.6774E 01	3.5275E-03
7.0505E 01	1.0715E 00	2.5855E 00	5.1435E 02	-5.5705E 03	-1.5995E 03	-1.6045E 03	0.2505E 02	1.2155E 01	1.8735E-03	1.5925E 01	2.3185E-03
7.1155E 01	1.0805E 00	2.1545E 00	7.0655E 02	-5.5955E 03	-1.9115E 03	-1.8045E 03	0.3225E 02	4.3115E 01	1.0425E-03	1.5965E 01	2.1505E-03
7.2535E 01	8.7005E-01	1.0395E 00	7.7405E 02	-5.6405E 03	-1.9215E 03	-1.7195E 03	5.0685E 02	5.4255E 00	8.7115E-04	1.0465E 01	1.4415E-03
7.4005E 01	5.4775E-01	1.0455E 00	8.2275E 02	-5.6795E 03	-1.9305E 03	-1.7495E 03	5.2735E 02	3.8005E 00	5.8805E-04	6.8865E 00	1.0645E-03
7.4215E 01	5.6005E-01	9.3965E-01	8.2905E 02	-5.6925E 03	-1.9305E 03	-1.7525E 03	5.2905E 02	3.8215E 00	5.8075E-04	6.8165E 00	9.3205E-04
7.4495E 01	5.1775E-01	2.0015E-01	8.2815E 02	-5.7025E 03	-1.9405E 03	-1.7585E 03	5.3745E 02	3.9905E 00	6.1455E-04	1.6715E 00	2.5075E-04
7.4995E 01	5.1605E-01	2.5855E-01	8.2815E 02	-5.7025E 03	-1.9405E 03	-1.7585E 03	5.3745E 02	3.9905E 00	6.1455E-04	1.6715E 00	2.5075E-04
7.6295E 01	7.2005E-01	0.0000	8.4045E 02	-5.7015E 03	-1.9395E 03	-1.7625E 03	5.4245E 02	4.0555E 00	7.2015E-04	0.0000	0.0000
7.9145E 01	1.0955E 00	0.0000	8.9715E 02	-5.7515E 03	-1.9895E 03	-1.8025E 03	5.5255E 02	7.0805E 00	1.0945E-03	0.0000	0.0000
8.3045E 01	7.1005E-01	0.0000	9.3575E 02	-5.7005E 03	-1.9585E 03	-1.8025E 03	5.4305E 02	4.5915E 00	7.1015E-04	0.0000	0.0000
8.5855E 01	6.2005E-01	0.0000	9.5805E 02	-5.7045E 03	-1.9665E 03	-1.8025E 03	5.4405E 02	4.0955E 00	6.2015E-04	0.0000	0.0000
8.8715E 01	5.4505E-01	0.0000	9.8445E 02	-5.7035E 03	-1.9815E 03	-1.8025E 03	5.4375E 02	5.5935E 00	8.4015E-04	0.0000	0.0000
8.8715E 01	8.4555E-01	0.0000	9.8445E 02	-5.7035E 03	-1.9815E 03	-1.8025E 03	5.4375E 02	5.5935E 00	8.4015E-04	0.0000	0.0000

READING = 0088 BLOCK = 20A TIME = 305.701 MACH 7.3 PT = 998.749 TT = 3085.7 PAGE 6

X	DRAG	CDRAG	CF	MC
4.600E 01	8.475E 01	8.475E 01	2.248E+03	3.879E+02
4.625E 01	1.725E+01	9.492E 01	2.920E+03	3.999E+02
4.675E 01	5.988E 00	9.889E 01	2.910E+03	4.656E+02
4.725E 01	8.100E 00	9.899E 01	2.585E+03	3.575E+02
4.750E 01	8.302E 00	1.033E 02	2.525E+03	3.852E+02
4.800E 01	1.558E 01	1.192E 02	2.707E+03	1.940E+02
4.825E 01	8.870E 00	1.236E 02	2.663E+03	2.427E+02
4.850E 01	1.040E 00	1.297E 02	2.659E+03	2.534E+02
4.875E 01	2.286E 01	1.471E 02	3.113E+03	5.019E+02
4.900E 01	4.267E 00	1.534E 02	3.169E+03	5.412E+02
4.950E 01	8.565E 00	1.620E 02	3.291E+03	5.367E+02
4.975E 01	8.561E 00	1.705E 02	3.515E+03	5.002E+02
5.000E 01	1.209E+01	1.790E 02	3.712E+03	5.579E+02
5.025E 01	2.106E+01	1.704E 02	3.860E+03	5.293E+02
5.050E 01	1.188E+01	1.710E 02	3.101E+03	5.901E+02
5.075E 01	1.133E 01	1.823E 02	3.058E+03	5.688E+02
5.100E 01	8.181E 00	1.905E 02	3.081E+03	5.312E+02
5.125E 01	8.317E 00	1.988E 02	3.119E+03	4.894E+02
5.150E 01	1.394E 01	2.128E 02	3.240E+03	3.582E+02
5.175E 01	9.595E+02	2.138E 02	3.050E+03	3.763E+02
5.200E 01	8.876E 00	2.157E 02	2.988E+03	3.225E+02
5.225E 01	1.179E 01	2.275E 02	2.814E+03	3.032E+02
5.250E 01	1.518E 01	2.426E 02	2.860E+03	2.195E+02
5.275E 01	8.322E 00	2.459E 02	2.816E+03	2.292E+02
5.300E 01	8.407E 00	2.507E 02	2.879E+03	1.980E+02
5.325E 01	1.660E 00	2.524E 02	2.814E+03	1.915E+02
5.350E 01	1.488E 00	2.539E 02	2.666E+03	1.498E+02
5.375E 01	3.888E 00	2.577E 02	2.716E+03	1.658E+02
5.400E 01	2.519E+01	2.580E 02	2.884E+03	1.628E+02
5.425E 01	8.825E+01	2.587E 02	3.068E+03	1.590E+02
5.450E 01	8.251E+01	2.591E 02	3.568E+03	1.324E+02
5.475E 01	1.477E 00	2.606E 02	2.970E+03	1.549E+02
5.500E 01	1.098E 00	2.617E 02	2.969E+03	1.415E+02
5.525E 01	3.619E 00	2.653E 02	2.838E+03	9.402E+03
6.550E 01	8.497E 00	2.697E 02	2.989E+03	2.113E+02
6.575E 01	8.392E 00	2.781E 02	3.317E+03	1.949E+02
6.600E 01	8.781E 00	2.868E 02	3.830E+03	1.808E+02
6.610E 01	1.154E 01	2.943E 02	3.[illegible]	1.926E+02
6.650E 01	1.565E 00	2.979E 02	3.559E+03	1.805E+02
6.652E 01	1.614E+01	2.981E 02	3.637E+03	1.810E+02
6.675E 01	8.184E+01	2.989E 02	3.832E+03	1.799E+02
6.685E 01	8.797E 00	3.057E 02	3.892E+03	1.271E+02
6.900E 01	2.068E 00	3.068E 02	3.863E+03	1.151E+02
6.925E 01	2.587E 00	3.107E 02	3.901E+03	8.871E+03
7.050E 01	2.051E 00	3.128E 02	3.350E+03	7.077E+03
7.115E 01	1.527E 00	3.183E 02	3.328E+03	8.276E+03
7.253E 01	2.982E 00	3.173E 02	3.248E+03	8.823E+03
7.300E 01	2.408E 00	3.189E 02	3.233E+03	8.524E+03
7.321E 01	2.103E+01	3.201E 02	3.188E+03	3.254E+03
7.496E 01	8.532E+01	3.210E 02	3.198E+03	2.165E+03
7.496E 01	1.362E+03	3.210E 02	3.109E+03	2.159E+03
7.629E 01	5.157E+01	3.215E 02	3.171E+03	3.181E+03
7.918E 01	1.248E 00	3.228E 02	3.212E+03	8.508E+03
8.300E 01	1.360E 00	3.292E 02	3.131E+03	3.787E+03
8.585E 01	5.880E+01	3.287E 02	3.098E+03	2.780E+03
8.671E 01	2.400E+01	3.251E 02	3.130E+03	3.551E+03

ORIGINAL PAGE IS
OF POOR QUALITY

REACTNG = 0088 BLOCK = 20A TTMF = 305.701 MACH 7.3 PT = 998.709 TT = 3085.7

B	NORAL	F(RAD	CF	MC
0.8715 01	0.000	5.25 E 02	5.1501=03	5.5525=03

REACTNG = 0088 BLOCK = 20A TTMF = 305.701 MACH 7.3 PT = 998.709 TT = 3085.7

RAMJET PERFORMANCE

ENGINE PERFORMANCE

CALCULATED THRUST	830.	(LBF)
MEASURED THRUST	778.	(LBF)
CALCULATED SPECIFIC IMPULSE	1473.	(LBF-SEC/LBM)
MEASURED SPECIFIC IMPULSE	1419.	(LBF-SEC/LBM)
CALCULATED THRUST COEFFICIENT	0.8327	
MEASURED THRUST COEFFICIENT	0.5585	

REGENERATIVE-COOLED ENGINE PERFORMANCE CALCULATED

STREAM THRUST	3853.	(LBF)
NET THRUST	735.	(LBF)
SPECIFIC IMPULSE	1717.	(LBF-SEC/LBM)
THRUST COEFFICIENT	0.5088	

MOMENTUM AND FORCES

INLET FRICTION DRAG	84.7	(LBF)
INLET MOMENTUM CHANGE	-806.8	(LBF)
COMBUSTOR FRICTION DRAG	213.1	(LBF)
COMBUSTOR STRUT DRAG	-13.09	(LBF)
COMBUSTOR MOMENTUM CHANGE	810.	(LBF)
NOZZLE FRICTION DRAG	27.12	(LBF)
NOZZLE STRUT DRAG	-0.00	(LBF)
NOZZLE MOMENTUM CHANGE	627.	(LBF)
NOZZLE PRESSURE INTEGRAL	858.	(LBF)
EXTERNAL FRICTION DRAG	0.00	(LBF)
EXTERNAL PRESSURE INTEGRAL	0.	(LBF)
TOTAL EXTERNAL DRAG	-728.	(LBF)
TOTAL STRUT DRAG	-13.09	(LBF)
CAVITY FORCE	-527.	(LBF)
CALCULATED LOAD CELL FORCE	-825.	(LBF)
MEASURED LOAD CELL FORCE	-877.	(LBF)
FUEL VACUUM SPECIFIC IMPULSE	0.0	0.0 -150.0 -127.2

STATIONS

NOMINAL FUEL LEADING EDGE	50.588 (IN)
STRUT TRANSLATION	1.7389 (IN)
INLET THROAT	80.800 (IN)
COWL LEADING EDGE	34.421 (IN)
NOZZLE SHROUD TRAILING EDGE	74.981 (IN)
NOZZLE PLUG TRAILING EDGE	88.713 (IN)
STRUT LEADING EDGE	57.877 (IN)
STRUT TRAILING EDGE	88.477 (IN)
COMBUSTOR EXIT	88.477 (IN)

INLET

ANGLE OF ATTACK	0.000	(DEGREES)
MASS FLOW RATIO	0.9880	
ADDITIVE DRAG COEFFICIENT	0.0000	
LIFTING PRESSURE RECOVERY EFFICIENCY	0.1018	
DELTA PT2	0.0901	(PSI)
TOTAL PRESSURE RECOVERY = SUPERSONIC	0.3212	
TOTAL PRESSURE RECOVERY = SUBSONIC	0.1027	
INLET PROCESS EFFICIENCY = SUPERSONIC	0.9030	
INLET PROCESS EFFICIENCY = SUBSONIC	0.9132	
KINETIC ENERGY EFFICIENCY = SUPERSONIC	0.9320	
KINETIC ENERGY EFFICIENCY = SUBSONIC	0.8834	
ENTHALPY AT P0 = SUPERSONIC	-33.49	(BTU/LBM)
ENTHALPY AT P0 = SUBSONIC	3.09	(BTU/LBM)

COMBUSTOR

FUEL-AIR RATIO	0.0283			
EQUIVALENCE RATIO	0.903			
COMBUSTOR EFFICIENCY	0.782			
TOTAL PRESSURE RATIO	0.0721			
COMBUSTION EFFECTIVENESS	0.7188			
INJECTOR DISCHARGE COEFFICIENTS	0.8193	0.8615	1.0544	0.8354

NOZZLE

VACUUM STREAM THRUST COEFFICIENT = CS	0.9368
NOZZLE COEFFICIENT = CT	0.8554
PROCESS EFFICIENCY	0.8391
KINETIC ENERGY EFFICIENCY	0.8573

FUEL INJECTORS

INJECTORS	STATION	VALVE
13	40.600	B
11	42.722	
10	44.300	
23	50.147	C
22	54.254	E
21	56.157	
20	57.472	
0	64.222	C

1-29-75
Reg. Corr.

RAMJET PERFORMANCE

SUMMARY REPORT

	P	T	h		GAMMA	MOLWT	SONV	MACH	VEL	B	W/A	W	A/AC	PUMTP	D	IVAC	PHI	ETAC
WIND TUNNEL		1	0	5														
0.000	747.249	2962	659.4	(785)	1.2949	28.852	2571											
0.000	0.386	399	-33.4	(96)	1.3987	28.851	980	6.007	5888	1.824	0.10656	26.947	0.9873	5029	9.751	180.6		
SPIKE TIP WS		2	0	8														
0.000	16.050	2962	659.4	(785)	1.2948	28.851	2571											
0.000	16.305	2898	638.9	(765)	1.2969	28.851	2543	0.398	1013	2.081	0.10656	26.947	0.9873	4972	1.678	184.5		
WIND TUNNEL		3	0	6														
0.000	747.249	2962	659.4	(785)	1.2949	28.852	2571											
0.000	0.379	396	-33.9	(95)	1.3986	28.851	977	6.027	5890	1.824	0.10507	26.570	0.9873	4960	9.618	180.7		
SPIKE TIP WS		4	0	6														
0.000	16.050	2962	659.4	(785)	1.2948	28.851	2571											
0.000	16.361	2898	639.8	(766)	1.2968	28.851	2544	0.392	996	2.081	0.10507	26.570	0.9873	4960	1.627	180.7		
INLET THROAT		5	0	3														
40.400	306.013	2912	644.1	(770)	1.2965	28.851	2550											
40.400	15.225	1398	214.8	(348)	1.3550	28.851	1804	2.569	8635	1.880	0.98482	26.947	0.1114	4316	66.058	160.2		
INLET UPWASH		6	0	3														
40.400	306.013	2912	644.1	(770)	1.2965	28.851	2550											
40.400	13.085	1340	200.5	(330)	1.3582	28.851	1771	2.660	8711	1.880	0.85893	26.947	0.1225	4357	62.890	161.7		
INLET DNWASH		7	0	8														
40.400	123.009	2912	644.1	(770)	1.2965	28.851	2550											
40.400	106.393	2813	614.6	(742)	1.2995	28.851	2510	0.485	1216	1.983	0.85893	26.947	0.1225	4357	10.236	161.7		
COMBUSTOR	0	8	1	3														
40.410	305.431	2911	644.1	(770)	1.2965	28.851	2550											
40.410	15.238	1395	215.0	(348)	1.3549	28.851	1805	2.567	8634	1.881	0.98470	26.947	0.1114	4316	66.028	160.1		
COMBUSTOR	0	9	2	21														
41.300	181.326	2875	602.0	(730)	1.3060	28.319	2657											
41.300	20.398	1690	292.5	(463)	1.3419	28.319	2070	2.077	4300	2.064	0.95378	27.152	0.1111	4210	63.742	155.6	0.26	0.07
COMBUSTOR	0	10	3	21														
41.310	195.865	2747	566.6	(806)	1.3035	28.237	2669											
41.310	20.487	1607	293.0	(439)	1.3467	28.237	2025	2.122	4297	2.051	0.95357	27.152	0.1112	4209	63.678	155.6	0.26	0.01
COMBUSTOR	0	11	4	21														
41.375	195.709	2765	561.7	(802)	1.3041	28.225	2624											
41.375	20.783	1605	296.2	(439)	1.3469	28.225	2025											
								2.112	4276	2.049	0.95501	27.152	0.1110	4200	63.485	154.7	0.26	0.00
COMBUSTOR	0	12	5	3														
41.500	185.140	2814	561.0	(811)	1.3027	28.258	2635											
41.500	22.541	1663	309.0	(461)	1.3429	28.258	2069	2.029	4191	2.056	0.95523	27.152	0.1110	4183	62.304	154.0	0.26	0.03
COMBUSTOR	0	13	6	8														
42.460	137.484	3053	654.4	(893)	1.2902	28.564	2728											
42.460	31.824	2169	388.1	(611)	1.3199	28.565	2325	1.628	3785	2.101	0.90585	27.152	0.1121	4108	55.835	151.3	0.26	0.26
COMBUSTOR	0	14	7	5														
44.095	110.337	3008	634.9	(1055)	1.2839	27.240	2467											
44.095	57.112	3135	677.9	(900)	1.2804	27.212	2708	1.051	2647	2.146	0.91334	27.152	0.1161	4160	46.408	151.0	0.26	0.74
COMBUSTOR	0	15	8	2														
44.310	109.989	3010	637.8	(1055)	1.2837	27.213	2467											
44.310	56.841	3157	682.7	(907)	1.2795	27.221	2716	1.026	2786	2.146	0.91175	27.152	0.1163	4146	59.477	150.9	0.26	0.75
COMBUSTOR	0	16	9	8														
44.800	109.284	3038	632.7	(1048)	1.2844	27.260	2879											
44.800	62.186	3161	693.5	(915)	1.2788	27.211	2726	0.988	2639	2.145	0.90820	27.152	0.1167	4088	37.692	150.5	0.26	0.74
COMBUSTOR	0	17	10	6														
44.810	109.228	3037	632.6	(1048)	1.2844	27.260	2879											
44.810	62.188	3161	693.5	(915)	1.2789	27.211	2726	0.988	2639	2.145	0.90821	27.152	0.1167	4088	37.697	150.5	0.26	0.74
COMBUSTOR	0	18	11	8														
46.250	102.947	3001	617.0	(1003)	1.2916	23.594	2696											
46.250	58.797	2709	510.5	(869)	1.3039	23.595	2424	0.958	2613	2.336	0.86595	27.465	0.1236	4095	35.184	149.1	0.65	0.21

AIRESEARCH MANUFACTURING COMPANY OF CALIFORNIA

ORIGINAL PAGE IS OF POOR QUALITY

READING # 0064 FLOW # 211 TIME # 293.811 MACH 0.0 P1 # 747.249 T1 # 2962.2 PAGE 2

	P	T	n		GAMMA	PHI-T	SIGMA	MACH	VEL	S	A/A	A	A/A*	RUPIM	G	INAC	PRI	ETAC
COMBUSTOR	0	19	12	2														
46.260	102.423	3082	898.9(1063)		1.2918	23.595	2898											
46.260	96.773	2710	514.4(869)		1.3038	23.596	2729	0.958	2613	2.330	0.886582	27.405	0.1239	4096	35.148	149.1	0.85	0.21
COMBUSTOR	0	20	13	4														
47.310	99.066	3317	835.2(1083)		1.2890	23.656	2975											
47.310	93.517	2925	486.5(942)		1.2932	23.657	2808	0.965	2709	2.350	0.880524	27.405	0.1332	4238	33.903	154.1	0.85	0.31
COMBUSTOR	0	21	14	2														
47.335	99.025	3321	834.9(1080)		1.2798	23.680	2976											
47.335	93.396	2930	486.5(943)		1.2930	23.662	2819	0.965	2707	2.350	0.880434	27.405	0.1333	4236	33.832	154.2	0.85	0.31
COMBUSTOR	0	22	15	4														
48.110	95.289	3547	820.8(1104)		1.2842	24.110	3186											
48.110	93.585	3145	472.3(1316)		1.2824	24.115	2883	0.965	2781	2.374	0.750362	27.405	0.1429	4363	32.427	158.9	0.85	0.80
COMBUSTOR	0	23	16	6														
48.775	89.817	3213	881.8(1165)		1.2867	21.328	3165											
48.775	84.264	2736	448.0(973)		1.3026	21.327	2882	1.006	3130	2.564	0.899499	27.786	0.1552	4863	34.001	180.6	1.06	0.23
COMBUSTOR	0	24	17	2														
48.785	89.756	3216	881.7(1166)		1.2865	21.328	3166											
48.785	84.156	2737	448.3(973)		1.3026	21.329	2883	1.006	3135	2.564	0.899808	27.786	0.1552	4865	34.004	180.7	1.06	0.23
COMBUSTOR	0	25	18	4														
49.315	87.003	3339	857.3(1213)		1.2815	21.448	3188											
49.315	80.475	2760	460.5(984)		1.2944	21.448	2894	1.175	3396	2.582	0.852871	27.786	0.1662	4572	34.480	184.6	1.06	0.26
COMBUSTOR	0	26	19	4														
50.725	79.884	3664	828.8(1339)		1.2835	21.768	3252											
50.725	81.687	3093	540.8(1070)		1.2871	21.772	2971	1.280	3743	2.612	0.556043	27.786	0.1950	4815	32.304	173.3	1.06	0.36
COMBUSTOR	0	27	20	4														
52.825	74.658	3857	813.4(1414)		1.2522	21.977	3305											
52.825	22.012	2979	237.5(1056)		1.2848	21.993	2941	1.474	4337	2.628	0.456068	27.786	0.2379	5066	30.736	183.1	1.06	0.42
COMBUSTOR	0	28	21	3														
53.325	73.421	3873	814.5(1421)		1.2511	21.999	3309											
53.325	20.337	2948	214.8(1043)		1.2856	22.017	2926	1.521	4451	2.630	0.437426	27.786	0.2486	5136	30.257	184.8	1.06	0.42
COMBUSTOR	0	29	22	4														
54.075	72.313	3919	808.4(1438)		1.2462	22.052	3321											
54.075	18.580	2940	195.2(1040)		1.2849	22.073	2919	1.567	4575	2.634	0.41233	27.786	0.2631	5203	29.313	187.2	1.06	0.44
COMBUSTOR	0	30	23	5														
54.635	71.455	3930	802.4(1444)		1.2471	22.078	3324											
54.635	18.000	2901	189.5(1022)		1.2861	22.098	2897	1.625	4708	2.635	0.389942	27.786	0.2782	5263	28.529	189.4	1.06	0.45
COMBUSTOR	0	31	24	4														
55.760	69.335	3940	597.9(1064)		1.2834	22.141	3338											
55.760	15.446	2918	135.7(1028)		1.2845	22.167	2899	1.659	4809	2.640	0.366010	27.786	0.2963	5329	27.361	191.8	1.06	0.48
COMBUSTOR	0	32	25	5														
56.260	54.190	4056	595.8(1554)		1.2083	22.217	3440											
56.260	14.776	3505	162.8(1253)		1.2539	22.216	3102	1.535	4760	2.684	0.294994	27.786	0.3678	5503	21.620	198.1	1.06	0.61
COMBUSTOR	0	33	26	5														
56.315	61.977	4106	595.8(1511)		1.2352	22.201	3366											
56.315	11.885	2909	74.3(1021)		1.2830	22.299	2885	1.770	5107	2.656	0.289401	27.786	0.3690	5507	23.333	198.2	1.06	0.50
COMBUSTOR	0	34	27	3														
56.455	61.779	4114	594.8(1515)		1.2346	22.270	3367											
56.455	11.500	2912	71.3(1022)		1.2828	22.310	2885	1.774	5118	2.657	0.291894	27.786	0.3717	5515	23.210	198.5	1.06	0.50
COMBUSTOR	0	35	28	9														
56.535	55.262	4037	594.5(1443)		1.2160	22.600	3437											
56.535	14.335	3452	124.9(1232)		1.2566	22.691	3063	1.565	4824	2.681	0.289516	27.786	0.3675	5540	22.128	198.7	1.06	0.61
COMBUSTOR	0	36	29	3														
56.815	56.084	4021	593.3(1436)		1.2119	22.580	3433											
56.815	13.947	3465	117.2(1213)		1.2569	22.674	3066	1.592	4881	2.679	0.289419	27.786	0.3688	5536	22.315	199.3	1.06	0.60
COMBUSTOR	0	37	30	4														
57.041	57.000	4357	592.3(1611)		1.2107	22.522	3421											
57.041	13.256	3681	98.3(1164)		1.2651	22.597	3022	1.645	4972	2.674	0.289374	27.786	0.3693	5548	22.095	199.7	1.06	0.58

ORIGINAL PAGE IS OF POOR QUALITY

READING = 0066 BLOCK = 211 TIME = 293.811 MACH 0.0 PT = 747.249 TT = 2962.2

	P	T	H	GAMMA	MOLWT	SONV	MACH	VEL	S	W/A	R	A/AC	NUMIH	Q	IVAC	PHI	ETAC
COMBUSTOR	0	38	31 5														
57.705	84.452	4123	589.3(1518)	1.2342	22.292	3369											
57.705	10.920	2880	86.7(1061)	1.2843	22.332	2860	1.832	5239	2.653	0.28908	27.786	0.3753	5574	23.537	200.0	1.06	0.51
COMBUSTOR	0	39	32 7														
58.785	112.805	3418	585.8(1241)	1.2755	21.825	3165											
58.785	6.112	1722	-82.4(581)	1.3368	21.829	2301	2.518	5783	2.558	0.28724	27.786	0.3777	5585	25.813	201.0	1.06	0.31
COMBUSTOR	0	40	33 6														
60.795	53.278	4711	579.8(1751)	1.1857	22.921	3481											
60.795	10.650	3893	187.3(1404)	1.2278	23.097	3208	1.458	4650	2.692	0.29723	27.786	0.3650	5572	21.479	200.5	1.06	0.72
COMBUSTOR	0	41	34 4														
62.215	55.181	4657	574.5(1729)	1.1909	22.876	3472											
62.215	10.598	3800	134.8(1367)	1.2347	23.031	3182	1.474	4691	2.687	0.30529	27.786	0.3553	5561	22.255	200.1	1.06	0.70
COMBUSTOR	0	42	35 5														
64.670	47.992	4991	584.7(1863)	1.1578	23.246	3516											
64.670	20.759	4488	227.3(1644)	1.1735	23.532	3336	1.252	4109	2.706	0.28938	27.786	0.3749	5542	18.479	199.5	1.06	0.88
COMBUSTOR	0	43	36 5														
65.055	43.940	5082	583.0(1900)	1.1500	23.339	3529											
65.055	21.122	3869	206.9(1718)	1.1583	23.637	3373	1.153	3888	2.713	0.26903	27.786	0.4032	5539	16.455	199.4	1.06	0.97
COMBUSTOR	HEGEN	44	37 4														
65.055	43.940	5136	616.9(1924)	1.1481	23.265	3550											
65.055	21.971	4750	326.2(1758)	1.1548	23.562	3402	1.121	3814	2.723	0.26903	27.786	0.4032	5563	15.947	200.2	1.06	0.97
NOZZLE	AE	45	38 5														
87.291	43.940	5082	583.0(1870)	1.1500	23.339	3529											
87.291	1.412	3005	-600.0(1025)	1.2622	24.082	2798	2.733	7648	2.713	0.05600	27.786	1.9371	7306	0.657	262.9	1.06	0.97
NOZZLE	PO	46	39 5														
87.291	43.940	5082	583.0(1870)	1.1500	23.339	3529											
87.291	0.386	2275	-868.9(745)	1.2851	24.083	2457	3.467	8518	2.713	0.02255	27.786	4.8107	7832	2.985	281.9	1.06	0.97
NOZZLE	AE HEGEN	47	40 5														
87.291	43.940	5136	616.9(1924)	1.1481	23.265	3550											
87.291	1.408	3101	-567.6(1063)	1.2584	24.081	2838	2.712	7694	2.723	0.05600	27.786	1.9371	7367	0.700	265.1	1.06	0.97
NOZZLE	PO HEGEN	48	41 5														
87.291	43.940	5136	616.9(1924)	1.1481	23.265	3550											
87.291	0.386	2340	-862.6(769)	1.2828	24.083	2489	3.457	8604	2.723	0.02214	27.786	4.8988	7916	2.981	284.9	1.06	0.97
FICTIVE	COMBUSTR	67	60 6														
65.055	300.913	5341	583.0(2006)	1.1666	23.611	3622											
65.055	0.386	1425	-1180.3(444)	1.3264	24.083	1975	4.740	9361	2.546	0.03958	27.786	2.7416	8356	5.757	306.7	1.06	1.00
FICTIVE	NOZZLE	68	61 6														
87.291	25.255	4908	536.7(1860)	1.1481	23.300	3492											
87.291	1.408	3499	-398.4(1224)	1.2278	24.058	2980	2.296	6841	2.755	0.05600	27.786	1.9371	6861	5.954	264.5	1.06	0.97

READING = 0004 FLUX = 211 IT-F = 243.811 MACH 6.0 P1 = 747.284 T1 = 2962.2 PAGE 8

XAMS	P-1F	P-1F	PTA	WDX	P-1F	S-CE	CA-ALL	P-1B/P50	P-1B/P10	P-0B/P50	P-0B/P10
0.9811E-01	1.0425E 00	0.000	-4.347E-01	0.000	0.000	0.000	2.470E-02	2.653E 00	1.372E-03	0.000	0.000
1.8366E 01	1.0425E 00	0.000	-3.014E 01	0.000	0.000	0.000	1.634E 02	2.653E 00	1.372E-03	0.000	0.000
3.0708E 01	2.2655E 00	0.000	-1.651E 02	0.000	0.000	0.000	5.053E 02	5.700E 00	2.951E-03	0.000	0.000
3.5088E 01	3.8405E 00	0.000	-3.447E 02	0.000	0.000	0.000	6.849E 02	1.007E 01	5.206E-03	0.000	0.000
3.5198E 01	3.9428E 00	5.706E 00	-4.282E 02	0.000	0.000	0.000	6.956E 02	1.015E 01	5.251E-03	1.475E 01	7.628E-03
3.5208E 01	3.9425E 00	5.686E 00	-4.282E 02	0.000	0.000	0.000	6.957E 02	1.016E 01	5.253E-03	1.467E 01	7.586E-03
3.5558E 01	4.0315E 00	5.880E 00	-4.360E 02	0.000	0.000	0.000	7.209E 02	1.043E 01	5.393E-03	9.834E 00	5.085E-03
3.5868E 01	3.9285E 00	2.125E 00	-4.506E 02	-2.582E 02	-2.582E 02	0.000	7.529E 02	1.017E 01	5.257E-03	5.499E 00	2.844E-03
3.6068E 01	3.8655E 00	2.417E 00	-4.408E 02	-2.610E 02	-2.610E 02	0.000	7.729E 02	1.000E 01	5.171E-03	7.549E 00	3.904E-03
3.6488E 01	4.2125E 00	4.621E 00	-4.742E 02	-2.678E 02	-2.678E 02	0.000	8.104E 02	1.090E 01	5.637E-03	1.190E 01	6.185E-03
3.7018E 01	4.2205E 00	8.772E 00	-5.027E 02	-2.855E 02	-2.758E 02	-9.471E 00	8.764E 02	1.092E 01	5.647E-03	1.753E 01	9.083E-03
3.7328E 01	4.1015E 00	8.051E 00	-5.141E 02	-2.933E 02	-2.810E 02	-1.263E 01	9.003E 02	1.061E 01	5.488E-03	2.083E 01	1.077E-02
3.8038E 01	3.8355E 00	1.326E 01	-5.270E 02	-3.148E 02	-2.933E 02	-1.948E 01	9.834E 02	9.925E 00	5.132E-03	3.436E 01	1.777E-02
3.8348E 01	5.3925E 00	1.561E 01	-5.259E 02	-3.220E 02	-2.995E 02	-2.248E 01	1.018E 03	1.395E 01	7.215E-03	4.04UE 01	2.089E-02
3.8758E 01	7.3995E 00	1.587E 01	-5.287E 02	-3.354E 02	-3.091E 02	-2.629E 01	1.044E 03	1.914E 01	9.896E-03	4.004E 01	2.071E-02
3.8818E 01	7.7158E 00	1.585E 01	-5.268E 02	-3.377E 02	-3.107E 02	-2.690E 01	1.072E 03	1.997E 01	1.032E-02	3.998E 01	2.068E-02
3.9018E 01	8.6808E 00	1.568E 01	-5.285E 02	-3.449E 02	-3.162E 02	-2.871E 01	1.094E 03	2.248E 01	1.162E-02	4.058E 01	2.098E-02
3.9328E 01	1.4726E 01	1.005E 01	-5.318E 02	-3.577E 02	-3.261E 02	-3.160E 01	1.130E 03	3.551E 01	1.836E-02	4.154E 01	2.148E-02
3.9508E 01	1.6526E 01	1.387E 01	-5.387E 02	-3.654E 02	-3.322E 02	-3.319E 01	1.150E 03	4.277E 01	2.211E-02	3.589E 01	1.856E-02
3.9818E 01	1.7136E 01	9.950E 00	-5.540E 02	-3.802E 02	-3.442E 02	-3.598E 01	1.167E 03	4.434E 01	2.293E-02	2.575E 01	1.332E-02
4.0008E 01	1.7496E 01	9.686E 00	-5.678E 02	-3.696E 02	-3.520E 02	-3.759E 01	1.209E 03	4.526E 01	2.341E-02	2.550E 01	1.323E-02
4.0408E 01	2.1706E 01	9.798E 00	-5.901E 02	-4.119E 02	-3.899E 02	-4.209E 01	1.256E 03	5.050E 01	2.523E 01	2.522E 01	1.305E-02
4.0418E 01	2.1886E 01	9.745E 00	-5.968E 02	-4.165E 02	-3.704E 02	-4.214E 01	1.257E 03	5.058E 01	2.942E-02	2.522E 01	1.304E-02
4.1308E 01	3.1358E 01	9.438E 00	-5.854E 02	-4.993E 02	-4.107E 02	-8.462E 01	1.302E 03	8.114E 01	4.196E-02	2.443E 01	1.263E-02
4.1318E 01	3.1408E 01	9.435E 00	-5.865E 02	-5.000E 02	-4.152E 02	-8.544E 01	1.303E 03	8.142E 01	4.210E-02	2.442E 01	1.263E-02
4.1378E 01	3.2158E 01	9.412E 00	-6.942E 02	-5.094E 02	-4.187E 02	-9.093E 01	1.371E 03	8.321E 01	4.303E-02	2.436E 01	1.260E-02
4.1508E 01	3.3498E 01	1.159E 01	-7.089E 02	-5.219E 02	-4.255E 02	-1.024E 02	1.380E 03	8.666E 01	4.481E-02	3.006E 01	1.552E-02
4.2468E 01	3.5328E 01	2.032E 01	-7.472E 02	-7.078E 02	-4.844E 02	-2.235E 02	1.501E 03	9.142E 01	4.727E-02	7.330E 01	3.790E-02
4.4098E 01	5.7418E 01	5.081E 01	-7.494E 02	-1.102E 03	-6.162E 02	-4.855E 02	1.499E 03	1.486E 02	7.683E-02	1.470E 02	7.603E-02
4.4318E 01	5.8368E 01	5.700E 01	-7.484E 02	-1.150E 03	-6.367E 02	-5.216E 02	1.725E 03	1.581E 02	8.072E-02	1.475E 02	7.629E-02
4.4808E 01	6.6948E 01	5.784E 01	-7.535E 02	-1.245E 03	-6.859E 02	-6.092E 02	1.785E 03	1.734E 02	8.958E-02	1.487E 02	7.687E-02
4.4818E 01	6.6848E 01	5.745E 01	-7.538E 02	-1.240E 03	-6.869E 02	-6.110E 02	1.784E 03	1.731E 02	8.950E-02	1.487E 02	7.688E-02
4.4258E 01	5.8808E 01	5.873E 01	-8.767E 02	-1.729E 03	-8.309E 02	-8.984E 02	1.963E 03	1.523E 02	7.877E-02	1.520F 02	7.860E-02
4.4268E 01	5.8608E 01	5.874E 01	-8.699E 02	-1.732E 03	-8.319E 02	-9.006E 02	1.964E 03	1.522E 02	7.870E-02	1.520E 02	7.861E-02
4.7318E 01	5.2988E 01	5.780F 01	-5.192E 02	-2.034E 03	-9.298E 02	-1.124E 03	2.094E 03	1.370E 02	7.087E-02	1.544E 02	7.986E-02
4.7338E 01	5.3098E 01	5.470E 01	-5.104E 02	-2.001E 03	-9.319E 02	-1.129E 03	2.097E 03	1.374E 02	7.105E-02	1.545E 02	7.989E-02
4.8118E 01	5.7338E 01	5.139E 01	-3.797E 02	-2.285F 03	-9.999E 02	-1.283E 03	2.194E 03	1.483E 02	7.668E-02	1.330E 02	6.877E-02
4.8778E 01	4.4208E 01	4.420E 01	-2.315E 02	-2.454E 03	-1.055E 03	-1.398E 03	2.277E 03	1.140E 02	5.894E-02	1.140E 02	5.894E-02
4.8788E 01	4.4168E 01	4.416E 01	-2.292E 02	-2.456E 03	-1.056E 03	-1.400E 03	2.278E 03	1.143E 02	5.909E-02	1.143E 02	5.909E-02
4.9318E 01	3.8478E 01	3.847E 01	-1.150E 02	-2.570E 03	-1.099E 03	-1.480E 03	2.345E 03	9.957E 01	5.149E-02	9.957E 01	5.149E-02
5.0728E 01	3.1698E 01	3.169E 01	1.443E 02	-2.671E 03	-1.204E 03	-1.667E 03	2.522E 03	8.201E 01	4.241E-02	8.201E 01	4.241E-02
5.2628E 01	2.2018E 01	2.201E 01	4.000E 02	-3.243E 03	-1.340E 03	-1.903E 03	2.769E 03	5.697E 01	2.946E-02	5.697E 01	2.946E-02
5.3328E 01	2.0348E 01	2.038E 01	4.950E 02	-3.362E 03	-1.369E 03	-1.953E 03	2.852E 03	5.263E 01	2.722E-02	5.263E 01	2.722E-02
5.4078E 01	1.8578E 01	1.858E 01	5.703E 02	-3.436E 03	-1.409E 03	-2.027E 03	2.948E 03	4.809E 01	2.487E-02	4.809E 01	2.487E-02
5.4838E 01	1.6808E 01	1.680E 01	6.389E 02	-3.540E 03	-1.447E 03	-2.099E 03	3.046E 03	4.396E 01	2.274E-02	4.396E 01	2.274E-02
5.5768E 01	1.5498E 01	1.549E 01	7.138E 02	-3.617E 03	-1.489E 03	-2.182E 03	3.164E 03	4.006E 01	2.072E-02	4.006E 01	2.072E-02
5.6268E 01	1.4788E 01	1.478E 01	8.017E 02	-3.735E 03	-1.509E 03	-2.220E 03	3.209E 03	3.824E 01	1.977E-02	3.824E 01	1.977E-02
5.6318E 01	8.5128E 00	1.476E 01	8.958E 02	-3.741E 03	-1.511E 03	-2.231E 03	3.216E 03	2.203E 01	1.139E-02	3.824E 01	1.987E-02
5.6458E 01	8.5168E 00	1.450E 01	9.050E 02	-3.756E 03	-1.516E 03	-2.242E 03	3.234E 03	2.206E 01	1.139E-02	3.752E 01	1.940E-02
5.6538E 01	1.4398E 01	1.434E 01	9.112E 02	-3.768E 03	-1.518E 03	-2.249E 03	3.245E 03	3.723E 01	1.925E-02	3.723E 01	1.925E-02
5.6818E 01	1.3998E 01	1.399E 01	9.297E 02	-3.801E 03	-1.528E 03	-2.273E 03	3.280E 03	3.620E 01	1.872E-02	3.620E 01	1.872E-02
5.7048E 01	1.3268E 01	1.326E 01	9.629E 02	-3.867E 03	-1.535E 03	-2.293E 03	3.309E 03	3.431E 01	1.774E-02	3.431E 01	1.774E-02
5.7768E 01	1.0928E 01	1.092E 01	9.757E 02	-3.910E 03	-1.556E 03	-2.355E 03	3.402E 03	2.826E 01	1.461E-02	2.826E 01	1.461E-02
5.8788E 01	8.1128E 00	8.112E 00	9.954E 02	-4.000E 03	-1.580E 03	-2.428E 03	3.532E 03	1.958E 01	8.130E-03	1.958E 01	8.130E-03
5.9798E 01	1.8658E 01	1.865E 01	9.981E 02	-4.186E 03	-1.617E 03	-2.569E 03	3.740E 03	4.309E 01	2.228E-02	4.309E 01	2.228E-02
6.2218E 01	1.8598E 01	1.859E 01	9.981E 02	-4.342E 03	-1.645E 03	-2.677E 03	3.972E 03	4.294E 01	2.221E-02	4.294E 01	2.221E-02

READING = 0000 BLOCK = 211 TIME = 293.811 MACH 6.0 PT = 747.249 TT = 2962.2

XAMB	P-IB	P-PB	PDA	QDX	W-IB	Q-DB	CA-ALL	P-IB/P30	P-IB/P10	P-DB/P30	P-DB/P10
6.488E 01	2.078E 01	2.078E 01	9.981E 02	-4.595E 03	-1.716E 03	-2.878E 03	4.289E 03	5.372E 01	2.778E-02	5.372E 01	2.778E-02
6.505E 01	2.085E 01	2.139E 01	9.981E 02	-4.642E 03	-1.730E 03	-2.912E 03	4.337E 03	5.396E 01	2.790E-02	5.537E 01	2.863E-02
6.509E 01	2.085E 01	2.146E 01	9.981E 02	-4.647E 03	-1.731E 03	-2.915E 03	4.342E 03	5.396E 01	2.790E-02	5.550E 01	2.872E-02
6.529E 01	1.982E 01	2.186E 01	9.981E 02	-4.671E 03	-1.739E 03	-2.932E 03	4.368E 03	5.129E 01	2.652E-02	5.648E 01	2.917E-02
6.695E 01	1.127E 01	9.250E 00	1.171E 03	-4.840E 03	-1.790E 03	-3.050E 03	4.583E 03	2.917E 01	1.508E-02	2.394E 01	1.238E-02
6.782E 01	8.199E 00	9.135E 00	1.363E 03	-4.894E 03	-1.806E 03	-3.088E 03	4.665E 03	2.122E 01	1.097E-02	2.364E 01	1.222E-02
6.839E 01	8.670E 00	8.952E 00	1.561E 03	-4.953E 03	-1.821E 03	-3.132E 03	4.760E 03	1.209E 01	6.250E-03	1.799E 01	9.303E-03
6.911E 01	3.658E 00	4.910E 00	1.690E 03	-5.009E 03	-1.833E 03	-3.176E 03	4.848E 03	9.466E 00	4.895E-03	1.271E 01	6.571E-03
6.972E 01	2.880E 00	4.187E 00	1.773E 03	-5.055E 03	-1.840E 03	-3.215E 03	4.922E 03	7.248E 00	3.747E-03	1.083E 01	5.603E-03
7.067E 01	1.974E 00	3.060E 00	1.867E 03	-5.120E 03	-1.850E 03	-3.271E 03	5.036E 03	5.106E 00	2.642E-03	7.914E 00	4.095E-03
7.110E 01	1.600E 00	2.802E 00	1.899E 03	-5.146E 03	-1.853E 03	-3.294E 03	5.088E 03	4.141E 00	2.141E-03	7.252E 00	3.750E-03
7.203E 01	1.822E 00	1.885E 00	1.995E 03	-5.215E 03	-1.863E 03	-3.353E 03	5.213E 03	4.715E 00	2.438E-03	4.878E 00	2.523E-03
7.353E 01	1.952E 00	7.650E-01	2.054E 03	-5.249E 03	-1.868E 03	-3.381E 03	5.272E 03	5.052E 00	2.613E-03	1.980E 00	1.024E-03
7.358E 01	1.953E 00	7.600E-01	2.056E 03	-5.249E 03	-1.868E 03	-3.381E 03	5.272E 03	5.054E 00	2.613E-03	1.967E 00	1.017E-03
7.486E 01	2.145E 00	0.000	2.099E 03	-5.306E 03	-1.875E 03	-3.431E 03	5.424E 03	5.551E 00	2.871E-03	0.000	0.000
7.771E 01	2.110E 00	0.000	2.184E 03	-5.319E 03	-1.888E 03	-3.431E 03	5.523E 03	5.461E 00	2.824E-03	0.000	0.000
8.161E 01	1.450E 00	0.000	2.280E 03	-5.334E 03	-1.903E 03	-3.431E 03	5.628E 03	3.753E 00	1.940E-03	0.000	0.000
8.442E 01	1.380E 00	0.000	2.292E 03	-5.340E 03	-1.917E 03	-3.431E 03	5.662E 03	3.571E 00	1.847E-03	0.000	0.000
8.728E 01	1.745E 00	0.000	2.329E 03	-5.371E 03	-1.940E 03	-3.431E 03	5.705E 03	4.516E 00	2.335E-03	0.000	0.000
8.729E 01	1.746E 00	0.000	2.329E 03	-5.371E 03	-1.940E 03	-3.431E 03	5.705E 03	4.518E 00	2.336E-03	0.000	0.000

ORIGINAL PAGE IS
OF POOR QUALITY

REACTION = 0.000 CYCLE = 211 TIME = 299.811 CALM 0.0 P1 = 197.249 T1 = 2982.2

X	CHAR.	CUMAC	CF	MC
4.040E 01	1.177E 02	1.177E 02	2.184E-03	4.259E-02
4.041E 01	1.739E-01	1.179E 02	2.165E-03	4.200E-02
4.130E 01	1.722E 01	1.351E 02	2.801E-03	4.704E-02
4.131E 01	1.955E-01	1.353E 02	2.850E-03	5.224E-02
4.137E 01	1.191E 00	1.365E 02	2.394E-03	5.305E-02
4.150E 01	2.255E 00	1.388E 02	2.805E-03	5.847E-02
4.246E 01	1.66EE 01	1.554E 02	2.512E-03	6.716E-02
4.469E 01	2.532E 01	1.807E 02	2.818E-03	7.906E-02
4.431E 01	3.367E 00	1.83EE 02	3.059E-03	7.230E-02
4.480E 01	7.037E 00	1.90EE 02	3.074E-03	7.231E-02
4.481E 01	1.355E-01	1.91CE 02	3.073E-03	7.230E-02
4.625E 01	2.053E 01	2.115E 02	3.337E-03	8.052E-02
4.626E 01	1.3E1E-01	2.11EE 02	2.902E-03	7.84UE-02
4.731E 01	1.319E 01	2.24HE 02	2.905E-03	7.573E-02
4.733E 01	5.13EE-01	2.251E 02	3.017E-03	7.207E-02
4.811E 01	9.596E 00	2.347E 02	2.981E-03	7.170E-02
4.877E 01	8.A31E 00	2.434E 02	3.206E-03	8.220E-02
4.878E 01	1.326E-01	2.435E 02	2.959E-03	8.924E-02
4.931E 01	6.669E 00	2.502E 02	2.899E-03	8.594E-02
5.072E 01	1.705E 01	2.672E 02	2.845E-03	5.867E-02
5.282E 01	2.392E 01	2.911E 02	2.848E-03	4.815E-02
5.332E 01	5.A06E 00	2.967E 02	2.921E-03	4.202E-02
5.407E 01	8.301E 00	3.050E 02	2.896E-03	4.013E-02
5.4A3E 01	4.143E 00	3.13EE 02	2.887E-03	3.730E-02
5.576E 01	9.557E 00	3.227E 02	2.865E-03	3.542E-02
5.626E 01	5.158E 00	3.284E 02	2.839E-03	3.2UEE-02
5.631E 01	4.665E-01	3.284E 02	3.02AE-03	2.814E-02
5.695E 01	1.215E 00	3.27EE 02	2.850E-03	2.733E-02
5.653E 01	7.22UE-01	3.283E 02	3.372E-03	2.74UE-02
5.8A1E 01	2.530E 00	3.30EE 02	3.011E-03	2.93AE-02
5.704E 01	1.947E 00	3.326E 02	2.989E-03	2.859E-02
5.776E 01	6.333E 00	3.391E 02	2.926E-03	2.505E-02
5.878E 01	9.212E 00	3.483E 02	2.787E-03	1.781E-02
6.079E 01	1.A25E 01	3.84AE 02	2.542E-03	1.704E-02
6.221E 01	1.125E 01	3.75EE 02	3.105E-03	3.138E-02
6.468E 01	2.013E 01	3.959E 02	3.140E-03	3.305E-02
6.505E 01	2.719E 00	3.987E 02	3.343E-03	3.137E-02
6.509E 01	2.830E-01	3.989E 02	3.455E-03	3.177E-02
6.529E 01	1.945E 00	4.00AE 02	3.453E-03	3.103E-02
6.695E 01	1.218E 01	4.125E 02	3.390E-03	2.274E-02
6.762E 01	9.480E 00	4.170E 02	3.378E-03	2.054E-02
6.839E 01	4.704E 00	4.217E 02	3.342E-03	1.504E-02
6.911E 01	3.751E 00	4.255E 02	3.303E-03	1.20UE-02
6.972E 01	2.780E 00	4.283E 02	3.273E-03	1.104E-02
7.067E 01	3.722E 00	4.32CE 02	3.219E-03	8.051E-03
7.110E 01	1.479E 00	4.335E 02	3.198E-03	7.822E-03
7.263E 01	4.786E 00	4.382E 02	3.170E-03	6.850E-03
7.353E 01	2.239E 00	4.405E 02	3.125E-03	5.40AE-03
7.354E 01	3.294E-03	4.405E 02	3.125E-03	5.4U1E-03
7.486E 01	1.22CE 00	4.417E 02	3.177E-03	7.063E-03
7.771E 01	2.609E 00	4.443E 02	3.159E-03	7.409E-03
8.101E 01	2.470E 00	4.468E 02	3.08AE-03	5.590E-03
8.442E 01	1.119E 00	4.479E 02	3.067E-03	5.304E-03
8.728E 01	9.912E-01	4.48AE 02	3.083E-03	6.303E-03
8.729E 01	0.000	4.480E 02	3.084E-03	6.305E-03

AIRESEARCH MANUFACTURING COMPANY OF CALIFORNIA

NOZZLE PERFORMANCE

ENGINE PERFORMANCE

CALCULATED THRUST	1741.	(LBF)
MEASURED THRUST	1904.	(LBF)
CALCULATED SPECIFIC IMPULSE	6135.	(LBF-SEC/LBM)
MEASURED SPECIFIC IMPULSE	6342.	(LBF-SEC/LBM)
CALCULATED THRUST COEFFICIENT	0.7179	
MEASURED THRUST COEFFICIENT	0.7845	

STREAMTUBE CALCULATED ENGINE PERFORMANCE

STREAM THRUST	8878.	(LBF)
NET THRUST	1908.	(LBF)
SPECIFIC IMPULSE	6205.	(LBF-SEC/LBM)
IMPLST COEFFICIENT	0.7590	

INLET

ANGLE OF ATTACK	0.000	(DEGREES)
MASS FLOW RATIO	0.9875	
ADDITIVE DRAG COEFFICIENT	0.0060	
LIPPING PRESSURE RECOVERY EFFICIENCY	0.1031	
DELTA PT2	0.1171	(PSI)
TOTAL PRESSURE RECOVERY = SUPERSONIC	0.9095	
TOTAL PRESSURE RECOVERY = SUBSONIC	0.1050	
INLET PROCESS EFFICIENCY = SUPERSONIC	0.6902	
INLET PROCESS EFFICIENCY = SUBSONIC	0.6957	
KINETIC ENERGY EFFICIENCY = SUPERSONIC	0.9815	
KINETIC ENERGY EFFICIENCY = SUBSONIC	0.8847	
ENTHALPY AT P0 = SUPERSONIC	-8.09	(BTU/LBM)
ENTHALPY AT P0 = SUBSONIC	27.76	(BTU/LBM)

INJECTION AND FORCES

INLET MOMENTUM DRAG	117.7	(LBF)
INLET REFLECTION DRAG	-713.9	(LBF)
COMBUSTOR MOMENTUM DRAG	680.9	(LBF)
COMBUSTOR STRUT DRAG	-2.46	(LBF)
COMBUSTOR CURVATURE DRAG	1263.	(LBF)
NOZZLE FRICTION DRAG	49.75	(LBF)
NOZZLE STRUT DRAG	0.00	(LBF)
NOZZLE MOMENTUM DRAG	1202.	(LBF)
NOZZLE PRESSURE INTEGRAL	1331.	(LBF)
EXTERNAL FRICTION DRAG	18.14	(LBF)
EXTERNAL PRESSURE INTEGRAL	-1702.	(LBF)
TOTAL EXTERNAL DRAG	-1700.	(LBF)
TOTAL STRUT DRAG	-2.46	(LBF)
CAVITY FORCE	-1577.	(LBF)
CALCULATED LOAD CELL FORCE	-1566.	(LBF)
MEASURED LOAD CELL FORCE	-1593.	(LBF)
FUEL VALVE SPECIFIC IMPULSE	0.00	0.00 0.00

COMBUSTOR

FUEL-AIR RATIO	0.0311	
EQUIVALENCE RATIO	1.000	
COMBUSTION EFFICIENCY	0.989	
TOTAL PRESSURE RATIO	0.1436	
COMBUSTION EFFECTIVENESS	0.8708	
INJECTOR DISCHARGE COEFFICIENTS	0.7499	0.7784 0.7005

NOZZLE

VACUUM STREAM THRUST COEFFICIENT = CS	0.9334	
NOZZLE COEFFICIENT = CF	0.8904	
PROCESS EFFICIENCY	0.8248	
KINETIC ENERGY EFFICIENCY	0.8440	

STATICS

NOMINAL CURL LEADING EDGE	34.884	(IN)
SPINE TRANSLATION	0.3140	(IN)
INLET THROAT	47.800	(IN)
CURL LEADING EDGE	54.194	(IN)
NOZZLE SHROUD TRAILING EDGE	73.534	(IN)
NOZZLE PLUG TRAILING EDGE	87.291	(IN)
STRUT LEADING EDGE	56.455	(IN)
STRUT TRAILING EDGE	65.055	(IN)
COMBUSTOR EXIT	65.055	(IN)

FUEL INJECTORS

INJECTORS	STATION	VALVE
1A	60.900	
1B	61.300	B
1C	60.300	
2A	60.700	C
2C	60.100	A
3A	59.865	
3B	59.250	
4	60.800	

ORIGINAL PAGE IS OF POOR QUALITY

APPENDIX B

COOLING LOSS CALCULATION

The cooling loss distribution was determined from the temperature difference between thermocouples imbedded in the engine surfaces and cooling water temperatures. Standard heat transfer equations were used to obtain local heat transfer coefficicnet and heat loss. The calculated heat losses were than adjusted proportionately to agree with the overall heat loss as determined from the overall water temperature rises and flow rates in inner and outer bodies.

The calculation was divided into four steps: (a) calculate local overall heat transfer coefficients, (2) determine local water and wall temperatures, (3) calculate local heat loss, and (4) adjust local heat loss to agree with the overall cooling loss. Physical dimensions for cooling passages are presented in Table B-1. The detailed equations are presented below.

Step 1: Local overall heat transfer coefficient

Because of different construction of water cooling passage, the overall heat transfer coefficient was calculated from two different equations. Equation (1) was used for standard channel flow without fins applicable to inner body and portions of outerbody as indicated. Equation (2) was used for finned passage applicable to a portion of outerbody only.

$$U = \frac{1}{\frac{3600}{h} + \frac{\ell}{k}} \text{ Btu/sec-ft}^2\text{-}^{o}\text{F} \qquad (1)$$

for innerbody and portions of outerbody $34.848 \leq x \leq 40.375$ and $66.836 \leq x < 73.224$.

where $$h = 0.023 \frac{k}{D_h} \left(\frac{3600\, D_h \dot{W}}{A_c \mu} \right)^{0.8} \left(\frac{C_p \mu}{k} \right)^{0.4} \text{ Btu/hr-ft}^2\text{-}^{o}\text{F}$$

$$A_c = \frac{\pi}{4(144)} (D_o + D_i)(D_o - D_i), \text{ sq ft}$$

$$D_h = \frac{D_o - D_i}{12}, \text{ ft}$$

$$C_p = 1 \text{ Btu/lbm } ^{o}\text{R}$$

$$\dot{W} = \text{lbm/sec}$$

$\mu \left(\frac{\text{lbm}}{\text{hr-ft}} \right)$ and $k \left(\frac{\text{Btu}}{\text{hr-ft-}^{o}\text{F}} \right)$ were evaluated at averaged wall temperature, T_W, and cooling water temperature T_c. $\frac{\ell}{k} \approx 1.4 \frac{\text{sec-ft}^2\text{-}^{o}\text{F}}{\text{Btu}}$

$$U = \frac{1}{\frac{1}{C_{TOT}} + 1.4} \text{ Btu/sec-ft}^2\text{-}^{o}\text{F} \qquad (2)$$

TABLE B-1

AIM COOLANT PASSAGE DIMENSIONS AND WALL TEMPERATURE IDENTIFICATIONS

X	D_o, in.	D_i, in.	Cos α	T_W Rdg	Channel
			Innerbody		
0.595	-	-	-	-	-
35.79	15.19	14.51	.9336	47-S	303
40.02	17.85	17.53	.9945	49-S	305
42.0	18.196	18.076	.9986	50-S	306
44.8	18.596	18.436	.9986	51-S	307
60	18.39	18.25	1	13-I and 14-I	308,290
64.8	18.39	18.25	1	15-I	309
68.08	17.508	17.231	.9397	11-NP	310
70.79	15.377	14.796	.9397	12-NP	311
81.3	7.386	5.668	.9272	14-NP	312
86.976	-	-	-	-	-
			Outerbody		
34.848	-	-	-	-	-
36.54	19.062	18.832	.9926	60-CO	313
37.04	19.282	18.992	.9926	54-C	314
39.01	19.881	19.551	.9926	55-C	315
40.0	20.160	19.760	.9926	56-059-C	316,292 only
41.98	20.229	19.919	.9976	39-0	317
42.58	20.317	20.007	.9976	40-0	318
43.79	20.494	20.184	.9976	41-0	319
45.23	20.700	20.390	.9976	42-0	320
46.51	20.891	20.581	.9976	43 to 46-0	289,293,294,295
47.02	20.965	20.655	.9976	47-0	321
49.0	21.259	20.949	.9976	49-0	322
50.01	21.406	21.096	.9976	50 and 52-0	323, 296
51.51	21.627	21.317	.9976	54-0	324
52.01	21.70	21.39	.9976	55-0	325
53.0	21.847	21.537	.9976	56-0	326
56.0	22.289	21.979	.9976	59-61-0	327,297,298
57.01	22.436	22.126	.9976	62-0	328
57.47	22.51	22.2	.9976	63-0	329
58.97	22.51	22.2	.9976	64-0	330
59.98	22.51	22.2	.9976	65-0	331
60.97	22.51	22.2	.9976	66-0	332
62.47	22.51	22.2	.9976	67 to 69-0	333,299,300
63.49	22.51	22.2	.9976	70-0	334
64.48	22.51	22.2	.9976	71-0	335
65.22	22.51	22.2	.9976	72-0	336
67.33	23.63	23.13	.9744	12-N	301
68.81	24.22	23.84	.9744	13-N	302
70.36	24.96	24.58		14-N	337
72.3	25.16	24.907		15-N	338
73.224	-	-	-	-	-

for a portion of outerbody $40.375 < x < 66.836$.

where $$C_{TOT} = \left[\frac{A_f}{A_o}\left(\frac{1}{mb}\right) + \frac{A_p}{A_o}\right] h$$

$$h = \frac{j\dot{W}C_p}{A_c Pr^{2/3}} \quad Btu/sec\text{-}ft^2\text{-}^oF$$

$$A_c = \text{net flow area} = \left(1 - \frac{t}{b}\right)\left(1 - \frac{t}{N}\right)\frac{b}{2}\,\frac{(D_o + D_i)\,\pi}{144}$$

$$= 0.00147(D_o + D_i),\ ft^2$$

$$mb = \sqrt{\frac{2h}{kt}}\,b = \frac{0.155}{12} \times 60 \times \sqrt{\frac{24}{30}\,\frac{h}{.006}} = 8.96\sqrt{h}$$

$$\frac{A_f}{A_o} = 2Nb = 4.90$$

$$\frac{A_p}{A_o} = 1 - Nt = 0.904$$

N = number of fins per inch = 16

t = fin thickness = 0.006 in.

b = fin height = 0.155 in.

j = j(Re), (see curve, Figure B-1)

$$D_h = \frac{2(1 - Nt)(b - t)}{(1 - Nt) + N(b - t)} = 0.00683 \text{ ft}$$

$$Re = \frac{D_h\dot{W}}{A_c\mu} \times 3600$$

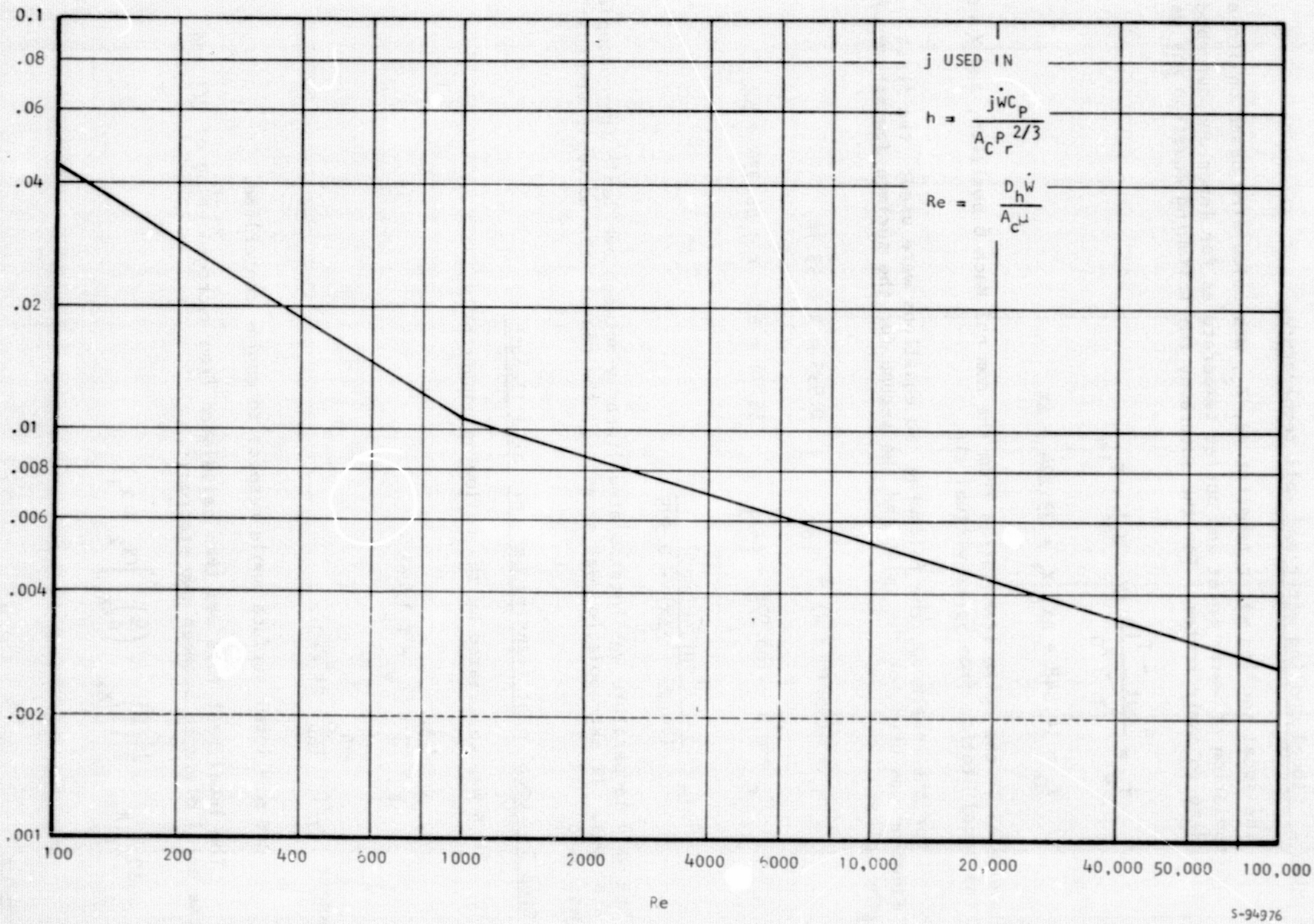

Figure B-1. Colburn j Factor For AiResearch Offset Plate-Fin Surface (16R-.155-.086)

Step 2: Local cooling water and wall temperatures

The local cooling water temperature, T_c, was calculated based on linear interpolation of water inlet and outlet temperatures for inner and outerbodies according to their routes. For the outerbody the following equation was used:

$$T_c = \frac{T_{out} - T_{in}}{X_1 - X_0} (X - X_0) + T_{in}$$

$$X_0 = 34.848 + \Delta X, \quad X_1 = 73.224 + \Delta X$$

where ΔX is the spike translation from the nominal Mach 6 position, and X is the local station from spike virtual tip.

For the innerbody, the foilowing two equations were used: the first equation was used for the spike and the second for the surface downstream of the spike.

$$T_c = m(55.76 - x) + T_{in} \qquad 0.595 \leq X \leq 55.76$$

$$T_c = m\left[x - (86.976 + \Delta X)\right] \qquad 55.76 + \Delta X < X \leq 86.976 + \Delta X$$

$$m = \frac{T_{out} - T_{in}}{(86.976 + \Delta X) - 0.595}$$

The wall temperature was interpolated linearly between available thermocouple stations. If extrapolation was necessary, the nearest thermocouple temperature was used.

Step 3: Local heat transfer per unit axial length

This was calculated by the following equations

$$\frac{Q}{\ell} = \frac{UA_T}{\ell} (T_w - T_c)/\cos \alpha$$

where $A_T/\ell = \frac{\pi D_o}{144}$ $ft^2/in.$

$\cos \alpha$ = local surface angle respect to engine centerline.

The local heat loss was then calculated from averaged value of Q/ℓ and the axial distance between two stations:

$$\Delta Q_{X_1, X_2} = \frac{1}{2}\left[\left(\frac{Q}{\ell}\right)_{X_1} + \left(\frac{Q}{\ell}\right)_{X_2}\right](X_2 - X_1)$$

At the extremes of the outerbody, the heat losses were calculated as follows

$$\Delta Q = \left(\frac{Q}{\ell}\right)_{36.54 + \Delta X} [36.54 - 34.848] \text{ Btu/sec}$$

for $34.848 + \Delta X \leq X \leq 36.54 + \Delta X$

$$\Delta Q = \left(\frac{Q}{\ell}\right)_{72.3+\Delta X} [73.224 - 72.3] \text{ Btu/sec}$$

for $72.3 + \Delta X \leq X \leq 73.224 + \Delta X$

At the extremes of the innerbody, namely, the inlet spike and nozzle cone sections, the heat loss was calculated from

$$\Delta Q = 0.5 \left[\left(\frac{Q}{\ell}\right)_{35.79}\right] \cdot [35.79 - 0.595]$$

for $0.595 \leq X \leq 35.79$

$$\Delta Q = 0.5 \left[\left(\frac{Q}{\ell}\right)_{81.3+\Delta X}\right] [86.976 - 81.3]$$

for $81.3 \leq X \leq 86.976$

The overall heat loss was then calculated from the summation of all local heat losses

$$\left(Q_{\text{overall}}\right)_{\text{calc.}} = \sum_{\text{inner}} \Delta Q + \sum_{\text{outer}} \Delta Q$$

Step 4: Heat loss from water flow rate and temperature rise

These were calculated as follows

$$\left(Q_{\text{overall}}\right)_{H_2O} = \dot{W}_o C_p \left(T_{\text{out}} - T_{\text{in}}\right)_{\text{outerbody}} + \dot{W}_i C_p \left(T_{\text{out}} - T_{\text{in}}\right)_{\text{innerbody}}$$

$\dot{W}_o = 89.7$ lb/sec, $W_i = 27.4$ lb/sec, $C_p = 1.0$

A correction factor, K, was then determined

$$K = \frac{\left(Q_{\text{overall}}\right)_{H_2O}}{\left(Q_{\text{overall}}\right)_{\text{cal.}}}$$

which was applied to all heat losses, ΔQ, determined from Step 3. Note that in the calculation of Q from water temperature rise, the strut heat loss was not directly included because

(a) The strut body ΔT could not be calculated due to bad measurements

(b) The heat loss from two of the struts was included in the innerbody water ΔT due to the coolant path through the struts

(c) The strut leading edge loss was low (< 30 Btu/sec) and would not significantly affect overall performance.

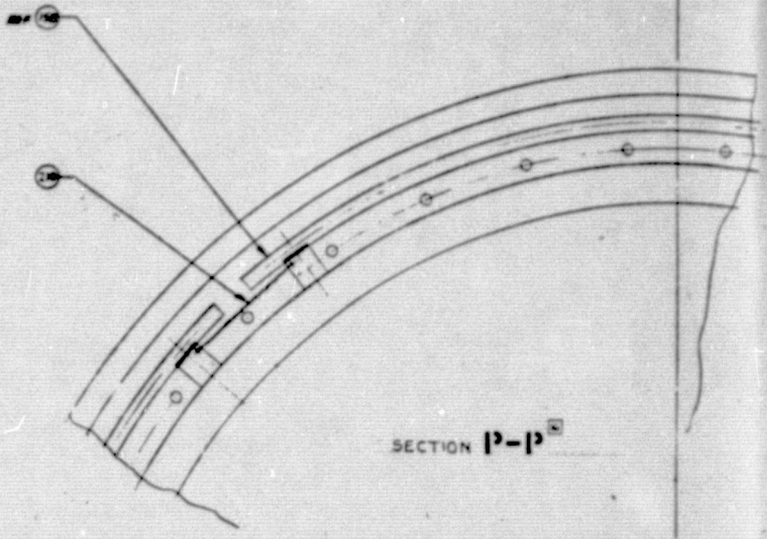

SECTION P-P

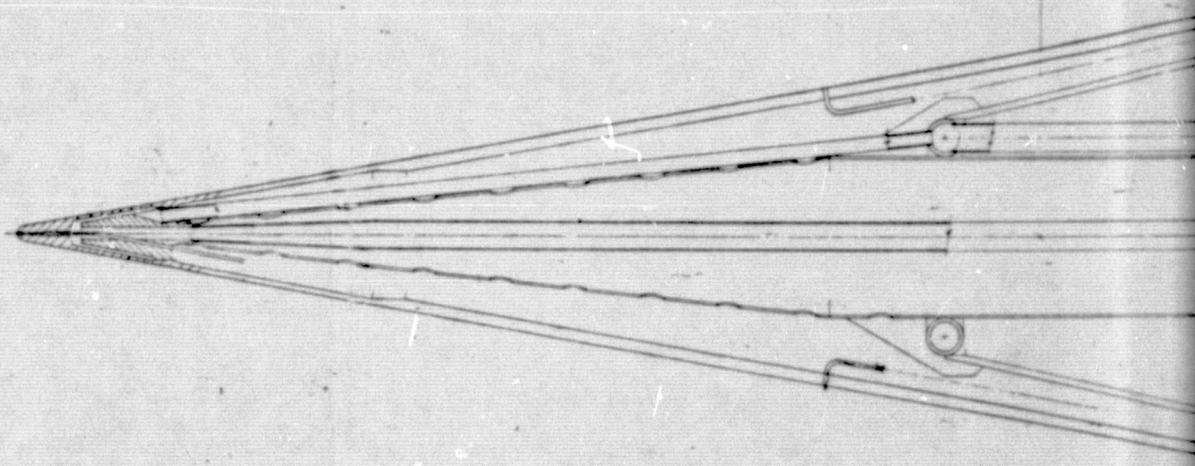

ORIGINAL PAGE IS
OF POOR QUALITY

FOLDOUT FRAME

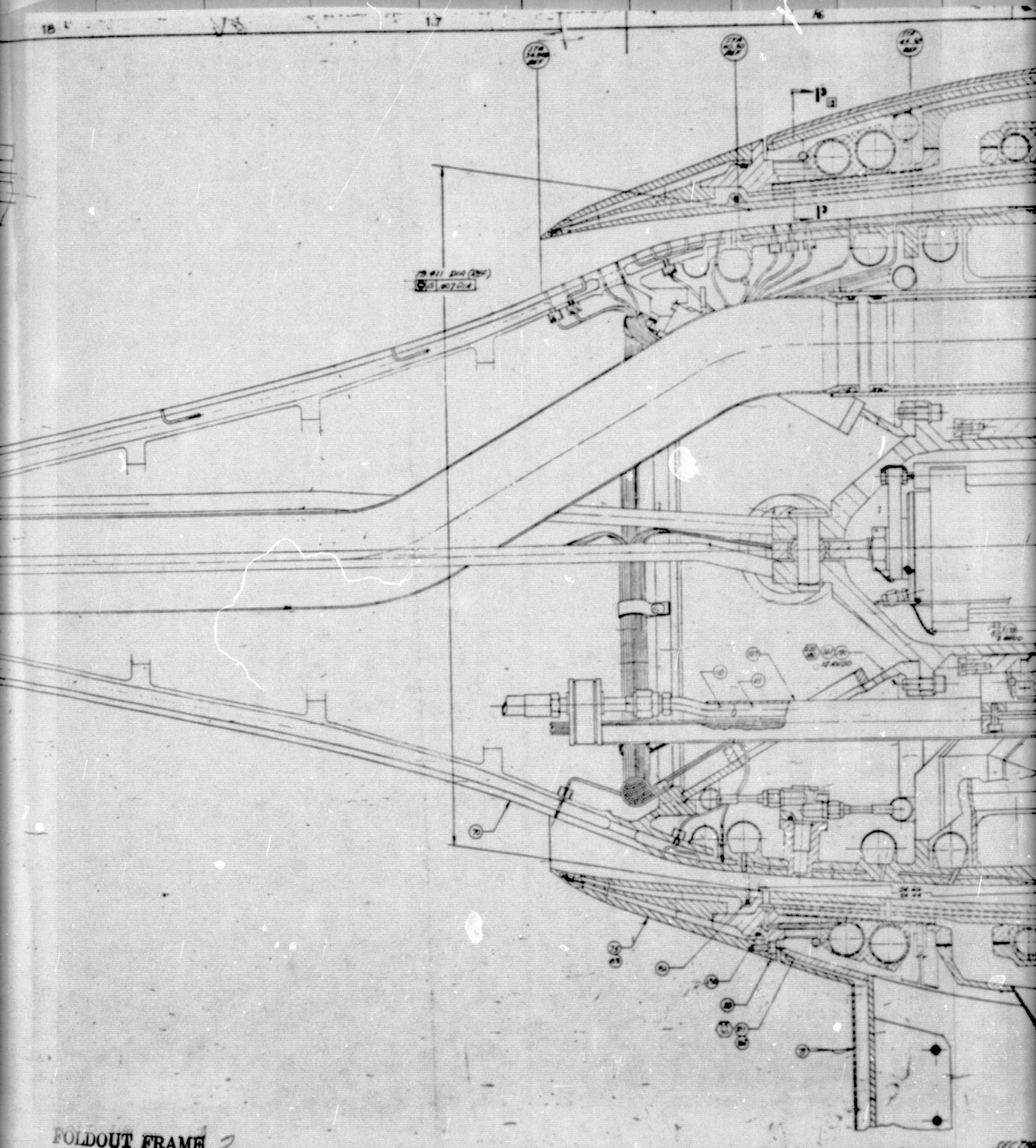

FOLDOUT FRAME 2

950501

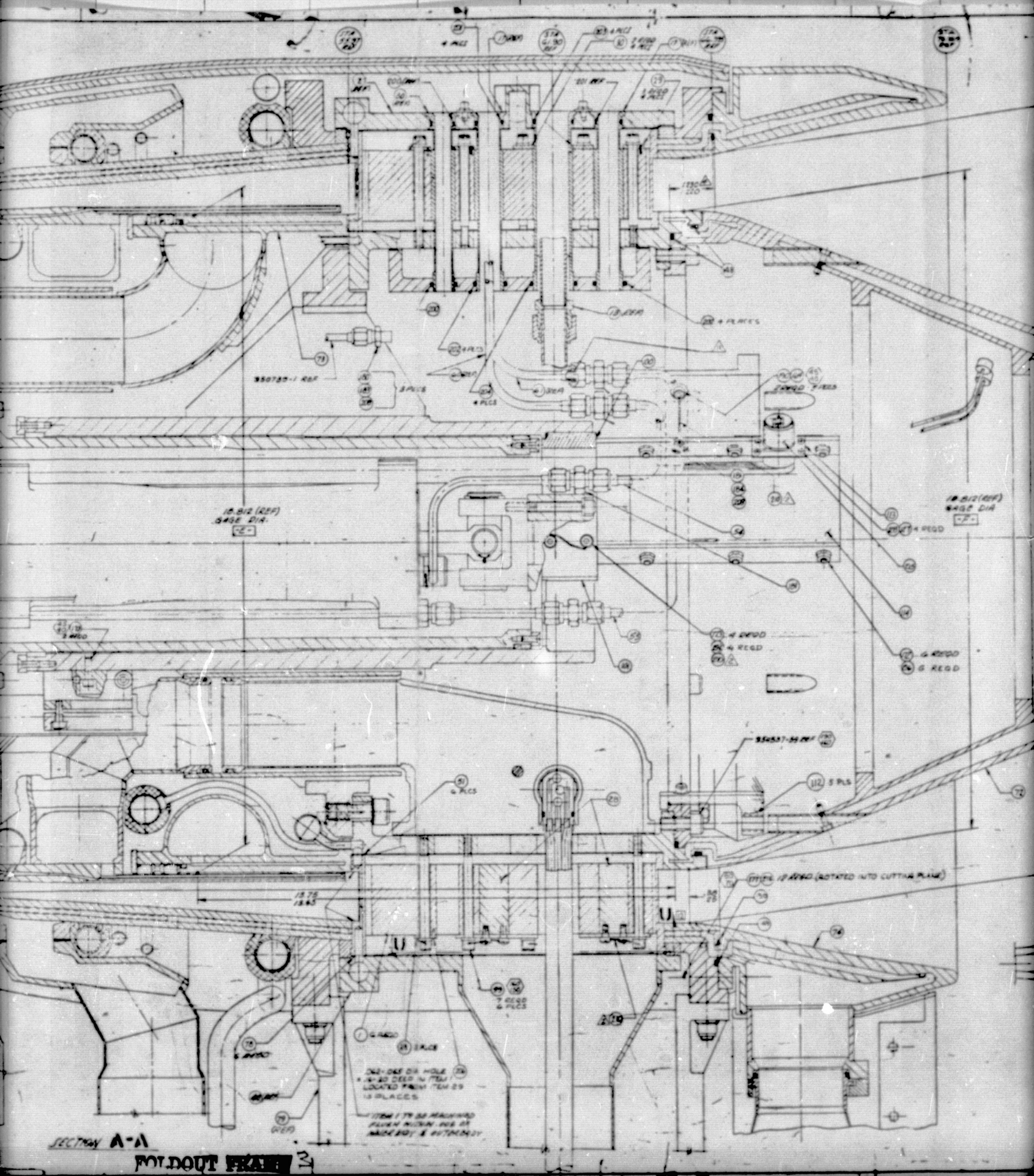
10.812 (REF) BASE DIA.
10.812 (REF) BASE DIA
4 REQD
6 REQD
5 PLS
7 REQD 6 PLCS
6 REQD
4 PLACES
3 PLCS
4 PLCS
6 PLCS
4 PLACES
4 REQD
6 REQD
5 PLS
6 REQD
6 REQD
6 REQD

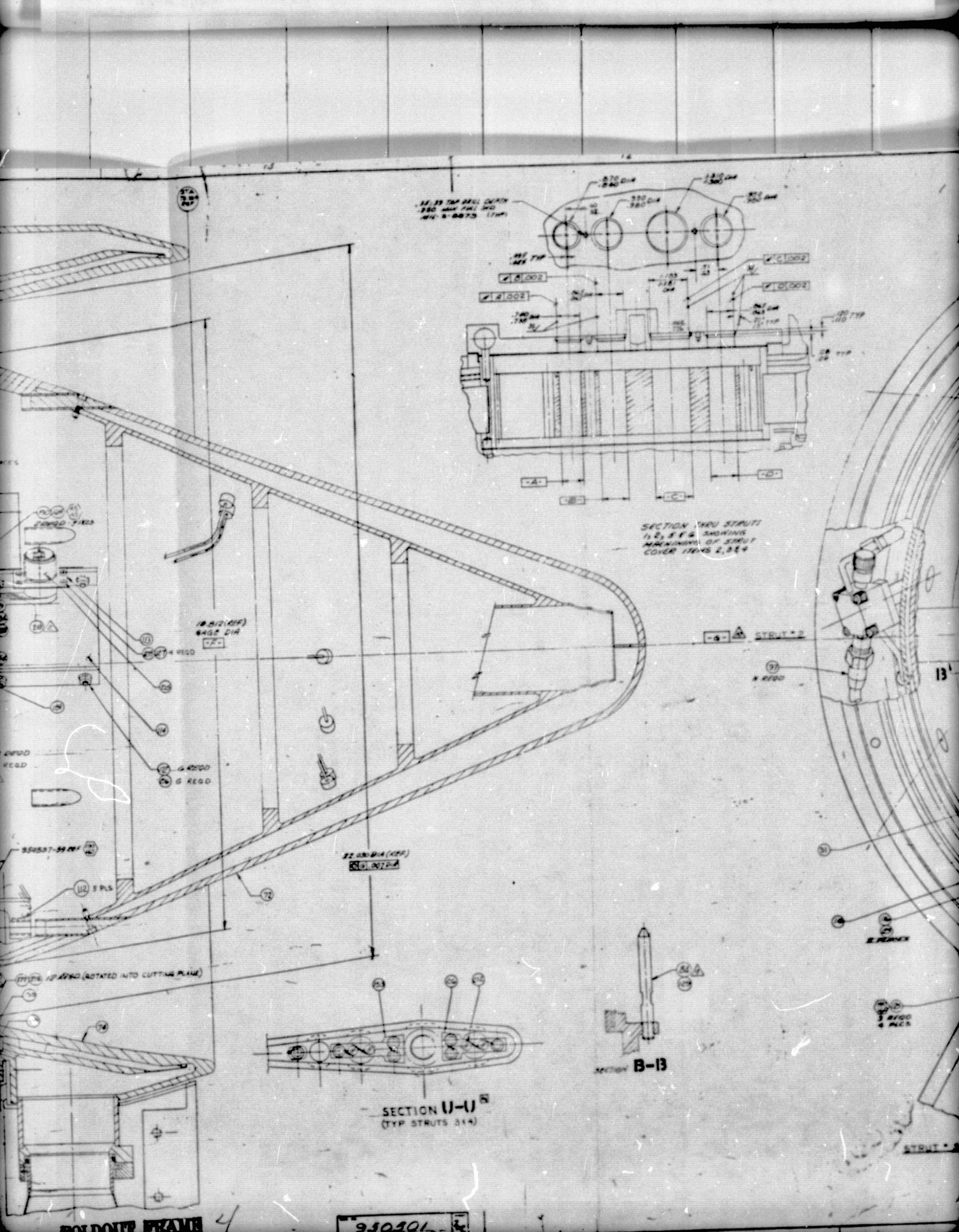
SECTION THRU STRUTS 1, 2, 5 & 6 SHOWING MACHINING OF STRUT COVER ITEMS 2, 3 & 4
STRUT "2"
STRUT "5"
SECTION B-13
SECTION U-U
(TYP STRUTS 3 & 4)
10 REQD (ROTATED INTO CUTTING PLANE)
BOLDOUT FRAME

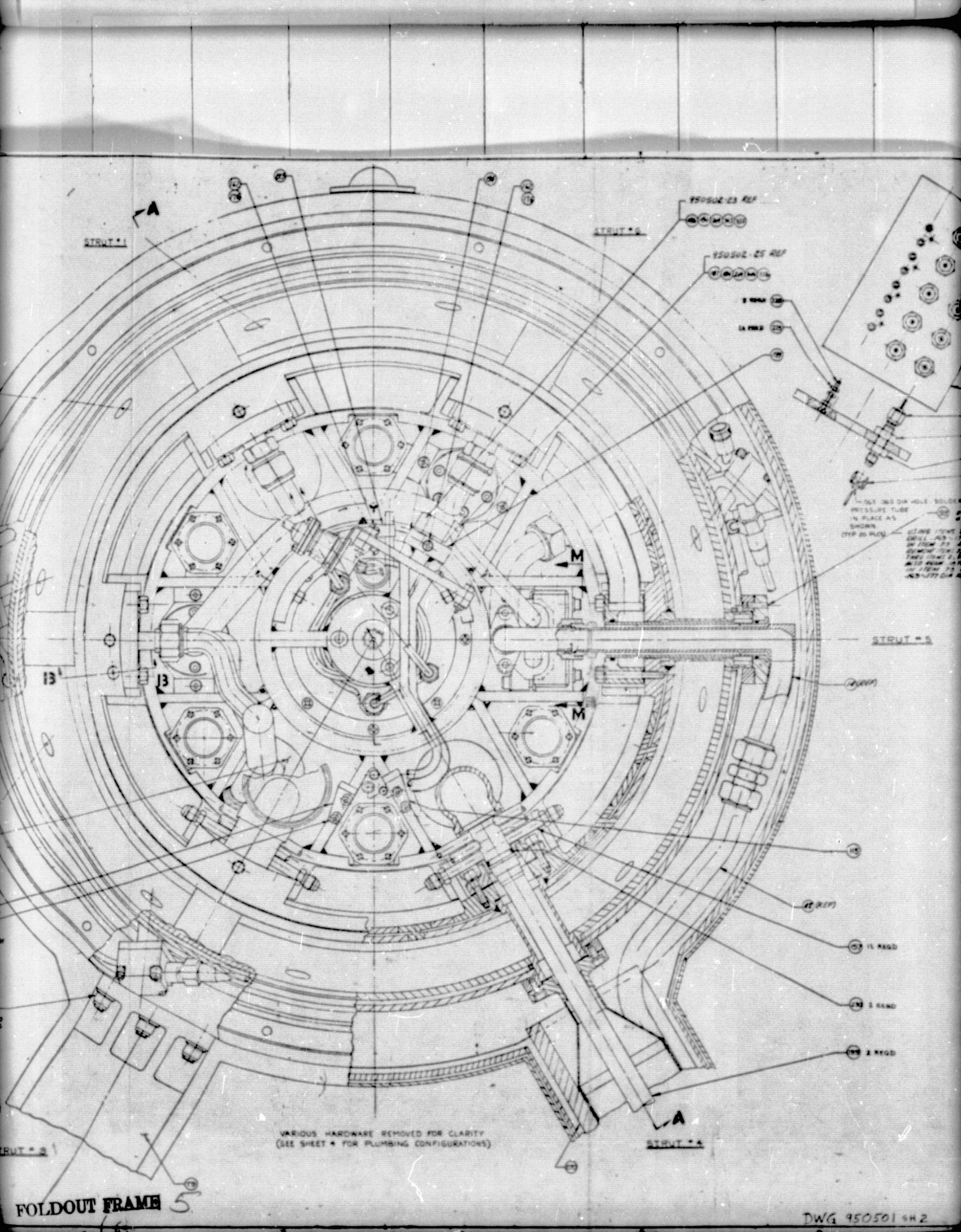

FOLDOUT FRAME 5

DWG 950501 SH 2

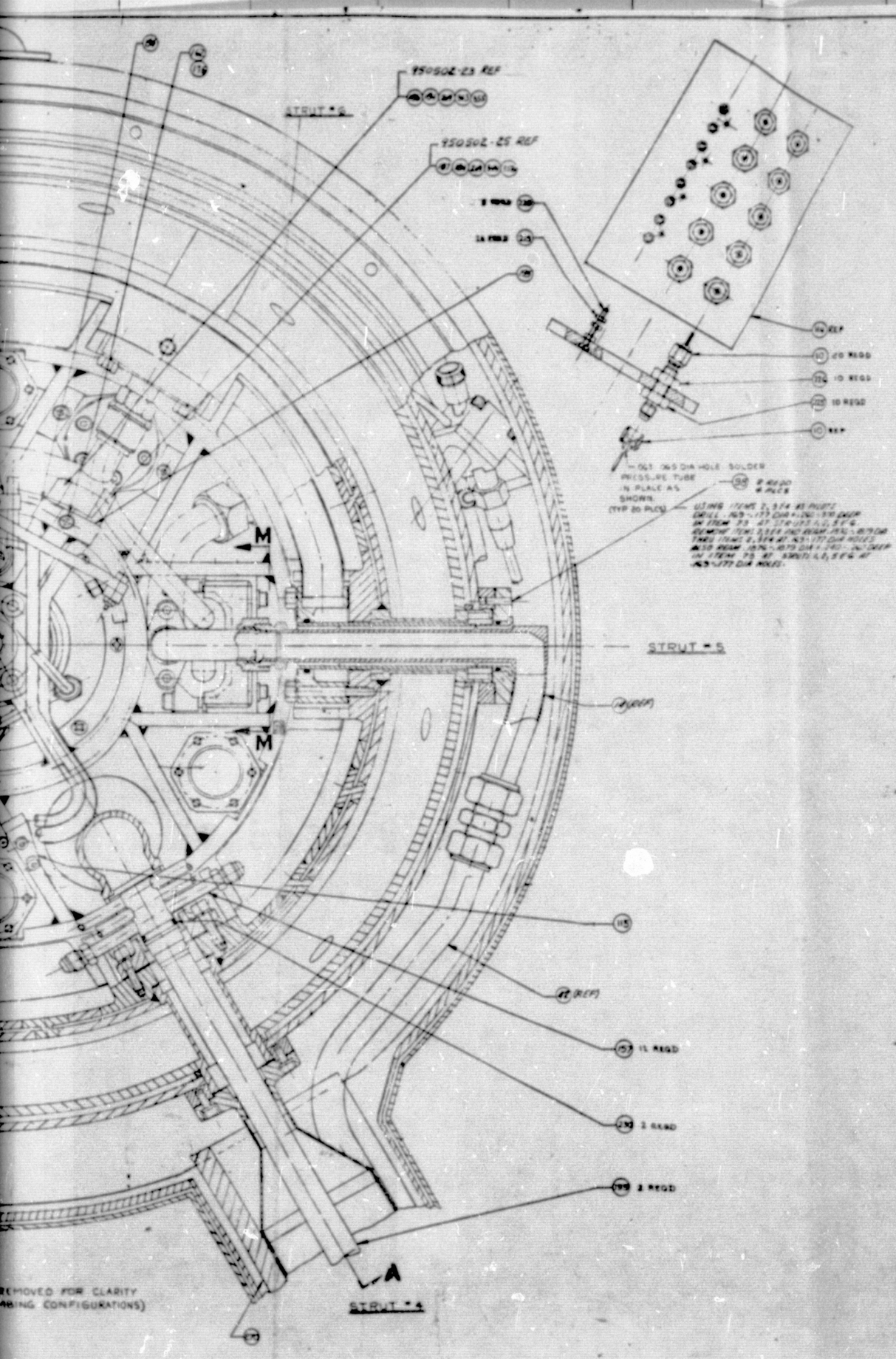
950502-23 REF
STRUT "6"
950502-25 REF
STRUT "5"
STRUT "4"
M
M
A
(REF)
11 REQD
2 REQD
2 REQD
20 REQD
10 REQD
10 REQD
(REF)
(REF)
(REF)

22 21 20

SECTION S-S

SECTION N-N

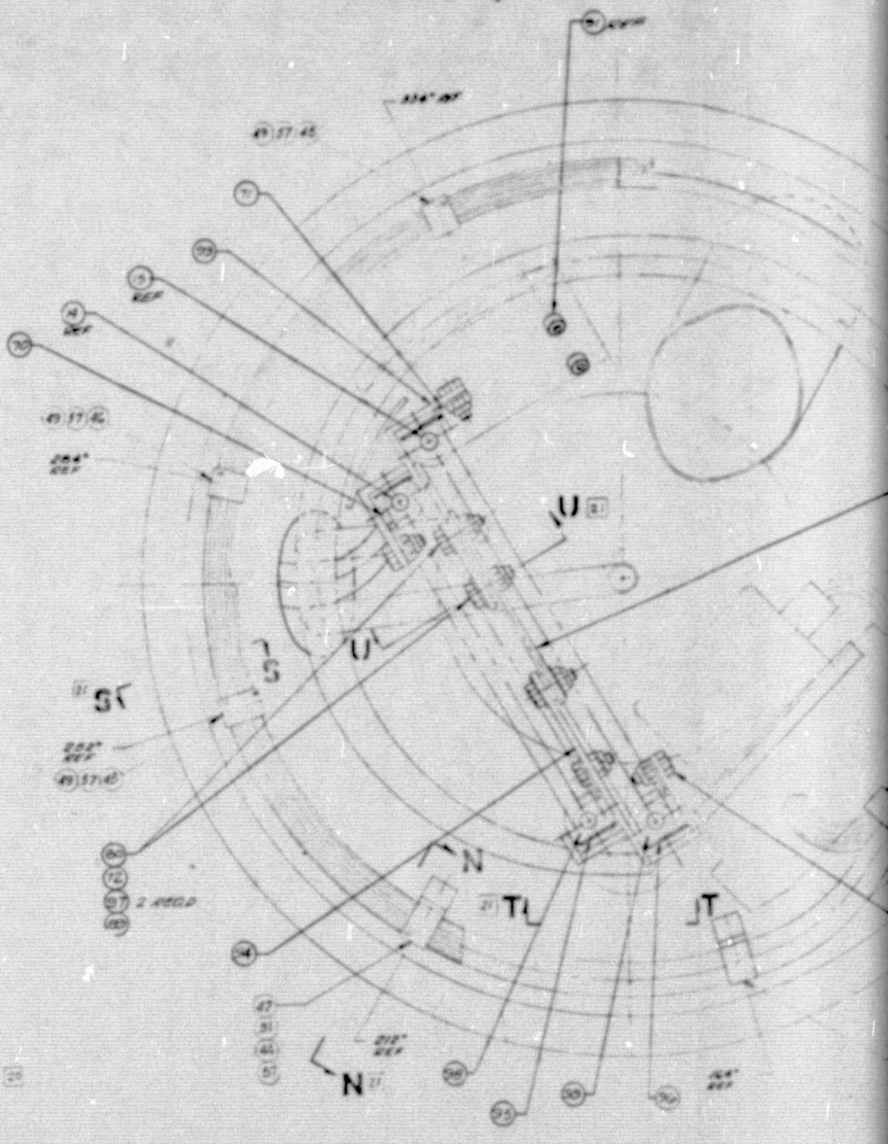

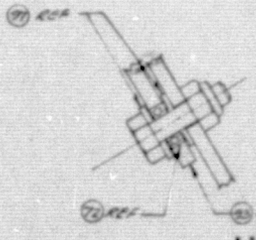

SECTION U-U

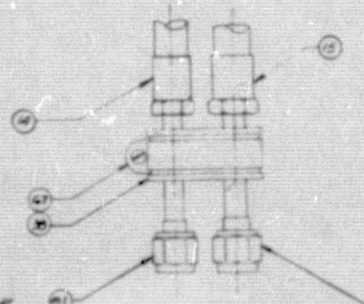

VIEW T-T

SECTION M-M
ALL OTHER ITEMS REMOVED FOR CLARITY
LOOKING AFT

ORIGINAL PAGE IS
OF POOR QUALITY

FOLDOUT FRAME

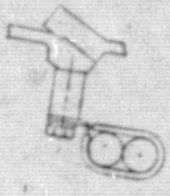

SECTION R-R
TYP 2 PLCS
@ 100° & 130°

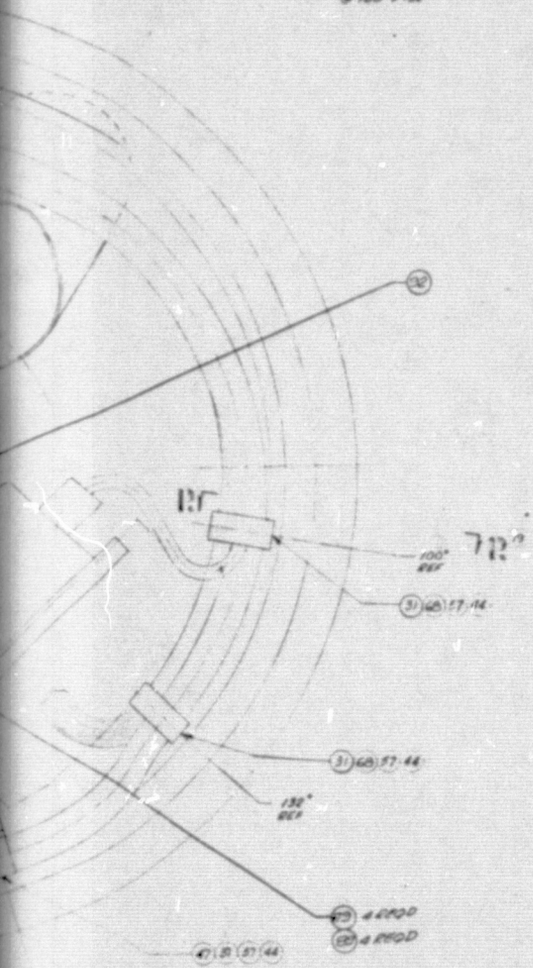

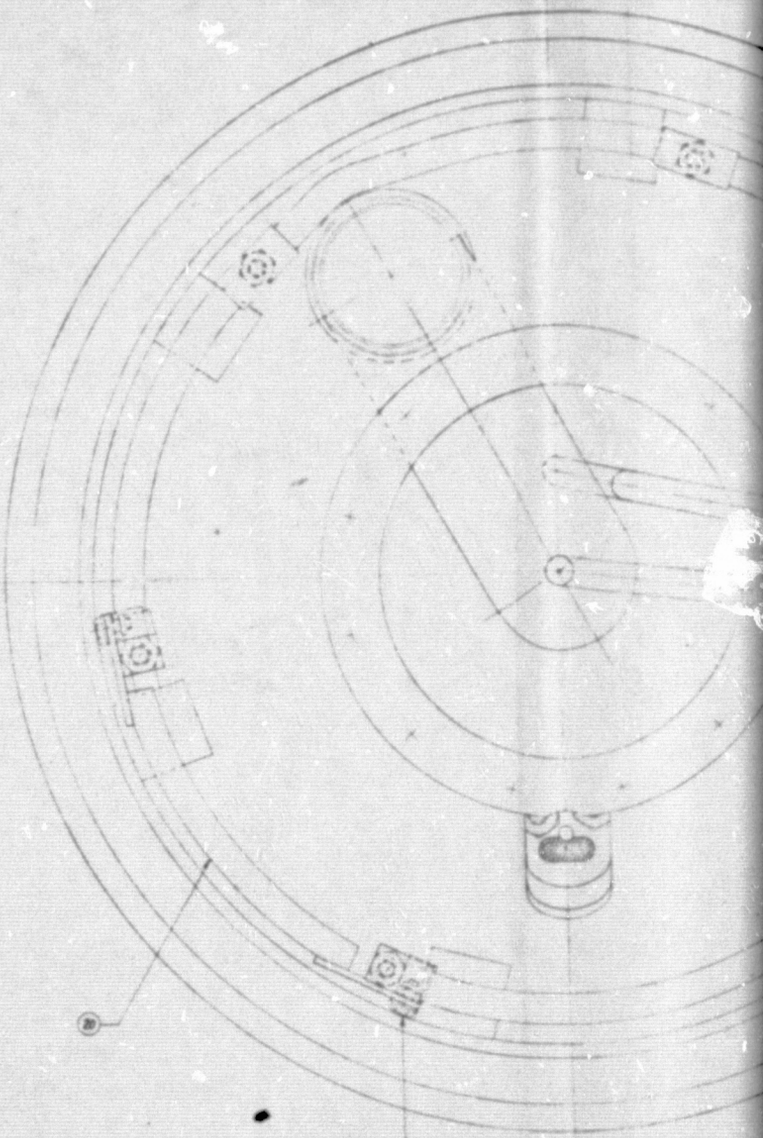

SECTION L-L
LOOKING FORWARD

FOLDOUT FRAME 2

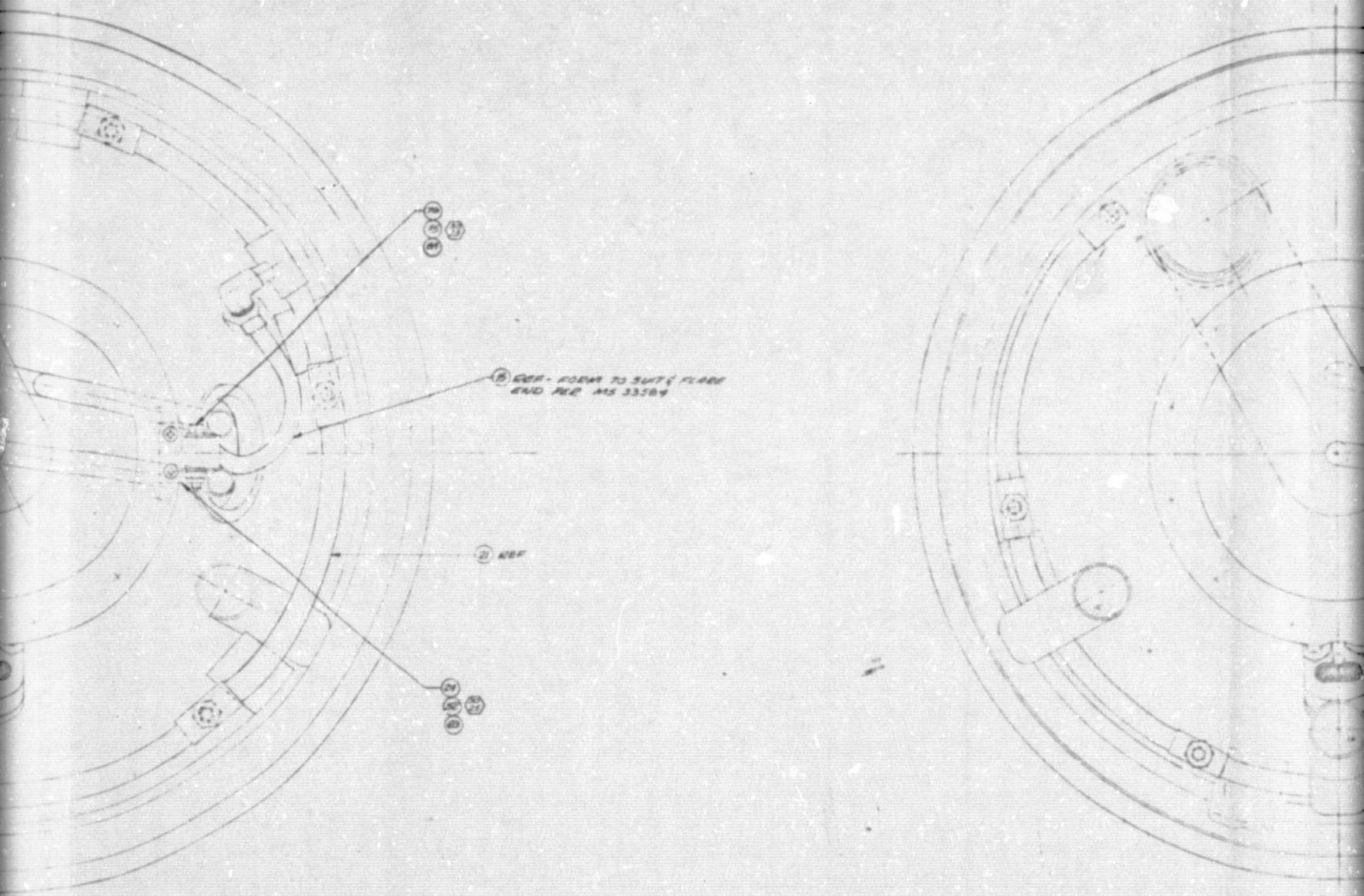

ECTION L-L
HR FASTENERS & SEALANT ONLY
KING FORWARD

FOLDOUT FRAME 5

REVISIONS				
DWT	LTR	DESCRIPTION	DATE	APPROVED
	C.T.	AS PER ITEM 2 OF CONTROLLING REVISION LETTER ADDED SHEET 2		

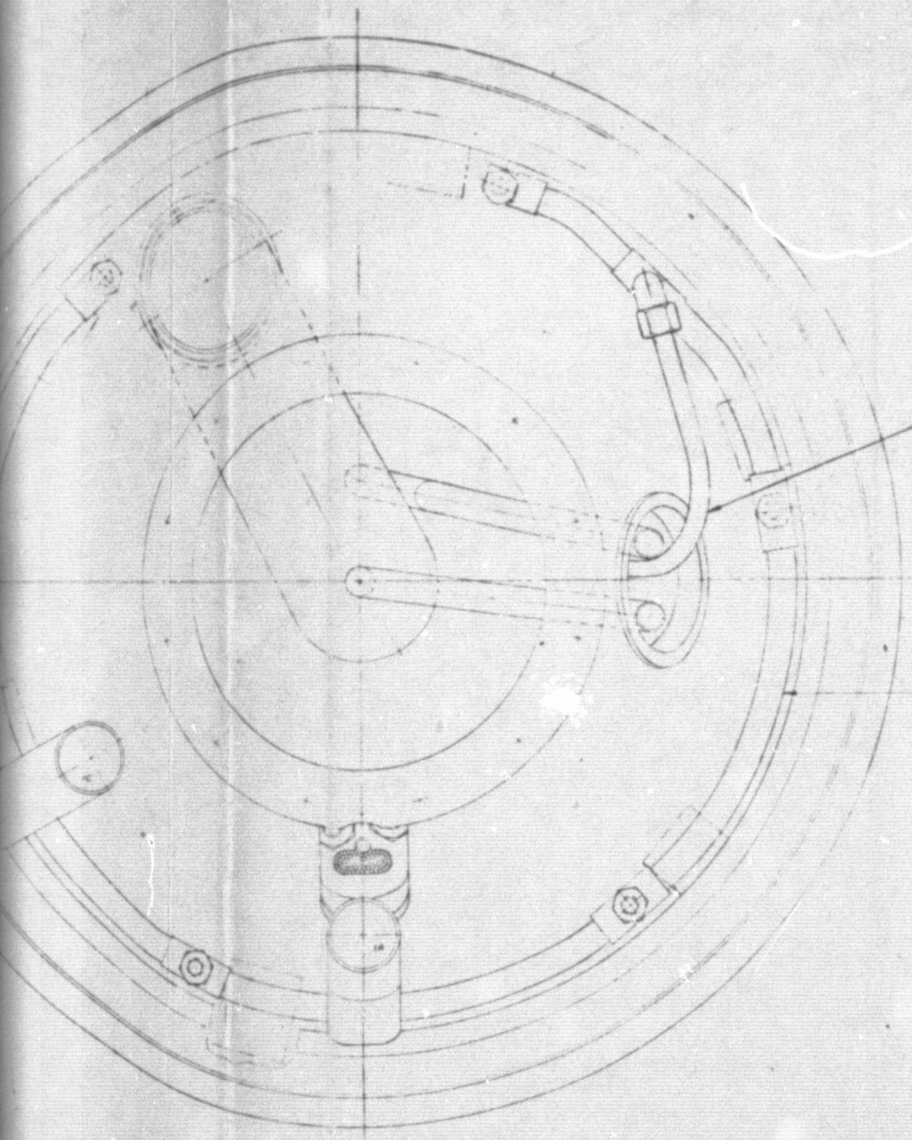

(14) REF - FORM TO SUIT ↓ FLARE END PER MS33584

(22) REF

SECTION K-K (B)

DEPICTING ↓ LINES & BRACKET ONLY

LOOKING FORWARD

* SEE SHEET 1 FOR CONTROLLING REVISION LETTER

FOLDOUT FRAME

FOLDOUT FRAME 4 C-5

J	70210	950502
SCALE		SHEET OF

950502

FOLDOUT FRAME

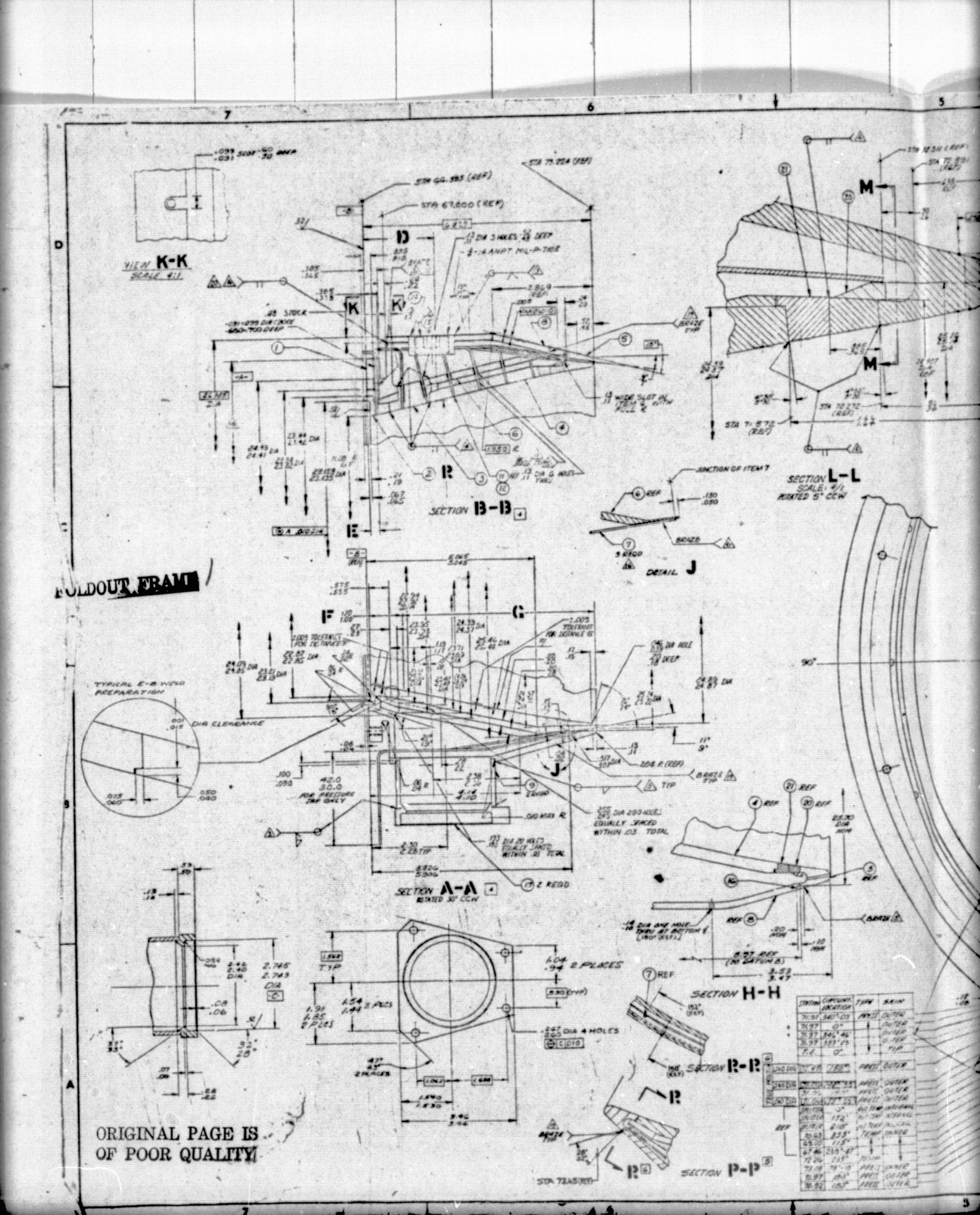

ORIGINAL PAGE IS
OF POOR QUALITY

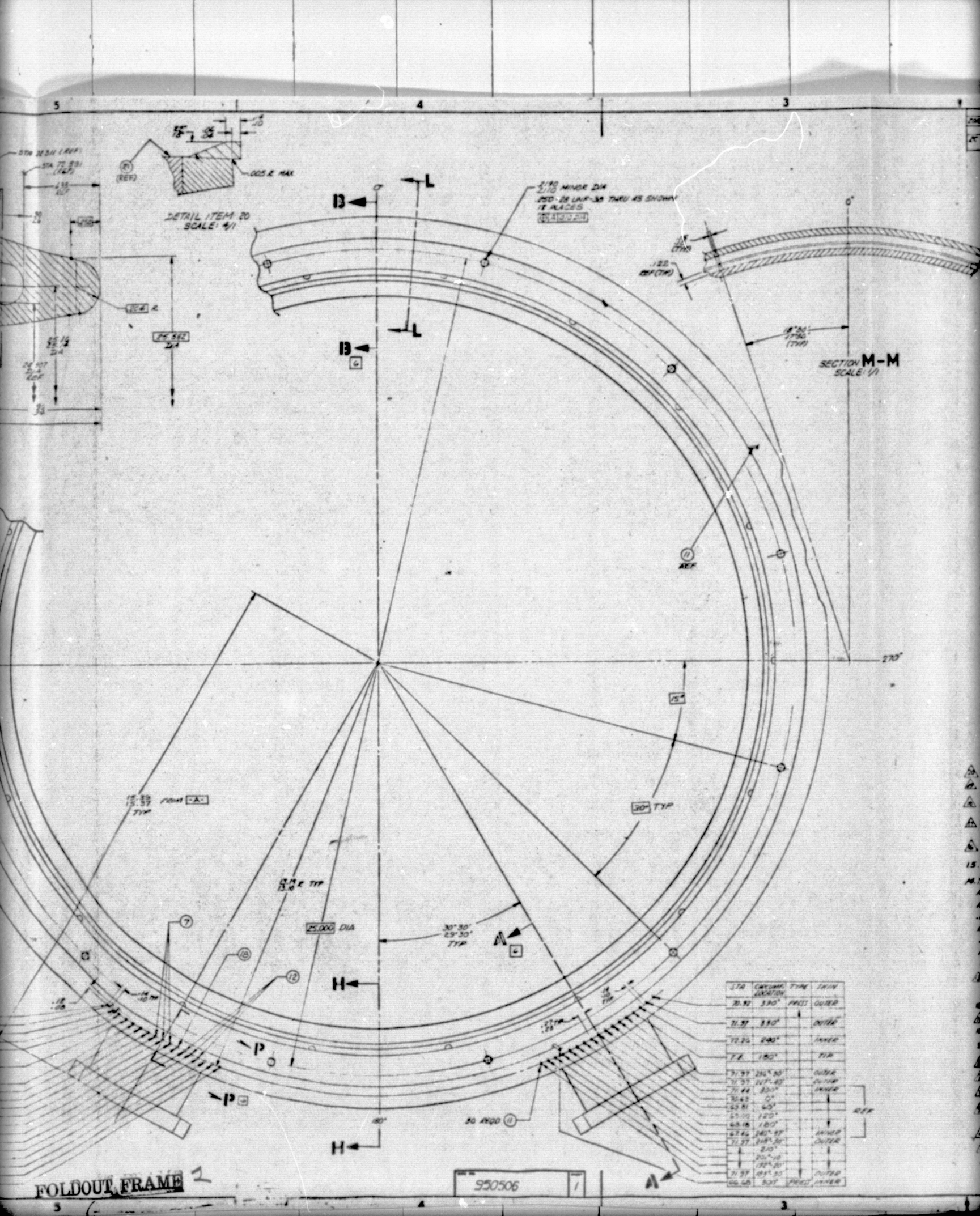
DETAIL ITEM 20
SCALE: 4/1
SECTION M-M
SCALE: 1/1
25.000 DIA
30° TYP
15° TYP
270°
180°
30 REQD
950506
FOLDOUT FRAME 2

ITEM	QTY	DESCRIPTION	DATE	APPROVED
	K	ADDED PARTS LISTED 8-9-72		
	L	REVISED TABLE OF CONTOUR COORDINATES		

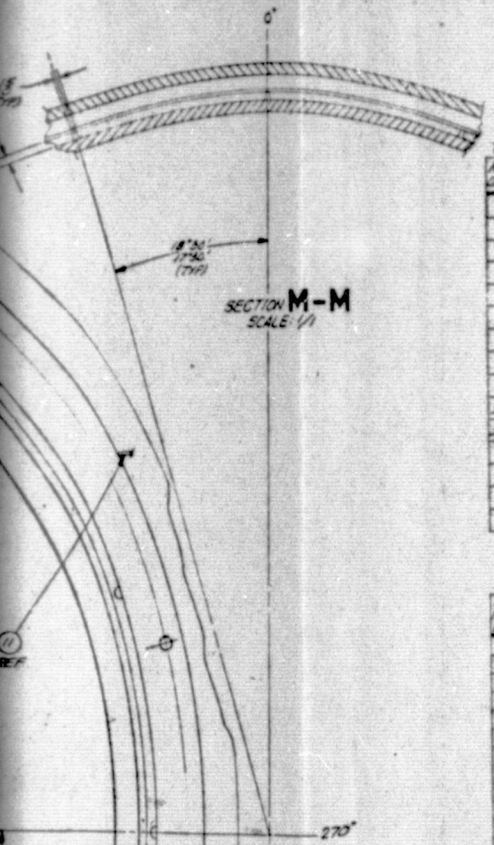

TABLE OF INSTRUMENTATION TYPE AND LOCATION

AXIAL STATION ON LAYOUT (REF)	IE	CIRCUMFERENTIAL LOCATION	S
66.48	.885	330°	PRESS
67.44	1.065	243°-27'	WALL
68.18	1.785	180°	WALL
69.00	2.405	120°	WALL
69.81	3.415	60°	WALL
70.43	4.235	0°	WALL
71.44	5.045	300°	WALL
72.26	5.865	240°	WALL
73.03	6.685	178°-17'	WALL
SHROUD BASE	TRAILING EDGE	0°	PRESS
SHROUD BASE	TRAILING EDGE	180°	PRESS
67.46	1.065	239°-41'	TC 2
69.00	2.605	115°	TC #2 / ITEM 12
70.69	4.295	359°	TC #2 / ITEM 18
72.26	5.865	295°	TC #2 / ITEM 12

TABLE OF CONTOUR COORDINATES

AXIAL STATION FROM STA 66.240 (IN LAYOUT REF)	ID	IR	STATION REF.
.240	-.415	11.022	65.380
.480	-.175	11.042	66.220
.780	.125	11.087	66.520
1.000	.345	11.132	66.740
1.460	.805	11.232	67.200
2.000	1.345	11.348	67.740
2.500	1.845	11.454	68.240
3.040	2.385	11.578	68.780
3.520	2.865	11.670	69.260
4.000	3.345	11.773	69.740
4.540	3.885	11.883	70.280
5.080	4.425	11.989	70.820
5.420	4.765	12.052	71.160
5.920	5.265	12.146	71.660
6.520	5.865	12.249	72.260
7.180	6.525	12.349	72.920
7.240	6.585	12.357	72.980
7.306	6.651	12.365	73.046

TABULATION OF INSTRUMENTATION OUTER SKIN

AXIAL STATION	CIRCUMF. LOCATION	TYPE
70.32	180°	PRESS
70.32	330°	
71.06	144°-24'	
71.06	150°	
71.06	156°-36'	
71.97	180°	
	183°-30'	
	196°-20'	
	203°-10'	
	210°	
	216°-50'	
	223°-40'	
	236°-30'	
	330°	
	340°-03'	
	346°-42'	
	353°-23'	
71.97	0°	
72.45	150°	PRESS

REVISIONS				
ZONE	LTR	DESCRIPTION	DATE	APPROVED
	A			
	B	ADDED GENERAL NOTE 14		
TC		ADDED "V" TO SEAL FACE		
2C		DELINEATED THERMOCOUPLE AT STA 72.32 FROM 72.26		
7D				
7C				
	C			
	D			
4B				
4B				
7A				
4B				
4B				
7A				
7A				
7A

TABLE OF CONTOUR CORD VALUES

A	27.148	26.196	25.007	23.809	22.479	21.650	19.625	18.734	17.680	16.590	15.845	15.140	12.740	11.403	9.790
R	3.237	3.411	3.633	3.895	4.122	4.338	4.782	4.945	5.256	5.518	5.776	5.926	6.640	7.140	8.607
LAYOUT STATION (REF)	18.140	19.834	20.443	21.691	22.830	23.859	25.915	26.764	27.830	28.904	29.455	30.164	32.760	34.083	37.310

7.439	6.962	6.698	6.468	5.720	5.000	4.580	2.100	5.111	4.651	-1.500	-1.600	-2.400	-2.900	-10.849
8.735	8.874	8.942	9.000	9.036	9.180	9.314	9.415	9.492	9.514	9.574	9.224	9.450	9.478	9.493
38.090	39.538	38.926	39.132	39.260	40.500	42.500	43.400	44.500	45.000	46.700	47.200	47.600	48.950	55.763

TABLE OF INSTRUMENTATION TYPE AND LOCATION

B	44.905	31.400	21.500	14.300	10.500	10.000	9.900	9.500	9.208	8.500	8.000	7.500	7.500	7.000	6.500
CIRCUMFERENTIAL LOCATION	G	0° 90° 180° 270°	0°	0°	0° 90° 180° 270°	0°	0°	0°	0° 90° 180° 270°	0°	0°	0° 90° 180° 270°	0°	0°	0° 90° 180° 270°
LAYOUT STATION (REF)	5.93	14.40	24.00	30.600	35.000	35.500	35.700	36.100	36.520	37.200	37.500	38.000	38.000	38.500	39.000
TYPE	7	7	3	1	2	7	4	3	8	6	2	7	9	1	7

6.000	5.500	5.500	4.000	3.600	3.600	3.500	3.000	2.050		0.83	0.30		-1.575	-2.475	
0°	0° 90° 180° 270°	0°	0°			0°	0°	0° 90° 180° 270°		0°			0° 90° 180° 270°		
32.500	40.000	41.000	41.130			42.000	42.500	43.450		44.850	44.950		47.375	48.17	

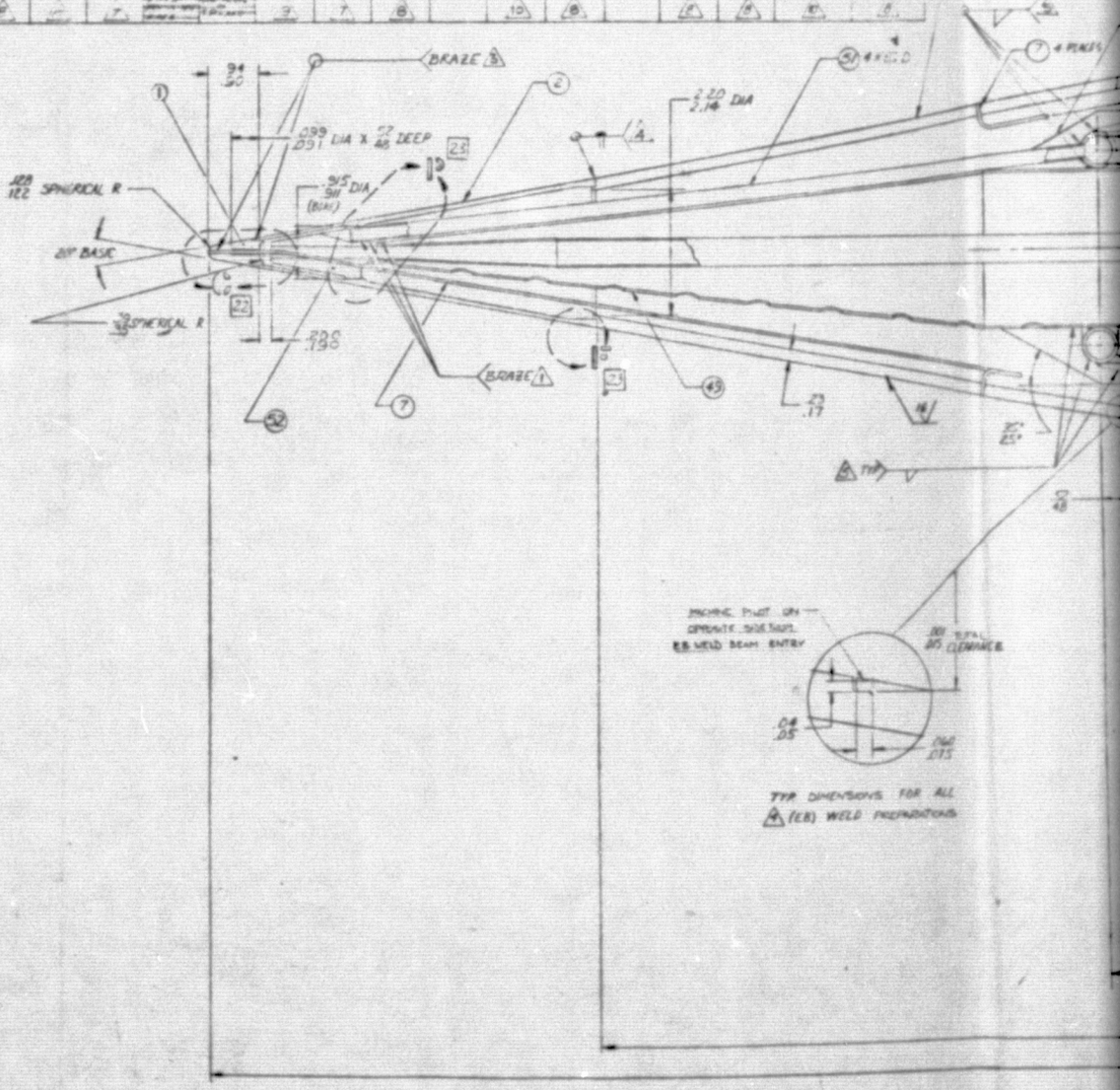

FOLDOUT FRAME

ORIGINAL PAGE IS
OF POOR QUALITY

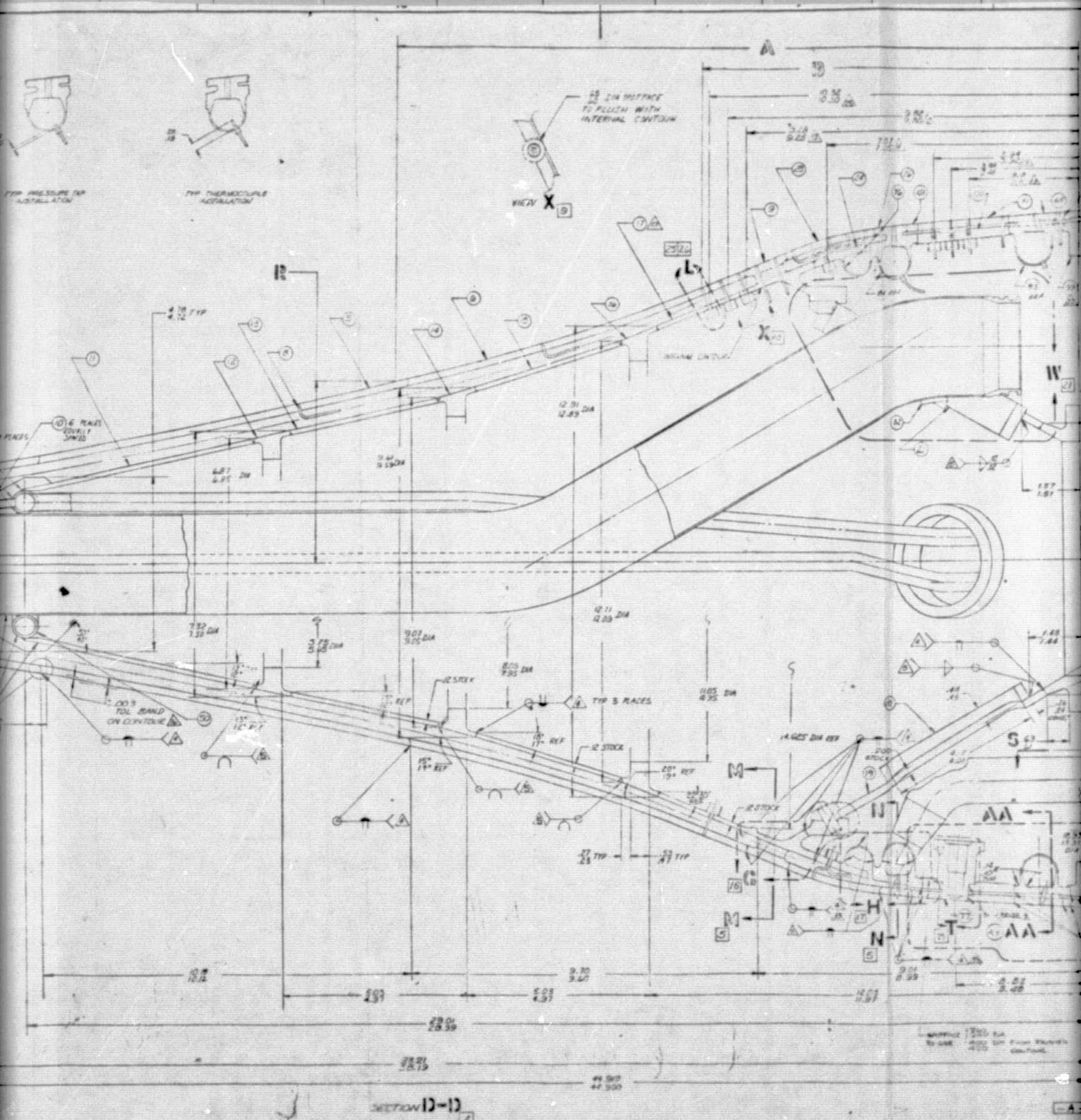

FOLDOUT FRAME 2

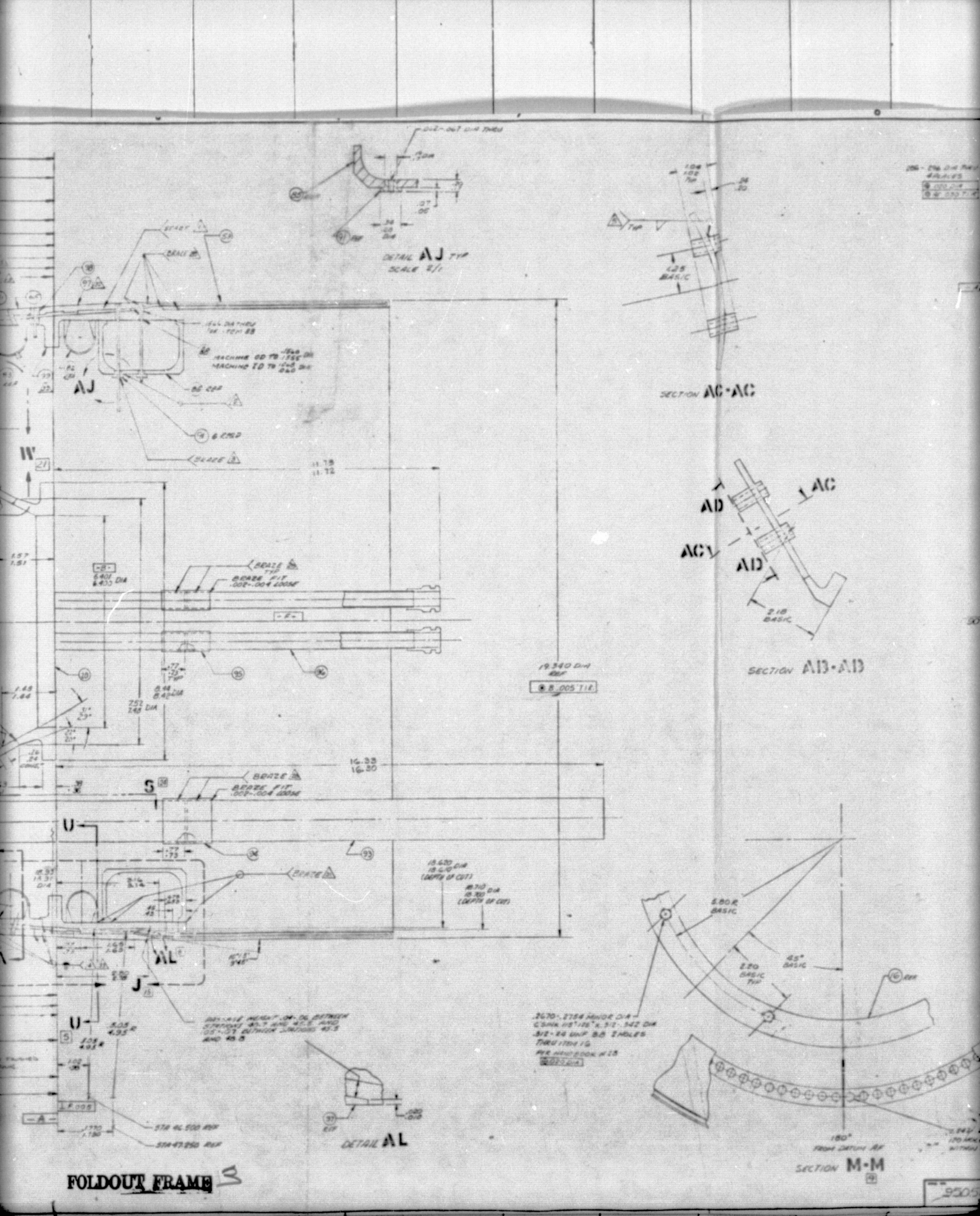
DETAIL AJ TYP
SCALE 2/1
SECTION AC-AC
SECTION AD-AD
SECTION M-M
DETAIL AL
AJ
AL
AC
AD
BRAZE
BRAZE FIT .003-.004 LOOSE
180° FROM DATUM AF
FOLDOUT FRAME 3

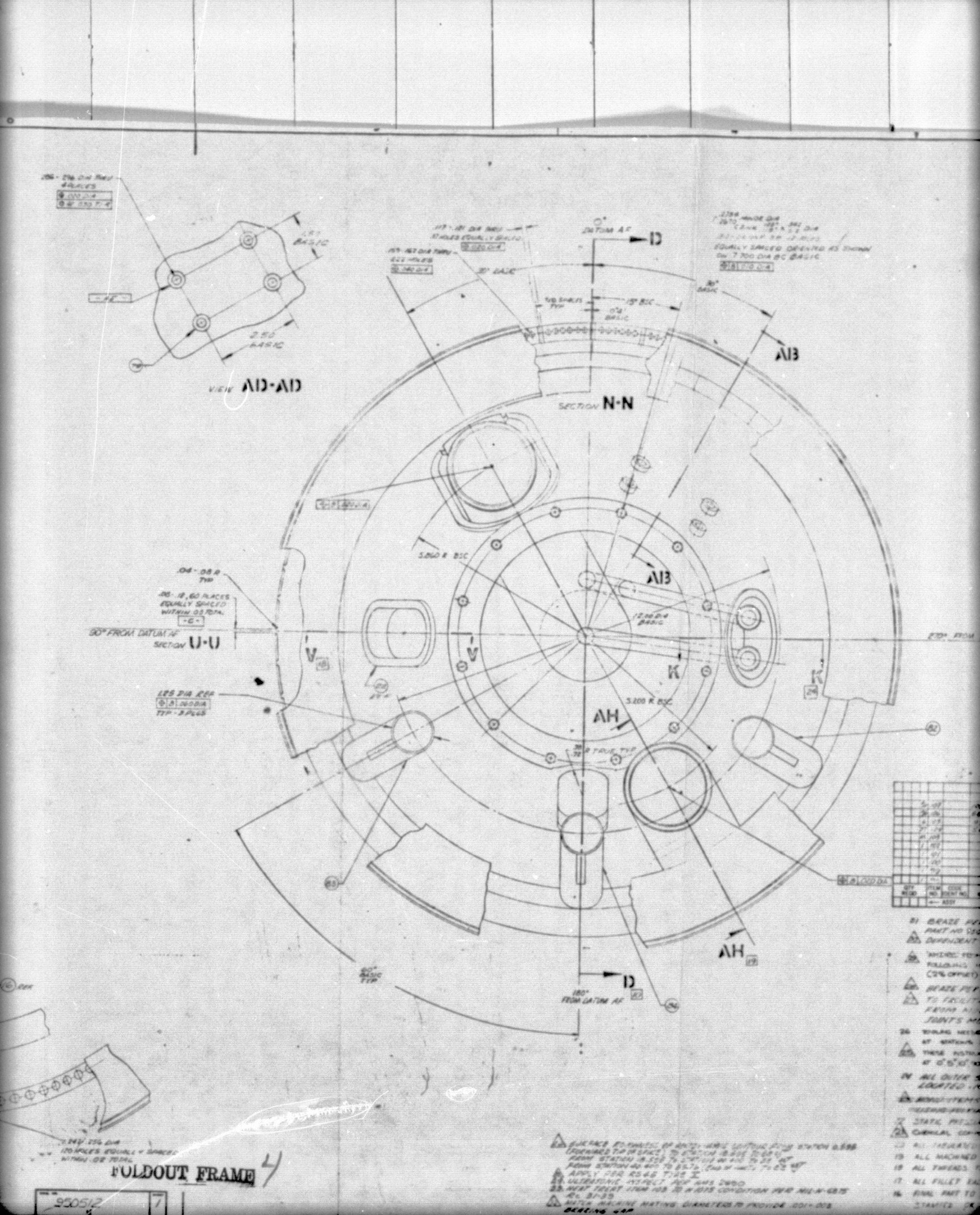

FOLDOUT FRAME 4

950512

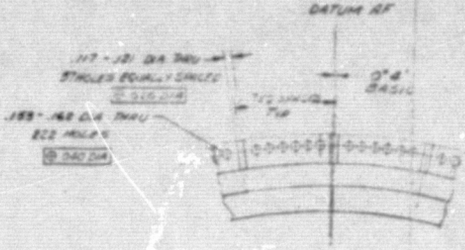

PART SECTION AA-AA

270° FROM DATUM AF

FOLDOUT FRAME 5

QTY REQD	ITEM NO.	CODE IDENT NO.	PART OR IDENTIFYING NO.	NOMENCLATURE OR DESIGNATION	SYM	ZONE
				← ASSY		

PARTS LIST

QTY REQD	ITEM NO.	CODE IDENT NO.	PART OR IDENTIFYING NO.	NOMENCLATURE OR DESIGNATION	SYM	ZONE
				← ASSY		

PARTS LIST

B1 BRAZE PER WBS-27 USING EMS 94850

A2 PART NO 950667-6 MAY BE SUBSTITUTED FOR ITEM 6, AS REQ'D DEPENDENT ON ROUTING TO BE DETERMINED ON WELDMENT

A3 "AMZIRC" FROM AMERICAN METAL CLIMAX INC. HEAT TREATED TO ROLLING NON-DEPLETED - UTS-45,000 PSI, YIELD STRENGTH (2% OFFSET) = 38,000 PSI, ELONGATION = 12 %

A4 BRAZE PER WBS-27 USING FILLMET 7 (AMS 4786)

A5 TO FACILITATE MANUFACTURE, ITEM 17 MAY BE MADE FROM MORE THAN ONE PIECE, AND ADDITIONAL WELD JOINTS MUST CONFORM TO WELD NOTE A4

A6 TOOLING NEEDED TO CORRECT FINAL GROWTH TO .060 ON DIAMETER AT STATIONS 38.5 AND 43.5 DURING PROOF PRESSURE TEST

A7 THESE INSTRUMENTATION BOSSES TO BE LOCATED CIRCUMFERENTIALLY AT 0°, 5°, 10°, 90°, 95°, 175°, 180°, 185°, 270°, 275°, 355° FROM DATUM 0°

A8 ALL OUTER SHELL THERMOCOUPLE JUNCTIONS TO BE LOCATED -.145 +.155 FROM INNER SURFACE.

A9 BOND ITEMS 58, 58, 59 TO INNER SHELL

A10 STATIC PRESSURE TEST ASSEMBLY TO 300 PSIA BEFORE FINAL MACHINING

A11 CHEMICAL COMPOSITION OF N-200 PER ASTM B-160 (FORGING), B-162 (SHEET)

A12 ALL TABULATED DIMENSIONS ARE LOCAL

A13 ALL MACHINED SURFACES 125 EXCEPT AS NOTED IN NOTE 36

A14 ALL THREADS TO BE PER HANDBOOK H-28

A15 ALL FILLET RADII .19 / .11

A16 FINAL PART TO BE STAMPED OR TAGGED #

NASA RAMJET R&D

A1 THIS INSTRUMENTATION BOSS TO BE LOCATED CIRCUMFERENTIALLY AT 5° FROM DATUM 0°

A2 THESE INSTRUMENTATION BOSSES TO BE LOCATED CIRCUMFERENTIALLY AT 0°, 5°, 10°, 15°, 90°, 95°, 180°, 185°, 270°, 275°, 350°, 355° FROM DATUM 0°

A3 THIS INSTRUMENTATION BOSS TO BE LOCATED CIRCUMFERENTIALLY ON DATUM 0°

A4 THESE INSTRUMENTATION BOSSES TO BE LOCATED CIRCUMFERENTIALLY AT 0°, 5° FROM DATUM 0°

A5 THESE INSTRUMENTATION BOSSES TO BE LOCATED CIRCUMFERENTIALLY AT 0°, 90°, 180°, 270° FROM DATUM 0°

A6 THERMOCOUPLE BRAZED THRU

A7 THERMOCOUPLE THRU CLEARANCE HOLE

A8 PRESSURE TUBE BRAZED OR WELDED THRU

A9 PRESSURE TUBE THRU CLEARANCE HOLE

A10 INSTRUMENTATION TUBES TO BE INSTALLED LONG ENOUGH TO REACH 4.50 AFT OF PLANE 'A' ALLOWANCE MUST THEN BE MADE FOR 4.25 EXTENSION GIVING SPACE TRAVEL.

A11 WELD PER WBS 18

A12 ELECTRON BEAM (E.B.) PER WBS 35

A13 BRAZE PER WBS 27 USING Ag-BA

A14 BRAZE PER WBS 27 USING NICROBRAZE MS 94539)

A15 BRAZE PER WBS 27 USING FILLMET NO. 7 (AMS 4786)

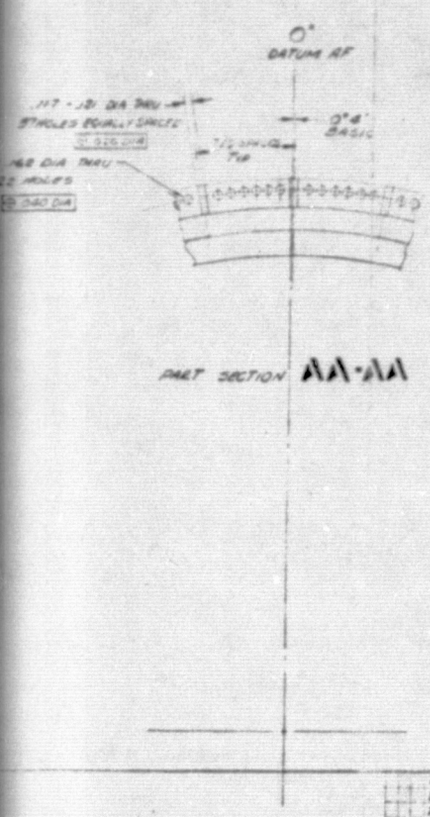

FOLDOUT FRAME 6

FOLDOUT FRAME 5

QTY REQD	ITEM NO	CODE IDENT NO	PART OR IDENTIFYING NO	NOMENCLATURE OR DESCRIPTION	SYM	ZONE
			← ASSY	PARTS LIST		

ORIGINAL PAGE IS
OF POOR QUALITY

FOLDOUT FRAME 1

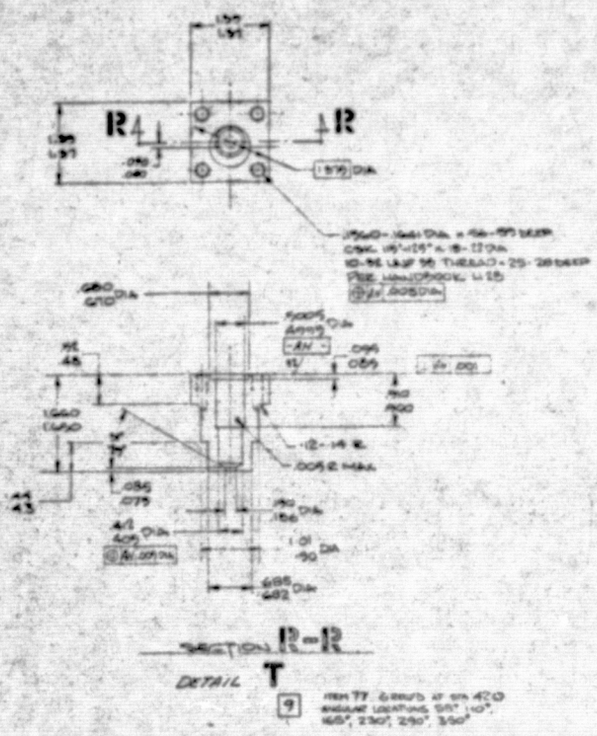

DETAIL T

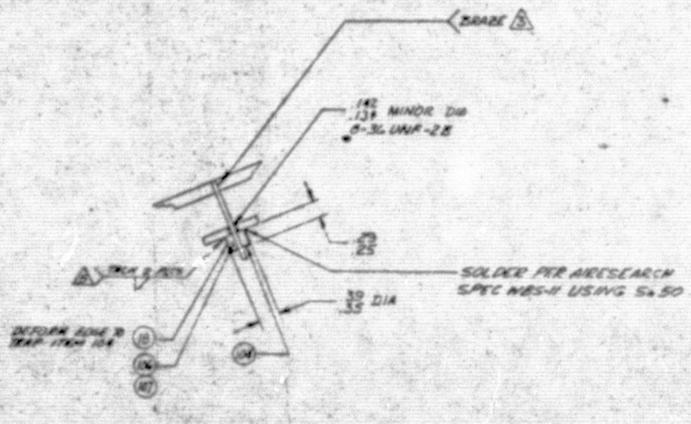

DETAIL L

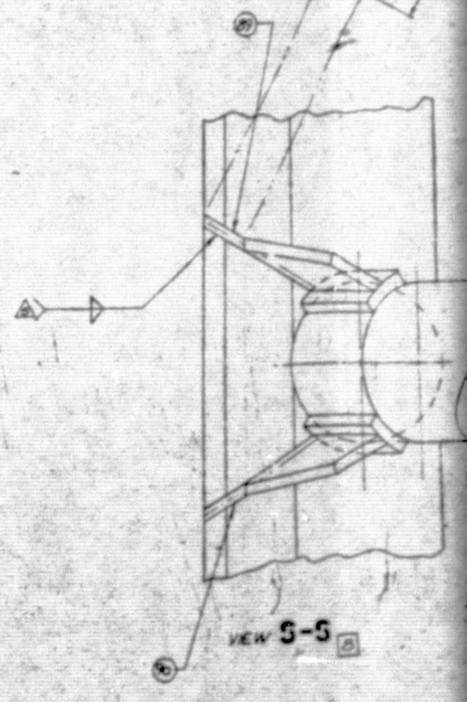

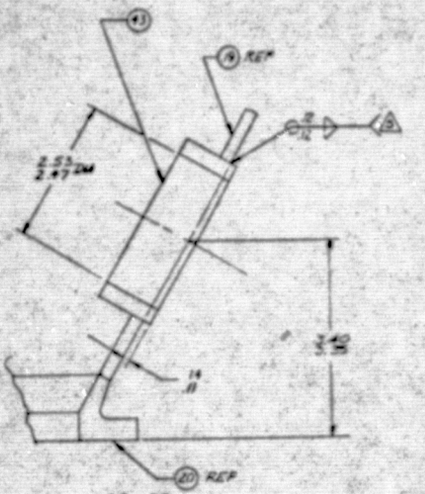

SECTION K-K 4

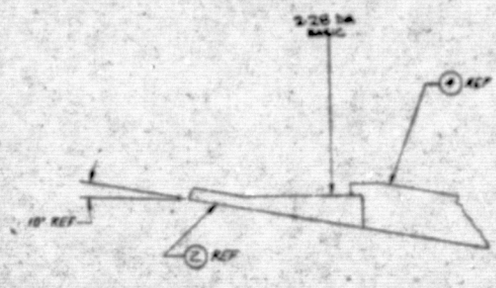

DETAIL F 12 SCALE 4:1

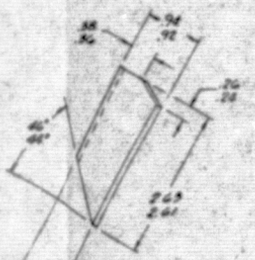

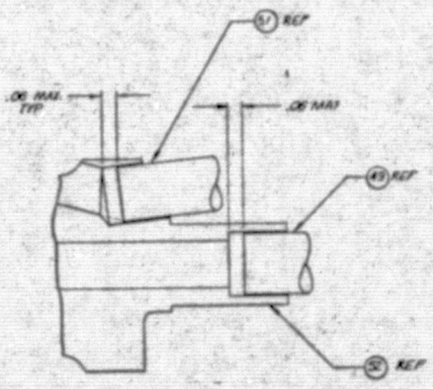

DETAIL P 12 SCALE 4:1

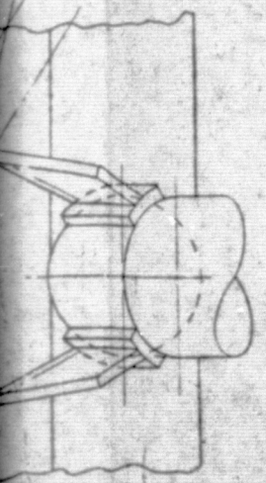

S-S 8

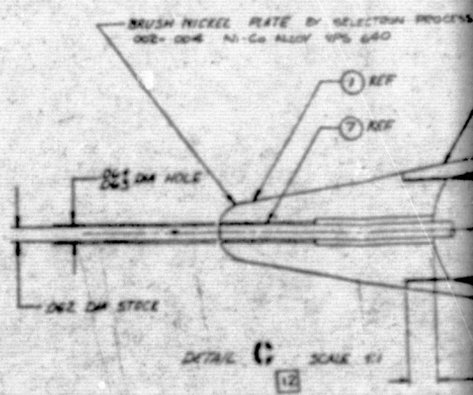

DETAIL C 12 SCALE 4:1

FOLDOUT FRAME 2

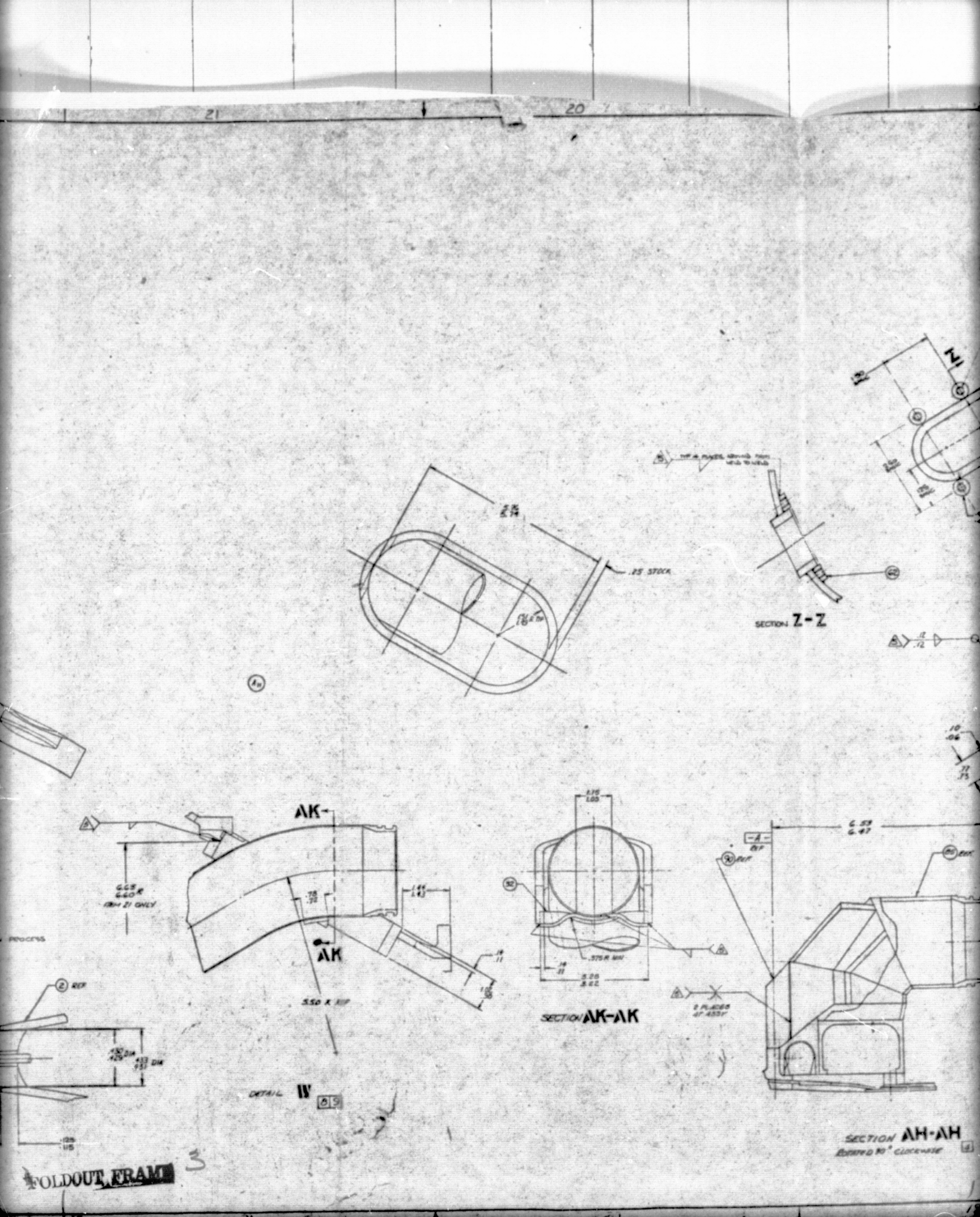
.25 STOCK
SECTION Z-Z
AK
5.50 R REF
DETAIL IV
SECTION AK-AK
.375 R MIN
SECTION AH-AH
ROTATED 90° CLOCKWISE
FOLDOUT FRAME

SECTION Z-Z
SECTION V-V
5
DETAIL AE
SCALE 4/1
DETAIL H
9
SECTION AH-AH
ROTATED 90° CLOCKWISE
4
DETAIL AF
SCALE 8/1
FOLDOUT FRAME 4
960512
2

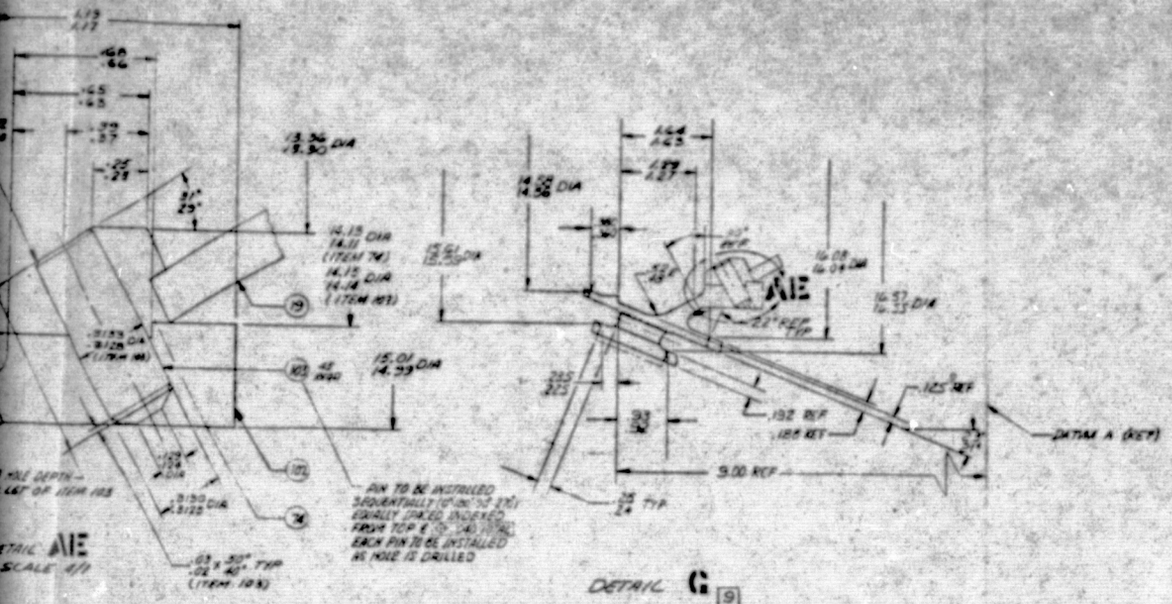

DETAIL G [9]

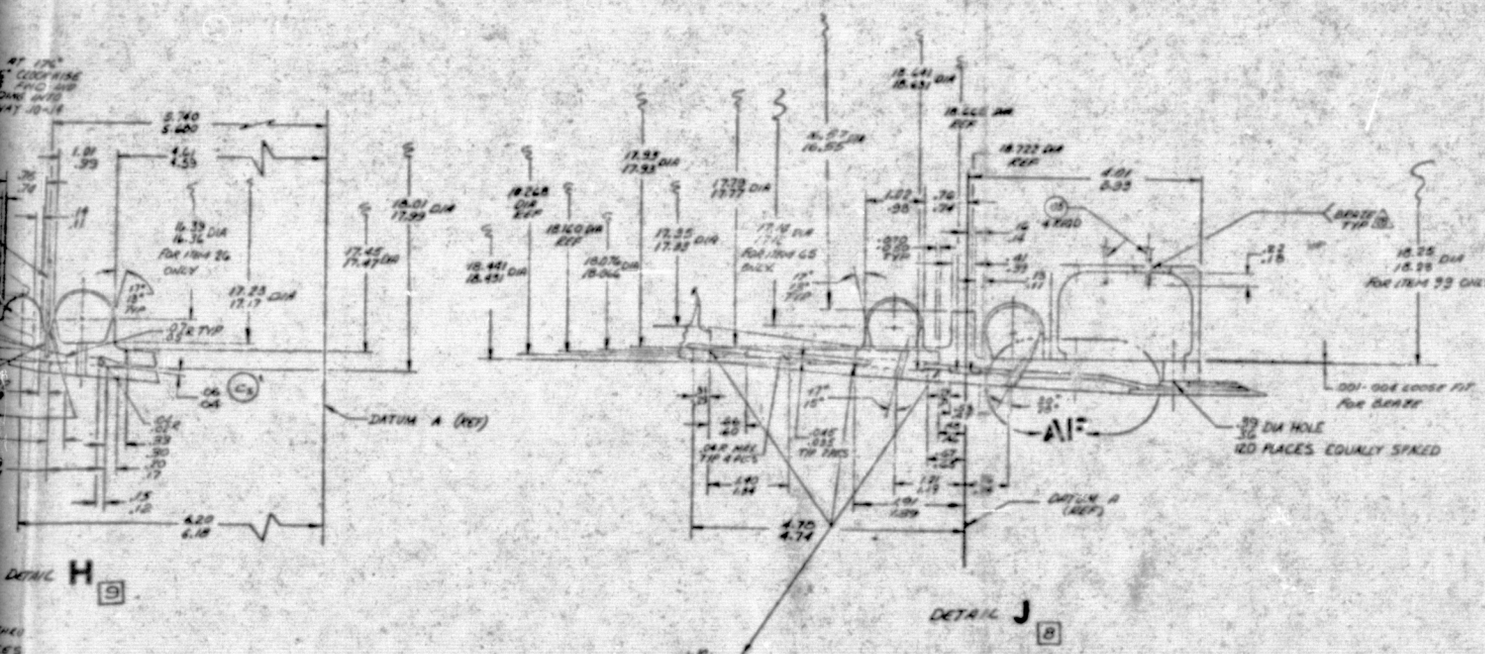

DETAIL H [9]

DETAIL J [8]

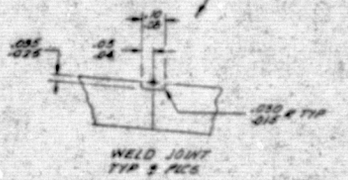

FOLDOUT FRAME

NOTES: UNLESS OTHERWISE SPECIFIED

NEXT ASSY	USED ON		
APPLICATION			

950512 12

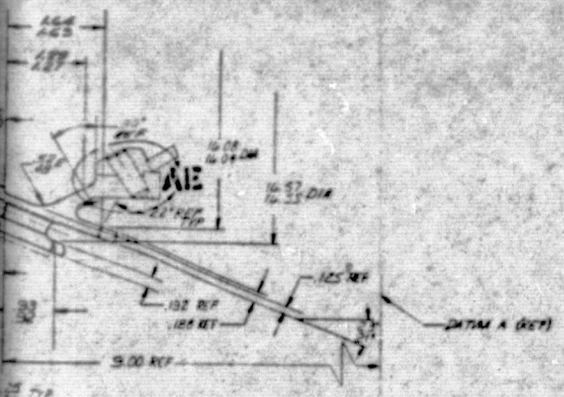

DETAIL G [9]

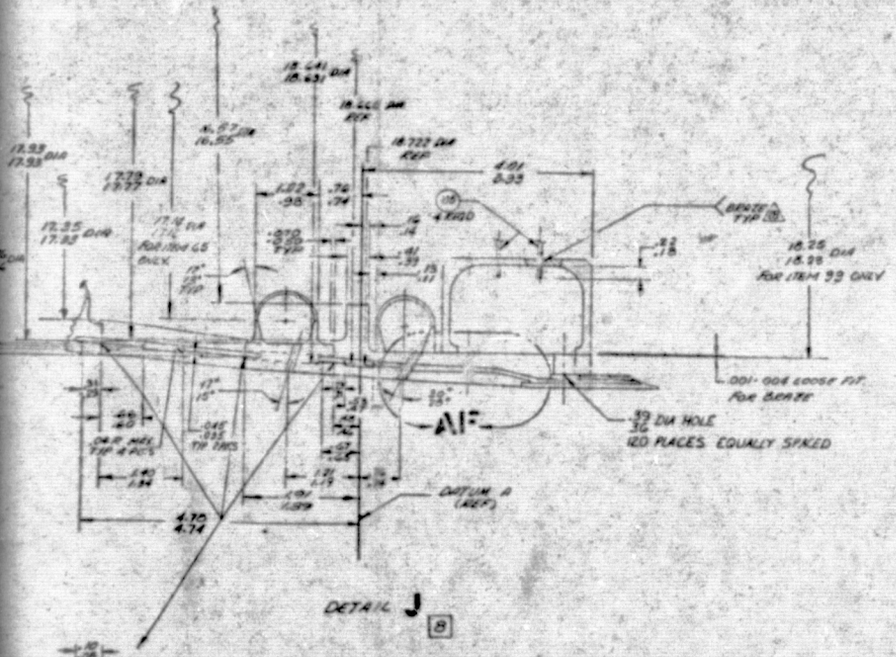

DETAIL J [8]

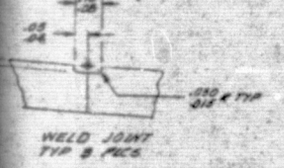

ZONE	LTR	DESCRIPTION	DATE	APPROVED
3/8	A	[illegible]	[illegible]	[illegible]
16	B	91. ADDED (18.35-18.37)-(18.59 DIA) REF. ADDED .005-.007 RAD. TYP. 92. ADDED .05-.07 RAD. TYP. ADDED .05-.07 CHAM. TYP. 93. ADDED (.85-.91) DIA. TYP. .005-.009 RAD. TYP. 94. ADDED (.70-.74) DIA. TYP. (18.72 REF) 95. ADDED (.30-.34) DIA. TYP. (20.51 REF) 96. ADDED VIEW K	[illegible]	[illegible]
7/8	C	DELETED VIEW "C-C" (3-2) TYP AND (8-1) TYP		
8/8	F	ADDED VIEW "F"		
7/8		ADDED ALL AROUND SYMBOL TO HOLE CALLOUT		
3/8		MARKED ⚠ ⚠		
2/8		MODIFIED NICKEL PLATING		
7/8		ADDED VIEW DEPICTING ITEMS 61 & 62	[illegible]	[illegible]
4/8	J	ADDED HOLE "K" REF. VIEW L	[illegible]	[illegible]
6/8	H	a) ADDED DIMS TO VIEW F DEPICTING ITEMS 31, 34, 35, 63, 64, 65, 66, 67		
6/8		b) ADDED ITEMS 70, 72, 74 TO VIEW G		
7/8		c) ADDED DIMS TO VIEW M DEPICTING ITEM 216		
7/8		d) ADDED VIEW AS DEPICTING ITEMS 74-76		
5/8		e) ADDED DIMS IN VIEW J OUT OF ALIGNMENT		
2/8		f) ALTERED DIMS OF ITEMS 37 & 38 IN NEW S-S AND PROJECTED VIEW	[illegible]	[illegible]
8/8	N	a) REVISED TOLERANCE .004 IN (.245-.249)	[illegible]	[illegible]
7/8		b) REVISED .791-.811 TO .795-.811	[illegible]	[illegible]
3/8	S	[illegible]	[illegible]	[illegible]
7/8	T	[illegible]	[illegible]	[illegible]
7/8	U	[illegible]	[illegible]	[illegible]
7/8		[illegible]	[illegible]	[illegible]
8/8	Y	21. 18.54-18.58 DIA (18.43-18.51 DIA)		
4/8		22. ADDED DIM. .960-.980		
8/8		23. .093-.098 (.085-.090) DIA		
2/8		24. ADDED SECTION AA-AA		
4/8		25. REVISED DIM. .030-.050 x 45°-60° TYP 8 PLACES		
4/8		26. DETAIL AF. ADDED FEATURE CONTROL SYMBOL	3-30-70	
7/8	Z	1. DELETED NOTE 19 "ALL DIM. TO BE HELD AFTER FINAL PLATING"		
4/8		2. ADDED DIMENSIONS 4.34-4.36 AND .06-.10	4-2-70	[illegible]
4/8	AA	INCORPORATED ECN DATED 5-15-70	[illegible]	[illegible]
4/8	AB	INCORPORATED ECN DATED 5-25-70	[illegible]	[illegible]
4/8	AC	INCORPORATED ECN DATED 6-1-70	[illegible]	[illegible]
4/8	AD	INCORPORATED ECN DATED 6-5-70	[illegible]	[illegible]
4/8	AE	INCORPORATED ECN DATED 6-15-70	[illegible]	[illegible]
4/8	AF	INCORPORATED ECN DATED 6-17-70	[illegible]	[illegible]
4/8	AG	INCORPORATED ECN DATED 7-1-70	[illegible]	[illegible]
4/8	AA	ADDED ITEMS 104, 105, 106 & 107 & ZIP AND DIMS PERTAINING TO SAME	[illegible]	[illegible]

FOLDOUT FRAME 6

4 SEE SHEET 1 FOR CONTROLLING CHANGE LETTER

QTY REQD	ITEM NO.	SPEC NO.	PART OR IDENTIFYING NO.	NOMENCLATURE OR DESCRIPTION	SYM ZONE
		ASSY		PARTS LIST	

NOTES: UNLESS OTHERWISE SPECIFIED

APPLICATION

AIRESEARCH MANUFACTURING COMPANY

INLET SPIKE ASSEMBLY, NON-REPAIRABLE

SIZE	FSCM NO.	DWG NO.	REV
J	70210	950512	

SCALE FULL SHEET 2 OF 2

950512 2

16 15 14

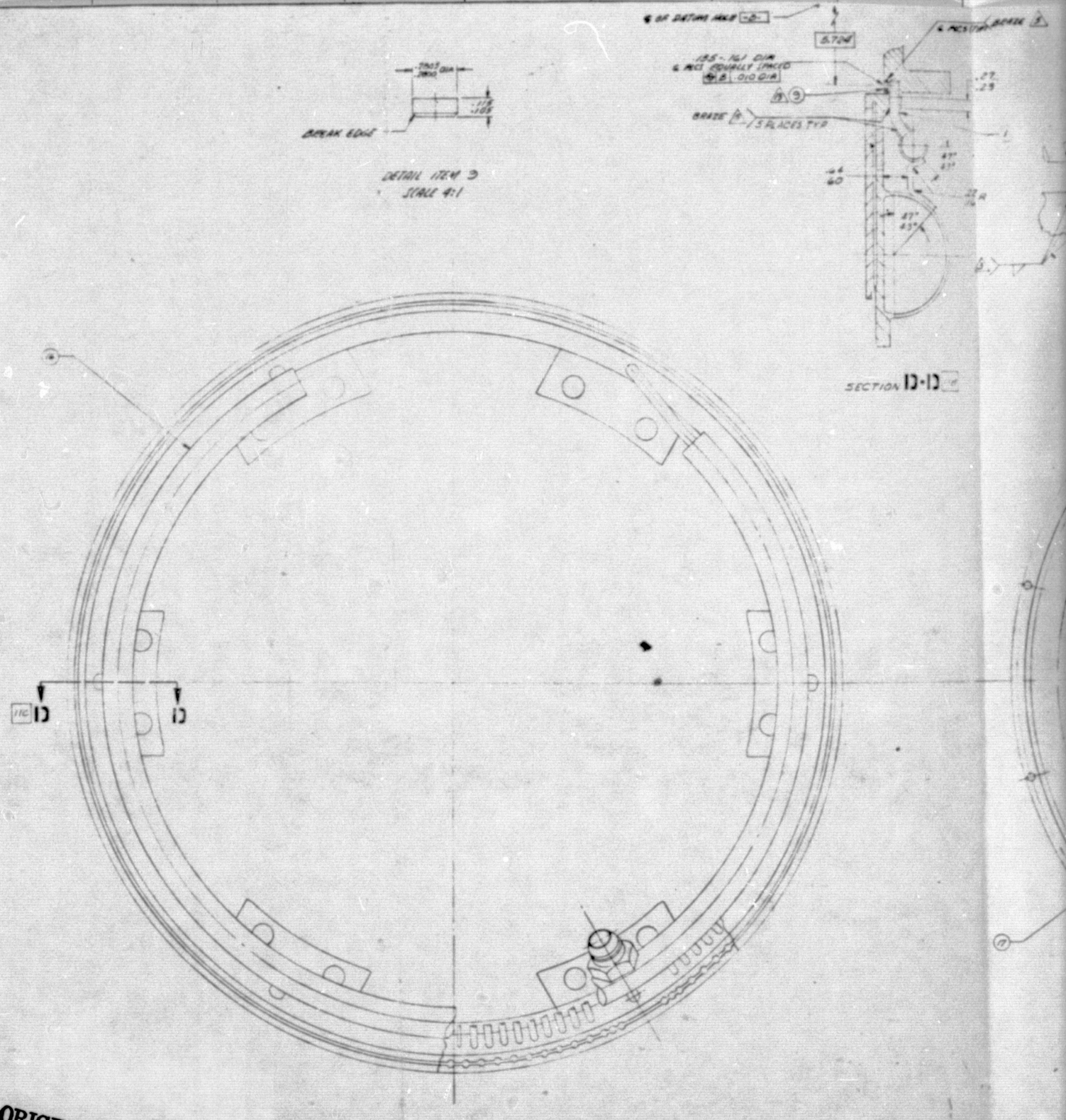

ORIGINAL PAGE IS
OF POOR QUALITY

FOLDOUT FRAME

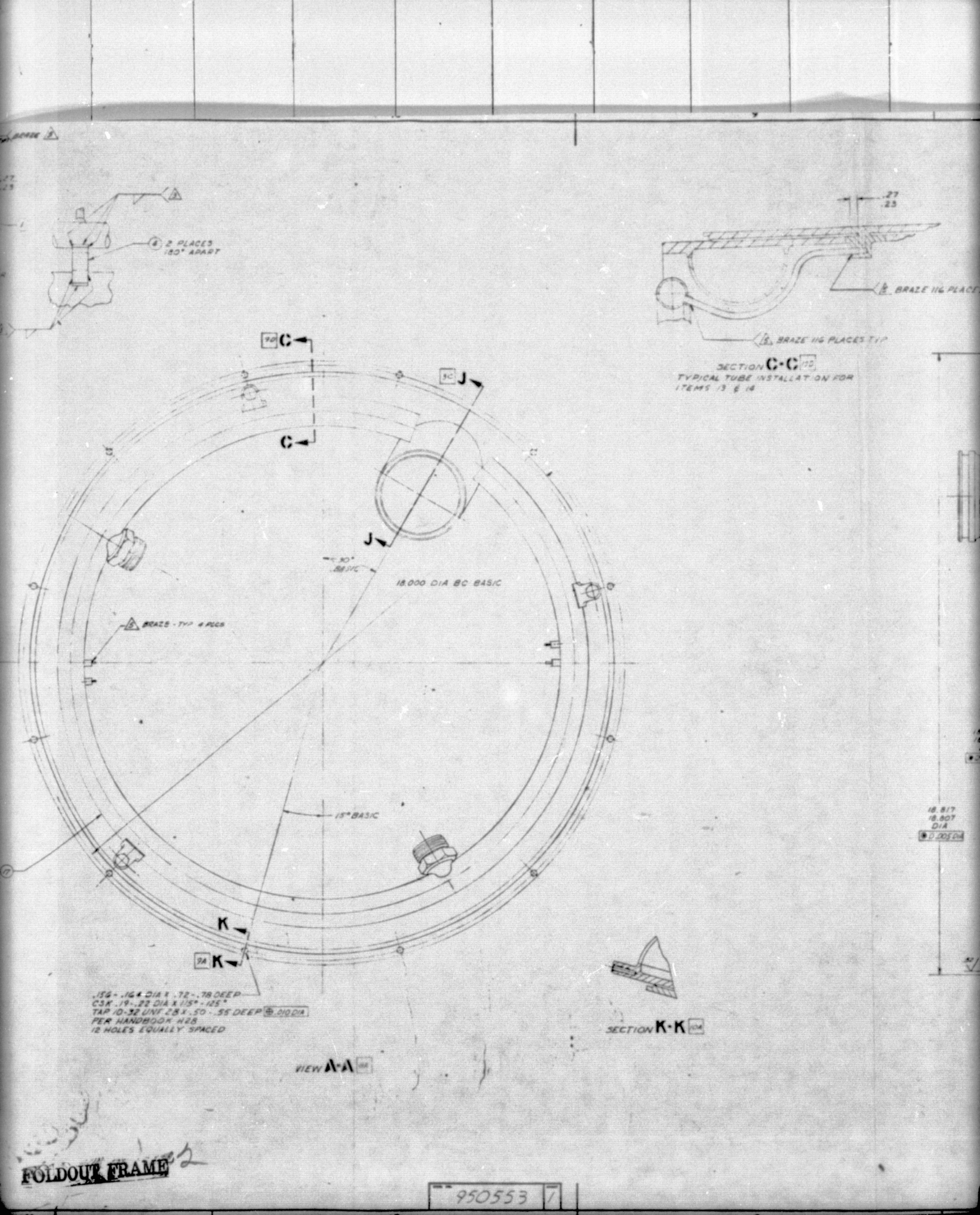
2 PLACES 180° APART
.27 .23
BRAZE 116 PLACES
BRAZE 116 PLACES TYP
SECTION C-C
TYPICAL TUBE INSTALLATION FOR ITEMS 13 & 18
C
J
30° BASIC
18.000 DIA BC BASIC
BRAZE - TYP 4 PLCS
15° BASIC
K
.154 - .164 DIA X .72 - .78 DEEP C'SK .19 - .22 DIA X 115° - 125° TAP 10-32 UNF 2B X .50 - .55 DEEP Ⓜ .010 DIA PER HANDBOOK H28 12 HOLES EQUALLY SPACED
VIEW A-A
SECTION K-K
18.817 18.807 DIA
.005 DIA
FOLDOUT FRAME 2
950553

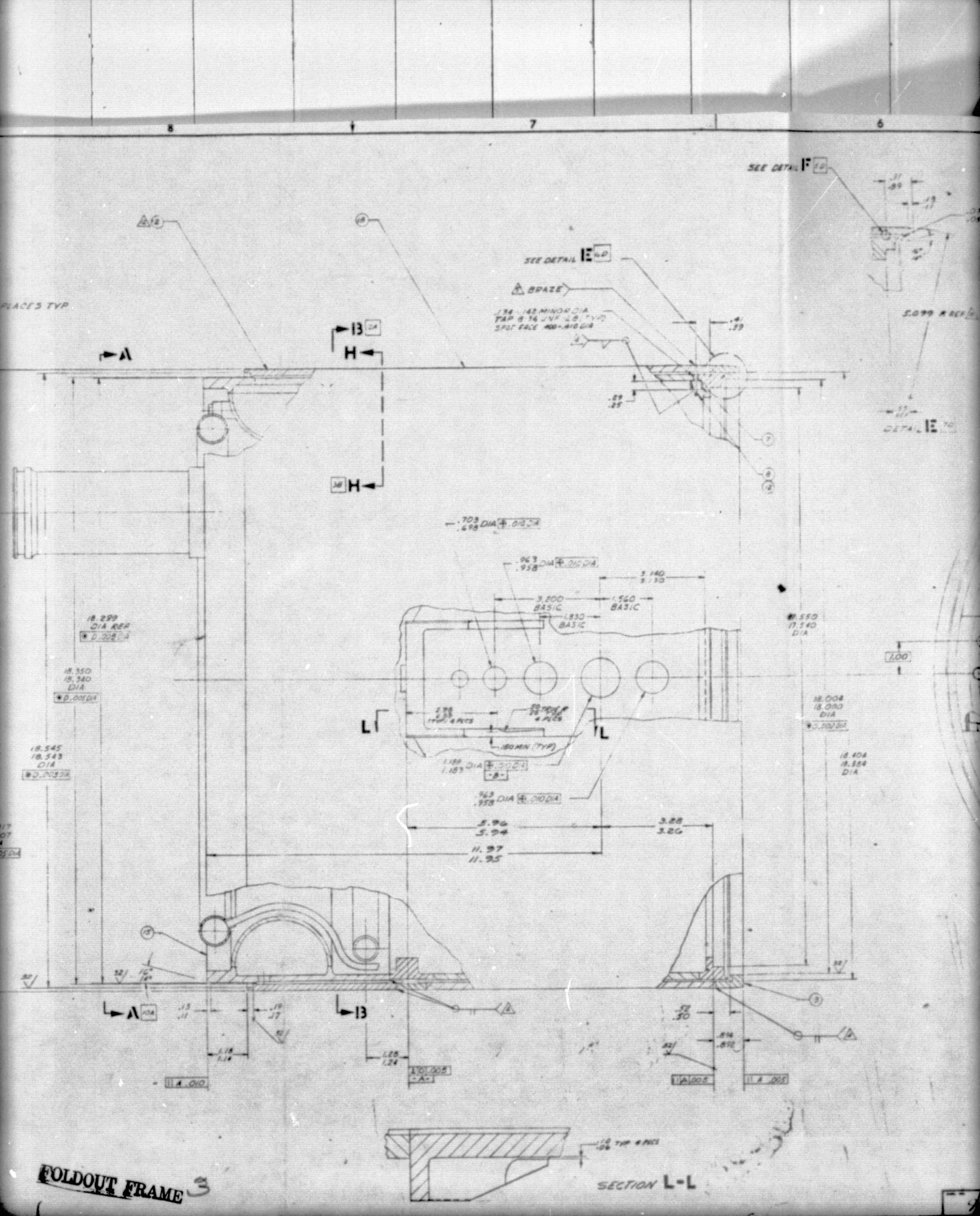
SEE DETAIL F
SEE DETAIL E
BRAZE
PLACES TYP
A
B
H
L
18.299 DIA REF
18.350 18.340 DIA
18.545 18.543 DIA
18.550 17.540 DIA
18.004 18.000 DIA
18.404 18.384 DIA
.703 .698 DIA
.963 .958 DIA
3.140 3.130
3.300 BASIC
1.560 BASIC
1.830 BASIC
1.00
.180 MIN. (TYP)
5.96 5.94
3.28 3.26
11.97 11.95
.10 .06 TYP 4 PLCS
SECTION L-L
FOLDOUT FRAME 3

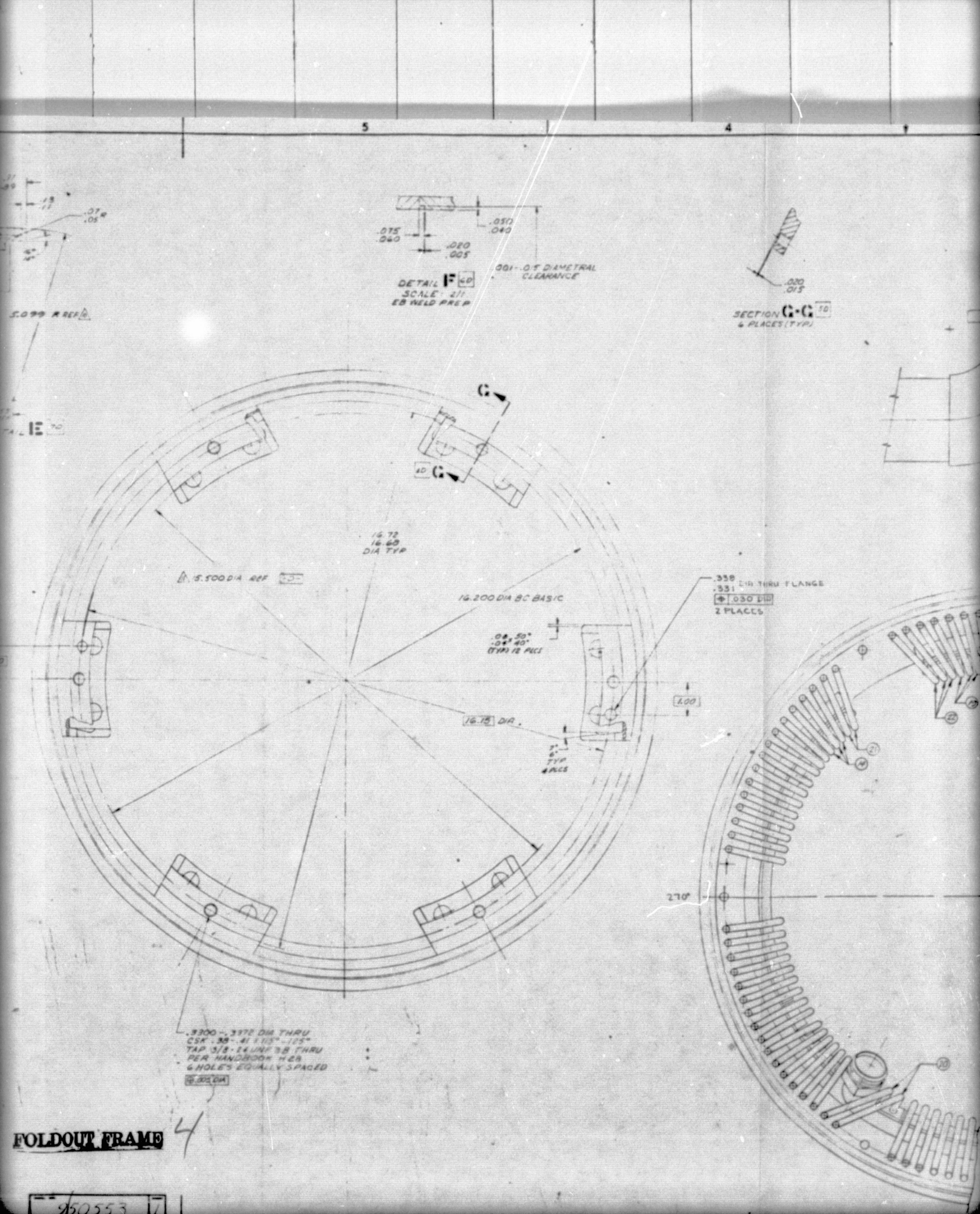
5
4
.075
.040
.050
.040
.020
.005
.001 - 0.5 DIAMETRAL CLEARANCE
DETAIL F (6.0)
SCALE: 2/1
EB WELD PREP
.020
.015
SECTION G-G (10)
6 PLACES (TYP.)
5.099 REF (6)
DETAIL E (7.0)
G
G (4.0)
16.72
16.60
DIA TYP
15.500 DIA REF (5.5)
16.200 DIA BC BASIC
.338
.331 DIA THRU FLANGE
.030 M B
2 PLACES
.04 50°
.04 40°
(TYP) 12 PLCS
4.00
16.15 DIA.
3°
6°
TYP
6 PLCS
270°
.3300 - .3372 DIA THRU
CSK .38 - 41 X 113° - 125°
TAP 3/8 - 24 UNF 3B THRU
PER HANDBOOK H-28
6 HOLES EQUALLY SPACED
.005 M A
FOLDOUT FRAME
4

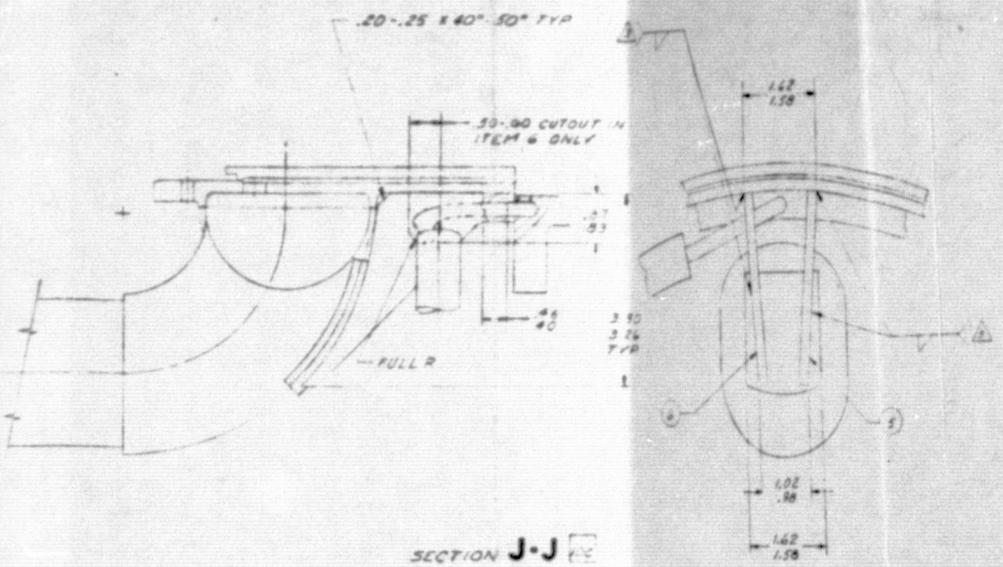

SECTION J-J
ROTATED 30° CCW

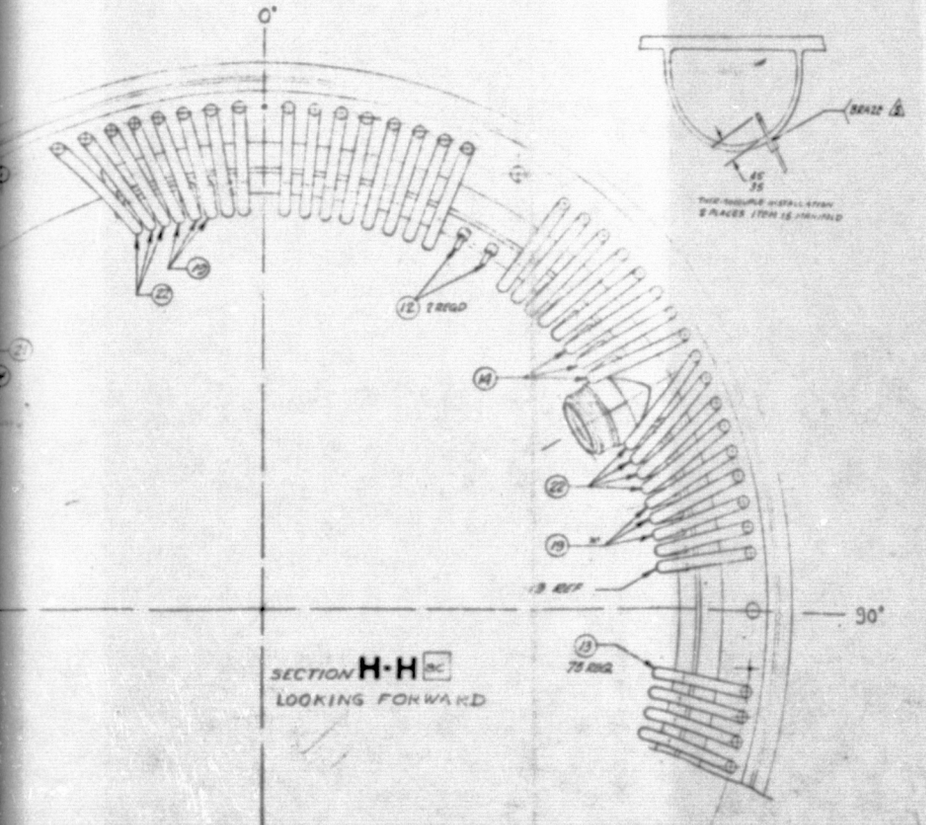

SECTION H-H
LOOKING FORWARD

TABLE OF INSTRUMENTATION

HYDROGEN MANIFOLD	STATION LOCATION	54.00	54.50	55.25	56.00	60.00
TH COUPLE STATIONS	TYPE	THROUGH STAT. PRESS TH COUPLE	STATIC PRESS	TH COUPLE		
2	2	QUANTITY	1	4	1	4
90°-270°	85°-275°	CIRCUMFERENTIAL LOCATION	0°	0° 90° 180° - 270°	0°	82°30' 178°30' 262°30' 358°30'

FOLDOUT FRAME 5

FOLDOUT FRAME

ITEM	QTY	PART NO.	DESCRIPTION
22	1	950570-4	TUBE, INJECTOR 2 PASS
21	1	950570-3	TUBE, INJECTOR 3 PASS
20	1	950570-1	TUBE, INJECTOR 4 PASS
19	1	950570-2	TUBE, INJECTOR
18	1	950573-1	MANIFOLD ASS'Y, HYDROGEN
17	1	950569-1	MANIFOLD ASS'Y, WATER
16	1	950569-2	MANIFOLD ASS'Y, FUEL
15	1	950599-1	MANIFOLD, FUEL
14	1	950530-1	TUBE, INJECTOR SUPPORT
13	1	950554-1	TUBE, INLET FUEL STRAIGHT
12	2	950607-2	THERMOCOUPLE
11			
10			
9	23		SPACER
8	18		TUBE, STATIC PRESSURE
7	1		BOSS
6	1		GUSSET
5	1		GUSSET
4	1		BRACKET
3	1		BRACKET
2	1		RING, END
1	1		RING

LIST OF MATERIAL

REVISIONS			
APPLICATION			

INNERBO... VON-RE...

950553

J 70210

SCALE

NOTES: UNLESS OTHERWISE SPECIFIED

1. ITEM 3 TO BE MACHINED AS ONE WITH ITEM 19.
2. SUPPORT ITEM 2 DURING PRESSURE TESTING
3. MEASURE PILOT DIA ON NOZZLE PLUG 950537 E MACH'G THIS DIA TO GIVE .000 +.002 LOOSE FIT DIA
4. MACHINE SURFACE FLUSH WITH MATING SURFACE WITHIN .005 R MAX OF NOZZLE PLUG WHEN BOLTED TOGETHER
5. √ ALL OVER
6. CHEMICAL COMP. OF N-200 PER ASTM B-160
7. PART TO BE STAMPED OR TAGGED NASA - RAMJET R&D
8. DIMENSIONING & TOL PER USASI Y14.5-1966
9. BRAZE PER MBS-27 USING ASTM 84y-84
10. WELD PER MBS-35 (ELECTRON BEAM)
11. WELD PER MBS-18 (TIG)
12. PRESSURE TEST HYDROGEN PASSAGES TO 700 PSIA. LEAKAGE: 1×10^{-7} CC/SEC. HELIUM AT 1 ATM DIFF
13. PRESSURE TEST WATER PASSAGES TO 300 PSIA BEFORE FINAL MACHINING

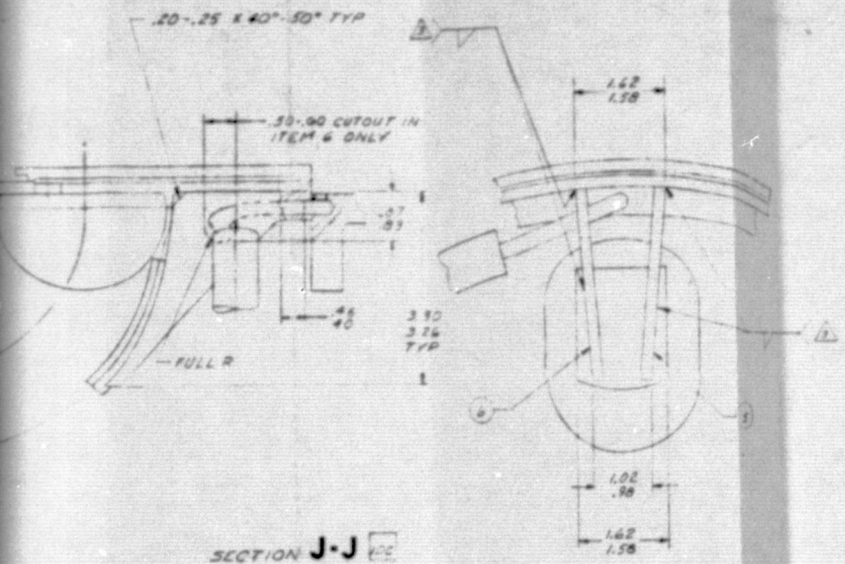

SECTION J-J
ROTATED 30° CCW

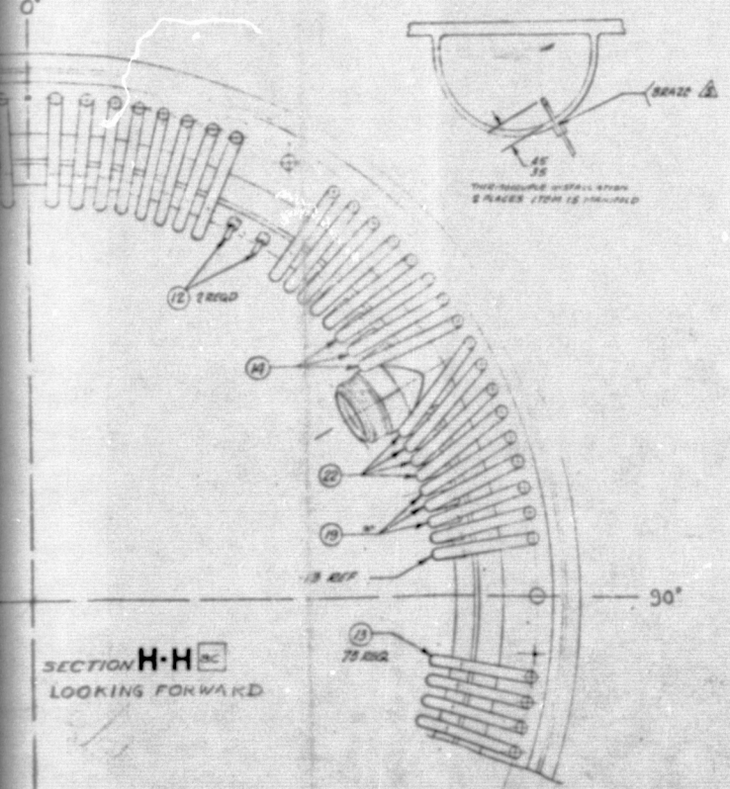

SECTION H-H
LOOKING FORWARD

REVISIONS				
LTR	ZONE	DESCRIPTION	DATE	APPROVED
A	10	[illegible]		
B	10	AS PER PURCHASE SPECIFICATION ADDED ITEM 3 AS [illegible] [illegible] [illegible] ADDED ADDED NOTE 4 ADDED ITEM 3 IN LIST		
C	10	ITEM 3 QUALITY TO BE 90 ITEM 19 QUANTITY SHALL BE ITEM 19 QUANTITY SHALL BE ADDED ITEM 20, 21 & 22 ADDED SECTION H-H .50-.90 WAS .90-.52 SECTION H-H REVISED TO SHOW ITEM 19, 20, 21 & 22 ADDED DIM 3.26-3.38, 3.14-3.34, .99-1.97 1.299-1.410 WAS 1.258-1.300 CONCENTRICITY ABOUT .005 ADDED SYMBOLS [illegible] [illegible] [illegible]		

TABLE OF INSTRUMENTATION

HYDROGEN MANIFOLD	STATION LOCATION	54.00	54.50	55.25	56.00	60.00	64.80	64.80
TH COUPLE	STATIC PRESS	TYPE	TH COUPLE	STAT. PRESS	TH COUPLE	STATIC PRESS	TH COUPLE	TH COUPLE	STAT. PRESS
2	2	QUANTITY	1	4	1	4	3	1	1
90°-270°	95°-275°	CIRCUMFERENTIAL LOCATION	0°	0° - 90° 180° - 270°	0°	82°30', 178°30', 0°, 20°; 264°30', 358°30', 240°	5°	0°	

FOLDOUT FRAME 6

ITEM NO.	PART NO.	QTY	DESCRIPTION	CODE IDENT	MATERIAL AND SPECIFICATION	ZONE
			ASSY		LIST OF MATERIAL	
22	950570-1		TUBE, INJECTOR 8° OFFSET			
21	950570-3		TUBE, INJECTOR 5° OFFSET			
20	950570-2		TUBE, INJECTOR 11° OFFSET			
18	950510-2		TUBE, INJECTOR STRAIGHT			
17	950571-1		INNERBODY, REAR			
16	950561-1		MANIFOLD ASSY, HYDROGEN			
15	950469-1		MANIFOLD ASSY, WATER			
14	950599-1		INNERBODY, FWD			
13	950530-1		TUBE, INJECTOR STRAIGHT			
12	950556-1		TUBE, INJ. FOR THERMOCOUPLE			
10	950467-2		THERMOCOUPLE			
9		-23	SPACER		3/8 DIA BAR	
8		-19	TUBE, STATIC PRESSURE			
7		-17	BOLT			
6		-11	GUSSET			
5		-9	SPACER			
4		-5	BRACKET			
3		-7	RING, END			
2		-5	RING			
1		-1	[illegible]			

UNLESS OTHERWISE SPECIFIED DIMENSIONS ARE IN INCHES. MACHINED FILLET RADII .015-.030. SURFACE ROUGHNESS PER MIL-STD-10. DIMENSION LIMITS INDICATED PLUS/MINUS UNLESS OTHERWISE SPECIFIED.	SIGNATURES	DATES	AEROJET-GENERAL CORPORATION	
			INNERBODY ASSY, NON REPAIRABLE	
			SIZE: J	FSCM NO: 70210
			DWG NO: 950553	
			SCALE:	SHEET

950553 1

FOLDOUT FRAME 5

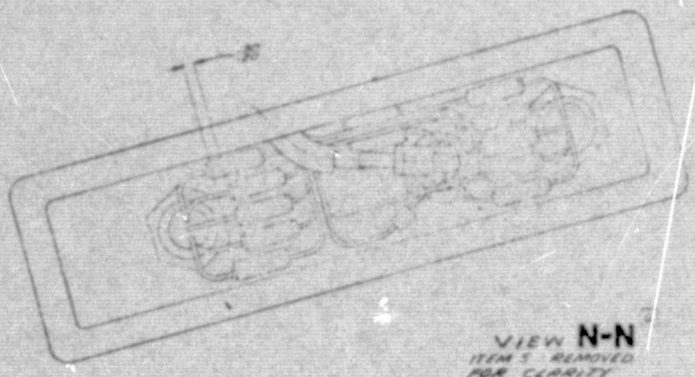

VIEW N-N
ITEM 5 REMOVED FOR CLARITY

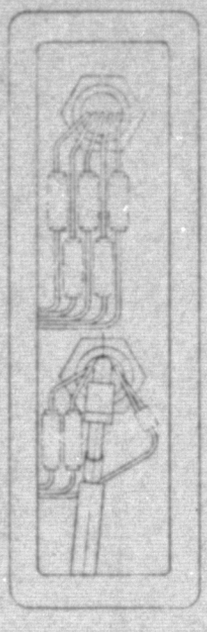

VIEW M - M
ITEM 6 REMOVED FOR CLARITY

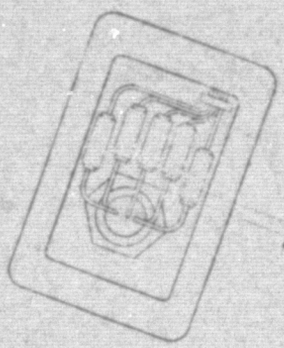

VIEW P - P
ITEM 9 REMOVED FOR CLARITY

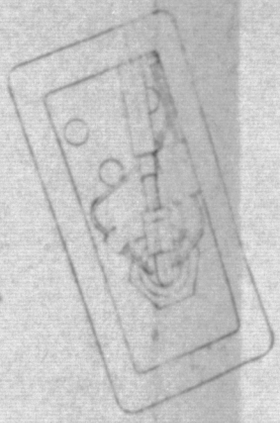

VIEW P - P
ITEM 8 REMOVED FOR CLARITY
TYPICAL 2 PLACES

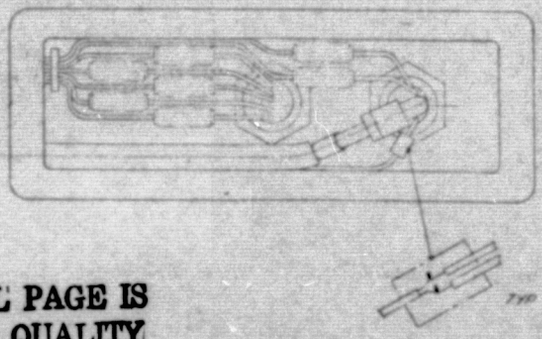

TYP 5 PLCS

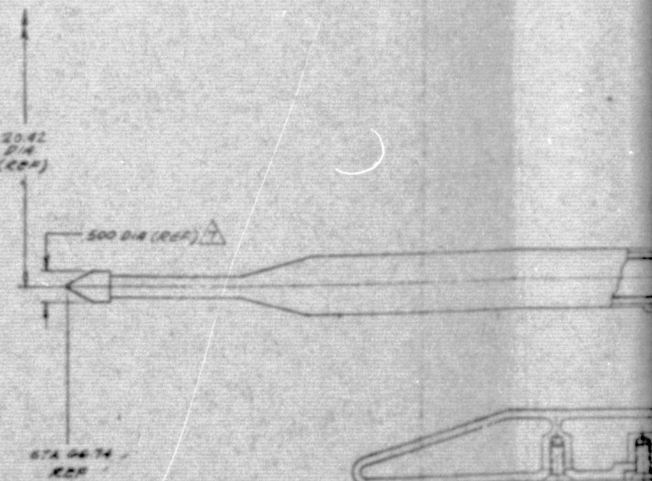

ORIGINAL PAGE IS
OF POOR QUALITY

VIEW L-L
ITEM 7 REMOVED FOR CLARITY

FOLDOUT FRAME

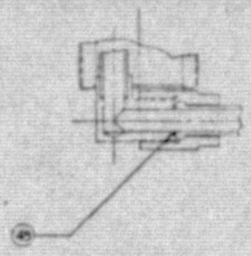

SECTION J-J
(TYPICAL 5 PLCS)
SCALE 2/1

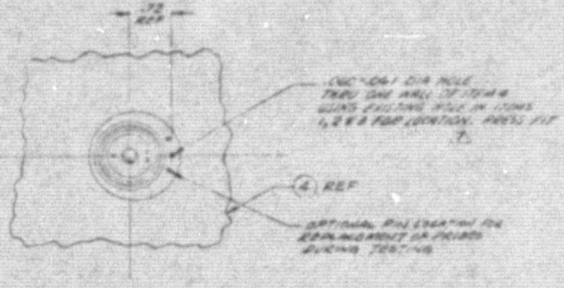

SECTION K-K
(TYPICAL 10 PLCS)

P-P
REMOVED
FOR CLARITY
(2 PLCS)

M

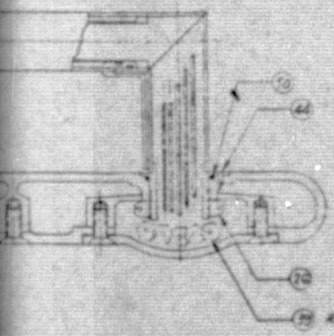

SECTION B-B
(TYPICAL 5 PLCS)

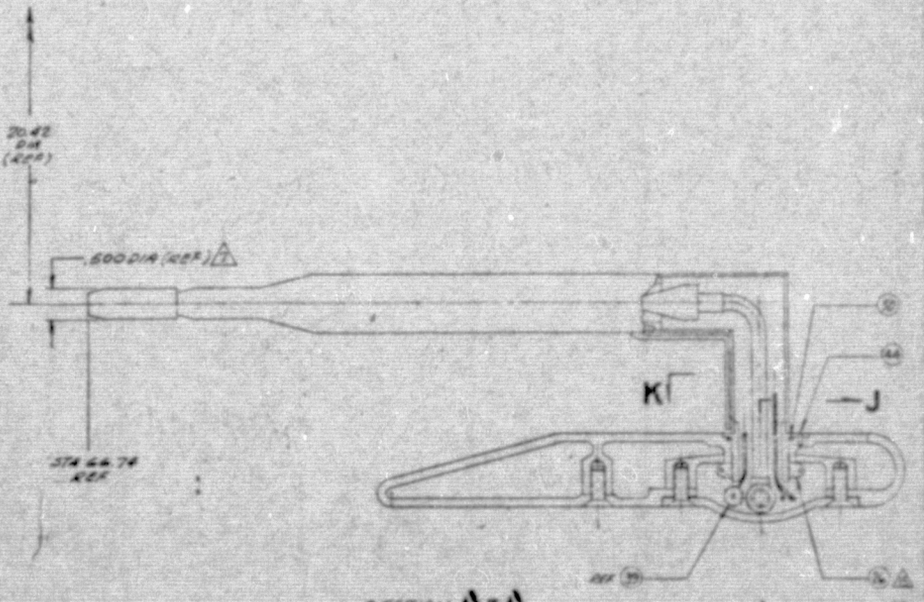

SECTION A-A
ROTATED 10° CW
(TYPICAL 5 PLCS)

K

950592

FOLDOUT FRAME 2

10 9 8

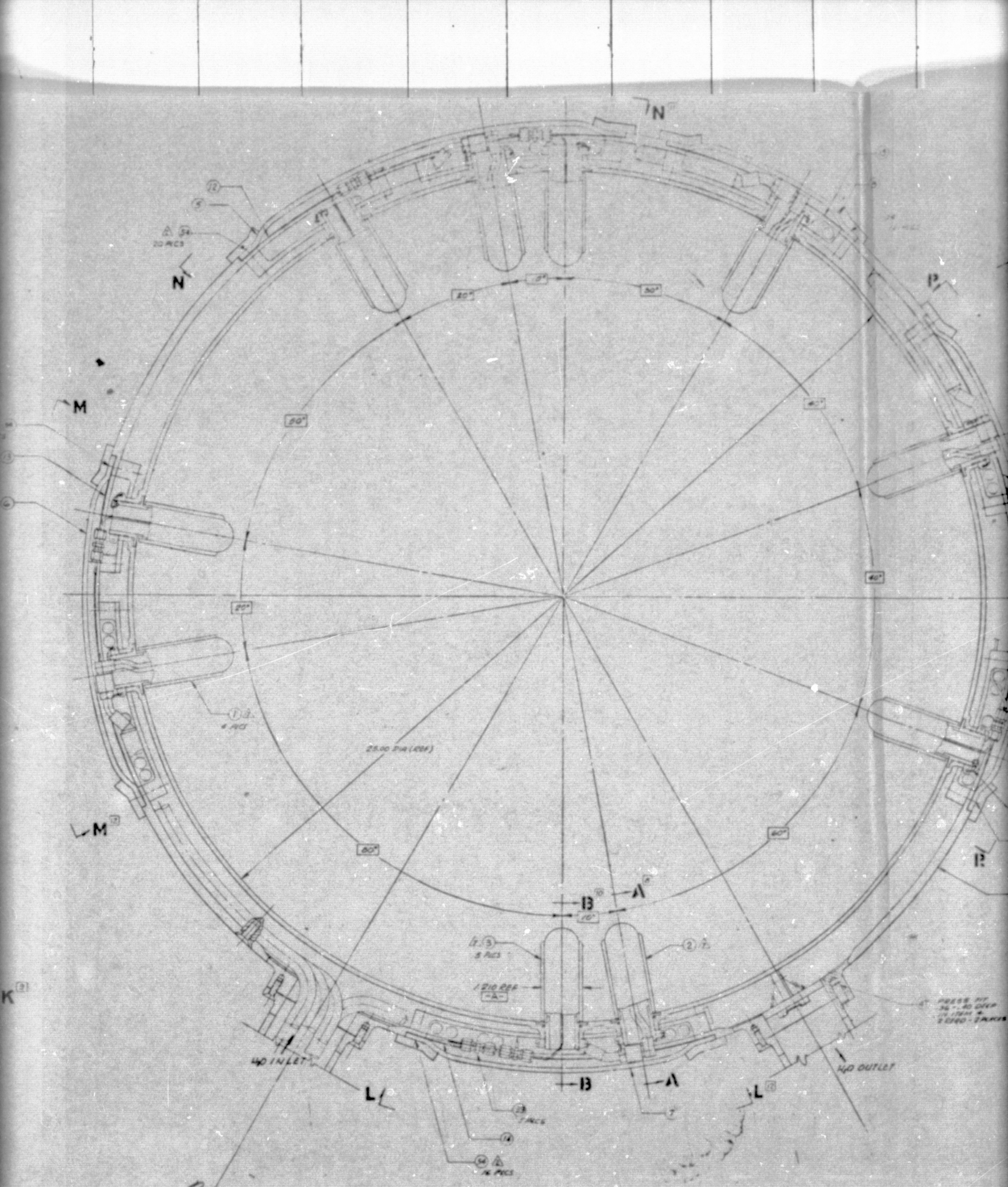

FOLDOUT FRAME 3

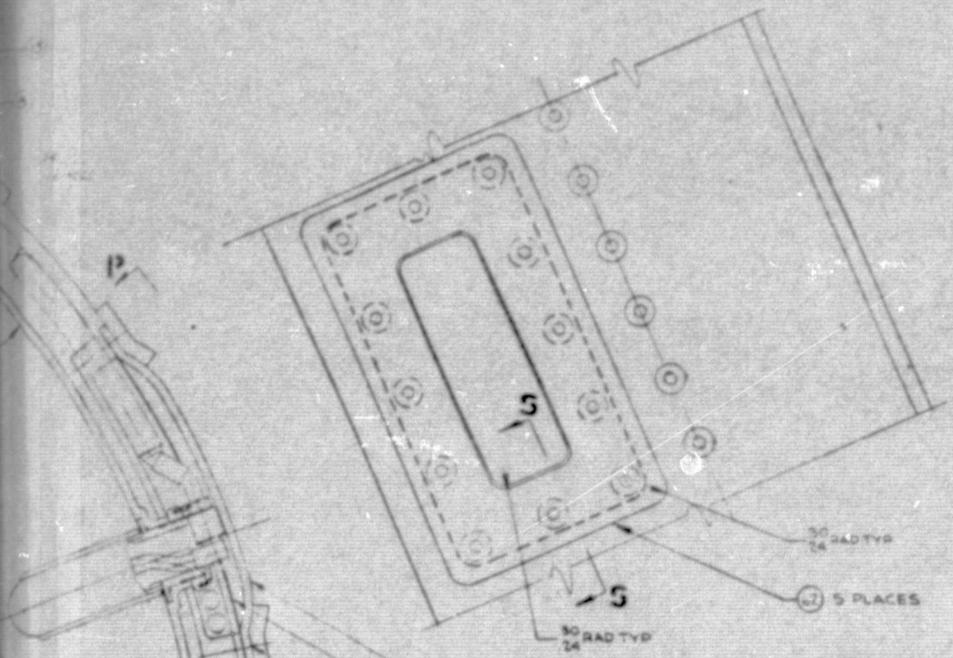

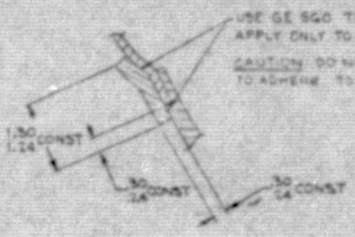

USE GE SG0 TO INSTALL ITEM 42
APPLY ONLY TO SURFACES SHOWN (TYP)

CAUTION: DO NOT ALLOW RTV 560 TO ADHERE TO SCREW HEADS

SECTION S-S
SCALE 1/1
ITEM 42 REF 5 PLACES
OPTION: WAVES ARE MOLDED MAY BE MORE THAN ONE PIECE

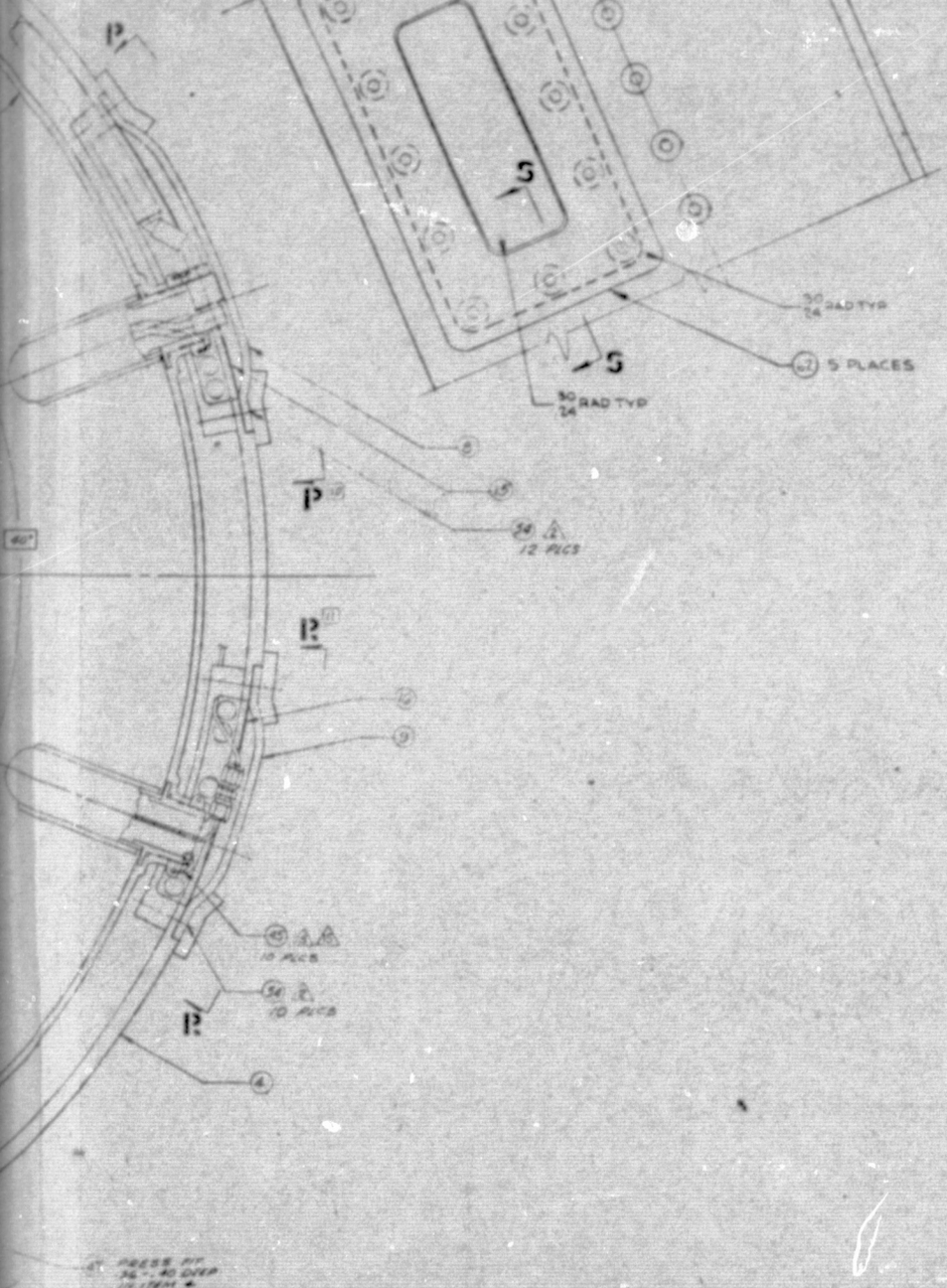

PRESS FIT
.24 - .40 DEEP
SEE ITEM 4
FOR TORQUE - SPECS

FOLDOUT FRAME 4

950592 F

STALL ITEM 61
FACES SHOWN (TYP)
LLOW 36560
EW HEADS

REV	ZONE	DESCRIPTION
		ADDED ITEM 61
		ADDED ITEM 61 TO FIELD OF DRAWING SHT 1 (1)
		ADDED NOTE 13
		ADDED SECTION B-B

ITEM	QTY	PART OR IDENTIFYING NO.	NOMENCLATURE OR DESCRIPTION	MATERIAL
61	AR	SS 560	RTV POTTING COMPOUND	
60		36-4A SIZE	FITTING	
59		-9	WIRE UNDER GALATA WOO LOPPER TX CONDUCTOR	
58		-1	THERMOCOUPLE UNDER CHROMEL-ALUMEL TX	
57		-5	SLEEVE (3100 X 15 I.D.) (1.0 D.) CHROMEL-ALUMEL	
56		-9	CONNECTOR, TUBE (FOR CHROMEL-ALUMEL WIRE)	
55				
54	51	33907 CR 187 3-8	SCREW	
53	24	33907 CR 187 4-40	SCREW	
52				
51	2	MS16998/3 NYLOK	CLAMP	
50		MS16998/3	SCREW	
49	1	4284 6 (1451) 1004-5	TAPE SEAL	
48	1	4284 6 (1451) 1004-5	TAPE SEAL	
47	1	4284 6 (1451) 1007-2	TAPE SEAL	
46		668-080-9108	PLUG, STRAIGHT	
45		MS 900-229	O-RING	
44		MS 20995 N40	WIRE, SAFE	
43		MS 9385-02	PIN, COTTER	
42		MS 24673-2	SCREW	
41		MS 9385-2	PLUG	
40		AN 924-10K	NUT	
39	0.1570	0.0174-316	FITTING, FERRULE	
38	0.1570	100-6-316	UNION	
37		950928-1	SLEEVE, TUBE	
36		950928-2	SLEEVE, TUBE	
35				
34				
33		950843-1	GASKET, BASE PLATE	
32		950871-1	INSTRUM. CELL COVER	
31		950818-1	GASKET, MOUNTING	
30		950817-1	GASKET, COVER, CELL	
29		950815-1	PLATE, BASE	
28		950812-2	LEG ASSY	
27		950812-1	LEG ASSY	
26		950798-1	NUT, DAM	
25		950820-14	TUBE ASSY	
24		950820-11	TUBE ASSY	
23		950820-13	TUBE ASSY	
22		950820-10	TUBE ASSY	
21		950820-16	TUBE ASSY	
20		950827-1	TUBE ASSY	
19				
18		950826-1	TUBE ASSY	
17		950815-1	FITTING, GAS SAMPLE	
16		950814-3	GASKET, COVER ACCESS	
15		950814-4	GASKET, COVER ACCESS	
14		950814-3	GASKET, COVER ACCESS	
13		950814-3	GASKET, COVER ACCESS	
12		950814-1	GASKET, COVER ACCESS	
11		950814-2	COVER, LEG	
10		950841-1	COVER, LEG	
9		950815-5	COVER, ACCESS	
8		950815-4	COVER, ACCESS	
7		950815-3	COVER, ACCESS	
6		950815-2	COVER, ACCESS	
5		950815-1	COVER, ACCESS	
4		950594-1	SUPPORT RING ASSY	
3		950595-1	PITOT STATIC PROBE	
2		950593-1	THERMOCOUPLE PROBE	
1		950592-1	INSTRUMENTATION RIG	

△9 APPLY PER ENGINEERING INSTRUCTIONS (DEPT 94-9)
△12 TORCH BRAZE PER WPS 27 USING AMS 4769
△13 AFTER BRAZING ITEM 38 IN PLACE INSPECT FOR SOUNDNESS OF BRAZE (A) VISUALLY (B) PENETRANT INSPECT PER MIL-I-6866
△14 AFTER BRAZING ITEM 37 IN PLACE PRESSURE TEST TUBE ASSY TO 95 ±5 PSIG NO LEAKAGE PERMITTED.
△15 TORQUE VALUE TO 95-105 INCH POUNDS
△16 FITTING & PASTENER TORQUE REQUIREMENTS PER AF 872
△18 BRAZE PER ALIGNMENT STRUCTURE DRG 27 USING AMS 4766 (SILVER 5) BRAZING ALLOY
△19 BRAZING GAP .002-.004 DIAMETRAL CLEARANCE
△20 BRAZE PER WPS 27 USING AMS 4777
△21 PRESSURE TUBES & THERMOCOUPLES SHALL BE SECURED WITH ASSOCIATED TERMINATION PER DRAWING EXCEPT THRU EXIT LEG, PLACE ITEM 26
△22 ITEM 59 SHALL BE BRAZED IN PLACE - 2 PASS PER SCHEDULE
△23 PRESSURE TEST ASSY PRIOR TO FINAL INSTALLATION AND BRAZE TO THE PLATE
△24 FOLLOWING OPERATIONS TO BE WITHIN 1.000 TOTAL OF BASE FOR POSITION WITH RESPECT TO DATUM A AFTER FINAL INSTALLATION
△25 IDENTIFICATION MARKING PER ARCAIR CLASS 1 (USING 5 INCH CHARACTERS)
△26 PROBE SHAFTS WHERE ARE TO BE SEALED (ITEM 48)
△27 THERMOCOUPLE JUNCTION PER CALIBRATION INSTRUCTION
△28 BRAZE PER MIL-B-7883 USING (SILVER) AMS 34850
△29 TORQUE VALUE TO 75-85 INCH POUNDS
△30 TORQUE VALUE TO 30-40 INCH POUNDS

FOLDOUT FRAME

UNLESS OTHERWISE SPECIFIED	NAME	DATE
DRAWN		
CHECKED		
ENGR APPR		
MFG APPR		
COMPTROLLER		

NORTH AMERICAN MANUFACTURING COMPANY

INSTRUMENTATION RIG
HYPERSONIC RESEARCH ENGINE
(B-1 M)

SIZE	CAGE NO.	DRAWING NO.	SHEET
J	70210	950592	

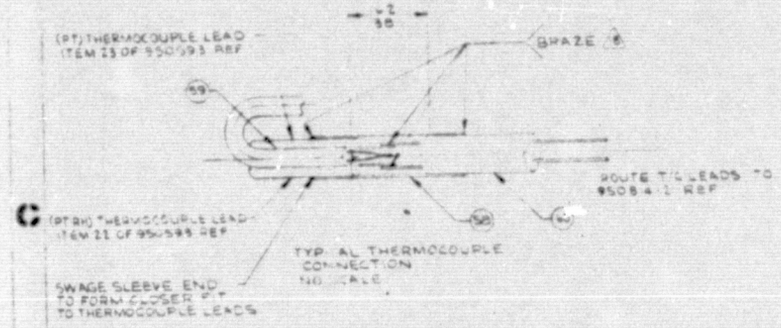

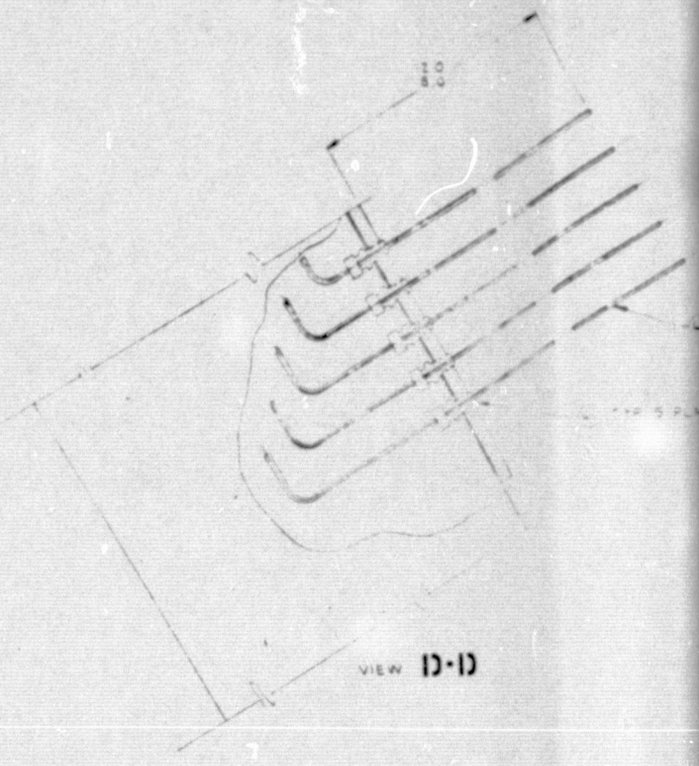

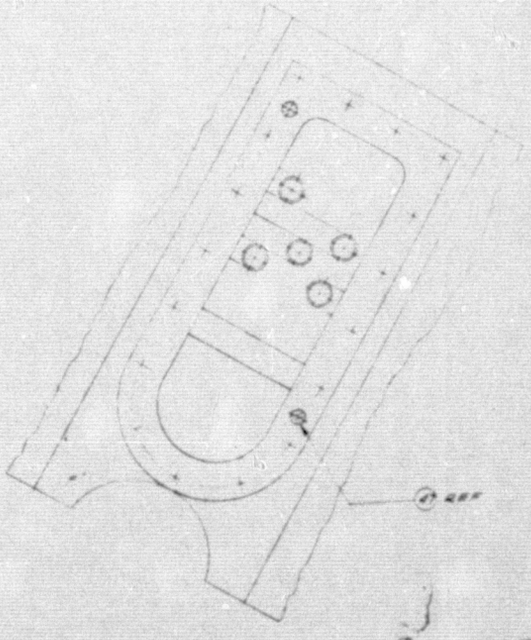

ORIGINAL PAGE IS
OF POOR QUALITY

FOLDOUT FRAME

21 20

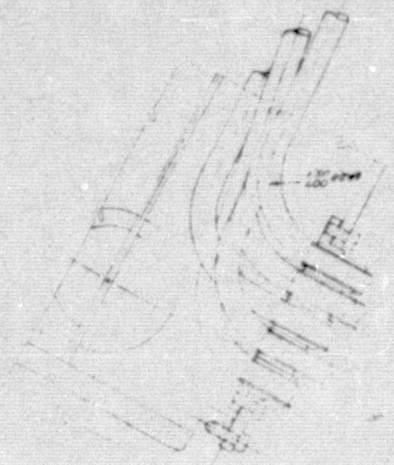

SECTION G-G

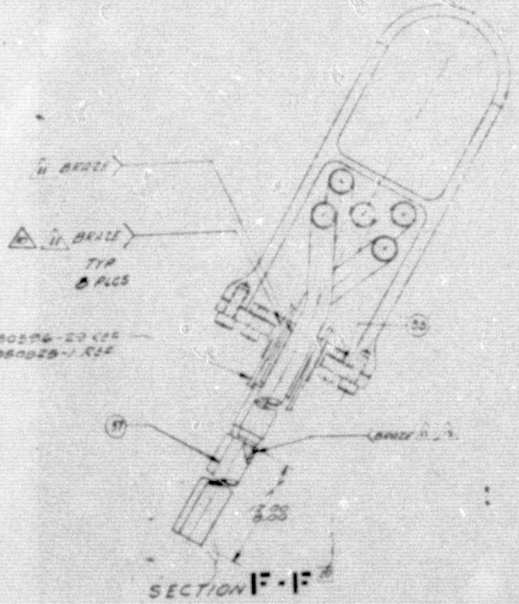

SECTION F-F

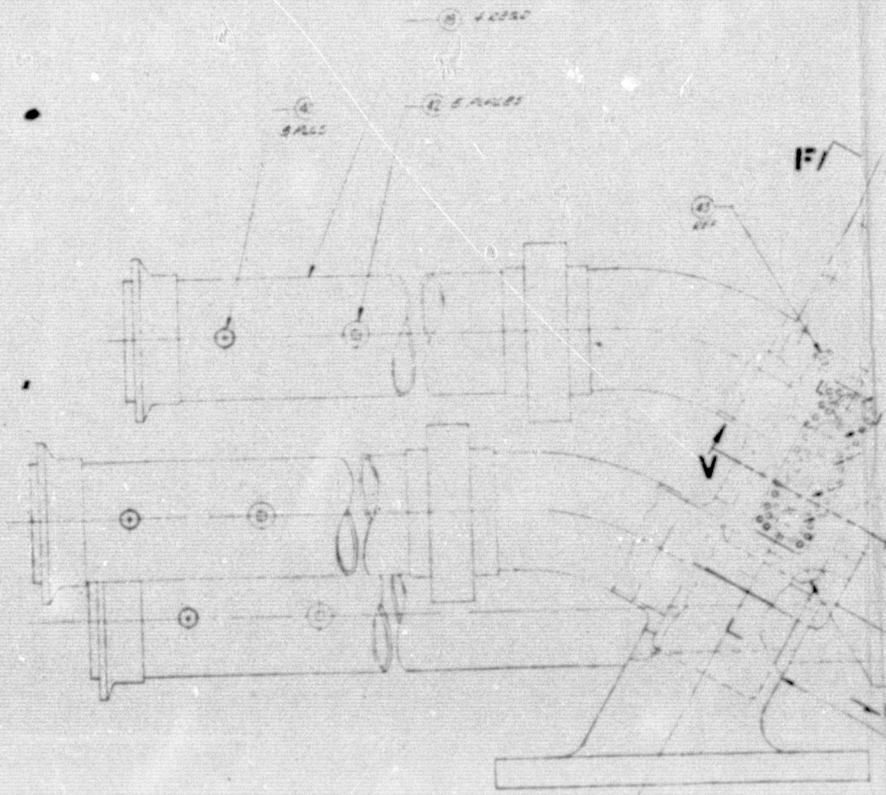

FOLDOUT FRAME 2

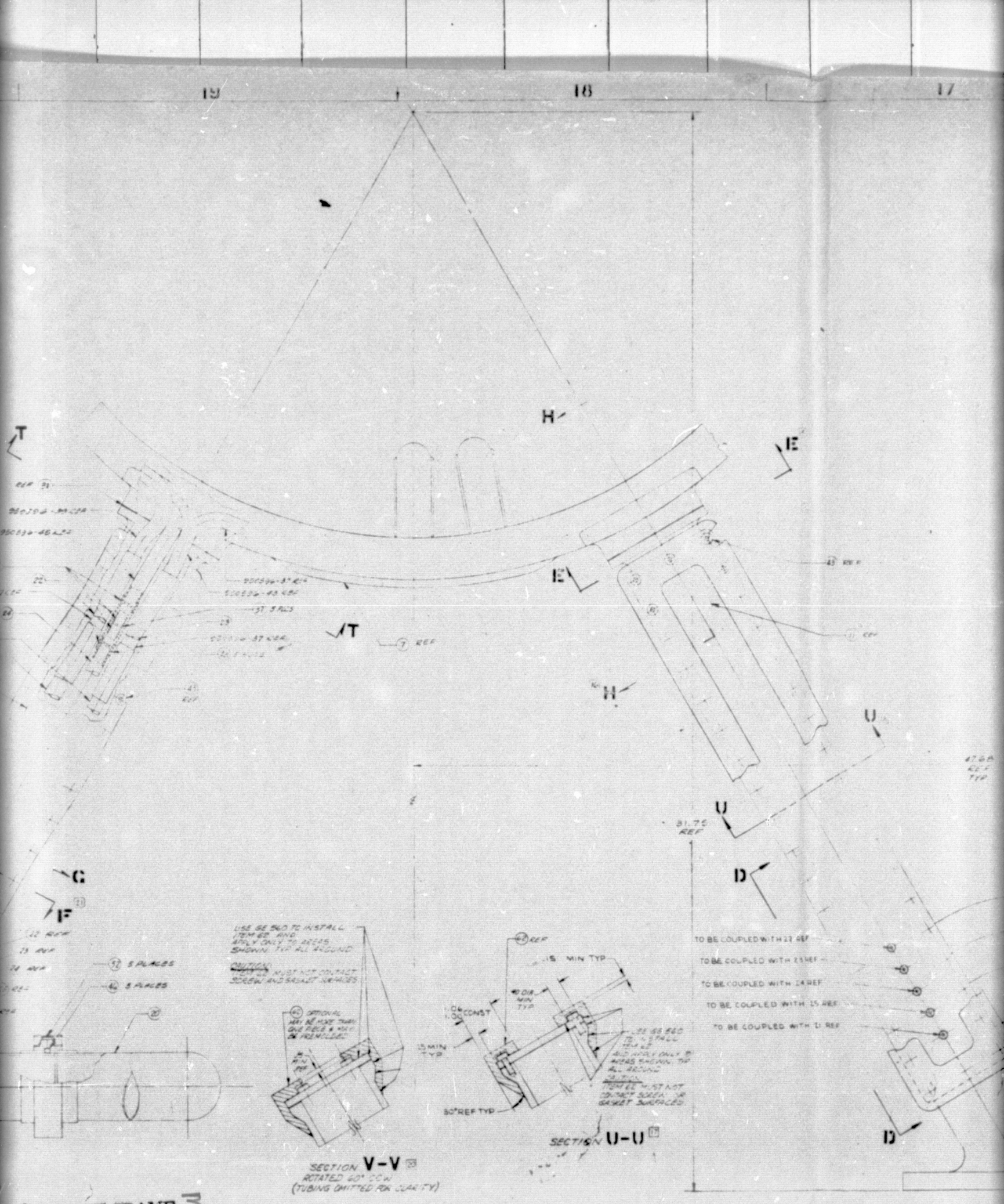

FOLDOUT FRAME 3

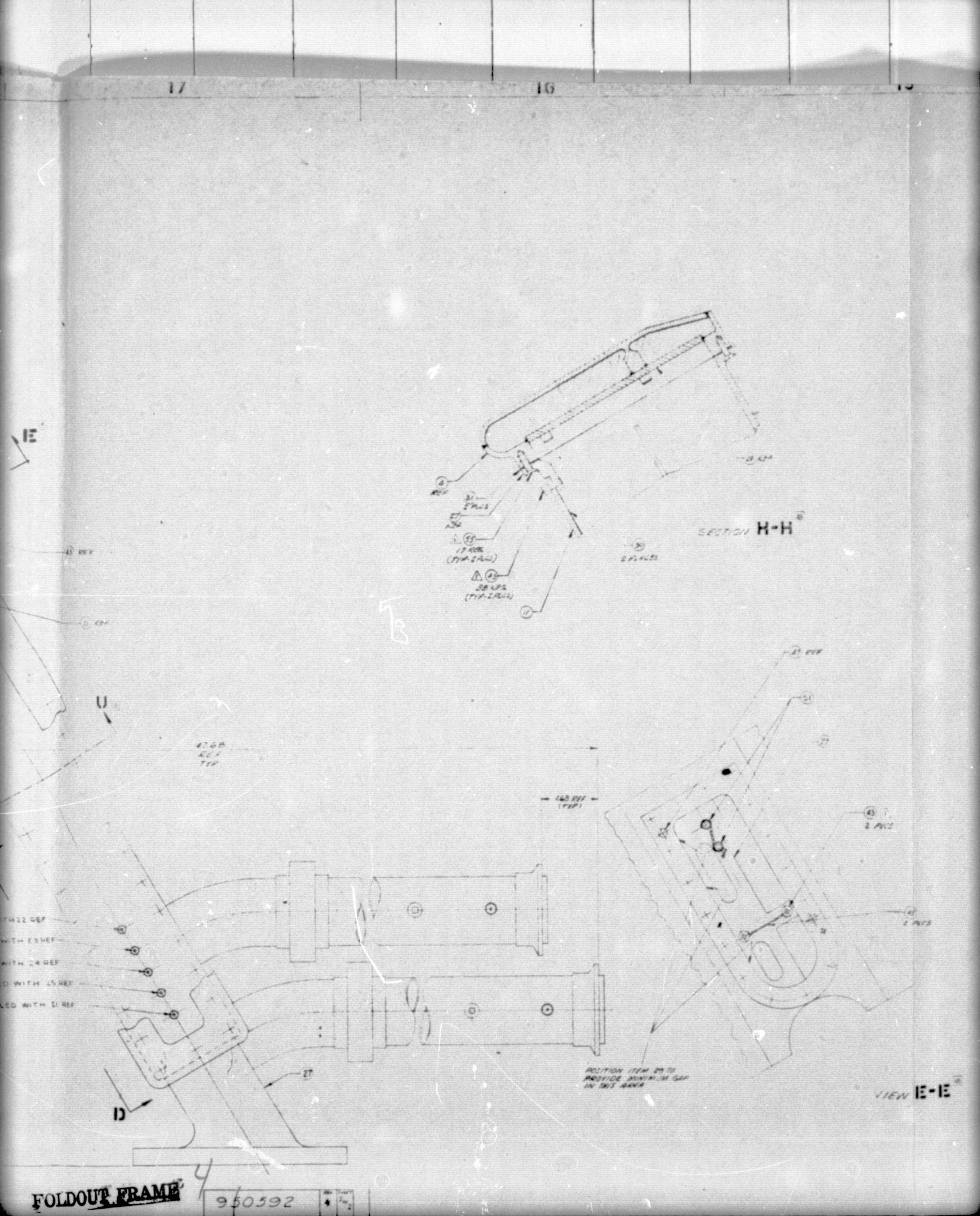
17
16
SECTION H-H
VIEW E-E
POSITION ITEM 29 TO PROVIDE MINIMUM GAP IN THIS AREA
2 PLCS
FOLDOUT FRAME
950592

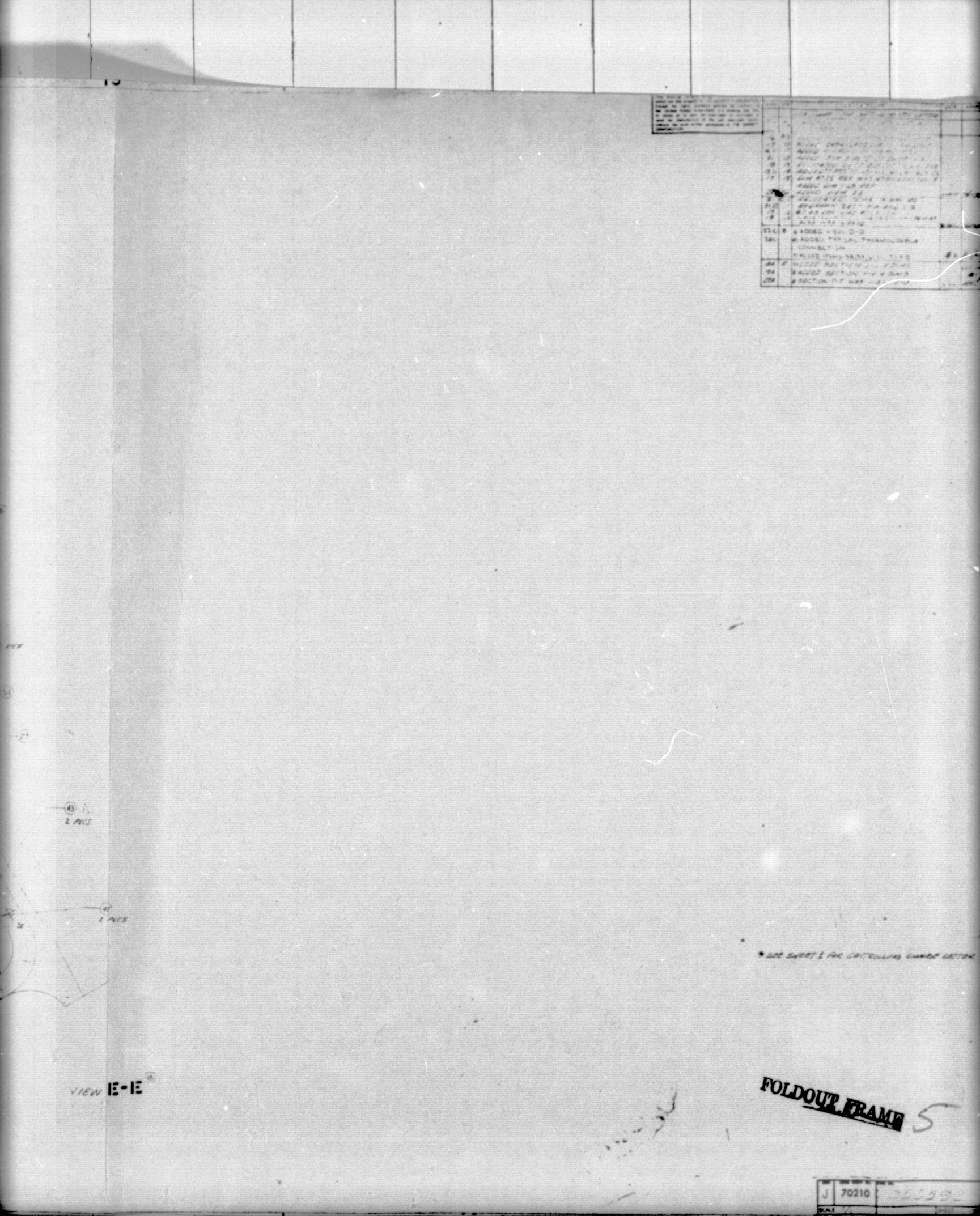
2 PLCS
2 PLCS
* SEE SHEET 2 FOR CONTROLLING NUMBER LETTER
VIEW E-E
FOLDOUT FRAME 5
J 70210

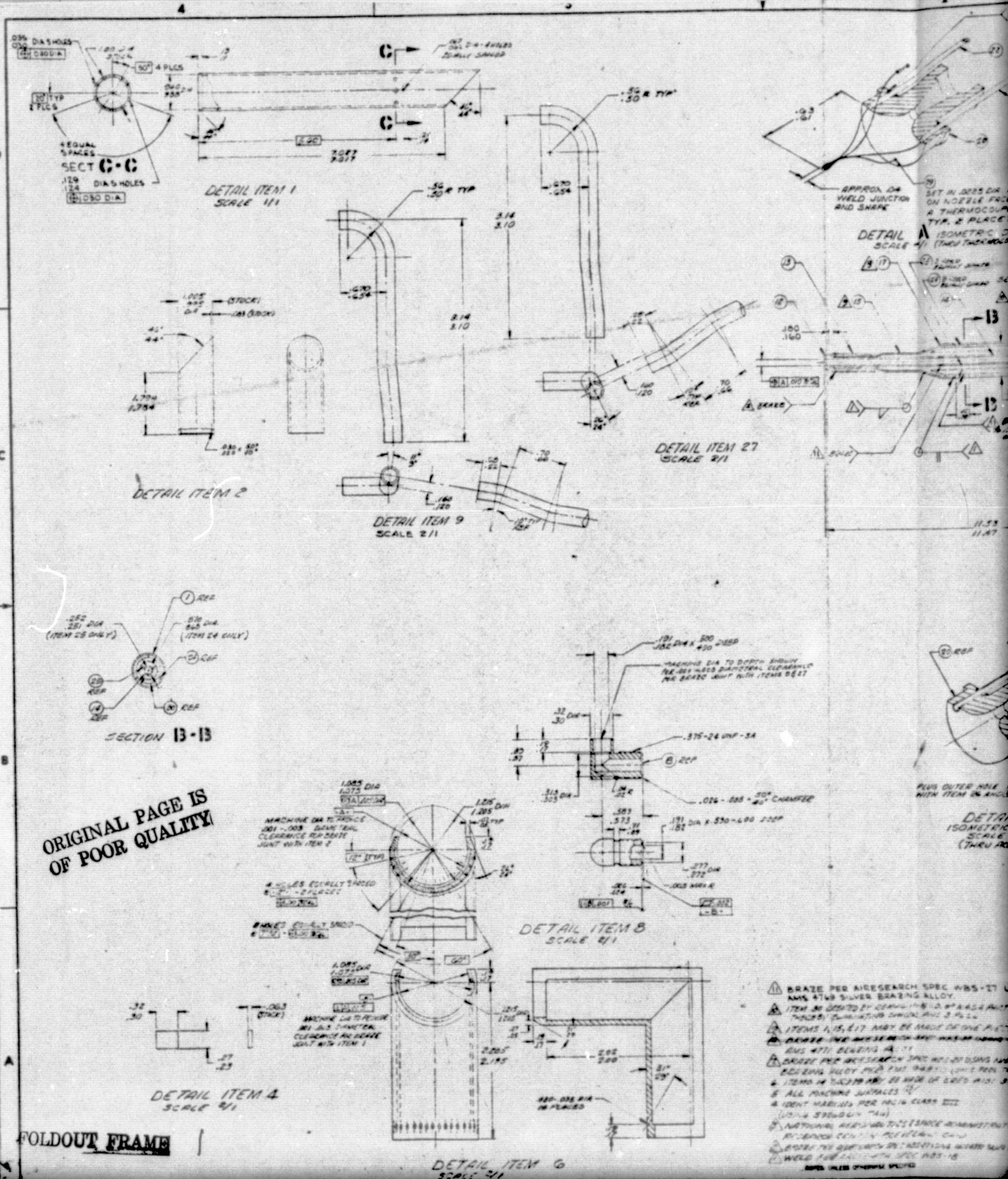

ORIGINAL PAGE IS OF POOR QUALITY

FOLDOUT FRAME 1

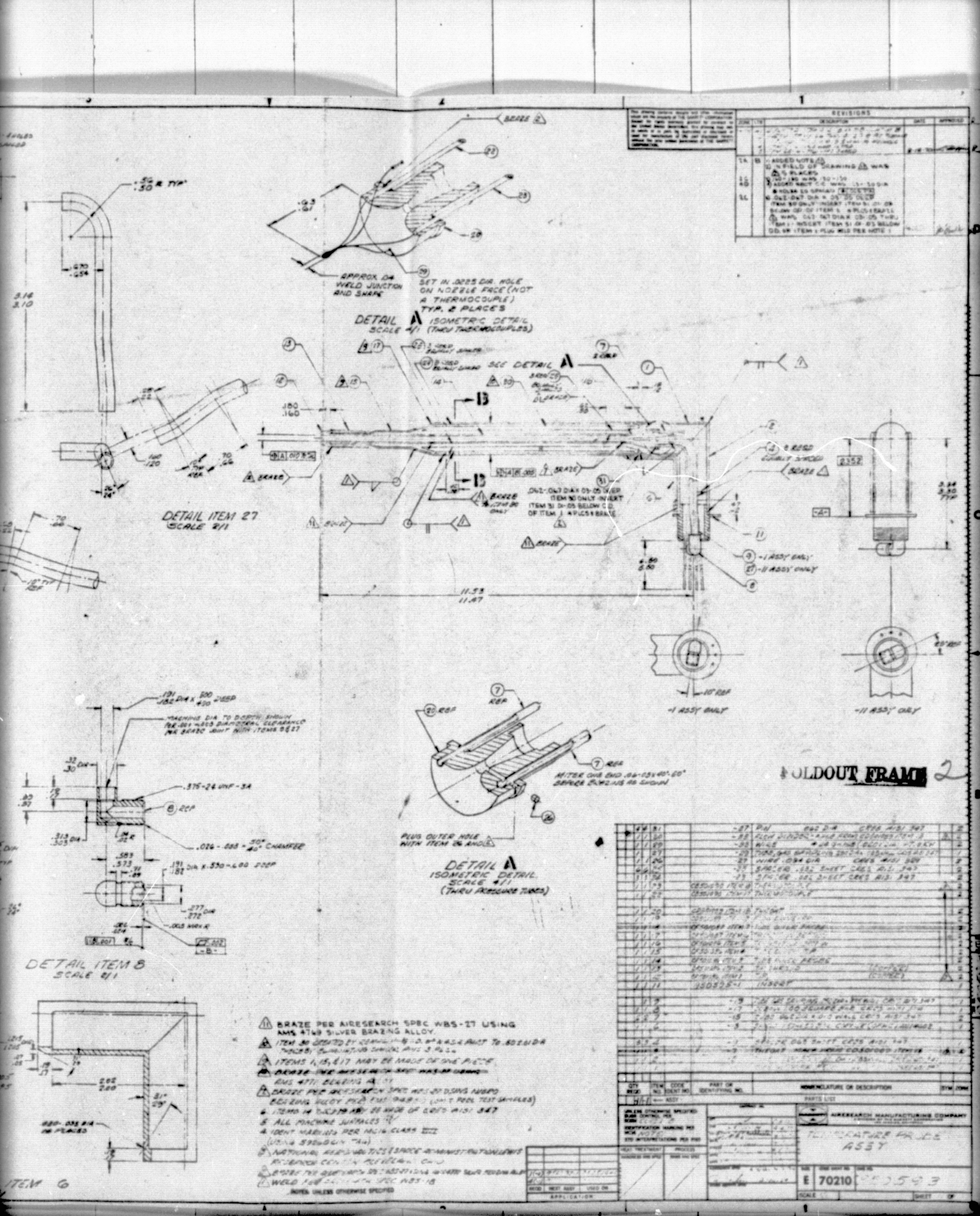
DETAIL A
ISOMETRIC DETAIL
SCALE 4/1
(THRU THERMOCOUPLES)
APPROX .04 WELD JUNCTION AND SHAFT
SET IN .0225 DIA. HOLE ON NOZZLE FACE (NOT A THERMOCOUPLE) TYP. 2 PLACES
SEE DETAIL A
DETAIL ITEM 27
SCALE 2/1
DETAIL ITEM 8
SCALE 8/1
DETAIL A
ISOMETRIC DETAIL
SCALE 4/1
(THRU PRESSURE TUBES)
-I ASSY ONLY
-II ASSY ONLY
FOLDOUT FRAME 2
ITEM 6
REVISIONS
NOTES UNLESS OTHERWISE SPECIFIED
AIRESEARCH MANUFACTURING COMPANY
E 70210

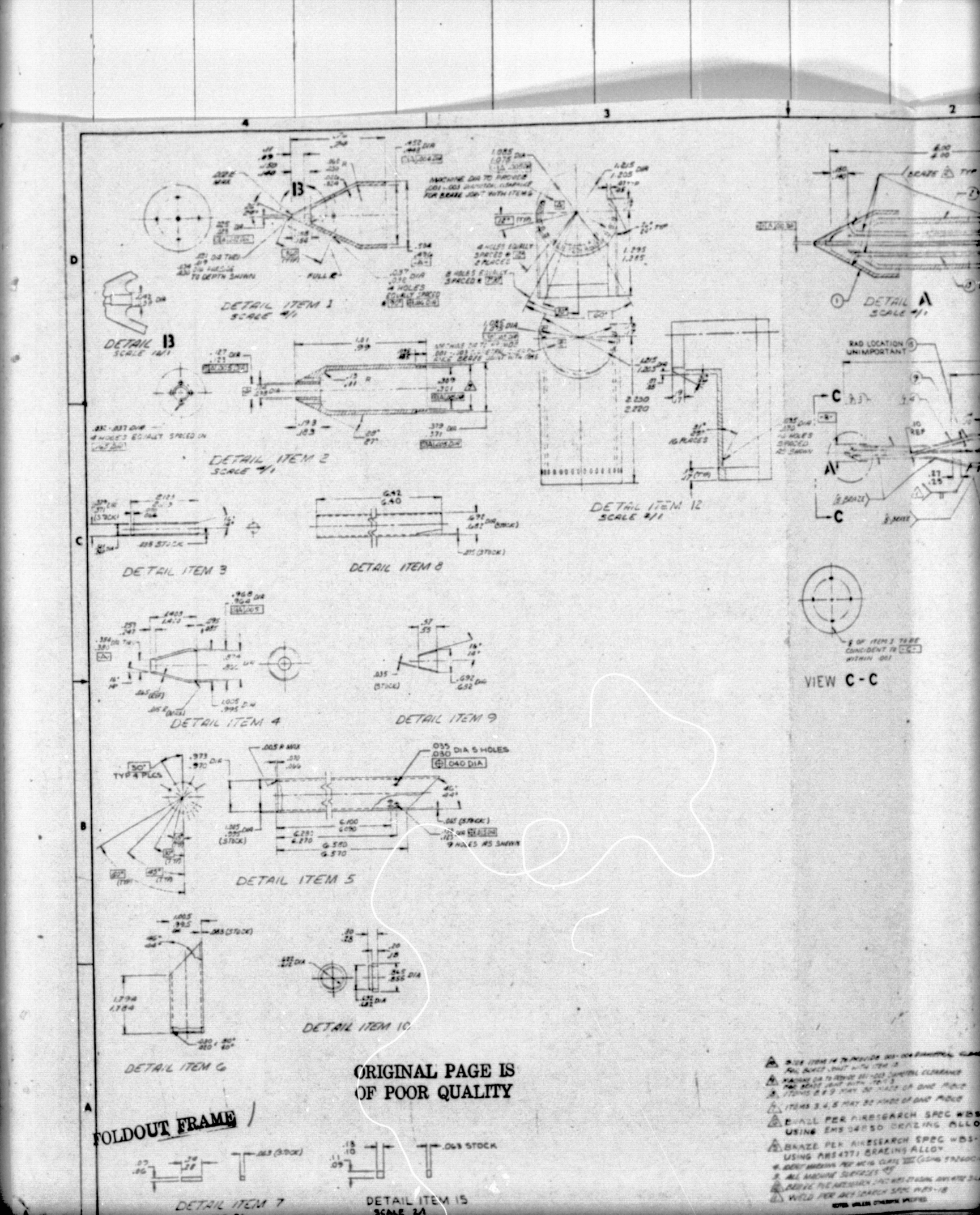

ORIGINAL PAGE IS
OF POOR QUALITY

FOLDOUT FRAME 1

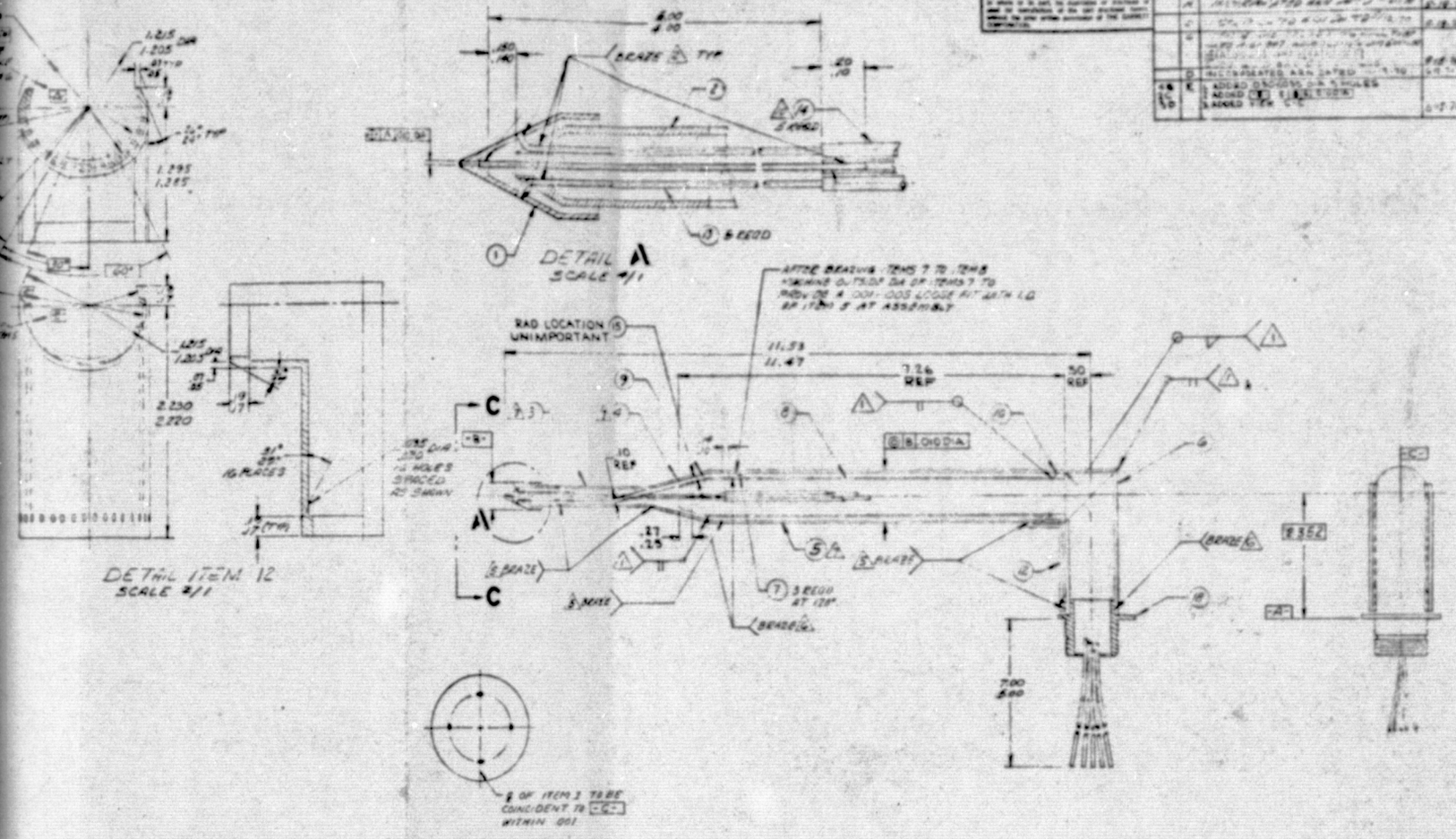

FOLDOUT FRAME 2

ITEM NO.	IDENT NO.	PART OR IDENTIFYING NO.	NOMENCLATURE OR DESCRIPTION	QTY PER ASSY
		930558-1	INSERT	
13	-37		SPACER .063 SHEET CRES AISI 347	3
12	-35		TUBE .062 WALL TUBING CRES AISI 347	2
11	-33		PLATE .87 DIA CRES WELD TUBING CRES AISI 347	2
10	-29		SHIELD 1.30 x 1.50 DIA CORRUGATED	1
9	-25		CAP TUBE 1.00 DIA BAR CRES AISI 321	1
8	-23		PRESSURE PLATE .187 SHEET CRES AISI 321	1
7	-19		TUBE .062 WALL .87 DIA CRES AISI 347	2
6	-17		SPACER .063 SHEET CRES AISI 347	2
5	-15		[illegible]	1
4	-13		[illegible]	2
3	-9		[illegible]	1
2	-7		[illegible]	1
1	-5		[illegible]	1

PARTS LIST

UNLESS OTHERWISE SPECIFIED
DIMENSIONS ARE IN INCHES
TOLERANCES ON
FRACTIONS ± 1/32
DECIMALS .XX ± .01
.XXX ± .005
ANGLES ± 1°
STD INTERPRETATIONS PER MIL-STD-8

AIRESEARCH MANUFACTURING COMPANY
A DIVISION OF THE GARRETT CORPORATION
LOS ANGELES, CALIFORNIA

PITOT STATIC PROBE ASSEMBLY

SIZE E | CODE IDENT NO. 70210 | DRAWING 930534

SCALE | SHEET

NEXT ASSY | USED ON
APPLICATION

NOTES UNLESS OTHERWISE SPECIFIED

A. SIZE ITEMS 14 TO PROVIDE .001-.004 DIAMETRAL CLEARANCE FOR BRAZE JOINT WITH ITEM 13
B. MACHINE DIA TO PROVIDE .001-.003 DIAMETRAL CLEARANCE FOR BRAZE JOINT WITH ITEM 3
C. ITEMS 8 & 9 MAY BE MADE OF ONE PIECE
D. ITEMS 3, 4, 5 MAY BE MADE OF ONE PIECE
E. BRAZE PER AIRESEARCH SPEC WBS-27 USING EMS 04850 BRAZING ALLOY (UNIT PEEL TEST 5 LBS/IN)
F. BRAZE PER AIRESEARCH SPEC WBS-27 USING AMS 4771 BRAZING ALLOY
G. IDENT MARKING PER MIL-STD-130 CLASS III (USING 93260C-14 TYPE)
H. ALL MACHINE SURFACES 63
J. REMOVE FLUX RESIDUE AND ANY STAINING AND AFTER SILVER BRAZING ALLOY
K. WELD PER AIRESEARCH SPEC WBS-18

ORIGINAL PAGE IS
OF POOR QUALITY

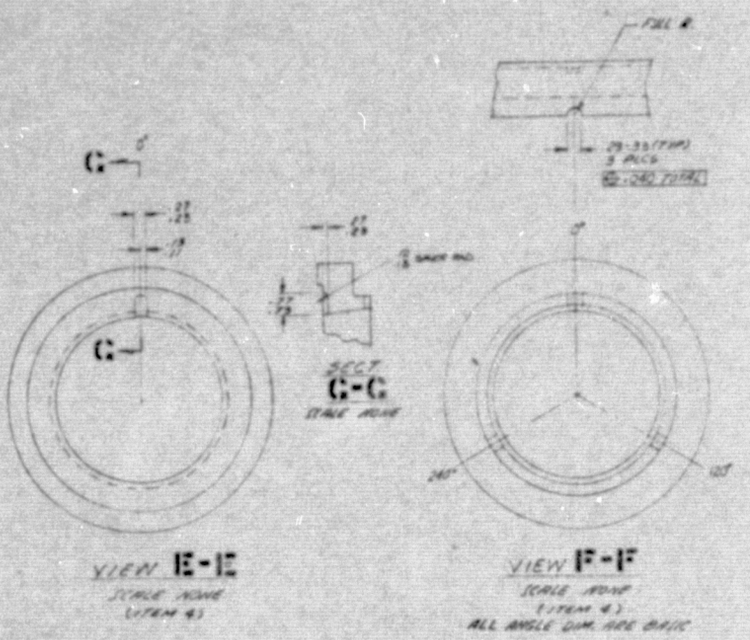

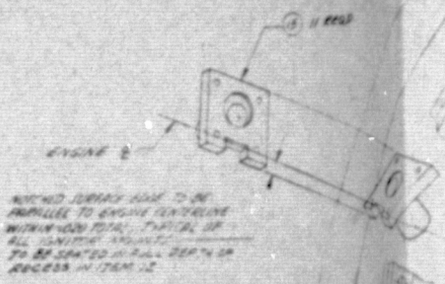

AERODYNAMIC CONTOUR ⚠

STATION	40.500	40.594	41.494	42.994	43.294	41.794	35.740	37.000	38.000	38.700	41.900	65.740	65.997	66.245	66.392
R	9.695	9.720	9.870	9.870	9.855	10.135	10.873	10.955	11.000	11.019	11.018	11.015	11.025	11.048	11.007

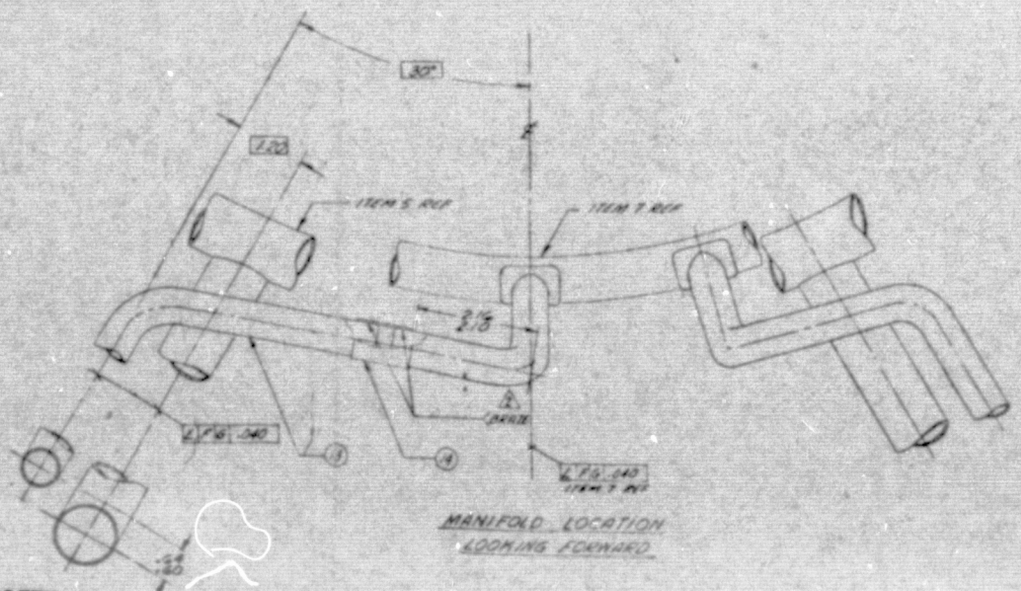

MANIFOLD LOCATION
LOOKING FORWARD

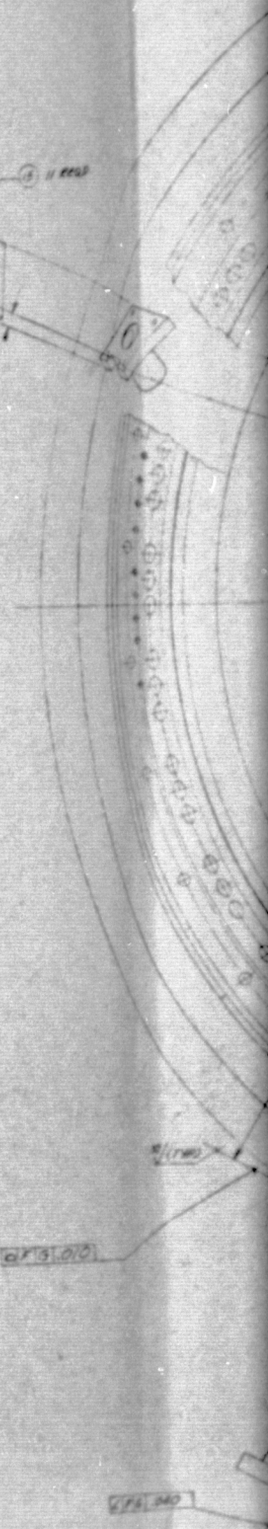

FOLDOUT FRAME

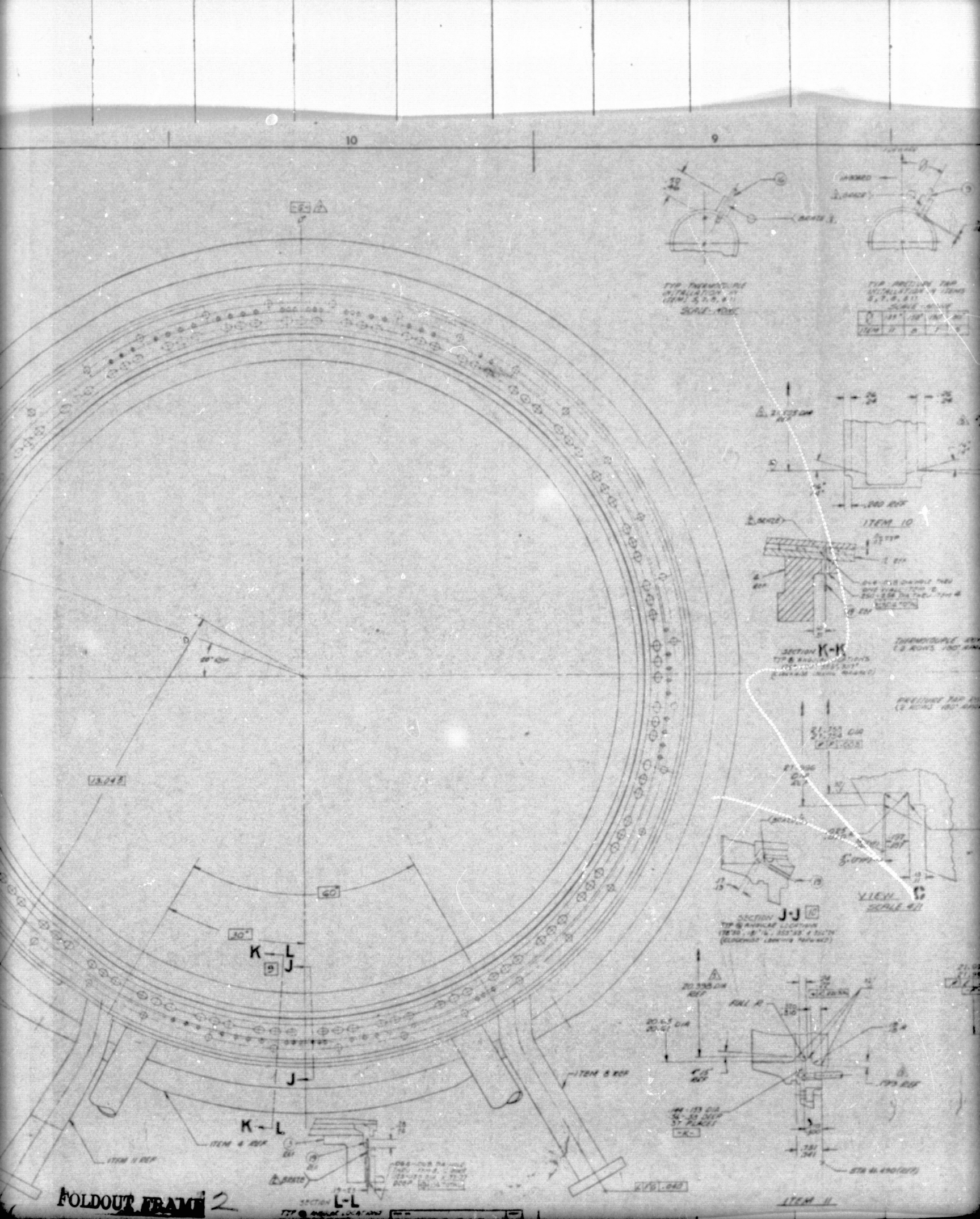
K - L
J
K - L
J
60°
30°
ITEM 6 REF
ITEM 11 REF
ITEM 5 REF
SECTION L-L
SECTION K-K
SECTION J-J
ITEM 10
ITEM 11
VIEW C
SCALE 4/1
FULL R
STA 40.410 (OUT)
FOLDOUT FRAME 2

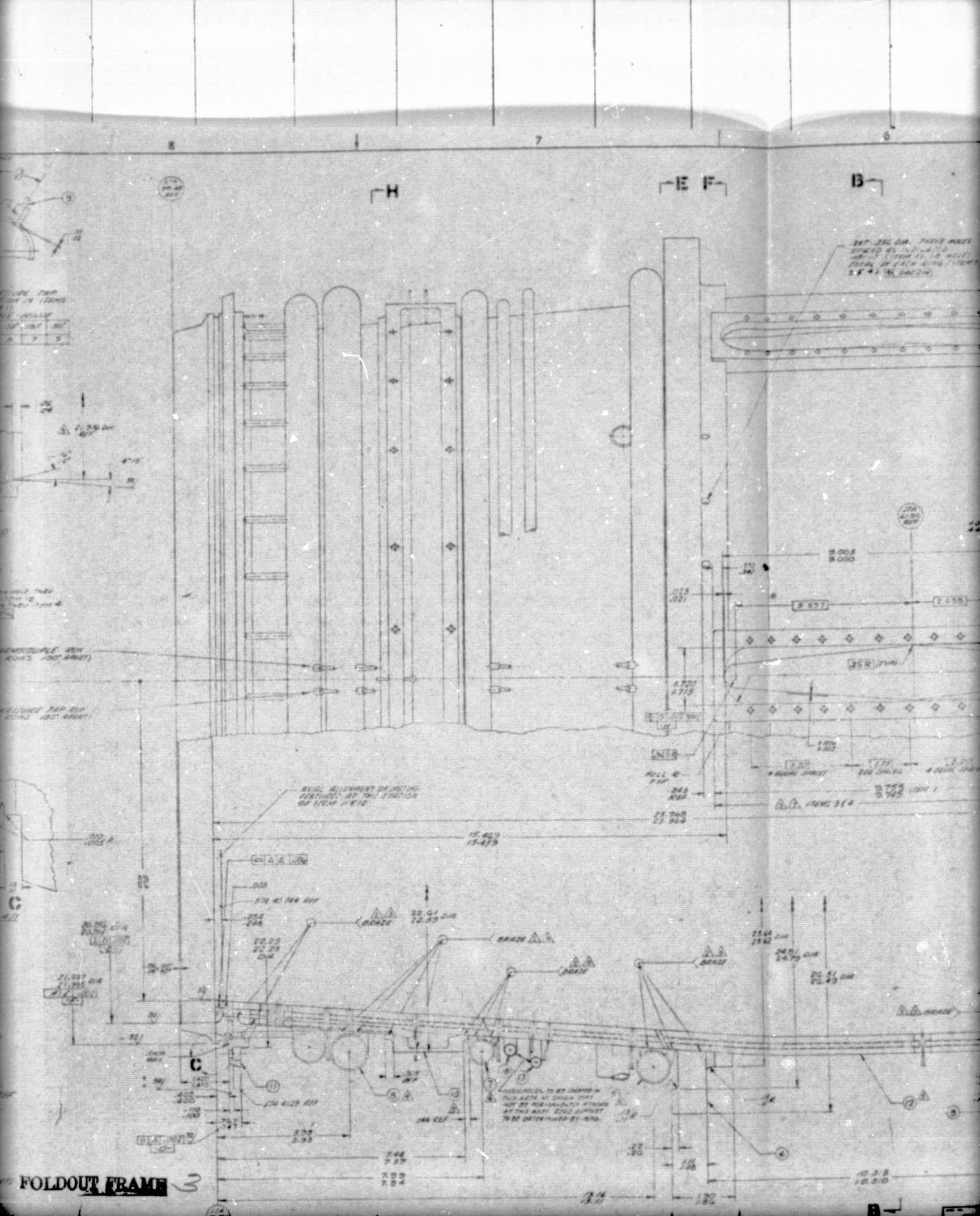

FOLDOUT FRAME 3

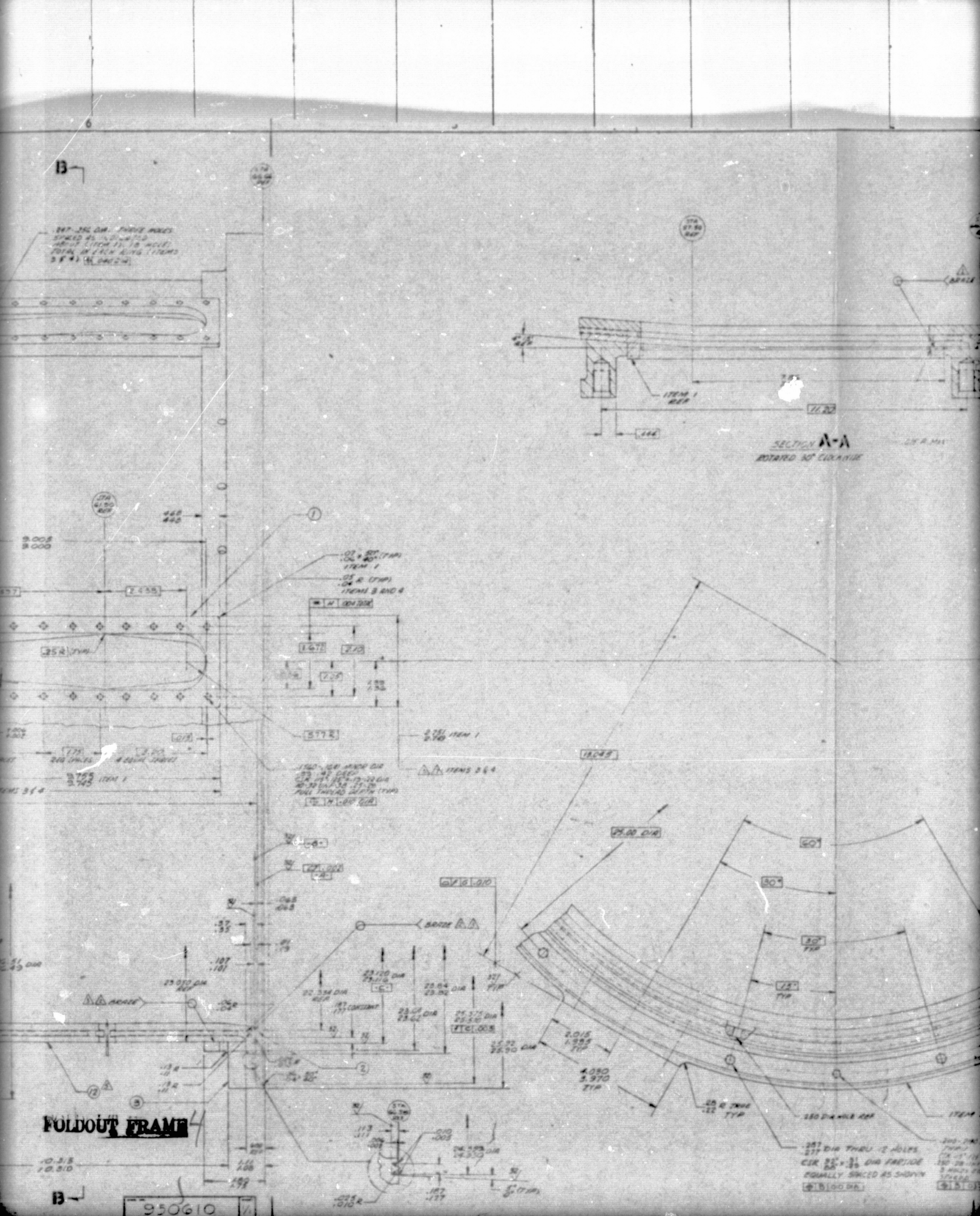
SECTION A-A
ROTATED 30° CLOCKWISE
FOLDOUT FRAME
950610

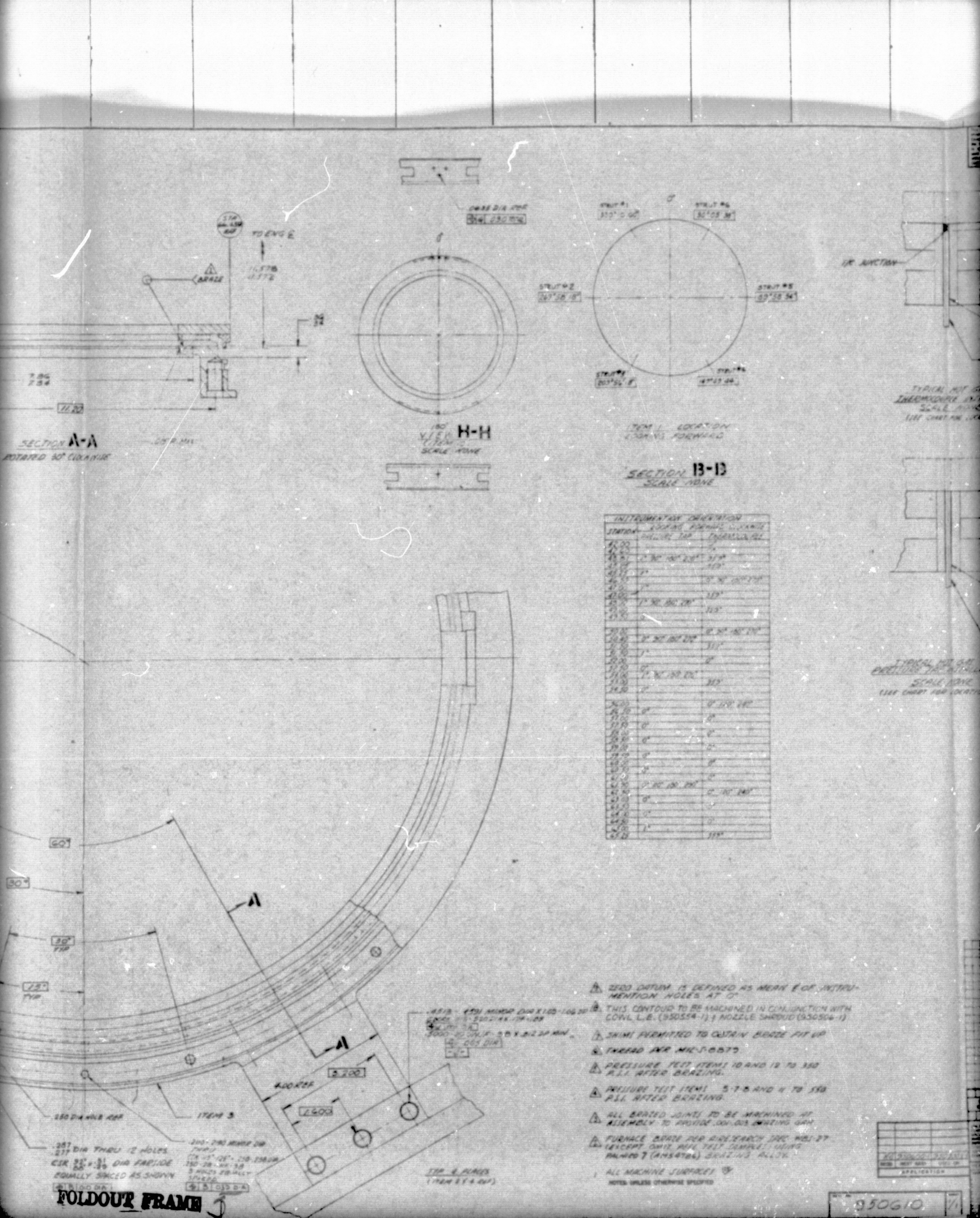
SECTION A-A
ROTATED 30° CLOCKWISE
H-H
SCALE NONE
SECTION B-B
SCALE NONE
INSTRUMENTATION ORIENTATION
STATION
AXIAL RADIAL CLEARANCE
CIRCUMFERENTIAL
TO EDGE
BRAZE
STRUT #1
STRUT #2
STRUT #3
STRUT #4
STRUT #5
STRUT #6
I.R. JUNCTION
60°
30°
A
A
.250 DIA HOLE REF
ITEM 3
4.00 REF
2.200
2.600
ITEM 4 PLACES
(ITEM 3 & 4 REF)
FOLDOUT FRAME
950610

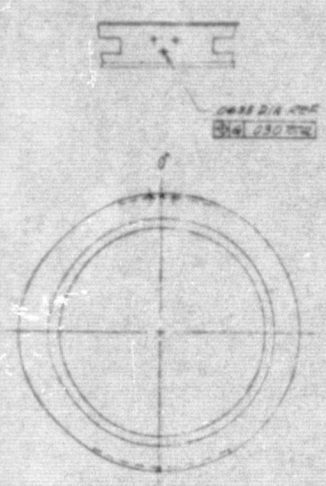

180° VIEW H-H (ITEM 9) SCALE NONE

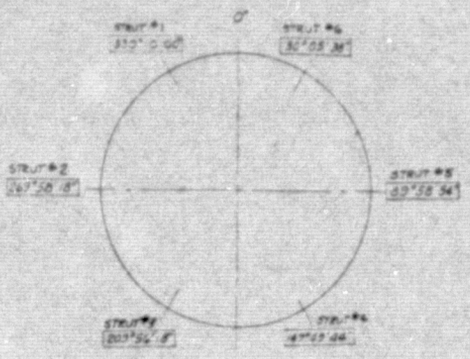

ITEM 1 LOCATION LOOKING FORWARD

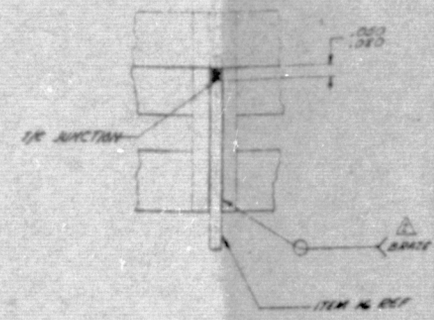

TYPICAL HOT GAS THERMOCOUPLE INSTALLATION SCALE NONE (SEE CHART FOR LOCATION)

SECTION B-B SCALE NONE

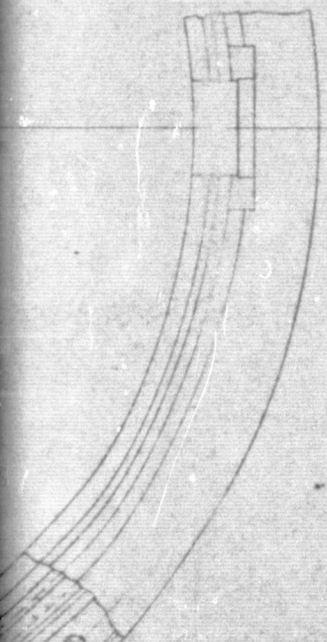

INSTRUMENTATION ORIENTATION		
STATION	LOOKING FORWARD CLOCKWISE	
	PRESSURE TAP	THERMOCOUPLE
49.00		0°
49.50	0°, 30°, 180°, 210°	315°
49.75		345°
50.00	0°	
50.25		0°, 30°, 180°, 210°
50.50	0°	
50.75		330°
51.00		
51.50	0°, 30°, 180°, 210°	
51.75		315°
52.00	0°	
52.25	0°, 30°, 180°, 210°	
52.50		300°
52.75	0°	
53.00	0°, 30°, 180°, 210°	
53.25		285°
53.50	0°	
53.75		0°, 30°, 180°, 210°
54.00		0°, 120°, 240°
54.50	0°	
55.00	0°	
55.50	0°	
56.00	0°	
56.50	0°	
57.00	0°	
57.50	0°	
58.00	0°	
58.50	0°	
59.00	0°, 180°, 210°	
59.50	0°	
60.00	0°	
60.50	0°	
61.00	0°	
61.50	0°	
62.00	0°, 180°, 210°	
62.50	0°	
63.00	0°	
63.50	0°	
64.00	0°	
64.50	0°	
65.00	0°	
65.50	0°	

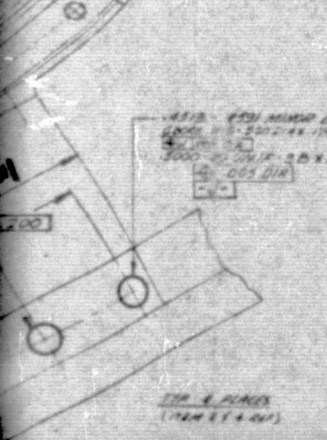

TYP 4 PLACES (ITEM 8,9 & 10)

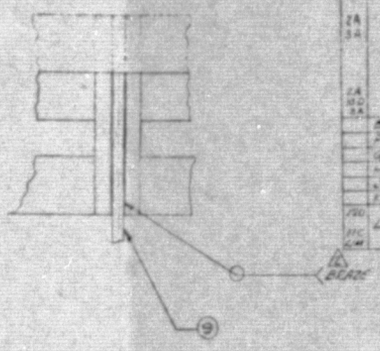

TYPICAL HOT GAS PRESSURE TAP INSTALLATION SCALE NONE (SEE CHART FOR LOCATION)

FOLDOUT FRAME

ITEM NO	QUANT	PART OR IDENTIFYING NO	NOMENCLATURE OR DESCRIPTION	MATL
10	A	950809-1	THERMOCOUPLE	98
11	B	950786-1	MANIFOLD ASSY - OX	74
12	C	950788-1	MANIFOLD ASSY - FU	74
13/6		950467-2	THERMOCOUPLE	90
14/5		950636-1	BOLT, HEAT MONITOR	150
15/14		950613-1	COLLAR	134
16/13		950655-1	TUBE, 24 INLET	134
17	6	.26	INJECTOR ASSY - SEE ITEM 9 PAGE 7	CA
18	1	.23	MANIFOLD ASSY NO. 1B - SEE ITEM 3 PAGE 7	74
19	1	.21	MANIFOLD ASSY - SEE ITEM 2 PAGE 7	74
20	3	.19	TUBE .062 OD X .010 WALL - 90 DEG ELBOW	90
21	1	.17	MANIFOLD ASSY 4 - SEE ITEM 950629-1	74
22	1	.15	MANIFOLD ASSY 2A - SEE ITEM 950629-1	74
23	6			
24	1	.11	MANIFOLD ASSY 3A - SEE ITEM 950629-1	74
25	1	.9	FUEL OUTBOARD FLANGE - SEE ITEM 950629-1	6A
26	1	.7	FUEL OUTBOARD ASSY - SEE ITEM 950629-1	6A
27	1	.5	FUEL UNIT	134

QTY REQD	ITEM NO	CODE IDENT NO	PART OR IDENTIFYING NO	NOMENCLATURE OR DESCRIPTION	SPEC ITEM

PARTS LIST

REVISIONS				
SYM	ZONE	DESCRIPTION	DATE	APPROVED
		INCORPORATED NEW DATED 1-6-67		
		INCORPORATED NEW DATED 1-6-67		
		INCORPORATED NEW DATED 1-6-67	

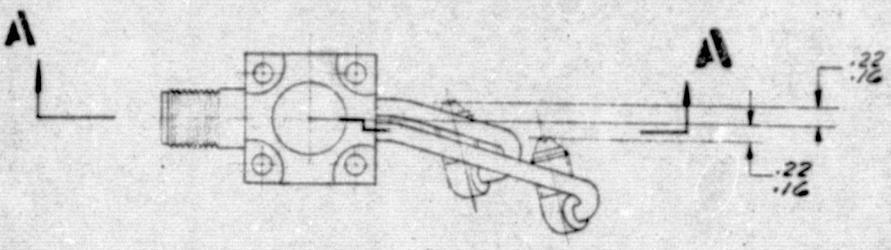

-1 ASSEMBLY

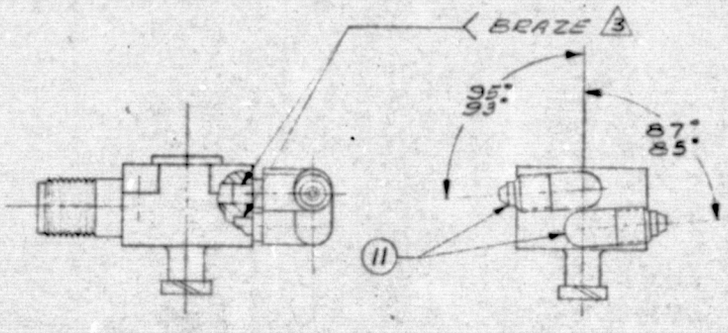

-2 ASSEMBLY

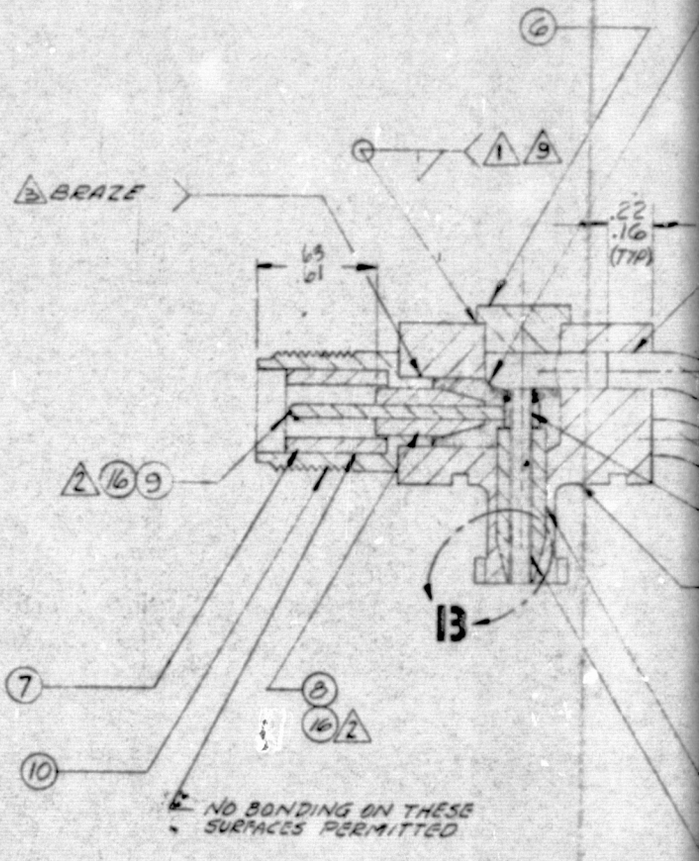

SECTION A-A
SCALE 2/1

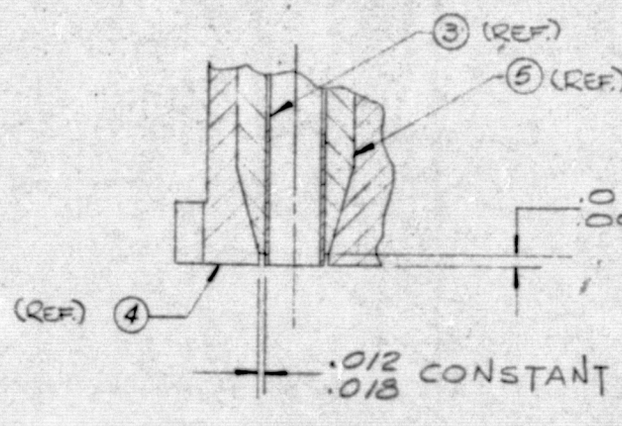

VIEW B
SCALE 5/1

2 CAUTION: DURING WELDING OPERATION NECESSARY PROTECTION IS MANDANTORY TO PREVENT DAMAGE TO SURROUNDING BONDED
8 SOLDER PER AIRESEARCH SPEC AF-209 WITH Sn 40/60 SOLDER PER QQ-
7 APPLY ITEM 17 PER AIRESEARCH SPEC RS161. AS INDICATED USING CARE NOT TO OBSTRUCT OPENINGS IN ITEMS 3 & 4
6. HELIUM LEAK TEST ASSY 4×10^{-7} CC/SEC HELIUM AT 1 ATM DIFF
5. PRESSURE TEST ASSY PER AMS 2615 AT 615 ± 10 PSIA
4. IDENT MARKING PER MC16 CLASS IIII (USING S926OCIN TAG)
3 BRAZE PER WBS-27 EXCEPT OMIT PEE SAMPLES USING PALNIRO 7 PER AMS 4786
2 BOND IN PLACE WITH ITEM 17 OBTAINED FROM AMERICAN THERMOC CORP., MINEOLA, N.Y. IN THE FOLLOWING MANNER: PRE-DRY AT 120°-150° ONE HALF TO ONE HOUR. THEN HEAT CEMENTED PART AT A RATE NOT 30° F/MIN UNTIL TEMPERATE REACHES AT LEAST 1100° F IN ARGON AT -35° TO -65° F DEW POINT
1 WELD PER SPEC WBS 18

NOTES-UNLESS OTHERWISE SPECIFIED

ORIGINAL PAGE IS
OF POOR QUALITY

FOLDOUT FRAME 1

This drawing contains designs and other information which are the property of THE GARRETT CORPORATION. Except for rights expressly granted by contract to the United States Government, this drawing may not, in whole or in part, be duplicated or disclosed or used for manufacture of the part disclosed herein, without the prior written permission of THE GARRETT CORPORATION.

REVISIONS

LTR	DESCRIPTION	DATE	APPROVED
A	1) GIN 2 WAS 'BOND IN PLACE USING ITEM 15 'ASTROCCRAM', MFG. BY AMERICAN THERMOCATALYTIC CORP MINEOLA, N.Y. 2) ADDED GIN 8, TYPE A-LP TO ITEM 16, 239-002-9001 TO ITEM 15, ADDED "PER AIRESEARCH SPEC RS161" TO GIN 1, ADDED GIN 9, ADDED LOCAL NOTE 'NO BONDING ON THESE SURFACES PERMITTED	5-18-70	9-Taylor

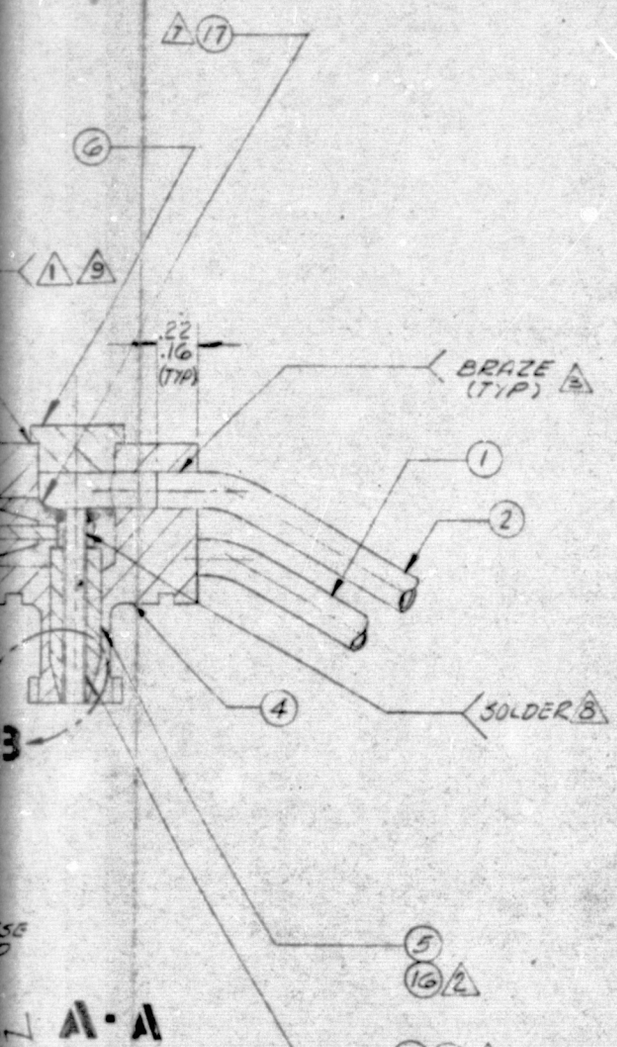

FOLDOUT FRAME 2

QTY REQD	ITEM NO.	CODE IDENT NO.	PART OR IDENTIFYING NO.	NOMENCLATURE OR DESCRIPTION	SYM
AR AR	17		239-002-9001	COMPOUND POTTING	
AR AR	16		TYPE A-LP	ADHESIVE	8
2	11		950797-1	ELBOW, LONG IGNITOR	
1	10		950633-1	BOSS	
1	9		950639-1	PIN ASSY	
1	8		950643-1	INSULATOR PIN	
1	7		950646-1	INSULATOR CONN	
1	6		950637-1	CAP	
1	5		950644-1	INSULATOR TUBE	
1	4		950622-1	BODY	
1	3		950678-1	TUBE	
1	2		950790-1	TUBE ASSY	
1	1		950783-1	TUBE ASSY	
-2	-1		← ASSY		

PARTS LIST

ESSARY PROTECTION
SURROUNDING BONDED COMPONENTS
40/60 SOLDER PER QQ-S-571
AS INDICATED
ITEMS 3 & 4
M AT 1 ATM DIFF
615 ± 10 PSIA
NG S926OCIN TAG)
EPT OMIT PEEL TEST
FER AMS 4786
M AMERICAN THERMOCALYTIC
R: PRE-DRY AT 120°-150°F FOR
PART AT A RATE NOT EXCEEDING
T 1100°F IN ARGON ATMOSPHERE

18

SPECIFIED.

REQD	NEXT ASSY	USED ON
(2)	950502-1	950500-1-1
1(-1)	750600-1	950501-1-1

APPLICATION

HEAT TREATMENT	PROCESS
HARDNESS AND SPEC	NAME AND SPEC

UNLESS OTHERWISE SPECIFIED:
DIMENSIONS ARE IN INCHES.
MACHINE FILLET RADII .015 — .030
SURFACE ROUGHNESS PER USAS B46.1-62
BURR CONTROL PER SOB3
DIMENSION LIMITS HELD AFTER PLATING
IDENT MARKING PER MC15 AMPED
DIMENSIONING AND TOL PER USAS Y14.5-66

CONTRACT NO.

DFT	L. DOMICO	2/11/70
ENGR		2-26-70
VALUE ENGR		
MATL	C. Capuano	3-26-70
STRESS		
APPD		3-26-70
APPD	D. [illegible]	3-26-70
AIRESEARCH APPD		
	3-30-70	
OTHER ACTIVITY APPD		

GARRETT AIRESEARCH MANUFACTURING COMPANY
A DIVISION OF THE GARRETT CORPORATION
LOS ANGELES, CALIFORNIA

IGNITOR ASSY

SIZE	CODE IDENT NO.	DWG NO.
D	70210	950627

SCALE 1/1 | SHEET 1 OF 1

950627

ORIGINAL PAGE IS
OF POOR QUALITY

MATCH DRILL ITEM 31 WITH ITEM 23
AS SHOWN:
.123-.130 DIA THRU PERPENDICULAR TO
SURFACE "J" OF ITEM 31 ⌖.010 DIA
.1696-.1675 MINOR DIA THRU
CSK .115°-.125° x .19-.22 DIA
10-32 UNJF-6B THRU PER MIL-S-8879
36 PLACES ⌖.005 DIA
.195-.201 DIA THRU ITEM 31 ONLY
CSK 99°-101° x .375-.385 DIA
36 PLACES ⌖.005 DIA

J SURFACE
REF (31)
REF (23)
.030
.015 GAP

SECTION E-E
SCALE 2/1

REF (31)
REF (2)

VIEW D-D
ROTATED 90° CW

℄ OF LEG (REF)
.245 REF
(1) TYP

VIEW L-L

100° FLAT HD SCREW
10-32 x .150 LONG
36 REQ'D (REF)

FOLDOUT FRAME

27.710
DIA REF

22.75
DIA (REF)
-A-

-B-

D

D

L

15.00
GAGE DIM.

100° FL
10-32
2 - R

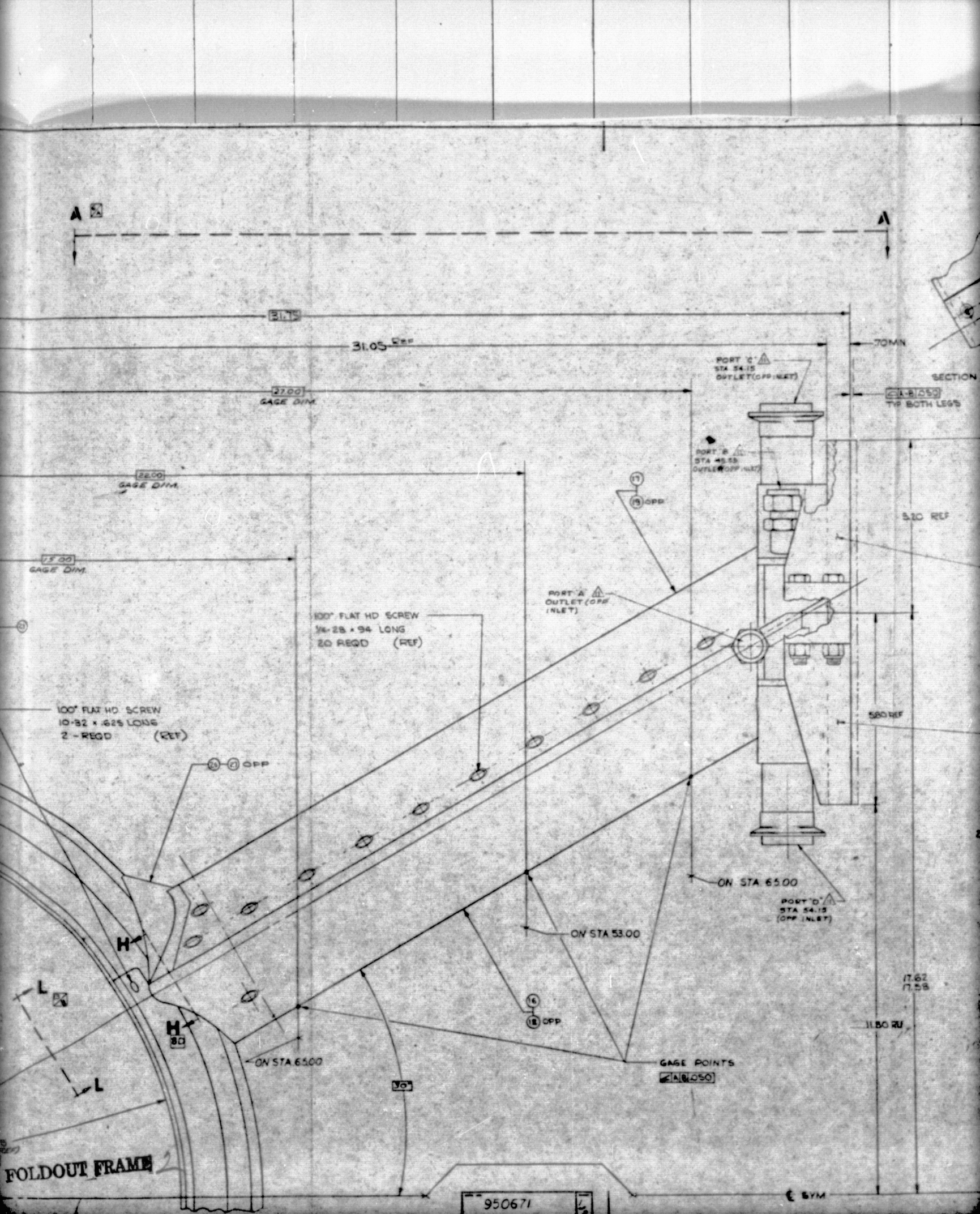
A
A
31.75
31.05 REF
.70 MIN
PORT 'C' ⚠1
STA 54.13
OUTLET (OPP INLET)
SECTION
A-B
TYP BOTH LEGS
27.00
GAGE DIM.
PORT 'B' ⚠1
STA 45.53
OUTLET (OPP INLET)
22.00
GAGE DIM.
17
19 OPP
5.20 REF
15.00
GAGE DIM.
PORT 'A' ⚠1
OUTLET (OPP INLET)
100° FLAT HD SCREW
1/4-28 x .94 LONG
20 REQD (REF)
100° FLAT HD SCREW
10-32 x .625 LONG
2 - REQD (REF)
23
21 OPP
5.80 REF
ON STA 65.00
PORT 'D' ⚠1
STA 54.13
(OPP INLET)
ON STA 53.00
H
L
H
80
16
18 OPP
17.62
17.58
11.80 RU
ON STA 65.00
GAGE POINTS
A B C D
30°
FOLDOUT FRAME 2
950671
E SYM

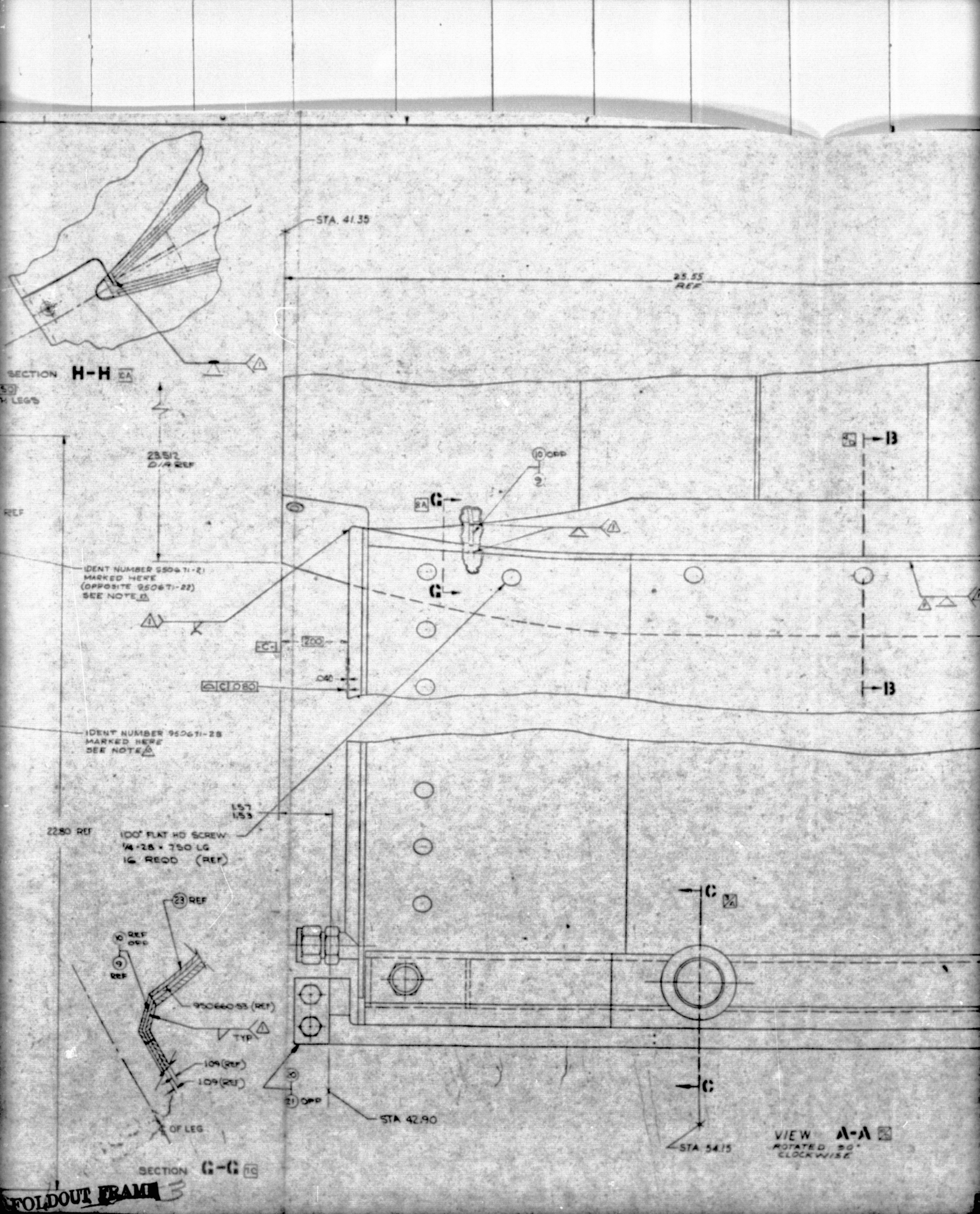

FOLDOUT FRAME 3

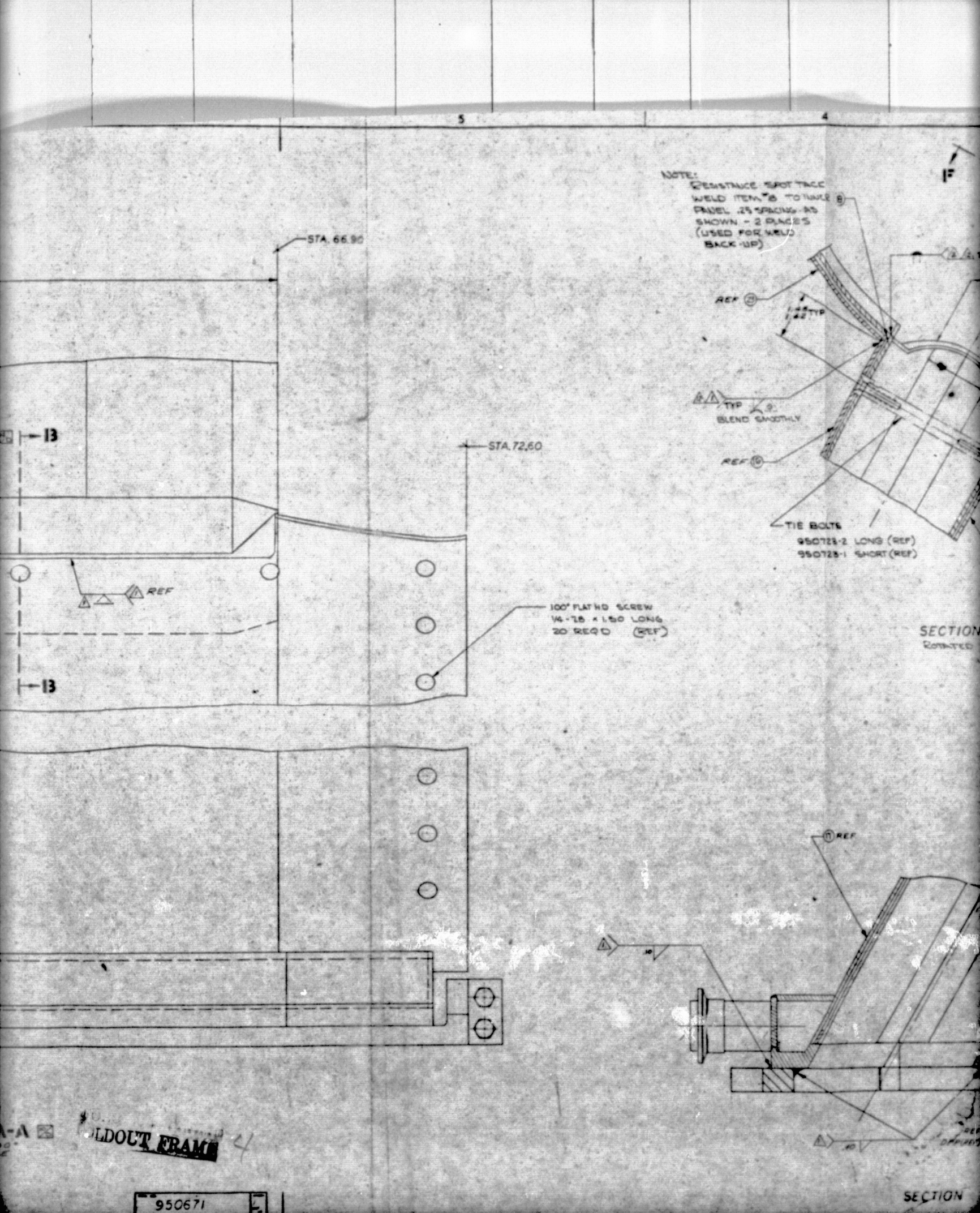
5
4
NOTE:
RESISTANCE SPOT TACK WELD ITEM 8 TO ITEM 9 PANEL .25 SPACING AS SHOWN - 2 PLACES (USED FOR WELD BACK-UP)
STA. 66.90
STA. 72.60
13
13
REF
100° FLAT HD SCREW
1/4-28 x 1.50 LONG
20 REQ'D (REF)
REF
TYP
BLEND SMOOTHLY
TIE BOLTS
950728-2 LONG (REF)
950728-1 SHORT (REF)
SECTION
ROTATED
REF
SECTION
A-A
OLDOUT FRAME
950671

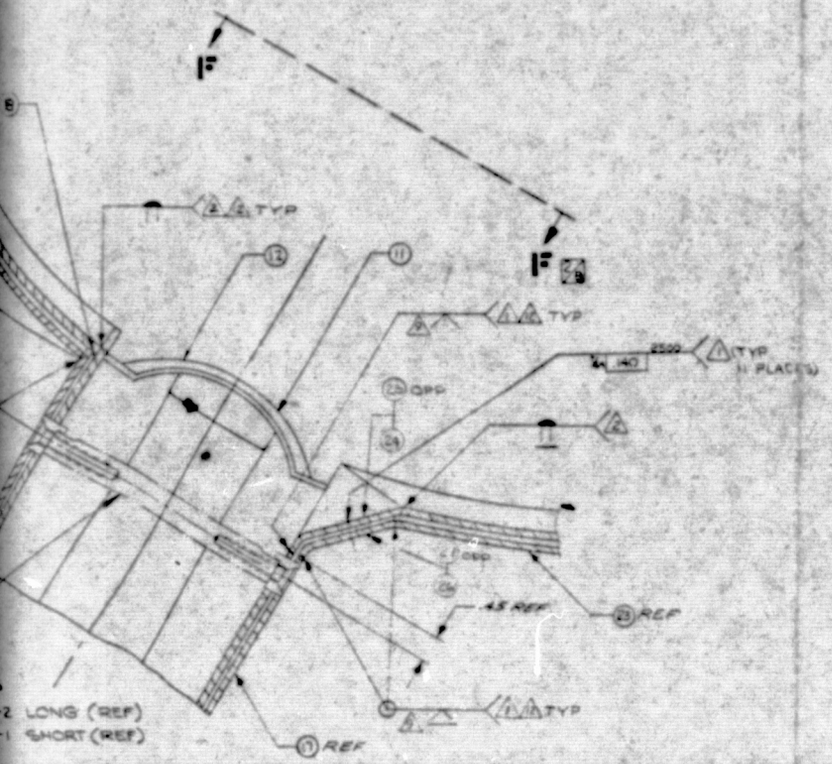

SECTION B-B
ROTATED 60° C.W.

X BASIC	P BASIC	W BASIC
0.000	13.60	2.500
1.750	13.60	2.031
3.350	13.60	1.592
4.760	13.25	1.227
6.700	12.98	0.000

SECTION K-K

VIEW F-F

SECTION C-C

6. MAY BE PURCHASED FROM: CRAWFORD FITTING CO (CRAWFORD) #9506, SOLON IN., SOLON, OHIO
4. APPLY PER RS-13
13. PROOF PRESSURE TEST CIRCUIT "A" ONLY AT ROOM TEMPERATURE USING STRESSCOAT PER SUBMARK #6 OR EQUIVALENT
12. RADIOGRAPHIC INSPECTION PER MIL-STD-453
11. PRESSURE TEST PER 950671-1 HYDROSTATICALLY:
H₂O COOLANT CIRCUIT "A" [illegible] PSI FOR [illegible]
H₂O " " "B" [illegible] PSI
H₂O " " "C" [illegible] PSI
H₂O " " "D" [illegible] PSI
NOTE: 950722-1 GASKET, OUTER COWL & 950721-1 GASKET, MANIFOLD MAY BE USED TO PERFORM THE TEST.

6. -1 ASSY. FOR PURPOSES OF FINAL MARKING & PROOF TEST ONLY, FOLLOWING PROOF TEST -1 ASSY. SHALL BE DISASSEMBLED AND PHYSICALLY IDENTIFIED AS:
950671-21 FOR OUTER COWL ASSY., SIDE SEC. RIGHT
950671-22 FOR OUTER COWL ASSY., SIDE SEC. LEFT
950671-23 FOR OUTER COWL ASSY., BOTTOM SEC.
7. 80% TO 99% PENETRATION
8. MATCH DRILL MANIFOLD ASSY., ITEM 31, AS SHOWN
9. FLUORESCENT PENETRANT INSPECT PER MIL-I-6866, TYPE I OR TYPE II
10. CRES AMS 5721
5. ALL DIMENSIONS ARE FINISHED DIMENSIONS OF (-1) ASSY. DETAIL PART DIMENSIONS WILL BE DETERMINED BY MFG.
2. WELD PER AIRESEARCH SPEC WBS-42 (SPOT WELD)
3. MACHINED SURFACES 125
1. WELD PER AIRESEARCH SPEC WBS-35 (EB WELD)
14. WELD PER AIRESEARCH SPEC WBS-18

NOTES: UNLESS OTHERWISE SPECIFIED

QTY REQ'D

950671

X BASIC	R BASIC	W BASIC
0.000	13.60	2.500
1.750	13.60	2.031
3.390	13.60	1.598
4.760	13.25	1.227
6.700	12.98	0.000

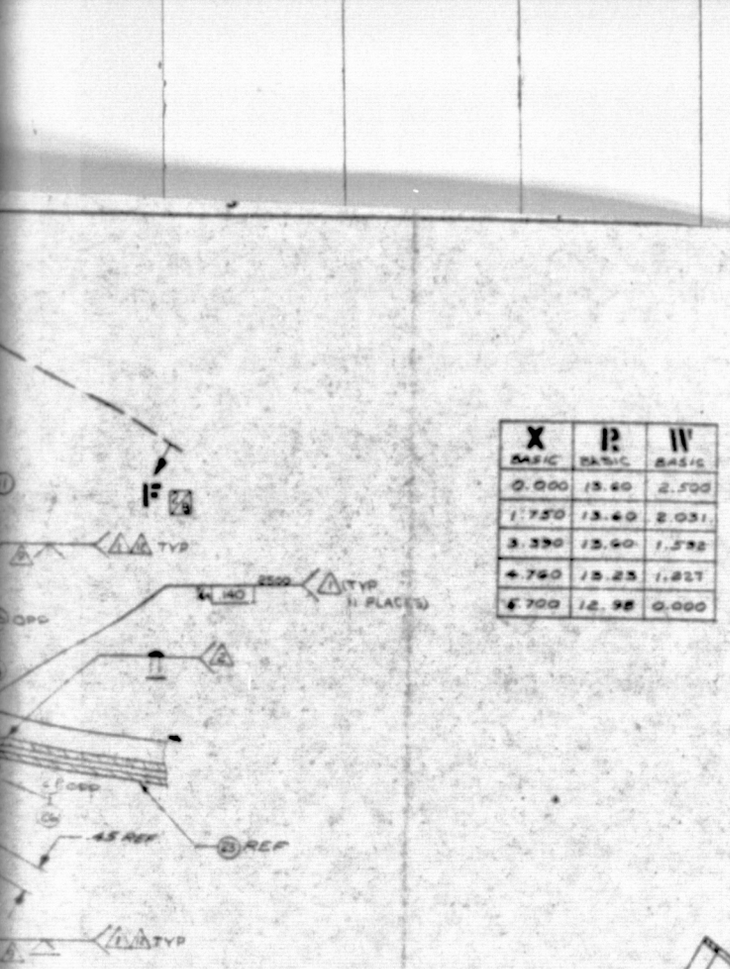

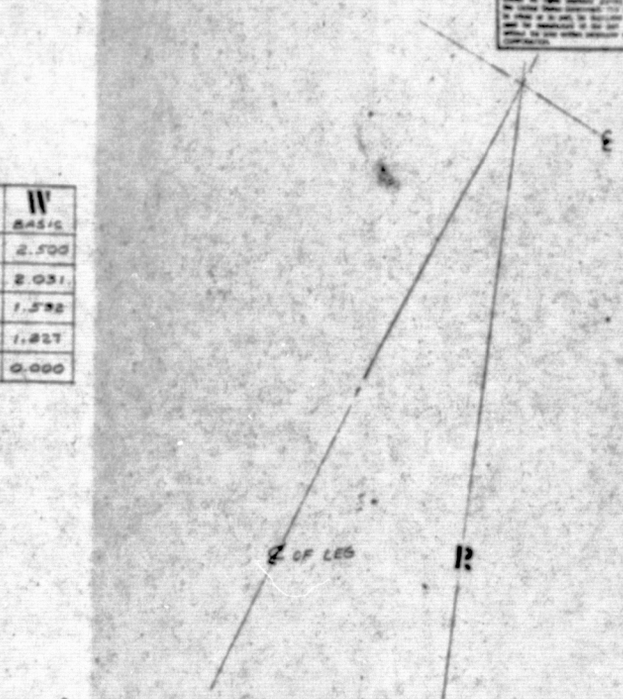

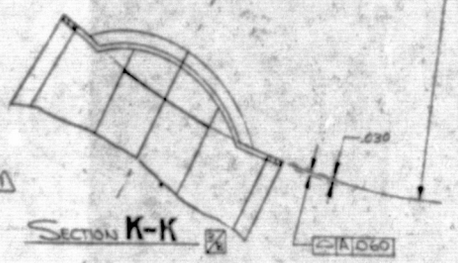

SECTION K-K

FOLDOUT FRAME

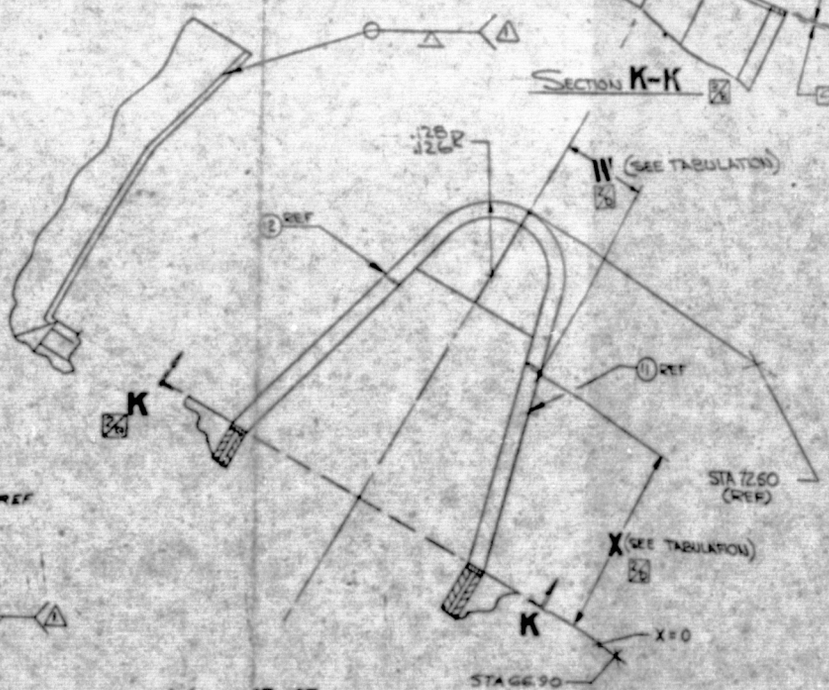

VIEW F-F

QTY REQD	ITEM NO	IDENT NO	PART OR IDENTIFYING NO.	NOMENCLATURE OR DESCRIPTION
	46		950693-3	RING, SEAL
	45		950693-1	RING, SEAL
1	44		MS 9245-18	PIN, COTTER
	43		MS 9541-04	PIN, STRAIGHT
AR AS			EY-909-300	ADHESIVE
8	40		NAS1351C04-4	SCREW
8	39		MS 35338-42	WASHER, LOCK
1	38		-25 OPP -27	SUPPORT
1	37		950933-1	CLAMP
4	36		950552-1	PLATE ASSY
1	35		950590-1	SEAL RETAINER ASSY
1	34		950528-2	MANIFOLD ASSY
1	33		950528-1	MANIFOLD ASSY
2	32		-33	PLATE .100 SHEET
1	31		-25	MANIFOLD ASSY MAKE FROM 950629-1
		SHOWN	-27	SUPPORT
			-29	FITTING MAKE FROM 950-6-12SH-SEL
2	29		-31	ELBOW .750 O.D. CRES WALL TUBING
2	28			
	27		950668-2	LEFT OUTER PANEL - FAIRING ASSY
	26		950664-1	RIGHT OUTER PANEL - FAIRING ASSY
	25		950664-6	LEFT INNER PANEL - FAIRING
	24		950664-5	RIGHT INNER PANEL - FAIRING
1	23		950660-1	DRUM ASSY, OUTER COWL
	22			
1	21		950668-2	MOUNT PLATE, OUTER COWL - LEFT
1	20		950663-1	MOUNT PLATE, OUTER COWL - RIGHT
	19		950661-2	LEG SIDE SEC. COWL ASSY - LEFT
	18		950662-1	INNER LEG COWL ASSY - LEFT
	17		950661-1	LEG SIDE SEC. COWL ASSY, RIGHT
	16		950662-2	INNER LEG COWL ASSY, RIGHT
	15		-23	OUTER COWL ASSY, BOTTOM SECTION
	14		-23 OPP - 21	OUTER COWL ASSY SIDE SECTION LEFT
	13		-21	OUTER COWL ASSY SIDE SECTION RIGHT
	12		-1900PP - 19	LEFT TOP HEADER .109 SHT
2	11		-19SHOWN	RIGHT TOP HEADER .109 SHT
2			-18OPP - 17	DIVIDER LEFT .125 ACRC STEEL
	10		-17SHOWN	DIVIDER RIGHT .125 ACRC STEEL
	9		-15	SPACER MAKE CRES CIL
2	8		-13OPP - 13	RIGHT LEG ASSY MATCHED MACHINED
	7		-13SHOWN	LEFT LEG ASSY MATCHED MACHINED
	6		-11	OUTER COWL ASSY, FAIRING INNER PANEL
	5		-9	OUTER COWL ASSY PAINTED OUTER PANEL
	4		-7	OUTER COWL WELD ASSY, MATCHED LEG
	3		-5	OUTER COWL ASSY, MATCHED
	2		-3	OUTER COWL ASSY, MACHINED
	1		-1	OUTER COWL ASSY, WELDED

NOTES UNLESS OTHERWISE SPECIFIED

COWL ASSY, OUTER, WELDED

J 70210 950571

950671

IS MAY BE PURCHASED FROM CRAWFORD FITTING CO (PARKER-LOK) 29500 SOLON RD., SOLON, OHIO

4 APPLY PER R S -13

13 PROOF PRESSURE TEST CIRCUIT "A" ONLY AT AMBIENT TEMPERATURE USING STRESSCOAT FOR ENGINEERING INTERPRETATION

12 RADIOGRAPHIC INSPECTION PER MIL-STD-453.

11 PRESSURE TEST PER 950671-1 HYDROSTATICALLY

H2O	COOLANT CIRCUIT	"A" 240-300 PSI
H2O	"	"B" 240-300 PSI
H2O	"	"C" 200-240 PSI
H2O	"	"D" 240-300 PSI

NOTE: 950728-1 GASKET, OUTER COWL & 950721-1 GASKET, MANIFOLD MAY BE USED TO PERFORM THE TEST

10 -1 ASSY IS FOR PURPOSES OF FINAL MACHINING & PROOF TEST ONLY. FOLLOWING ABOVE TEST -1 ASSY SHALL BE DISASSEMBLED AND PHYSICALLY IDENTIFIED AS:
950671-21 FOR OUTER COWL ASSY, SIDE SEC. RIGHT
950671-23 FOR OUTER COWL ASSY, SIDE SEC. LEFT
950671-25 FOR OUTER COWL ASSY, BOTTOM SEC.

9 80% TO 99% PENETRATION

8 MATCH DRILL MANIFOLD ASSY., ITEM 31, AS SHOWN

7 FLUORESCENT PENETRANT INSPECT PER MIL-I-6866, TYPE I OR TYPE II

6 CRES AISI 321

5 ALL DIMENSIONS ARE FINISHED DIMENSIONS OF (-1) ASSY. DETAIL PART DIMENSIONS WILL BE DETERMINED @ MFG

4 WELD PER AIRESEARCH SPEC MBS-42 (SPOT WELD)

3 MACHINED SURFACES 90

2 WELD PER AIRESEARCH SPEC MBS-35 (EB WELD)

1 WELD PER AIRESEARCH SPEC MBS-19

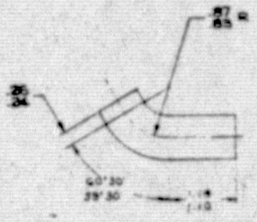

DETAIL ITEM 28

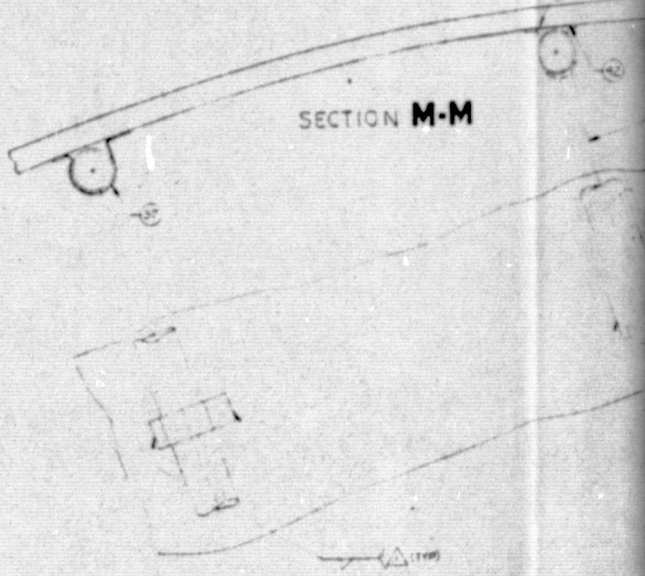

SECTION M-M

DETAIL ITEM 29
NUT & FERRULE OMITTED FOR CLARITY

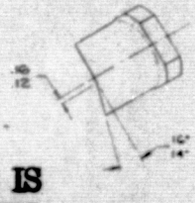

ORIGINAL PAGE IS
OF POOR QUALITY

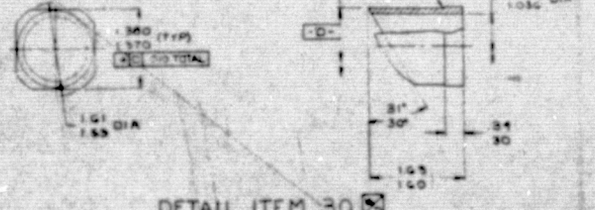

DETAIL ITEM 30
(ITEM 38 OPP.)

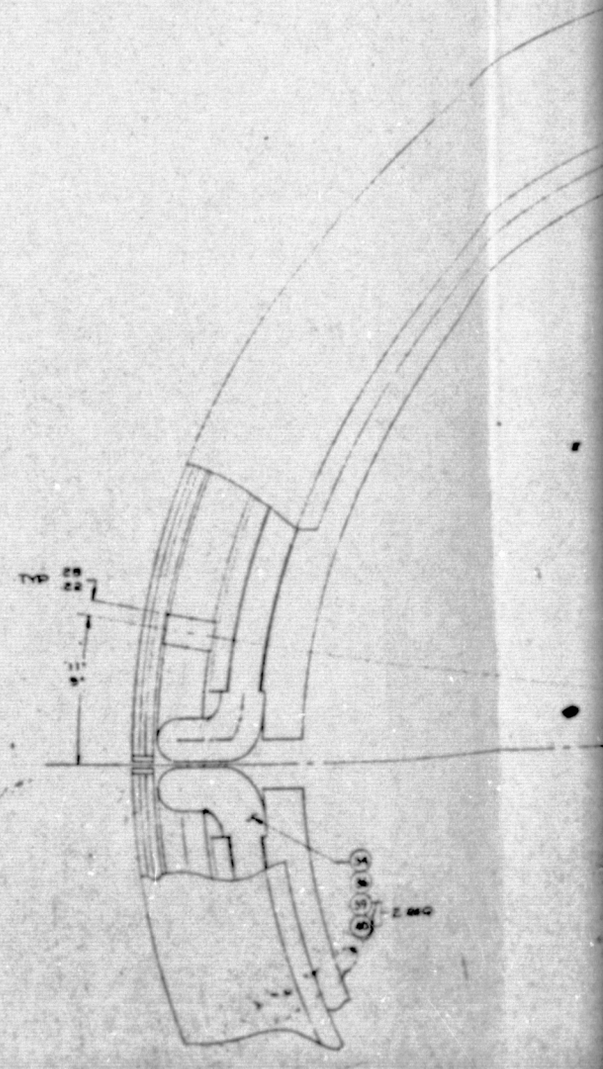

FOLDOUT FRAME

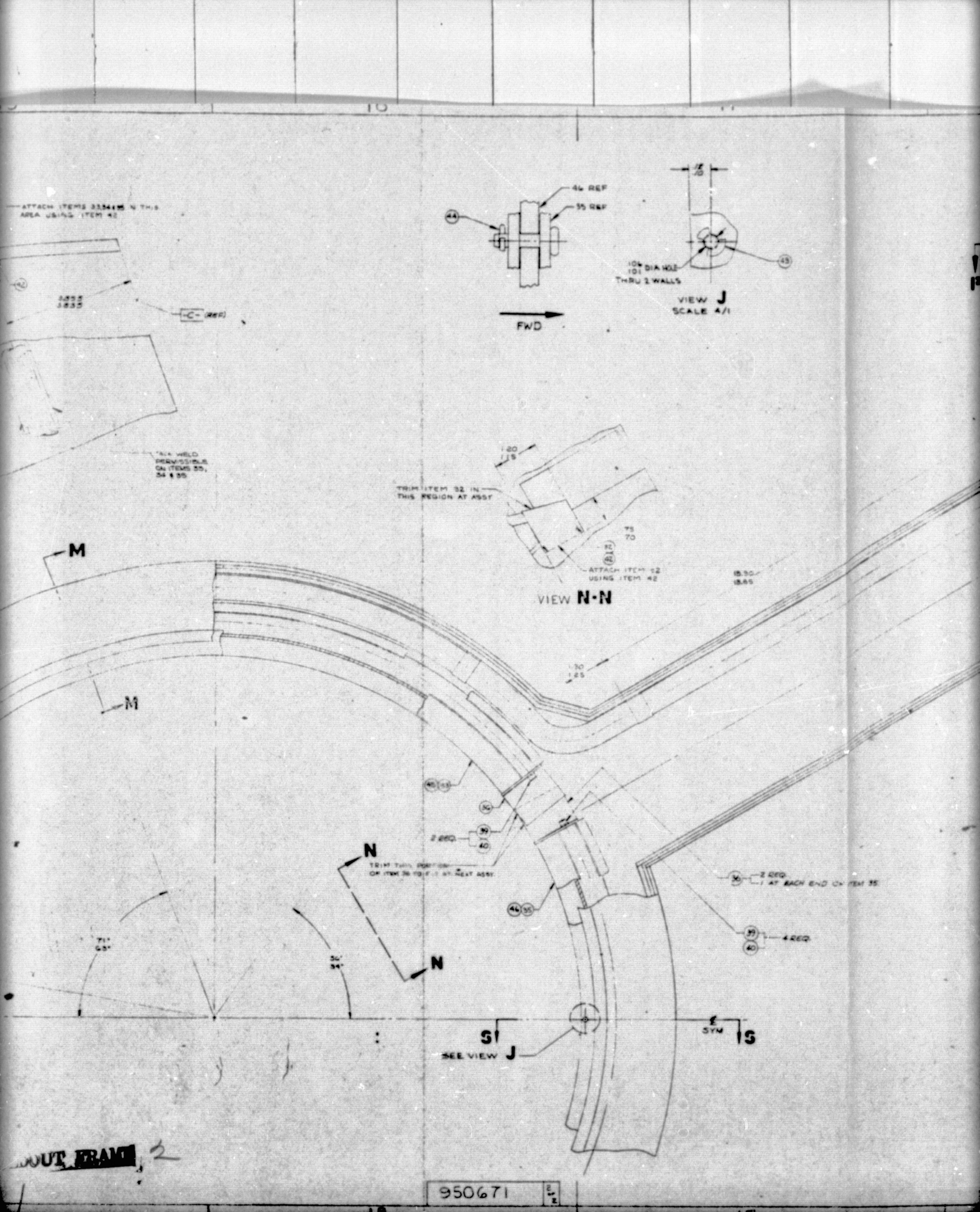

OUT FRAME 2

950671 2/2

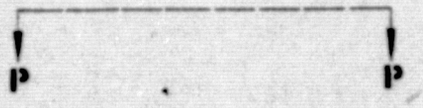

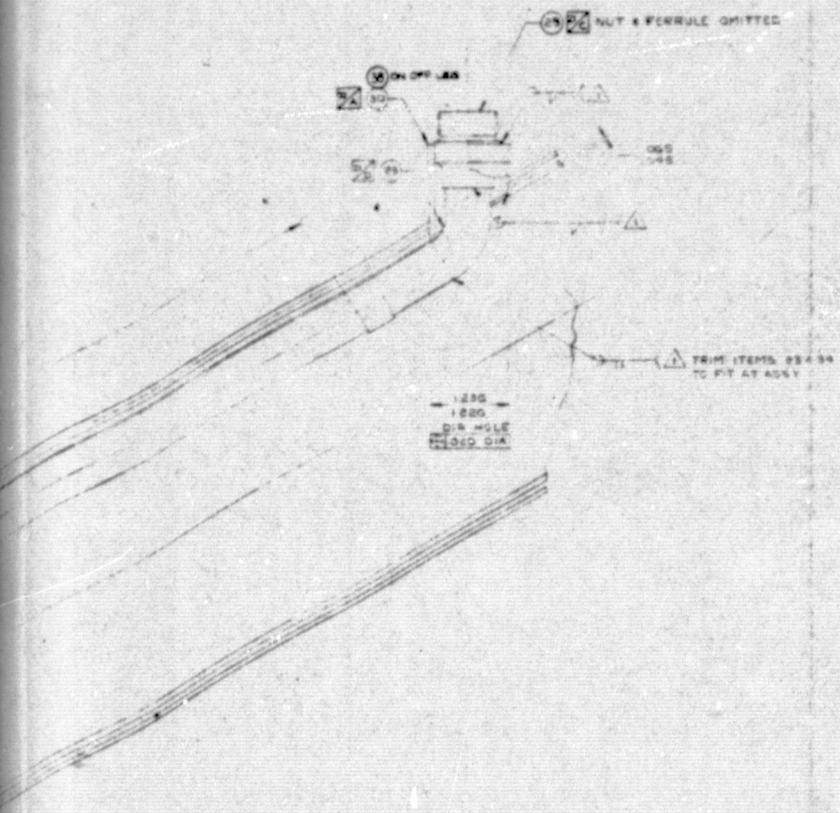

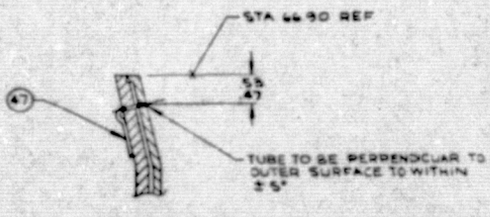

SECTION S-S
SCALE 1/1

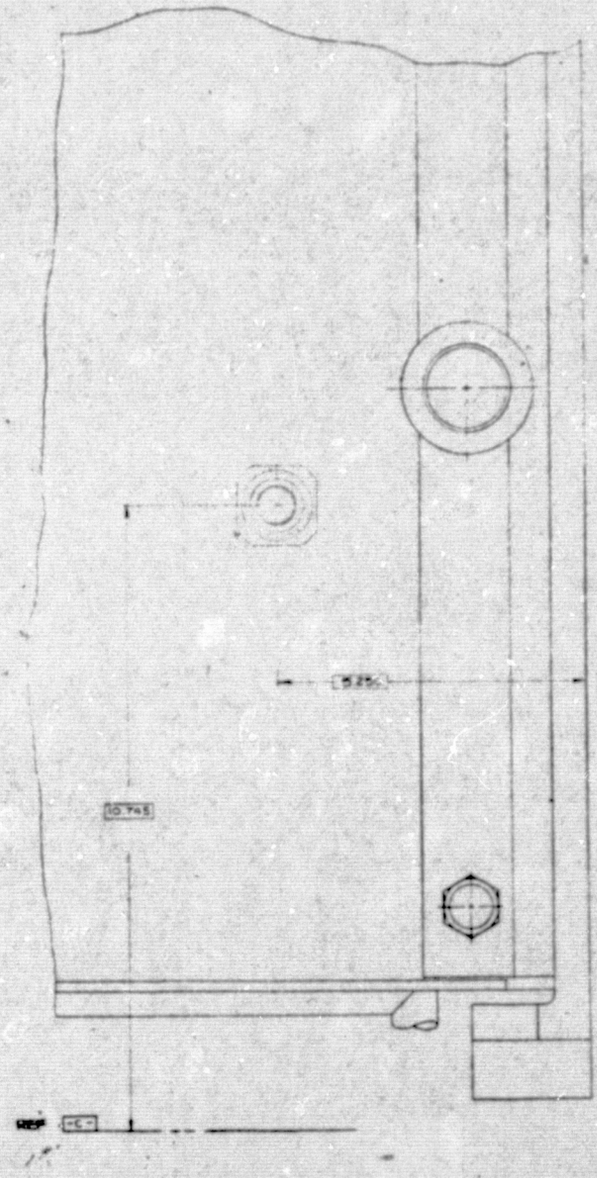

VIEW P-P

FOLDOUT FRAME 3

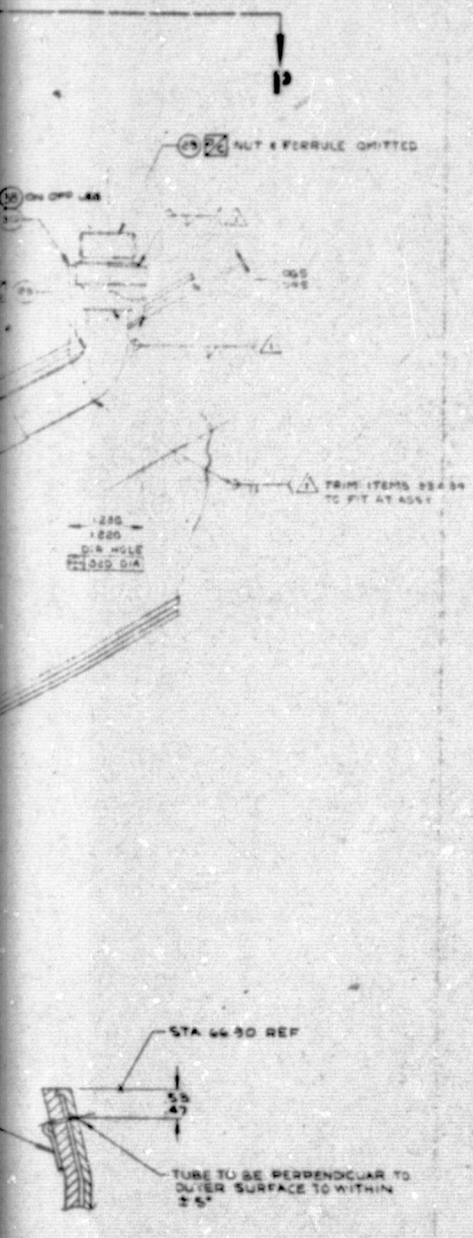

SECTION S-S
SCALE 1/1

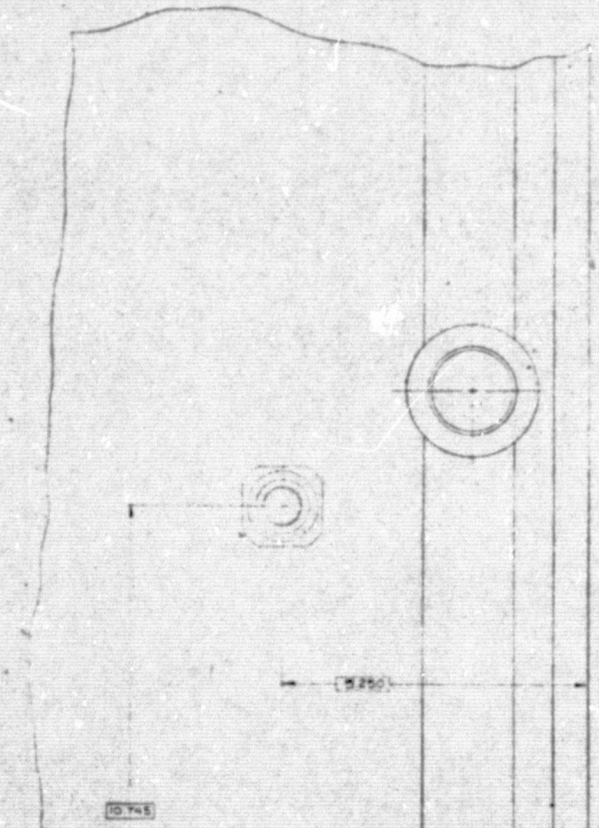

VIEW P-P

LTR	DESCRIPTION	DATE	APPROVED
NEW	ADDED SEAT S-S		
NEW	ADDED VIEW J		

* SEE SHEET 1 FOR CONTROLLING REVISION LETTER

FOLDOUT FRAME 4

3

J 70210 950671